Green Energy and Technology

Pedro Pérez-Higueras
Eduardo F. Fernández *Editors*

High Concentrator Photovoltaics

Fundamentals, Engineering and Power Plants

Springer

Green Energy and Technology

More information about this series at http://www.springer.com/series/8059

Pedro Pérez-Higueras · Eduardo F. Fernández
Editors

High Concentrator Photovoltaics

Fundamentals, Engineering and Power Plants

Springer

Editors
Pedro Pérez-Higueras
University of Jaén
Jaén
Spain

Eduardo F. Fernández
University of Santiago de Compostela
Santiago de Compostela
Spain

ISSN 1865-3529 ISSN 1865-3537 (electronic)
Green Energy and Technology
ISBN 978-3-319-15038-3 ISBN 978-3-319-15039-0 (eBook)
DOI 10.1007/978-3-319-15039-0

Library of Congress Control Number: 2015934682

Springer Cham Heidelberg New York Dordrecht London

Printed on acid-free paper

Springer International Publishing AG Switzerland is part of Springer Science+Business Media (www.springer.com)

Contents

Editors and Contributors

About the Editors

Dr. Pedro Pérez-Higueras is professor at the University of Jaén (Spain) and he researches since more than 20 years in the field of photovoltaic energy. In the last seven years, he has worked in High Concentrator Photovoltaics Technology and his research interest covers the developing, characterization and modelling of concentrator photovoltaic devices and optimal design of power plants. He has collaborated in more than 30 R&D projects with different companies and institutions and he has published more than 100 papers in the most prestigious peer-review journals and congresses related to solar energy.

Dr. Eduardo F. Fernández has worked around 10 years in the field of solar energy and Concentrator Photovoltaics. During this time he has been involved in research projects in prestigious research institutes, universities and private companies. His research interest covers the developing, characterization and modelling of concentrator photovoltaic devices and systems. He has been granted a project funded by the Spanish/Galician government and European Union for developing high concentrator photovoltaic modules based on new concepts and configurations between the optical elements and high efficiency solar cells. Recently, he has received the Juan de la Cierva fellowship, the most prestigious grant for young researchers of the Spanish government. He has published numerous papers in the most prestigious peer-review journals and congresses related to high concentrator photovoltaic technology.

Contributors

Carlos Adame-Sánchez University of Castilla-La Mancha, Castilla-La Mancha, Spain

Juan D. Aguilar-Peña University of Jaén, Jaén, Spain

Jorge Aguilera University of Jaen, Jaen, Spain

Florencia Almonacid IDEA Research Group, University of Jaén, Jaen, Spain

Juan de la Casa IDEA Research Group, University of Jaén, Jaén, Spain

Daniel Chemisana Applied Physics Section of the Environmental Science Department, Polytechnic School, University of Lleida, Lleida, Spain

A.B. Cueli CENER (Renewable Energy National Centre), Sarriguren, Spain

César Domínguez Instituto de Energía Solar, Universidad Politécnica de Madrid, Ciudad Universitaria, Madrid, Spain

J. Díaz CENER (Renewable Energy National Centre), Sarriguren, Spain

Eduardo F. Fernández University of Santiago de Compostela, Santiago de Compostela, Spain; IDEA Research Group, University of Jaén, Jaen, Spain

Francisco J. Gallego-Álvarez University of Jaén, Jaén, Spain

Pablo García-Linares CEA-LITEN, National Institute for Solar Energy (INES), Le Bourget-du-Lac, France

Antonio J. García-Loureiro University of Santiago de Compostela, Santiago de Compostela, Spain

Ivan González-Luchena University of Castilla-La Mancha, Castilla-La Mancha, Spain

Antonio González-Rodríguez University of Castilla-La Mancha, Castilla-La Mancha, Spain

L.A. Guerrero Panamericana University, Aguascalientes, Mexico

Christian A. Gueymard Solar Consulting Services, Colebrook, USA

S. Gutiérrez Panamericana University, Aguascalientes, Mexico

Joan E. Haysom SUNLAB Centre for Research in Photonics, University of Ottawa, Ottawa, Canada

Karin Hinzer SUNLAB Centre for Research in Photonics, University of Ottawa, Ottawa, Canada

Leocadio Hontoria-García University of Jaén, Jaén, Spain

Soteris A. Kalogirou Department of Mechanical Engineering and Materials Sciences and Engineering, Cyprus University of Technology, Limassol, Cyprus

Yong Sin Kim School of Electrical Engineering, Korea University, Seoul, South Korea

A.R. Lagunas CENER (Renewable Energy National Centre), Sarriguren, Spain

Tapas K. Mallick Environment and Sustainability Institute, University of Exeter, Penryn Campus, Penryn, Cornwall, UK

Adel Mellit Faculty of Sciences and Technology, Renewable Energy Laboratory, Jijel University, Jijel, Algeria

L. Micheli Environment and Sustainability Institute, University of Exeter, Penryn, Cornwall, UK

J. Moracho CENER (Renewable Energy National Centre), Sarriguren, Spain

Emilio Muñoz-Cerón Center for Advanced Studies in Energy and Environment, University of Jaén, Jaén, Spain; IDEA Research Group, University of Jaén, Jaén, Spain

Francisco J. Muñoz-Rodríguez IDEA Research Group, University of Jaén, Jaén, Spain

G. Nofuentes IDEA Research Group, University of Jaén, Jaén, Spain

I. Petrina CENER (Renewable Energy National Centre), Sarriguren, Spain

Pedro Pérez-Higueras IDEA Research Group, University of Jaén, Jaén, Spain

P. Rodrigo Panamericana University, Aguascalientes, Mexico

José A. Ruiz-Arias University of Malaga, Malaga, Spain

Catalina Rus-Casas University of Jaén, Jaén, Spain

Sundaram Senthilarasu Environment and Sustainability Institute, University of Exeter, Penryn Campus, Penryn, Cornwall, UK

Katie Shanks Environment and Sustainability Institute, University of Exeter, Penryn Campus, Penryn, Cornwall, UK

Greg P. Smestad Sol Ideas Technology Development, San José, California, USA

D.L. Talavera IDEA Research Group, University of Jaén, Jaén, Spain

Steve Tomosk Telfer School of Management, University of Ottawa, Ottawa, Canada

David Wright Telfer School of Management, University of Ottawa, Ottawa, Canada

Aggelos Zacharopoulos Centre for Sustainable Technologies, School of the Built Environment, Ulster University, Newtownabbey, Co. Antrim, UK

Introduction

Jorge Aguilera

Abstract Concentrating photovoltaics (CPV) is an alternative to flat-plate module to produce cost-competitive electricity. It is based on the use of an optical system of decreased cost that is able to concentrate solar light on a very small surface (high-efficiency solar cell). It has numerous benefits such as greater energy density, greater efficiency, and lower surface and lower semiconductor material requirements. Nevertheless, some technical and economic barriers must be removed to decrease the electricity production costs using this technology and to make it really cost-competitive. In the past years, researchers in CPV technology have experimented with important technological advances that are mainly focused on the increase the high-efficiency solar cells. Recently, a four-junction solar cell, with an efficiency of 44.7 % under 297 suns and the expectations to reach 50 % in next years, has been developed. Despite such technological advances, CPV technology has a marginal position in the photovoltaic market and must show, even still, a long-term reliability similar to the flat-plane PV module to improve its position in the market. Some arguments could explain this situation: the high competition of the flat-plane PV, the lack of CPV-module testing methods and standards, and the lack of trust of private sector investors. For CPV technology to gain momentum, it is necessary to continue economical and technical support of development and testing of pilot projects to show long-term reliability and achieve a better understanding of the CPV technology performance, which would result in greater confidence of the private sector.

1 Introduction

From the beginnings, CPV technology appeared like a real alternative to flat-plate modules to produce cost-competitive electricity to concentrate the solar light on a very small surface (high-efficiency solar cell). Its benefits are clear: greater energy

J. Aguilera (✉)
University of Jaen, Jaen, Spain
e-mail: aguilera@ujaen.es

P. Pérez-Higueras and E.F. Fernández (eds.), *High Concentrator Photovoltaics*,
Green Energy and Technology, DOI 10.1007/978-3-319-15039-0_1

density, greater efficiency, and lower surface and semiconductor areas. Comparing its position on the learning curve of flat-plate modules, CPV technology is further behind. Taking into account the continuous increase of solar cell efficiency, CPV technology shows an extremely high potential for a decrease in cost. Nevertheless, linked to these advantages there appear to be some technical barriers that must be eliminated to dramatically decrease electricity-production costs.

When light falls onto a monojunction solar cell, only photons with energy greater than the band gap energy are able to break covalent bonds to create electron-hole pairs, which are separated by the device structure and produce electrical current. This current can be used to power an electric circuit. Photons with lower energy cannot produce more electricity. Multijunction (MJ) solar cells try to eliminate such losses by having various subcells placed of different semiconductor material, and, thus they have a different band gap energy. The subcell placed on the top has the greater band gap energy, and the rest of the subcells are ordered by decreasing band gap. In this sense, spectrum solar range used to produce electricity is wider [1, 2] and the efficiency increases.

The efficiency of MJ solar cells increases with the number of cells that form the stack, but this increase is less each time the overall number of cells increases [3]. In practice, MJ solar cells are limited to five or six subcells, and, in fact, the best results are obtained with triple-junction monolithic solar cells.

Concerning the optical concentrator, it can be simple, or it can consist of primary and secondary optical devices. The primary optical device collects and concentrates direct normal irradiation (DNI), and the secondary optical device distributes light uniformly across the solar cell. The use of a secondary optical device allows an increase of the uniformity of the DNI, thus improving the performance of the system [4, 5]. Currently, research lines are focused to improve the design to decrease the nonuniformity on different subcells [6]. Different optical concentrators are currently being used (parabolic dishes, Fresnel lenses, linear parabolic reflectors, etc.), but most of the CPV systems use optical devices based on Fresnel lenses [7].

In the past years, researcher in CPV technology has experimented with important technological advances mainly focused on two research lines: (1) the increase of high-efficiency solar cells; and (2) the improvement of optical concentrators.

Concerning solar cells, Table 1 shows the evolution of efficiency records from previous years. A relative increase in efficiency, nearly 20 %, has been seen in only 10 years. It is worth mentioning that on 2013, the Sharp Company reached an efficiency of 44.4 % with a three-junction (InGaP/GaAs/InGaAs) solar cell under 302 suns, and Fraunhofer Institute reported an efficiency of 44.7 % with a four-junction (GaInP/GaAs/GaInAsP/GaInAs) solar cell under 297 suns. The efficiency of MJ solar cells not only is the highest in PV technologies, but also there is an expectation to obtain 50 % in following years [8, 9].

These results join together some intrinsic advantages of CPV technology—such as the decrease of solar cell material requirement for the same capacity, lowers balance-of-system costs (BOS), greater energy density, decreased land costs—all of which make this technology very attractive for massive electricity production.

Table 1 Evolution of the indoor efficiency record for 2003–2013

Date	Type of cell	Suns	Efficiency (%)
Q4 2003 [10]	GaInP/GaAs/Ge (2 terminals)—spectrolab	309×	36.9
Q4 2004 [11]	GaInP/GaAs/Ge (2 terminals)—spectrolab	175×	37.3
Q4 2005 [12]	GaInP/GaInAs/Ge (2 terminals)—spectrolab	236×	39.0
Q4 2006 [13]	GaInP/GaInAs/Ge (2 terminals)—spectrolab	179×	39.3
Q4 2007 [14]	GaInP/GaInAs/Ge (2 terminals)—spectrolab	240×	40.7
Q4 2008 [15]	GaInP/GaAs/GaInAs (2 terminals)—NREL	140×	40.8
Q4 2009 [16]	GaInP/GaInAs/Ge (2 terminals)—spectrolab	364×	41.6
Q4 2010 [17]	InGaAp/GaAs/InGaAs (2 terminals)—spire	406×	42.3
Q4 2011 [18]	GaInP/GaAs/GaInNAs (2 terminals)—solar junction	418×	43.5
Q4 2012 [19]	InGaAp/GaAs/InGaAs (monolithic)—sharp	306×	43.5
Q4 2013 [20]	InGaP/GaAs/InGaAs (monolithic)—sharp	302×	44.4
Q4 2013 [21]	GaInP/GaAs//GaInAsP/GaInAs—(Fraunhoffer institute)	297×	44.7

However, despite such technological advances, CPV technology must show, even still, a long-term reliability similar to that of the flat-plane PV module to consolidate a stronger market position.

In the present context—in which the price of conventional crystalline silicon PV modules has decreased sharply from €3.5/W to €0.5/W [22], which is linked to the absence of a small- to medium-size application market, which would in turn facilitate CPV technology to reach a maturity—it is complicated to think about CPV obtaining a solid position in terms of market penetration during the short term. In fact, CPV technology has marginal participation in the global PV market. According to the European Photovoltaic Industry Association (EPIA), the total PV power installed in 2012 was approximately 102 GW, of which only 100 MW can be attributed to CPV technology. These figures show a share participation of <0.1 % [23]. Despite very limited market share, it is worth mentioning that at the end of 2013, the total power of CPV technology was approximately 160 MW [24, 25], which represents a 60 % increase compared with the previous year. The following three arguments could be made for this situation.

Argument No. 1

The first argument is the low cost, the very well-known good reputation, and the highly reliable technology of the flat-plane PV. In fact, in the last 10 years, the market penetration of PV has increased greatly worldwide. Such technology has shown a high degree of maturity and has earned PCV the confidence not only of public institutions but also of private companies regarding its capacity to produce cost-competitive electricity.

Trying to obtain the present privileged position of flat-plane PV has not been easy, and it has required an enduring collaboration of many actors (governmental

bodies on both national and local levels, decision makers, private companies, electric utilities, national government organizations, etc.) that were able to launch a wide variety of promotional strategies and dissemination programmes worldwide. In fact, in past years, economies of scale have been a key factor in the sharply decreased the costs of flat-plane PV, and CPV must be able to follow a steeper learning curve [26]. So, for a relatively novelty technology such as CPV to compete in such scenario assumes the facing of manifold challenges.

The use of CPV has numerous benefits such as greater energy density, greater efficiency, and needs for lower surface and semiconductor material requirements, thus resulting in a decrease of the associated costs. Nevertheless, additional costs are needed due to use of optical devices, lenses, trackers, and operation and managements costs, etc. Therefore, it is necessary to remove some technical and economic barriers to decrease the electricity production costs using this technology and to make it truly competitive in the marketplace.

Argument No. 2

The second argument is the lack of CPV-module testing methods and standards [27, 28]. Many years ago, numerous domestic and international consensus standards (IEC 61215, IEC 60904, IEC 61853, etc.) were developed for the design qualification and type approval of terrestrial crystalline silicon for the rating of flat-plane photovoltaic modules under different meteorological conditions, etc. Therefore, based on the use of such testing methods and standards, it is possible to study and compare the performance of different module types and to accurately predict how much energy a PV module will deliver under real meteorological conditions during a specific period of time. This information has been used by government bodies, prospective owners, private companies, etc., to study by means of classical investment analysis in order to project the profitability of PV projects and to analyze the "bankability" of this technology. In general, all of the standards published and elaborated by the International Electrotechnical Commission and different International Organizations (National Renewable Energy Laboratory, ASTM International, Institute for Environmental Protection and Research, etc.) that are relevant for photovoltaics have been well accepted for the PV market. Ultimately, they have contributed to increase the confidence in PCV technology and to pave and make easier the development of PV. In CPV technology, the present situation is far from here, and it can be characterized by a lack of testing methods and standards for rating and studying the performance of CPV modules.

A short time ago, the International Electrotechnical Commission published the first part of IEC-62670 standard [29], which defines standard test conditions under which suppliers must measure the CPV system and deliver the main electrical parameters of CPV modules. The second and third part of this standard was not published until date [30]. Both parts will define the procedure to evaluate generated energy and determine the performance ratio of CPV plants. The lack of standards for CPV modules to analyze CPV modules performance under different meteorological conditions is one of the most important technological barrier, and it would be necessary to remove it as soon as possible to drive the sector to take off.

Argument No. 3
Finally, the third argument is the lack of trust of private sector investors in a relatively new technology that must show a long-term reliability. In this sense, it is necessary to develop a methodology that permits anlaysis of the bankability of CPV projects to decrease the risk of investing in them. Such a methodology would be based on the evaluation of the real performance of a CPV through on-site experimental campaigns [31, 32]. The conducting of experimental campaigns would allow development of a database to deeper analyze CPV performance and to forecast energy production over the long term. An accurate prediction of the energy production of a CPV plant would increase investors confidence in this technology. Table 2 shows some of the strengths, weaknesses, opportunities, and threats (SWOT diagram) to high-CPV technology [33, 34].

Forecasting the evolution of the market for a new technology is a complex issue mainly due to the lack of historical data and because of rapid advances that occur during the first stages of development. In addition, this evolution will be dependent on other factors such as the economic crisis, support programs implemented by several countries, etc. However, the increase forecasts for CPV technology are optimistic, and numerous technical reports have predicted a rapid increase of the global market share [35–37]. To achieve this goal, a crucial issue will be not only to continue the economical and technical support of development and testing of pilot projects but also to foster the installation of multi-MW PV plants. In this way, it will provide establishment of quality, safety, and reliability standards as well as a better understanding of CPV technology performance under real meteorological

Table 2 SWOT diagram for HCPV technology

Strengths	Weaknesses
• High efficiency • Modularity and scalability • Mature technology • Several pilot MW plants installed • Widely used materials (steel, glass, aluminum, plastics) • High-energy yield (kWh/kWp) for high-DNI locations • Low LCOE for high DNI locations • Smaller area per MW than flat plate	• Only suitable for locations with high DNI • Not suitable for building integration • Need for high-accuracy tracking • Higher cost per Wp • Low production and installed capacity • Long-term reliability not proven • Few years of field performance data • Lack of standardization of power rating or system acceptance criteria
Opportunities	**Threats**
• Market emergence of utility-scale projects • Specific political incentives • Perceived as a distinctive technology • Green/local job creation policies • More cost decrease potential than CSP plants • Lower maintenance cost than CSP plants	• Perceived technology risk • Decreasing costs of flat-plate • Perceived high cost • Bankability • Energy storage is easier in CSP plants

LCOE levelised cost of electricity; *CSP* concentrated solar power

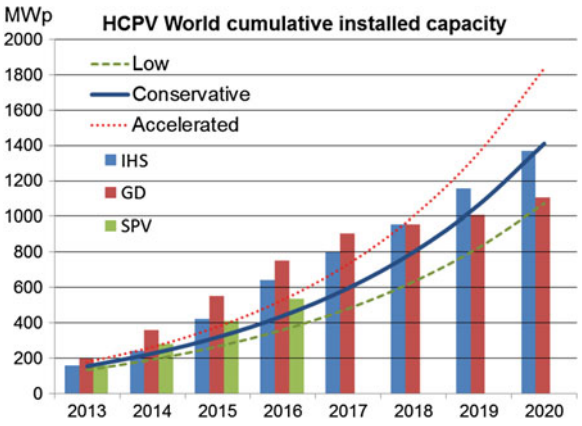

Fig. 1 Market forecast performed by three private companies: GD, and SPV. The forecast of HCPV world cumulative capacity is based on three scenarios: 1 a base case with annual growth of 30 % (*conservative*), 2 a pessimistic case with annual growth of 27 % (*low*), and 3 an optimistic case with annual growth of 33 % (*accelerated*) [39]. solar solution; *GD* Global data; *SPV* SPV market research

conditions. The undertaking of large projects, such as the installation of 44-MW CPV in South Africa or a 50-MW CPV in China, shows the path we must take to allow CPV technology to really gain share in the marketplace [38] (Fig. 1).

References

1. Meusel M, Adelhelm R, Dimroth F, Bett AW, Warta W (2002) Spectral mismatch correction and spectrometric characterization of monolithic III-V multijunction solar cells. Prog Photovoltaics Res Appl 10(4):243–255
2. Kinsey GS, Edmondson KM (2009) Spectral response and energy output of concentrator multijunction solar cells. Prog Photovolt Res Appl 17(5):279–288
3. Pérez-Higueras P, Muñoz E, Almonacid G, Vidal PG (2011) High concentrator photovoltaics efficiencies: present status and forecast. Renew Sustain Energy Rev 16:1810–1815
4. Ota Y, Nishioka K (2012) Three-dimensional simulating of concentrator photovoltaic modules using ray trace and equivalent circuit simulators. Solar Energy 86(1):476–481
5. Victoria M, Herrero R, Domínguez C, Antón I, Askins S, Sala G (2013) Characterization of the spatial distribution of irradiance and spectrum in concentrating photovoltaic systems and their effect on multi-junction solar cells. Prog Photovolt Res Appl 21(3):308–318
6. Mendes-Lopes J, Benítez P, Zamora P, Miñano C (2013) 9-Fold Fresnel Köhler concentrator for increased uniform irradiance on high Concentrations. AIP Conf Proc 1556:75
7. Zubi G, Bernal-Agustín JL, Fracastoro GV (2009) High concentration photovoltaic systems applying III-V cells. Renew Sustain Energy Rev 13(9):2645–2652
8. Law DC, King RR, Yoon H, Archer MJ, Boca A, Fetzer CM, Mesropian S, Isshiki T, Haddad M, Edmondson KM, Bhusari D, Yen J, Sherif RA, Atwater HA, Karam NH (2010) Future technology pathways of terrestrial III-V multijunction solar cells for concentrator photovoltaic systems. Solar Energy Mater Solar Cells 94(8):1314–1318

9. Luque A (2011) Will we exceed 50 % efficiency in photovoltaics? J Appl Phys 110(3):031301
10. Green MA, Emery K, King DL, Igari S, Warta W (2004) Solar cell efficiency tables (version 23). Prog Photovolt Res Appl 12(1):55–62
11. Green MA, Emery K, King DL, Igari S, Warta W (2005) Solar cell efficiency tables (version 25). Prog Photovolt Res Appl 13(1):49–54
12. Green MA, Emery K, King DL, Hisikawa Y, Warta W (2006) Solar cell efficiency tables (version 27). Prog Photovoltaics Res Appl 14(1):45–51
13. Green MA, Emery K, King DL, Hishikawa Y, Warta W (2007) Solar cell efficiency tables (version 29). Prog Photovolt Res Appl 15(1):35–40
14. Green MA, Emery K, Hishikawa Y, Warta W (2008) Solar cell efficiency tables (version 31). Prog Photovolt Res Appl 16(1):61–67
15. Green MA, Emery K, Hishikawa Y, Warta W (2009) Solar cell efficiency tables (version 33). Prog Photovolt Res Appl 17(1):85–94
16. Green MA, Emery K, Hishikawa Y, Warta W (2010) Solar cell efficiency tables (version 35). Prog Photovolt Res Appl 18(2):144–150
17. Green MA, Emery K, Hishikawa Y, Warta W (2011) Solar cell efficiency tables (version 37). Prog Photovolt Res Appl 19(1):84–92
18. Green MA, Emery K, Hishikawa Y, Warta W, Dunlop ED (2012) Solar cell efficiency tables (version 39). Prog Photovolt Res Appl 20(1):12–20
19. Green MA, Emery K, Hishikawa Y, Warta W, Dunlop ED (2013) Solar cell efficiency tables (version 41). Prog Photovolt Res Appl 21(1):1–11
20. Green MA, Emery K, Hishikawa Y, Warta W, Dunlop ED (2014) Solar cell efficiency tables (version 43). Prog Photovolt Res Appl 22(1):1–9
21. Dimroth F, Grave M, Beutel P, Fiedeler U, Karcher C, Tibbits TND, Oliva E, Siefer G, Schachtner M, Wekkeli A, Bett AW, Krause R, Piccin M, Blanc N, Drazek C, Guiot E, Ghyselen B, Salvetat T, Tauzin A, Signamarcheix T, Dobrich A, Hannappel T, Schwarzburg K (2014) Wafer bonded four-junction GaInP/GaAs//GaInAsP/GaInAs concentrator solar cells with 44.7 % efficiency. Prog Photovolt Res Appl 22(3):277–282
22. Energy Trend (http://www.energytrend.com)
23. Global Market Outlook for photovoltaic 2013–2017. EPIA
24. HIS Solar Solution (2013) Concentrated PV (CPV) report 2013—CPV on the edge of market breakthrough. USA
25. Mints P (2013) The current status of CPV 2013. PV-insider. UK
26. Merkle EW, Tölle R, Sturm M (2012) High-efficient low-cost photovoltaics: recent developments, the economic perspective is concentrator PV capable of breaking the economic barrier (Chap. 9). Springer, Berlin
27. Muller M, Kurtz S, Rodríguez J (2013) Procedural considerations for CPV outdoor power ratings per IEC 62670. AIP Conf Proc 1556:125
28. Muñoz E, Vidal PG, Nofuentes G, Hontoria L, Pérez-Higueras P, Terrados J, Almonacid G, Aguilera J (2010) CPV standardization: an overview. Renew Sustain Energy Rev 14(1):518–523
29. IEC 62670-1 Photovoltaic concentrators (CPV)—performance testing. Part 1: standard conditions. International Electrotechnical Commission (IEC), edition 1.0 2013-09. Geneva ISBN 978-2-8322-1120-5
30. Procedural considerations for CPV outdoor power ratings per IEC 62670
31. Gupta R (2013) CPV expansion and bankability required. Renew Energy Focus 14(4):12–13
32. Leloux J, Lorenzo E, García-Domingo B, Aguilera J, Gueymard CA (2014) A bankable method of assessing the performance of a CPV plant. Appl Energy 118:1–11
33. Dominguez C (2012) Optical and electrical characterization of high-concentration photovoltaic systems. Ph.d., E.T.S.I. Telecomunicación (UPM). http://oa.upm.es/10378/
34. Pérez Higueras P et al (2010) Propuesta para un Marco Regulatorio para la Concentración Fotovoltaica en España (2010–2020), ISBN: 978-84-692-9987-6. http://www10.ujaen.es/sites/default/files/users/ceaema/publicaciones/libros/Propuesta_de_un_marco_regulatorio_para_la_CPV.pdf

35. Prior B, Seshan C (2011) Concentrating photovoltaics 2011: technology, cost, and markets. GTM Res
36. The World Market for Concentrated PV (CPV)—2012. IMS Research, 2012
37. Concentrated Photovoltaic (CPV) (2013) 2012—global market size, average installation price, market share, regulations and key country analysis to 2020. GlobalData
38. PV insider http://news.pv-insider.com/concentrated-pv/bankability-not-easy-proposition-so-cpv-finds-novel-ways-March
39. Talavera DL et al (2015) Levelised cost of electricity in high concentrated photovoltaic grid connected systems: spatial analysis of Spain, Applied Energy 151, 49–59

Multijunction Concentrator Solar Cells: Analysis and Fundamentals

Eduardo F. Fernández, Antonio J. García-Loureiro and Greg P. Smestad

Abstract Multijunction (MJ) concentrator solar cells are primarily constructed of III-V semiconductor materials. The high solar-conversion efficiencies of these devices are dependent on precise control of growth conditions using one of several techniques such as molecular beam epitaxy, metal organic chemical vapour, or metal organic vapour-phase epitaxy deposition. The use of several junctions in an MJ tandem stack allows these devices to achieve efficiencies that are not possible for single-junction devices. Their behaviour is consequently complex, but it can be understood through an examination of the external quantum efficiency and the temperature dependence of each cell in the stack. This chapter lays out a systematic approach for understanding the spectral and temperature dependence of the overall MJ device by way of consideration of its component subcells. The efficiency of the cell as a function of temperature and concentration is described for both lattice-matched and metamorphic triple-junction (TJ) solar cells. The electrical characteristics and current–voltage curves are described from these considerations, and the performance of MJ solar cells under real operating conditions are then presented by considering a term describing the overall thermal factor and another term for the spectral factor. These terms can be understood from the background presented in the previous sections. Finally, the power output for the complete cell incorporated into a Fresnel lens based high-concentration photovoltaic system is presented for a particular geographic location using meteorological data.

1 Introduction

Multijunction (MJ) solar cells comprised of III-V materials are routinely used in space applications, for example, on satellites, unmanned space probes, planetary landers, and the International Space Station (ISS) [1, 2]. In contrast, when these

E.F. Fernández (✉) · A.J. García-Loureiro
University of Santiago de Compostela, Santiago de Compostela, Spain
e-mail: eduarferfer@gmail.com

G.P. Smestad
Sol Ideas Technology Development, San José, California, USA

P. Pérez-Higueras and E.F. Fernández (eds.), *High Concentrator Photovoltaics*,
Green Energy and Technology, DOI 10.1007/978-3-319-15039-0_2

solar cells are used for terrestrial applications, they are used together with concentrator optics so that the cell cost becomes a small fraction of the overall system cost. This creates several challenges to overcome that stem from the increase in the irradiance on, and temperature of, the cell [3–5]. The MJ solar cell approach offers significant advantages and disadvantages that can only be understood by analysing a given design's composition and performance from a fundamental perspective. This is the goal of this chapter.

An MJ solar cell is a quantum solar converter based on the use of two or more subsolar cells (subcells) comprised of semiconductor materials with different energy gaps (i.e., band-gaps, E_{gap}). It can take the form of a spectral splitting system [1, 4, 5] or stacked tandem junctions. Both approaches can be accomplished by using different stoichiometric semiconductor materials or by varying the composition of semiconductor alloys. An example of a stacked tandem device was first introduced in the late 1970s. It used two subcells each with a p–n junction: The bottom cell was based on gallium arsenide (GaAs) and the top cell (exposed to sunlight) was based on aluminium gallium arsenide. A different approach was later developed by the National Renewable Energy Laboratory based on an indium gallium phosphide (or InGaP alloy) junction on top of a GaAs middle junction grown on a germanium (Ge) substrate. This formed a triple-junction (TJ) tandem cell [1–5]. Further refinements replaced the GaAs with InGaAs alloys. The stacked-subcell approach has resulted in MJ cells of >40 % solar conversion efficiency [6–8]. Further work includes quantum well and quantum dot layers as well as inverted metamorphic (IMM) TJ solar cells [1, 9]. Combinations of GaAs and GaSb have also shown promise [5].

The basic idea in all such MJ cells is to improve the solar conversion efficiency, η, of the whole solar cell by optimizing the light absorption and photocurrent generation of each subcell for a narrow wavelength range. As shown in Table 1, a single-junction (SJ) solar cell, built with only one light-absorber material, has a maximum theoretical (thermodynamic) efficiency at a one-sun concentration of 30–34 % in sunlight. To improve on this efficiency, it is necessary to concentrate the sunlight on the cell and/or to interconnect several subcells. The efficiency limit increases to approximately 86.8 % for an infinite number of subcells at the maximum concentration ratio that can be achieved on Earth [10, 11].

Table 1 is for a cell temperature of 298 K. If the cell temperature increases beyond this, thermodynamics requires that the cell voltage decreases [12, 13]. An approximate relationship holds for the open circuit voltage, V_{oc}, at a given temperature, T, as follows:

$$\frac{d(qV_{oc})}{dT} = -\frac{E_{gap} - qV_{oc}}{T} \tag{1}$$

Here, q is the charge on an electron. In actual solar cells, this temperature dependence often leads to solar conversion efficiencies that are lower at greater cell temperatures. The temperature dependence of several key cell parameters will be the topic of subsequent chapters.

Table 1 The maximum solar conversion efficiency for tandem cells as a function of the number of subcells in the stack, n, for different concentration ratios, X [10, 11]

Concentration ratio (X)	No. of cells in the stack (n)	Maximum efficiency (η)
1	1	31.0
	2	42.9
	3	49.3
	…	–
	∞	68.2
100	1	35.2
	2	48.4
	3	55.6
	…	–
	∞	76.2
46,300	1	40.8
	2	55.7
	3	63.9
	…	–
	∞	86.8

The theoretical analysis assumes blackbody radiation for the sun, rather than the AM1.5 standard solar spectrum, but the general results (and the efficiency values) are quite similar if the actual solar spectrum is considered

Although the efficiencies obtained in actual cells are noteworthy and have improved over time, there exists a considerable gap between theoretical and experimental values. This is due to one or more loss mechanisms operating in solar cells. For example, not every photon that a subcell absorbs gives rise to an electron-hole pair that is collected at the electrical contacts. This is reflected by an external quantum efficiency (EQE) that is less than unity [1, 4, 6]. In addition, there are both optical losses, such as those from parasitic absorption by interconnection layers, and electrical losses, such as those caused by internal series and shunt resistance. In the section that follows, an overview of MJ concentrator solar cells is presented, and the precise growth conditions necessary to create MJ devices are outlined. Then an analysis of the whole MJ cell will be presented that allows one to characterize and understand the losses of a particular design. This leads to the ability to predict the performance of MJ cells under the actual conditions found under deployment in a high-concentrator photovoltaics (HCPV) system.

2 Overview of MJ Concentrator Solar Cells

The key to the success of modern III-V solar cells is based on the development of advanced growth technologies, mainly molecular beam epitaxy, metal organic chemical vapour deposition, metal organic vapour phase epitaxy and other similar techniques [14–17]. It is necessary to have high-accuracy epitaxial growth to obtain

a highly efficient MJ solar cell. This means that there is little difference between the lattice constants of adjacent layers. The growth techniques allow for unprecedented control on the atomic level of the semiconductor devices. This makes it possible to grow new materials, including pseudomorphic and alloy multiple compositions, for example, Si_xGe_{1-x}, $Al_xGa_{1-x}As$, or $In_xGa_{1-x}As$, where x is the mole fraction that specifies the composition of the alloy [18]. It is necessary to consider that the alloy components are distributed uniformly over the whole layer without any type of clustering. This is reasonable in the case of solar cells due to the dimension of the active region of these devices compared with the lattice constant.

A semiconductor material has many types of properties [19–22], but the most relevant considerations in the design of an efficient MJ solar cell are the energy gap and the lattice constant. The energy gap is equivalent to the energy that is necessary to free a bond electron in the crystal, thereby creating a hole in the valance band and an electron in the conduction band. In this case, it corresponds to the minimum energy of the photon to be absorbed for the semiconductor material. The lattice constant is the physical dimension of the unit cell in the crystal lattice of the semiconductor. The ideal situation should be that the different materials of multi-layer semiconductor devices have the same lattice constant, or at least as close as possible, to decrease the number of defects and thermal, mechanical, and electrical stresses. The results of such stresses are recombination centers within the band-gap that lead to efficiency losses. In most cases, it is not a trivial matter to grow a mechanically and electrically stable solar cell, and thus it is necessary to consider a critical thickness of the semiconductor layer that corresponds to the maximum thickness of the material necessary to avoid dislocations and similar defects that can act as recombination centres [23]. Figure 1 shows the energy gap versus lattice constant for several elements and alloy materials [24]. In the case of an alloy composition of three or more materials—as in $Al_xGa_{1-x}As$, $In_xGa_{1-x}P$, or $Ga_xIn_{1-x}As_yP_{1-y}$ with two molar fractions, x and y—the lattice constant and the energy band-gap of the resulting material is a complex function of the mole fraction.

An MJ solar cell with two, three, or more junctions is a set of the same number of p–n junctions made from different materials, stacked on the top of each other, including metallic contacts on the top and bottom of the solar cell [25–27]. The idea

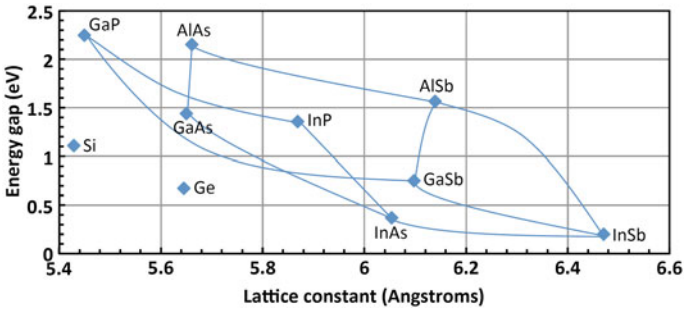

Fig. 1 Energy band-gap versus lattice constant for several semiconductors used in MJ HCPV cells

is to subdivide the incident solar spectrum into several parts to be absorbed for the different subsolar cells; each one has an optimized efficiency for a certain range of wavelengths in the spectrum of the incident sunlight. The goal is to find the best and most advantageous band-gap combination for each subsolar cell to convert the total incident solar light with the maximum possible efficiency. It is also necessary to take into account low-resistance metal contacts for obtaining a high-efficiency solar cell. There are several possibilities to connect the different p–n junctions, but one of the most efficient methods is to use a tunnel junction with very low resistance and very thin layers to decrease, as much as possible, the absorbed light in these layers [28]. In addition to all of the previously mentioned factors, one should not overlook the importance of the semiconductor materials and the thickness of the various subcells as part of the design. This is necessary to obtain the best current balance among all of the subcells. The ideal situation is when all of the subcells generate the same light-generated current under the relevant spectral conditions outdoors. However, there is inevitably a subcell of the MJ with the lowest current, which limits the total current of the MJ because the p–n junctions are connected in series [29]. The total device voltage is the sum of the voltage of each subcell minus the voltage of the tunnel junctions because they are in reverse bias. A typical structure of a TJ solar cell is depicted in Fig. 2. In this case, each subcell is based on several materials with different band-gaps. The p–n solar cell with the highest band-gap is located on the top of the MJ solar cell stack to absorb the highest-energy photons, and the other subcells are placed in decreasing order of the band-gap with the aim to capture photons with less energy (longer wavelengths). The plot shows the air mass (AM) 1.5 direct (AM1.5D, ASTM G-173-03) reference spectrum [30] with the dashed vertical lines indicating the band-gaps for the top [gallium indium

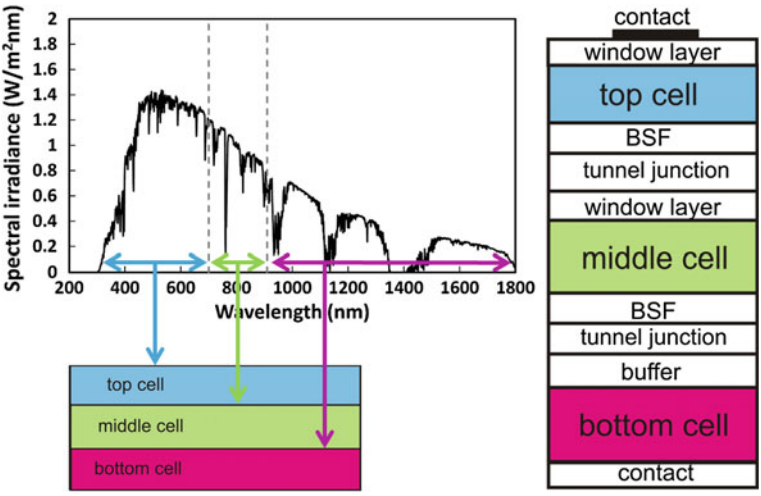

Fig. 2 Portions of the solar spectrum absorbed in a TJ solar cell (*left*) and a schematic of a typical monolithic TJ HCPV solar cell (*right*)

phosphide (GaInP; 1.88 eV)] and middle [gallium indium arsenide (GaInAs) (1.41 eV)] subcells. The bottom subcell in this example is Ge (0.67 eV). Absorption of the photons is determined by the energy gap of the semiconductor material alloy and its absorption coefficient [19]. The latter parameter indicates how far into material photons of a specific energy can penetrate before they are absorbed by the material. To improve the efficiency of the MJ solar cell, each one is designed to absorb only one part of the spectrum of sunlight (e.g., AM1.5D). Window layers should be included on the top subcells to decrease the surface recombination velocity, and a back surface field (BSF) layer should also be used to minimize scattering and loss of charge carriers at the tunnel junction [31]. It is necessary that both layers should be as transparent as possible so the photons can be absorbed in the active regions of the device. This is shown in Fig. 2 (right side).

One of the main problems of the MJ solar cell is related to the various lattice constants of the semiconductor alloy material of each layer and the need to grow an MJ solar cell when several materials with different lattice constants are necessary to obtain the highest overall device efficiency. If the materials of the separate p–n junctions have the same lattice constant, then it is easier to grow the MJ solar cell. In this approach, the cells are called lattice-matched (LM) cells. [32]. The main disadvantage of this strategy is that the materials with different band-gaps selected for the subcells should have the same, or a very close, lattice constant. This constraint decreases maximum efficiency because it is not possible to select the best materials for each subcell in terms of band-gap. One approach to increase the number of possible semiconductor materials that can be selected is to use materials with different lattice constants but with thin layers to decrease the stress in the structure. These solar cells are called metamorphic-mismatched (MM) cells. This option increases the list of possible materials that can be used, but it still limits the flexibility to select the best materials for the subcells. This problem is critical when four or more different materials with several lattice constants are necessary to create an MJ solar cell [33].

There is another device structure called inverted-metamorphic (IMM) [34–36]. In this case, the MJ solar cell is grown in an inverted order on a suitable substrate starting with the top subcell. Later, the original growth substrate is removed, and the front metallic contact is deposited on the top layer [37]. In addition, more flexible techniques exist that use materials with different lattice constants. For example, it is possible to mechanically stack cells to connect several separate subcells or use fabrication by way of wafer bonding [38–40]. This last method combines semiconductor materials with different lattice constants by forming semiconductor bonds at the common interface layer. Each subcell, or group of subcells, are grown on different substrates and then joined together. Afterward, the substrate of the top cell is removed. For this process to succeed, it is necessary to have high-quality, low-roughness surfaces. A good example of this technique is a four-junction device comprised of GaInP/GaAs//gallium indium arsenide phosphide (GaInAsP)/GaInAs, which has an efficiency of approximately 45 % [41].

In the case of the application of the device in an HCPV system, optimization of the front metal grid pattern is essential for a specific irradiance level and solar concentration (i.e., 500× to 1000×). The main objective is to maximize light absorption and decrease, as much as possible, the ohmic and shadow losses generated for the metal grid [31]. The design and analysis of MJ solar cells begins with this criterion and by considering their behaviour versus the input solar spectrum, temperature, and electrical properties.

3 Analysis of the Behaviour of MJ Solar Cells

The behaviour of MJ solar cells is inherently different than that of conventional SJ solar cells. The internal series connection of several junctions with different band-gaps makes these devices more sensitive to incident spectral irradiance. In addition, the electrical parameters and temperature dependencies are significantly influenced by the irradiance level. In this section, the basic aspects for understanding the performance of MJ solar cells under different operating regimes are presented.

3.1 EQE

The external quantum efficiency (EQE) offers valuable information for understanding the performance of a solar cell. The EQE, as a function of wavelength, represents the ratio of the number of electrons collected at the external contacts of the cell to the number of incident photons as follows:

$$\mathrm{EQE}\,(\lambda) = \frac{\text{number of electrons}}{\text{number of photons}\,(\lambda)} \tag{2}$$

The wavelength interval for measurements of EQE (λ) typically ranges from 1 to 10 nm. EQE can be related to the spectral response (SR). The SR represents the amperes generated per watt of incident light of a given wavelength and can be expressed as follows:

$$\mathrm{SR}\,(\lambda) = \frac{q\lambda}{hc}\mathrm{EQE}\,(\lambda) \tag{3}$$

where q is the electric charge, λ is the wavelength, h is Planck's constant, and c is the speed of light. Given this relationship, the short-current density (J_{sc}) of a cell for a particular spectral distribution $E(\lambda)$ can be estimated as follows:

$$J_{sc} = \int \mathrm{SR}(\lambda)E(\lambda)\mathrm{d}\lambda \tag{4}$$

The J_{sc} is measured at the point at the I-V curve where $V = 0$ and is typically expressed in mA/cm^2. The standard (or reference) spectral distribution for AM1.5D is shown in Fig. 2. However, as will be described in a subsequent chapter, the actual spectral distribution under the operating conditions found for an MJ cell used in a deployed (real-world) HCPV system is a function of the location of the system as well as the time of year and time of day.

As discussed previously, to improve the conversion efficiency, MJ solar cells are based on several junctions interconnected in series in which each subcell responds to a particular band of the spectrum. Because of this, the short-current density of an MJ solar cell is the subcell with the lowest current. This is usually expressed as follows:

$$J_{sc} = \min\left(\int \mathrm{SR}_i(\lambda)E(\lambda)\mathrm{d}\lambda\right) \tag{5}$$

where the index i represents the junction, or subcell, considered in the MJ solar cell.

Figure 3 shows the EQE, at 25 and 75 °C, of an LM GaInP/GaInAs/Ge solar cell as an example of the number of photons collected in each spectral band of a typical MJ solar cell. This plot shows the EQE's variation with temperature. As can be seen, the absorption range is mainly determined by the band-gap. Because of this, the key to understanding the variations of EQE with temperature is by considering the change of the band-gap energy (E_{gap}) versus temperature. This variation can be explained with the Varshni relation as shown [42]:

$$E_{gap}(T) = E_{gap}(0) - \frac{\alpha T^2}{T + \beta} \tag{6}$$

where $E_{gap}(0)$ is the band-gap energy at 0 K, and α and β are material constants. The Eq. (6) shows that the energy gap decreases as the temperature increases. Hence, as the device temperature increases, the MJ solar cell is able to absorb photons with lower energy. This explains the shift in EQE for the top, middle and bottom junctions at longer wavelengths as shown in Fig. 3. In addition, a loss in EQE for the middle and bottom junctions at shorter wavelengths is also observed. This can be mainly explained due to the gain in EQE at longer wavelengths by the junction directly above. This effect is also observed to a lesser degree in the EQE of the top junction, probably due to the decrease with temperature of the band-gap energy of the window layer of the MJ solar cell [43, 44].

The effect of temperature on the EQE described previously clearly suggests that the influence of temperature on the electrical parameters of an MJ solar cell is more complex than in an SJ device. The J_{sc} of the current-limiting junction increases with temperature due to the decrease of its energy gap. However, this increase is lessened by the effect of the junction immediately above because the current of this

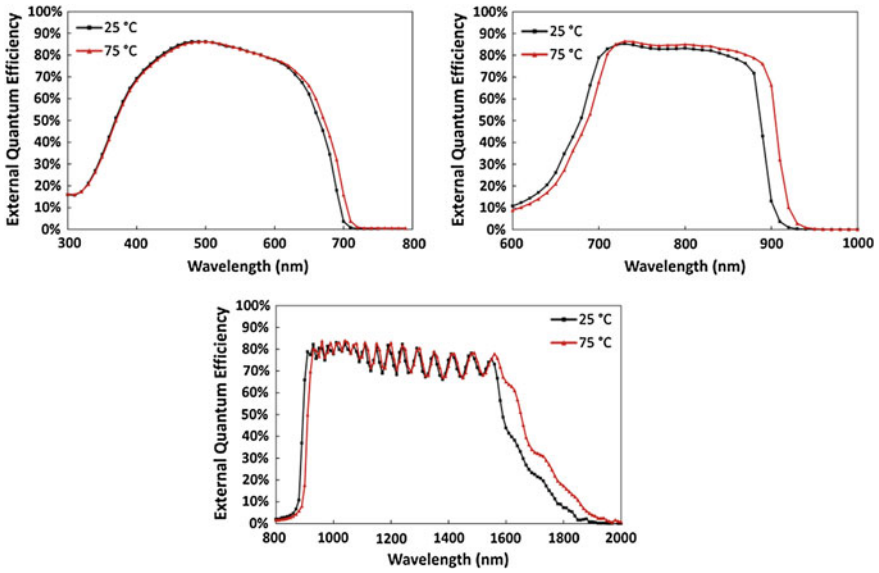

Fig. 3 Experimental EQE of the top junction (*top left*), middle junction (*top right*), and bottom junction (*bottom*) of an LM GaInP/GaInAs/Ge TJ solar cell at 25 and 75 °C [48, 49]. The oscillations in the external quantum efficiency for the Ge subcell are due to optical interference effects from the many thin layers above it [50, 51]

junction is also increased with temperature. Bearing this in mind, the temperature coefficient of an MJ solar cell (dJ_{sc}/dT) can be expressed as follows [45]:

$$\frac{dJ_{sc}}{dT} = \frac{dJ_{sc,i}}{dT} - \frac{dJ_{sc,i-1}}{dT} \tag{7}$$

where ($dJ_{sc,i}/dT$) and ($dJ_{sc,i-1}/dT$) are the temperature coefficient of the limiting-junction and the temperature coefficient of the junction above, respectively. This phenomenon implies that (dJ_{sc}/dT) depends on the incident spectrum and that the temperature coefficient of the whole MJ cell could not be always positive. At the same time, the I-V characteristics of an MJ solar cell are strongly affected by the current balance among the junctions. Hence, the influence of temperature on the rest of the electrical parameters is also expected to be affected by the incident spectral distribution and the limiting junction [46, 47].

3.2 *Influence of the Input Spectrum*

It is well known that MJ solar cells have a larger spectral dependence than SJ solar cells because of the series connection of several subcells with different energy gaps

[52]. This is shown graphically in Fig. 2. Taking this into account, the temperature dependence of the electric parameters of an MJ solar cell are also expected to be influenced by the incident spectrum as was previously commented on. To clarify this issue, Fig. 4 shows the main electrical parameters of an LM GaInP/GaInAs/Ge solar cell under illumination by different spectra at 25 and 75 °C. The spectra are expressed through the spectral matching ratio (SMR) index for the top and middle subcells as shown [53]:

$$SMR(top/middle) = \frac{J_{L,top}}{J_{L,top}^{1.5D}} / \frac{J_{L,middle}}{J_{L,middle}^{1.5D}} \tag{8}$$

where $J_{L,top}$ and $J_{L,middle}$ are the photo current densities of the top and middle junctions, respectively. Figure 4 (top left) shows J_{sc} versus SMR for the two temperatures. A maximum at SMR = 1 can be seen. This maximum represents the spectral condition where the top and middle subcells generate the same current (current-matched condition). Around this point, J_{sc} decreases due to the current limitation in one of the subcells. On the left side of the maximum, the current of the middle subcell is increased, whereas the current of the top subcell is decreased. This corresponds to red-rich spectra, and the top subcell is limiting the current (SMR < 1). On the right side of the maximum, the current of the top subcell is increased, whereas the current of the middle subcell is decreased. Hence, these

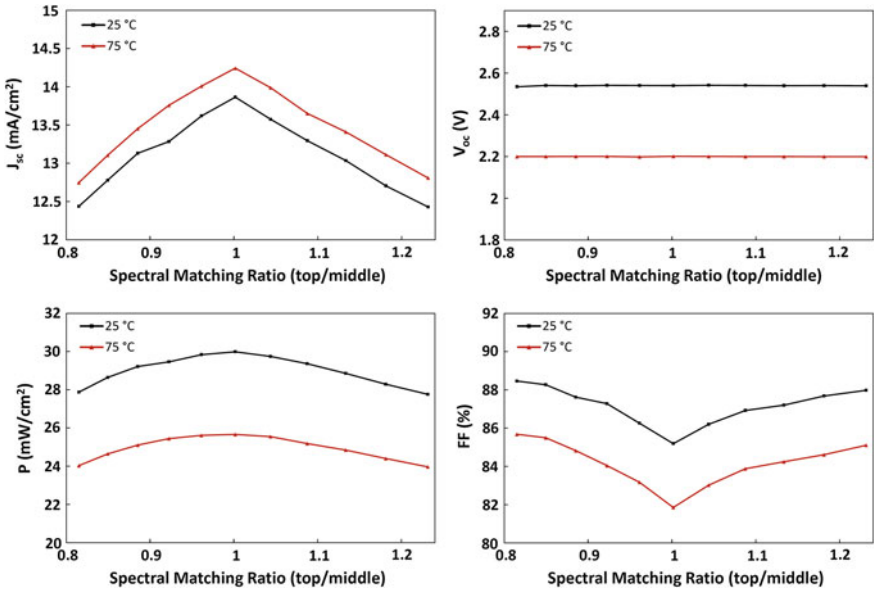

Fig. 4 Experimental short-circuit current density (J_{sc}), open-circuit voltage (V_{oc}), P, and FF versus SMR for the top and middle subcells at 25 and 75 °C of an LM GaInP/GaInAs/Ge solar cell. SMR = 1 corresponds to AM1.5D, ASTM G173-03, 1000 W/m^2 where the three subcells generate the same current as under reference conditions [55, 56]

spectral conditions are more blue-rich, and the middle subcell is limiting the current (SMR > 1). Related to temperature, the cell shows an increase in current with temperature more or less independent of the SMR. The open-circuit voltage (V_{oc}) versus SMR for the two temperatures is shown in Fig. 4 (top right). As can be seen, no significant dependence on incident spectrum is found. In addition, the cell shows a decrease in open-circuit voltage with a temperature independent of the SMR. Figure 4 (bottom left) shows the maximum power density (P) versus SMR for the two temperatures. P shows a similar behaviour to J_{sc} under spectral changes. A maximum in P at SMR = 1 can be observed. In addition, around the maximum, P decreases due to the current limitation by one of the subcells. Regarding temperature, the cell again shows a decrease in temperature more or less independent of the spectral changes. The fill factor (FF) versus SMR for the two temperatures is given in Fig. 4 (bottom right). In this case, FF shows the opposite behaviour compared with J_{sc} and P under spectral changes but with less variation. There is a minimum at SMR = 1, and the FF increases around it. As for the previous parameter, the cell shows a decrease in temperature more or less independent of the spectral changes. The different behaviour of the FF under spectral changes can be explained by analysing the relationship between FF and the rest of the electrical parameters as follows:

$$\mathrm{FF} = \frac{P}{J_{sc} V_{oc}} \tag{9}$$

V_{oc} can be considered independent of incident spectrum as a first approximation. At the same time, J_{sc} shows a larger spectral influence than P. Hence, the FF grows when J_{sc} decreases because P decreases to a lesser extent under spectral changes. This behaviour exhibited by the FF under spectral variations can be used as a tool to evaluate the current-matching among the subcells of an MJ solar cell under operating conditions [54].

As presented, the electrical parameters of an MJ solar cell are strongly influenced by the spectral distribution. However, the temperature dependences of MJ solar cell parameters can be considered independent of spectrum with a low margin of error [49, 55, 57].

3.3 *Influence of Optical Concentration*

MJ solar cells show an important spectral dependence as was previously commented on. In addition to this, the I-V parameters of MJ concentrator solar cells are also affected by the illumination level. Furthermore, the temperature coefficients of the electrical parameters are also affected by the optical concentration under operating conditions [58].

Under uniform irradiance, the short-circuit current can be considered linear with respect to the concentration and is usually expressed as:

$$I_{sc} = X \cdot I_{sc,1\ sun} \tag{10}$$

where X is the concentration factor or effective concentration, and $I_{sc,1sun}$ is the short-circuit current at one sun (1000 W/m^2). The concentration factor is sometimes called the "concentration ratio" and is given the symbol "C" in some texts. Accordingly, the absolute temperature coefficient of I_{sc} can be expressed as a function of concentration as follows:

$$\frac{dI_{sc}}{dT} = X \frac{dI_{sc,1\ sun}}{dT} \tag{11}$$

The rest of the electrical parameters and temperature coefficients show a more complex relationship versus concentration. To clarify this point, Fig. 5 shows the main electrical parameters of an LM GaInP/GaInAs/Ge solar cell under different concentration levels at 25 and 65 °C.

Figure 5 (top) shows V_{oc} versus concentration for the two temperatures. As can be seen, V_{oc} grows with a logarithmic dependence as the concentration increases. For subcells connected in series, this dependence can be expressed as [57]:

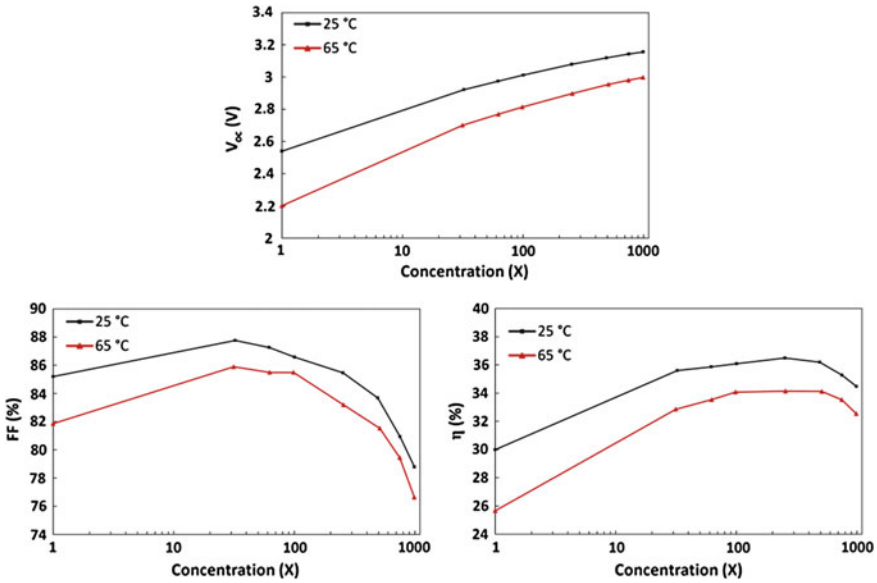

Fig. 5 Experimental open-circuit voltage (V_{oc}), FF, and efficiency (η) versus concentration (X) at 25 and 65 °C of an LM GaInP/GaInAs/Ge solar cell [61, 62]. The front metal grid of the cell is optimized for operating at concentrations between 250× and 500×

$$V_{oc} = \sum_{i=1}^{n} V_{oc,i,1\ sun} + \frac{kT}{q}\sum_{i=1}^{n} m_i \ln(X) = V_{oc,1\ sun} + \frac{mkT}{q}\ln(X) \tag{12}$$

where n is the number of subcells in series, $V_{oc,1sun}$ is the open-circuit voltage at one sun, m is the diode ideality factor, k is Boltzmann's constant, and q is the electric charge. As is also shown in Fig. 5 (top), the temperature dependence of V_{oc} decreases with concentration. This can be explained by writing Eq. (11) as follows:

$$\frac{dV_{oc}}{dT} = \frac{dV_{oc,1\ sun}}{dT} + \frac{mk}{q}\ln(X) \tag{13}$$

The first term on the right, which is the temperature coefficient at one sun, is negative. The second term on the right is positive and increases with concentration such that the temperature coefficient of V_{oc} decreases in absolute value versus concentration. It is important to note that to know V_{oc} and dV_{oc}/dT at a particular concentration ratio from their values at one sun, the value of the ideality factor should be known. Reported ideality factors for TJ solar cells are usually in the range 3–4 for concentration levels from 1× to 1000× [58]. The ideality factor is influenced by the recombination mechanism and the concentration ratio (which determines the injection level) [59]. The dominant recombination mechanism for an MJ solar cell has been shown to be different at low and high irradiance levels. The trend is toward the radiative limit (m = 1 for each subcell) as concentration increases [57, 60]. Because of this, it is necessary to perform an analysis of m as a function of concentration [$m = m(X)$] to accurately predict V_{oc} and dV_{oc}/dT. This behaviour can be seen in the change and decrease of the slope of V_{oc} as a function of $\ln(X)$ shown in Fig. 5 (top).

Figure 5 (bottom left) shows the FF versus concentration for the two temperatures. As can be seen, the FF increases with concentration ≤30×. Above this point, the FF decreases gradually due to series resistance losses. As in the previous case, the temperature dependence of FF decreases with concentration. This can be explained by writing the temperature coefficient of the FF as [45]:

$$\frac{dFF}{dT} = \frac{\ln\left(V_{oc,1,\ sun}\frac{qT}{mkT} + \ln(X) + 1\right)\left(\frac{dV_{oc,1\ sun}}{dT}\frac{q}{mkT} - V_{oc,1\ sun}\frac{q}{mkT^2}\right)}{\left(V_{oc,1\ sun}\frac{q}{mkT} + \ln(X) + 1\right)^2} \tag{14}$$

This equation expresses the variation of the temperature coefficient for FF with concentration assuming a negligible series resistance. As shown, the numerator is negative and grows in absolute value with concentration. However, the denominator increases to a larger extent with concentration. As a result, dFF/dT decreases in absolute value with concentration, and this explains the behaviour described previously.

Figure 5 (bottom right) shows the efficiency (η) versus concentration for the two temperatures. As can be seen, η increases with concentration until >250×. This

increase is dominated by the logarithmic increase of V_{oc} with the intensity of the light. However, as the concentration increases, this effect is counterbalanced by the decrease of the FF due to series resistance losses. As a result, the efficiency is decreased above a certain concentration level. As in the previous cases, the temperature dependence of η is decreased with concentration. This can be explained by writing the temperature coefficient of η as shown [61]:

$$\frac{1}{\eta}\frac{d\eta}{dT} = \frac{1}{V_{oc}}\frac{dV_{oc}}{dT} + \frac{1}{FF}\frac{dFF}{dT} + \frac{1}{I_{sc}}\frac{dI_{sc}}{dT} \tag{15}$$

The temperature coefficients of V_{oc} and FF decrease with concentration, whereas the temperature coefficient of I_{sc} is kept constant. Furthermore, in Eq. (15), the dominant term is the temperature coefficient of V_{oc}. Hence, the temperature coefficient of η should decrease with concentration and will be mainly given by the temperature coefficient of V_{oc} as follows:

$$\frac{1}{\eta}\frac{d\eta}{dT} \approx \frac{1}{V_{oc}}\frac{dV_{oc}}{dT} \tag{16}$$

It is important to note that this approximation may not be valid at increased concentration levels due to the strong decrease of dV_{oc}/dT as discussed in the literature [45]. However, experimental results show that the temperature coefficient of η can be approximated using Eq. (16) with a low margin of error until concentration levels reach even the extreme values of 10,000× [60].

Table 2 shows an example of the relative temperature coefficients of η and V_{oc} of an LM and MM TJ solar cell at different concentration levels. As was discussed, the temperature coefficients of V_{oc} and η are similar and decrease with concentration for both types of MJ solar cells. In addition, the MM solar cell shows a slightly greater temperature dependence than the LM solar cell.

Table 2 Experimental temperature coefficients of η and V_{oc} of an LM and an MM GaInP/GaInAs/Ge TJ solar cell at different concentration levels [61]

	LM		MM	
X	$1/\eta\ d\eta/dT$ (%/K)	$1/Voc\ dVoc/dT$ (%/K)	$1/\eta\ d\eta/dT$ (%/K)	$1/Voc\ dVoc/dT$ (%/K)
1	−0.257	−0.241	−0.305	−0.272
100	−0.134	−0.160	−0.188	−0.184
250	−0.132	−0.143	−0.179	−0.172
500	−0.129	−0.129	−0.172	−0.162
750	−0.117	−0.126	−0.163	−0.151
1000	−0.109	−0.122	−0.157	−0.147

4 Equivalent Circuit Models of MJ Solar Cells

An MJ solar cell can be considered as several series connected p–n junctions. Each junction can be represented by an equivalent circuit model. The most frequently used models are the single exponential model (SEM) and the double exponential model (DEM) [59]. Figure 6 shows an example of the equivalent circuits of a TJ solar cell by connecting the three subcells circuits in series.

Taking into account the SEM model, the current density of each subcell can be mathematically expressed as follows:

$$J = J_{\mathrm{sc},i} - J_{0,i}\left(\exp^{\frac{(V_i + JR_{\mathrm{s},i})}{m_i V_\mathrm{T}}} - 1\right) - \frac{V_i + JR_{\mathrm{s},i}}{R_{\mathrm{p},i}} \tag{17}$$

where each i subcell is characterized by a set of five parameters: the short-current density ($J_{\mathrm{sc},i}$), the diode-saturation current density ($J_{0,i}$), the diode ideality factor (m_i), the series resistance ($R_{\mathrm{s},i}$), and the shunt (or parallel) resistance ($R_{\mathrm{p},i}$). V_T is the semiconductor thermal voltage given by $V_\mathrm{T} = kT/q$.

Equation (17) combines the different recombination mechanisms into one diode term that takes place in an MJ solar cell. Bearing this in mind, the current density of each subcell can be more accurately expressed by the DEM model as shown:

$$J = J_{\mathrm{sc},i} - J_{01,i}\left(\exp^{\frac{(V_i + JR_{\mathrm{s},i})}{m_{1,i} V_\mathrm{T}}} - 1\right) - J_{02,i}\left(\exp^{\frac{(V_i + JR_{\mathrm{s},i})}{m_{2,i} V_\mathrm{T}}} - 1\right) - \frac{V_i + JR_{\mathrm{s},i}}{R_{\mathrm{p},i}} \tag{18}$$

where each i subcell is characterized by a set of seven parameters: the short-current density ($J_{\mathrm{sc},i}$), the diode-saturation current densities ($J_{01,i}$, $J_{02,i}$), the diode ideality factors ($m_{1,i}$, $m_{2,i}$), the series resistance ($R_{\mathrm{s},i}$), and the shunt resistance ($R_{\mathrm{p},i}$). The first diode term represents the surface and bulk region recombination, which usually dominates at high irradiance levels with $m_{1,i} \approx 1$, and the second diode term

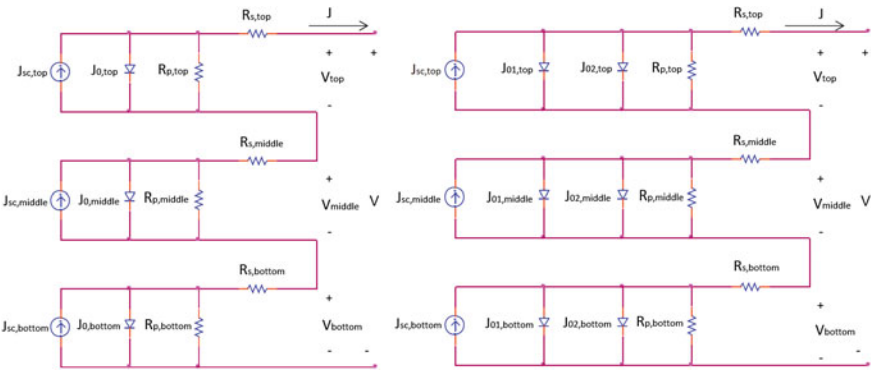

Fig. 6 Equivalent circuit models of a TJ solar cell by using the SEM (*left*) and the DEM (*right*)

represents the depletion region recombination, which usually dominates at low irradiance levels with $m_{2,i} \approx 2$ [57].

The total voltage of the MJ solar cell, neglecting the voltage decrease on the tunnel junctions [63], can simply be obtained by adding the voltages of each subcell as shown:

$$V = \sum_{i=1}^{n} V_i \tag{19}$$

The model's parameters described previously depend on the operating conditions, such as concentration and cell temperature, for the MJ solar cell [64]. At the same time, current MJ solar cells are usually fabricated monolithically and incorporate only two electrical terminals. Because of this, the separate measurement of the individual subcells and the determination of their parameters is a complex task [65]. Some investigators have proposed different methods to obtain the parameters of the subcells by making different assumptions and simplifications. Examples of extraction methods based on the SEM scheme can be found in the literature [46, 55, 59, 66–68] as can results from those based on the DEM scheme [59, 69–71]. It is important to note that these studies usually estimate the parameters at a particular set of operating conditions. Furthermore, the ability to translate the parameters at a desired operating condition is still challenging; thus the application of these models is often limited. Figure 7 shows an example of the modelled I-V characteristics of a typical GaInP/GaInAs/Ge device using Eqs. (17) and (19) by setting $R_{s,i} = 0$ and $m_i = 1$ under 1× concentration.

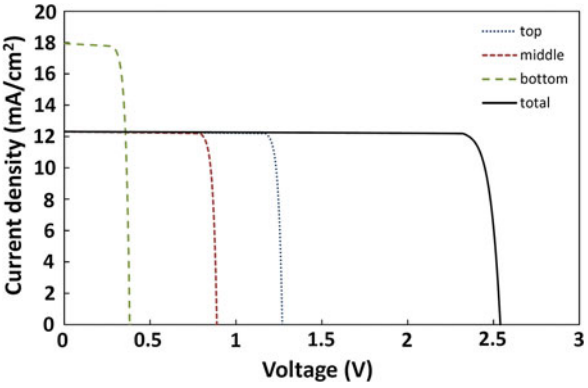

Fig. 7 Modelled I-V characteristics of each individual subcell and for the whole device of an LM GaInP/GaInAs/Ge solar cell under reference conditions (AM1.5D, ASTM G173-03, 1000 W/m^2, 25 °C)

5 Performance of MJ Solar Cells Under Real Operating Conditions

Currently the use of MJ solar cells for terrestrial applications is limited to HCPV due to their relatively high cost. HCPV technology is based on the use of less expensive optical elements to collect direct incidence sunlight and concentrate it to approximately 300× to 2000× on the surface of the solar cell. The aim is to decrease the cost of electricity, thus decreasing the semiconductor material by the use of the less expensive optics [72–75].

Under actual conditions, the performance of MJ solar cells in an HCPV system will be affected by time-varying atmospheric parameters. Therefore, it is necessary to quantify the impacts of the different phenomena to accurately estimate their performance. In this section, a discussion is presented on the main parameters that affect the behaviour of MJ solar cells outdoors. A procedure to quantify these parameters is addressed.

5.1 Thermal Factor

As presented in Sect. 3, the operating temperature of an MJ solar cell affects its electrical performance. Under real operating conditions, the cell temperature is not constant because it is affected by the changes in the direct normal irradiance (DNI), air temperature (T_{air}), and wind speed (W_s) [76, 77].

As already discussed, the effect of temperature on the electrical parameters of MJ solar cells can be quantified, with a low margin of error, using linear coefficients. Bearing this in mind, the effect of cell temperature on the power output can be quantified as shown:

$$\mathrm{TF} = 1 - \gamma(T_c - T_c^*) \tag{20}$$

where TF is defined as the thermal factor (TF), γ is the maximum power temperature coefficient at the operating concentration, T_c is the cell temperature, and T_c^* is the cell temperature under reference conditions (T_c^* = 25 °C).

In contrast, direct measurement of the cell temperature in HCPV systems is a complex task due to the special features that arise because the cells are surrounded by different peripheral elements [78]. Because of this, the scientific community has devoted considerable effort to develop methods for indirectly predicting the cell temperature in HCPV devices from different parameters (i.e., atmospheric parameters and/or easily measurable parameters in the concentrator) [77]. Among the different procedures, the methods based on atmospheric parameters present the advantage of allowing estimation of the cell temperature for a specific location without directly measuring the concentrator. Because of this, they are a more useful

tool for the electrical characterization at a desired location if the atmospheric data are available.

A simple method based on linear coefficients as a function of DNI, T_{air}, and W_s has been proposed [76]. The procedure is based on the following relation as follows:

$$T_c = T_{air} + a_1 \mathrm{DNI} + a_2 W_s \tag{21}$$

where a_1 and a_2 are specific coefficients of the concentrator. In addition, if we assume that the influence of W_s does not play an important role in the estimation of cell temperature, Eq. (21) can be simplified as:

$$T_c = T_{air} + a_1 \mathrm{DNI} \tag{22}$$

A slightly more sophisticated expression as a function of the same atmospheric parameters has been proposed [79]. In this case, the cell temperature is obtained as follows:

$$T_c = T_{air} + b_1 \mathrm{DNI}\left(\exp^{\left(-\frac{W_s}{2W_0}\right)} + b_2\right) \tag{23}$$

where b_1, b_2, and W_0 are specific coefficients of the concentrator. As in the previous relations, the method assumes that the cell temperature is proportional to DNI, but it uses an exponential correction based on the wind speed.

5.2 Spectral Factor

As was discussed in Sect. 3, the performance of MJ solar cells shows strong spectral dependence. Furthermore, the spectral distribution of incident irradiance is affected by atmospheric parameters and changes during the course of day, month, or year. In particular, the atmospheric parameters with the largest influence on the spectral irradiance and on the performance of MJ solar cells are, in order of importance, AM, aerosol optical depth (usually quantified at 500 or 550 nm), and precipitable water [80–84].

As was also mentioned, the performance of MJ solar cells under spectral variation is mainly determined by the current balance among the subcells. This effect can be quantified through the spectral factor (SF) as [84]:

$$\mathrm{SF} = \frac{\min\left(J_{sc,i} E_b(\lambda)\right) \int E_{b,\mathrm{ref}}(\lambda)\mathrm{d}\lambda}{\min\left(J_{sc,i}\left(E_{b,\mathrm{ref}}(\lambda)\right)\right) \int E_b(\lambda)\mathrm{d}\lambda} \tag{24}$$

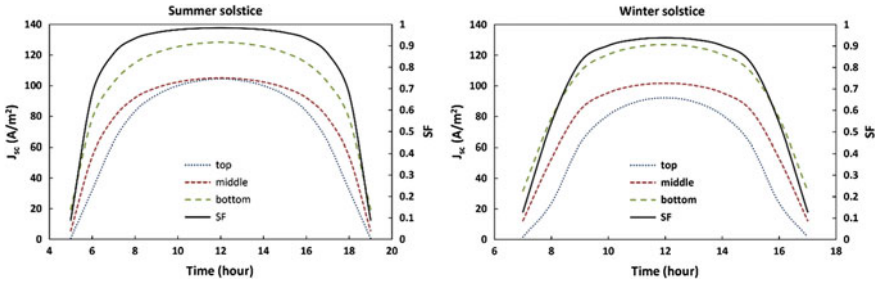

Fig. 8 Simulated SF and short-circuit current densities of an LM GaInP/GaInAs/Ge solar cell with an SOG Fresnel lens as a primary optic at the summer and winter solstices in Granada, southern Spain. The other parameters are kept constant at the reference values defined by the AM1.5D, ASTM G-173-03 reference spectrum [30]

where the short-circuit current density of each i junction in a concentrator is given by:

$$J_{\mathrm{sc},i} = \int E_b(\lambda)\eta_{\mathrm{opt}}(\lambda)\mathrm{SR}_i(\lambda)\mathrm{d}\lambda \tag{25}$$

where $E_b(\lambda)$ is the incident direct normal spectral distribution, $E_{b,\mathrm{ref}}(\lambda)$ is the direct reference spectrum, and $\eta_{\mathrm{opt}}(\lambda)$ is the optical efficiency of the concentrator.

Equation (24) evaluates the performance of an MJ solar cell as a function of the mismatch among the short-circuit current densities of the different junctions relative to the value obtained under illumination by the reference spectrum. To explain this in more detail, Fig. 8 shows the simulated SF and short-circuit current densities of

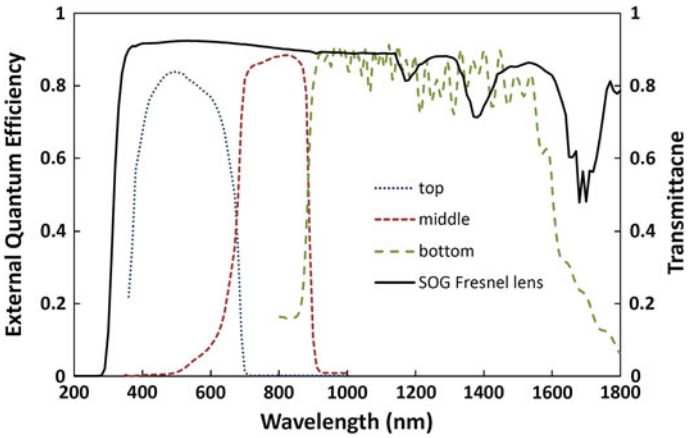

Fig. 9 External quantum efficiency of an LM GaInP/GaInAs/Ge solar cell and the transmittance of an SOG Fresnel lens. Refer to this plot, together with the solar spectrum shown in Fig. 2, for the discussion and results found in this section

each junction for an LM GaInP/GaInAs/Ge solar cell with a silicone-on-glass (SOG) Fresnel lens as a primary optic (see Fig. 9 for the EQE and transmittance) for 2 example days at Granada, southern Spain. The complete procedure followed is explained in detail in the next subsection.

To show a contrasting variation between data, the summer and winter solstices were selected as shown in Fig. 8. These days represent the minimum and maximum daily average AM values, respectively. As can be seen, the behaviour of the SF is similar for both days. The maximum spectral losses are produced at sunrise and sunset when the AM values are greater, and the minimum spectral losses are produced at midday when the AM values are lower. Although the behaviour of the SF is similar on both days, the spectral losses are significantly greater on the winter solstice than at the summer solstice with average SF values of approximately 0.7 and 0.8, respectively. This difference can be explained by taking into account that the AM values are significantly greater at the winter solstice than at the summer solstice. This can be also observed from the analysis of the short-circuit current densities of the top and middle junctions. As can be seen for low AM values, the top and middle junctions yield similar currents. However, for high AM values, the top junction strongly limits the current, thus resulting in an overall decrease of the SF of the MJ solar cell [80, 84].

5.3 Power Output

The power output of the cell is a key parameter because it allows knowledge of the energy yield of a particular photovoltaic device. The power produced by an MJ solar cell as a function of the incident DNI can be expressed as shown:

$$P = \mathrm{DNI} \cdot A_{\mathrm{cell}} \cdot X \cdot \eta_{\mathrm{cell}} \tag{26}$$

where η_{cell} is the efficiency of the cell at the operating concentration, and other conditions are held at the reference conditions. The effective concentration can be related to the geometric concentration (C_{geo}) of the HCPV device as shown:

$$X = \eta_{\mathrm{opt}} \cdot C_{\mathrm{geo}} \tag{27}$$

where geometric concentration is defined as:

$$C_{\mathrm{geo}} = \frac{A_{\mathrm{lens}}}{A_{\mathrm{cell}}} \tag{28}$$

where A_{lens} is the area of the primary optics, A_{cell} is the area of the cell, and η_{opt} is the optical efficiency.

By itself, Eq. (26) neglects the cell temperature and spectral effects. Combining Eqs. (20), (24), and (26), the power generated by an MJ solar cell can be more accurately expressed as:

$$P = \mathrm{DNI} \cdot A_{\mathrm{cell}} \cdot \eta_{\mathrm{opt}} \cdot C_{\mathrm{geo}} \cdot \eta_{\mathrm{cell}} \cdot \mathrm{TF} \cdot \mathrm{SF} \tag{29}$$

This equation estimates the power output of an MJ solar cell in a concentrator as a function of its temperature and direct normal incidence characterized by its irradiance (W/m^2) and spectral distribution.

Figure 12 shows an example of the simulated annual power density of an MJ solar cell with an SOG Fresnel lens as a primary optic in Granada, southern Spain. The external quantum efficiency of the cell and transmittance of the Fresnel lens used are plotted in Fig. 9. The system has a geometric concentration of 700×, an optical efficiency of 85 %, and a cell efficiency under reference conditions of 38.5 %.

To quantify the effect of cell temperature, the times series of air temperature is estimated from the maximum, minimum, and average values obtained from the NASA atmospheric database for an entire year [85–87]. The cell temperature was calculated using Eq. (22) from the air temperature and considering a_1 = 0.06 °C/Wm^{-2}. Once the cell temperature is obtained, the TF is estimated using Eq. (20) and by taking γ = −0.12 %/°C as shown in Fig. 10.

The spectral distribution of the direct normal irradiance for the whole year was simulated using the simple model of the atmospheric radiative transfer of sunshine (SMARTS) [88]. The AM was calculated as a function of the Sun's zenith angle (θ) as [89]:

$$\mathrm{AM} = \frac{1}{\cos\theta + 0.45665\theta^{0.07}(96.4836 - \theta)^{-1.697}} \tag{30}$$

and the monthly average values of aerosol optical depth at 550 nm and precipitable water were gathered from the Aerosol Robotic Network data set [90]. In addition, Granada is a nonindustrialized medium-size city; therefore, the rural aerosol model

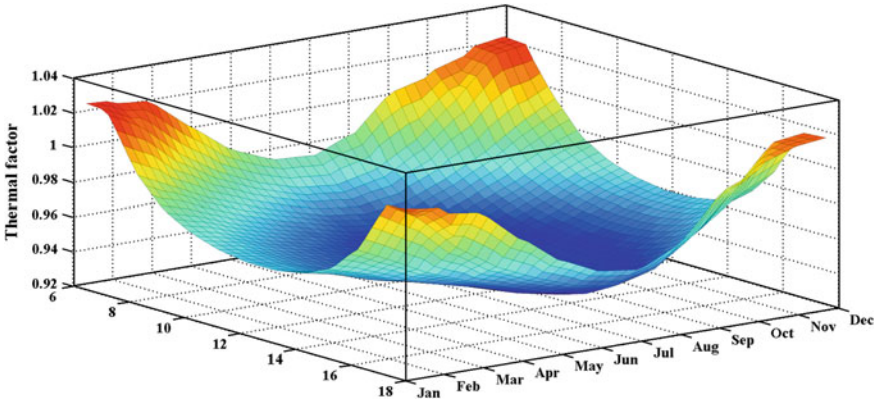

Fig. 10 Simulated annual TF for an LM GaInP/GaInAs/Ge solar cell with an SOG Fresnel lens as primary optics in Granada, southern Spain. The system has a geometric concentration of 700×, an optical efficiency of 85 %, and a cell efficiency under reference conditions of 38.5 %

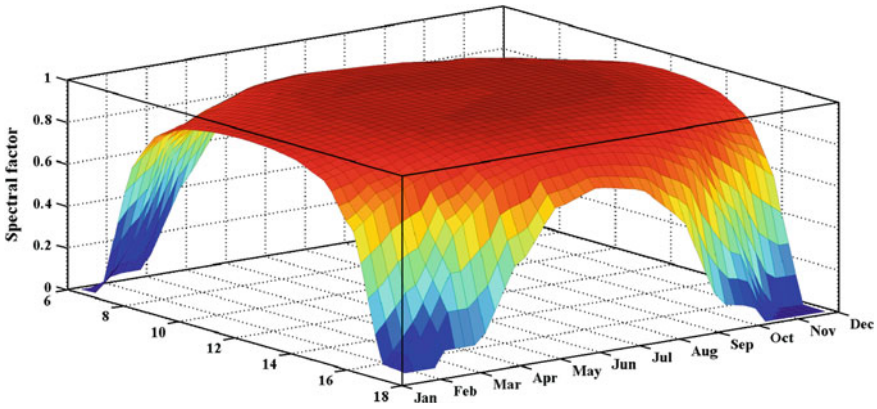

Fig. 11 Simulated annual SF for an LM GaInP/GaInAs/Ge solar cell with an SOG Fresnel lens as primary optics in Granada, southern Spain. The system is the same as the one described for Figs. 10 and 12

was selected. The rest of the input parameters for the SMARTS model were held constant at their reference values defined by the standard AM1.5D, ASTM G-173-03 at which MJ solar cells and HCPV devices are rated [30]. Once the spectral distribution is available, the SF was obtained using Eqs. (24) and (25), and the data for the external quantum efficiency and lens transmittance shown in Fig. 9. The result is shown in Fig. 11.

Finally, the power density of the cell per unit area is predicted using Eq. (29) every 10 min for the whole year as a function of the simulated DNI, TF, and SF values. This is shown in Fig. 12. In this figure, the generated power density ranges

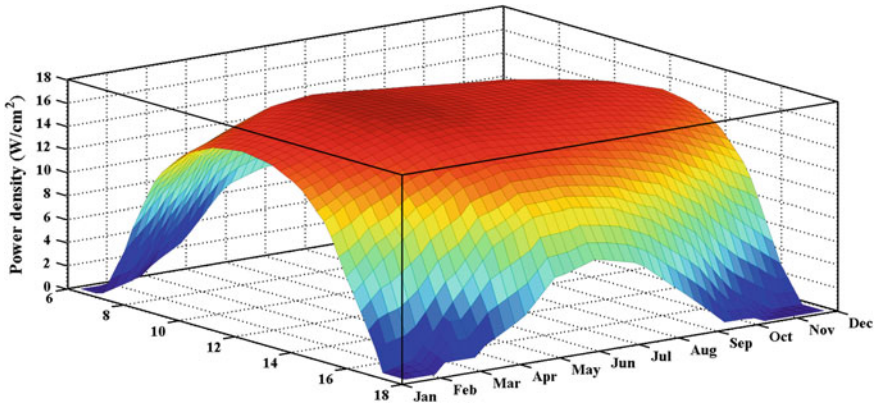

Fig. 12 Simulated annual power density for an LM GaInP/GaInAs/Ge solar cell with an SOG Fresnel lens as primary optics in Granada, southern Spain. The calculation utilized (Eq. 29) and the results shown in Figs. 10 and 11

from 0 to 18 W/cm^2 and is dominated by the incident DNI. In contrast, the TF and the SF lead to power losses as can be seen in Figs. 10 and 11. In particular, the SF ranges from 0 to 1, whereas the TF ranges from 0.9 to 1. Based on this, it could be concluded that the spectral effects produce greater energy losses than the temperature effects. However, as can be seen in Fig. 10, the maximum thermal losses are produced at midday and at summer months when the contribution to the final annual energy yield is at a maximum. In contrast, as can be seen in Fig. 11, the maximum spectral losses are produced at sunrise and sunset and at winter months when the contribution to the annual energy yield is lower than in the previous case. This implies that the spectral losses do not necessarily dominate the energy losses of an MJ solar cell in a concentrator under real operating conditions for a particular period of time. To analyse the factor that leads to greater energy losses, the TF and SF terms of Eq. (29) must be carefully analysed and compared. Thermal and spectral losses change during the course of a day, month, or year and for each location. Consequently, this type of analysis should be performed for a given period of time and a specific location to accurately analyse and quantify the impact of the spectral and thermal effects on the energy harvested.

The procedure based on Eq. (29) described previously for estimating the maximum power of an HCPV device was evaluated at the Centre of Advanced Studies in Energy and Environment at the University of Jaen in Southern Spain. The electrical parameters of an HCPV module were monitored together with the main atmospheric parameters during the course of 2 years (2013–2014). The HCPV module was made up of 20 TJ LM GaInP/GaInAs/Ge solar cells with an area of 0.763 cm^2 interconnected in series and each with the EQE shown in Fig. 9. The module used SOG Fresnel lenses with the transmittance shown in Fig. 9 as a primary optical element. The secondary optical element for each cell consisted of a

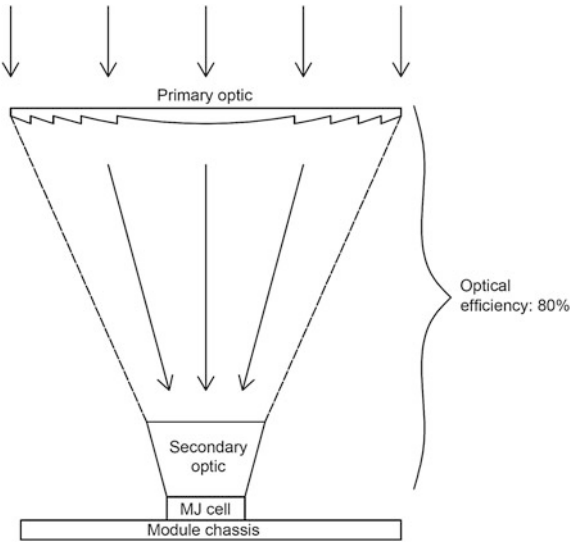

Fig. 13 Schematic diagram of a single receiver of the HCPV module under study

Table 3 RMSE, MBE, and R^2 between actual and predicted output power for an HCPV MJ cell

RMSE (%)	MBE (%)	R^2
3.46	−1.26	0.98

truncated pyramid reflective cup that used an aluminium film layer to enhance its reflectivity. The module had a geometric concentration of 700× and used passive cooling to ensure that MJ solar cells operate at their optimal operation range, which is 50–80 °C. The module had a nominal maximum power of 280 W under reference conditions (DNI = 1000 W/m^2, T_C = 25 °C, spectrum = AM1.5D) [91]. Figure 13 shows a schematic diagram of a single receiver of the HCPV module under study.

Table 3 shows the root mean square error (RMSE), the mean bias error (MBE), and the determination coefficient (R^2) between actual and predicted data. This shows that the procedure described above is valid for estimating the maximum power of an HCPV device at a particular location if high-quality atmospheric parameters are available.

6 Conclusions

MJ concentrator solar cells are complex devices because they consist of several devices stacked in optical and electrical series. This allows them to reach efficiencies that are not possible with SJ devices. The analysis of their behavior, however, is still possible from consideration of their external quantum efficiency, band-gaps, and temperature coefficients of individual subcells. This allows the influence of the input spectrum to be considered so that the short-circuit current, open circuit voltage, and FF can nonetheless be understood as a function of temperature, input spectrum, and irradiance that is a result of the optical concentration factor. A lumped parameter approach that considers a TF and an SF allows the estimation of the power output for real HCPV systems. These factors, when combined with atmospheric and meteorological data, allow for the calculation of the power output as a function of time of day and time of year.

Future work can consider this approach for different geographic locations and for several complex conditions faced by real HCPV systems in the field. The analysis can also be expanded to consider lattice-MM and other device structures such as the IMM. Not considered in the above basic description is the effect of transient irradiance, partial shadowing or cell mismatching. This can also be considered in more complex modelling efforts. The general conclusion is that the behaviour of MJ concentrator solar cells and modules can, and must, be understood from a fundamental perspective for large-scale HCPV deployment to be successfully undertaken.

References

1. Philipps S, Dimroth F, Bett A (2013) In: McEvoy A, Castañer L, Markvart T (eds) Solar cells: materials, manufacture and operation. Elsevier, Amsterdam, p 353
2. Bailey S, Raffaelle R (2012) In: McEvoy AMT, Castañer L (eds) Practical handbook of photovoltaics fundamentals and applications. Elsevier, Boston, p 863
3. Algora C In: Luque A, Andreev V (eds) Concentrator photovoltaics. Springer, Berlin, p 89
4. Olson J, Friedman D, S Kurtz (2003) In: Luque A, Hegedus S (eds) Handbook of photovoltaic science and engineering. Wiley, New York, p 359
5. Fraas L (2014) Low-cost solar electric power. Springer, Cham, p 97
6. Kurtz S, Geisz J (2010) Multijunction solar cells for conversion of concentrated sunlight to electricity. Opt Express 18(9):A73–A78
7. King R, Shusari D, Larrabee D, Liu X-Q, Rehder E, Edmond-son K, Cotal H, Jones R, Ermer J, Fetzer C, Law D, Karam N (2012) Solar cell generations over 40 % efficiency. Prog Photovolt Res Appl 20:801–815
8. Tanabe K (2009) A review of ultrahigh efficiency III-V semiconductor compound solar cells: multijunction tandem, lower dimensional, photonic up/down conversion and plasmonic nanometallic structures. Energies 2:504–530
9. Wilt D, Stan M (2012) High efficiency multijunction photovoltaic development. Ind Eng Chem Res 51(37):11931–11940
10. Landsberg P, Markvart T (2013) In: McEvoy A, Castañer L, Markvart T (eds) Solar cells: materials, manufacture and operation. Elsevier, Amsterdam, p 55
11. de Vos A (1992) Endoreversible thermodynamics of solar energy con-version. Oxford University Press, New York, p 120
12. Smestad G, Ries H (1992) Luminescence and current-voltage characteristics of solar cells and optoelectronic devices. Sol Energy Mater Sol Cells 25:51–71
13. Smestad G (2002) Optoelectronics of Solar Cells. SPIE, Bellingham, p 57
14. Tobin S, Vernon S, Bajgar C, Wojtczuk SJ, Melloch M, Keshavarzi A, Stellwag T, Venkatensan S, Lundstrom M, Emery K (1990) Assessment of MOCVD and MBE growth GaAs for high-efficiency solar cell applications. IEEE Trans Electron Devices 37(2):469–477
15. Ptak A, Johnston S, Kurtz S, Friedman D, Metzger W (2003) A comparison of MBE- and MOCVD-grown GaInNAs. J Cryst Growth 251(1–4):392–398
16. Bett A, Adelhelm R, Agert C, Beckert R, Dimroth F, Schubert U (2001) Advanced III-V solar cell structures grown by MOVPE. Sol Energy Mater Sol Cells 66(1–4):541–550
17. Jackrel D, Bank S, Yuen H, Wistey M, Harris J, Ptak A, Johnston S, Friedman D, Kurtz S (2007) Dilute nitride GaInNAs and GaInNAsSb solar cells by molecular beam epitaxy. J Appl Phys 101(11):114916
18. Malik R (1989) III-V semiconductor materials and devices. Elsevier, Amsterdam
19. Simon MS, Kwok KN (2006) Physics of semiconductor devices. Wiley, New York
20. Levinshtein ME, Rumyantsev SL, Shur MS (2001) Properties of advanced semiconductor materials: GaN, AIN, InN, BN, SiC, SiGe. Wiley, New York
21. Green M (2003) Third generation photovoltaics. Springer, Berlin
22. Mokkapati S, Jagadish C (2009) III-V compound SC for optoelectronic devices. Mater Today 12(4):22–32
23. Washburn J, Kvam EP, Liliental-Weber Z (1991) Defect formation in epitaxial crystal growth. J Electron Mater 20(2):155–161
24. Cohen M, Bergstresser T (1966) Band structures and pseudopotential form factors for fourteen semiconductors of the diamond and zinc-blende structures. Phys Rev 141(2):789–796
25. Yamaguchi M, Takamoto T, Araki K, Ekins-Daukes N (2005) Multi-junction III-V solar cells: current status and future potential. Sol Energy 79(1):78–85
26. Dimroth F (2006) High-efficiency solar cells from III-V compound semiconductors. Physica Status Solidi C: Conf 3(3):373–379

27. King R, Bhusari D, Larrabee D, Liu X-Q, Rehder E, Edmondson K, Cotal H, Jones R, Ermer J, Fetzer C, Law D, Karam N (2012) Solar cell generations over 40% efficiency. Prog Photovolt Res Appl 20(6):801–815
28. Walker A, Thériault O, Wilkins M, Wheeldon J, Hinzer K (2013) Tunnel-junction-limited multijunction solar cell performance over concentration. IEEE J Sel Topics Quantum Electron 19(5):1–8
29. Guter W, Schöne J, Philipps S, Steiner M, Siefer G, Wekkeli A, Welser E, Oliva E, Bett A, Dimroth F (2009) Current-matched triple-junction solar cell reaching 41.1 % conversion efficiency under concentrated sunlight. Appl Phys Lett 54(22)
30. ASTM G 173-03e1 (2012) Standard tables for reference solar spectral irradiance: direct normal and hemispherical on 37 tilted surface
31. Cotal H, Fetzer C, Boisvert J, Kinsey G, King R, Hebert P, Yoon H, Karam N (2009) III-V multijunction solar cells for concentrating photovoltaics. Energy Environ Sci 2(2):174–192
32. García I, Rey-Stolle I, Galiana B, Algora C (2009) A 32.6 % efficient lattice-matched dual-junction solar cell working at 1000 suns. Appl Phys Lett 94(5):0535509
33. Araki K, Yamaguchi M, Kondo M, Uozumi H (2003) Which is the best number of junctions for solar cells under ever-changing terrestrial spectrum? In: 3rd World conference on photovoltaic energy conversion, pp 307–312
34. Yoon H, Haddad M, Mesropian S, Yen J, Edmondson K, Law D, King R, Bhusari D, Boca A, Karam N (2008) Progress of inverted metamorphic III-V solar cell development at Spectrolab. In: 33rd IEEE photovoltaic specialists conference
35. Geisz J, Kurtz S, Wanlass M, Ward J, Duda A, Friedman D, Olson J, McMahon W, Moriarty T, Kiehl J (2007) High-efficiency GaInPGaAsInGaAs triple-junction solar cells grown inverted with a metamorphic bottom junction. Appl Phys Lett 91(2):023502–023502
36. Geisz J, Friedman D, Ward J, Duda A, Olavarria W, Moriarty T, Kiehl J, Romero M, Norman A, Jones K (2008) 40.8 % efficient inverted triple-junction solar cell with two independently metamorphic junctions. Appl Phys Lett 93(12):123505
37. King R, Law D, Edmondson K, Fetzer C, Kinsey G, Yoon H, Krut D, Ermer J, Sherif R, Karam N (2007) Advances in high-efficiency III-V multijunction solar cells. Adv OptoElectron
38. Tanabe K, Fontcuberta i Morral A, Atwater H, Aiken D, Wanlass M (2006) Direct-bonded GaAs/InGaAs tandem solar cell. Phys Lett 89(10):102106
39. Derendorf K, Essig S, Oliva E, Klinger V, Roesener T, Philipps S, Benick J, Hermle M, Schachtner M, Siefer G, Jäger W, Dimroth F (2013) Fabrication of GaInP/GaAs//Si solar cells by surface activated direct wafer bonding. IEEE J Photovolt 3(4):1–6
40. Häussler D, Houben L, Essig S, Kurttepeli M, Dimroth F, Dunin-Borkowski R, Jäger W (2013) Aberration-corrected transmission electron microscopy analyses of GaAs/Si interfaces in wafer-bonded multi-junction solar cells. Ultramicroscopy 134:55–61
41. Dimroth F, Grave M, Beutel P, Fiedeler U, Karcher C, Tibbits T, Oliva E, Siefer G, Schachtner M, Wekkeli A, Bett A, Krause R, Piccin M, Blanc N, Drazek C, Guiot E, Ghyselen B, Salvetat T, Tauzin A, Signamarcheix T (2014) Wafer bonded four-junction GaInP/GaAs//GaInAsP/GaInAs concentrator solar cells with 44.7 % efficiency". Prog Photovolt Res Appl 22(3):277–282
42. Varshni YP (1967) Temperature dependence of the energy gap in semiconductors. Physica 34:149–154
43. Aiken D, Stan M, Murray C, Sharps P, Hills J, Clevenger B (2002) Temperature dependent spectral response measurements for III-V multi-junction solar cells. In: 29th conference record of the IEEE photovoltaic specialists conference
44. Helmers H, Schachtner M, Bett A (2013) Influence of temperature and irradiance on triple-junction solar subcells. Sol Energy Mater Sol Cells 116:144–152
45. Braun A, Katz EGJ (2013) Basic aspects of the temperature coefficients of concentrator solar cell performance parameters. Prog Photovolt Res Appl 21(5):1087–1094

46. Domínguez C, Antón I, Sala G (2010) Multijunction solar cell model for translating I-V characteristics as a function of irradiance, spectrum, and cell temperature. Prog Photovolt Res Appl 18(4):272–284
47. Friedman D (1996) Modelling of tandem cell temperature coefficients. In: 25th conference record of the IEEE photovoltaic specialists conference
48. Meusel M, Baur C, Létay G, Bett A, Warta W, Fernandez E (2003) Spectral response measurements of monolithic GaInP/Ga(In)As/Ge triple-junction solar cells: measurement artifacts and their explanation. Prog Photovolt Res Appl 11(8):499–514
49. Fernández E, Loureiro A, Higueras P, Siefer G (2011) Monolithic III-V triple-junction solar cells under different temperatures and spectra. In: Proceedings of the 8th spanish conference on electron devices, CDE'2011, Art no 5744222
50. Baudrit M, Algora C (2008) Modeling of GaInP/GaAs dual-junction solar cells including tunnel junction. In: 33rd IEEE photovoltaic specialists conference
51. Siefer G, Baur C, Bett A (2010) External quantum efficiency measurements of Germanium bottom subcells: measurement artifacts and correction procedures. In: 35th IEEE Photovoltaic Specialists Conference
52. Faine P, Kurtz S, Riordan C, Olson J (1991) The influence of spectral solar irradiance variations on the performance of selected single-junction and multijunction solar cells. Solar Cells 31(3):259–278
53. Domínguez C, Anton I, Sala G, Askins S (2013) Current-matching estimation for multijunction cells within a CPV module by means of component cells. Prog Photovolt Res Appl 21(7):1478–1488
54. McMahon W, Emery K, Friedman D, Ottoson L, Young M, Ward J, Kramer C, Duda A, Kurtz S (2008) Fill factor as a probe of current-matching for GaInP/GaAs tandem cells in a concentrator system during outdoor operation. Prog Photovolt Res Appl 16(3):213–224
55. Fernández E, Siefer G, Almonacid F, Loureiro A, Pérez-Higueras P (2013) A two subcell equivalent solar cell model for III-V triple junction solar cells under spectrum and temperature variations. Sol Energy 92:221–229
56. Meusel M, Adelhelm R, Dimroth F, Bett A, Warta W (2002) Spectral mismatch correction and spectrometric characterization of monolithic III-V multi-junction solar cells. Prog Photovolt Res Appl 10(4):243–255
57. Siefer G, Bett A (2014) Analysis of temperature coefficients for III-V multijunction concentrator cells. Prog Photovolt Res Appl 22(5):515–524
58. Kinsey G, Hebert P, Barbour K, Krut D, Cotal H, Sherif R (2008) Concentrator multifunction solar cell characteristics under variable intensity and temperature. Prog Photovolt Res Appl 16 (6):503–508
59. Segev G, Mittelman G, Kribus A (2012) Equivalent circuit models for triple-junction concentrator solar cells. Sol Energy Mater Sol Cells 98:57–65
60. Braun A, Hirsch B, Vossier A, Katz E, Gordon J (2013) Temperature dynamics of multijunction concentrator solar cells up to ultra-high irradiance. Prog Photovolt Res Appl 21 (2):202–208
61. Fernández E, Siefer G, Schachtner M, García Loureiro A, Pérez-Higueras P (2012) Temperature coefficients of monolithic III-V triple-junction solar cells under different spectra and irradiance levels. AIP Conf Proc 1477:189–193
62. Siefer G, Baur C, Meusel M, Dimroth F, Bett A, Warta W (2002) Influence of the simulator spectrum on the calibration of multi-junction solar cells under concentration. In: 29th IEEE photovoltaic specialists conference
63. Guter W, Bett A (2006) I-V characterization of tunnel diodes and multijunction solar cells. IEEE Trans Electron Devices 53(9):2216–2222
64. Ben Or A, Appelbaum J (2014) Dependence of multi-junction solar cells parameters on concentration and temperature. Solar Energy Mater Solar Cells 130:234–240
65. Karcher C, Helmers H, Schachtner M, Dimroth F, Bett A (2014) Temperature-dependent electroluminescence and voltages of multi-junction solar cells. Prog Photovolt Res Appl 22 (7):757–763

66. Wanlass M, Emery K, Gessert T, Horner G, Osterwald C, Coutts T (1989) Practical considerations in tandem cell modeling. Solar Cells 27(1–4):191–204
67. Ben Or A, Appelbaum J (2013) Estimation of multi-junction solar cell parameters. Prog Photovolt Res Appl 21(4):713–723
68. Ben Or A, Appelbaum J (2013) Performance analysis of concentrator photovoltaic dense-arrays under non-uniform irradiance. Solar Energy Mater Solar Cells 117:110–119
69. Reinhardt K, Lewis B, Kreifels T (2000) Multijunction solar cell iso-junction dark current study. In 28th IEEE photovoltaic specialists conference
70. Nishioka K, Takamoto T, Agui T, Kaneiwa M, Uraoka Y, Fuyuki T (2005) Evaluation of temperature characteristics of high-efficiency InGaP/InGaAs/Ge triple-junction solar cells under concentration. Sol Energy Mater Sol Cells 85(3):429–436
71. Nishioka K, Sueto T, Uchida M, Ota Y (2010) Detailed analysis of temperature characteristics of an InGaP/InGaAs/Ge triple-junction solar cell. J Electron Mater 39(6):704–708
72. Zubi G, Bernal-Agustín J, Fracastoro G (2009) High concentration photovoltaic systems applying III-V cells. Renew Sustain Energy Rev 13(9):2645–2652
73. Pérez-Higueras P, Muñoz E, Almonacid G, Vidal P (2011) High concentrator photovoltaics efficiencies: present status and forecast. Renew Sustain Energy Rev 15(4):1810–1815
74. Fernández E, Pérez-Higueras P, Garcia Loureiro A, Vidal P (2013) Outdoor evaluation of concentrator photovoltaic systems modules from different manufacturers: first results and steps. Prog Photovolt Res Appl 21(4):693–701
75. Luque A, Sala G, Luque-Heredia I (2006) Photovoltaic concentration at the onset of its commercial deployment. Prog Photovolt Res Appl 14(5):413–428
76. Almonacid F, Pérez-Higueras P, Fernández E, Rodrigo P (2012) Relation between the cell temperature of a HCPV module and atmospheric parameters. Sol Energy Mater Sol Cells 105:322–327
77. Rodrigo P, Fernández E, Almonacid F, Pérez-Higueras P (2014) Review of methods for the calculation of cell temperature in high concentration photovoltaic modules for electrical characterization. Renew Sustain Energy Rev 38:478–488
78. Fernandez EF, Almonacid F, Rodrigo P, Pérez-Higueras P (2014) Calculation of the cell temperature of a high concentrator photovoltaic (HCPV) module: a study and comparison of different methods. Sol Energy Mater Sol Cells 121:144–151
79. Hornung T, Steiner M, Nitz P (2012) Estimation of the influence of Fresnel lens temperature on energy generation of a concentrator photovoltaic system. Solar Energy Mater Solar Cells 333–338:99
80. Kinsey G, Edmondson KM (2009) Spectral response and energy output of concentrator multijunction solar cells. Prog Photovolt Res Appl 17(5):279–288
81. Philipps S, Peharz G, Hoheisel R, Hornung T, Al-Abbadi N, Dimroth F, Bett A (2010) Energy harvesting efficiency of III-V triple-junction concentrator solar cells under realistic spectral conditions. Sol Energy Mater Sol Cells 94(5):869–877
82. Chan N, Brindley H, Ekins-Daukes N (2013) Impact of individual atmospheric parameters on CPV system power, energy yield and cost of energy. Prog Photovolt Res Appl 22(10):1080–1095
83. Chan N, Young TB, Brindley HE, Ekins-Daukes N, Araki K, Kemmoku YY (2012) Validation of energy prediction method for a concentrator photovoltaic module in Toyohashi Japan. Prog Photovolt Res Appl 21:1598–1610
84. Fernández E, Almonacid F, Ruiz-Arias JS-MA (2014) Analysis of the spectral variations on the performance of high concentrator photovoltaic modules operating under different real climate conditions. Sol Energy Mater Sol Cells 127:179–187
85. Surface meteorology and Solar Energy. Available: https://eosweb.larc.nasa.gov/sse/
86. Erbs D, Klein S, Beckman WA (1983) Estimation of degree-days and ambient temperature bin data from monthly-average temperatures. Ashrae J 25:60–65
87. Almonacid F, Pérez-Higueras P, Rodrigo P, Hontoria L (2013) Generation of ambient temperature hourly time series for some Spanish locations by artificial neural networks. Renew Energy 51:285–291

88. Gueymard C (2001) Parameterized transmittance model for direct beam and circumsolar spectral irradiance. Sol Energy 71(5):325–346
89. Kasten F, Young AT (1989) Revised optical air mass tables and approximation formula. Appl Opt 28(22):4735–4738
90. Aerosol Robotic Network. Available: http://aeronet.gsfc.nasa.gov/
91. IEC (2013) IEC 62670-1 ed1.0 Photovoltaic concentrators (CPV)—performance testing—part 1: standard conditions

Characterization of Multijunction Concentrator Solar Cells

César Domínguez and Pablo García-Linares

Abstract This chapter summarizes the state of the art in instruments and methods for the characterization of concentrator multijunction (MJ) solar cells (MJSC). The current-voltage characteristic (I–V curve) under illumination and the spectral response or quantum efficiency (QE) are the main properties of a solar cell. The measurement of the I–V curve as a function of light concentration provides the most relevant information on cell performance such as peak efficiency or series resistance losses. Concentrator solar simulators should fulfill strict spatial uniformity and spectral requirements to provide accurate measurements. Precise spectral tunability is required to reduce errors in the measurement of latest-generation cell architectures, especially those not based on a germanium bottom cell with an excess of current. The main types of concentrator solar simulators are described, and advice on appropriate reference sensors and measurement precautions is provided. Spectral characterization under controlled simulator conditions is essential to analyze MJ cell behavior under the ever-varying spectral conditions found in real operation. The relevance of the QE is that it allows calculating the photocurrent generated by each subcell under a particular spectral irradiance and diagnosing possible malfunctioning of the different regions of the cell. Cell electroluminescence (EL) is also discussed as a useful tool for assessing defects. Spatially resolved EL can be used to analyze solar cell internal defects, sheet resistivity, or thermal inhomogeneity under steady concentrated light. Typical characterization set-ups, test procedures, and potential instrumentation issues are discussed for QE and EL.

C. Domínguez (✉)
Instituto de Energía Solar, Universidad Politécnica de Madrid, Ciudad Universitaria, 28040 Madrid, Spain
e-mail: cesardd@ies-def.upm.es

P. García-Linares
CEA-LITEN, National Institute for Solar Energy (INES), Le Bourget-du-Lac, France

P. Pérez-Higueras and E.F. Fernández (eds.), *High Concentrator Photovoltaics*, Green Energy and Technology, DOI 10.1007/978-3-319-15039-0_3

1 Introduction

Motivated by the interest of the satellite industry and a growing number of companies working on terrestrial concentrator systems, the progress on multijunction solar cells (MJSC) has been accelerated from the beginning of the century. The increasing record efficiencies achieved boost the interest of their use as a source of electricity in terrestrial photovoltaic (PV) plants. Appropriate characterization methods are essential for the development and optimization of concentrator cells achieving the highest efficiencies and energy yield on the field. However, the successive new generations of MJ cells employ an increasingly diverse range of semiconductor materials and architectures. Thus, classical PV characterization methods and standards become insufficient or inappropriate.

This chapter summarizes the state of the art in instruments and methods for the evaluation of concentrator cell performance. The majority of the instrumentation issues described is related specifically to the measurements of MJ cells due to their use of multiple subcells with different bandgaps that are internally series-connected and make a broader use of the spectrum than conventional silicon cells. The current-voltage characteristic (I–V curve) under illumination and the spectral response are the main properties of a solar cell. Cell electroluminescence (EL) is also discussed as a useful tool for assessing defects. Typical characterization set-ups, test procedures, and potential instrumentation issues are discussed.

2 Quantum Efficiency

Quantum efficiency (QE) is a key measurement for photovoltaic devices in general and MJSC in particular. This technique has been applied to MJSC for almost 30 years [1]. Regarding conventional single-junction cells, QE helps diagnosing possible malfunctioning of the different parts or regions of the cell [2] such as low carrier collection in the base, emitter, depletion region, high front surface recombination, poor back surface passivation, antireflection coating (ARC), etc. In MJSC, the aforementioned electronic and optical performance features can be identified and quantified through QE for each of the subcells integrating the whole device [3]. The characterization of the spectral collection of each junction separately provides valuable information that can be employed to establish an adequate comparison between them. The relevance of the QE is that it allows calculating the short-circuit current (I_{sc}) generated by each subcell. Because MJSC are devices composed of different types of materials with different bandgaps, they can absorb a different portion of the sunlight spectrum. In addition, each material forms a p–n junction, which is series-connected monolithically to the next junction in a cascade configuration with no physical access to its individual terminals [4]. The possibility of determining the photogenerated current delivered by each subcell is essential during the design of a MJSC for a particular set of operation conditions because the smallest one limits the performance of the rest of the device. Obtaining the QE is a

straightforward method to provide accurate feedback on the layer structure design, the quality of the epitaxial process, or the convenience of a particular processing step during the fabrication of the cell.

2.1 Definitions

To appropriately begin with the description of this technique, a number of useful definitions that best fit this characterization technique are reviewed.

- External QE: number of carriers collected per incident photon directly measured on the photovoltaic device terminals and therefore including the reflection of the incident light produced on its front surface. It may be relative or absolute.
- Internal QE: number of carriers collected per incident photon resulting from the measurement of the photovoltaic device once the reflected component of the incident light has been subtracted. It may be relative or absolute.

The relation that links both internal (QE_{int}) and external QE (QE_{ext}) through the spectral reflectivity ($R(\lambda)$) is shown in (1):

$$QE_{ext} = QE_{int}[1 - R(\lambda)] \tag{1}$$

Three different expressions of the QE corresponding to a $Ga_xIn_{1-x}P$ p–n junction that constitutes the top cell of a triple-junction MJSC are illustrated in Fig. 1. The three curves included in the figure show the main differences between the aforementioned definitions: the absolute external QE is smaller than its internal counterpart because it includes in the denominator (i.e., the number of photons), the incident photons that are reflected on the cell surface, $R(\lambda)$ in (1), and thus never penetrate into the active semiconductor layers of the cell. The relative QE corresponding to the external QE is also represented.

The QE is then obtained from the ratio between two magnitudes which are measured for this type of characterization: the number of photogenerated carriers

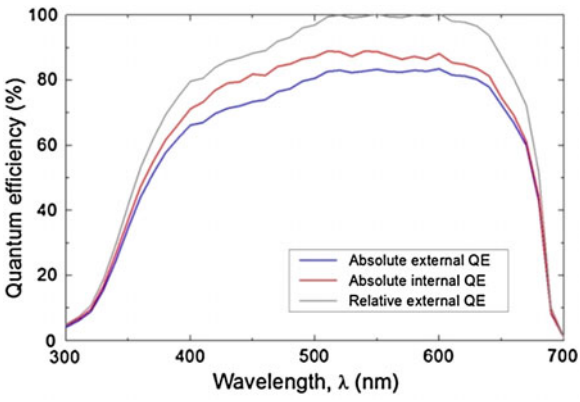

Fig. 1 QE plot of a $Ga_xIn_{1-x}P$ p–n junction where the absolute external and internal QE are shown together with relative external QE

(i.e., electrons) and the number of photons from the solid angle of the aforementioned light beam that excites the device under test. In the following section, the set-up used to carry up this experimental technique is reviewed.

2.2 The QE Characterization Set-up

A typical QE set-up adapted to the measurement of MJSC requires a number of elements, some of which are indispensable and others that are just recommended but usually included for practical reasons. These elements, depicted in Fig. 2a, are listed and described hereafter.

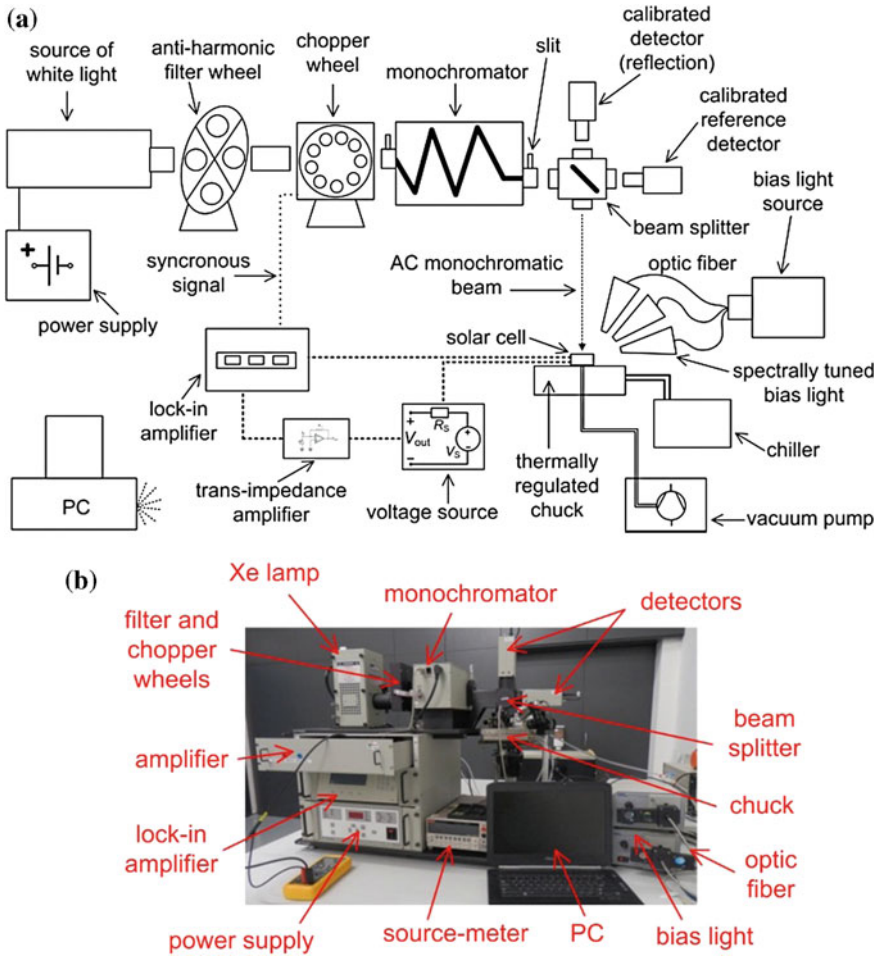

Fig. 2 Description of a QE system applied to the characterization of MJSC where the different elements are indicated. **a** Sketch of the QE system. **b** Picture of an actual QE system

Source of white light and power supply
The QE characterization system is spectrally resolved because it uses monochromatic light to excite the solar cell. This monochromatic light is selected from a source of white light, typically produced by a Xe arc lamp or a quartz tungsten halogen lamp with the power supply being provided by a tunable stable power module. Xe sources are ultraviolet (UV) and visible-rich. They have a relatively continuous spectrum in the 200- to 700-nm range, but in exchange they are slightly more unstable than halogen lamps, which are more infrared (IR)-rich (their spectra usually peak around the near-IR); however, they are also inexpensive to operate and easy to handle. These halogen lamps are often combined with deuterium lamps, which complement the relatively poor UV response. Power supplies in the range of 50–1000 W are often offered by specialized market suppliers.

Monochromator
This element converts the white light focused at its entrance into a monochromatic beam. It typically works with diffracting gratings that spatially separate the spectral components of the light. These gratings have a specific spectral response characterized by particular peak efficiency and an operating range. A monochromator often hosts more than one grating. The input and output openings are regulated by a set of slits, the aperture widths of which enable tuning of the spectral resolution of the output monochromatic beam. The selected wavelength at the output is remotely controlled by software, which sweeps a portion of the operating spectrum with a fixed step.

Antiharmonic filter-wheel
A set of longpass and/or bandpass filters disposed on a wheel that is automatically controlled as a function of the scanning spectral range helps prevent harmonics and stray light, which would hinder the QE measurement located in the optical path.

Calibrated detectors
A photovoltaic detector is required to measure the light impinging on the solar cell under test. The fact that it is calibrated allows determining the absolute components of the QE. The calibrated detector used for the acquisition of the reflected component allows the measurement of the internal QE.

Lock-in amplifier and chopper
The electrical signals being handled in the QE characterization are low because the initial luminous power from the white light source is strongly decreased throughout its optical path, especially in the monochromator (there exists a trade-off between monochromaticity and power of the light beam). For this reason the test light is chopped, and the resulting modulated signal is demodulated, thus increasing the signal-to-noise ratio (SNR) with the lock-in amplifier synchronous-detection technique.

Transimpedance amplifier
This optional element of the QE set-up is used to amplify the signal level as well as to convert the current photogenerated by the test cell and from the calibrated detectors into a proportional voltage signal. This stage is located before the lock-in entrance because it can only accept voltage signals.

Personal computer
A personal computer is used to run the software employed to synchronize the different elements of the set-up, save the relevant data from each measured point, and set the desired parameters of each measurement.

Thermally regulated chuck and vacuum pump
The solar cell or PV receiver is fixed onto a chuck, which, by means of the vacuum produced by a vacuum pump, is thermally regulated with a close-cycle water chiller, thermoelectric assembly or equivalent cooling system.

Bias light
As it will be reviewed later, the QE characterization of an MJSC requires a bias light that is absorbed by all of the subcells from the device except the one under test. Halogen lamps equipped with a combination of longpass and shortpass filters and guided to the sample with optic fibers can be used. Another possible configuration can be implemented with lasers of different wavelengths. This solution provides greater irradiance, but it is less versatile.

Voltage source
Another feature of the QE particularly applied to MJSC is the need for an electrical voltage bias. This can be provided by an electrical active load, such as a voltage source or a source-meter, which must operate in at least two quadrants.

2.3 The QE Characterization Applied to MJSC

The electrical configuration of the subcells within a MJSC makes necessary the use of an alternative continuous bias light to saturate the junctions (in terms of photogeneration) that are not meant to respond during each measurement, making the one under test to limit the device performance and hence, command the operation [4]. In contrast, a voltage bias is necessary to avoid reverse bias of the solar cell sub-junction under test.

In Fig. 3a, a simplified sketch is shown of the front metallization of a concentrator solar cell during QE characterization. The figure represents the relative position of the monochromatic test light spot within a small concentrator cell surface, which can significantly affect the absolute value of the measurement. This effect is magnified on cells with a finger pitch in the range of the test light spot dimension. This is explained by the fact that a different equivalent shading factor is produced as a function of the position of the spot. If the position of the spot is slightly varied throughout the cell surface, a different portion of the finger metallization will be illuminated, and a different response will be measured. This uncertainty has been characterized for this particular example. The result is shown in Fig. 3b, where a 3 % difference exists between the two extreme equivalent shading situations.

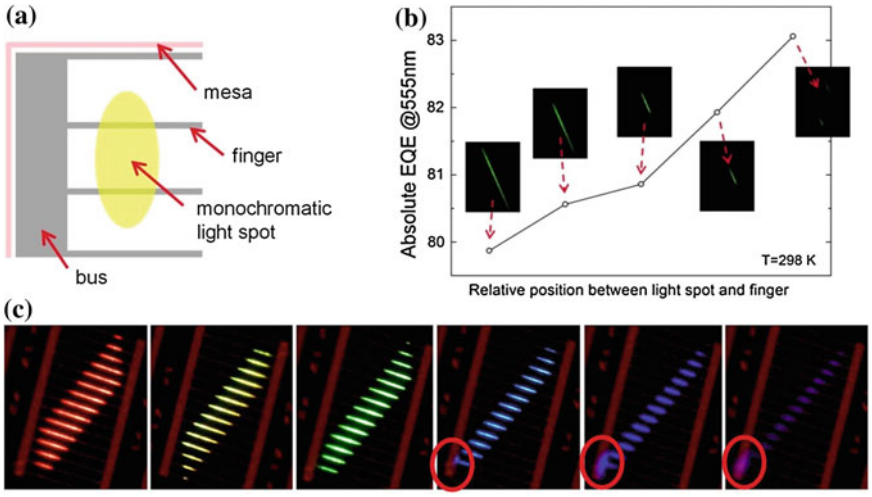

Fig. 3 **a** Sketch of a concentrator solar cell illuminated with a test light spot where the finger pitch is approximately as large as the spot dimension. **b** Example of a QE measurement as a function of the position of the test light spot. **c** Concentrator solar cell illuminated by different visible wavelengths

Chromatic aberration of the test light spot passing through the refractive optics of the QE system may also be responsible for a large artifact. This can be the case when the test cell and the test light spot have approximately the same size. Obviously, if the light spot is larger than the cell, an absolute measurement cannot be appropriately performed because part of the test light will be lost. However, chromatic aberration can make the light spot partly impinge the busbar when varying the test wavelength (Fig. 3c).

2.3.1 Light Bias

A light bias system with a special spectral distribution is one of the essential elements of a QE characterization system applied to MJSC. This is explained by the fact that series-connected circuits share a common current. A MJSC under illumination is limited (and commanded) by the p–n junction that generates the smallest photocurrent, and therefore a light bias is required to externally photogenerate an excess of current in the junctions that are not to be measured so that the one under test commands the device, and its response can be appropriately acquired. The photocurrent in excess produced in the junctions that are not to be measured is either radiatively and nonradiatively recombined by that same junction or performed through the shunt resistance.

In principle, a QE measurement must be performed at a certain current bias. Actually, because the QE feature can be used to calculate its I_{SC} at one sun (through the integration with the solar spectrum), a current bias level of approximately one

sun should circulate across the device. In general, the chopped test light from the monochromator is weak and very far from the one-sun (0.1 Wcm^{-2}) irradiance. As a result, the cell electrical response during the QE measurement is far from one-sun illumination conditions unless a bias light is also applied to the junction under test. However, when all of the junctions that constitute the MJSC have a linear response with respect to the incident light, there should be no need to apply such bias light also to the junction under test.

Another figure of merit of the light sources used to bias the different MJSC junctions is the power density provided by each of them. The larger the power density of the bias lights, the smaller the artifact associated with small shunt resistance of the cell. The effect of this artifact and ways to compensate for it will be discussed in an upcoming section.

Different types of bias light systems are generally used in commercial and homemade QE characterization systems:

- A set of lasers with a characteristic emission wavelength is centered within each of the junction QE response ranges. The laser provides an excellent power density, which is a positive point in favor of this choice. Regarding the linearity issue, the laser solution will be effective in case the power of the lasers can be tuned so that one of them is used to bias the junction under test close to one sun, and the rest of the coherent sources are used to saturate the rest of the junctions. Commercial lasers are not always tunable, and, in addition, their use may require increasing the security of the laboratory environment. Natural substitutes for them are the laser-diodes or directly the use of diodes with the maximum possible collimation to increase the power density.
- White light sources with optical filters, like the ones presented in the sketch in Fig. 2, are a versatile, easy-to-use, and inexpensive solution. Halogen lamps, whose light is redirected with optic fiber, and a set of long-pass, band-stop, and short-pass filters, such as the ones whose transmission responses are shown in Fig. 4c–e, respectively, can be used to provide the appropriate bias light. Actually, the bias of the junction under test can be tuned simply by choosing a different cut-off wavelength for the filters. The negative point in this case is that high irradiances are not easily achieved with these white light sources.

Typical QE signatures from a triple and quadruple MJSC are shown in Fig. 4a, b, respectively. A quadruple cell with a bandgap distribution approximately such as the one shown here has recently obtained a record efficiency [5]. Each of the junctions from the MJSC requires a light bias with a particular spectrum to be measured. These lights have been obtained in this case by means of halogen lamps tuned with long-pass, band-rejected, and short-pass filters as the ones represented in that same figure.

2.3.2 Voltage Bias

The application of an external voltage bias is also an important element in the QE characterization applied to MJSC. The reason is that the junction under test must be

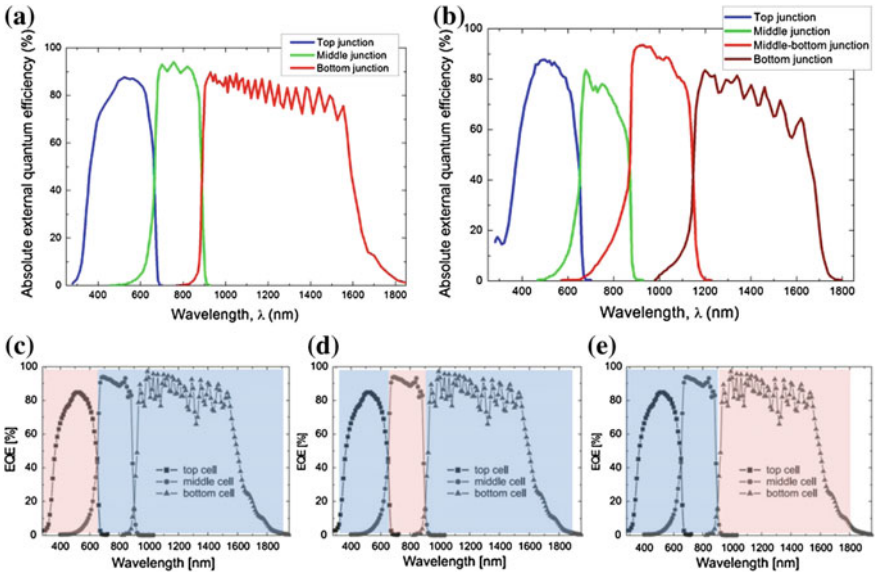

Fig. 4 Absolute QE of a triple-junction cell (**a**) and a quadruple-junction cell (**b**). **c**–**e** show long-pass, band-stop and short-pass filters, respectively, selected to measure the QE of top, middle and bottom junctions. *Blue* and *pink* colors represent the transmitted and filtered components, respectively (color in online)

at zero volts during its characterization, and the difficulty with this is that the MJSC is a series-connected, two-terminal device with no access to any of the intermediate terminals. The external voltage (V_{ext}) at the cell terminals equals the sum of the individual voltages of the junctions. A voltage bias produced by an external source must be applied to provide the appropriate bias conditions to the test junction.

The voltage scheme of the MJSC is expressed in Eq. (2), where V_{top}, V_{middle}, and V_{bottom} are the bias voltage of the top, middle, and bottom junctions, respectively. According to this simple relationship, we can deduce that the junction under test would be reverse-biased if no V_{ext} is applied (i.e., for $V_{ext} = 0$ V) because it would become naturally biased at a reverse voltage equal in absolute value to the sum of the other two junctions' voltages.

$$V_{ext} = V_{top} + V_{middle} + V_{bottom} \tag{2}$$

A graphic representation of the I–V curve of the MJSC, including each individual subjunction I–V curve, is presented in Fig. 5a. In this case, the operating point of the electrical-equivalent circuit of the triple-junction cell corresponds to a situation where a QE experiment is being performed on the top junction with no external voltage bias ($V_{ext} = 0$ V). The monochromatic test light is absorbed by the top junction, and the two other sources of bias light are absorbed by the middle and

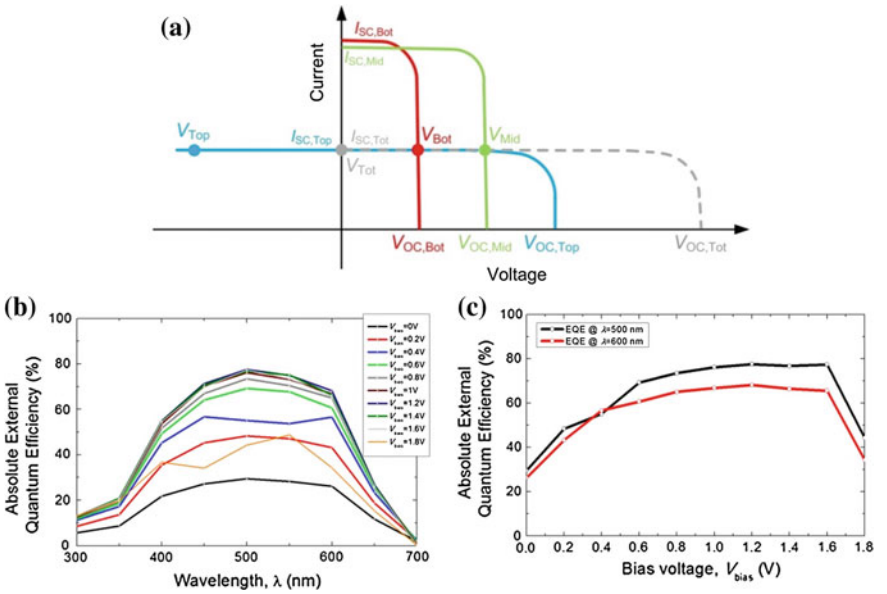

Fig. 5 **a** Sketch of the I–V curves of the MJSC (*dashed gray*) as well as from each of the other subcells. The top cell of the triple-junction cell is represented with a *solid blue line*, the middle cell with a *green solid line*, and the bottom cell with a *red solid line*. **b** QE as a function of V_{ext}. **c** QE at λ = 500 nm and λ = 600 nm as a function of V_{ext} from 0 V to 1.8 V (color in online)

bottom junctions. The test light from the monochromator is supposed to have a much lower irradiance, which is the reason why $I_{SC,Top}$ is lower than $I_{SC,Mid}$, and $I_{SC,Bot}$ and equal to $I_{SC,Tot}$ (short-circuit current measured at the whole-device terminals). This same electrical operating point could also correspond to a situation where an additional bias light illuminates (with a lower irradiance than the other two bias lights) the test junction. This strategy would pursue biasing the total device current close to the one-sun operation point. As represented in the figure, the voltage distribution of the MJSC is as follows: because no external voltage is applied, the transimpedance amplifier imposes zero volts on the cell output voltage and V_{Tot} as well as the middle and bottom junction operating voltages, V_{Mid} and V_{Bot}, are close to their corresponding V_{OC}; therefore the test junction operating voltage, V_{Top}, becomes reverse-biased at approximately—($V_{OC,Bot}$ + $V_{OC,Mid}$). Because this is unacceptable for the QE measurement of that p–n junction, a compensating external bias voltage of $V_{ext} \sim (V_{OC,Bot} + V_{OC,Mid})$ must be applied on the MJSC terminals to impose $V_{OC,Top} = 0$.

Once it has been stated that an external voltage must be applied during the measurement of the QE of an MJSC, the procedure to select the appropriate value will be detailed. First, it must be added that the estimation of this V_{ext} depends on the cell internal voltage distribution, i.e., the voltage supplied by each junction, which cannot be directly measured. The V_{ext} selected for each subcell measurement depends on the V_{OC} of the MJSC, which in turn depends on the number of subcells

of the structure, the bandgaps of the different materials that constitute each subcell junction, and the spectral irradiance of the bias illumination.

As recommended in Ref. [6], V_{ext} must be obtained from the sum of the mean values of V_{OC} and voltage at the maximum power point (V_{MPP}) of all subcells not to be measured, i, regarding bias light conditions: $V_{ext} = 1/2 \sum_i \left(V_{OC}^i + V_{MPP}^i\right)$. But these values cannot be easily known for a particular illumination and corresponding spectral distribution. Therefore, a simple method is here proposed and exemplified for a triple-junction cell:

- Sum all bandgaps present in the structure:
  $E_G(\text{sum}) = E_G(\text{Top}) + E_G(\text{Mid}) + E_G(\text{Bot})$
  $= 1.85\,\text{eV} + 1.4\,\text{eV} + 0.75\,\text{eV} \;\; = 4\,\text{eV}$
- make a proportionality coefficient (C_j) for each junction:
  $C_{Top} = 1 - (1.85/4) = 0.54;\; C_{Mid} = 1 - (1.4/4) = 0.65;$
  $C_{Bot} = 1 - (0.75/4) = 0.81.$
- and measure the cell V_{OC} provided by the bias light used for the measurement of the QE of each junction (V_{OC}^j) :
- Apply $V_{ext} = V_{OC}^j \cdot C_j$

At this point, an assumption is made regarding a linear relationship between the V_{OC} of a subcell and its material bandgap (E_G) for all of the junctions present in the structure when illuminated equivalently. This approximation is reasonably verified if only direct III–V semiconductor materials subcells constitute the MJSC, although a correction factor must be used when an indirect bandgap material is present. A correction factor may also be required when the difference between the irradiance with which a particular test junction is illuminated is much larger than the irradiance used for biasing the rest of the junctions during that measurement.

The QE of a junction is particularly sensitive to the applied external voltage when the shunt resistance is degraded. An example of the influence of V_{ext} on the QE measurement of a junction with a relative small shunt is shown in Fig. 5b. In this case, the whole QE curve is measured with a 50-nm step for V_{bias} between $V_{ext} = 0$ V and 1.8 V. At low V_{ext}, the junction is reverse-biased, and its QE is small. The response increases as V_{ext} increases until it reaches approximately 1 V where it remains relatively stable for a wide range of V_{ext}. For V_{ext} close to the cell V_{OC}, in this case 1.8 V, the QE collapses. Figure 5c shows the evolution of the response of the junction for two particular wavelengths, λ = 500 nm and λ = 600 nm.

2.3.3 Artifacts Caused by Shunt Resistance and Radiative Coupling

A junction affected by a small (degraded) shunt resistance presents a typical artifact consisting of the response of an adjacent junction throughout its whole absorption range [6, 7]. This is often the case in the current commercial triple-junction, lattice-matched structures (GaInP/GaInAs/Ge). Actually, the Ge bottom junction is

usually characterized by a relatively poor shunt resistance, which presents a strong artifact response in at least one of the adjacent cells (mostly in the middle subcell). The explanation of the physical mechanism that produces this artifact is out of the scope of this work, and its fundamentals are extensively reviewed in Ref. [6]. The work by Meusel et al. also explains that the magnitude of the artifact depends on the irradiance level of the external bias light. Therefore, increasing the intensity of these bias lights directly impacts this parasitic response, the origin of which (low shunt resistance) cannot be avoided.

The artifact, when present, is easily recognizable in the absolute QE from the bottom cell of a commercial triple-junction cell such as the one shown in Fig. 6a. It presents a scaled version of the middle junction response in the same absorption range of that junction (between 670 and 880 nm) corresponding to the short wavelengths of the black solid curve in the figure. Another effect of the artifact is the decrease of the QE signature corresponding to the actual absorption range of the bottom junction (from 880 to 1800 nm). Actually, Siefer et al. [8] deduced that the loss of response in the bottom cell range is proportional to the artifact manifested in the middle cell absorption range. Their work also proposes a procedure to compensate and correct this parasitic response to obtain the artifact-free real response of the bottom junction (gray solid line in Fig. 6a). The correction procedure, based on data treatment, is here detailed:

- Plot both middle and bottom cell absolute external QE in the same graph. Scale down the whole middle junction QE until reaches the parasitic level produced by the bottom subcell. The scaling factor (Sf_{mid}) will be later used in the data treatment.
- Subtract the scaled middle cell QE from the bottom cell QE only in the range of the middle cell spectral response.

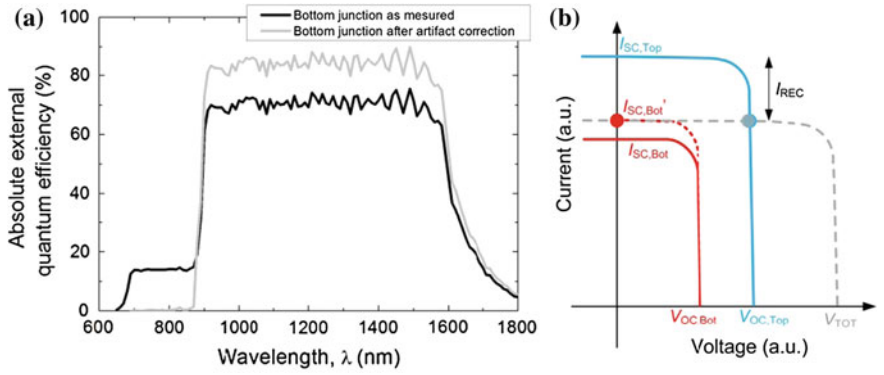

Fig. 6 **a** Bottom cell of an MJSC before and after data treatment used to correct the artifact caused by shunt resistance. **b** Sketch of I–V curves corresponding to subcells showing the radiative coupling

- Correct the bottom junction response within the range corresponding to wavelengths longer than the absorption threshold of the middle junction (generally from 880 to 1800 nm) by dividing the QE values by $(1 - \mathrm{Sf_{mid}})$.
- Plot together the result of the subtraction between the parasitic response of the bottom cell and the scaled middle cell within the absorption range of the middle cell and the rest of the bottom response scaled up a factor $1/(1 - \mathrm{Sf_{mid}})$ to compose the corrected artifact-free bottom absolute external QE.

The integration of the new bottom QE curve with the solar spectrum will now correspond to the photogenerated current produced by this junction, which was not the case with the curve directly obtained from the measurement comprising the artifact and before data treatment correction. Therefore, the corrected QE can be reliably used to adjust a solar simulator for a measurement of the I–V curve.

Luminescence or radiative coupling effects produced by the radiative recombination of the higher bandgap junctions of an MJSC at an energy corresponding to their bandgap edge [as in a light-emitting diode (LED)] and toward the smaller bandgap junctions is another performance feature that has gathered the attention of the scientific community lately [9–12].

Once the higher bandgap junction has emitted through the next junction and this has absorbed the incoming flux (the junction next to it has the largest probability of absorption of the light rather than the lower junctions because (1) it is located before in the optical path and (2) its absorption coefficient is generally greater than the smaller bandgap cell), this intermediate junction can reemit to the smallest junction in a cascade process. Regarding the emission from lower-bandgap junctions, any luminescence from the bottom junction that is not reabsorbed is lost. The QE signature of a junction affected by radiative coupling shows a tail in the QE response range corresponding to the junction that is at the origin of the emission and a decrease of the QE level within the absorption range of the junction. The effect is thus similar to the one already tackled regarding the low shunt resistance artifact. It is important to note that although the QE tail is produced by a particular measurement condition, its presence does not necessarily imply that radiative coupling will take place in the same way under realistic operating conditions [13].

High-quality, direct-bandgap junctions have a large radiative-to-nonradiative recombination ratio and emit in the surrounding of the bandgap wavelength when operating in relatively large forward bias, which is the normal operation under real conditions. This emission is captured by the lower junction, thereby creating an extra photocurrent. This effect is sketched in Fig. 6b where the I–V curves of the top and bottom individual junctions of a double-junction cell, denoted as “top” and “bot” in the plot and respectively represented in blue and red solid lines, are represented together with the I–V curve measured on the device terminals. In this case, the high-bandgap or top cell produces a strong radiative coupling, and most of its emission is absorbed by the low-bandgap or bottom junction rather than sent out of the cell through its front surface plane. Equation (3) is then verified, where $I'_{\mathrm{SC,Bot}}$ and $I_{\mathrm{SC,Bot}}$ are the short-circuit currents of the bottom junction with and without taking into account the radiative coupling, and I_{LC} is precisely the current produced

by the radiative coupling from the top cell into the bottom cell. The fact that most of the emission from the top cell radiative recombination is directed to the junction underneath instead of escaping from the front surface of the device happens because the difference between the refractive index of the medium out of the cell and that of the top junction is large (note that $n_{out} = 1$ and $n_{in} > 3.5$) compared to the difference in refractive index between the two subcell semiconductor materials. Luminescence from the top junction enhances the photocurrent of its adjacent junction, thus shifting its I–V curve upward. This in turn shifts the operating point of the top junction up and therefore decreases the recombination current, which then decreases the luminescence in an iterative process [11]. The dashed red line represents the equilibrium I–V curve of the bottom cell once the photocurrent produced by the radiative coupling has been taken into account. The difference between the top cell short-circuit current ($I_{SC,Top}$) and $I'_{SC,Bot}$ is denoted as I_{REC}. This value corresponds to the total excess of current photogenerated in the top junction that will recombine within that junction, so that (4) is verified. The dashed gray line represents the equilibrium I–V curve of the tandem.

$$I'_{SC,Bot} = I_{SC,Bot} + I_{LC} \tag{3}$$

$$I_{SC,Top} = I'_{SC,Bot} + I_{REC} \tag{4}$$

Steiner et al. proposed in [9] a method to identify, measure, and correct the radiative components produced by a particular measurement conditions so the appropriate QE signatures can be obtained. The latter allows tuning the solar simulator so that realistic one-sun conditions prevail.

2.4 *Influence of the Incident Angle and Temperature on the QE Applied to MJSC*

The QE of a solar cell has a dependence on temperature as has been reviewed in the previous chapter [14]. As the temperature increases, the bandgap of a semiconductor material decreases, and this produces a shift in the optical absorption edge. A sketch of the temperature-dependent external QE of the top and middle junction is shown in Fig. 7a, b. As the temperature increases, the decrease of the QE at high wavelengths shifts toward longer wavelengths. The figure shows how the short wavelength edge of the top cell remains the same because it only depends on the absorption edge of the window layer and the corresponding surface recombination velocity. This will be the case unless the window layer also suffers a noticeable shift with temperature. The shift produced in the long wavelengths of the top junction at high temperature is proportional to the shift suffered by the short wavelengths of the bottom junction at those same temperatures. A systematic work on the influence of temperature on the GainP/Ga(In)As/Ge triple-junction cell, including a thorough analysis of its effect on each junction of the QE, can be found in references [15, 16].

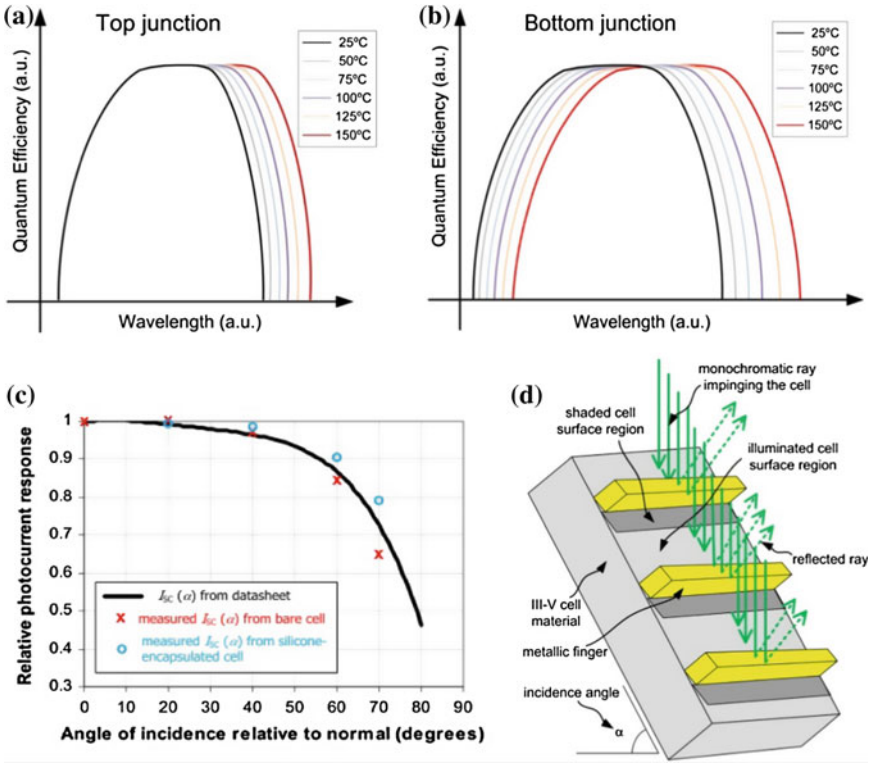

Fig. 7 **a**, **b** Sketch of the QE of the top and bottom junctions of a MJSC as a function of temperature. **c** Relative photocurrent response as a function of the incidence angle, $I_L(\alpha)$. Data from the datasheet are shown together with data from QE characterization from two samples, i.e., with and without a silicone encapsulant. **d** Sketch of a concentrator cell surface and incident rays in a situation where the fingers are orientated transversal with respect to the plane of tilt

Relative photocurrent response as a function of the incidence angle, $I_L(\alpha)$, such as the one shown in Fig. 7c, is a common figure of merit that can be found in commercial MJSC datasheets. Such a characteristic (represented in the figure with a dark solid line) is acquired by means of I–V characterization; however, it can also be obtained from angular-dependent analysis of the absolute QE. Figure 7c represents $I_L(\alpha)$ obtained from the integration of the absolute QE of the limiting junction of an equivalent MJSC described by the datasheet curve for two cases, i.e., with and without a silicone encapsulant (respectively represented by blue hollow circles and red crosses).

QE characterization as a function of the incidence angle (α) and temperature can also be used to study the optical coupling between the ARC and the transparent element used to encapsulate the cell in certain concentrated photovoltaic (CPV) configurations (a silicone-based material generally is used). This optical coupling is modified because of the dependence of the refractive index with

temperature, which modifies the design conditions. This optical coupling has a direct effect on the spectral response of each subcell. A performance analysis of each individual junction of the MJSC for the case of a bare cell and a silicone-encapsulated cell is assessed in [17] to evaluate differences in the optical coupling for each junction as a function of α and T.

Some subtleties exist regarding the QE characterization procedure of a concentrator cell as a function of α. Figure 7d shows a sketch of a concentrator cell with the metal fingers transversally oriented with respect to the plane of tilt. Under this configuration, the metallization is expected to block a significant part of the incident light. This shading produced by the fingers decreases the measured absolute QE, and therefore the I_{SC} obtained is underestimated. Conversely, a longitudinal orientation does not block the incident light. There is not a bad or a good way to orient the finger metallization with respect to the tilt plane because under real illumination inside a concentrator, the light bundle will impinge at every angle; however, at the very least, the measurement of the different samples should be performed under the same conditions.

3 Eectroluminescence

Electroluminescence (EL) is another characterization technique that is widely used for the characterization of an MJSC. It is based on the application of an external current bias (I_{bias}) to the cell (in the opposite direction of the photogenerated current) that is transported through the p–n junction associated diodes and produces a separation of its quasi-Fermi levels, which in turn induce carrier recombination within the cell. Part of this recombination is nonradiative (e.g., Shockley Read Hall and Auger), but another part is radiative, which consists of the emission of photons. Part of these photons are emitted within the cell volumen; they are reabsorbed by the semiconductor (this phenomenon is known as "photon recycling"), and others are emitted out of the cell by its front surface as occurs in an LED. When the semiconductor recombines radiatively, a flux of photons of energy close to the material bandgap is created. Actually, the emission is a Gaussian distribution centered on the wavelength corresponding to the semiconductor bandgap. In the case of an MJSC subjected to EL, the voltage bias corresponding to the current injected into the device is divided into the different p–n junctions, creating a voltage difference in each of them, which in turn is associated with a particular luminescence. Therefore, an MJSC composed of n subcells that are subjected to EL will produce a luminescence of n populations of photons, each of them characterized by photons with energies corresponding to each of the n bandgaps. In most cases, the subcell materials from a high-efficiency concentrator MJSC are III–V semiconductors characterized by direct bandgaps, which have a strong emission, contrary to indirect semiconductor materials such as silicon. Actually, the bottom junction of the conventional lattice-matched MJSC approach (GaInP/Ga(In)As/Ge) is made of Ge, an indirect group IV semiconductor, the emission of which is much less strong than the emission from the middle and top junctions.

This characterization technique has been applied in its spatial resolution format to Si cells allowing the determination of some important diode parameters such as minority carrier diffusion lengths [18–20] or the series resistance component produced by the front-grid metallization [21]. In turn, the spectrally resolved version of the EL can be used to gather information on the mechanisms related to the recombination of the cell [22]. This can be performed thanks to the reciprocity relation between QE and EL [23]. Regarding MJSC, other more complex techniques have been developed to extract information and enable accurate modeling on sheet and shunt resistance present in individual subcells using a combined EL and photoluminescence technique that avoids the coupling effects between subcells.

There are two main types of EL characterizations applied to MJSC, both of which are shown in Fig. 8:

- Spatially resolved EL, in which the MJSC, placed on a thermally regulated chuck, is excited by an external I_{bias} produced by a current (or a voltage) source. It produces an EL flux that is spectrally selected by a bandpass filter (so that only one of the subcells is imaged) before being detected by a charge-coupled device (CCD) camera where the emission is captured, digitalized, and sent to the computer for subsequent data treatment. The data resulting from this characterization technique consists of an image of the EL intensity map exiting the front-surface of the device corresponding to each of the junctions that constitute the MJSC.
- Spectrally resolved EL (Fig. 9), in which the EL is captured by a concentrator optics which sends it to the entrance of a monochromator before passing through a chopper wheel that modulates it to create a synchronous signal that will be later demodulated by means of a lock-in amplifier. The different spectral components of the emission are selected by the monochromator, which are redirected toward a calibrated detector. This detector, made of a semiconductor material of a bandgap lower or equal than the bottom cell material bandgap, produces a current signal proportional to the monochromatic light received and

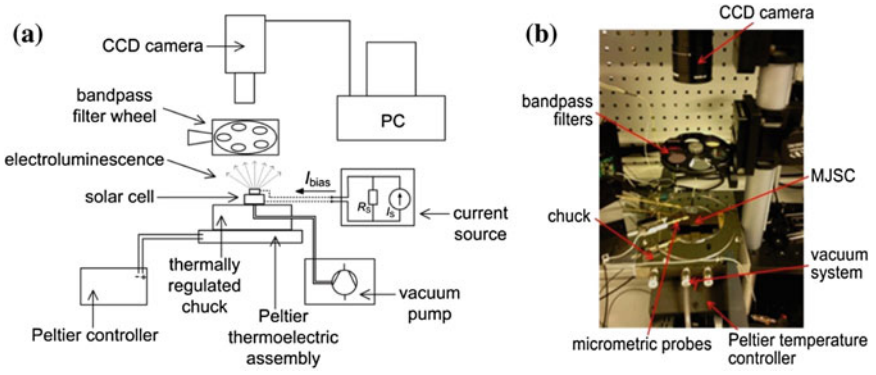

Fig. 8 **a** Sketch of a spatially resolved EL system. **b** Picture of the EL system with descriptions of the parts

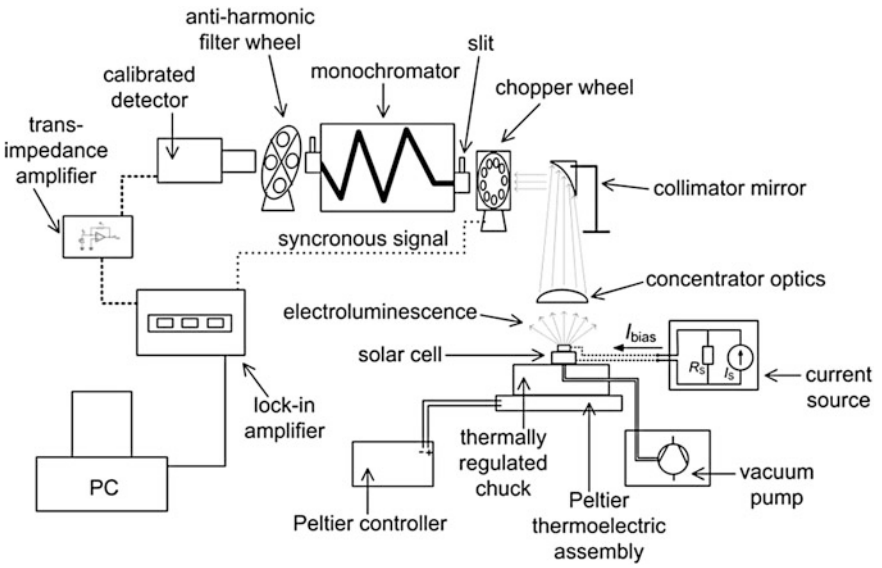

Fig. 9 Sketch of a spectrally resolved EL system

sends this signal to a transimpedance amplifier, which amplifies and converts it to a voltage signal that can be processed by the lock-in amplifier. The lock-in reads the actual value of the emission of the MJSC at each particular wavelength and sends this information to the computer that commands the whole EL system. The spectral information is then reconstructed to show the peaks corresponding to the emission from the cell.

3.1 Spatial EL

As shown by the work of Zimmerman on EL applied to the characterization of MJSC [24–29], this technique can be useful for the identification of defects present in these devices.

3.1.1 Shunt-Type Defects

Shunt-type defects can appear in MJSC during different stages of the production of the CPV receiver used in CPV modules, i.e., during the epitaxial growth of the wafer, during the processing of the metal contacts and mesa patterns of the cell, or even during the dicing or the encapsulation of the individual cells into the receivers. These kinds of defects can also be formed and enlarged during the life cycle of the

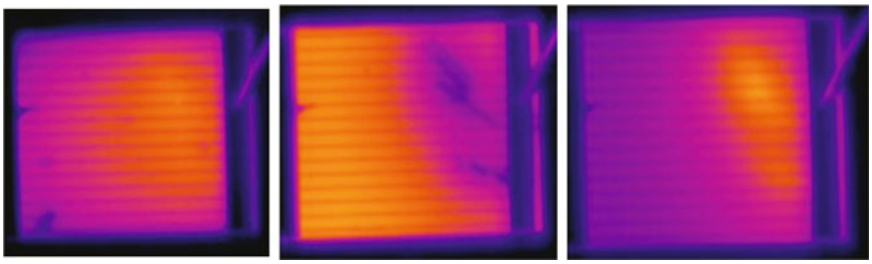

Fig. 10 Example of spatial EL showing a large shunt defect in an MJSC

CPV system. In any case, spatial EL is a useful technique to identify these defects, and it is actually the most commonly used technique, together with the dark I–V curve, to assess the degradation of the devices after accelerated aging experiments [29–33].

Shunt defects, often found on the Ge junction of GaInP/Ga(In)As/Ge commercial triple-junction cells, are expected to decrease the lifetime of a CPV system because the current leaked through them heats up locally a spot of the cell producing a thermal runaway that can trigger a chain effect that is one of the main drivers of infant mortality. A shunt defect located in one of the junctions of an MJSC is observed as a dark region in that junction. This is caused by the alternative path that exists for the injected current, which is now transported through the lower shunt resistance instead of through the diode. This in turn creates a lower biasing of the associated diode (i.e., lower quasi-Fermi level separation), which decreases the radiative recombination or EL. The adjacent junctions show a brighter EL caused by redistribution of the current in the surroundings of the shunted area, which induces a greater current density through the shunted cell element, in turn producing a higher bias and a correspondingly greater luminescence. An example of the EL signature from an MJSC affected by a shunt defect is shown in Fig. 10.

3.1.2 Other Defects Present in MJSC Imaged by EL

Shunts are not the only defects that can be imaged by EL. The technique can be used to identify possible cracks in the structure derived from the mechanical stress to which the whole device is subjected. Surface defects such as scratches—occuring during manipulation of the cell while it is being mounted on the carrier or CPV receiver, from semiconductor inhomogeneities produced by growth defect, or from semiconductor damage from any other origin—can also be imaged by EL. In all of these cases, the emission from dark areas corresponding to the defects is not generally more intense in the adjacent junctions. However, it is important to verify that the defect observed by EL is not caused by a particle deposited on the front surface of the cell that can be easily removed by blowing with clean air as it shown in Fig. 11a where an elongated thin particle produces a shade similar to a semiconductor crack. These particles can be identified by microscopy observation of the cell surface.

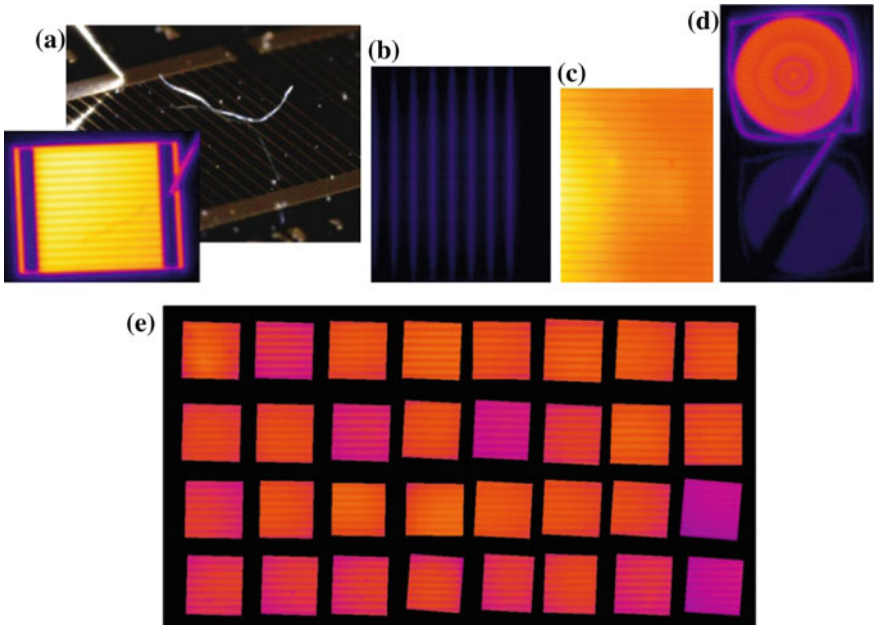

Fig. 11 **a** Elongated particle on a cell under EL. **b** EL from a junction with a high lateral resistivity. **c** Example of crowding effect produced from the busbar. **d** EL from the adjacent device to the one being contacted. **e** Image of the relative EL homogeneity analysis (RELHA) method for the wafer inhomogeneity characterization

Spatial EL can also be used to test the sheet resistivity ($\rho_{\square}$, measured in ohms/square or Ω/□) of a specific emitter layer. $\rho_{\square}$ is defined as ρ/t, where ρ is the emitter layer resistivity and t the thickness of the layer. Figure 11b shows the emission from an MJSC top junction with a high $\rho_{\square}$, where the so-called crowding effect is present. The crowding effect consists of the inhomogeneous distribution of the EL produced by a voltage loss gradient induced by the lateral flow of current. The model and simulation tool developed in [25] is based on this principle. In the case of the figure, the current injected by the bus bars flows through the fingers, and then, when it must be transported laterally throughout the whole surface, the high $\rho_{\square}$ hinders its lateral spreading, and the carriers recombine within the regions next to the fingers (actually the image shows the EL in false blue color apparently coming from the fingers because of diffraction effect produced by the thin metallization). The crowding effect is also shown in Fig. 11c and is caused in this case by the high series resistance introduced by the metal fingers when the current is injected from only one busbar. This effect can be used to test the validity of the front metallization, or the emitter thickness and/or resistivity, in terms of series resistance for a particular concentrated illumination (i.e., associated with an I_{SC} that

is not supposed to produce a significant voltage decrease throughout its transport within the semiconductor).

In Fig. 11d, a problem probably originating by a defective mesa is noted. Indeed, the mesa should electrically isolate the cells in the wafer; however, in this experiment the cell adjacent to the one contacted with the probes emits when biased, thus implying that part of the current flows from the contacted cell to the one next to it.

Relative EL homogeneity analysis can be applied to processed wafers before dicing. This technique allows the diagnosis of the wafer crystalline homogeneity at each junction level by mapping the EL signature (acquired under precisely the same electrical and optical conditions) of individual cells throughout the whole wafer [34]. An example of this is shown in Fig. 11e where the different (false) colors of the EL from each cell define an epitaxial quality mapping.

EL has also been proposed for the identification of thermal inhomogeneities induced by the presence of voids at the bonding interface between the rear metallization of the cell and the substrate. This technique is applied by injecting very high currents that emulate the operating conditions of the MJSC under concentration such that the thermal runaway is produced and can be detected by this enhanced EL characterization [35].

3.2 Spectral EL

Spectrally resolved EL is a useful tool used to verify the bandgap of a particular subcell from the MJSC structure (by means of the wavelength of the EL peak) and the crystalline quality of the junction (intensity of the EL peak). In MJSC, it can be used together with the QE to infer the internal distribution of the cell external voltage between the different subcells present in the structure as well as the diode-quality factor [36–38]. The technique, authored by T. Kirchartz, analyzes EL spectra at different injection intensities and employs the reciprocity theorem [23] to derive the I–V curves of each individual junction. The reciprocity theorem relies on the following equation:

$$\phi_{\text{emission}}(E) = \text{QE}(E) \cdot \phi_{\text{blackbody}}(E) \cdot \left[\exp\left(\frac{qV}{kT}\right) - 1\right] \tag{5}$$

where ϕ_{emission} is the spectral emission, $\phi_{\text{blackbody}}$ is the blackbody photon flux, V is the internal voltage applied to the p–n junction, and kT/q is the thermal voltage.

Spectral EL as a function of temperature has also been studied [39] showing subcell V_{OC} and carrier concentration. This technique has also been experimentally verified for V_{OC} measurements acquired under concentrated illumination. The extraction of the subcell bandgaps allows identifying an increase of temperature produced by an enhancement in current density.

4 I–V Characteristic

The I–V curve of a solar cell is probably the most common characterization in photovoltaics and in MJSC in particular [40]. It renders valuable information on the electronic properties of the p–n junction when measured under dark conditions and allows studying the electrical performance, such as I_{SC}, V_{OC}, fill-factor (FF), and efficiency (η), when acquired under illumination. The dark curve of a solar cell is a useful tool to monitor the degradation of a solar cell during a particular operation period (which can be the normal degradation over time or the product of an accelerated process) or possible damage that occurred during manipulation (e.g., bonding or encapsulation) of the cell. In the case of the dark curve of the cell, the electronic parameters of the diode and the associated series and shunt resistance can be fitted to a model. The Shockley model of the diode is often used employing one or two diodes. In the second case, two recombination regimes are identified: (1) the low-voltage regime, which is dominated by Shockley Read Hall recombination in the space charge region and characterized by a low exponential slope in the range of $q/2kT$, where q is the electric charge, T is the temperature, and k is the Boltzmann constant and (2) the high-voltage regime, which is dominated by recombination in the neutral zones and characterized by an exponential slope of q/kT.

This type of characterization requires a simple set-up easily implementable in any laboratory. Figure 12 shows two types of systems proposed for the measurement of the I–V curve where the solar cell is represented on the left with a current source in parallel with a diode. The set-up from Fig. 12a can be used under illumination and is based on a variable load that takes the role of the power supply, providing the cell biasing, which is swept within the operation range of the cell, and the voltmeters register both the cell voltage (V_{cell}) and current (I_{cell}) as the measurement of the voltage at the calibrated shunt terminals.

A measurement performed with a source-meter in four-wire mode is shown in Fig. 12b. In this case, the power supply (I_{source}) can be set to the current or voltage source. In the first case, the current from the source is synchronized and commanded by the reading from the ammeter I_{meter}, which provides feedback to adjust I_{source} to the

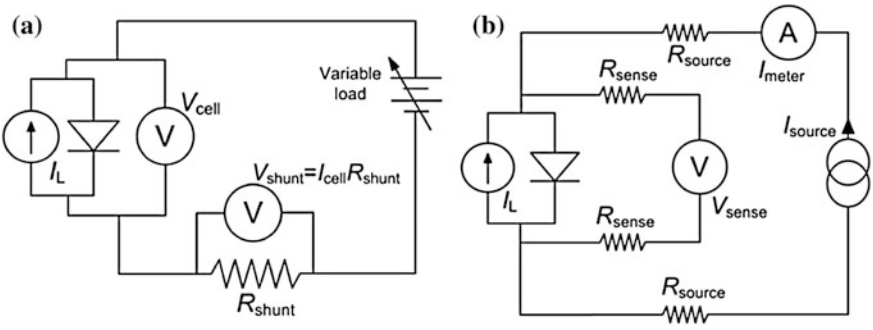

Fig. 12 Typical I–V characterization set-ups. **a** A system based on a variable load and **b** a system based on a source-meter in four-wire mode

desired current level, and the voltage is measured by V_{sense}. In the voltage source mode, I_{source} is commanded by V_{sense}, which provides feedback to fix a particular cell-voltage bias. The current is measured by the ammeter. In both cases, two physically independent circuits, called "sense" and "source," are present allowing the sense circuit to drain a negligible current because the impedance of the voltmeter is very large. As a consequence, the voltage decrease in the resistance associated with the sense circuit, R_{sense}, is also negligible, and V_{cell} measures the actual voltage at the cell terminals (this requires the shortest and less resistive common electrical path between sense and source circuits before the cell terminals so that the voltage decrease remains small). The resistance of the source circuit does not affect the measurement in this case because a voltage decrease induced in this circuit only demands a greater voltage on I_{source} terminals. The four-wire mode is suitable for high or medium current measurement, whereas the conventional two-wire mode is suitable for very low current measurements. The latter is a consequence of errors in the current reading produced by the current drained through the sense circuit because of the noninfinite impedance of the voltmeter, which allows the conduction of very small currents (they can be in the range of pA in a performing source-meter) in the circuit in parallel to the one where the actual measurement is performed. The two-wire mode must be selected, which modifies the source-meter circuitry and allows the measurement of the voltage on the I_{source} terminals.

Most I–V set-ups implement techniques to decrease the noise of the measurement either by repeating each point multiple times, repeating the whole curve multiple times (and averaging afterwards), or increasing the time constant related to the duration of the acquisition.

5 Cell Testing Under Concentrated Light

The ultimate performance indicator for concentrator solar cells is their I–V curve under high light intensity, i.e., test conditions resembling real operation within a CPV module. This section describes state-of-the-art characterization techniques for solar cells under concentration, notably at the solar simulator. Typical simulator requirements, measurement procedures, instrumentation issues, and performance parameters are detailed in this section. Most subtleties are linked to the use of monolithic multijunction cells, which are very sensitive to the incident spectrum because of their internal series connection.

5.1 International Standards on Concentrator Cells

International standards organizations, such as American Society for Testing and Materials International or International Electrotechnical Commission (IEC), have issued several standard specifications and test procedures on the calibration and

characterization of PV cells. In particular, ASTM standard E2236-10 describes methods for determining the performance of nonconcentrator MJSC [41]. However, no international standard is yet available on the measurement of concentrator solar cells.

Only very recently has the IEC issued technical specification IEC TS 62789 on the parameters to be specified for concentrator PV cells, both multijunction and single-junction, with recommendations on appropriate measurement methods. Specifically, it defines the measurement conditions under which the concentrator cell performance must be reported [42]:

- Design irradiance in kW/m2 (equivalent to "suns"),
- spectral distribution AM1.5 direct (as specified in the future IEC 60904-3 Ed. 3.0, which is similar to the ASTM G173-03 distribution [43]), and
- 25 °C cell temperature.

Furthermore, IEC Technical Committee 82 is also about to release several other standards related to PV concentrators or MJ cells:

- IEC 60904-1-1: Measurement of current-voltage characteristics of multijunction PV devices. It will describe requirements and measurement conditions to be fulfilled specifically when measuring the I–V curve of a multijunction cell.
- IEC 60904-3 Ed. 3.0, Photovoltaic devices–Part 3: Measurement principles for terrestrial PV solar devices with reference spectral irradiance data. It will include the reference spectral irradiance distribution AM1.5 direct.
- IEC 60904-9 Ed. 3.0, Photovoltaic devices Part 9: Solar simulator performance requirements. The upcoming norm will extend the requirements to take into account MJSC.
- IEC 62787, CPV solar cells and cell-on-carrier assemblies (reliability qualification).

5.2 Solar Simulators

Solar simulators are used to measure solar cells under readily available synthetic illumination and repeatable operating conditions. These devices illuminate a designated test area with a light that resembles the sun's light according to some predefined characteristics (typically spatial uniformity, temporal, stability and spectral distribution) in such a way that makes the device under test perform like under some predefined reference conditions.

A solar simulator also includes means for measuring said performance, i.e., the I–V curve of the device as well as the measurement conditions. At least light intensity, spectral irradiance and temperature are evaluated.

The quality and particular features required for a solar simulator depend on the purpose of the measurements to be performed. Calibration, power rating, or comparison between cell technologies require very low measurement uncertainty and therefore strict requirements for the simulator. Sorting of cells at the production line or qualification tests before and after some aging tests can allow, on the contrary, larger bias errors provided the repeatability (precision) of measurements is still high.

5.2.1 Requirements

The quality of solar simulators is classified according to three characteristics: the spatial uniformity of the irradiance, the match to a reference spectral irradiance distribution, and the temporal stability of the irradiance during a measurement (ASTM E927, IEC 60904-9, JIS C 8912). Each characteristic can be classified in three different levels according to the specifications met: A—the strictest requirements, and B or C—the most flexible requirements. No classification is given according to the angular distribution of the light beam over the receiver, although its description might be required. However, the aforementioned norms do not take into account requirements specific to multijunction cells or the use of concentration; thus, supplementary constraints must be considered.

Light Intensity

CPV cells have are evaluated over a wide range of concentration levels, typically from 1 sun to more than 1000 suns. The unit 1-sun refers to a total irradiance of 1000 W/m^2 under AM1.5 direct reference spectrum. Thus, the unit "kW/m^2" can be used interchangeably with "suns." The ASTM G173-03 is the international standard definition of AM1.5D spectrum, although an IEC version will be published in the third edition of the IEC 60904-3. The G173 spectrum actually integrates to a total irradiance of 900.1 W/m^2, so it is normalized to 1000 W/m^2 to achieve 1-sun conditions. Many laboratories count on one highly tunable solar simulator for the measurement at 1 sun and another one with less stringent specifications for high-intensity measurements due to the difficulty of tuning the spectrum of high-intensity simulators [44].

Spatial Uniformity of the Irradiance

Although concentrators hardly ever cast uniform light on the cell, spatial homogeneity is a typical requirement to solar simulators. If the intensity of the light is not uniform over the test area, uncertainty in the measurement of the incident irradiance is high and reproducibility of the results more difficult. The spatial nonuniformity of the irradiance is calculated through the maximum and minimum light intensities found over the defined test area. To do this, the irradiance is measured throughout a matrix of equally spaced test positions over the test plane. ASTM E927 gives detailed recommendations about the minimum proportion of the area that should be checked. Nonuniformity is calculated as the ratio between the difference and the average of the maximum and minimum values of irradiance. In IEC 60904-9, class A is achieved if nonuniformity is <2 % over the designated test area.

The size of the sensor has an influence on the measured uniformity. If a sensor in the same size as the device under test, irradiance variations with a shorter length might be hidden. Thus, a slight change in the location of the DUT aperture at the test plane would introduce unknown levels of measurement uncertainty (hidden bias error).

Depending on the concentration achieved by the simulator and its design, the irradiance map might be very dependent on the height of the solar cell aperture. Special care should be taken if the DUT and the reference cell are not the same height to perform proper irradiance corrections.

Furthermore, this nonuniformity map may well be a function of wavelength [45]. Therefore, if the device under test is an MJ cell, uniformity should be studied separately for the spectral region corresponding to each subcell. This is typically performed using component cells (i.e., single-junction cells with the same relative spectral response as the subcells in a MJ cell). When lamps are used, the spatial uniformity can also fluctuate with time.

Temporal Instability

Measurement uncertainty also depends on the stability of the irradiance during measurement of the I–V curve. In the case of pulsed simulators, this is measured using a reference cell simultaneously with the current-voltage pairs. For steady-state simulators, two readings before and after I–V curve measurement are enough to check stability. For multiflash measurements triggered by a light sensor, temporal stability has to do with the maximum variation of irradiance that can be found between the detection of the reference level and the acquisition of the I–V pair; thus, it actually depends on the sampling rate of the data acquisition system. Again, class A is achieved if the instability is not >2 %. Nevertheless, instabilities may be corrected through I–V curve translation procedures such as those defined in IEC 60891 norm [46].

Temporal fluctuations of the irradiance are wavelength-dependent [47, 48]; therefore, they should be evaluated for every spectral region of interest separately, i.e., using component cells if MJ cells are concerned [45].

Spectral Distribution

Under current international norms, the similarity between simulator and reference spectra is evaluated through the percentage of the total irradiance is found in different spectral ranges (typically 100-nm wide) [49]. The reference percentages are calculated from the integration of the AM1.5D spectral irradiance over each wavelength bin. A “spectral match” is then calculated for every interval as the ratio of the simulator percentage to the reference percentage. Class A is achieved if all ratios are within 0.75–1.25. Current norms were conceived for crystalline silicon devices, so the spectral match is only studied up to 1100 nm. Most III–V MJ cells will require extending the study down to the bandgap energy of the bottom junction, which is typically 1800 nm for Ge-based triple-junction cells.

The I–V curve of a two-terminal MJ cell is greatly dependent on incident spectrum due to the series connection of its subcells in series. Accurate measurements require the spectrum of the solar simulator to be adjusted such that the photocurrent of each subcell is the same as under a reference spectrum or that the

concentration level is the same for every subcell. In other words, the current balance between any two subcells must be the same as under the reference spectrum. However, the spectral match described previously cannot assure that the appropriate current balance is achieved; thus, significant measurement errors might be introduced even if a class A simulator is used [50].

Current Balance and Spectral-matching Ratio

Thus, spectral quality can be evaluated more significantly through the ratio of the current balance between two subcells under the simulator spectrum to that under the reference spectrum. This quantity is often referred to as the "spectral matching ratio" and is calculated as in (6). This ratio can be given for every pair of subcells—top to middle, middle to bottom, and top to bottom—in a triple-junction cell [51].

$$\mathrm{SMR}_{j-\mathrm{subcell}}^{i-\mathrm{subcell}} = \frac{\left(I_{L,i}^{E_{\mathrm{sim}}} \Big/ I_{L,j}^{E_{\mathrm{sim}}}\right)}{\left(I_{L,i}^{E_{\mathrm{AM1.5D}}} \Big/ I_{L,j}^{E_{\mathrm{AM1.5D}}}\right)} \tag{6}$$

The solar simulator should be capable of assuring a value of spectral-matching ratio (SMR) equal to one between every pair of junctions. This is equivalent to ask for the same concentration level at every subcell. Although implicitly given by previous conditions, we can also define the requirement of having the same subcell to limit the overall current as under reference spectrum.

Said requirement is obviously device-dependent, so this is more of a measurement consideration. The simulator requirement would rather be the possibility of having the spectrum tuned so that SMR = 1 is fulfilled. For solar simulators with a fixed spectrum that cannot be tuned, the SMR between every pair of junctions must be known to perform appropriate I–V curve corrections. Component cells matched to the subcells in the device under test are often used for this purpose. Depending on the way that the simulator spectrum can be adjusted (filtering, mixture of multisources, flash lamp triggering voltage, etc.), there may be only some types of multijunction cell technologies for which the SMR can be adjusted to 1. Therefore, information on which types of MJ cell technologies for which the simulator adjustable should be a simulator specification.

For lattice-matched, Ge-based triple-junction cells, it is usually assumed that a moderate mismatch in the spectral region of the bottom junction introduces negligible changes in the measured performance. First, the Ge subcell generates a large excess of photocurrent under the reference spectrum and therefore hardly limits the overall current. Second, the contribution of this subcell to the overall voltage is small, so even if the subcell voltage changes due to variations in the intensity of the bottom spectral region, the cell voltage is less affected. For instance, a 30 % excess of intensity in the bottom region would lead to an overestimation of the FF of only 1 % [52]. For these reasons, the spectral requirements can be somewhat relaxed for the bottom cell in this case.

This is no longer the case for the latest concepts of MJ with record efficiencies, in which either the bottom subcell current does not have such an excess of current (as in Ge-based metamorphic cells or in four-junction solar cells) or when other bottom cell materials with a larger bandgap energy are used. In these cases, imprecise spectral balance between any two subcells can lead to significant measurement errors, typically efficiency overestimations. For instance, a 30 % excess of intensity in the spectral region of a 1-eV GaInAs bottom subcell would lead to a 4 % error in the FF [53].

5.2.2 Types of Solar Simulators

The illumination system of a solar simulator typically comprises an optical assembly of one or more light sources and other optical elements that guide, collimate, mix, or homogenize the light to create the prescribed light beam over the test plane. Gas discharge lamps achieve the highest radiances, especially if they are pulsed. Flash lamps filled with noble gases can be triggered to conduct very large current densities for a short time producing radiances that resemble blackbody radiation with an equivalent temperature greater than that of the sun (approximately 5800 K). Xenon-filled flash lamps produce a high similarity with solar white light. The maximum intensity of flash lamps can be controlled varying the discharge voltage, which determines the maximum current density. Continuous Xe arc lamps are also used, but they produce very large spectral emission lines that must be carefully filtered. Moreover, their spectrum shows a red-shift with ageing, i.e., the proportion of power in the longer wavelengths increases with bulb use [54]. Their intensity can be controlled through the current load. In general, for the same irradiance level and illuminated area, a continuous illumination system requires greater complexity and provides poorer spatial uniformity of the irradiance.

Alternatively, tungsten halogen lamp arrays are also used, but they cannot provide the solar spectrum alone because they feature a low color temperature (in the range of 3000 K). Infrared light-rejecting filters (dichroic filters or "hot mirrors") are used to improve the similarity with the solar spectrum. Thus, they are frequently used as complementary lights for multisource solar simulators to precisely adjust the combined spectrum or even to perform spectral sweeps, which are useful for the characterization of multijunction devices [55]. Their intensity is varied with load current, so is their spectral distribution.

An arrangement of several light sources, spectral filters, and homogenizing lenses is usually required to create a continuous light beam with the necessary quality for a calibration laboratory [56].

Solar simulators can be either steady-state or pulsed. Depending on the measurement scheme, pulsed simulators can be either single-pulse or multiflash. Continuous and single-pulse simulators measure the whole I–V curve without interruption of the light intensity. Multiflash simulators, on the contrary, measure only one current-voltage pair per flash pulse (see Fig. 13). However, multiple irradiance values can be recorded during the same values, so the measurement

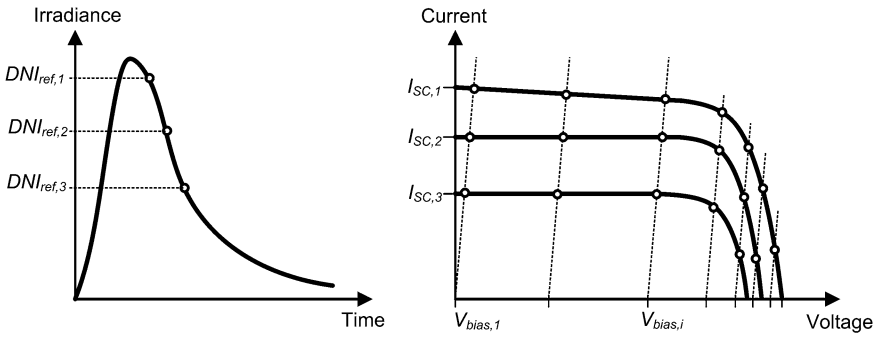

Fig. 13 Multiflash testing scheme. I–V points are taken at as many irradiance levels (DNI_i) as desired throughout the flash decay, which trigger the data acquisition (*left*). Each flash pulse is taken at a fixed bias voltage ($V_{bias,i}$), and both the current and voltage of the device under test are recorded simultaneously with the irradiance (*right*)

provides a family of I–V curves at different concentration levels [57]. This is a convenient feature when measuring concentrator cells, the performance of which must typically be analyzed as a function of a large range of concentration levels.

Single-pulse simulators generate a plateau of light intensity with the minimum duration possible to perform the complete voltage sweep. Because the irradiance must be stable during the pulse, the energy required is much greater than that of multiflash pulse. The fast voltage sweep of single-pulse measurements can introduce transient-related artifacts. Both multiflash and single-flash pulses may introduce transient artifacts in high-capacitance devices such as heterojunction or other high-efficiency silicon devices [58, 59]. Continuous simulators, on the contrary, can usually assume that the device is in electrical equilibrium.

Tuning Light Spectrum

When MJ cells are considered, simulator architecture becomes more complex to allow tuning the spectral balance between subcells. As a general rule, the larger the number of junctions in the device under test, the larger the number of spectrally tunable elements that must be incorporated. For instance, at Fraunhofer ISE, a three-source sun simulator is used for the calibration of triple-junction solar cells [60]. However, the mixture of different light beams can also be performed using a single light source but creating different optical paths whose intensity and spectrum can be independently adjusted and then combined together. The different light paths are created simply by taking different solid angles of the emitted angle, which are guided using mirrors [61], beam splitters [62], refractive optics, or fiber optics [63]. Dichroic mirrors or spectral filters are typically used to adjust the spectrum of each optical path [61–64]. Neutral-density filters (preferably metallic meshes) and diaphragm apertures are used for varying light intensity. The different light paths can be combined at the simulator output or at the test plane using integrator optics,

diffusers, or mirrors. A final stage for homogenizing and varying overall intensity is often used.

The Spectrolab T-HIPSS pulsed simulator uses a single high-intensity flash lamp and 19 mirrors with independent variable-aperture shutters and interferential filters to tune the spectrum on the test plane [61]. Each mirror reflects the light from the lamp toward the test plane so that the 19 images overlap. Each aperture is independently adjusted to create the desired spectral mixture. The overall intensity can also be adjusted by means of nickel meshes with variable transmission levels (from 0.1 to 60 %), thus achieving a range of intensities from 100 to 1500 suns. Optionally, a final mask can be used to enhance uniformity. The X-Sim Simulator, developed by Fraunhofer ISE and Aescusoft, uses 6 independent channels with a similar principle to tune the spectrum for MJ cells with up to 6 junctions [64].

Multiflash solar simulators introduce a valuable additional variable for spectral adjustments, i.e., the spectrum emitted by the lamp varies as the light intensity decreases [65]. Because only one current-voltage point is taken per pulse, the moment at which the point is measured varies the spectral conditions. However, this varies irradiance as well, so this adjustment must be compensated by the variation of other simulator features. For instance, purely mechanical adjustments, such as varying the distance between the lamp and the output or the opening of a diaphragm, can easily compensate irradiance variations.

A sample set-up of a low-cost concentrator solar simulator is shown in Fig. 14. It is able to measure the I–V curve of Ge-based triple-junction solar cells under variable concentration, i.e., less than 1 to more than 1000 suns [66, 67]. It uses the

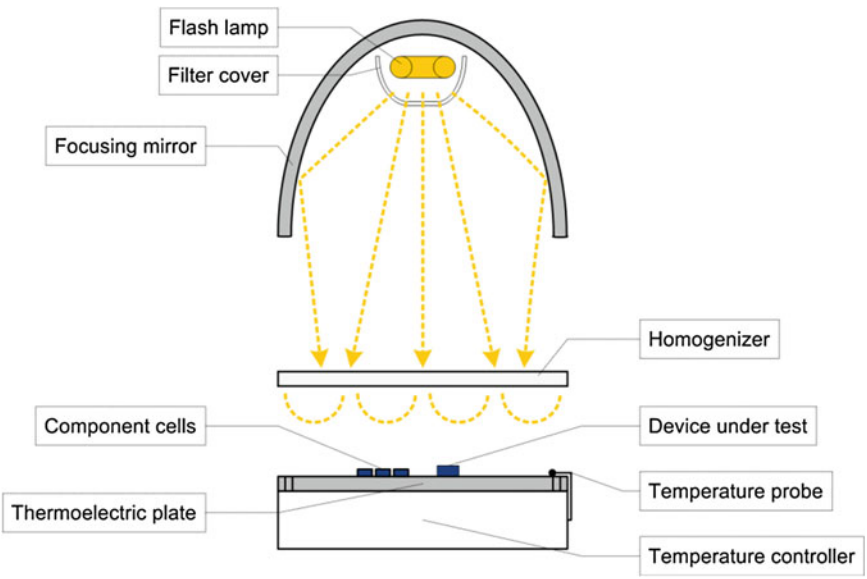

Fig. 14 Simple concentrator flash simulator developed at IES-UPM suns [66, 67]

decay of the flash pulse to produce the desired sweep of irradiance levels and spectra. But conversely, the irradiance here can also be changed by varying the distance from the lamp to the receiver plane, therefore keeping the same spectrum. Up to two additional stages of spectral filters can be included to add spectral flexibility (around the flash lamp and on the homogenizer at the simulator output). The simplicity of the concept has allowed Solar Added Value to prepare a commercial version of the system (Helios 3030-XX) for high-speed automatic testing of up to multiple receivers simultaneously.

5.3 Measurement Conditions

5.3.1 Irradiance and Spectrum

Light intensity or concentration level is typically measured at the solar simulator by means of a PV reference device. Truly radiometric (thermal) sensors cannot be used with pulsed simulators due to their slow response. Furthermore, reference PV cells matched to the device under test can filter out discrepancies between simulator and reference spectra outside the absorption region (otherwise collected by a thermal sensor). This decreases spectral mismatch corrections and hence uncertainty. Linearity between the incident irradiance and the photocurrent of the PV reference device is usually assumed to calculate effective concentration (X), as in Eq. (7). If linearity cannot be assumed, the reference cell must be calibrated at multiple concentration levels [50].

$$X = \frac{I_{\mathrm{SC,ref}} \cdot \mathrm{MM}}{I^{*}_{\mathrm{SC,ref}}} (\mathrm{suns}) \tag{7}$$

where I_{SC} is the short-circuit current of the reference cell under the simulator—taken as an approximation of its photocurrent—and I_{SC}* is its calibrated short-circuit current under AM1.5D reference spectrum and 25 °C cell temperature. MM is a mismatch factor that takes into account the differences in spectral response between the device under test ($\mathrm{SR_{DUT}}$) and the reference sensor ($\mathrm{SR_{ref}}$) in relation to both the simulator spectrum (E_{sim}) and the reference spectrum ($E_{\mathrm{AM1.5D}}$), under which the calibrated current has been obtained. It is calculated as defined in the norm IEC 60904-7:

$$\mathrm{MM} = \frac{\int \mathrm{SR_{ref}}(\lambda)\, E_{\mathrm{AM1.5D}}(\lambda)\, \mathrm{d}\lambda}{\int \mathrm{SR_{ref}}(\lambda)\, E_{\mathrm{sim}}(\lambda)\, \mathrm{d}\lambda} \frac{\int \mathrm{SR_{DUT}}(\lambda)\, E_{\mathrm{sim}}(\lambda)\, \mathrm{d}\lambda}{\int \mathrm{SR_{DUT}}(\lambda)\, E_{\mathrm{AM1.5D}}(\lambda)\, \mathrm{d}\lambda} \tag{8}$$

If the spectral response of the device under test and the reference unit are identical (i.e., the two cells are of the same technology), or if the simulator spectrum and the reference spectrum are identical, then MM = 1.

A multijunction cell cannot be used as a reference irradiance sensor because spectral conditions different from the reference AM1.5D might yield the same calibrated value if the limiting subcell changes.

Component "Isotype" Cells

When multijunction cells are concerned, concentration level or irradiance must be evaluated for each subcell separately [44]. The so-called "component cells" are used to estimate the photo current at each subcell and hence its concentration level. Component cells are single-junction cells with the same (relative) spectral response as each subcell in an MJ cell. A component cell is often grown using a similar stack of semiconductors as the multijunction cell but where only one junction is a diode. The others junctions are left electrically inactive by growing isotype junctions. This is why they are also known as "isotype" cells. The inactive layers are still optically absorbent, though, so the active diode in principle features the same spectral response as the subcell in the MJ cell.

If the photocurrent of the component cells under standard test conditions is known ($I^*_{Li-\text{component}}$), they can be used as reference sensors to calculate the effective concentration $X_{i\text{-subcell}}$ at which the subcells are operating under any particular simulator light:

$$X_{i-\text{subcell}} = \frac{I_{Li-\text{subcell}}}{I^*_{Li-\text{subcell}}} = \frac{I_{Li-\text{component}} \cdot \text{MM}_i}{I^*_{Li-\text{component}}} = X_{i-\text{component}} \cdot \text{MM}_i \qquad (9)$$

where MM_i stands for the spectral mismatch factor between the i-component cell and the corresponding MJ subcell, in relation to simulator and reference spectra, as obtained in Eq. (8).

Luminescent coupling should be considered as a possible source of error because it has been found to produce significant changes in the effective spectral response of multijunction cells. This process is nonlinear and dependent on illumination intensity or voltage bias, so its effect varies with the spectral content and from component cells to actual subcells [11]. Inactive layers of a component cell can still absorb and reemit part of the incident light, which is then collected by the succeeding active junction.

The combined use of component cells makes up a spectral sensor for evaluating the spectral content of the light at any given moment. For instance, in a pulsed simulator where the spectrum changes continuously with time, they can provide a time-resolved measurement of the spectrum throughout the pulse [65, 68] (even in pulses with a plateau, the spectrum is known to fluctuate). The spectral matching ratio already described provides a measurement of the balance of light intensity between any two subcell regions.

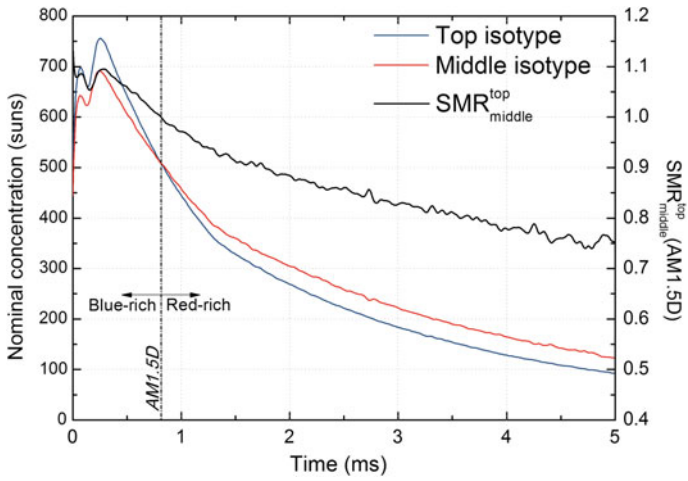

Fig. 15 Effective concentration on component "isotype" cells and resultant SMR throughout a sample Xe flash pulse

$$\mathrm{SMR}_{j-\mathrm{component}}^{i-\mathrm{component}} = \frac{\left(I_{L,i}^{E_{\mathrm{sim}}} \Big/ I_{L,j}^{E_{\mathrm{sim}}}\right)}{\left(I_{L,i}^{E_{\mathrm{AM1.5D}}} \Big/ I_{L,j}^{E_{\mathrm{AM1.5D}}}\right)} = \frac{\left(I_{L,i}^{E_{\mathrm{sim}}} \Big/ I_{L,i}^{E_{\mathrm{AM1.5D}}}\right)}{\left(I_{L,j}^{E_{\mathrm{sim}}} \Big/ I_{L,j}^{E_{\mathrm{AM1.5D}}}\right)} = \frac{X_{i-\mathrm{component}}}{X_{j-\mathrm{component}}} \qquad (10)$$

For a triple-junction cell, effective AM1.5D reference spectrum is assured in terms of spectral balance when SMR (*top to middle*) and SMR (*middle to bottom*) are equal to one. The main spectral balance in Ge-based cells is that between the top to middle junctions, so the simulator spectrum is said to be blue-rich when SMR (*top to middle*) is >1 and red-rich when it is <1 (Fig. 15).

Commercial encapsulated component cells, such as the BPI-SF1 sensor from Black Photon Instruments, are available for measuring simulator spectra. The set includes a GaInP cell for sensing the 340- to 700-nm region, a GaAs cell for the 700- to 900-nm region, and another optional channel for the 900- to 1750-nm region. The cells are sealed within a hermetic glass enclosure with an opening angle of ±25°.

Spectroradiometric Measurements

Regardless of the spectral analysis with component cells, a radiometric measurement of the simulator spectrum is usually required

- if no component cells are available for the particular technology under test,
- for calculating the spectral MM between the device under test and the reference cell(s), or
- for assessing the spectral match of the simulator to reference AM1.5D.

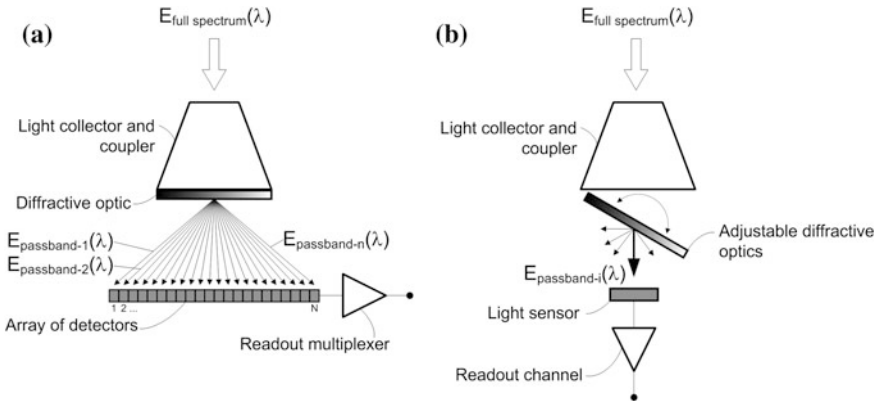

Fig. 16 Typical spectroradiometer architectures when measuring the light spectrum of cell solar simulators **a** array-detector monochromator and **b** scanning monochromator

Broadband spectroradiometers are used for this purpose covering at least the spectral range defined by the absorption of the device under test. The spectral range significant for conventional PV is 300–1100 nm, but it extends to 1800 nm when considering III–V 3J cells. A high spectral resolution is required for characterizing the emission spikes produced by Xe flash lamps. These spikes demand a large dynamic range to achieve high enough SNR in their surroundings. The length of the measurement interval is called "integration time," which is used to vary the sensitivity of the instrument. The measurement of pulsed light sources imposes a trade off for the integration time: A very short time is needed to keep spectrum constant, but this highly decreases the SNR. The dark current or thermal noise of the detector is very much affected by the working temperature and the integration time. Active cooling may be needed for low light or long integration time measurements.

Mainly two types of spectroradiometers are used: array-detector and scanning monochromators (Fig. 16). Array-detector monochromators separate different wavelengths spatially using a diffraction grating, which are then projected on a detector array such as a CCD sensor or a photodiode array. Each pixel of the array corresponds to a different wavelength. Linear arrays exist in the range of hundreds or thousands of pixels, so very high spectral resolutions can be achieved (on the order of ≥0.1 nm) even when a very broad spectrum is considered. To cover the whole UV visible near infrared spectral range, two or more diffraction gratings are used, which cast the light on separate detector arrays made of different semiconductors. The shortest integration times of most detector arrays are in the range of 1–10 ms, which is too long for flash pulses without a plateau: Irradiance and spectrum will vary significantly during that time. Nevertheless, detector arrays with integration times down to 10 μs do exist (e.g., Toshiba TCD1304AP), although several instrumentation issues linked to the quality of the electronic shutter, the linearity of the sensor, and the readout electronics raise serious doubts on the measurement accuracy [69, 70]. For instance, depending on the kind of readout electronics, the

integration time of every pixel occurs in parallel (simultaneously) or in series (delayed by the time of reading one pixel). If the latter is the case, the delay between the first and the last pixels (wavelengths) may be in the range of the integration time, and hence they would correspond to different snapshots of the pulse, so the measured spectrum would actually be a distorted mixture of different spectra.

A scanning monochromator measures a single wavelength at a time usually by mechanically changing the position or alignment of the monochromator elements (filter wheel, mirrors, grating, etc.) to vary the pass-band that is projected on a single detector. The main drawback of this type of instrument is that it requires the spectrum to be kept constant throughout the whole minutes-long measurement, which is not possible in pulsed simulators. In the latter case, a different pulse must be triggered for measuring each wavelength, and hence the measurement can take hours [71]. Nevertheless, this set-up allows performing time-resolved measurements of a single wavelength provided that the detector can be used as an analog scope [72]. Therefore, this is the most convenient spectroradiometer for analyzing the spectrum of short flash pulses without a plateau provided that the repeatability between flash pulses is high.

A cosine-response irradiance probe is used to collect the light on the designated test area, typically dome-shaped polytetrafluoroethylene diffusers or integrating spheres that focus the collected light into the numerical aperture of an optical fiber that takes the light into the monochromator.

5.3.2 Cell Temperature

Continuous simulators do not allow direct measurement of cell temperature under concentrated light because large temperature gradients may exist between the measurement chuck and the cell or even within the cell itself [56]. Moreover, the temperature probe itself may affect the temperature due to the small of thermal capacity of the cell. The strict correlation between V_{OC} and cell temperature can be used to provide a close loop feedback to the temperature plate provided that the V_{OC} <25 °C is known. The latter can be found, for instant, by letting the solar cell reach room temperature in the dark and then recording the V_{OC} while opening a high-speed electronic shutter that shaded the simulator's light: The highest V_{OC} recorded is the one under the initial steady-state temperature [73]. Then the temperature plate cools down the solar cell until the reference V_{OC} is achieved again.

In contrast, a pulsed solar simulator can be assumed to illuminate the cell without changing its temperature provided that the pulse duration is short enough, say, in the range of 1 ms [73, 74]. However, the actual temperature increase is dependent on the thermal mass of the cell and its substrate and on how well are they thermally attached to the test plate.

The measurement chuck should include an active temperature controller, such as a Peltier-cell thermoelectric heater or a water-cooled platform, able to produce temperature variations of approximately 80 °C. Vacuum is in general desired for a good heat transfer to the measurement chuck. The temperature should be monitored

using small of thermistors or thermocouples installed as close as possible to the solar cell embedded in the test block or in the cell substrate where possible. The cell is heated up to the desired temperature, and the I–V measurement is taken once the cell has reached thermal equilibrium. If good thermal conductivity is achieved between the cell and the measurement chuck, a negligible gradient from the cell to the temperature probe can be assumed in dark conditions under moderate plate temperatures.

5.4 I–V Curve Measurement Precautions

To measure the I–V characteristic of the PV device, solar simulators employ a variable load to make the device work at different working points across the I–V curve. Then the voltage and current across the device are measured for every working condition simultaneously with the incident irradiance. If the linearity of the current with irradiance is known for the particular test device and reference sensor, corrections can be made to account for the variability of the irradiance between the measured points, thus translating all of the current measurements to a single reference irradiance level. Voltage can also be corrected for light fluctuations if the effective ideality factor of the device is known because the open-circuit voltage increases with the logarithm of the photocurrent, but it is weighted by the ideality factor. The changes in the voltage losses due to the series resistance depend also on the photocurrent.

The aforementioned dependence of PV devices on temperature is also taken into account. Algebraic methods, such as the one in the IEC 60891 standard, use linear temperature coefficients to correct both current and voltage. Analytical modeling of the device (such as in the lumped diode model) can also be used to extract translation equations for the voltage [75]). To carry out these corrections, the temperature of the device must be measured. This quantity is difficult to measure because a temperature probe can rarely be installed directly on the cell surface. Usually the back surface of the substrate is used for sensing it, but a gradient will exist between the cell and the probe. With concentrated light, this gradient can be very large even across the cell itself, with dozens of degrees °C in the range of 1 cm [76]. The required uncertainty level in the performance of the device determines the accuracy required for the temperature measurement (this relationship can be extracted from the thermal coefficient of the maximum power point).

Many different measurement schemes can be used to produce the required sweep of voltage and current across the device. The particular scheme used may be determined by the type of simulator used—i.e., continuous, single-pulse or multi-flash—or by the electric characteristics of the test specimen. Resistive and capacitive loads are the simplest passive loads and are typically chosen for very high-power systems or when custom measurement systems are required. However, they cannot operate beyond the power quadrant of the I–V curve. Automatic source meters can actively bias the PV device to reverse or forward voltages, i.e., beyond

the I_{SC} and V_{OC}, but usually the maximum current or power do not allow the measurement of large modules. Programmable bipolar power supplies allow the same measurement scheme, but equipment for much greater powers is commercially available. Capacitive loads and bipolar power supplies also have the advantage of very fast voltage sweeps, so they are the usual options for pulsed solar simulators.

5.5 Performance Under Concentration

5.5.1 Nominal Efficiency

Nominal efficiency is determined from the current-voltage characteristic of the solar cell under the design concentration, reference spectrum, and 25 °C cell temperature. According to the IEC 62789 specification, the I–V curve measured should be shown along with the values of I_{SC}, V_{OC}, V_{MP}, I_{MP}, FF, and efficiency as well as measurement conditions.

To provide nominal efficiency, an accurate calculation of the incident power is required, i.e., the product of irradiance and solar cell area. However, the definition of cell area can be problematic. In contrast to flat plate, a concentrator cell may include active zones not intended to be illuminated. For instance, the bus bars might be separated by a security margin from the cell edge. This margin is actually photoactive but is left dark in real operation. These wasted areas are not included by the manufacturer within the designated illumination area, so they should be carefully masked when measuring the cell under the wide beam of the simulator. Otherwise, the actual illuminated area should be used in the calculation of the efficiency rather than the designated illumination area.

5.5.2 Performance as a Function of Concentration

Concentrator cells may be operated under a wide range of irradiance conditions depending on the particular concentrator architecture and the available solar resource. At the design level, it is important to characterize the concentration under which the optimal conversion efficiency is achieved to provide appropriate feedback to the cell manufacturer or the CPV system designer. In contrast, to estimate actual energy yield outdoors, a good knowledge of the variation of performance with intensity is required. For measuring this relationship, a simulator is required that is able to create variable intensity while keeping constant spectrum and temperature. According to IEC 62789, concentrator cell specifications should include the plot efficiency and V_{mp} as a function of irradiance in units of kW/m^2 (almost equivalent to “suns”).

I–V parameters as a function of concentration can also be used to fit typical diode model parameters of the solar cell such as the effective ideality factor or the

series resistance. Despite actually being composed of several subcells in series, we can assign a lumped-diode model to an MJ solar cell. From the Shockley equation, the dependence of V_{OC} on the concentration factor (X) can be easily derived [75]:

$$\Delta V_{OC}(X) = V_{OC}(X) - V_{OC}^{*} = n\frac{kT}{q}\ln X \tag{11}$$

where $V_{OC}(X)$ and V_{OC}^{*} are the open-circuit voltages of the MJ solar cell under concentration and 1-sun reference conditions, respectively; q is the electron charge; k is Boltzmann's constant; T is the temperature; and n is the diode ideality factor. In the case of an MJ cell, n becomes an effective parameter with a value typically between 3 and 4 [77]. Therefore, the effective ideality factor n can be extracted from the relationship between the growth of the open-circuit voltage ΔV_{OC} and the logarithm of the concentration. The plot of concentration versus open-circuit voltage allows also analyzing the characteristic curve of the solar cell without the influence of the series resistance [78] because no series resistance losses happen at V_{OC}. We can approximate the voltage at the maximum power point (V_{MP}) in a similar way:

$$V_{MP}(X) \cong V_{MP}^{*} + n\frac{kT}{q}\ln X - I_{MP}(X)R_S \tag{12}$$

where R_S is the series resistance, and $I_{MP}(X)$ is estimated as X times I_{MP}^{*}, the current at the maximum power point under reference conditions. Hence:

$$P_{MP}(X) \cong X \cdot P_{MP}^{*} + X \cdot I_{MP}^{*} \cdot \Delta V_{OC}(X) - (X \cdot I_{MP}^{*})^2 R_S \tag{13}$$

The conversion efficiency is calculated by dividing the maximum power (P_{MP}) by the incident light flux, which is the product of the incident irradiance $G(X)$ and the cell active area (A_{cell}) (Fig. 17):

$$\eta(X) = \frac{P_{MP}(X)}{G(X)A_{cell}} \cong \frac{P_{MP}^{*} + I_{MP}^{*} \cdot n\frac{kT}{q}\ln X - X(I_{MP}^{*})^2 R_S}{G^{*}A_{cell}} \tag{14}$$

Now the effective series resistance can be estimated from the relationship between efficiency and concentration, differentiating (14):

$$\frac{d\eta}{dX} \cong \frac{I_{MP}^{*}\left(n\frac{kT}{q}\frac{1}{X} - I_{MP}^{*}R_S\right)}{G^{*}A_{cell}} \tag{15}$$

Both terms in the difference describe the two dominant trends in the curve efficiency versus concentration because the derivative corresponds to its slope. The efficiency peaks when X makes both terms equal, and the derivative becomes zero. Furthermore, for large concentration factors well beyond peak efficiency, the derivative of the efficiency becomes asymptotically:

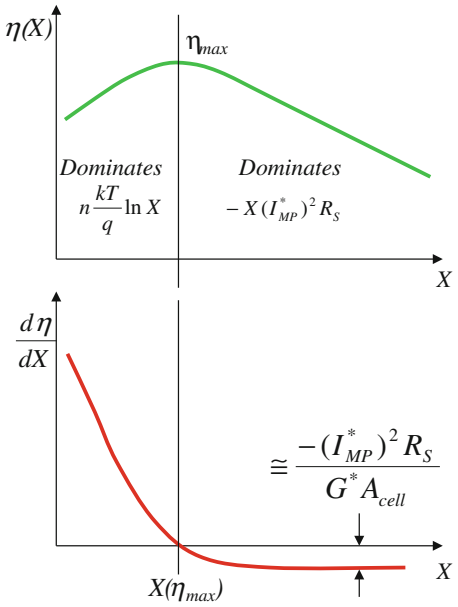

Fig. 17 Efficiency as a function of concentration allows extracting the effective series resistance of the MJ cell. For concentration ratios well above peak efficiency, the decrease of efficiency is dominated by the series resistance losses

$$\frac{\mathrm{d}\eta}{\mathrm{d}X} \cong \frac{-(I^*_{\mathrm{MP}})^2 R_{\mathrm{S}}}{G^* A_{\mathrm{cell}}} \tag{16}$$

and hence the series resistance can be obtained from the asymptotic slope of the curve under high concentration:

$$R_{\mathrm{S}} \cong -\frac{\mathrm{d}\eta}{\mathrm{d}X}\frac{G^* A_{\mathrm{cell}}}{(I^*_{\mathrm{MP}})^2} \tag{17}$$

5.6 Temperature Coefficients

Temperature coefficients are valuable information for modelling performance and predicting outdoor performance depending on the actual operating conditions. They can be obtained simply by measuring the I–V curve of the cell under a large range of temperatures. Because the voltage temperature coefficient is dependent on concentration, it should be studied for several light intensities or, at least, under the expected operating irradiance [77, 79].

The use of the AM1.5D spectrum is critical for extracting the thermal coefficient of I_{SC} and also FF because they are dependent on the spectral content of the light [80, 81]. The use of solar simulators can lead to large inconsistencies due to the influence of gas discharge spectral emission lines, e.g., unfiltered Xe lamps produce

very large spikes in the 800- to 1000-nm region, which mainly affects the middle junction. This effect is very dependent on the proximity of the subcell bandgap to said emission lines. An alternative procedure uses temperature-dependent quantum efficiency measurements, and their product with the reference spectrum yields the expected photocurrent. In any case, the I_{SC} temperature coefficient should be extracted for each subcell independently. For this purpose, the simulator spectrum is varied to make the other subcells have an excess of current.

If the reference cells are not calibrated under all of the desired temperature values, they should be kept under 25 °C while the device under test is heated up. However, the spectral mismatch factor between the DUT board and the reference cells must be reestimated for each value of temperature as the DUT spectral response changes.

5.7 Spectral Characterization

Because MJ concentrator cell are subject to ever-varying spectral conditions in real operation, characterization of their spectral sensitivity is desired. This involves adjusting the simulator spectrum to produce a large range of different spectral conditions, so that each junction limits the cell current (or at least those subcells likely to limit the current in real operation under the concentrator).

5.7.1 Spectrometric Characterization

Spectrometric characterization is used to describe the behavior of MJ cells under varying spectral conditions that fulfill an additional restriction: The sum of the effective irradiance on all subcells is a constant [7, 62]. Each spectrum is set so the photocurrents follow (18). This restricts the observed variations to be only related to spectral variations and not to changes in the concentration level. The simulator spectrum is tuned to produce a large range of different current balances between subcells. Each IV parameter measured is then plotted versus the ratio between the current of one of the subcells to its current under reference conditions.

$$\frac{I_{L,i}^{E_{\text{sim}}}}{I_{L,i}^{E_{\text{AM1.5D}}}} + \frac{I_{L,j}^{E_{\text{sim}}}}{I_{L,j}^{E_{\text{AM1.5D}}}} = 2 \tag{18}$$

5.7.2 Subcell-Limitation Diagrams

Another technique makes use of a component cell to evaluate the current matching between subcells of an MJ cell under any given spectrum [51, 82, 83]. If the MJ cell current is limited by one of its subcells, the current of the corresponding component

cell will vary with light intensity in the same proportion. If the spectral distribution changes, the current of the other component cells will vary with a different trend. We can use this to identify the limiting subcell when a noticeable variation of the spectrum occurs. For this purpose, the MJ cell's I_{SC} is recorded simultaneously with the effective concentration given by each component cell, and the spectrum of the light is intentionally varied so as to produce a large sweep of SMR values. The SMR between any two subcells likely to be limited in real operation should be analyzed. Next, the cell's I_{SC} is normalized by the concentration of each component cell as follows:

$$I_{\mathrm{N},i-\mathrm{component}} = \frac{I_{\mathrm{SC,MJ}}}{X_{i-\mathrm{component}}} [A/\mathrm{sun}] \tag{19}$$

where $I_{\mathrm{N},i\text{-component}}$ indicates the MJ cell current normalized to the concentration factor of the *i*-component cell. If one of the subcells is limiting the current for a range of different spectra, $I_{\mathrm{N},i\text{-component}}$ will be constant throughout this spectral sweep provided that the spectral response of the MJ subcells and the corresponding component cells is exactly the same.

To make linearity explicit, the normalized ratios are plotted against the spectral sweep in terms of SMR. The two plots in Fig. 18 present a sample subcell-limitation diagram for a three-junction cell current matched under AM1.5D. Here, the MJ cell current has been normalized by the top and middle concentration factors to obtain $I_{\mathrm{N,top}}$ and $I_{\mathrm{N,middle}}$, respectively. In the spectral zone labeled *A*, the MJ current normalized to the top-cell *X* remains constant (the MJ cell is said to *follow* the top component cell), so in this zone $I_{\mathrm{SC,MJ}} \approx I_{L,\text{top-subcell}}$. This knowledge is used to "calibrate" the top-subcell's current sensitivity $I_{L,\mathrm{top}}$* as a function of the top-component *X*, as in (20). Analogously, in zone *B* the middle subcell is limiting the MJ cell.

$$\{\text{Zone } A\} : I^*_{L,\mathrm{top}} = \left.\frac{I_{\mathrm{SC,MJ}}}{X_{\mathrm{top}-\mathrm{component}}}\right|_{I_{\mathrm{SC,MJ}} \approx I_{L,\mathrm{top}}} [A/\mathrm{sun}] \tag{20}$$

$$\{\text{Zone } B\} : I^*_{L,middle} = \left.\frac{I_{\mathrm{SC,MJ}}}{X_{\mathrm{middle}-\mathrm{component}}}\right|_{I_{\mathrm{SC,MJ}} \approx I_{L,middle}} [A/\mathrm{sun}] \tag{21}$$

These two calibration values can be used to determine the overall current-matching (CM) under the reference spectrum $E_{\mathrm{AM1.5D}}(\lambda)$.

$$CM^{\mathrm{top}}_{\mathrm{middle}}(E_{\mathrm{AM1.5D}}(\lambda)) = \frac{I^*_{L,\mathrm{top}}(E_{\mathrm{AM1.5D}}(\lambda))}{I^*_{L,\mathrm{mid}}(E_{\mathrm{AM1.5D}}(\lambda))} \tag{22}$$

Moreover, the current photogenerated at each subcell can be estimated for any arbitrary simulator intensity and spectrum by means of the component-cells:

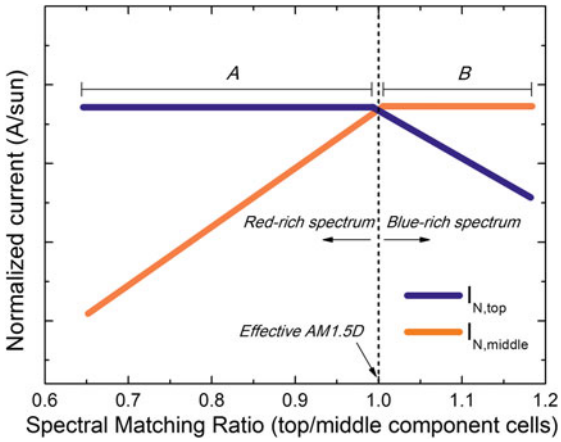

Fig. 18 Sample subcell-limitation graph for the top and middle subcells of a conventional three-junction cell

$$I_{L,i-\text{subcell}} = X_{i-\text{component}} \cdot I^{*}_{L,i-\text{subcell}}[A] \tag{23}$$

The current-matching ratio under any particular illumination spectrum $E_i(\lambda)$ can be directly obtained through the value of SMR, as shown in (24).

$$\begin{aligned} \text{CM}^{\text{top}}_{\text{middle}}(E_i(\lambda)) &= \frac{I_{L,\text{top}}(E_i(\lambda))}{I_{L,\text{middle}}(E_i(\lambda))} = \frac{X_{\text{top}}(E_i(\lambda))}{X_{\text{middle}}(E_i(\lambda))} \cdot \frac{I^{*}_{L,\text{top}}(E_{\text{AM1.5D}}(\lambda))}{I^{*}_{L,\text{mid}}(E_{\text{AM1.5D}}(\lambda))} \\ &= \text{SMR}^{\text{top}}_{\text{middle}}(E_i(\lambda)) \cdot \text{CM}^{\text{top}}_{\text{middle}}(E_{\text{AM1.5D}}(\lambda)) \end{aligned} \tag{24}$$

However, the subcell-limitation graph may deviate from this ideal analysis if the spectral responses of the component cells do not match the subcells in the MJ device. In this case, the spectral mismatch error MM defined previously should be introduced again. Nevertheless, habitually, this mismatch is found to be a monotonic trend of the normalized I_{sc}, so its bias can be estimated and removed.

6 Summary

The main measurement methods used in the characterization of MJ concentrator solar cells have been described. The relevance of the spectral response [$S(\lambda)$] is that it allows calculating the photocurrent (I_L) generated by each subcell under a particular spectral irradiance and diagnosing possible malfunctioning of the different regions of the cell. The variations of $S(\lambda)$ with beam incidence angle and cell temperature are useful for understanding current losses when the cell is used within a concentrator.

The EL is based on the application of an external current bias (I_{bias}) to the cell, which induces a strong carrier recombination within the cell, part of which generates photons with energies corresponding to each subcell bandgap. Spatially resolved EL can be used to analyze solar cell internal defects, sheet resistivity, or thermal inhomogeneity during operation.

The measurement of the I–V curve as a function of light concentration provides the most relevant information on cell performance such as peak efficiency or series resistance losses. Concentrator solar simulators should fulfill strict spatial uniformity and spectral requirements to provide accurate measurements. Precise spectral tunability is required to decrease errors in the measurement of latest-generation cell architectures, especially those not based on a Ge bottom cell with an excess of current. The main types of concentrator solar simulators have been described and advice on appropriate reference sensors and measurement precautions provided. Spectral characterization under controlled simulator conditions is essential to analyze MJ cell behavior under the ever-varying spectral conditions found in real operation.

References

1. Burdick J, Glatfelter T (1986) Sol Cells 18:301
2. Hovel HJ (1975) Semiconductors and semimetals. In: Solar cells, Vol 11. Academic Press, Inc., New York
3. Bertness KA, Kurtz SR, Friedman DJ, Kibbler AE, Kramer C, Olson JM (1994) Appl Phys Lett 65:989
4. Luque AL, Viacheslav A (eds) (2007) Concentrator photovoltaics. Springer, Berlin, pp 67–87
5. Dimroth F, Grave M, Beutel P, Fiedeler U, Karcher C, Tibbits TND, Oliva E, Siefer G, Schachtner M, Wekkeli A, Bett AW, Krause R, Piccin M, Blanc N, Drazek C, Guiot E, Ghyselen B, Salvetat T, Tauzin A, Signamarcheix T, Dobrich A, Hannappel T, Schwarzburg K (2014) Prog Photovolt Res Appl 22:277
6. Meusel M, Baur C, Létay G, Bett Aw, Warta W, Fernandez E (2003) Prog Photovolt Res Appl 11:499 (2003)
7. Meusel M, Baur C, Siefer G, Dimroth F, Bett AW, Warta W (2006) Solar energy material solar cells, vol 90, p 3268
8. Siefer G, Baur C, Bett AW (2010) In: Proceedings of the 35th IEEE photovoltaics specialists conference PVSC, pp 000704–000707
9. Steiner MA, Geisz JF, Moriarty TE, France RM, McMahon WE, Olson JM, Kurtz SR, Friedman DJ (2013) IEEE J Photovolt 3:879
10. Lim SH, Li J-J, Steenbergen EH, Zhang Y-H (2013) Prog Photovolt Res Appl 21:344
11. Steiner MA, Geisz JF (2012) Appl Phys Lett 100:251106
12. Steiner MA, Kurtz SR, Geisz JF, McMahon WE, Olson JM (2012) IEEE J Photovolt 2:424
13. Kurtz SR, Emery K, Olson JM (1994) In: Conference record of the twenty fourth IEEE photovoltaics specialists conference—1994, 1994 IEEE first world conference photovoltaics energy conversion, vol 2, pp 1733–1737
14. Varshni YP (1967) Physica 34:149
15. Henning Helmers MS (2013) Sol Energy Mater Sol Cells 116:144
16. Kinsey GS, Edmondson KM (2009) Prog Photovolt Res Appl 17:279

17. Garcia-Linares P, Dominguez C, Voarino P, Besson P, Baudrit M (2014) In: Proceedings of IEEE 40th photovoltaics specialists conference PVSC 2014, pp 3298–3303
18. Fuyuki T, Kondo H, Yamazaki T, Takahashi Y, Uraoka Y (2005) Appl Phys Lett 86:262108
19. Giesecke JA, Kasemann M, Warta W (2009) J Appl Phys 106:014907
20. Würfel P, Trupke T, Puzzer T, Schäffer E, Warta W, Glunz SW (2007) J Appl Phys 101:123110
21. Hinken D, Ramspeck K, Bothe K, Fischer B, Brendel R (2007) Appl Phys Lett 91:182104
22. Kirchartz T, Rau U (2007) J Appl Phys 102:104510
23. Rau U (2007) Phys Rev B 76:085303
24. Zimmermann CG (2009) IEEE Electron Device Lett 30:825
25. Zimmermann CG (2006) J Appl Phys 100:023714
26. Zimmermann CG (2010) In: Proceedings of the 35th IEEE photovoltaics specialists conference PVSC, pp 001783–001787
27. Nesswetter H, Lugli P, Bett AW, Zimmermann CG (2013) IEEE J Photovolt 3:353
28. Zimmermann CG (2013) Appl Phys Lett 102:233506
29. Nelson WB (2009) Accelerated testing: statistical models, test plans, and data analysis. Wiley, New York
30. Núñez N, Vázquez M, González JR, Algora C, Espinet P (2010) Microelectron Reliab 50:1880
31. Espinet-Gonzalez P, Algora C, OrlandoV, Nunez N, Vazquez M, Bautista J, Xiugang H, Barrutia L, Rey-Stolle I, Araki K (2012) In: Proceedings of the IEEE 38th photovoltaics of specialists conference PVSC, vol 2, pp 1–6
32. Espinet-González P, Algora C, Núñez N, Orlando V, Vázquez M, Bautista J, Araki K (2014) Prog Photovolt Res Appl n/a
33. Bosco N, Sweet C, Ludowise M, Kurtz S (2012) IEEE J Photovolt 2:411
34. Garcia-Linares P, Dominguez C, Voarino P, Besson P, Baudrit M (2014) In: Proceedings of AIP conference. AIP Publishing, pp 110–113
35. Mabille L, Mangeant C, Baudrit M (2013) In: Proceedings of IEEE 39th photovoltaics specialists conference PVSC, pp 3416–3420
36. Kirchartz T, Rau U, Hermle M, Bett AW, Helbig A, Werner JH (2008) Appl Phys Lett 92:123502
37. Kirchartz T, Rau U, Kurth M, Mattheis J, Werner JH (2007) Thin Solid Films 515:6238
38. Roensch S, Hoheisel R, Dimroth F, Bett AW (2011) Appl Phys Lett 98:251113
39. Karcher C, Helmers H, Schachtner M, Dimroth F, Bett AW (2014) Prog Photovolt Res Appl 22:757
40. Friedman DJ, Olson JM, Kurtz S (2010) In: Luque A, Hegedus S (eds) Handbook of photovoltaics Science and engineering. Wiley, New York, pp 314–364
41. ASTM (2010) E2236-10 Standard test methods for measurement of electrical performance and spectral response of nonconcentrator multijunction photovoltaic cells and modules. ASTM International, West Conshohocken
42. IEC (2014) IEC/TS 62789 photovoltaic concentrator cell documentation, 1.0 edn. International Electrotechnical Commission, Geneva
43. ASTM (2008) G173-03 standard tables for reference solar spectral irradiances: direct normal and hemispherical on 37° tilted surface. ASTM International, West Conshohocken
44. Emery K, Meusel M, Beckert R, Dimroth F, Bett A, Warta W (2000) In: Conference record of the twenty-eighth IEEE photovoltaics specialists conference 2000, pp 1126–1130
45. Nishi D, Ueda T, Ohshima H, Hishikawa Y (2013) In: AIP conference proceedings. AIP Publishing, pp 133–137
46. IEC (2009) 60891 Photovoltaic devices—procedures for temperature and irradiance corrections to measured I-V characteristics. International Electrotechnical Commission, Geneva
47. Galleano R, Dunlop ED, Halton D (2004) In: Proceedings of 19th European photovoltaics solar energy conference. Paris, France

48. Kiehl J, Emery K, Andreas A (2004) In: Proceedings of 19th European photovoltaics solar energy conference and exhibition
49. IEC (2007) 60904-9 Photovoltaic devices—part 9: solar simulator performance requirements. International Electrotechnical Commission, Geneva
50. Pravettoni M, Galleano R, Dunlop ED, Kenny RP (2010) Meas Sci Technol 21:115901
51. Domínguez C, Antón I, Sala G, Askins S (2012) Prog Photovolt Res Appl n/a
52. Osterwald CR, Wanlass MW, Moriarty T, Steiner MA, Emery KA (2014) In: AIP conference proceedings. AIP Publishing, pp 149–153
53. Osterwald C, Wanlass M, Moriarty T, Steiner M, Emery K (2014) Effects of spectral error in efficiency measurements of GaInAs-based concentrator solar cells. NREL
54. Emery KA (1986) Sol Cells 18:251
55. Adelhelm R, Bücher K (1998) Sol Energy Mater Sol Cells 50:185
56. Emery K (2011) In: Luque A, Hegedus S (eds) Handbook of photovoltaics science and engineering. Wiley, Chichester, pp 797–840
57. Keogh W, Cuevas A (1997) In: Proceedings of IEEE 26th photovoltaics specialists conference
58. King DL, Gee JM, Hansen BR (1988) In: Proceedings of IEEE photovoltaics specialists conference. Twente, Las Vegas
59. Ossenbrink HA, Zaaiman W, Bishop J (1993) In: Conference record of the twenty third IEEE photovoltaics specialists conference, pp 1194–1196
60. Siefer G, Baur C, Meusel M, Dimroth F, Bett AW, Warta W (2002) In: Conference record of the twenty-ninth IEEE photovoltaics specialists conference 2002, pp 836–839
61. Jungwirth D, Eigler LC, Espiritu S (2008) In: Proceedings of 33rd IEEE photovoltaics specialists conference, pp 1–6
62. Meusel M, Adelhelm R, Dimroth F, Bett Aw, Warta W (2002) Prog Photovolt Res Appl 10:243
63. Moriarty T, Jablonski J, Emery K (2012) In: Proceedings of 38th IEEE photovoltaics specialists conference PVSC, pp 001291–001295
64. Schachtner M, Hoheisel R, Sabuncuoglu F, Siefer G, Bett AW, Darou S, Spinner D (2011) Hamburg, Germany
65. Domínguez C, Antón I, Sala G (2008) Opt Express 16:14894
66. Antón I, Domínguez C, Sala G, Martínez M, Díaz V, Álvarez JL, Alonso J (2005) In: Proceedings of 3rd international conference on solar concentrations for generation of electricity or hydrogen. NREL/CD-520-38172, Scottsdale
67. Domínguez C, Anton I, Sala G (2010) Prog Photovolt 18:272
68. Peharz G, Rodriguez JPF, Siefer G, Bett AW (2008) In: Proceedings of international conference on solar concentrations for generation of electricity, ICSC-5. Palm Desert
69. Hohl-Ebinger J, Siefer G, Warta W (2007) In: Proceedings of 22nd European photovoltaics solar energy cenference and exhibition. Milano, Italy, pp 425–428
70. Myers DR, Cannon TW (1997) In: AIP conference proceedings on National Renewable Energy Laboratory. NREL/Sandia National Laboratory (SNL) photovoltaics program review meeting. American Institute of Physics, Lakewood, pp 395–406
71. Cannon TW (1998) In: AIP conference proceedings of national center photovoltaics NCPV 15th program review meeting. American Institute of Physics, pp 623–628
72. Andreas AM, Myers DR (2008) In: Proceedings of SPIE. San Diego, p 70460I
73. Moriarty T, Emery K (1999), pp 301–311
74. Muller M, Deline C, Marion B, Kurtz S, Bosco N (2011) In: AIP conference proceedings. AIP Publishing, pp 331–335
75. Sala G (1989) In: Luque A (ed) Solar cells and optics for photovoltaic concentration. Adam Hilger, Bristol, pp 239–245
76. Mathur RK, Mehrotra DR, Mittal S, Dhariwal SR (1984) Sol Cells 11:175
77. Kinsey GS, Hebert P, Barbour KE, Krut DD, Cotal HL, Sherif RA (2008) Prog Photovolt Res Appl 16:503
78. Wolf M, Rauschenbach H (1963) Adv Energy Convers 3:455

79. Virshup GF, Chung B-C, Ladle Ristow M, Kuryla MS, Brinker D (1990) In: Conference record of the twenty first IEEE photovoltaics specialists conference 1990, vol 1, pp 336–338
80. Aiken D, Stan M, Murray C, Sharps P, Hills J, Clevenger B (2002) In: Conference record of the twenty-ninth IEEE photovoltaics specialists conference, pp 828–831
81. Siefer G, Bett AW (2002) Prog Photovolt Res Appl n/a
82. Domínguez C, Victoria M, Herrero R, Askins S, Antón I, Sala G (2012) In: AIP conference proceedings. American Institute of Physics, pp 127–130
83. Garcia I, McMahon WE, Steiner MA, Geisz JF, Habte A, Friedman DJ (2015) IEEE J Photovolt 5:438

High-Concentration Optics for Photovoltaic Applications

Katie Shanks, Sundaram Senthilarasu and Tapas K. Mallick

Abstract The concept of a high-concentration optical system is introduced detailing the various design types and focusing only on those aimed at photovoltaic (PV) applications. This will include point focus, line focus, imaging, nonimaging, and the classical cassegrain set-up. The theory of high-concentration optics is explained in terms of idealised concepts and maximum limits for each concentrator type and combination. The optical system is broken down into the different stages and materials possible in a high-concentration configuration. The physics of reflective and refractive optics are described, and their associated errors, advantages and a brief overview of past milestones, and recent research trends in the area of high-concentration PVs are presented. Current primary and secondary optics are geometrically explained covering Fresnel, parabolic, heliostat, compound parabolic, hyperboloid, v-trough, and dome-shaped optics. This chapter also covers examples of new secondary optics, such as the three-dimensional crossed-compound parabolic concentrator and the square elliptical hyperboloid concentrator. The aim of this chapter is to provide the basic optical behaviour of high-concentration designs aimed at PV applications considering their geometry, materials, and reliability.

1 Introduction

1.1 Concentrator Concepts

High-concentration optics are in the range of 100–2000 suns [1], a recently modified definition due to their need for dual axis tracking. The development of solar concentrator technology over the years has included improvements in concentration solar cells, cooling systems, and optical accuracy. The concentration ratio

K. Shanks (✉) · S. Senthilarasu · T.K. Mallick
Environment and Sustainability Institute, University of Exeter, Penryn Campus, Penryn, Cornwall TR10 9FE, UK
e-mail: kmas201@exeter.ac.uk

P. Pérez-Higueras and E.F. Fernández (eds.), *High Concentrator Photovoltaics*, Green Energy and Technology, DOI 10.1007/978-3-319-15039-0_4

definition also lacks conformity because this can be linked to the geometrical concentration ratio, optical concentration ratio (similar to optical efficiency), or intensity concentration ratio (flux concentration ratio) [2]. Care should be taken when a concentrating system is being described what is being used, although often it is the designed geometrical concentration ratio quoted along with an optical efficiency, which, when multiplied, should give the flux concentration ratio.

In terms of a concentrator PV (CPV) system, multiple concentrator optics (including low concentration devices <10 suns) can be involved. In this way a high-concentrator PV (HCPV) system can be classified as a single-stage, two-stage, or greater-stage system, although fewer stages are desired to decrease complexity and additional uncertainties. The preferred outline of a high-concentration optical system within an HCPV system consists of primary and secondary optics. The primary optics initially collect incident light, and typical examples include the Fresnel lens and the parabolic reflector. The secondary optics are of medium to low concentration and can be referred to as "receiver optics" when in optical contact with the PV. These secondary optics can increase the concentration of the system but are used more often with the aim of improving the system's acceptance angle and the irradiance distribution on the PV. Receiver optics introduced to a concentrator design which improve the irradiance distribution are also suitably referred to as homogenisers. Two examples of different HCPVs are given in Fig. 1.

CPV systems can be categorised in a variety of ways such as concentration ratio, primary optic type, tracking method, geometry, and number of stages. Figure 1a could be described as a two-stage refractive concentrator consisting of a primary

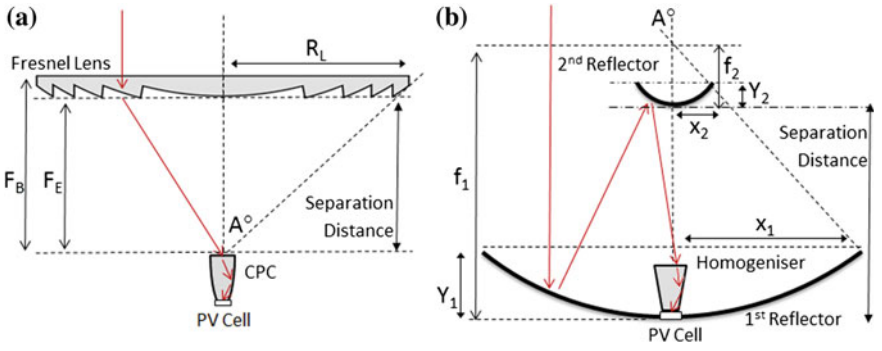

Fig. 1 **a** Primary Fresnel lens with secondary compound parabolic concentrator (CPC). Parameters that may be considered during the design of such a system are given: radius of the Fresnel lens R_L, back focal length F_B; effective focal length F_E; and separation distance and maximum angle of incident rays on the secondary, A. **b** A classical cassegrain set-up of a primary parabolic dish reflector with a hyperboloid secondary reflector and crossed V-trough dielectric filled homogeniser as a receiver optic. Example of design parameters to be considered in a cassegrain are shown: primary paraboloid's radius x_1; depth of the paraboloid y_1; and focal length f_1. Similarly, examples for the secondary are hyperboloid radius x_2; depth y_2; and focal length f_2. The separation distance between the two reflectors is again displayed as is the maximum incidence angle of light on the secondary A, which can relate the two reflectors' geometry

Fresnel lens and secondary CPC. Figure 1b shows the classic cassegrain set-up, which typically consists of a parabolic primary reflector, a secondary paraboloid or hyperboloid secondary, and a tertiary crossed V-troughed dielectric filled homogeniser. In both of these, if the original two-dimensional (2D) geometries were translated linearly, then they would be described as "line-focus systems." Figure 1a would become a linear Fresnel lens with a linear (or 2D) CPC focusing on a line of solar cells, and Fig. 1b would become a parabolic trough similarly focusing on linear optics and receivers. A line-focus CPV system, also referred to as a 2D design, is normally used for solar thermal concentrator systems where the receiver may be a transparent pipe carrying water or another liquid medium to be heated. There is often a point-focus version to every line-focus geometry and vice versa, where by way of rotational or translational symmetry the original 2D design is transformed into a three-dimensional (3D) one. Terms such as "crossed" or "rotated" could be used to describe how a 2D profile has been transformed into a 3D optic. A point-focus collector can be deliberately designed not to be symmetrical across any obvious axis, but an uneven irradiance distribution on the cell would be expected. Due to the popularity of line-focus systems with thermal heating, and the rareity of high-concentration linear optics [3], point source systems will be addressed more than linear systems in this chapter. It should also be obvious that with point-focus optics, a dual-axis tracking system is preferred for maximum performance, and a line-focus optical concentrator would require a single-axis tracking system.

Optics can also be classified as imaging or nonimaging where the former describes an optic that refracts light from an object in such a way as to maintain the image but produce a smaller form at the focal plane [4]. Nonimaging optics, such as the CPC and the nonimaging Fresnel lens, were designed later and tailored specifically for the collection of solar rays. This means that they were designed specifically to obtain high optical efficiencies and highly uniform flux distribution output and to cope with the characteristics of solar light [4]. This list of aims, however, does not necessarily require the same image to be replicated at the focal plane, and thus typically the image is distorted at the focal plane, and the term "nonimaging optics" was given. Nonimaging concentrators with very large numerical apertures (small aperture ratio or *f*-number) would have very large aberrations if used as image-forming systems [2]. Geometrical aberrations in the classic sense cause imaging optics to perform at a nonideal level. Image-forming concentrators must treat each ray in a similar fashion to replicate the image at the receiver.

This means all rays that pass through an imaging optic will be reflected once or pass through a refractive boundary only once along with all of the other rays. In this way, rays at varying angles or different incident positions, which would be lost, cannot be treated differently in an attempt to keep them within the system. Nonimaging concentrators such as the CPC, however, can apply different conditions to different rays and obtain ideal performance. Purely imaging optics are, however, capable of approaching the thermodynamic limit and even possibly attaining flux

levels greater than a nonimaging one; for both types, careful and tailored design decides which is optimum [5].

The ideal solar concentrating optical system would have 100 % optical efficiency, an output of uniform irradiance distribution (matching in shape and size to the PV receiver), maximum acceptance angle, high optical tolerance, and durability (hence high reliability). It would also preferably be cheap to manufacture, lightweight, and easy to install. Each type of CPV system has advantages and disadvantages, and it is important to know the application and location to choose the most appropriate design.

1.2 Optical Physics Basics

1.2.1 Concentration Ratio

The concentration of an optic or system of optics can be defined as low (<10 suns), medium (10–100 suns), high (100–2000 suns), or ultrahigh (>2000 suns) concentration [1]. Under normal conditions, the maximum concentration ratio ($C_{\max}$) achievable on Earth due to the divergence of light from the Sun is 46,000× for a 3D system (full tracking) and only 216× for a 2D system (single-axis tracking) as calculated from the Sun's diameter [2, 6]. The resulting Eqs. (1) and (2) consider that the concentrator is immersed in refractive index, n, (for air this becomes 1) and θ_i as the input angle (i.e., effective solar angular radius: 4.7 mrad or 0.267°) [2, 6]:

For a linear concentrator, the maximum concentration equation is shown:

$$C_{\max} = \frac{n}{\sin \theta_i} \tag{1}$$

and for a point-focus concentrator:

$$C_{\max} = \left(\frac{n}{\sin \theta_i}\right)^2 \tag{2}$$

If we now use θ_o to represent the output (absorber) angle and NA to denote the numerical aperture ($NA = n \sin \alpha$), then the above can be written [7]:

$$C_{\max} = \left(\frac{n \sin \theta_o}{n \sin \theta_i}\right)^2 = \left(\frac{NA_o}{NA_i}\right)^2 \tag{3}$$

The previous equation can be used to calculate the maximum concentration possible of an optic by using the maximum acceptance angle as θ_i. Fresnel-reflective losses from the absorber can be avoided by limiting the θ_o to $<\pi/2$ [2, 7], but some antireflective coatings of solar cells can still have greater

reflectance values for off-axis incident light rays. The concentration ratio of a linear concentrator is usually given as the ratio of the transverse input and output dimensions [2]. As expected, the point-focus equivalent of a line-focus concentrator will always have an increased geometrical concentration ratio, but it is much easier to achieve an ideal concentrator design in 2D geometry such has been performed for the CPC. An ideal concentrator works perfectly for all rays within the acceptance angle.

The current concentration ratio range for commercial HCPV is 100–1000 suns [8]. Specific concentration limits for each type of concentrator is discussed in later sections.

1.2.2 Ideal Conditions and the Classic Cassegrain

Most optical concentrators are initially based on, or initially designed on, idealised concepts and conditions, and then they are developed to consider more accurately the practical environment. First assumptions may include the condition of incoming radiation from the Sun to be parallel and a specific irradiance value (e.g., 1000 W $/m^2$). The optical components are also idealised, assuming 100 % specular reflectance for mirrors, all wavelengths to be fully refracted for lenses, and no thermal effects on shape [9]. It would be difficult to include all uncertainties in the first steps of optical design, but some are essential and can significantly alter results. One must consider that these practical uncertainties are especially important at greater concentration ratios (which are more sensitive to error) and when incorporating multiple stages (errors build on each other) where these uncertainties intensify (see Fig. 2).

The line and spot in line- and point-focusing optics can only ever be realised in an idealized mathematical model. Manufacturing uncertainties (surface roughness and slope errors) and alignment errors (tracking error and component misalignment) give an effective distribution of errors for the system, which contribute to the Gaussian diameter seen in real measurements [3]. Parabolic reflectors are concentrators intended for distant sources (parallel light sources) where all incident light is reflected into the focal point. In this way, parabolic mirrors are popularly used in telescopes. The Sun is an extended source, not a point light source, with a light divergence of 4.7 mrad (0.27°) and where solar rays are not exactly parallel, but instead each ray can be described as a cone. This effect is amplified by multiple stage concentrators [10–12].

The classical cassegrain (shown in Fig. 1b) uses a primary parabolic-shaped reflector and a hyperboloid secondary. Other conic curves have been tried for the primary and secondary, but a hyperboloid secondary is preferred to allow greater optical tolerance. A cassegrain consisting of a parabolic primary and secondary is based on the theory of parabolas: Any parallel light incident on a parabolic dish will be reflected at such an angle as to pass through the focal point of that parabola. In this way, with a parabolic primary and secondary of coincident focal points, the

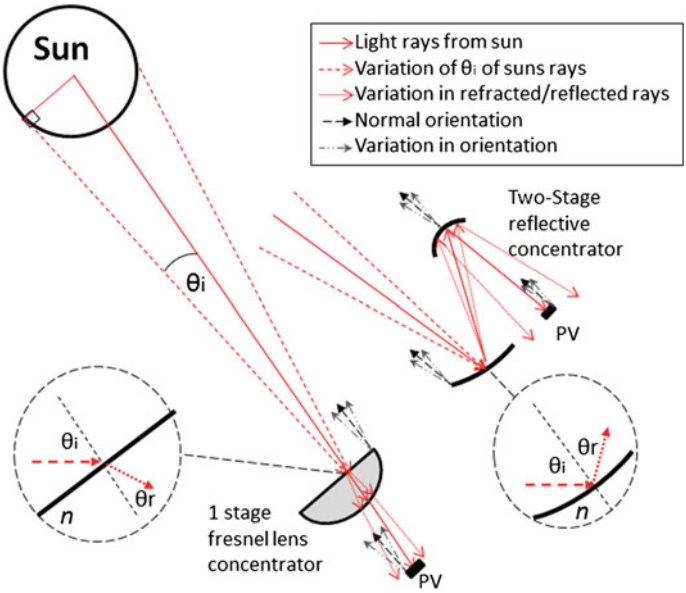

Fig. 2 Light rays from the Sun are shown to not be parallel, incident on a single-stage refractive concentrator and a two-stage reflective concentrator. Focus is given to the variation of incidence angle of a light ray from the Sun after refraction or reflection, which can cause final light rays missing the PV receiver. Magnifications of the incident rays undergoing refraction and reflection are also shown and labelled

parallel light would be concentrated and reproduced, thus giving a uniform irradiance distribution on a solar cell placed in the base of the first reflector. As mentioned, light from the Sun is not parallel, and so the paraboloids would need to be positioned off focus (afocal) to compensate, or another design such as the parabololoid-hyperboloid one could be used instead. Many have researched and commercialised the cassegrain design, and it holds the advantage of an upward-facing receiver. This can be easier to cool and structure without extensive shadowing on the primary. For HCPVs, shadowing within the cassegrain causes the loss of 1 sun, which is not significant compared with the hundreds of suns an HCPV is designed to produce. The dark image produced on the PV receiver may, however, affect the PVs efficiency. The shadow is $1/C$ of the total area where C is the geometrical concentration ratio.

Low optical tolerance is associated with the cassegrain design because it uses two reflective stages, thus compounding the reflective error and the uncertainty in incidence angle of the light rays (see Fig. 2). It often requires a tertiary optic to improve the acceptance angle, but there are methods to avoid this such as decreasing the path length of light rays within the system. This decreases the effect of error on the final light ray position [13]. The cassegrain reflector arrangement allows the PV receiver to be mounted below the main reflector. This geometry gives

easy access to the receivers during replacement and thus drastically lowers maintenance costs. Furthermore, the whole optical geometry can be designed using ray tracing and is usually considered a compact solar concentrator. The minimum aspect ratio of the cassegrain design has been calculated as one fourth [2], but the same has yet to be proven for a cassegrain design with a nonimaging (hence different ray path lengths) primary and/or secondary [10].

The final hurdle in any concentrator optic development is manufacturing and practical testing. Unless the design has a sufficiently high optical tolerance then errors in geometry replication and alignment will decrease the performance. Practical considerations—such as fluctuations in temperature, moisture, wind, and shadowing—can also affect results as expected.

1.2.3 Optical Tolerance, Etendue, and Solar Tracking

One of the main challenges of concentration optics is the decrease in acceptance angle as concentration ratio is increased due to etendue. Optical tolerance refers to all possible alignment uncertainties within the optical system including component misalignment, cell position uncertainty, and tracking error. For high and ultra-high concentrator optics, this is difficult to overcome without compromising another attribute such as optical efficiency or irradiance distribution. Conventionally, the acceptance angle of an optical system is taken to be the offset angle from normal solar incidence, which achieves 90 % of the normal incidence power. This value may be different for $\theta > 0$ and $\theta < 0$ in an asymmetric concentrator (or one with asymmetric errors). If the acceptance angle is maximised, then it decreases the need for highly accurate and more expensive optics, structure, and tracking. A minimum requirement for the angular tolerance, θ_t, and hence the acceptance angle of a system, is to exceed the effective solar angular radius, θ_i. Assuming that $\sin\theta_t \approx \theta_t$, the following equation is formed [14]:

$$\theta_t \leq \frac{n \sin\theta_o}{\sqrt{C_g}} - \theta_i \tag{4}$$

The acceptance angle or optical tolerance for high-concentration devices, such as parabolic dishes and Fresnel lenses, without additional optics can be expected to be very low ($\pm \approx 0.5^\circ$ or less) [15–17]. However, there are exceptions to this with increasing focus on improving acceptance angles for HCPVs [13].

High-concentration optics have the limitation of requiring continuous tracking. The acceptance angle can be determined from the variation of optical efficiency as a function of the incident angle of the input light rays. However, there is slight variation in the value at which to measure the acceptance angle (e.g., 95–80 % of the normal incidence maximum). During practical testing, the short circuit current or power output can be used to measure acceptance angle, but each gives slightly differing results [18].

During the day the Sun is viewed as having a daily rotation about its north-south axis. It then also has a seasonal north-south motion of $\pm 23^{\circ}27'$ away from the equator [19]. Due to the Earth's axial tilt and elliptical orbit, the Sun's noontime position also slightly changes. Jagoo [19] give the derivation for the Sun's position equation as well as a comparison of the theoretical azimuth and theoretical altitude with measured values at different times of the day. Single-axis trackers follow the east–west motion of the Sun during the day but are unable to fully consider the seasonal variation. Dual-axes trackers give optimal performance year-round. However, trackers introduce their own error and cost and are less resistant to natural extremes, which could permanently damage the system. Dynamic trackers use sensors to generate a differential signal when the device is not positioned optimally for available incident light. Although easy to build and maintain, these devices fail to discriminate between the obscured Sun and a bright spot in a broken cloud [19]. The chronological tracker maintains the receiver normal to the Sun using a built-in clock and is typically single-axis. This type of tracker requires frequent manual adjustments, thus making it difficult to accurately follow both daily and seasonal variations and only works over a portion of the time because it rotates 15°/h.

1.2.4 Reflection and Refraction

Snell's law of refraction dictates that any ray travelling through a medium with refractive index n_1, which is then incident on the surface of another medium of refractive index n_2, will have a path described by:

$$n_1 \sin \alpha_1 = n_2 \sin \alpha_2 \tag{5}$$

where α_1 and α_2 are the angles the ray makes with the normal of the surface before (angle of incidence) and after refraction (angle of refraction). Snell's law can also be applied to the case of reflection where the refractive medium is replaced by a mirror. In this scenario, the ray will continue to stay in the same medium of refractive index n_1, and so Eq. (5) becomes Eq. (6) where α_2 is referred to as the angle of reflection:

$$\begin{aligned} n_1 \sin \alpha_1 &= n_1 \sin \alpha_2 \\ \alpha_1 &= \alpha_2 \end{aligned} \tag{6}$$

Total internal reflection (TIR) occurs when a light ray comes into contact with a less optically dense medium (lower refractive index) than the medium it is currently travelling in and if the angle of incidence is greater than the critical angle for TIR. The critical angle for TIR can be calculated using Snell's law by letting $\theta_2 = \frac{\pi}{2}$ and rearranging for θ_1, which now represents the critical angle θ_c:

$$\theta_c = \sin^{-1}\left(\frac{n_2}{n_1}\right) \tag{7}$$

When a mirror is placed against the surface of a lens (n_2 now > n_1), TIR is lost, and the rays will be reflected with the mirror's reflectance properties (approximately 90 %). By leaving an air gap between the two materials both the TIR and refracted rays, which do not meet the TIR criteria (otherwise lost), are kept within the optical system.

The surface of both reflective and refractive surfaces must be smooth to avoid the scattering of light. The previous equations assume optically smooth interfaces between two lossless media, but light can be partially or fully absorbed, refracted, and reflected. For lenses, a rough finish will decrease TIR or alter the refraction direction intended; for mirrors, a greater proportion of the light will be diffusely reflected (scattered) instead of specularly reflected (direct). On a very smooth surface, lines normal to neighbouring points along that surface are parallel to each other, and multiple light rays reflect specularly, all with the same definite angle pertaining to Eq. (6). In diffuse reflection, all of the reflected rays still behave in accordance with the law of reflection, but the roughness of the surface means normals along the surface vary. Because the angle of incidence depends on the normal line at the exact point a ray hits, the incident angles for a set of parallel rays will not be the same, and each reflected ray will have a different angle of reflection, hence scattering occurs.

Gaussian scattering can be applied to optical surfaces using Eq. (8) within simulations to produce more accurate irradiance distributions, which will be affected by nonideal factors in the optics [20].

$$R(\alpha) = R_0 \exp\left[-0.5(\alpha/\sigma)^2\right] \tag{8}$$

where R_0 is the radiance in the specular direction, and σ is the SD of a Gaussian distribution in degrees (0.2).

High-concentration optics very rarely will be able to use any diffuse irradiance. Most materials exhibit a mixture of specular and diffuse reflection along with absorption and transmittance (refraction); examples are given in Materials for HCPV Optics . For most interfaces, the fraction of light increases with increasing angle of incidence until, in scenarios capable of TIR, the critical angle is surpassed.

The refractive index is also wavelength dependent, and although this variation can be negligible at certain solar energy wavelengths and for relevant materials, for high-concentration optics it can compromise the refractive optical design, thus limiting the concentration ratio (such as for Fresnel lenses) and affecting the reliability of the system by way of the optical efficiency, acceptance angle, and irradiance distribution.

Most solar concentrators will be encased for protection including a transparent cover material forming the input aperture of the collector system. There are two parallel interfaces for this as well as any other panes used (e.g., air/glass and

glass/air) with reflection at each interface. Every transparent material exhibits some absorption due to the interaction of incident radiation with the molecular structure of the medium. Norton [21] discussed the effect of incidence angle on the transmittance of light and indexed sources of material data to replicate the theoretical absorbance/transmittance as well as strength and other properties important for solar collectors.

When using a refractive optic, care must be taken that TIR does not work against the design by reflecting light backwards instead of toward the receiver. This is negligible when the optic is in optical contact with the solar cell, but errors in the interface (mismatched slopes, grooves, cracks, bubbles) will allow for air ($n = 1$) and unwanted reflection. Antireflection coatings for solar cells are common, but information about the angle of incidence required is limited. The coating could decrease reflection for approximately normal incident rays but increase it for wide-angled rays. For final-stage refractive optics, which have a greater portion of output rays at wide angles, the overall energy incident on the solar cell would be decreased.

1.3 Historical Overview

1.3.1 HCPV Optical-Design Milestones and Current Trends

John Hadley introduced parabolic mirrors into practical astronomy in 1721 when he used one to build a reflecting telescope with little spherical aberration [22]. Before that, telescopes used spherical mirrors. The first reported use of an external flat reflector in a solar thermal concentrator was in 1911 by Shuman for a water-pumping system powered by a flat-plate reflector assembly [21]. Lighthouses also commonly used parabolic mirrors to collimate a point of light from a lantern into a beam before being replaced by more efficient Fresnel lenses in the Nineteenth century [23]. Augustin Jean Fresnel was the first to discover the use of Fresnel lenses in 1822 as glass collimators in lighthouses [24, 25]. Only when less costly materials such as poly(methylmethacrylate) (PMMA) were discovered were Fresnel lenses implemented as solar energy collectors in the 1950s. In the late 1970s, the first modern Fresnel lens CPV system was built at Sandia National Laboratories [26]. Interest in Fresnel lense solar concentrators increased in the second half of the twentieth century [4].

In the 1960s, Giovanni Francia was the first person to apply the Fresnel reflector concentrator concept for industrial thermal processes in Italy [27]. The compound parabolic concentrator (CPC) was the first 2D concentrator ever designed, also in the 1960s, but the theory was not explicitly explained until the 1970s when the generalized entendue was derived [2].

Regarding concentration measurements, since the first ultra-high flux measurements were performed at the University of Chicago in 1988, there has been very rapid progress including experimental investigation of laser pumping and materials

processing experiments performed at the National Renewable Energy Laboratory High-Flux Solar Furnace and the Weizmann Institute Solar Tower [2].

Concentrating solar technologies have passed the testing and small-scale power-production phases and are now being commercialised [19]. A noticeable trend in large solar concentrator designs is the shift from continuos surfaces to segmented surfaces of optics, e.g., using many smaller flat or circular facets to make a large parabolic dish. Evidence shows that this is now one method to improve the performance of reflector concentrators as shown by Zanganeh et al. [28]. Solar dish concentrators based on ellipsoidal polyester membrane facets and V-groove reflectors have been showing improved irradiance distributions whilst still obtaining optical efficiencies of >80 % [28]. Nilsson et al. [11] proposed a stationary asymmetric parabolic solar concentrator with a microstructured reflector surface; three different microstructures were tested for their effect on irradiance distribution and optical efficiency. The highest optical efficiency reached 88 %, and all distributions decreased distribution peaks. For high concentration, an array of small concentrators per cell module is the safer design considering manufacturing, maintenance, damage, and replacement [9], and it is the same for systems with mulitple concentrators per cell.

Third-generation organic PVs have begun to be tested under concentrated sunlight as well. Organic PVs are a potentially low-cost, lightweight, and flexible alternative to inorganic PVs, but they have poor durability. Under concentration levels <10 suns, the short-circuit current increases with concentration in a linear fashion, whereas the open circuit voltage increases logarithmically [29]. At >10 suns, heating of the organic PV material causes a decrease in the open circuit voltage [29]. At present only low-concentration optics—such as light funnels, wedges, luminescent concentrators, and small reflective dishes—are being used with organic PVs.

2 Primary Optics

The majority of HCPV concentrators will be point focus and require two-axis tracking. They are well suited for large field installations in the 10–100-MW range [8] rather than smaller scale systems or for domestic use. High-concentration optics are only suited to sunny areas where direct sunlight is available due to their high dependency on normal incident light rays and specular reflectance rather than diffuse.

2.1 Fresnel Lens

The most developed refractive concentrator is the Fresnel lens, which is made up of a chain of prisms (see Fig. 3) where each prism contributes a section of the slope of the lens surface but without the material of the full body of a conventional singlet [4].

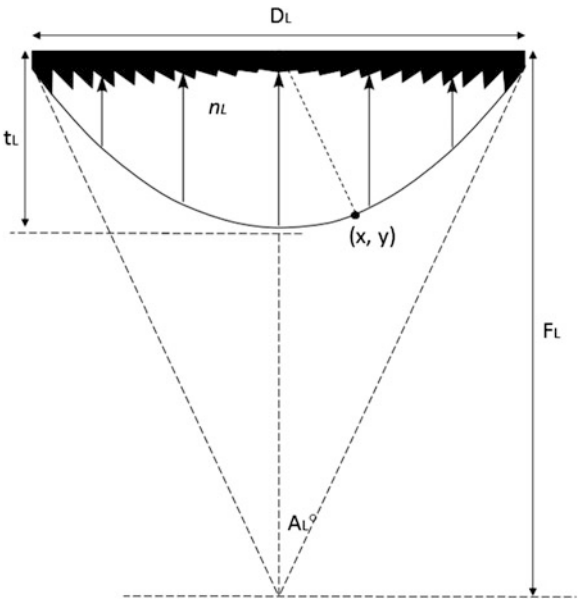

Fig. 3 The conversion from a conventional convex lens to a compact Fresnel lens by way of truncation. Dimensions and geometry of the lens are shown: diameter of the lens D_L; original thickness t_L; original focal length (which is now termed the "back focal length" of the Fresnel lens) F_L; refractive index of the lens n_L; and the maximum angle of concentration A_L

According to Fermat's principle that all rays have an equal path length, then the following equation can be obtained for a full-bodied aspheric convex lens [26]:

$$F_L + (n_L + 1)t_L = \sqrt{(F_L - y_L)^2 + x^2} + n_L y \tag{9}$$

By substituting $D_L/2$ for × and the thickness of the lens t_L for y, the following equation relates the focal length to the thickness [26]:

$$\frac{t_L}{D_L} = \frac{\sqrt{F_L^2/D_L^2 + 1/4} - F_L/D_L}{n_L - 1} \tag{10}$$

For a solid lens, only the angular orientations of the outer surfaces on which light is incident and transmitted are relevant to the focusing action. The thickness of the inner medium is not important and in fact absorbs more energy the longer the light travels in the medium. So by collapsing the convex lens down to minimise the thickness, the rays should approximately still focus in the same area but require less lens material to do so.

The centre of curvature of each ring in a Fresnel lens can be designed to recede along the axis according to its distance from the centre to eliminate spherical aberration. Fresnel reflection causes approximately 8 % loss within the Fresnel lens, and for easy mold removal any vertical lines shown in a Fresnel diagram are typically actually inclined at 2° [26].

In a Fresnel lens, the discretisation and the sharp edges of the prisms, which are absent in the convex, are a source of unwanted diffracted rays. Consequently, the Fresnel lens is a much poorer imaging lens than the original smooth convex lens; however, as stated previously, imaging of the source is not necessary in power collection. This small percentage of loss is greatly outweighed by the relative lightness and compactness of the Fresnel lens. The convex lens would not be used in a commercial HCPV system as a primary optic. In general, high-concentrating Fresnel lenses are actually also avoided commercially because in large structures mainly formed from glass, such lenses are still considered unwieldy, heavy, and expensive [9]. This gives more reason for modular designs with Fresnel lenses focusing toward very small solar cells ($100\ \text{mm}^2$) or all focusing to one PV receiver.

The *f*-number (relative aperture) of a Fresnel lens is the focal length over the diameter. Because the *f*-number is increased, the irradiance is decreased. They are typically point-focus circular-faced lenses, although line-focus Fresnel lenses have been designed, and they can be cut to square shapes to increase the packing factor. The maximum concentration ratio of a single Fresnel lens, which is limited by chromatic aberration, is approximately 1000× [30]. However, by combining a diverging polycarbonate (PC) lens and a converging PMMA lens, the concentration limit can be increased up to 8500× [31].

There are two types of Fresnel lens: imaging and nonimaging [12]. The nonimaging Fresnel lens has a lower manufacturing cost, but the performance is far from optimum due to the low acceptance angle and decreased geometrical optical efficiency [32]. However, nonimaging Fresnel lenses are considered less sensitive to chromatic aberration, especially when the design process considers multiple wavelengths such as in the case of the domed Fresnel lens [17]. In the case of imaging Fresnel lenses, the output image can be altered by aberrations due to inaccurate manufacturing of the prism tips and grooves [4]. However, acceptance angles close to the theoretical maximum and 100 % geometrical optical efficiencies are [32–34]. For both types, ray-tracing software can be used to improve the optical efficiency, acceptance angle, chromatic aberration, spot shape, and flux uniformity. For Fresnel lenses, there is a compromise to be made between module thickness and the above mentioned list of attributes, which increase as thickness decreases [23].

The irradiance distribution for Fresnel lenses, such as for many concentrator optics, is originally a Gaussian shape, which is difficult to match to a square solar cell. However, an asymmetrical curved Fresnel lens, which has very good uniform irradiance (ratio of maximum and minimum irradiance points <2), is possible [32]. There are significant manufacturing problems with this type of Fresnel lens due to the nonsymmetric design and problems in molding the curved lens [32]. A hybrid Fresnel-based concentrator with a significantly improved uniformity, compared with a traditional Fresnel lens, can be obtained by tailoring the order of the Fresnel prisms as shown in Fig. 4 (adapted from Zhuang and Yu [35]).

The use of an aspheric lens (Fresnel or not) to obtain high concentration by eliminating spherical aberration is widely known, and the profile can be calculated using Fermat's principle. When considering chromatic aberration, ray-tracing

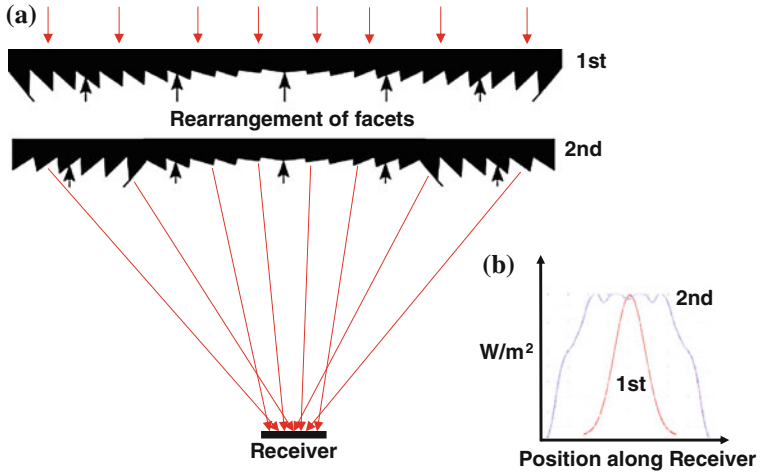

Fig. 4 **a** Diagrammatic representation of improved Fresnel-based concentrator and **b** irradiance distribution profile on the receiver [35]

methods or calculations involving two or more wavelengths are an effective method to decrease the dispersion of the focus beam. A dome-shaped nonimaging Fresnel lense can be made in such a way with improved optical efficiency and less transmission of infrared rays, which may or may not be beneficial to the PV material being used.

Fresnel lenses offer high optical efficiencies and low production costs, which explains their development as PV concentrators over the years.

2.2 Parabolic Reflectors

The point-focus parabolic dish and line-focus parabolic trough can be concave or convex (inverse) where the active side (that which is used to redirect the light) faces the source. The parabolic dish is a paraboloid of revolution, a surface obtained by revolving part of a parabola about its axis of symmetry. The parabola shown in Fig. 5 may be represented in cartesian coordinates by:

$$D_r^2 = 8\, F_r\, t_r \tag{11}$$

and:

$$4\tan(A_r/2) = \frac{2x}{F_r} \tag{12}$$

As shown in Fig. 1b, when two parabolas have coincident focal points and hence the same angle A, then the following equation relates the two:

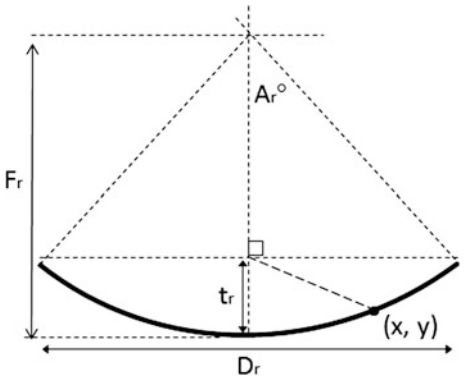

Fig. 5 Dimensions and geometry of a parabolic curve reflector in two dimensions

$$\frac{x_1}{f_1} = \frac{x_2}{f_2} \tag{13}$$

Parabolic troughs are usually designed for low to medium concentration ratios with a half-acceptance angle two to three times the apparent angular width of the Sun's disk. The maximum concentration ratio of a parabolic trough concentrator, which can attain high optical efficiency and high acceptance angles without the aid of a secondary optic, is limited to $\sim 70\times$ [36]. Beyond this, the parabolic trough is suitable for concentrations up to 200 suns and although possible, it is rarely used for HCPV applications [3]. The use of a second concentrator is needed to bring the concentration value as close to the limit as possible. Therefore, the usual approach is to take advantage of the low aspect ratio values of focusing primary optics and use second-stage concentration at the receiver to increase the overall concentration value. Parabolic trough concentrators are the most proven and commercially tested solar thermal concentrator technologies, and the California Mojave Desert has nine large commercial-scale solar power plants in operation [19], but the parabolic dish is used for HCPV systems.

Large paraboloids are difficult to manufacture accurately, and sometimes smaller flat or conic mirror facets are arranged to approximate the paraboloid shape. The trough is inherently easier to manufacture and can be performed so by bending a flat reflective sheet [3].

A parabolic dish (point-focusing) solar collector is advantageous compared with other collector systems due to the absence of cosine losses and the increased concentration ratio compared with the line-focusing parabolic trough [37]. The 3D parabolic dish can be thought of as the most efficient high-concentration optic with the fewest restrictions, but maximizing their full potential is very expensive compared with the point-focus Fresnel lens [19]. Parabolic dishes have greater optical efficiencies than that of the linear Fresnel reflector or central receivers where cosine losses ensue.

As for their performance at high-concentration ratios, although parabolic reflectors on their own can reach high optical efficiencies or have relatively uniform

irradiance distribution (by matching receiver size to beam radius), they cannot perform both unless other optical stages are used due to the gaussian shape of light from the Sun [38, 39].

Parabolic mirrors for dish power-generation systems are generally constructed from one large parabola per dish, although less expensive techniques, such as forming the dish from an array of small mirrors, are becoming more common [9].

2.3 Linear Fresnel Reflector and Heliostat Fields

Linear Fresnel reflectors (LFRs) implement flat mirrors in strips at increasing tilt positions at further distances from the receiver (usually positioned above the LFR). Most LFR systems are solar thermal, and research into receiver shapes and areas has been conducted. They have been classed as low-concentration optics in the past, but they can be used as medium concentrators. To reach greater concentrations, bent or parabolic mirrors are needed in place of the flat mirrors, and hence LFRs are sometimes not considered as high-concentration optics, but their parabolic or similarly curved counterparts would be. The central receiver set-up has the advantage of being a stationary fixed receiver, which is easy to structure and support, and it decreases the weight and strain on moving optics. This can be adoptable for any collector field-tower receiver set-up, and typical support tower heights are up to 10 × 15 m tall [9].

Abbas et al. [40] reviewed LFRs and described how the variation of the total power impinging onto the receiver and its flux map along the day has traditionally been identified as a major handicap for LFR technology. This problem is first due to the optical efficiency of the solar field, which varies more than in trough collectors [41], as well as the change on total radiation falling within the field, which is caused by the zenith angle.

The linear Fresnel reflector has the ability to "reshape" the mirror surface, which is a major advantage compared with the trough system. Solar movement across the sky can be compensated for by simple adjustment of the mirror elements rather than requiring movement and control of the reflector/receiver unit as a whole. This simplifies the support and tracking structure leading to fewer implementation costs [9].

Linear Fresnel reflector systems have relatively low initial cost, and because the reflector strips are ground-mounted, wind loads on the reflector strips are low.

Fields of heliostats are similarly used for thermal power towers and some smaller-scale PV central receivers have gained growing interest, but at present their use as HCPV optics is rare. Plans for space solar-concentrator optics, which would direct light toward solar fields on Earth, consist of a lightweight array of heliostat mirror satellites in a constellation in low Earth orbit (1000 km). Although this may seem far-etched, NASA is developing a solar sail due to be finished by 2015. The Earth-based solar fields, which would receive the extra 6 $kWh/m^2/day$, are already being constructed [8]. This idea involves taking advantage of the dawn-to-dusk

sunsynchronous orbit adopted, i.e. a near-polar orbit of inclination angle 99° rotating at 1°/d, to remain consistently normal to the Sun's rays.

On the Earth's surface, each heliostat has a dual-axis tracking system, and the overall field usually takes on a circular or semicircular array [21].

3 Secondary and Final-Stage Optics

In high-concentration optics, secondary optics are necessary for high performance and high reliability. Due to the low optical tolerance of HCPVs, this is important even during prototype stages where manufacturing and alignment is perhaps not optimum. This is even more important for optical systems of multiple stages, such as the cassegrain, and as the concentration ratio is increased. As one can imagine, tertiary optics are common depending on the design of the optical system, and a wide range of shapes is used. Reflective secondary optics tend to have increased flux uniformity and colour-mixing effects, but dielectric secondariness using TIR can withstand more internal reflections without much loss [42]. Too many reflections in both optics results in severe light ray loss by way of Fresnel losses, not meeting TIR criteria, or in light being reflected back (opposite direction of receiver). The three main families of final stage optics are the dome-shaped lens, the compound parabolic concentrator (CPC), and the light funnels (light cones). Although all are capable of increasing the concentration ratio, irradiance distribution, and/or acceptance angle on the solar cell(s), the optimum receiver optic will depend on the design and constraints of the system.

Nonimaging secondary optics can improve the irradiance uniformity and eliminate shadowing better than imaging secondary optics for certain systems. The nonimaging secondary optic can be formed by rotating a segment of curve from a linear, quadratic, and even cubic order function [10].

3.1 The Revolved Conics

This section refers to the ellipsoid, paraboloid, hyperboloid, and even the sphere (the circle can be argued to be and not be a true conical shape) as revolved conics producing 3D point source optics. These are typically used as the second stage of reflection in the cassegrain set-up described earlier, and thus their size should be kept low to avoid shadowing effects on the primary. Although these secondary optics will share the same advantages and disadvantages as the larger primary versions, due to their smaller size they are easier to manufacture accurately. They will also undoubtedly introduce their own errors into the optical system, but these too are easier to minimise on a small scale than in the high-concentrating versions. The revolved conics are imaging optics, and so microscopic and macroscopic imperfections will increase the focusing point diameter and cause lower concentration.

As mentioned in the Introduction, high concentration is difficult to achieve with line-focusing optics, but the combination of two linear optics can produce an overall point focus capable of high-concentration ratios up to 2000 suns [3]. This is performed by the primary linear optic focusing in one plane along its length to create a line focus and then the secondary linear optic focusing that line to a point. In this set-up, the path of most rays within the optical system are longer than in the conventional point source counterpart, and so further beam spread is incurred as is increased shadowing from the oblong secondary optic, but accurate manufacturing is more economic.

A 2D profile of a dome lens can be designed that redirects all incoming rays from the first-stage (and possibly second-stage) optic toward the cell. The 3D lens is then rotated around the optical axis. The dome lens typically uses less material than a CPC and can be easier to manufacture [20]. The significant advantage of the dome-shaped lens is the uniform irradiance distribution it can provide on the cell [20]. A ball lens can also be used as a secondary optic, but this would perhaps still require a tertiary optic at the receiver. Due to the ball lens 3D symmetry, any expansion due to heat should not affect the performance of the ball lens to redirect the light rays to the intended destination. However, the weight and support of the ball lens is more difficult to accommodate.

The paraboloid, ellipsoid, and hyperboloid mirrors are typically used as secondary reflectors wherein the latter is more tolerable to errors and hence can improve the acceptance angle of a system when replacing a secondary paraboloid. The ellipsoid, semisphere, and sometimes even flat mirrors are used in arrays to emulate a larger parabolic dish with simultaneously high optical efficiency and irradiance distribution.

Many novel secondary optics have been aimed at improving irradiance distribution on the PV receiver, but most of these require the input aperture to be fully illuminated, which—although possible in HCPVs—does then limit the acceptance angle.

3.2 The CPC and Its Variations

The 2D profile of the CPC can be described as having focal points of both parabola sides located at the intersection between the opposite parabola and the receiver. The compound parabolic concentrator is designed using the edge-ray principle and is considered an ideal concentrator in two dimensions. This means that no rays within the acceptance angle are lost, and hence it achieves maximum theoretical concentration. All rays entering at the extreme collecting angle are conserved on the output exit aperture with no loss of rays. The length is bound by the extreme rays at θ_i where both rays reach the receiver. The focal length can be given as [2]:

$$f = \frac{a'}{1 + \sin\theta_i} \tag{14}$$

where α' is half the exit aperture.

The overall length is [2]:

$$L = \frac{a(1 + \sin\theta_i \cos\theta_i)'}{\sin^2\theta_i} \tag{15}$$

And the entry aperture diameter in:

$$a = \frac{a'}{\sin\theta^i} \tag{16}$$

From Eqs. (16) and (1), the CPC matches the maximum theoretical concentration ratio. In the ideal 2D CPC design, the rays incident on the rim of the exit aperture are said to be at the boundaries of failure regions, which in 3D designs are realised for skew rays. A 3D CPC can be made from revolving the 2D profile (circular), by crossing two linear CPCs (square), or by more complex computation methods for specific geometries such as the rotationally asymmetrical compound parabolic concentrator [43].

In the 3D CPC (Fig. 6a, b), there is a 3-fold infinity of rays as opposed to the 2-fold infinity in the 2D design, and the rays outside the meridian sections can no longer be guaranteed accommodation in the same way as the 2D rays (because the light ray can now be skewed) and hence be reflected out of the CPC.

The linear dielectric-filled CPC can also be designed to account for the acceptance angle inside the dielectric due to refraction using:

$$\sin\theta_i\ (n - (2/n)) \quad \text{or} \quad \sin\theta_i'(1 - (2/n^2)) \tag{17}$$

From this equation, it is preferable to choose refractive materials with a refractive index greater than the square root of 2, but in the case of 3D, rays will still be lost. The dielectric-filled CPC takes advantage of TIR and increases the collecting angle for the same length as a reflective CPC. Thus, this gives the possibility of a higher acceptance angle or shortening of the CPC [2].

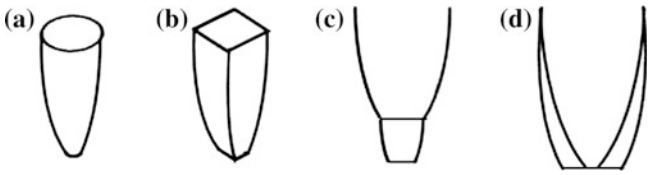

Fig. 6 Variations of CPC. **a** Revolved CPC. **b** Crossed CPC. **c** CCPC. **d** Lens-walled CPC

The CCPC (Fig. 6b) has been found to be an ideal concentrator for a half acceptance angle of 30° and outperforms the revolved CPC as a static solar concentrator at 3.6× concentration [44]. The square-apertured CCPC is also preferable due to its higher packing factor when arrayed side by side, and less PV material is wasted in manufacturing because of the efficiency of cutting square PV cells rather than circular ones. However, the CCPC, like the CPC, does not have a good output irradiance distribution for a flat receiver, and hot spots can reach 50× the energy of the incident rays [44]. The CCPC can be classed as a new type of secondary optic for HCPV systems, which requires further study.

In attempt to decrease the amount of material required in a CPC (the high length-to-width ratio) and hence decrease the weight and expense depending on the material used, the two-stage CPC [CCPC (see Fig. 6c)] is an option. The first stage is in the air with a regular reflective CPC; then, instead of a solar cell at the exit aperture, there is another transparent material filled CPC using TIR. Another method to decrease the length of the CPC is to use truncation, i.e., removing part of the entrance aperture end, which tends to a gradiant of 0. By doing so, there is little decrease in the concentration ratio with a sizeable decrease in the length. Truncation can increase the half acceptance angle of a CPC, but it also decreases the geometrical concentration ratio. The maximum concentration ratio can only be achieved by a full-height CPC without truncation [21]. Larger-opening angles can decrease wind-induced deviations, manufacturing tolerances, and sagging effects, whist through optimisation they can still yield high acceptance angles [36].

CPCs can absorb direct and diffuse solar radiation, and, as low concentration devices, their acceptance angle is much greater than that of high-concentration systems. Correspondingly, optical efficiency decreases slowly within the range of the acceptant angle the CPC is designed for, but it decreases rapidly beyond this range. The main disadvantage of the CPC is the very nonuniform irradiance distribution it outputs with a very high peak in the centre [20]. The lens-walled CPC (see Fig. 6d) is designed such that the the two parabolic curves of the 2D CPC profile are each rotated from the light-entry side to create a type of wedge shape with parabolic curves. The optical efficiency is lower than the original filled CPC or mirrored CPC, but the irradiance distribution is somewhat improved. The lens-walled CPC is also capable of higher acceptance angles [45]. One design of the lense-walled CPC reports $\sim$65 % optical efficiency at 0° incidence, which decreases slightly to $\sim$60 % at 20° from normal [45].

For an ideal CPC the exploitable part of the diffuse irradiance is 1/c but this contribution to a high concentrating system is negligible.

3.3 Light Funnels

Light funnels (light cones or homogenisers) all follow a funnel shape (Fig. 7) and are typically used in the same fashion as a funnel where their prime aim is to capture more stray light due to errors and redirect them toward the receiver. Light

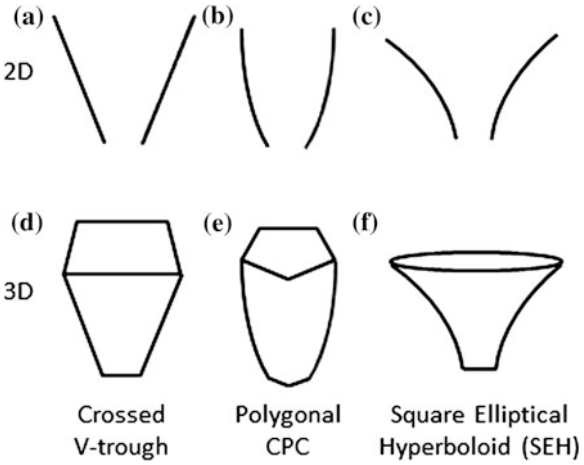

Fig. 7 Examples of 2D profiles and possible 3D transformations. **a** V-trough. **b** CPC. **c** Compound hyperbolic concentrator. **d** 3D square-apetured V-trough. **e** Polygonal apertured CPC. **f** Hyperboloid with an elliptical entry aperture and square-exit aperture

funnels can first be described by their 2D curves (Fig. 7a–c) where the side walls will be flat (V-trough), hyperbolic, or elliptical. However, the most popular cones are the CPC, as described previously, and simple V-shaped cones in order to save on manufacturing costs and decrease complexity. Further variations are possible when the 2D profile (V-shaped, CPC-shaped, or hyperbolic curved as shown in Fig. 7a–c) is translated into 3D where circular, square, or polygonal entry apertures can be realised (Fig. 7d–f). In this way we obtain the square-faced V-trough, the circular cone, the elliptical cone, and many more complex variations. Merged forms, including the circular-square cone, which has a circular entry merged with a square exit, are possible as well. Square solar cells are more common than circular, and hence square-exit faces are usually desired, but there are plenty of examples of circular cells with circular optics [42, 46].

At present, light funnels are all used in the same fashion in HCPVs which, as described, is to funnel light toward the receiver with the receiver being a solar cell, an array of solar cells, or possibly another type of low concentration optic that is attached to the solar cell(s) (specifically the two-stage CPC design and any variations would fit this description). In arrangements with an array of solar cells, the HCPV system will only work as efficiently as the lowest-performing cell. Hence, errors in irradiance distribution or tracking can severely limit the system's full potential. There is less risk of this happening with an accompanying optic or array of optics attached to the receiver.

The light cones are simple forms of nonimaging devices, some of which have been used for many years [2]. The advantage of these light cones is by far their simplicity yet effectiveness at increasing acceptance angle. They are not ideal optics; many of the light rays, even within a critical angle of incidence, can still be lost. In all of the designs there is a compromise between entry aperture width, which allows a greater acceptance of deviated rays, and slope or height of the walls. A smaller gradient in the walls results in smaller reflection angles, hence more

reflections and rays not meeting TIR criteria or reflecting backward out of the system. Similarly, if the height is increased to maintain the wall slope whilst increasing aperture width, then the ray will travel longer in the light funnel and incur a greater number of reflections resulting in the same problems.

The equation:

$$2y = (\pi/2) - \theta_1 \tag{18}$$

can be used to determine the length of a cone for a given entry aperture diameter, but some rays within θ_i can still be reflected out of the cone. The 2D V-trough is far from ideal as depicted by earlier literature [2]. The identification rays that are reflected out of axisymmetric cone shaped concentrators can be performed according to the procedure outlined by Winston et al. [2] for the CPC. The optical efficiency of a cone for rays within the acceptance angle is approximately 80 % with smaller-angled cones performing closer to ideal concentrators. A V-trough concentrator will have very high acceptance angles when its geometrical concentration ratio is <2 [47]. The crossed V-trough (inverted pyramid) and similar square-shaped light funnels are the simplest but most effective method to couple a circular primary optic with a square cell as well as homogenizing the irradiance distribution on the cell.

The square elliptical hyperboloid (SEH), which is based on the ideal trumpet concentrator, has recently been developed with an elliptical-entry aperture connected to a square-exit aperture by way of hyperbolic curves (Fig. 7f) [48]. A concentration ratio of 6× for the SEH is the optimum for use as a stationary solar concentrator despite its low optical efficiency of 55 %. The main use of this type of concentrator, however, is for building integrated PV applications, and its performance as a final-stage light funnel still has to be tested. The SEH designed for 4× concentration ratio has a greater optical efficiency of 68 % and may be more suited to HCPV optical systems.

One particular type of optic, which has no concentration effect and is purely for ensuring that rays travel toward the receiver, is the straight-forward light pipe or light rod. The light rays are focused onto the surface in the same way as in a light funnel, but the width of the entry aperture is not greater than that of the receiver. The light rod would be used in optical systems where it is beneficial to position the solar cell outside the optical system or not in the location of focused rays (cooling purposes). The light rod can transport the light rays to the cell and act as a homogeniser to distribute rays evenly. If we ignore this homogenising effect, which would improve the performance of the cell, then technically the acceptance angle would be the same as when the receiver was placed at the entry-aperture position of the light rod. For that reason, it cannot be called a light funnel or cone that directly improves the acceptance angle. Depending on the condition of the focusing light rays, it may only improve the irradiance distribution by a small factor and will somewhat decrease the optical efficiency due to absorption and if too many internal reflections are incurred. The light rod is hence the simplest method purely to reposition the cell.

4 Materials for HCPV Optics

A critical task in any concentrating optic design is identifying the best possible materials. Ideally a material would have high optical efficiencies (90–100 % reflection or transmittance), high thermal and ultraviolet (UV) tolerance, physical durability against environmental conditions, and overall economical to produce. In some systems using both a refractive element and a reflective element, both refractive and reflective issues must be addressed, but with careful design they may complement each other. For example, a secondary mirror optic may correct for primary lens aberrations as long as they are not severe. Generally, reflective materials are more cost-effective than refractive materials [10].

4.1 Refractive Optics

Glass can withstand high temperatures and is typically the best choice for high-quality accurate optics. Most plastic materials have less effective light-transmission properties compared with glass and tend to degrade with heat and UV exposure. Glass can be used over decades in some applications (regular maintenance, such as cleaning, is still required), whereas plastics typically last for only a few years [21]. The combination of strength, flexibility, and light weight, however, makes plastics more attractive with an overall aim to save money on capital and running costs (less-expensive solar tracker systems are required for lighter systems). Polymers—such as PMMA, which has a refractive index of 1.49 (very close to that of glass)—are often used in solar concentrators with good solar spectrum matching and resistances to ageing. PMMA remains thermally stable up to at least 80° [4] and is perhaps the most popular polymer used in CPVs. Polyethylene is used widely in other areas, such as a plastic film, but it has a short lifetime of only 1 year [21]. Polyamide, polystyrene, acrylics, and PC have been investigated (at least as covers for flat-plate collectors), but more research is required, especially regarding their durability. Durability is a topic that lacks data in many areas. Testing requires several years to pass, although some advanced weathering simulations are possible as is modelling. High levels of temperature, humidity, and solar radiation have, however, been proven to accelerate ageing with thermal effects proving most detrimental.

The properties of plastic films are dependent on the length of the polymer chain: Longer chains result in less brittle material. However, degradation due to heating, light exposure, oxidation, and mechanical breaking (scratches and repeated flexing) split these long polymer chains [21].

Fresnel lenses have traditionally been manufactured out of PMMA, which, due to the dispersion curve, makes shorter wavelengths converge faster than longer wavelengths and hence causes longitudinal chromatic aberration (LCA). Fresnel lenses may be manufactured by hot-embossing, casting, extruding, laminating, compression-moulding, or injection-moulding thermoplastic PMMA [49]. Optical

or mirror-grade PMMA material may come from the automotive, lighting, or skylight industries. Applicable formulations of optical-grade poly(dimethylsiloxane) (PDMS) material are shared with the aerospace, electronics, and light-emitting diode industries. A heavier lens technology consists of acrylic or silicone facets patterned on a glass superstate as researched in the late 1970s [50, 51]. PMMA and PDMS can be adhered to a glass superstate and patterned as a Fresnel lens. PC is sometimes suggested as an alternative to PMMA due to its significantly greater resilience, which prevents mechanical fracture and fatigue. However, PC has a smaller spectral bandwidth, less optical transmittance, and lower resistance to scratches [52]. It suffers more from optical dispersion, chromatic aberration, and solar-induced photo oxidation [53–56].

PMMA has a transmittance of $\sim$95 % and has a low glass-transition temperature meaning that high-temperature treatments, such as calcination, which is a preparation method of antireflective and antifogging coatings, cannot be used on PMMA material. Zhou et al. [57] successfully fabricated antifogging and antireflective coatings on Fresnel lenses by way of spin-assembling silica nanoparticles without any high-temperature posttreatments and reached a transmittance of 98.5 %. Super hydrophilic coatings (antifogging) can effectively prevent water condensation on transparent substrates, which can alter light concentration in CPV systems. Another way to achieve an antireflective property on PMMA (refractive index = 1.49) is to layer a single coating of refractive index 1.22. However, at present there are no bulk materials that possess such a low refractive index [57], but nanoporous coatings have voids leading to a lower refractive index and better antireflective properties [57].

As mentioned previously, the acceptance angle decreases with greater concentration ratios. To combat this trade-off between concentration ratio and half acceptance angle in CPCs, a large refractive index dielectric medium could be used to form the solid concentrator instead of the common mirror one. However, this increases the weight and amount of material required for manufacturing. The lens-walled CPC, which uses less material and thus decreases the weight, has a lower optical efficiency partly due to the low transmissivity of the lens material chosen for the lens-walled CPC and so could be improved with different materials.

Computer-controlled diamond turning machines, as well as other modern materials and molding techniques, have significantly improved the design and accuracy of refractive optics such as Fresnel lenses [24]. Similarly, computer-aided design and machining has improved the quality of reflective optics, but in both cases good-quality prototyping can be expensive when requiring smooth and accurate geometries.

4.2 Reflective Optics

Reflective concentrators do not suffer from selective wavelength absorption and dispersion associated with dielectric lenses. They use less material than any other equal concentration system because they are not filled with an optical material.

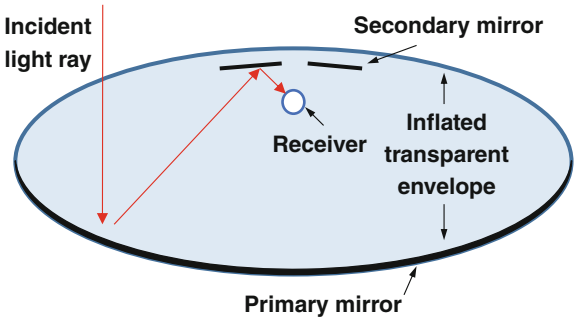

Fig. 8 Diagram of inflatable solar concentrator optics for solar thermal application. The primary mirror consisting of a silicone coated fiberglass fabric with an aluminum mirror layer [59]

They are, however, said to be more prone to manufacturing errors and are less tolerant to slope error than lenses.

In general, the optical efficiency of reflective concentrators is a coupled function of both the geometry and the mirror reflectivity. A common approximation for the effect of reflectivity on optical efficiency follows from the pioneering work of Rabl [58].

Polymer mirror films can be used as a low-cost option for reflective surfaces and have low weight and costs compared with a curved glass or polished aluminium mirror. They are, however, difficult to apply, especially to 3D shapes, and if not properly applied will not replicate the intended curve or line intended.

V-trough concentrators are one of the easiest-constructed of all low-concentrating systems: They can be fabricated from a single aluminium sheet. Bader et al. [59] attempted to lower the manufacturing costs of solar concentrators by investigating the use of pneumatic polymer mirrors. By applying slight pressure over an inflatable elastic enclosure, two opposing cylindrical curved surfaces were obtained. These encompassed a transparent foil on one side and a silicone coated fibreglass fabric with an aluminium mirror sheet on the other side as shown in Fig. 8.

Wind-induced vibrations were eliminated due to the use of a concrete structure, which is more rigid and stronger than conventional metallic frames. Self-cleaning scratch-resistant foils were applied easily, and the high-quality mirror foils were well protected from the environment. There is a high potential for a cost decrease due to the cheaper and lightweight materials, which can also be easily transported. The concrete structure would be built on site. The cylindrically shaped optics, which suffer from optical aberration, were corrected somewhat with the use of a tailor-made secondary specular reflector incorporated in tandem with the primary cylindrical mirror. However, the resulting prototype was only suitable for thermal receivers, but it shows the variance of materials possible and how they may be used to reach high solar concentrations.

Parabolic reflectors designed for high concentrations in particular can be costly to build on such a large scale. They require stronger structures and more expensive solar trackers due to their weight and high accuracy requirement. A silvered mirror using smooth glass produces a common mirror with reflectivity >85 %. The smooth glass is covered from the back and sealed with an oxidation layer. These types of mirrors are only applicable as flat reflectors. Curves—such as the parabolae, hyperbolae, ellipse, or circular—are extremely difficult and hence costly to manufacture with accuracy. Manufacturing processes used include precise grinding, milling, polishing, and a variety of coating methods for a mirror finish. Flab et al. have manufactured a mirror with a reflectivity >94 %, which is successfully being used in Colorado [19].

Jagoo et al. constructed a very low cost parabolic dish with basic tools using wood, cement, silicone paste, and fibreglass [19]. A chrome polymer reflector with an adhesive back was used for this application. It had the advantages of high weathering durability, and the system reflected 82 % of the incident sunlight. Fiberglass is cheap, impermeable, and easy to use and mould.

Alanod is a reflective thin film comprised entirely of aluminium that has a total reflectivity of 95 %. Samples coated with a polymeric chemical to protect the alumina layer can survive for a few years. ReflecTech mirror film is a polymer-based film for concentrating sunlight in solar energy arrays. The film has an overall reflectivity of 94 % and is immune to water and UV radiation.

5 Conclusion

High-concentration optics for PV applications require all types of optics including low-concentration and nonconcentration devices. As the geometric concentration ratio is increased, the acceptance angle is decreased and errors in alignment, manufacturing, reflectivity, and refraction are more noticeable. The use of smaller optics to replicate a high-concentrating optic is becoming more popular as a means to achieve high optical efficiency as well as high irradiance uniformity on the receiver. Receiver optics are essential to increase the acceptance angle, and an array of possible optics have been outlined herein. The Fresnel lens and parabolic dish maintain the most popular form of high-concentrating optic for PV applications. A variety of possible materials has been given for both reflective and refractive optics along with manufacturing methods. Depending on the constraints of a project, different concentrator types, geometries, materials, and manufacturing methods will be chosen as optimum, but tailoring a design to an application is always important, especially for high-concentration optics for PV applications. This chapter provided many options for concentrator design and manufacturing and explains the basic optical behaviour and materials used today.

References

1. Chemisana D, Mallick T (2014) Building integrated concentrated solar systems. In: Enteria N, Akbarzadeh A (eds) Solar energy sciences and engineering applications, 1st edn. CRC Press, pp 545–788
2. Winston R, Miñano JC, Benitez P (2005) Nonimaging optics. Elsevier, London
3. Murphree QC (2001) A point focusing double parabolic trough concentrator. Solar Energy 70 (2):85–94
4. Xie WT, Dai YJ, Wang RZ, Sumathy K (2011) Concentrated solar energy applications using fresnel lenses: a review. Renew Sustain Energy Rev 15(6):2588–2606
5. Luque A, Andreev VM (2007) Concentrator photovoltaics. Springer, Berlin
6. Chaves J (2008) Introduction to nonimaging optics. CRC Press, Boca Raton
7. Goldstein A, Gordon JM (2010) Double-tailored nonimaging reflector optics for maximum-performance solar concentration. J Opt Soc Am A Opt Image Sci Vis 27 (9):1977–1984
8. Fraas LM (2014) Low-cost solar electric power. Springer International Publishing, Cham
9. Sangster AJ (2014) Electromagnetic foundations of solar radiation collection. Green energy and technology. Springer International Publishing, Cham
10. Chen YT, Ho TH (2013) Design method of non-imaging secondary (NIS) for CPV usage. Solar Energy 93:32–42
11. Nilsson J, Leutz R, Karlsson B (2007) Micro-structured reflector surfaces for a stationary asymmetric parabolic solar concentrator. Solar Energy Mater Solar Cells 91(6):525–533
12. Winston R, Miñano JC, Bentez P, Shatz N, Bortz JC (2005) Nonimaging optics. Elsevier, Melbourne
13. Dreger M, Wiesenfarth M, Kisser A, Schmid T, Bett AW (2014) Development and investigation of a CPV module with cassegrain mirror optics. In: CPV-10
14. Goldstein A, Gordon JM (2011) Tailored solar optics for maximal optical tolerance and concentration. Solar Energy Mater Solar Cells 95(2):624–629
15. Julio Chaves. Introduction to Nonimaging OpticsÂ (Google eBook). CRC Press, 2008
16. Goldstein A, Gordon JM (2011) Tailored solar optics for maximal optical tolerance and concentration. Solar Energy Mater Solar Cells 95(2):624–629
17. Akisawa A, Hiramatsu M, Ozaki K (2012) Design of dome-shaped non-imaging fresnel lenses taking chromatic aberration into account. Solar Energy 86(3):877–885
18. Yamdt MD, Cook JPD, Hinzer K, Schriemer H (2014) Optical channel variability and acceptance angle in CPV modules studied by active I-V response. In: CPV-10
19. Jagoo Z (2013) Tracking solar concentrators. Springer, The Netherlands
20. Victoria M, Domnguez C, Antón I, Sala G (2009) Comparative analysis of different secondary optical elements for aspheric primary lenses. Opt Express 17(8):6487–6492
21. Norton B (2014) Harnessing solar heat, volume 18 of lecture notes in energy. Springer, Netherlands
22. Wilson RN (2004) Reflecting telescope optics I. Springer, Berlin
23. Miller DC, Kurtz SR (2011) Durability of fresnel lenses: a review specific to the concentrating photovoltaic application. Solar Energy Mater Solar Cells 95(8):2037–2068
24. Leutz R, Suzuki A (2001) Nonimaging fresnel lenses: design and performance of solar concentrators. Springer, New York
25. Yeh N (2010) Analysis of spectrum distribution and optical losses under fresnel lenses. Renew Sustain Energy Rev 14(9):2926–2935
26. Luque A, Hegedus S (2003) Handbook of photovoltaic science. Wiley, England
27. Silvi C (2009) The pioneering work on linear fresnel reflector concentrators (LFC's) in Italy. In: Solarpaces conference. Italian Group for the History of Solar Energy (GSES)
28. Zanganeh G, Bader R, Pedretti A, Pedretti M, Steinfeld A (2012) A solar dish concentrator based on ellipsoidal polyester membrane facets. Solar Energy 86(1):40–47

29. Tromholt T, Katz EA, Hirsch B, Vossier A, Krebs FC (2010) Effects of concentrated sunlight on organic photovoltaics. Appl Phys Lett 96(7):073501
30. Languy F, Fleury K, Lenaerts C, Loicq J, Regaert D, Thibert T, Habraken S (2011) Flat fresnel doublets made of PMMA and PC: combining low cost production and very high concentration ratio for CPV. Opt Express 19(3):A280–94
31. Languy F, Habraken S (2013) Nonimaging achromatic shaped fresnel lenses for ultrahigh solar concentration. Opt Lett 38(10):1730–1732
32. González JC (2009) Design and analysis of a curved cylindrical fresnel lens that produces high irradiance uniformity on the solar cell. Appl Opt 48(11):2127–2132
33. Leutz R, Suzuki A, Akisawa A, Kashiwagi T (1999) Design of nonimaging fresnel lens for solar concentrators. Solar Energy 65:379
34. Kritchman EM, Friesem AA, Yekutieli G (1979) Highly concentrating fresnel lenses. Appl opt 18:2688–2695
35. Zhuang Z, Yu F (2014) Optimization design of hybrid fresnel-based concentrator for generating uniformity irradiance with the broad solar spectrum. Opt Laser Technol 60:27–33
36. Canavarro D, Chaves J, Collares-Pereira M (2013) New second-stage concentrators (XX SMS) for parabolic primaries; comparison with conventional parabolic trough concentrators. Solar Energy 92:98–105
37. Palavras I, Bakos GC (2006) Development of a low-cost dish solar concentrator and its application in zeolite desorption. Renew Energy 31(15):2422–2431
38. Baig H, Heasman KC, Mallick TK (2012) Non-uniform illumination in concentrating solar cells. Renew Sustain Energy Rev 16(8)5890–5909
39. Shanks K, Sarmah N, Mallick TK (2013) The design and optical optimisation of a two stage reflecting high concentrating photovoltaic module using ray trace modelling. In: PVSAT-9
40. Abbas R, Muñoz Antón J, Valdés M, Martnez-Val JM (2013) High concentration linear Fresnel reflectors. Energy Convers Manage 72:60–68
41. Morin G, Dersch J, Platzer W, Eck M, Häberle A (2012) Comparison of linear fresnel and parabolic trough collector power plants. Solar Energy 86(1)1–12
42. Jaus J, Peharz G, Gombert A, Pablo J, Rodriguez F, Dimroth F, Eltermann F, Wolf O, Passig M, Siefer G, Hakenjos A, Riesen S, Bett AW (2009) Development of flatcon modules using secondary optics. IEEE, pp 1931–1936
43. Abu-Bakar SH, Muhammad-Sukki F, Ramirez-Iniguez R, Mallick TK, Munir AB, Yasin SHM, Rahim RA (2014) Rotationally asymmetrical compound parabolic concentrator for concentrating photovoltaic applications. Appl Energy 136:363–372
44. Sellami N, Mallick TK (2013) Optical efficiency study of PV crossed compound parabolic concentrator. Appl Energy 102:868–876
45. Guiqiang L, Gang P, Yuehong S, Jie J, Riffat SB (2013) Experiment and simulation study on the flux distribution of lens-walled compound parabolic concentrator compared with mirror compound parabolic concentrator. Energy 58:398–403
46. Andreev V, Ionova E (2003) Concentrator PV modules of "all-glass" design with modified structure. In: Proceedings of 3rd world conference on photovoltaic energy conversion, 2003
47. Tang R, Liu X (2011) Optical performance and design optimization of V-trough concentrators for photovoltaic applications. Solar Energy 85(9):2154–2166
48. Sellami S, Mallick TK (2013) Optical characterisation and optimisation of a static window integrated concentrating photovoltaic system. Solar Energy 91:273–282
49. Leutz R, Fu L, Annen HP (2009) Stress in large-area optics for solar concentrators. In Dhere NG, Wohlgemuth JH, Ton DT (eds) SPIE Solar Energy + Technology. International society for optics and photonics, pp 741206–741206–7
50. Egger JR (1979) Manufacturing fresnel lens master tooling for solar photovoltiac concentrators
51. Lorenzo E, Sala G (1979) Hybrid silicone-glass Fresnel lens as concentrator for photovoltaic applications. In: Proceedings of the silver jubilee congress 1:536–539
52. Miller DC, Kempe MD, Kennedy CE, Kurtz SR (2009) Analysis of transmitted optical spectrum enabling accelerated testing of CPV designs preprint. In: SPIE
53. John E Greivenkamp. *Field Guide to Geometrical Optics*. 2004

54. Kasarova SN, Sultanova NG, Ivanov CD, Nikolov ID (2007) Analysis of the dispersion of optical plastic materials. Opt Mater 29(11):1481–1490
55. Andrady A (1997) Wavelength sensitivity in polymer photodegradation. Polymer 128:47–94
56. Andrady AL, Hamid SH, Hu X, Torikai A (1998) Effects of increased solar ultraviolet radiation on materials. J Photochem Photobiol B Biol 46:96–103
57. Zhou G, He J, Ligang X (2013) Antifogging antireflective coatings on fresnel lenses by integrating solid and mesoporous silica nanoparticles. Microporous Mesoporous Mater 176:41–47
58. Rabl A (1976) Comparison of solar concentrators. Solar Energy 18(2):93–111
59. Bader R, Haueter P, Pedretti A, Steinfeld A (2009) Optical design of a novel two-stage solar trough concentrator based on pneumatic polymeric structures. J Solar Energy Eng 131 (3):031007

The High-Concentrator Photovoltaic Module

P. Rodrigo, L. Micheli and F. Almonacid

Abstract High-concentrator photovoltaic (HCPV) modules incorporate solar cells, optical devices, cooling mechanisms, and other elements in an assembly to provide the functions required to concentrate sunlight and obtain electricity. The variety of designs for configuring HCPV modules is introduced in this chapter. Thermal management, an important aspect to be considered in the design of these modules, is discussed, as are the possibilities and innovations for implementing cooling mechanisms. The behavior of HCPV modules is complex because of the different interdependent elements and involved processes and because of the changing operating conditions in the field. The experimental analysis of available modules has motivated progress in understanding this complex behavior. The influence of different atmospheric parameters on such behavior is analyzed in this chapter. In addition, existing models for the electrical characterization of HCPV modules are reviewed. Many of these models have been recently developed and are intended for a more accurate simulation of the behavior, for easier implementation, or for meeting specific needs of the HCPV industry. The availability of reliable models to predict the energy harvested by HCPV is important to promote this photovoltaic technology.

1 Introduction

High-concentrator photovoltaic (HCPV) modules are used in HCPV systems to convert unconcentrated sunlight to electricity. These assemblies include optical elements, solar cells, cooling mechanisms, and other peripheral elements that can be

P. Rodrigo (✉)
Panamericana University, Aguascalientes, Mexico
e-mail: prodrigo@up.edu.mx

L. Micheli
Environment and Sustainability Institute, University of Exeter, Penryn, Cornwall, UK
e-mail: lm409@exeter.ac.uk

F. Almonacid
Jaén University, Jaén, Spain
e-mail: facruz@ujaen.es

P. Pérez-Higueras and E.F. Fernández (eds.), *High Concentrator Photovoltaics*,
Green Energy and Technology, DOI 10.1007/978-3-319-15039-0_5

arranged in many different configurations. Multijunction concentrator solar cells and optical configurations for HCPV modules have been analyzed elsewhere in this book. The thermal management of the modules and the design of cooling mechanisms will be analyzed in this chapter. These are important topics because of the large light-concentration factors focused on small areas in HCPV modules.

The research community and the industry are involved in developing better designs and manufacturing processes to improve HCPV module efficiencies. To achieve this goal, progress in understanding the real behavior of the HCPV modules in the field is required. Because prototypes and commercial HCPV modules are available, the experimental analysis of these devices becomes feasible. The behavior of HCPV modules strongly depends on the behavior of the solar cells inside. The main influencing atmospheric parameter is clearly direct normal irradiance (DNI), but there are many other aspects in the design and many other atmospheric variables that have nonnegligible influence.

Progress in understanding HCPV module behavior has allowed the development of models for the electrical characterization of these devices. Taking into account the classical models for conventional photovoltaic technologies, some researchers have recently developed models and tools that are able to reproduce the behavior of HCPV modules with greater accuracy and/or are more adapted to the specific needs and circumstances of the HCPV industry. These models are helpful for improving designs and energy prediction, among other applications, and are essential to promote HCPV technology.

This chapter is structured as follows: Sect. 2 is an overview of the components and fundamentals of HCPV modules; Sect. 3 gives an introduction to the behavior of HCPV modules mainly based on the analysis of outdoor measurements and the influence of atmospheric parameters; Sect. 4 discusses the cooling mechanisms in HCPV modules and several topics related to thermal management in these devices; Sect. 5 is a review of existing models for the electrical characterization of HCPV modules with emphasis on identifying the inputs, requirements, procedures, and applicability of the different proposals; because some of these models use the temperature of the cells inside the module as input, Sect. 6 reviews existing models for estimating this temperature from atmospheric parameters and/or direct measurements on the modules. Comparative tables of the characteristics of the reviewed models are given, which can help in the choice of the most suitable model for each specific application. The conclusions of the chapter are presented in Sect. 7.

2 Fundamentals and Components of HCPV Modules

The HCPV module is the fundamental unit used in HCPV systems to convert unconcentrated sunlight to electricity. This unit must provide different functions: concentration of the incident light, homogenization of the concentrated light in some designs, photovoltaic effect, heat dissipation, environmental protection,

electrical isolation, electricity removal, and fixing to the tracking structure. As can be realized, all of these functions can be obtained by means of many possible configurations and designs [1, 2].

A typical configuration based on point-focus Fresnel lenses, which has reached commercial acceptance, is shown in Fig. 1. In this configuration, each solar cell has its own optics. The module is composed of several solar receivers integrated with the primary lens, and the different receivers are electrically interconnected usually in a series configuration. The primary lenses in the example shown in the figure are Fresnel lenses, which focus the light on a specific area, are the so called point-focus Fresnel lenses. The solar receivers are composed in this case of a secondary optical element for light homogenization, a small solar cell, a bypass diode for safe-guarding the solar cell in cases of unusual operation such as partial shading, a heat-sink for passive cooling, and electrical connections to pass the electricity to the adjacent receivers or outside the module. These kinds of modules must be always be pointed toward the sun to be able to properly focus the solar rays on the solar cells surfaces, so they are mounted on two-axis solar trackers.

The main factors that determine the structure of an HCPV module are the optical configuration and its associated geometric concentration factor, the kind of solar cells, and the mechanisms for heat removal. The optical configuration allows obtaining a high light concentration level on a small area. Point-focus optical configurations require two-axis solar trackers, whereas linear-focus configurations can use single or dual-axis trackers. Other configurations allow separating the assembly of solar cells from the solar collectors. The different possibilities of optical designs are analyzed elsewhere in this book. The small semiconductor area

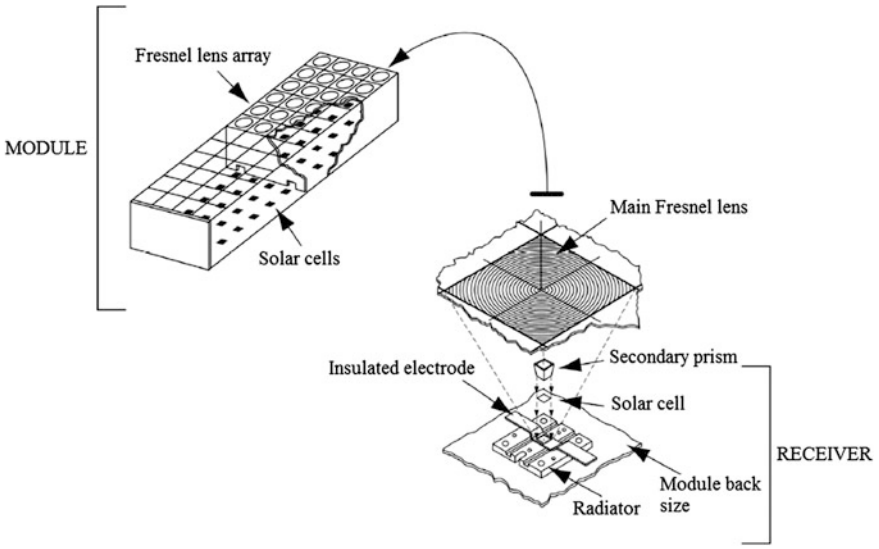

Fig. 1 Structure of an HCPV module based on point-focus Fresnel lenses. *Source* IEC 62108 [1]

required in HCPV modules usually allows incorporating high-efficiency multi-junction III–V solar cells, which otherwise would be too expensive for terrestrial applications. These cells are also analyzed in a previous chapter. In contrast, the design of cooling mechanisms is a large topic of interest in HCPV and will be discussed in Sect. 4 of this chapter. Cooling mechanisms are required in HCPV modules to limit the solar cell operating temperature and to decrease temperature differences between the cells in the module and across each individual cell. Better thermal designs of the solar receivers and the use of different kinds of heat exchangers contribute to improve heat removal. Passive cooling uses the natural motion of a fluid, whereas active cooling uses a small part of the generated energy to force the circulation of a fluid. Air is usually used as exchanger fluid, whereas water or other high thermally conductive fluids can also be used if available. There are many possibilities to implement cooling mechanisms, and innovative technologies are being investigated. These options, combined with the variety of optical configurations, offer a wide field for the design of HCPV modules.

The instantaneous efficiency of an HCPV module is defined as the quotient between the electrical power output and the luminous power input. Under normal operating conditions, the electrical power output corresponds to the module maximum power (P_{max}) because of the use of inverters with maximum power point tracking. The luminous power available for the module is calculated from the incident DNI, which is the only component of solar radiation that can be focused on the solar cell surfaces by the optical elements in the HCPV module. Thus, the instantaneous efficiency of an HCPV module is shown by (Eq. 1):

$$\eta_{mod} = \frac{P_{max}}{DNI \cdot A_{mod}} \tag{1}$$

with A_{mod} being the module area. Different values of efficiency can be calculated if we consider only the area of the primary optical elements or the whole area of the module including frames and separation elements. DNI must be corrected for angle of incidence for modules using single-axis tracking.

In contrast, the standard efficiency of an HCPV module depends on the operating conditions taken as a reference. These conditions have been recently normalized in the standard IEC 62670-1 [3], which allows two sets of standard conditions: (1) concentrator standard operating conditions [i.e., CSOC: 900 W/m^2 of DNI, 20 ºC ambient temperature, 2 m/s of wind speed, and standard direct normal AM 1.5 spectrum]; and (2) concentrator standard test conditions [i.e., CSTC: 1000 W/m^2 of DNI, 25 ºC cell temperature (T_c), and standard direct normal AM1.5 spectrum]. HCPV modules should always incorporate on their data sheets and nameplates the conditions at which the module was rated.

The efficiency of an HCPV module is lower than the efficiency of the solar cells inside. The nonideal properties of transmission, absorption, and reflection of the optical elements play an important role. The efficiency of an HCPV module can be broken down as (Eq. 2):

$$\eta_{\text{mod}} = \eta_{\text{cell}} \cdot \eta_{\text{opt}} \cdot (1 - L) \tag{2}$$

with η_{cell} being the efficiency of the solar cells, η_{opt} the efficiency of the optical elements, and L a factor considering other kinds of losses. Among these other losses, Joule effect in electrical connections and wires and mismatch effects between receivers can be cited. Mismatch can be caused by small differences in the alignment of the solar receivers, temperature differences between the solar cells, dispersion of solar cells parameters due to manufacturing tolerances, etc. An HCPV module is composed of a number of interdependent elements that configure a complex system, so many factors can influence its efficiency and its behavior.

The real efficiency of the commercially available HCPV modules is difficult to analyze. The companies usually provide incomplete information because of limited experience and commercial strategies. In 2011, an analysis of published efficiencies led to statistically represent the efficiency of commercial HCPV modules by a normal distribution with a mean of 24 % and an SD of 4 % [4]. However, HCPV module technology is rapidly evolving. The challenges in the design and manufacturing of HCPV modules include reaching greater efficiencies as well as decreasing weight and cost, improving angular acceptance, and ensuring long-term reliability.

3 Analysis of the Behavior of HCPV Modules

The main components that determine the electrical behavior of an HCPV module are the solar cells, which are usually multijunction III–V solar cells. However, as was commented in the previous section, an HCPV module is an assembly of different elements (solar cells, primary and secondary optical elements, cooling devices, protection elements for outdoor operation, bypass diodes, electrical connections, etc.). This means that the electrical behavior of an HCPV module cannot be exclusively explained by the behavior of the solar cells inside. Although solar cells are the critical component, HCPV modules must be analyzed as a whole for a better understanding of their behavior in the field.

Experimental analysis of the behavior of HCPV modules can be performed indoors under controlled conditions with the help of a sun simulator or outdoors under real conditions by mounting and measuring the studied modules on a solar tracker. The analysis shown in this section is mainly based on outdoor measurements, which can be more representative of the real behavior in the field, although there are also important studies performed indoors.

Efficiency and maximum power of HCPV modules can be considered the most important electrical parameters to be analyzed. They are key parameters in many applications, for instance, in predicting the harvested energy in HCPV systems. However, it must be taken into account that the electrical behavior of an HCPV module is only fully described by knowing the current-voltage characteristic (I–V)

curve under any given environmental conditions. Therefore, many other electrical parameters—such as short-circuit current, open-circuit voltage, or fill factor among others—can be interesting for different studies.

As a starting point of the analysis, and considering that solar cells are the most important components in HCPV modules, it can be assumed that the variables influencing solar cell behavior will be also important in the behavior of HCPV modules. Because multijunction solar cells are influenced by changes in irradiance, cell temperature, and incident light spectrum [5–7], the behavior of HCPV modules should depend at least on DNI (the only component of solar radiation that can be focused on the solar cells by the optical elements), T_c, and direct sunlight spectrum $E(\lambda)$ [8–11]. So, in a first approximation, the functional dependence of HCPV modules behavior could be expressed as:

$$\text{Curve } I\text{-}V = f(\text{DNI}, T_c, E(\lambda)) \tag{3}$$

Of course, this functional dependence can be extended or written in different ways. Some of the involved variables can be expanded. For instance, T_c in a passively cooled HCPV module depends on DNI, ambient temperature, or wind speed among others [12]. Direct sunlight spectrum depends on air mass, aerosol optical depth, or precipitable water among others [13]. Moreover, other variables could be added to the function, for instance, lens temperature, which itself depends on several atmospheric parameters. However, Eq. (3) is quite synthetic and could be considered representative of the main variables that influence HCPV module behavior taking into account that it can be written in many other more or less descriptive ways.

Among the variety of factors that influence HCPV module behavior, different studies have shown that the three most important variables to be considered are DNI, T_c, and air mass. This does not mean that the electrical behavior of HCPV modules can be determined exclusively from these three variables, but a reasonable approximation of the real behavior can be performed by analyzing these three inputs. Of course, other factors must be analyzed for a better understanding.

Next, taking this into account, Sects. 3.1, 3.2, and 3.3, respectively, analyze the influence of DNI, T_c, and air mass on several electrical parameters. Section 3.4 briefly comments on the influence of other involved factors.

3.1 Influence of Direct Normal Irradiance

Direct normal irradiance is by far the most important variable that determines HCPV module behavior [11]. HCPV module maximum power (a key electrical parameter in many studies) is strongly and decisively influenced by DNI. Figure 2 plots the maximum power of an HCPV module obtained through an outdoor experimental campaign covering a wide range of operating conditions versus DNI without filtering any other variable that can influence HCPV module behavior. The

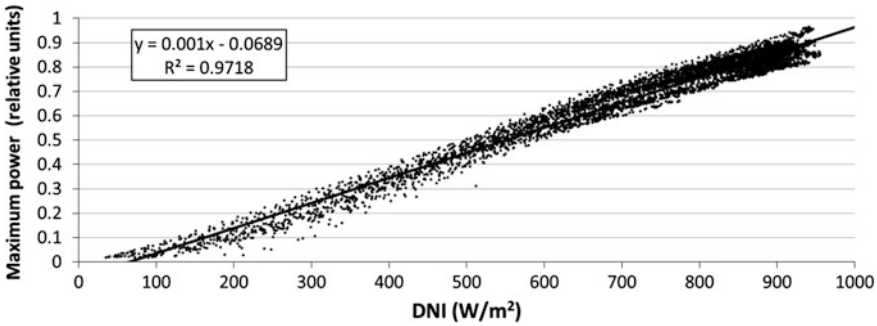

Fig. 2 Maximum power normalized to the rated maximum power at concentrator standard test conditions versus direct normal irradiance for an HCPV module measured outdoors at Jaén, South of Spain, during an experimental campaign of 8 months as well as the results of a linear regression of the data. The module was composed of 16 series-connected GaInP/GaInAs/Ge solar cells, with one domed Fresnel lens per cell with 550× concentration factor, and was passively cooled through a metal plate

represented maximum power has been normalized to the rated maximum power of the module at CSTC.

As can be seen, although there is some scatter when representing maximum power versus DNI (which indicates that there are other influencing variables), this scatter is narrowly bounded. Thus, these kinds of measurements highlight the decisive influence of DNI on HCPV module behavior. Moreover, if a linear regression of the collected data is performed, results indicate that the influence of DNI on maximum power is reasonably linear as shown in Fig. 2 where a correlation coefficient (R^2) of 0.9718 was obtained (close to unity). This means that a simple linear model that represents maximum power versus DNI could be used in preliminary studies that do not require a high degree of accuracy in the prediction. However, as was commented, most of the studies on HCPV modules require more in¯depth knowledge of their behavior; thus, other influencing factors must be usually considered.

3.2 Influence of Cell Temperature

A first consideration with respect to this parameter regards the meaning of the T_c in an HCPV module. Actually, not every cell in an HCPV module operates exactly at the same temperature. Measurements on the back plates of HCPV modules have shown that cells near the frame have lower temperatures depending on wind speed and direction and orientation of the module [14–16]. Thus, for Eq. (3) to make sense when applied to HCPV modules, the T_c variable must be considered as the average temperature of the cells in the module. We will simply refer T_c as the "cell temperature" in the module keeping this consideration in mind.

The T_c in an HCPV module influences electrical parameters such as open-circuit voltage, fill factor, short-circuit current, etc. The most affected parameter is open-circuit voltage so we will focus on the analysis of this one.

Figure 3 plots outdoor measurements of open-circuit voltage versus T_c collected during an experimental campaign performed on an HCPV module. In this graph, measured open-circuit voltages have been corrected to the reference irradiance of 1000 W/m^2 to try to remove the influence of DNI on this parameter by means of a logarithmic correction. In addition, the corrected voltages have been normalized to the rated open-circuit voltage of the module at CTSC.

The scatter in the graph can be caused by different reasons such as the difficulty of measuring the temperature of the cells inside an HCPV module operating in real conditions, different temperatures of the cells in the module, uncontrolled disturbances during the experiment, etc. However, these kinds of outdoor measurements suggest that open-circuit voltage decreases linearly when T_c increases. This suggested linear behavior could be represented by the regression line shown in Fig. 3. In fact, the influence of T_c on the open-circuit voltage of HCPV modules has also been studied indoors with the use of sun simulators, and an almost perfect fit to the linear behavior has been observed [9]. This decrease of open-circuit voltage with respect to T_c can be explained taking into account the influences of temperature on the intrinsic carrier concentration and the band-gap of the semiconductors that compose the multijunction solar cells in the module [17].

The behavior of open-circuit voltage in HCPV modules is similar to that in conventional flat-plate photovoltaic modules, in which open-circuit voltage is usually modelled with linear functions based on T_c by means of temperature coefficients provided by the manufacturers. However, typical values of these coefficients are different for flat-plate modules and for HCPV modules. HCPV

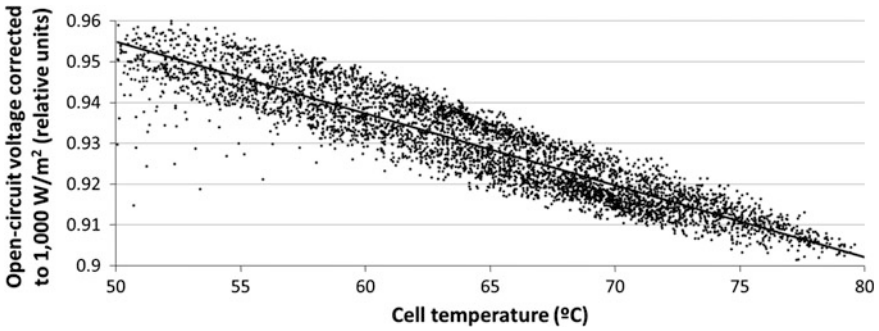

Fig. 3 Open-circuit voltage corrected to 1000 W/m^2 of irradiance and normalized to the rated open-circuit voltage at Concentrator Standard Test conditions versus T_c for an HCPV module measured outdoors at Jaén, south of Spain, during an experimental campaign of 8 months as well as linear regression of the data. The module was composed of six series-connected GaInP/GaInAs/Ge solar cells, with one squared flat Fresnel lens per cell with 500× concentration factor, passively cooled through a metal plate. A small PT100 sensor was placed inside the module close to one of the solar cells for the measurement of its operating temperature

modules typically show a lower dependence on T_c than conventional modules because of the specific properties of the materials that compose the multijunction solar cells [18, 19].

3.3 Influence of Air Mass

Air mass has been identified as the main atmospheric parameter that influences the sunlight spectrum, although the exact spectral content of the sunlight cannot be determined exclusively from this parameter. Because HCPV modules behavior is influenced by the behavior of the multijunctions cells inside, taking into account that these cells are very sensitive to the spectrum of the incident light and due to the importance of the air mass as an indicator of the spectral content of sunlight, it is reasonable to think that air mass should play an important role in the behavior of HCPV modules. Thus, different investigators have analyzed and tried to quantify the influence of air mass on HCPV module behavior [16, 20–25].

The effect of variations of the incident spectrum on HCPV modules is complex and affects different electrical parameters. However, the electrical parameter that probably better describes the influence of the spectrum is the module short-circuit current, so that we will focus on the analysis of the influence of air mass on this parameter.

Figure 4 plots outdoor measurements of short-circuit current versus air mass collected during an experimental campaign performed on an HCPV module. In this graph, measured short-circuit currents have been corrected to the reference

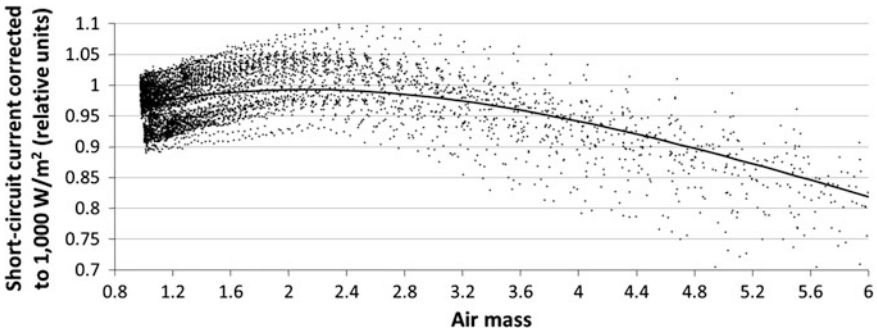

Fig. 4 Short-circuit current corrected to 1000 W/m^2 of irradiance and normalized to the rated short-circuit current at Concentrator Standard Test conditions versus air mass for an HCPV module measured outdoors at Jaén, south of Spain, during an experimental campaign of 8 months as well as regression curve modelled as a fourth-order polynomial. The module was composed of five series-connected GaInP/GaInAs/Ge solar cells, with one squared flat Fresnel lens per cell with 625× concentration factor, passively cooled through a finned heat exchanger. Air mass was calculated from the registered values of sun elevation angle with a pressure correction based on Jaén's altitude

irradiance of 1000 W/m^2 to try to remove the influence of DNI on this parameter by means of a linear correction. In addition, the corrected currents have been normalized to the rated short-circuit current of the module at CSTC. The resulting factor is known as normalized short-circuit current or spectral correction factor.

The scatter in the graph can be attributed to different reasons, but probably the main reason is that the spectral content of the incident sunlight is not fully determined by the air mass parameter, so there are other influencing atmospheric variables that have not been filtered. From the measurements in the graph, the behavior of the normalized short-circuit current with respect to air mass could be mathematically expressed in different ways. For instance, the graph shows a fourth–order polynomial whose coefficients have been adjusted from the set of measurements by multilinear regression analysis.

The obtained curve can be representative of the influence of air mass on normalized short-circuit current under the hypothesis that other involved variables are random and their influence, when collecting a large number of measurements and applying a regression procedure, cancels. If we examine this curve, two trends are observed. From low to high values of air mass, at first the normalized short-circuit current increases until reaching a maximum, and it gradually decreases afterward.

This behavior agrees with what could be expected if we take into account that HCPV module behavior is strongly influenced by the behavior of the multijunction solar cells inside. In these solar cells, which are usually composed of three monolithically grown series-connected subcells with each one having a different spectral response, the current is limited by the subcell with lower short-circuit current. Under real operating conditions, the limiting subcell can be either the top or the middle subcell depending on the spectrum of the incident light. In the regression curve shown in Fig. 4, the region on the left of the maximum would correspond to spectral conditions under which the middle subcell governs the current, whereas the region on the right would correspond to spectral conditions under which the top subcell governs the current. The curve maximum would represent the operating point at which both subcells generate the same current. Multijunction solar cells for terrestrial applications are usually designed to obtain maximum efficiency at the standard AM1.5d spectrum. In Fig. 4, the maximum of the curve does not exactly correspond to an air mass value of 1.5. This can be explained, among other reasons, by the influence of lense transmittance, which is not constant for every wavelength, that causes that the spectrum of the light that reaches the solar cells in the module does not necessarily correspond to the spectrum of the external sunlight that falls on the primary lenses [24].

3.4 Other Influencing Factors

Although air mass is the most important atmospheric variable that influences the sunlight spectrum, other atmospheric parameters have a nonnegligible influence on

the spectral content and thus affect HCPV module behavior. Among them, aerosol optical depth, precipitable water, or Ångström exponent can be cited [26, 27].

The change in the optical properties of the lenses used as primary concentrators in HCPV modules play a role in the electrical behavior of the modules. Both the net luminous power and the spectral content of the light that fall on the solar cells do not exclusively depend on DNI and the spectrum of the sunlight that falls on the primary lenses. Optical properties of the lenses, such as transmittance and focal length, change during the real operation of HCPV modules, and the characteristics of the light that finally reaches the solar cells varies accordingly. This effect is mainly function of the lens temperature, which varies with the atmospheric conditions [28].

Wind speed, characterized by magnitude and direction, has also a complex influence on HCPV module behavior. On the one hand, wind falling on the front side of an HCPV module causes cooling of the lenses, what usually improves their optical efficiency as well as the electrical output of the module. In contrast, a high-intermittent wind speed can cause vibrations of the tracking structure and cause misalignments that deteriorate the electrical output. Of course, wind falling on the back side of passively cooled HCPV modules improves heat dissipation and decreases T_c, which increases the module's efficiency. Another effect of wind is originating temperature differences between the solar cells in an HCPV module depending on its direction and the orientation of the module [29, 30].

There are many other factors that can affect the HCPV modules behavior such as tracking accuracy, deformations of the optical elements, module structure or tracker structure, degradation of the lenses, soiling on the primary optics, self-shading between trackers, etc. [31].

4 Cooling Mechanisms in HCPV Modules

In flat photovoltaic and low CPV systems, cooling is generally not required because of the large module surface and limited irradiance incident on the solar cells corresponding to terrestrial levels. Inversely, it becomes an important aspect for medium-, high-, and ultra-high concentrating CPV systems where the receiver surface area strongly decreases and the irradiance dramatically increases. Taking into account a typical 1 cm^2-sized multijunction solar cell integrated with a primary lens that receives 900 W/m^2 of DNI, and considering a 500× concentration factor, 20 % of optical losses, and 41.1 % of cell efficiency, it is expected that the device produces approximately 21 W of waste heat. A well-dimensioned cooling system is then essential to remove this heat and to keep the T_c in the range that concentrating photovoltaics usually operate, i.e., 50–80 °C [12, 32]. An amount of heat equal to the one generated must be removed from the cell to stop the temperature increasing and to let the system work at a steady state.

4.1 Targets of HCPV Cooling

Cell temperature in HCPV modules must be limited to enhance electrical efficiency, to decrease thermal stresses, and to avoid damages due to high operating temperatures. A reasonably low T_c is not the only requirement that an HCPV cooling system must meet. The uniformity of temperature must be taken into account considering both the spatial temperature distribution in each single cell; and the temperature variations among the different solar cells in the module. Internal temperature gradients across a solar cell are generally due to nonuniform illumination on the active area, and they cause power losses and may lead to damages [33]. In contrast, in a typical series-connected configuration of solar cells in an HCPV module, the output current intensity is affected by the worst-performing cell, whose current limits the performance of the other cells. Bypass diodes are generally installed to overtake this current-mismatch issue, which can take place when the irradiance on the cells is not the same across the series. An optimal HCPV cooling system should prevent the system from current-mismatch due to nonuniform temperature. Moreover, the cooler is generally required to be simple to grant high reliability and not to strongly affect the HCPV plant cost. A reliable system is essential: Any failure could cause damages to the cells and long interruptions in power generation.

4.2 Thermal Model of an HCPV Solar Receiver

Using the electrical resistance analogy, the thermal behavior of an HCPV solar receiver could be described through a simple one-dimensional thermal model. In this simplistic approach, the difference in temperature between the cell and that of the ambient environment corresponds to the driving potential for heat flow as the voltage is the driving potential for the current [34]. The aim of any model is to represent a real case in the most appropriate way. However, some approximations must be considered. The present equivalent thermal circuit is developed in one dimension perpendicularly to the widest surfaces of each layer. A common 1 cm^2-sized triple-junction solar cell is generally approximately 190 μm thick and is represented in Fig. 5 where three surfaces are named “A”, “B”, and “C”: If the heat is generated at the centre of the cell, the path to reach surface A is approximately 50 times shorter than the ones to reach surfaces B and C. The largest portion of the generated heat is then expected to flow along the lower-resistance path. The model considers uniform illumination on the cell and constant properties in any material along any direction. All of the temperature values in the model refer to the values at the top of each layer.

A scheme of the layers and a corresponding equivalent thermal circuit for a typical HCPV receiver is shown in Fig. 6. Because it is a one-dimensional model, all of the resistances are reported per unit area. It is important to highlight that

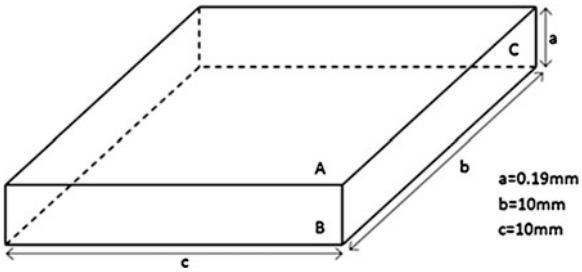

Fig. 5 Thermal scheme of a typical triple-junction solar cell. The heat source is placed in the centre of the volume and heat can follow the three paths—long *a*/2, *b*/2, or *c*/2—to reach one of the three surfaces, which are, respectively, named "*A*", "*B*", and "*C*"

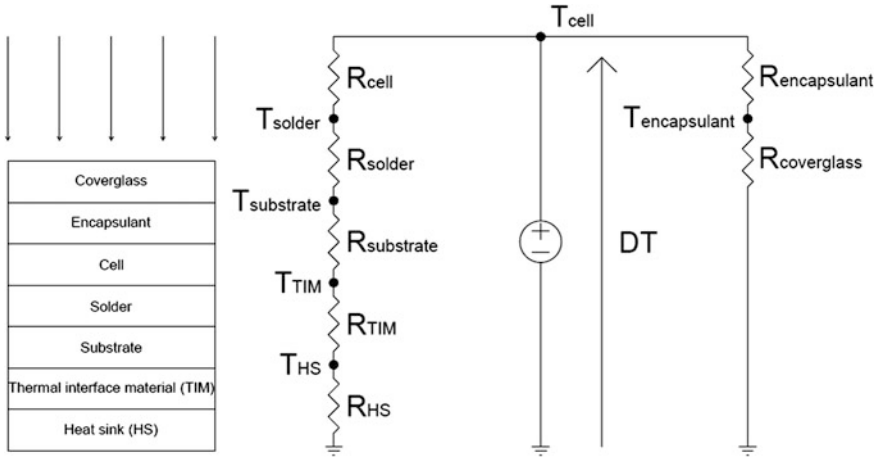

Fig. 6 Scheme of the layers that compose a typical HCPV receiver and one-dimensional equivalent thermal circuit

neglecting the conduction on the other two dimensions and the thermal exchanges in all of the layers others than the coverglass and the heat sink is a strongly limitative assumption. However, this approach can help to estimate the performances of the cooling system and has already been reported in literature [35].

Each layer of the assembly introduces a thermal resistance to the path between the cell and the environment, which, respectively, represent the source and the ground. The overall of thermal resistance of the heat path can be expressed as:

$$R_{\text{tot}} = \frac{T_{\text{cell}} - T_{\text{amb}}}{q_{\text{cell}}} \tag{4}$$

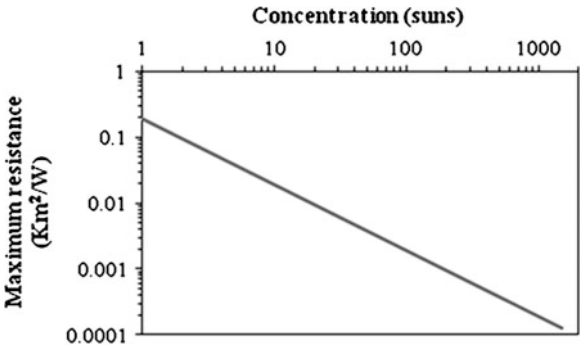

Fig. 7 Estimation of the maximum thermal resistance of the one-dimensional heat path per different concentration levels for a typical solar receiver with a 1 cm^2-sized triple-junction solar cell assuming a standard cell efficiency of 41.1 %. For thermal resistances lower than this cut-off value, the solar cell is expected to operate with temperatures <100 °C under environmental conditions of 20 °C air temperature

Taking into account a value of 21 W/cm^2, which can be representative of the waste heat produced by a 1 cm^2-sized triple-junction solar cell at 500 suns, a maximum operating temperature of 100 °C, and an ambient temperature of 20 °C, a cooling system with an overall resistance $<3.2 \times 10^{4}$ (m^2 K)/W must be designed for this cell. Whatever the concentration, the maximum cell's operating temperature is expected not to overtake 100 °C. In Fig. 7, the maximum values of heat path resistance are estimated for concentrations ≤1500 suns, assuming a standard cell efficiency of 41.1 %, taking into account that a fixed efficiency is a limitative approach but still useful to highlight the strong relation between concentration and thermal resistance. As can be seen, a greater concentration requires a lower thermal resistance. Any point below the line would let the cell to work at a temperature <100 °C. In particular, at constant concentration, the furthest the point from the line, the lower the temperature and thus the highest the cell's efficiency.

As shown in Fig. 6, the heat is removed by the cell first by conduction across the different layers of the receiver. There are two main paths that the heat can follow: The first one goes from the cell to the heat sink, and the second one goes up to the coverglass. Once in the bottom of the heat sink or at the top of the coverglass, the heat is transmitted to the environment through radiation and convection. In the following two sections, an analysis of the conductive heat exchange and the radiative and convective heat exchanges will be shown.

4.3 Conductive Heat Exchange in an HCPV Solar Receiver

The structure of the assembly, in terms of choice and order of the materials in the stack, is a primary topic concerning heat dissipation. Greater than 99 % of the heat

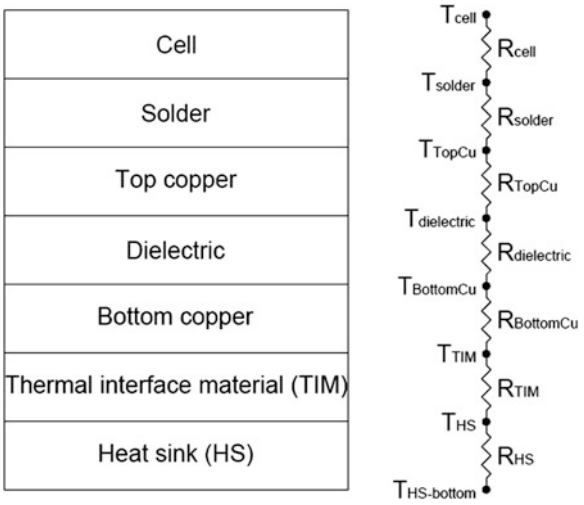

Fig. 8 Expanded scheme of the layers that compose a typical HCPV receiver below the solar cell as well as one-dimensional equivalent thermal circuit depiction

removed by a solar cell in an HCPV receiver is transferred by thermal conduction [36]. The receiver assembly is usually designed to be able to transfer the electrical energy, to dissipate the thermal energy, and to assure adequate mechanical support. The coverglass and the encapsulant are not usually required to perform high thermal conductivity: The thermal resistance of a clear silicone encapsulant is generally much greater than the one of the substrate's materials. For this reason, the present analysis will mainly focus on the layers placed below the cell (assuming the light hitting the upper side of the cell). A more detailed model of thermal transmission from the cell to the bottom of the substrate of a typical HCPV receiver (where the heat exchanger is located) is shown in Fig. 8.

In this model, the equivalent thermal resistance (R_{cond}) can be calculated as the sum of the individual layer resistances:

$$R_{\text{cond}} = R_{\text{cell}} + R_{\text{solder}} + R_{\text{TopCu}} + R_{\text{dielectric}} + R_{\text{BottomCu}} + R_{\text{TIM}} + R_{\text{HS}} \quad (5)$$

where each resistance can be estimated on the basis of typical values of thicknesses and thermal conductivities of the relative layer reported in Table 1. A GaInP/GaInAs/Ge solar cell is composed by multiple layers of different materials, but it is usually modelled as a single block of Ge for thermal purposes. An overall of thermal resistance of 3.35×10^{5} (m^2 K)/W results for the considered receiver.

Figure 9 shows the contribution of each layer to the global thermal resistance of the path. The thermal interface material placed between the substrate and the heat spreader is the largest challenge for heat dissipation representing approximately half of the overall of thermal resistance. New thermal interface materials that are able to grant greater thermal performances, such as the one made of several nano-layers of aluminium and nickel, are being investigated.

Table 1 Materials that compose the different layers of a typical HCPV receiver below the solar cell and numeric values of thickness and thermal properties chosen for the calculation of the overall of thermal resistance of the stack

Layer	Material	Thickness (mm)	Thermal conductivity at 25 °C (W/m K)	Resistance (K m^2/W)	Ref.
Cell	Ge	0.180	160	1.125×10^{-6}	[37]
Solder	Sn–Ag–Cu	0.125	78	1.602×10^{-6}	[38]
Substrate	Top copper	0.3	400	7.500×10^{-7}	[37]
	Aluminium nitride	0.63	285	2.210×10^{-6}	[37]
	Bottom copper	0.3	400	7.500×10^{-7}	[37]
Thermal interface material	Epo-tek	0.050	2.83	1.767×10^{-5}	[37]
Heat sink	Aluminium	1.5	160	9.375×10^{-6}	[37]

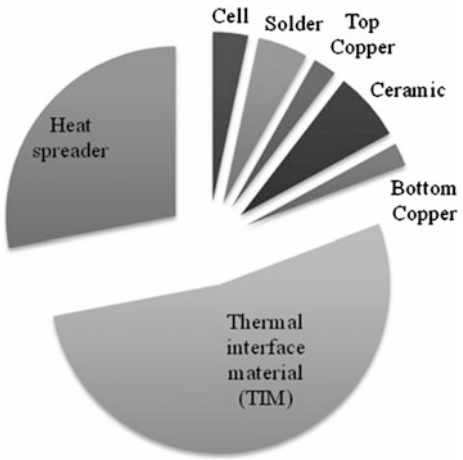

Fig. 9 Breakdown of the layers thermal resistances as obtained by the one-dimensional thermal model for an analyzed representative HCPV solar receiver with typical values of thickness and thermal properties of the layers

4.4 Radiative and Convective Heat Exchange in an HCPV Solar Receiver

So far, only the conductive transmission of heat has been considered. Once in the heat sink, the waste heat must be moved into an external system in order not to further affect the receiver. Any object placed in contact with a fluid exchanges heat with it through natural convection and radiation. This is the condition of a solar

receiver mounted in an outdoor CPV system. The rate of natural convection (q_c) is approximately proportional to the difference between the surface and the free stand fluid temperatures, respectively, reported as T_s and T_{amb}:

$$q_c = S \cdot h_c \cdot (T_s - T_{amb}) \tag{6}$$

where S stands for the area of the exchanging surface, and h_c represents the constant of proportionality, which is called the "convective heat transfer coefficient." It depends on the fluid, the state of the flow, and the geometry of the system. The heat transfer coefficient for air in free convection usually ranges between 3 and 25 W/(m^2 K) [34]. In contrast, radiation is a function of the difference between the temperature fourth powers:

$$q_r = \sigma \cdot S \cdot F_{1-2} \cdot \varepsilon \cdot \left(T_s^4 - T_{amb}^4\right) \tag{7}$$

where σ is the Stefan Boltzmann constant, approximately 5.67×10^{-8} W/(m^2 K^4); F_{1-2} is the view factor; and ε is the emissivity of the surface's material.

The simplest solution to dissipate the waste heat generated by the cell is to use a large, flat heat sink placed at the bottom of the heat spreader. Aluminium is the material generally chosen due to its good balance between thermal performances, weight, and costs. Combining the two previous equations and considering the only bottom surface, it is possible to calculate the minimum area (S_{HS}) required by the heat sink to work properly:

$$S_{HS} = \frac{q_{cell}}{h_c \cdot (T_s - T_{amb}) + \sigma \cdot F_{1-2} \cdot \varepsilon \cdot \left(T_s^4 - T_{amb}^4\right)} \tag{8}$$

Assuming all the 21 W heat generated by a cell to reach the heat sink, and, similar to the conditions in [39], an upper bound for emissivity of 0.09 and a view factor of 1, considering only the flat bottom surface of the receiver, and taking into account an optimistic value of 25 W/(m^2 K) for the air heat transfer coefficient, a heat sink surface temperature of 60 °C, an ambient temperature of 20 °C, and a dissipating area of 0.020 m^2 for the aluminium heat sink is required. It corresponds to an aluminium plate sizing 14.5 cm/side for cooling a 1 cm^2-sized cell. Taking instead into consideration a more conservative air heat transfer coefficient of 5 W/(m^2 K), the required surface increases to 0.105 m^2, which means a 32 cm × 32 cm wide aluminium heat sink.

Despite its simplicity and its exploitation in some applications, a flat heat sink might be not the best heat exchanger in terms of effectiveness, volume, weight, and cost. For these reasons, several active and passive designs have been developed to enhance the performance of the cooler in CPV applications and will be reported in the next section.

4.5 Designs of HCPV Coolers

The cooler is the last component of the heat path and its role is to transfer the heat to an external fluid. Coolers are generally classified as passive or active. Passive cooling does not require input of mechanical or electrical power because it acts through the exploitation of natural laws. In these systems, the motion of the fluid is due to the gradient of density induced by the nonuniform temperature of the fluid. Passive coolers have been considered more reliable than the active ones for microelectronics cooling [40] and are expected to decrease the probability of damage caused by cooling failures. In contrast, active cooling is obtained using a fraction of the cell power output, and, as such, a part of the energy output would not be available for further use. Active cooling does not dependent on the working conditions and has the main advantage of being generally more easily controllable than passive cooling.

The design of an HCPV cooler depends on many factors, which are not limited to the concentration and the outdoor conditions. First, the optics of the system usually play a fundamental role. The most typical optical configurations in HCPV systems are shown in Fig. 10. In reflecting systems where no secondary is applied, the receiver is usually located between the sun and the mirrors (Fig. 10a). This means that the receiver must be as compact as possible to decrease shading. Thanks to their higher thermal-exchange coefficients, active coolers can achieve better performance in limiting volume. If a secondary reflector is present (Fig. 10b), or if concentration is achieved through lenses (Fig. 10c), coolers would not create any risk of shadowing, and large areas for cooling are usually available.

Second, the number of cells and their distribution on the receiver are a key issue to be considered, and they are usually grouped in single-cell geometry, linear geometry, or densely packed geometry [35]. In the single-cell geometry,

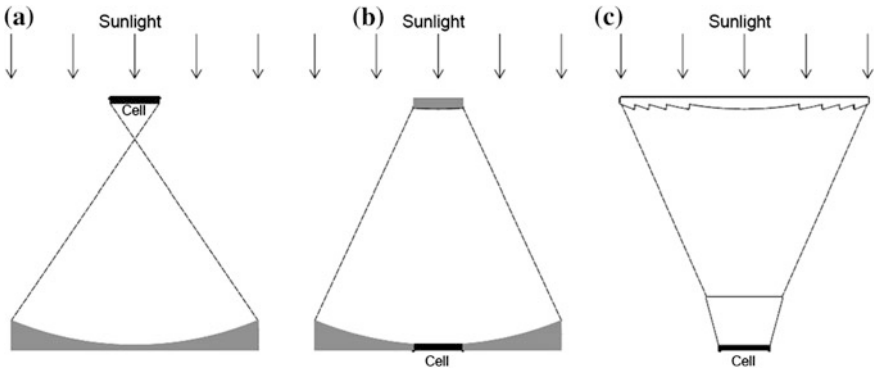

Fig. 10 Typical optical configurations for HCPV devices: only primary reflecting optics (**a**), both primary and secondary reflective optics (**b**), and refractive optics (**c**). In (**a**), the cooler must be compact to decrease shading, so active cooling can be a good choice. In (**b**) and (**c**), a larger area is available for the cooler, so passive cooling seems more suitable because of its reliability

concentrators focus sunlight onto an individual cell. This is a favorable configuration for cooling: Ideally, an area equal to the surface of concentrators is available for cooling purposes, thus favouring the employment of passive systems. In linear geometries, two sides of each cell are in contact with the adjacent cells decreasing the available cooling surface. In densely packed geometries, each cell is surrounded by cells on each side (excluding the cells on the side): The decreased areas available for cooling and the high thermal power densities make the application of passive cooling systems difficult.

Third, the choice of the fluid may depend on its availability. High thermally conductive fluids might be too expensive or not easy to provide in remote locations. Unfortunately water is not yet easy to access in many locations, especially in areas such as the desert lands, where irradiance is particularly high. For these reasons, air can result the best fluid to be exploited for both active or passive systems.

Last, the inclination angle of the receiver changes continuously because HCPV systems are usually tracked. Heat sinks in natural convection are especially affected by the inclination angle, and, in particular, a downward-facing heat sink is the worst positioning for passive cooling. Despite that, some technologies, such as the architectural design of the CPV, specifically requires such hidden cooling devices [41, 42].

The simplest passive way to increase the thermal transfer of any surface is the addition of fins [43]. The performances of the fins in an HCPV system depend on the number, the spacing, and the length [44], and are also affected by the inclination angle and the temperature difference [42]. The heat management of any heat sink can be enhanced by forced air flow. However, due to the low heat capacity of air, water cooling has been intensively applied in many high-concentrating systems: impinging jets [45], water-immersion [46], and heat pipes [47]. Beyond all of these proved technologies, more solutions, such as thermoelectric devices [48] or two-phase flows [49], can arise as a feasible way to provide efficient HCPV cooling. Due to the high power densities and the small volumes involved, micro- and nano-technologies can play an important role in HCPV cooling. Microchannels have already been successfully applied in CPV [50]. The suspension of high thermally conductive particles <100 nm into a fluid can enhance the performances of any system. Nanofluids have already been used in many applications [51], including PV/T cooling [52], but despite their potential, research into their applications for heat transfer purposes seems to have lost appeal [53]. Among the emerging passive microtechnologies, carbon nanotubes appears like the most promising solution [54]. More technologies, such as microfins, nano-wires, or miniature heat pipes and thermosyphons, can soon become suitable for HCPV. The integration of different technologies can lead to innovative and high-performing solutions: Hybrid schemes, such as hybridizations of jet impingement and microchannels [55, 56], have shown the capability of reaching high heat-transfer coefficients and improving the temperature uniformity [57]. In particular, hybridizations of jet impingement and microchannel have been tested for HCPV applications.

At the latest state-of-the-art, the quote of solar energy converted into heat is still greater in percentage than the one converted into electricity. The reuse of the waste

heat produced by HCPV already represents an opportunity to improve overall system efficiency and then to decrease the costs of the technology. According to Kribus et al. [58], adding a heat-recovery system to an actively or a passively cooled HCPV system would add no more than, respectively, 5 or 10 % to the installation cost. This cogenerative solution is referred to as "CPV/thermal" and is able to provide both electricity and heat at medium rather than at low temperatures [59]. The recovered heat can be used in many domestic and industrial processes such as air conditioning, water desalination, or water heating.

5 Models for the Electrical Characterization of HCPV Modules

In this section, some relevant models for the electrical characterization of HCPV modules are summarized. The electrical behavior of HCPV modules is only fully described by knowing the I–V curve under given environmental conditions. However, many applications do not require the whole I–V curve, which is difficult to obtain, but only use specific parameters. Among them, the critical parameter in most of the studies, for instance in the calculation of the harvested energy, is the module maximum power. Because of this, many of the proposed models for the electrical characterization of HCPV modules focus on the calculation of the maximum power, although some of them provide other electrical parameters.

As was commented in Sect. 3, a variety of factors influence the HCPV modules behavior. The three main factors are DNI, T_c, and direct sunlight spectrum. Direct normal irradiance is always used as input in the proposed models. Cell temperature is often explicitly taken into account, although sometimes it is implicitly considered by introducing into the model other variables that are supposed to make the determination. Direct sunlight spectrum is not considered an explicit input; different atmospheric parameters that help to quantify the spectral impact are normally used instead. With some exceptions, factors other than these three are not usually considered as being state-of-the-art.

Accuracy is an important desireable characteristic for the models. Low uncertainty in prediction is also a goal, an aspect that is very important if the model will be applied under conditions other than the ones used to test the model or for untested module designs. Developing models with more "physical sense" can contribute to decrease uncertainty—but taking into account that an HCPV module is a complex system and therefore some simplifications, empirical, or semiempirical procedures are always required to build a model—every existing proposal uses these procedures to a greater or lesser extent. Thus, extensive testing of each model is always needed and, at the end of all, the analysis of the successful cases over time is the best indicator of the quality of a model.

In contrast, accuracy and reliability are not the only characteristics searched by users, but applicability also plays a very important role. The different models

require different equipment or software packages to be applied, which are not always available in real circumstances. Certain aspects—such as the availability of module information, the technical resources for monitoring module behavior and atmospheric parameters, the availability of data sources and other technical and economic issues—are taken into account when choosing a model. The best model for a specific project is the one that better exploits the available resources to reach the project goals. Thus, it is a role of researchers to develop tools that provide solutions to the real problems affecting the industry.

Because of all of these reasons, the development of models for the electrical characterization of HCPV modules is still challenging, and new proposals are expected in the near future. Next a summary of existing models is presented, and a comparative table showing some of their characteristics is given.

- Model of the standard ASTM E 2527

This model, defined in [60], uses as inputs DNI, ambient temperature (T_{air}), and wind speed (W_s). Maximum power is calculated by Eq. (9):

$$P_{max} = \text{DNI} \cdot (a_1 + a_2 \cdot \text{DNI} + a_3 \cdot T_{air} + a_4 \cdot W_s) \tag{9}$$

Despite its simplicity, it is remarkable that the model does not use any spectral correction, which limits the degree of accuracy. However, parameters a_1, a_2, a_3, and a_4 can be obtained through regression analysis of outdoor measurements, data which are relatively easy to obtain, which facilitates the application of the model to different kinds of HCPV modules.

- Model of King et al. [61]

This classical model [61] is intended for characterizing different PV devices and, in particular, has been tested for HCPV modules. It quantifies spectral effects in a basic way through the air mass parameter, what is an advantage with respect to the previous model. Model inputs are the so-called "effective irradiance," the T_c, and the air mass.

The effective irradiance (B_{ef}) is a factor that tries to represent the irradiance that actually affects the HCPV module and is calculated by Eq. (10):

$$B_{ef} = [\text{DNI} \cdot f_1(\text{AM})]/\text{DNI}^* \tag{10}$$

with DNI^* being the reference DNI and $f_1(\text{AM})$ a spectral correction factor modeled as a fourth-order polynomial function of the air mass.

With these inputs, a set of equations allow the calculation of five points on the module I–V curve as represented by the following electrical parameters: short-circuit current (I_{sc}), open-circuit voltage (V_{oc}), maximum power point current (I_{mpp}), maximum power point voltage (V_{mpp}), current at a voltage $V_{oc}/2$ (I_x) and current at a voltage (V_{mpp} + V_{oc})/2 (I_{xx}). The module maximum power is obtained by the product $V_{mpp} \cdot I_{mpp}$. The model equations that allow calculation of the module maximum power (P_{max}) are as follows:

$$I_{\mathrm{mpp}} = \left(C_0 \cdot B_{\mathrm{ef}} + C_1 \cdot B_{\mathrm{ef}}^2\right) \cdot \left[I_{\mathrm{mpp}}^* + \alpha_{\mathrm{Impp}} \cdot \left(T_{\mathrm{c}} - T_{\mathrm{c}}^*\right)\right] \tag{11}$$

$$\delta = [m \cdot k \cdot (T_{\mathrm{c}} + 273.15)]/q \tag{12}$$

$$V_{\mathrm{mpp}} = V_{\mathrm{mpp}}^* + C_2 \cdot N_{\mathrm{s}} \cdot \delta \cdot \ln(B_{\mathrm{ef}}) + C_3 \cdot N_{\mathrm{s}} \cdot [\delta \cdot \ln(B_{\mathrm{ef}})]^2 + \beta_{\mathrm{Vmpp}} \cdot \left(T_{\mathrm{c}} - T_{\mathrm{c}}^*\right) \tag{13}$$

$$P_{\mathrm{max}} = V_{\mathrm{mpp}} \cdot I_{\mathrm{mpp}} \tag{14}$$

The meaning of the involved parameters can be read in [61]. These parameters are given by regression procedures from outdoor monitored data, what facilitates application to different HCPV modules, and the model accounts for spectral effects in a basic way so that a more accurate prediction than the previous one can be achieved. In addition, if monitored data includes the complete I–V curve of the module as acquired by a curve tracer, five points on the I–V curve can be predicted rather than only the maximum power point, which can be helpful for certain applications. Another advantage of the model is the wide experience on applications for a variety of technologies.

- Model of Peharz et al. [10]

The model of Peharz et al. [10] computes the maximum power of an HCPV module from DNI, T_{c}, and Z parameter inputs as Eq. (15):

$$P_{\mathrm{max}} = b_1 \cdot \mathrm{DNI} + b_2 \cdot Z^2 + b_3 \cdot Z + b_4 \cdot T_{\mathrm{c}} + b_5 \tag{15}$$

with Z-parameter being a factor that accounts for spectral effects on the module behavior [62]. This parameter represents the mismatch between the photocurrents of the top and middle subcells with respect to the reference AM1.5d spectrum and has positive values when the middle subcell limits the current and negative values when the top subcell limits the current. To obtain the value of this input, measurements of isotype cells (specific sensors equipped with the same kinds of solar cells than the analyzed module) are required, which implies a more expensive experimental set-up than that of the previous models. If these sensors are available, parameters b_1, b_2, b_3, b_4, and b_5 can be obtained by regression procedures of outdoor monitored data as with the previous models. The model is relatively easy to implement and provides better accuracy than the previous ones, what makes it attractive.

- Model of Chan et al. [8]

A more sophisticated model was proposed in [8], which uses as inputs DNI, module heat-sink temperature, ambient temperature, date and time, aerosol optical depth at 500 nm, and relative humidity.

The model makes use of SMARTS2 software to generate the direct sunlight spectrum from the atmospheric parameters used as inputs. It considers the transmittance function of the lenses to estimate the irradiance and spectrum actually

incident on the triple-junction solar cells. The photocurrent of each subcell is then calculated by considering its specific quantum efficiency profile where the dependency on temperature is modeled through the Varshni equation [63]. A triple-junction solar cell equivalent circuit is built to obtain the cell I–V curve, considering three two-diode equivalent circuits for the subcells, connected in series through resistors that represent the tunnel junctions. A parallel-connected diode is incorporated to model the bypass diode in the solar receiver. The electrical configuration of the receivers in the module is also modeled, and a circuit solver is used to obtain the module I–V characteristics. This I–V curve is finally corrected by using a Gaussian curve in an attempt to account for mismatch effects between receivers caused by small differences in optical alignment and cell manufacturing among other effects. All of these tools are integrated in a software package called Syracuse.

It is worth noting that to make use of this package, detailed knowledge of the materials and structures that compose the HCPV module—including the solar cells, optical devices, etc.—is required to parameterize the model. The investigators have shown a deep knowledge of these details by using transmittance functions of the optical elements and semiconductor physics models to obtain the subcells quantum efficiencies and values of the equivalent circuits' parameters, etc. With all this, they also needed to make outdoor measurements on the module and even use a sun simulator to complete the set of required parameters. However, the high accuracy makes it a very valuable tool.

- Model of Almonacid et al. [64]

As was shown in the description of the previous models, when more accuracy is searched for it seems to be more difficult to obtain the model parameters, i.e., simple outdoor measurements on the module and a basic knowledge of its materials are not enough to characterize the electrical behavior. Actually, the relations between the variables used as inputs and the HCPV module behavior become very complex, and the values of the parameters that define these relations become very difficult to determine.

Because of these difficulties, Almonacid et al. [64] tried to build a model whose parameters could be exclusively obtained from outdoor measurements on the module, which are relatively easy to obtain, and thus preserve good accuracy in the prediction. For this purpose, they made use of the ability of artificial neural networks (ANNs) to solve complex problems. Inputs chosen for the model were DNI, air mass, precipitable water, ambient temperature, and wind speed.

An ANN composed of three layers (input layer, hidden layer, and output layer) was built. The input layer had five nodes corresponding to the five input variables; the output layer had one node corresponding to the maximum power of the HCPV module; and the number of nodes of the hidden layer was empirically chosen by trying different network architectures and was finally established to be seven nodes. Two sets of outdoor measurements covering a wide range of operating conditions, known as the training set" and the "validation set," were then collected. The training set was used to adjust the weights and biases of the network architecture, i.e., the parameters that characterize the HCPV module behavior, through the

Levenberg Marquardt back-propagation algorithm, an iterative process that, at each step, computes the gradient and updates the network parameters based on the input vectors and output target vectors shown to the network. The validation set was used to avoid the possibility that the network memorizes the training examples, i.e., the error on the validation set was monitored during the training process, and the point at which the network began to overfit the data was detected. After these complex processes, the network is assumed to be properly configured to represent the HCPV module behavior. Subsequent analysis on datasets other than the one used to train and validate the network allows determining the quality and accuracy of the developed model.

The investigators reported good preliminary results. However, a difficulty of this model to be applied is that an advanced knowledge on complex ANN architectures and training algorithms is required to determine the model parameters, and this knowledge is not always available. In contrast, once the parameters are determined, the model becomes easy to use, and expertise on ANNs is not necessary for carrying out studies and predictions. Another aspect to be considered is that ANNs create certain mistrust in some PV professionals, although currently many PV applications are based on these tools.

- Model of Steiner et al. [65]

This model represents at the moment the highest level of complexity and sophistication in the field of HCPV module characterization [65]. The model can be regarded as an evolution of the Syracuse model previously described taking into account the change in the optical properties of the primary lenses as a function of temperature and the effect of small misalignments caused by a nonideal sun tracker. The variables used as inputs are DNI, lens temperature, module heat-sink temperature, date and time, aerosol optical depth at 500 nm, precipitable water, α_1 and α_2 Angstrom exponents, and deviation angles in azimuth and elevation with respect to the Sun's position. Thus, temperature sensor on the lens plate and tracking accuracy sensor should be incorporated to the experimental set-up to obtain full functionality, which makes the model application more expensive than the Syracuse one.

The spectral optical efficiency of the lenses is calculated by detailed finite element modeling considering thermal expansions of the materials, changes in the refractive index with the lens temperature, and applying ray-tracing techniques. The influence of misalignment of the tracker to the Sun on the module short-circuit current is modeled through an angular acceptance function specific of each module's configuration. These models combined with similar approaches than the one used in the Syracuse tool complete an advanced package for HCPV module electrical simulation called YieldOpt. As can be realized when reading the analysis reported by the investigators, the use of such advanced model implies increasing difficulty for obtaining the model parameters. However, important merits of the model are the high accuracy and the progress in understanding and quantifying some physical effects that influence HCPV module behavior.

- Model of Fernández et al. [66]

This model was recently reported and tries to combine an easy formulation and relative easiness for obtaining the model parameters with a high degree of accuracy [66]. It uses as inputs DNI, T_c, air mass (AM), and aerosol optical depth at 550 nm (AOD_{550}). The maximum power of an HCPV module is calculated as:

$$P_{max} = \frac{P^*}{DNI^*} \cdot DNI \cdot \left[1 - \delta\left(T_c - T_c^*\right)\right] \cdot \left[1 - \varepsilon(AM - AM_U)\right] \cdot \left[1 - \varphi\left(AOD_{550} - AOD_{550,U}\right)\right] \quad (16)$$

where P^*, DNI^*, and T_c^* are constant parameters that define reference conditions and δ is the temperature coefficient that represents the linear influence of T_c on maximum power. AM_U and $AOD_{550,U}$ are parameters dependent on the module design, especially on the optical properties of the lenses and physical properties of the multijunction solar cells, that represent the point at which the AM or AOD_{550} variables respectively begin to have a significant influence on the spectral losses. The ε parameter is used to model the influence of air mass on maximum power having a value of zero for $AM < AM_U$ and a constant value for $AM > AM_U$, and the φ parameter is used to model the influence of aerosol optical depth at 550 nm on maximum power having a value of zero for $AOD_{550} < AOD_{550,U}$ and a constant value for $AOD_{550} > AOD_{550,U}$.

The earlier versions of the model only included the air mass correction for quantifying spectral losses [22]. This spectral influence was mainly studied from outdoor measurements on HCPV modules by plotting normalized values of maximum power versus air mass values and was explained because low values of air mass usually correspond to spectral conditions at which the top and middle subcells almost generate the same current, whereas high values of air mass usually correspond to spectral conditions at which the top subcell strongly limits the current. With only this spectral correction, the model shown a reasonably good behavior for different HCPV modules and climates [67].

Later, the investigators published an in-depth study on the influence of different atmospheric parameters—including air mass, aerosol optical depth at 550 nm, precipitable water, and Angstrom exponent—on the spectral behavior of HCPV modules [26]. The spectral optical efficiencies of two kind of lenses (polymethyl methacrylate and silicon on glass) and the spectral responses of two kinds of triple-junction solar cells (lattice-matched and metamorphic) were combined to represent different possibilities in the design of HCPV modules, and real spectral conditions along a year at different places around the world were reproduced by means of atmospheric parameter databases and use of the SMARTS model. The influence of each atmospheric parameter on maximum power was analyzed by means of calculations of the spectral factor, which quantifies the differential performance of the HCPV modules between incident and reference spectra. The analysis reinforced preliminary conclusions based on outdoor measurements that led to the formulation of the "air mass" term in the model and led to adding a term

for modeling the aerosol optical depth influence while maintaining the model formulation, a term specially useful for climates characterized by medium-high turbidity levels. The first experimental tests of the latest version of the model led to good results and were reported in [66].

After completing the review of some existing models, shown in Table 2 are the main characteristics of these models for the electrical characterization of HCPV modules. In this table, the models have been classified by level of accuracy taking into account the errors calculated from the experimental tests performed by the investigators and reported in the literature. However, this classification is somewhat subjective. An in-depth analysis of the accuracy of the models would require using the same experimental set-up and instruments in all cases by testing the models in the same climates and with the same module designs, reproducing the tests in different places and with different module designs, calculating the same statistical parameters for representing the errors, etc. Another aspect to be considered is that there is not a unique method for determining the parameters of each model, and the chosen method affects the quality of the results. Because of these difficulties and due to the novelty of some proposals, there are only few comparative studies on the accuracy of the models [23]. Finally, it is important to remark that, whereas the models reviewed in this section are representative of the state-of-the-art, the list of models is not exhaustive, and other interesting approaches can be found in the literature.

6 Models for Estimating the Cell Temperature of an HCPV Module

As was shown when reviewing the characteristics of the models for the electrical characterization of HCPV modules, some of these models use the T_c as input, which is an important factor affecting the HCPV module behavior. This variable is usually considered as the average temperature of the cells inside the module because, as was commented previously, different cells have different temperatures in an HCPV module operating under real conditions. Obtaining the T_c input for a model is difficult because the direct measurement of this temperature, due to the specific design of HCPV modules, usually requires accessing inside the module [12]. Moreover, when the model is used to predict the module behavior only based on atmospheric databases, there is not a physical module to be measured. Thus, models for estimating T_c in HCPV modules based on easily measurable parameters on the module and/or atmospheric parameters are required for electrical characterization and for other purposes such as power rating [10, 68].

For conventional flat-plate photovoltaic modules, T_c can be adequately estimated using relatively simple methods based on measuring the temperature on the back of the module. Inversely, for HCPV modules, the use of concentrated light focused on a small cell area, as well as the use of cooling mechanisms, implies a complex

Table 2 Summary of characteristics of some existing models for the electrical characterization of HCPV modules

	ASTM	King et al. [61]	Peharz et al. [10]	Chan et al. [8]	Almonacid et al. [64]	Steiner et al. [65]	Fernandez et al. [66]
Inputs used to consider irradiance effects	DNI	DNI	DNI	DNI	DNI	DNI	DNI
Inputs used to consider temperature effects	Ambient temperature	Cell temperature	Cell temperature	Module heat-sink temperature	Ambient temperature	Module heat-sink temperature	Cell temperature
	Wind speed				Wind speed		
Inputs used to consider spectral effects	None	Air mass	Z parameter	Date/time	Air mass	Date/time	Air mass
				AOD_{500}	Precipitable water	AOD_{500}	AOD_{550}
				Ambient temperature		Precipitable water	
				Relative humidity		Angstrom exponents	
Additional inputs	None	None	None	None	None	Lens temperature	None
						Tracking accuracy	
Parameterization can be done from basic module information and/or outdoor measurements	Yes	Yes	No	No	Yes	No	Yes
Parameterization requires advanced module information and/or indoor measurements and/or the use of complex physical models	No	No	Yes	Yes	No	Yes	No
Parameterization requires advanced knowledge on Artificial Neural Networks	No	No	No	No	Yes	No	No
Specific software is required	No	No	No	Yes	No	Yes	No
The model provides electrical parameters other than maximum power	No	Yes	No	Yes	No	Yes	No
Accuracy level	Medium	Medium/High	High	Advanced	High	Advanced	High

thermal behavior, which makes it more difficult to estimate the T_c. Because of this, different models specific for HCPV modules have recently been developed.

These models can be classified into models based on direct measurements on the module and models based on atmospheric parameters. Models based on atmospheric parameters are mandatory when there is not a physical module to be measured, whereas models based on direct measurements are usually more accurate depending on the chosen method, available sensors, and module design, etc. The models based on direct measurements can be further classified into models based on module heat-sink temperature and models based on electrical parameters. The module heat-sink temperature can be typically measured at the root of a finned heat-exchanger on the back of the module for passively cooled designs. The measurement of this temperature is a way of decreasing uncertainty because estimating the heat-sink temperature is difficult and depends on a variety of factors such as ambient temperature, DNI, wind speed and direction, module electrical efficiency, or module design [14, 15, 69]. Models based on electrical parameters try to obtain T_c from the measurements of electrical parameters that are sensitive to the T_c such as the open-circuit voltage.

Next, some relevant proposals for estimating T_c in an HCPV module intended for electrical characterization are summarized, and a comparative table showing their main characteristics is given.

1. Models based on module heat-sink temperature

- Model of King et al. [61]

The classical model developed by King et al. [61] expresses T_c as a function of module heat-sink temperature (T_{h-s}) and DNI as:

$$T_c = T_{h-s} + (\mathrm{DNI}/\mathrm{DNI}^*) \cdot \Delta T \tag{17}$$

where DNI^* is the reference DNI, and ΔT is a constant parameter representing the temperature difference between the cell and the heat-sink at the reference irradiance. Obtaining the ΔT parameter requires monitoring a module with a T_c sensor under conditions around the reference irradiance, which implies difficulty in parameterizing the model.

- Model of Rubio et al. [70]

The model developed by Rubio et al. [70] uses similar assumptions to the previous one, i.e., T_c is calculated as a function of DNI and T_{h-s} as:

$$T_c = T_{h-s} + \rho \cdot \mathrm{DNI} \tag{18}$$

with ρ being the so-called "internal thermal resistance" of the module, a constant parameter that tries to represent in a simple way the module's thermal behavior. The main advantage of this model is that the value of the ρ parameter can be estimated without the need of monitoring the HCPV module if there is knowledge of the

material layers below the solar cell (thicknesses and thermal conductivity) as well as the geometric concentration ratio and optical efficiency of the module [32].

- Model of Fernández et al. [15]

Real HCPV power plants use inverters to keep the modules operating at maximum power point. When an HCPV module operates under this condition, part of the luminous power absorbed by the solar cells is not transformed to heat but converted to electricity. This implies that T_c values in an HCPV module operating under real conditions should depend on the rate of harvested energy. This effect was theoretically investigated by Yandt et al. [71], who predicted temperature differences ≤14 °C between the open-circuit condition and the maximum power point condition for the cells in an HCPV module. Later, Fernández et al. [15] simultaneously measured two identical HCPV modules in the same solar tracker, one at open-circuit and the other connected to an inverter, and observed differences in the T_c between 2 and 20 °C depending on the incident DNI with the major differences corresponding to the highest DNI levels. As a result of these observations, they proposed a model that accounts for the power harvested by the module to calculate T_c. This model was formulated as:

$$T_c = T_{h-s} + R\left[\mathrm{DNI} \cdot C_{geom} \cdot \eta_{opt} - P_{max}/(N \cdot A_{cell})\right] \tag{19}$$

As can be seen, the model depends on T_{h-s} and DNI inputs as with the previously described models, but it also incorporates the module maximum power (P_{max}) as input. R is the thermal resistance between the solar cell and the back of the module, which can be measured or estimated from physical properties of the materials behind the solar cell, C_{geom} is the geometric concentration factor, η_{opt} is the optical efficiency of the lenses, N is the number of solar cells in the module, and A_{cell} is the area of each cell.

2. Models based on electrical parameters

- Model of the standard IEC 60904-5

The standard IEC 60904-5 [72] defines a procedure for estimating the T_c in a photovoltaic device from measurements of the open-circuit voltage. This procedure has been tested for HCPV modules and is based on the following expresión:

$$V_{oc} = V_{oc}^{*} + N_s\left(nkT_{c(K)}/q\right)\ln(\mathrm{DNI}/\mathrm{DNI}^{*}) + \beta_{Voc}\left(T_{c(K)} - T_{c(K)}^{*}\right) \tag{20}$$

The expression can be rearranged to calculate the T_c in Kelvins ($T_{c(K)}$) from the measurements of open-circuit voltage (V_{oc}) and DNI. In the expression, some parameters are involved: k and q, respectively, represent the Boltzmann constant and the electron charge; N_s is the number of series-connected solar cells in the module; V_{oc}^{*}, DNI^{*} and $T_{c(K)}^{*}$ respectively represent the open-circuit voltage, DNI,

and T_c at predefined reference conditions; n is the effective diode ideality factor of the module, and β_{Voc} is the temperature coefficient of open-circuit voltage for the module.

n and β_{Voc} parameters can be adjusted from measurements of T_c, Voc and DNI performed on an HCPV module under different operating conditions. β_{Voc} is also usually provided by the module manufacturer, and n could be obtained from values published in the literature. However, a careful selection of these values is required because the model is very sensitive to both parameters and because there are many factors in the design of an HCPV module that can modify the value of these parameters.

An alternative to this method consists in measuring the module short-circuit current instead of the DNI. The DNI/DNI* quotient is replaced by the I_{sc}/I_{sc}^* quotient, and this way the method becomes exclusively dependent on electrical measurements. This alternative is known as the "$V_{oc} - I_{sc}$" method.

- Model of Peharz et al. [10]

The model developed by Peharz et al. [10] calculates the T_c in an HCPV module from electrical measurements of V_{oc}, and I_{sc} based on the following expression:

$$T_c = \frac{V_{oc} - a_1 \ln(I_{sc}) - a_2}{b_1 \ln(I_{sc}) + b_2} \tag{21}$$

This functional dependence was proposed from the analysis of the measurements performed on several HCPV modules in a sun simulator. This equipment allowed controlling the light intensity incident on the module by means of a flash bulb and the module temperature by means of several infrared light bulbs whose distance to the module back plate could be varied. Model parameters can be fitted from these kinds of indoor measurements or even from an outdoor experimental campaign as was shown in [68].

3. Models based on atmospheric parameters

- Model of Almonacid et al. [12]

The model developed by Almonacid et al. [12] uses linear coefficients to express the dependence of T_c on ambient temperature (T_{air}), DNI, and wind speed (W_s) by means of:

$$T_c = T_{air} + c_1 \cdot \mathrm{DNI} + c_2 \cdot W_s \tag{22}$$

As with the other models based on atmospheric parameters, the model parameterization must be performed from the analysis of outdoor measurements on an HCPV module equipped with a cell-temperature sensor.

- Model of Hornung et al. [28]

The model developed by Hornung et al. [28] is similar to the previous one with the difference that investigators tried to model the influence of wind speed by means of an exponential correction:

$$T_c = T_{air} + m \cdot \left[\exp\left(-0.5 W_s / W_{s,0}\right) + d\right] \cdot \mathrm{DNI} \tag{23}$$

Again, the model parameters must be obtained from the analysis of outdoor measurements.

- Model of Fernández et al. based on ANN [22]

This model is an attempt at improving the accuracy of the models based on atmospheric parameters by using the same atmospheric inputs: T_{air}, DNI, and W_s [32]. It is assumed that this aim can be reached by better capturing the complex relation between these three inputs and the T_c than the proposed analytical expressions. For this purpose, the ability of ANNs for characterizing complex and highly nonlinear processes was used. Neutral Network architecture is composed of three layers (a three-node input layer, a single-node output layer, and a five-node hidden layer) was built and trained through the Levenberg–Marquardt back-propagation algorithm by means of an extensive set of outdoor measurements. A comparative study on accuracy with respect to the linear model based on the same atmospheric parameters showed better performance of the ANN-based model. However, the model has the difficulties inherent to these kinds of approaches, i.e., parameterization is difficult especially if there is not advanced knowledge and experience in ANN-training algorithms.

There are several comparative studies on accuracy for some of the models reviewed in this section [32, 68]. These studies use the same datasets of atmospheric measurements and parameters directly measured on commercial HCPV modules for all of the compared models. The studies confirm that models based on direct measurements on the module are more accurate than models exclusively based on atmospheric parameters, i.e., the direct measurements on the module are an effective way of decreasing uncertainty. However, it is remarkable that the differences on accuracy are not very large, so the models based on atmospheric parameters are very useful tools when the HCPV module and the experimental set-up required for monitoring its behavior are not available. Of course, the choice of the most suitable model for a specific project is not trivial, and accuracy is not the only relevant factor. However, other factors, such as the aim of the project, the availability of technical resources and data sources, etc., must be taken into account.

The list of models reviewed in this section is not exhaustive, and other proposals can be found in the literature. In particular, some models implement more detailed approaches of the module thermal behavior by using tools such as finite element modeling [73, 74]. These models seem to be more oriented to improve module designs and heat-dissipation mechanisms than to characterize the electrical behavior. Table 3 summarizes the main characteristics of the models reviewed in this section.

Table 3 Summary of characteristics of some existing models for estimating the T_c in an HCPV module for electrical characterization

	Based on module heat-sink temperature			Based on electrical parameters		Based on atmospheric parameters		
Required inputs	King et al. [61]	Rubio et al. [70]	Fernández et al. [15]	IEC 60904–5	Peharz et al. [10]	Almonacid et al. [12]	Hornung et al. [28]	Fernández ANN [22]
	Heat-sink temp.	Heat-sink temp.	Heat-sink temp.	Voc	Voc	Ambient temp.	Ambient temp.	Ambient temp.
	DNI	DNI	DNI	DNI or Isc	Isc	DNI	DNI	DNI
			Max. power			Wind speed	Wind speed	Wind speed
Parameterization can be done from basic module information and/or values in the literature	No	Yes	Yes	Yes	No	No	No	No
Parameterization requires monitoring the behavior of a module	Yes	No	No	No	Yes	Yes	Yes	Yes
Parameterization requires advanced knowledge on artifical neural networks	No	No	No	No	No	No	No	Yes
The model requires direct measurements on a module to be applied	Yes	Yes	Yes	Yes	Yes	No	No	No

7 Conclusions

Solar cells and optical devices are not the only components to be considered in the design of an HCPV module. Mechanisms for thermal management and heat dissipation must be analyzed. Targets of cooling in HCPV modules are limiting the operation temperature of the solar cells, decreasing the temperature differences between cells, decreasing temperature gradients across each cell, ensuring reliability, and decreasing costs. The design of HCPV solar receivers is evolving to decrease the thermal resistance of the materials behind the solar cells. The addition of finned heat-exchangers is a simple way of improving heat dissipation, but many other alternatives are being investigated both for passive and active cooling.

Understanding the behavior of HCPV modules under real operating conditions is difficult. Experimental studies are required for analyzing the influence of the changing atmospheric conditions taking into account the variety of possible designs. The behavior of an HCPV module strongly depends on the behavior of the solar cells inside, but other elements of the assembly have an influence. DNI is the most important atmospheric variable. The temperature of the solar cells and the direct sunlight spectrum play a relevant role in HCPV modules. There are also additional factors to be considered.

Currently there are different models intended for reproducing the electrical behavior of HCPV modules. These models offer different levels of accuracy, although there are few comparative studies of the models using the same experimental set-up and testing conditions. Some models require specific software and/or unusual instruments to be applied; some others are relatively easier to implement. The choice of a model depends on the available resources and the aims of the project. The development of reliable models is important to promote HCPV technology, and new proposals are expected in the near future.

References

1. IEC 62108 (2007) Concentrator photovoltaic (CPV) modules and assemblies—design qualification and type approval, edn 1. Geneve
2. Sala G, Pachón D, Antón I (1999) Test, rating and specification of PV concentrator components and systems. C-rating project. Book1: classification of PV concentrators. Contract NNE-1999-00588
3. IEC 62670-1 (2013) Photovoltaic concentrators (CPV)—performance testing—part 1: standard conditions. Edition 1.0, Geneve
4. Pérez-Higueras PJ, Muñoz E, Almonacid G, Vidal PG (2011) High concentrator photovoltaics efficiencies: present status and forecast. Renew Sust Energy Rev 15:1810–1815
5. Fernández Eduardo F, Siefer G, Almonacid F, Loureiro AJG, Pérez-Higueras PJ (2013) A two subcell equivalent solar cell model for III–V triple junction solar cells under spectrum and temperature variations. Sol Energy 92:221–229
6. Philipps SP, Peharz G, Hoheisel R, Hornung T, Al-Abbadi NM, Dimroth F, Bett AW (2010) Energy harvesting efficiency of III–V triple-junction concentrator solar cells under realistic spectral conditions. Sol Energy Mat Sol Cells 94:869–877

7. Domínguez C, Antón I, Sala G (2010) Multijunction solar cell model for translating I–V characteristics as a function of irradiance, spectrum, and cell temperature. Prog Photov Res App 18:272–284
8. Chan NLA, Young TB, Brindley HE, Ekins-Daukes NJ, Araki K, Kemmoku YY (2013) Validation of energy prediction method for a concentrator photovoltaic module in Toyohashi Japan. Prog Photov Res App 21:1598–1610
9. Peharz G, Ferrer Rodríguez JP, Siefer G, Bett AW (2011) Investigations on the temperature dependence of CPV modules equipped with triple-junction solar cells. Prog Photov Res App 19:54–60
10. Peharz G, Ferrer Rodríguez JP, Siefer G, Bett AW (2011) A method for using CPV modules as temperature sensors and its application to rating procedures. Sol Energy Mater Sol Cells 95:2734–2744
11. Fernández Eduardo F, Pérez-Higueras PJ, García Loureiro AJ, Gómez Vidal P (2013) Outdoor evaluation of concentrator photovoltaic systems modules from different manufacturers: first results and steps. Prog Photov Res Appl 21:693–701
12. Almonacid F, Pérez-Higueras PJ, Fernández EF, Rodrigo P (2012) Relation between the cell temperature of a HCPV module and atmospheric parameters. Sol Energy Mat Sol Cells 105:322–327
13. Faine P, Kurtz S, Riordan C, Olson JM (1991) The influence of spectral solar irradiance variations on the performance of selected single-junction and multi-junctions solar cells. Sol Cells 31:259–278
14. Ota Y, Nagai H, Araki K, Nishioka K (2012) Temperature distribution in 820X CPV module during outdoor operation. AIP conference proceedings 1477:364–367
15. Fernández Eduardo F, Rodrigo P, Almonacid F, Pérez-Higueras PJ (2014) A method for estimating cell temperature at the maximum power point of a HCPV module under actual operating conditions. Sol Energy Mat Sol Cells 124:159–165
16. Strobach E, Faiman D, Kabalo S, Bukobza D, Melnichak V, Gombert A, Gerstmaier T, Roettger M (2014) Modeling a grid-connected concentrator photovoltaic system. Prog Photov Res App. doi:10.1002/pip.2467
17. Helmers H, Schachtner M, Bett AW (2013) Influence of temperature and irradiance on triple-junction solar subcells. Sol Energy Mat Sol Cells 116:144–152
18. Fernández Eduardo F, Siefer G, Schachtner M, García-Loureiro AJ, Pérez-Higueras PJ (2012) Temperature coefficients of monolithic III–V triple-junction solar cells under different spectra and irradiance levels. AIP Conf Proc 1477:189–193
19. Siefer G, Bett AW (2014) Analysis of temperature coefficients for III–V multijunction concentrator cells. Prog Photov Res App 22:515–524
20. Kinsey GS, Edmondson KM (2009) Spectral response and energy output of concentrator multijunction solar cells. Prog Photov Res App 17:279–288
21. Fernández Eduardo F, Rodrigo P, Fernández JI, Almonacid F, Pérez-Higueras PJ, García-Loureiro AJ, Almonacid G (2014) Analysis of high concentrator photovoltaic modules in outdoor conditions: influence of direct normal irradiance, air temperature, and air mass. J Renew Sust En 6:013102
22. Fernández Eduardo F, Almonacid F, Rodrigo P, Pérez-Higueras PJ (2013) Model for prediction of the maximum power point of a high concentrator photovoltaic module. Sol Energy 97:12–18
23. Rodrigo P, Fernández Eduardo F, Almonacid F, Pérez-Higueras PJ (2013) Models for the electrical characterization of high concentration photovoltaic cells and modules: a review. Renew Sust Ener Rev 26:752–760
24. McMahon WE, Emery KE, Friedman DJ, Ottoson L, Young MS, Ward JS, Kramer CM, Duda A, Kurtz S (2008) Fill factor as a probe of current-matching for GaInP/GaAs tandem cells in a concentrator system during outdoor operation. Prog Photov Res App 16:213–224
25. Aronova ES, Grilikhes VA, Shvarts MZ, Timoshi NH (2008) On the estimation of hourly power output of solar photovoltaic installations with MJ SCs and sunlight concentrators. In: 33rd IEEE photovoltaic specialists conference

26. Fernández Eduardo F, Almonacid F, Ruiz-Arias JA, Soria-Moya A (2014) Analysis of the spectral variations on the performance of high concentrator photovoltaic modules operating under different real climate conditions. Sol Energy Mat Sol Cells 127:179–187
27. Chan NLA, Brindley HE, Ekins-Daukes NJ (2014) Impact of individual atmospheric parameters on CPV system power, energy yield and cost of energy. Prog Photov Res App 22:1080–1095
28. Hornung T, Steiner M, Nitz P (2012) Estimation of the influence of fresnel lens temperature on energy generation of a concentrator photovoltaic system. Sol Energy Mat Sol Cells 99:333–338
29. Araki K, Kemmoku Y, Yamaguchi M (2008) A simple rating method for CPV modules and systems. In: 33rd IEEE photovoltaic specialists conference
30. García-Domingo B, Aguilera J, de la Casa J, Fuentes M (2014) Modelling the influence of atmospheric conditions on the outdoor real performance of a CPV (concentrated photovoltaic) module. Energy 70:239–250
31. Kurtz S, Muller M, Jordan D, Ghosal K, Fisher B, Verlinden P, Hashimoto J, Riley D (2014) Key parameters in determining energy generated by CPV modules. Prog Photov Res App. doi:10.1002/pip.2544
32. Fernández Eduardo F, Almonacid F, Rodrigo P, Pérez-Higueras PJ (2014) Calculation of the cell temperature of a high concentrator photovoltaic (HCPV) module: a study and comparison of different methods. Sol Energy Mat Sol Cells 121:144–151
33. Baig H, Heasman KC, Mallick TK (2012) Non-uniform illumination in concentrating solar cells. Renew Sustain Energy Rev 16:5890–5909
34. Mills A (1999) Basic heat and mass transfer. Prentice Hall, New Jersey
35. Royne A, Dey CJ, Mills DR (2005) Cooling of photovoltaic cells under concentrated illumination: a critical review. Sol Energy Mater Sol Cells 86:451–483
36. Cotal H, Frost J (2010) Heat transfer modeling of concentrator multijunction solar cell assemblies using finite difference techniques. In: IEEE photovoltaic specialists conference pp 213–218
37. Micheli L, Sarmah N, Luo X, Reddy KS, Mallick TK, Tapas M (2014) Design of a 16-cell densely-packed receiver for high concentrating photovoltaic applications. Energy Procedia (in press)
38. King J (1988) Material handbook for hybrid microelectronics. Artech House Publishers, Massachusetts
39. Kulkarni DP, Das DK (2005) Analytical and numerical studies on microscale heat sinks for electronic applications. Appl Therm Eng 25:2432–2449
40. Tseng YS, Fu HH, Hung TC, Pei BS (2007) An optimal parametric design to improve chip cooling. Appl Therm Eng 27:1823–1831
41. Mittelman G, Dayan A, Dado-Turjeman K, Ullmann A (2007) Laminar free convection underneath a downward facing inclined hot fin array. Int J Heat Mass Transf 50:2582–2589
42. Do KH, Kim TH, Han YS, Choi BI, Kim MB (2012) General correlation of a natural convective heat sink with plate-fins for high concentrating photovoltaic module cooling. Sol Energy 86:2725–2734
43. Bar-Cohen A, Iyengar M, Kraus AD (2003) Design of optimum plate-fin natural convective heat sinks. J Electron Packag 125:208
44. Natarajan SK, Mallick TK, Katz M, Weingaertner S (2011) Numerical investigations of solar cell temperature for photovoltaic concentrator system with and without passive cooling arrangements. Int J Therm Sci 50:2514–2521
45. Royne A, Dey CJ (2007) Design of a jet impingement cooling device for densely packed PV cells under high concentration. Sol Energy 81:1014–1024
46. Zhu L, Boehm RF, Wang Y, Halford C, Sun Y (2011) Water immersion cooling of PV cells in a high concentration system. Sol Energy Mater Sol Cells 95:538–545
47. Anderson W, Tamanna S, Sarraf D, Dussinger P, Hoffman R (2008) Heat pipe cooling of concentrating photovoltaic (CPV) systems. In: IEEE international energy conversation engineering conferences, p 1

48. Van Sark WGJHM (2011) Feasibility of photovoltaic—thermoelectric hybrid modules. Appl Energy 88:2785–2790
49. Valeh-e-Sheyda P, Rahimi M, Karimi E, Asadi M (2013) Application of two-phase flow for cooling of hybrid microchannel PV cells: a comparative study. Energy Convers Manag 69:122–130
50. Karathanassis IK, Papanicolaou E, Belessiotis V, Bergeles GC (2013) Multi-objective design optimization of a micro heat sink for concentrating photovoltaic/thermal (CPVT) systems using a genetic algorithm. Appl Therm Eng 59:733–744
51. Wong KV, De Leon O (2010) Applications of nanofluids: current and future. Adv Mech Eng 2010:1–11
52. Al-Shamani AN, Yazdi MH, Alghoul MA, Abed AM, Ruslan MH, Mat S et al (2014) Nanofluids for improved efficiency in cooling solar collectors—a review. Renew Sustain Energy Rev 38:348–367
53. Taylor R, Coulombe S, Otanicar T, Phelan P, Gunawan A, Lv W et al (2013) Small particles, big impacts: a review of the diverse applications of nanofluids. J Appl Phys 113:011301
54. Micheli L, Sarmah N, Luo X, Reddy KS, Mallick TK (2013) Opportunities and challenges in micro- and nano-technologies for concentrating photovoltaic cooling: a review. Renew Sustain Energy Rev 20:595–610
55. Barrau J, Perona A, Dollet A, Rosell J (2014) Outdoor test of a hybrid jet impingement/micro-channel cooling device for densely packed concentrated photovoltaic cells. Sol Energy 107:113–121
56. Barrau J, Rosell J, Chemisana D, Tadrist L, Ibañez M (2011) Effect of a hybrid jet impingement/micro-channel cooling device on the performance of densely packed PV cells under high concentration. Sol Energy 85:2655–2665
57. Sung MK, Mudawar I (2008) Single-phase and two-phase cooling using hybrid micro-channel/slot-jet module. Int J Heat Mass Transf 51:3825–3839
58. Kribus A, Kaftori D, Mittelman G, Hirshfeld A, Flitsanov Y, Dayan A (2006) A miniature concentrating photovoltaic and thermal system. Energy Convers Manag 47:3582–3590
59. Mittelman G, Kribus A, Dayan A (2007) Solar cooling with concentrating photovoltaic/thermal (CPVT) systems. Energy Convers Manag 48:2481–2490
60. ASTM E 2527 (2009) Standard test method for electrical performance of concentrator terrestrial photovoltaic modules and systems under natural sunlight. American Society for Testing and Materials
61. King DL, Boyson WE, Kratochvil JA (2004) Photovoltaic array performance model. Sandia National Laboratories, SAND2004-3535
62. Peharz G, Siefer G, Bett AW (2009) A simple method for quantifying spectral impacts on multi-junction solar cells. Sol Energy 83:1588–1598
63. Varshni YP (1967) Temperature dependence of the energy gap in semiconductors. Physica 34:149–154
64. Almonacid F, Fernández EF, Pérez-Higueras PJ, Rodrigo P, Rus-Casas C (2013) Estimating the maximum power of a high concentrator photovoltaic (HCPV) module using an artificial neural network. Energy 53:165–172
65. Steiner M, Siefer G, Hornung T, Peharz G, Bett AW (2014) YieldOpt, a model to predict the power output and energy yield for concentrating photovoltaic modules. Prog Photov Res Appl. doi:10.1002/pip.2458
66. Fernández Eduardo F, Almonacid F, Mallick TK, Pérez-Higueras PJ (2014) Analytical modelling of high concentrator photovoltaic modules based on atmospheric parameters. Int J Photoenergy (in press)
67. Fernández Eduardo F, Almonacid F, Sarmah N, Mallick T, Sánchez I, Cuadra JM, Soria-Moya A, Pérez-Higueras PJ (2014) Performance analysis of the lineal model for estimating the maximum power of a HCPV module in different climate conditions. AIP Conf Proc 1616:187
68. Rodrigo P, Fernández Eduardo F, Almonacid F, Pérez-Higueras PJ (2014) Review of methods for the calculation of cell temperature in high concentration photovoltaic modules for electrical characterization. Renew Sustain Energy Rev 38:478–488

69. Castro M, Domínguez C, Núñez R, Antón I, Sala G, Araki K (2013) Detailed effects of wind on the field performance of a 50 kW CPV demonstration plant. AIP Conf Proc 1556:256–260
70. Rubio F, Martínez M, Coronado R, Pachón JL, Banda P (2008) Developing CPV power plants —ISFOC experiences. In: IEEE photovoltaic specialists conference, pp 1–4
71. Yandt MD, Wheeldon JF, Cook J, Beal R, Walker AW, Thériault O et al (2012) Estimating cell temperature in a concentrating photovoltaic system. AIP Conf Proc 1477:172–175
72. IEC 60904-5 (2011) Photovoltaic devices—part 5: determination of the equivalent cell temperature (ECT) of photovoltaic (PV) devices by the open-circuit voltage method
73. Wang YN, Lin TT, Leong JC, Hsu YT, Yeh CP, Lee PH et al (2013) Numerical investigation of high-concentration photovoltaic module heat dissipation. Renew Energy 50:20–26
74. Steiner M, Siefer G, Bett AW (2012) An investigation of solar cell interconnection schemes within CPV modules using a validated temperature-dependent SPICE network model. Prog Photov Res App 22:505–514

Modeling of High-Concentrator Photovoltaic Systems for Utility-Scale Applications

Yong Sin Kim

Abstract The levelized cost of energy (LCOE) is widely used for evaluating the cost of energy generation across technologies. In a utility-scale high-concentrator photovoltaic system (HCPV), capacity factor (CF) and ground-coverage ratio (GCR) are the two fundamental drivers for determining the LCOE. However the LCOE is a complex function of various parameters, which is not explicitly defined in terms of these two factors. In this chapter, based on a cost function that simplifies the LCOE in terms of CF and GCR, the method for modeling utility-scale HCPV systems is considered.

1 Introduction

As the price of fossil fuel and environmental concern increases, so does the demand for renewable energy. Although numerous utility-scale photovoltaic (PV) systems have been researched and installed during the last several decades, the cost of energy generation has remained high compared with other types of energy-generation systems. In comparing the energy generation cost for utility-scale power plants, levelized cost of energy (LCOE) is widely used and defined as the cost of generating electricity over the system's lifetime accounting for initial investment, financing, cost for operations and maintenance, cost of fuel, and some other expenses [1, 2]. One of the essential way to reduce the LCOE of a utility-scale PV system is to optimize system-specific parameters through accurate system modeling.

There are two fundamental drivers for the LCOE of utility-scale PV systems: capacity factor (CF) and system ground-coverage ratio (GCR) [3–5]. CF represents the total amount of energy that the plant produces during a certain period of time divided by the total amount of energy that the plant would have produced at its full capacity, which depends on the locations of the site, PV and inverter efficiency, and

Y.S. Kim (✉)
School of Electrical Engineering, Korea University, Seoul, South Korea
e-mail: shonkim@korea.ac.kr

P. Pérez-Higueras and E.F. Fernández (eds.), *High Concentrator Photovoltaics*,
Green Energy and Technology, DOI 10.1007/978-3-319-15039-0_6

tracking method. GCR is defined as the ratio of total PV area to the total land used. The highest CFs are generated with dual-axis trackers that follow the sun throughout the day and keep the PV module oriented toward the sun for maximizing energy generation. The longer the time spent tracking the sun (indicating the higher CF), however, the more space between trackers is needed to minimize the self-shading effect [3–6]. As a result, GCR is reduced and LCOE increases due to additional overhead in terms of land requirements, site preparation and maintenance, electrical wiring, and trenching.

For accurately modeling utility-scale high-concentrator PV (HCPV) systems, conventional modeling based on flat panels is inadequate. Various tracking methods based on flat panels have been investigated in [4], in which energy yield—defined as the ratio of total energy generated to the peak energy—and GCR are mostly considered. However, unlike CF, energy yield does not consider time dependency and thus is not suitable because the insolation changes throughout the day. Furthermore, lack of an electrical model for power optimization lowers the accuracy in modeling the total power harvested under shading conditions.

HCPV systems with narrow acceptance angles requires accurate dual-axis tracking resulting in the trade-off between tracker array spacing, self-shading loss, and land use. When simulating utility-scale HCPV systems after modeling, the computational time for finding the optimum configuration for given system parameters increases exponentially as the number of trackers increases. In this chapter, system modeling, as well as the method by which to reduce computational time in simulating utility-scale HCPV Systems, will be covered.

2 Cost Function

Modeling starts from defining two-tracker space-related parameters, i.e., GCR and CF as

$$\mathrm{GCR} = \sum A_{\mathrm{module}} \Big/ A_{\mathrm{land}} \tag{1}$$

$$\mathrm{CF} = \int_{t_1}^{t_2} P(t)\mathrm{d}t / [(t_2 - t_1)P_{\max}] \tag{2}$$

where A_{module} is the area of a CPV module; A_{land} is the total land area for the system; $P(t)$ is the output power generated by the system at a given time t; and $P_{\max}$ is the maximum power available by the system. Then LCOE can be simplified as

$$\mathrm{LCOE} = \frac{\sum C}{\int_{t_1}^{t_2} P(t)\mathrm{d}t} = \frac{C_{\mathrm{others}} + C_{\mathrm{land}}A_{\mathrm{land}}}{\mathrm{CF}(t_2 - t_1)P_{\max}} \tag{3}$$

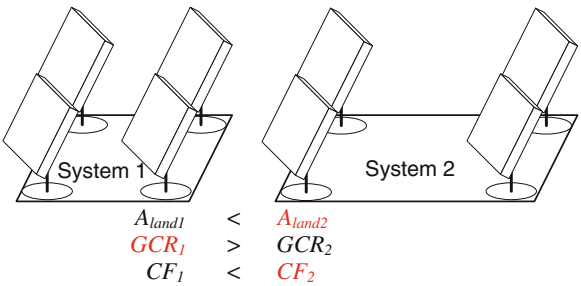

Fig. 1 Capacity factor (*CF*) versus ground coverage ratio (*GCR*) in CPV systems

where the sum of C is the cost over the system's lifetime, C_{land} is the cost of a unit land; and C_{others} is overall cost not related to land. With a system constant k, LCOE can be expressed as

$$\text{LCOE} = \frac{1 + C_{\text{land}} A_{\text{land}} / C_{\text{others}}}{\text{CF}(t_2 - t_1) P_{\max} / C_{\text{others}}} = \frac{1 + \frac{k}{\text{GCR}}}{\text{CF}(t_2 - t_1) P_{\max} / C_{\text{others}}} \tag{4}$$

Thus, the cost function F can be expressed by the relationship between CF and GCR with k as [7]:

$$F = \frac{1 + \frac{k}{\text{GCR}}}{\text{CF}} \propto \text{LCOE} \tag{5}$$

If F is minimized, so is LCOE because F is linearly proportional to LCOE. Previous analysis using complicated equations to calculate and minimize LCOE is now reduced to a simple equation that has one system parameter and two variables. Figure 1 shows trackers in two different systems. The total area of the system 1 is smaller than that of the system 2, resulting in higher GCR but less CF due to larger self-shading loss; this will be covered later in this chapter.

3 Solar Radiation

To estimate total power harvested from a system, it is crucial to have accurate solar radiation data at the site where the system is deployed. In this section, we describe the Sun's position, air mass (AM), and weather function to obtain direct normal irradiance (DNI) data on an hourly basis.

3.1 The Sun's Position

The Sun's apparent position varies with the location of observer and the time, which can be described by two angles: the elevation angle α and the azimuth angle

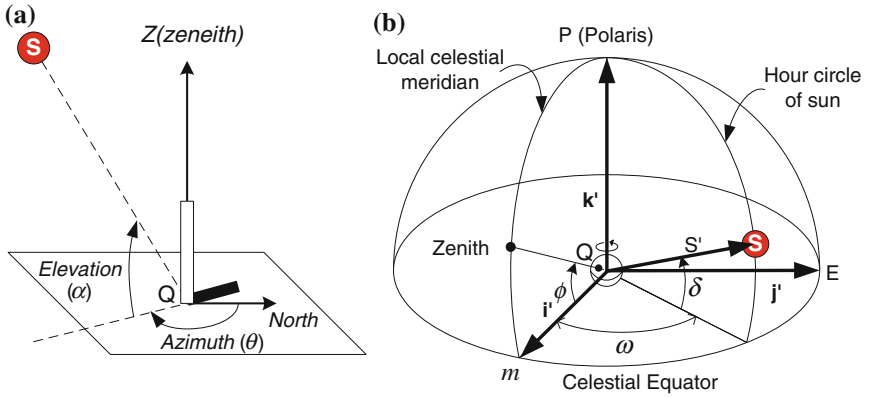

Fig. 2 **a** Earth surface coordinate system for an observer at location Q. **b** Earth center coordinate system with hour angel ω, declination δ, and latitude ϕ at location Q

θ as shown in Fig. 2a. The α is the angular height of the geometric center of the Sun from the horizon, and the θ is the clockwise angle on the horizontal plane from the north-pointing coordinate axis to the projection of the Sun's central ray. α and θ at location Q can be expressed in terms of the latitude ϕ, the declination of the Sun δ, and the hour angle ω in Fig. 2b as [8]:

$$\begin{aligned} \sin\alpha &= \cos\phi\cos\delta\cos\omega + \sin\phi\sin\delta \\ \cos\alpha\sin\theta &= \cos\delta\sin\omega \\ \cos\alpha\cos\theta &= -\sin\phi\cos\delta\cos\omega + \cos\phi\sin\delta \end{aligned} \tag{6}$$

3.2 Air Mass and Weather Function

Extraterrestrial radiation I_E, solar radiation incident outside of the earth's atmosphere, varies by ±3 % throughout a year depending on the Earth–Sun distance. It can be expressed as

$$I_E(n) = I_0 \cdot \left(\frac{\overline{R_{ES}}}{R_{ES}}\right)^2 \approx I_0\left[1 + 0.033\cos\left(\frac{360\cdot n}{365}\right)\right] \tag{7}$$

where $I_0 = 1367$ W/m^2 is the solar constant; R_{ES} is the actual earth-sun distance; $\overline{R_{ES}}$ is the average value of R_{ES}; and n is the nth day in a year [9]. Solar radiation, which is defined as solar energy received on the Earth's surface, is the sum of DNI and diffused radiation after scattering in the atmosphere. As the rays travel through the

atmosphere longer, solar radiation attenuates more due to increased probability of scattering and absorption. Solar radiation discussed in [4] neglects this attenuation.

AM describes the attenuation of solar radiation and is defined as the optical path length of solar radiation through the earth's atmosphere. AM incorporates the curvature of the earth as a function of α and can be expressed as [10]:

$$\mathrm{AM}(\alpha) = \frac{1}{\sin\alpha + 0.50572 \cdot (6.07995 + \alpha)^{-1.6364}} \tag{8}$$

Denoting I_{D} as the intensity of solar radiation reaching the earth's surface at normal incident, approximately 70 % of the radiation incident on the atmosphere is transmitted to the Earth's surface as [11]:

$$I_{\mathrm{D}}(n,\alpha) = I_{\mathrm{E}}(n) \cdot 0.7^{\mathrm{AM}(\alpha)^{0.678}} \tag{9}$$

However, sunlight intensity depends not only on the day of a year and the Sun's elevation but also on the site location as shown in Fig. 3. The α is a function of time. Thus, the intensity of direct normal incident of sunlight on an hourly basis needs to include the weather function $W(n)$ of the site as

$$I_{\mathrm{D}}(n,\alpha) = I_{\mathrm{E}}(n) \cdot W(n) \cdot 0.7^{\mathrm{AM}(\alpha)^{0.678}} \tag{10}$$

The monthly average DNI values from various sources, such as NASA and NREL (both TMY2 and TMY3 are available), as shown in Fig. 4, can be used for obtaining $W(n)$, which can be expressed as

$$\overline{I_{\mathrm{D}}(m)} = \frac{1}{n_{\mathrm{E}} - n_{\mathrm{S}}} \frac{2}{\alpha_{\max}} \int_{n_{\mathrm{S}}}^{n_{\mathrm{E}}} \int_{0}^{\alpha_{\max}} I_{\mathrm{E}}(n) \cdot W(n) \cdot 0.7^{\mathrm{AM}(\alpha)^{0.678}} \mathrm{d}\alpha \mathrm{d}n \tag{11}$$

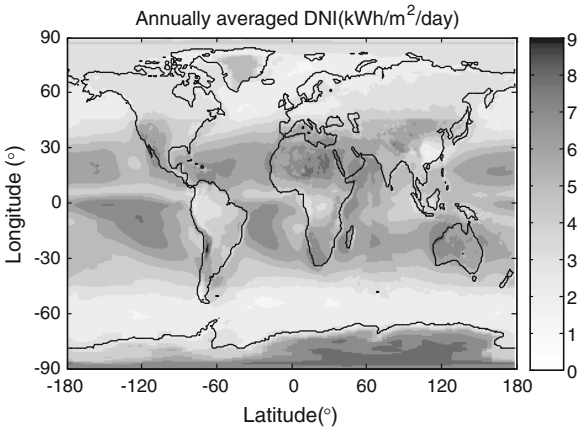

Fig. 3 Annually averaged DNI of the world

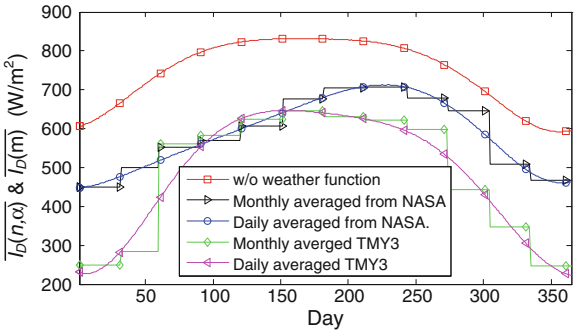

Fig. 4 Monthly and daily averaged direct normal incident radiation in a year for a location at latitude of 37° and longitude −120°

where m is the month of a year; and n_E and n_S are the end and the start days of the month, respectively. α_{max} represents the maximum α on the nth day. For the location at latitude of 37° and longitude −120°, for example, the fifth-order polynomial curve fit in the least-squares sense to the monthly averaged DNI from NASA gives

$$W(n) = 1.09 \times 10^{-12} n^5 - 9.10 \times 10^{-10} n^4 + 2.20 \times 10^{-7} n^3 \cdots - 1.04 \times 10^{-5} n^2 - 6.89 \times 10^{-4} n + 0.74 \tag{12}$$

Figure 4 also compares DNI values produce by Eqs. (9) and (10). The hourly DNI at the given location is depicted in Fig. 5. We will consider this hourly DNI data throughout the simulations.

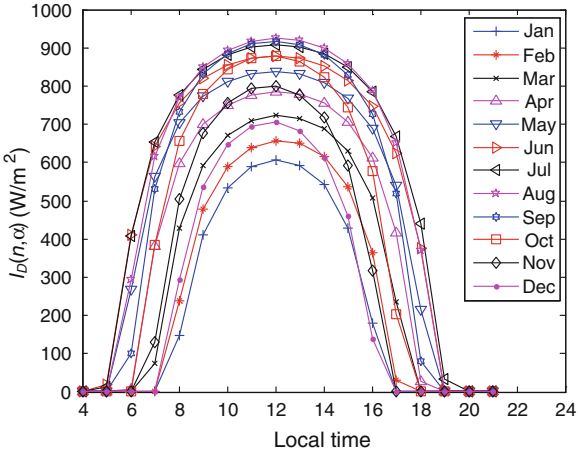

Fig. 5 Hourly direct normal incident radiation at latitude 37° and longitude −120° for the first day of each month

4 Self-shading by Dual-Axis Trackers

As discussed previously, HCPV systems with dual-axis trackers can maximize CF by tracking the Sun throughout a day. Especially in the morning and the evening, however, this tracker array poses a self-shading problem, which in turn causes power loss and thus reduces CF. To alleviate the self-shading problem, the optimal spacing between trackers should be determined [5, 7]. Figure 6 depicts a dual-axis tracker whose modules are normal to the sunlight in X–Z plane.

To obtain shaded area on the ground, we need to know the $L_0(t)$, and $L_S(t)$ at time t can be given by:

$$L_0(t) = \frac{H(t) - P}{\tan(\alpha(t))} = \frac{h/2/\cos(\alpha(t)) - P}{\tan(\alpha(t))} \tag{13}$$

$$L_S(t) = L(t) - L_0(t) = \frac{h}{\sin(\alpha(t))} - \frac{h/2/\cos(\alpha(t)) - P}{\tan(\alpha(t))} \tag{14}$$

where h is the height of the module array; P is the height of a pole; $H(t)$ is the hypotenuse of the right-angled triangle with one side formed by the half-height of the module array; and $\alpha(t)$ is the α at time t. Then, four vertices—$V_{LB}(t)$, $V_{LT}(t)$, $V_{RB}(t)$, and $V_{RT}(t)$—of the shaded area for the tracker located at (0, 0) can be obtained as

$$\begin{aligned}
V_{LB}(t) &= (-L_0(t)\cos\phi(t) - w/2 \cdot \sin\phi(t), L_0(t)\sin\phi(t) - w/2 \cdot \cos\phi(t)) \\
V_{LT}(t) &= (-L_S(t)\cos\phi(t) - w/2 \cdot \sin\phi(t), L_S(t)\sin\phi(t) - w/2 \cdot \cos\phi(t)) \\
V_{RB}(t) &= (-L_0(t)\cos\phi(t) + w/2 \cdot \sin\phi(t), L_0(t)\sin\phi(t) + w/2 \cdot \cos\phi(t)) \\
V_{RT}(t) &= (-L_S(t)\cos\phi(t) + w/2 \cdot \sin\phi(t), L_S(t)\sin\phi(t) + w/2 \cdot \cos\phi(t))
\end{aligned} \tag{15}$$

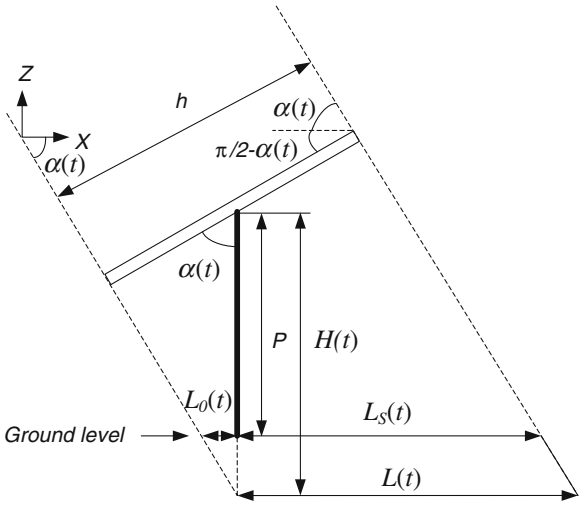

Fig. 6 Dimension of a dual-axis tracker at X–Z plane

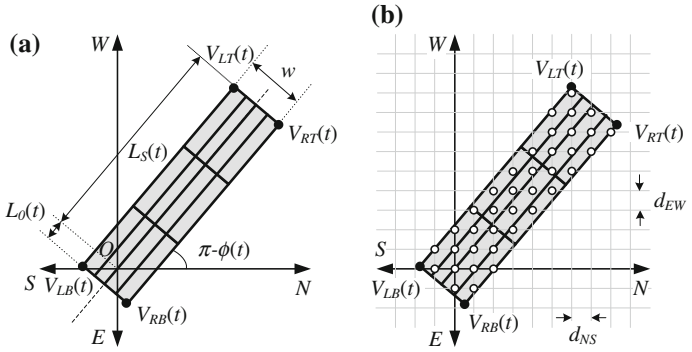

Fig. 7 Shadow by a dual-axis tracker with a 3-by-4 module array. **a** Shadow area on the ground. **b** Shadow matrix with grid

where w is the width of the module array; and $\phi(t)$ the θ as shown in Fig. 7a. When defining $V_{\mathrm{LB}}(t) = (x_{\mathrm{LB}}(t), y_{\mathrm{LB}}(t))$, $V_{\mathrm{LT}}(t) = (x_{\mathrm{LT}}(t), y_{\mathrm{LT}}(t))$, $V_{\mathrm{RB}}(t) = (x_{\mathrm{RB}}(t), y_{\mathrm{RB}}(t))$, and $V_{\mathrm{RT}}(t) = (x_{\mathrm{RT}}(t), y_{\mathrm{RT}}(t))$, four vertices of the (m, n) module in the M-by-N module array on a single tracker can be defined as

$$\begin{aligned}
V_{\mathrm{LB}}^{mn}(t) &= (x_{\mathrm{LB}}(t) + (m-1)(x_{\mathrm{LT}}(t) - x_{\mathrm{LB}}(t))/M + (n-1)(x_{\mathrm{RB}}(t) - x_{\mathrm{LB}}(t))/N, \\
&\qquad y_{\mathrm{LB}}(t) + (m-1)(y_{\mathrm{LT}}(t) - y_{\mathrm{LB}}(t))/M + (n-1)(y_{\mathrm{RB}}(t) - y_{\mathrm{LB}}(t))/N) \\
V_{\mathrm{LT}}^{mn}(t) &= \left(x_{\mathrm{LB}}^{mn}(t) + (x_{\mathrm{LT}}(t) - x_{\mathrm{LB}}(t))/M, y_{\mathrm{LB}}^{mn}(t) + (y_{\mathrm{LT}}(t) - y_{\mathrm{LB}}(t))/M\right) \\
V_{\mathrm{RB}}^{mn}(t) &= \left(x_{\mathrm{LB}}^{mn}(t) + (x_{\mathrm{RB}}(t) - x_{\mathrm{LB}}(t))/N, y_{\mathrm{LB}}^{mn}(t) + (y_{\mathrm{RB}}(t) - y_{\mathrm{LB}}(t))/N\right) \\
V_{\mathrm{RT}}^{mn}(t) &= \left(x_{\mathrm{RB}}^{mn}(t) + (x_{\mathrm{LT}}(t) - x_{\mathrm{LB}}(t))/M, y_{\mathrm{RB}}^{mn}(t) + (y_{\mathrm{LT}}(t) - y_{\mathrm{LB}}(t))/M\right)
\end{aligned} \tag{16}$$

Instead of calculating the shaded area for each tracker one by one, the shaded area can be efficiently obtained by using shadow- and Tracker-array matrixes. When letting a shadow matrix of the module array in the tracker be SM(t) with the solar north–south and the east–west grid as shown in Fig. 7b, each grid in the shaded area is assigned to a value of 1. With the same grid space, the (u, v) element of a Tracker-array matrix TA can be assigned to a value of 1 where a tracker is located at (u, v). Then the shadow matrix for the tracker array, SMA(t, u, v), can be calculated by a convolution as

$$\mathrm{SMA}(t, u, v) = \mathrm{TA}(u, v) \otimes \mathrm{SM}(t) \tag{17}$$

$$\mathrm{SMA}(t, u, v) = \sum_{p} \sum_{q} \mathrm{TA}(p, q)\mathrm{SM}(t, u - p, v - q) \tag{18}$$

where the installation site is sized by L_{EW}-by-L_{NS}; and $p = L_{EW}/d_{EW}$; and $q = L_{NS}/d_{NS}$. Then the shadow matrix for the all tracker arrays can be simplified as

$$\mathrm{SMA}(t) = \sum_{i=1}^{n_{EW}} \sum_{j=1}^{n_{NS}} \mathrm{SMA}(t, u_i, v_j) \tag{19}$$

where n_{EW} and n_{NS} are the number of tracker arrays in east–west and in north–south directions. From the shadow matrix, we can calculate the hours of shading for each grid points, $H_S(t_1, t_2)$, which describes how long each point is shaded by the tracker array for the given time from t_1 to t_2. Since the shadow matrix is discrete, we need to add time interval Δt, which leads to

$$H_S(t_1, t_2) = \Delta t \sum_{t=t_1}^{t_2} \mathrm{SMA}(t) \tag{20}$$

Figure 8a shows hours of shading by a single dual-axis tracker. The area beneath the module is most likely to be shaded, and the hours of shading are shaped like a butterfly. To identify how much a certain module in the tracker array is shaded at a given time t, SMA(t) in Eq. (19) can be rewritten as

$$\mathrm{SMA}(t) = \sum_{i=1}^{n_T} \sum_{j=1}^{n_S} \sum_{k=1}^{n_M} \mathrm{SMA}_{ijk}(t) \tag{21}$$

where n_T, n_S, and n_M are the number of trackers in the tracker array, strings in a tracker, and modules in a string, respectively. Defining $A_{ijk}(t)$ to be the shaded area on the ground by the kth module in the jth string on the ith tracker, the bar on it to be the self-shaded area on the module as shown in Fig. 8b, and the function $\sim$ to be

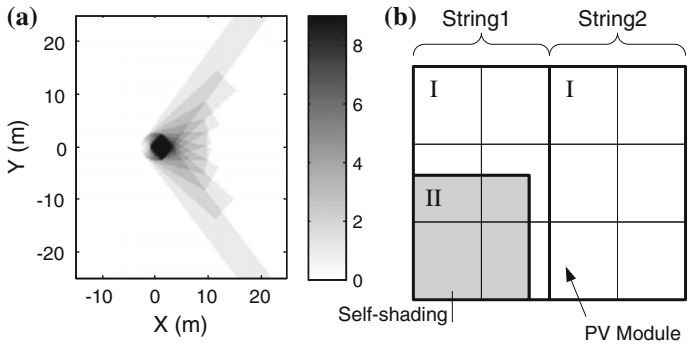

Fig. 8 **a** Hours of shading by a dual-axis tracker on January 1. **b** Example of self-shading in a 3-by-4 module array with two strings

the saturation function that makes each element be 1 if >1, then the fractions of self-shading on the module at a given time t can be obtained as

$$\begin{aligned} \mathrm{FS}_{ijk}(t) &= \overline{A_{ijk}(t)} \Big/ A_{ijk}(t) \\ &= \sum \sim \left[\mathrm{SMA}_{ijk}(t) - \sim \mathrm{SMA}_{ijk}(t)\right] \Big/ \sum \sim \mathrm{SMA}_{ijk}(t) \end{aligned} \tag{22}$$

5 Mismatch Between HCPV Modules

A PV module harvests its maximum energy when the voltage and the current are at its maximum power point $P_{\mathrm{MP}} = V_{\mathrm{MP}} \times I_{\mathrm{MP}}$. When a PV cell is shaded in a HCPV system, a bypass diode turns on and lets the string current flow with the reverse voltage across the cell. Deviations from the rated power of the individual cell or module can be caused by spectral mismatch, misalignment of optics, dirt, voltage drop on the cable, and so on. In [12], the effect of mismatch is analyzed using some worst-case scenarios. However, more generalizations is needed in planning utility-scale HCPV systems.

5.1 Power Losses Within a Module

Figure 9 shows current–voltage (I–V) and power–voltage (P–V) characteristics of a CPV module with two different tolerance values [13]. It is assumed that each parameter is normally distributed with 5 and 10 % SDs with their mean values. Each I–V curve has current steps that originated from a bypass diode connected to each cell. As tolerance increases, the voltage at the maximum power point also increases because of a decrease in the voltage drop across the internal series resistances. However, mismatches in current among cells increases accordingly and

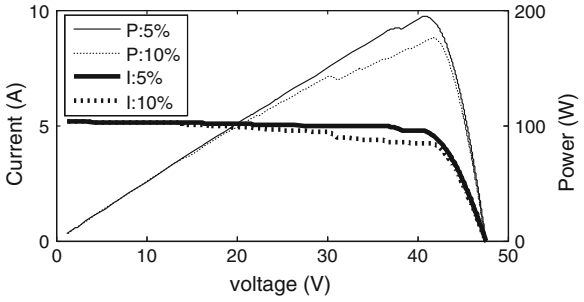

Fig. 9 I–V and P–V characteristics for a module with 5 and 10 % power tolerances

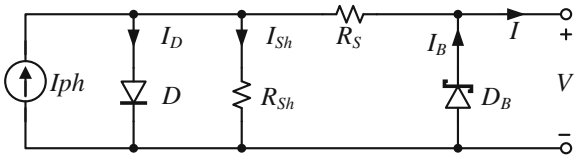

Fig. 10 Simple modeling of a PV cell

thus result in greater power loss. The mismatch losses increase from 0.9 to 6.2 % as tolerance increases from 5 to 10 %.

In HCPV system using multijunction PV cells, the high concentration of sunlight produces enough carriers to saturate the energy level of defects [14]. When the subcell generation–recombination current is neglected, a CPV cell with a bypass diode is modeled a shown in Fig. 10. The cell current I is given by

$$I = I_{\mathrm{Ph}} - I_{\mathrm{D}} - I_{\mathrm{Sh}} + I_{\mathrm{B}} \tag{23}$$

where I_{Ph}, I_{D}, I_{Sh}, and I_{B} are the PV currents that depend on irradiance and temperature, the internal diode current, the shunt current, and the bypass diode current, respectively. To understand the contribution of power losses, we instead consider five essential parameters including I_{Ph}, the diode saturation current I_{S}, the diode ideality factor n, the series resistance R_{S}, and the shunt resistance R_{Sh}. The simulation results based on these five parameters in terms of different tolerance given in Fig. 11 shows that power loss by mismatch is influenced by the order of $I_{\mathrm{Ph}} > n > R_{\mathrm{S}} \approx R_{\mathrm{Sh}} > I_{\mathrm{S}}$. Mismatch effects in the PV current are greater than others by more than several orders of magnitude regardless of the tolerance values.

5.2 Power Losses by Misalignments

Because the most dominant factor that causes power loss in HCPV systems is the mismatch in the PV current, HCPV system with a very narrow acceptance angle require highly accurate alignment control at the time of installation. Intramodule alignment can be accurately controlled in the factory. However, maintaining high

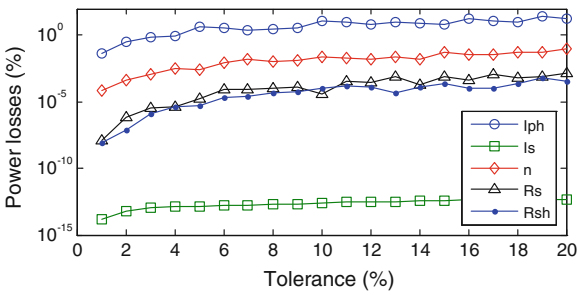

Fig. 11 Power losses in a CPV module by mismatches in various parameters

Fig. 12 *Bottom-right* view of misaligned HCPV modules

quality control during the time of installation is very difficult as can be seen from Fig. 12 [13]. Figure 13 shows a SolFocus prototype concentrator and its simulated optical efficiency $E(\theta_{C,i})$ according to the incident angle θ_C of the ith concentrator, which leads to the photocurrent of the ith cell as

$$I_{Ph,i} = I_{Ph0} \times E(\theta_{C,i}) \tag{24}$$

To account for module-to-module misalignments Eq. (24) can be redefined as

$$I_{Ph,i} = I_{Ph0} \times E(\theta_{C,i} + \theta_{M,j}) \tag{25}$$

where $\theta_{M,j}$ represents the angular misalignment of the jth module. Figure 14 shows the simulation results for power losses in 12 HCPV modules composed of 16 concentrators and all connected in series where σ_M is the SD of module-to-module alignment. Although the SD of $\theta_{C,j}$ is only $\sigma_C = 0.2°$, the module misalignment can easily be a dominant component by which to determine the power loss. By using an

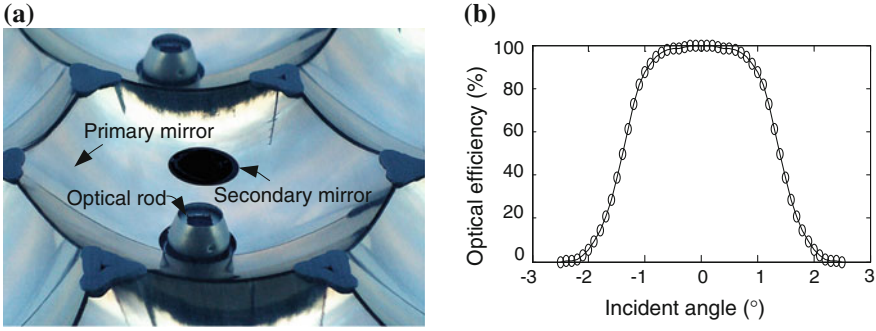

Fig. 13 SolFocus prototype HCPV concentrator. **a** Components. **b** Optical efficiency of the concentrator according to the incident angle

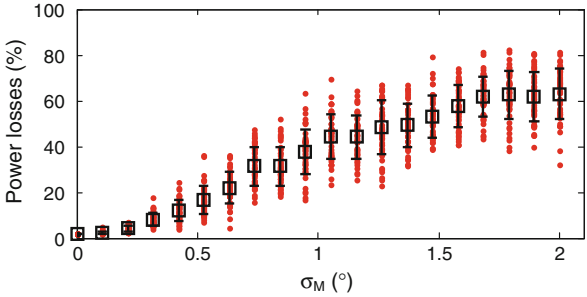

Fig. 14 Power losses by misalignment between modules (σ_C = 0.2°)

I–V curve as shown in Fig. 9, $V_{MP,ijk}$ and $I_{MP,ijk}$ can be obtained in term of voltage and current deviations, $\varepsilon_{V,ijk}$ and $\varepsilon_{I,ijk}$, as

$$V_{MP,ijk} = V_{MP}(1 + \varepsilon_{V,ijk}) \tag{26}$$

$$I_{MP,ijk} = I_{MP}(1 + \varepsilon_{I,ijk}) \tag{27}$$

6 Power-Optimization Strategies

As depicted in Fig. 15, various power-optimization strategies can be realized for HCPV systems [5, 13, 15]. Currently, centralized and string PV systems are mostly popular for utility-scale applications. However, considering mismatch and partial-shading losses, other types of distributed systems can be good candidates as

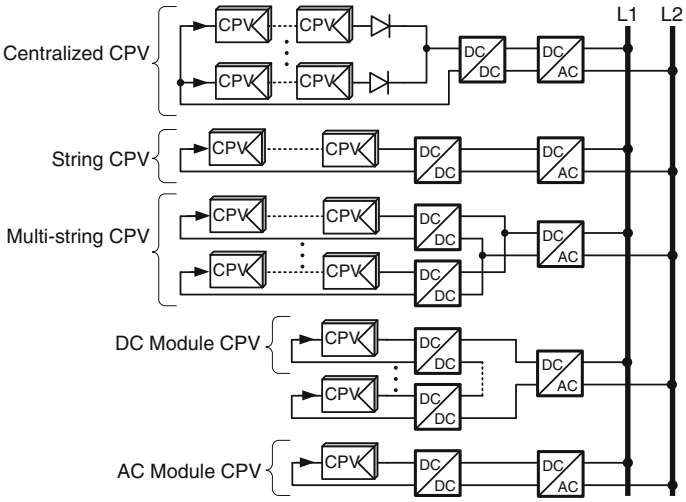

Fig. 15 Various power-optimization strategies of grid-tied HCPV systems

technology develops. Thus, quantifying the efficiencies of various strategies and choosing the optimum system are critical in lowering LCOE. In this section, various power-optimization strategies are investigated.

6.1 Centralized CPV System

Multiple string are connected in parallel followed by a single maximum power point tracker (MPPT) and an inverter, which makes each string voltage set the same. Let a CPV module have n_{BD} bypass diodes, and Eq. (22) be quantized by n_{BD} to consider mismatch and partial shading, then the DC power $P_{\mathrm{MP}}(t)$ based on each string can be obtained as

$$\mathrm{FS}_{ijk}(t) = \left\lceil n_{\mathrm{BD}}\mathrm{FS}_{ijk}(t)\right\rceil / n_{\mathrm{BD}} \tag{28}$$

$$V_{\mathrm{MP},ij}(t) = V_{\mathrm{MP}}\sum_{k=1}^{n_{\mathrm{M}}}\left[(1+\varepsilon_{\mathrm{V},ijk})(1-\mathrm{FS}_{ijk}(t)) - n_{\mathrm{BD}}V_{\mathrm{BD}}\mathrm{FS}_{ijk}(t)\right] \tag{29}$$

$$I_{\mathrm{MP},ij}(t) = \left\{\min(I_{\mathrm{MP},ijk}(t))\middle| k \in N, k \le n_{\mathrm{M}},\ \ \forall k : I_{\mathrm{MP},ijk}(t) \ge 0\right\} \tag{30}$$

$$P_{\mathrm{MP}}(t) = \left\{\sum_{i=1}^{n_{\mathrm{T}}}\max(V_{\mathrm{MP},ij}(t)\cdot\sum_{j=1}^{n_{\mathrm{S}}}I_{\mathrm{MP},ij}(t))\middle|\ j \in N, j \le n_{\mathrm{S}}\right\} \tag{31}$$

where $\mathrm{FS}_{ijk}(t)$ stands for the quantized shaded area using ceiling function to calculate the number of bypass diodes needed to be turned on. $V_{\mathrm{MP},ij}(t)$ and $I_{\mathrm{MP},ij}(t)$ are the maximum power point voltage and current of the jth string located in the ith tracker. Note that the efficiency of each DC/DC converter is reflected to the MPP voltage and current. The string current is assumed to be linearly proportional to the direct normal incident radiation I_{D} in Eq. (10) in terms of time.

6.2 String CPV System

Each string is connected to its own DC/DC converter and inverter for an individual MPPT, which makes each string independent of each other. A string CPV system offers a high DC string voltage range. Equation (28) through Eq. (31) are unchanged, and the DC power $P_{\mathrm{MP}}(t)$ based for each string can be obtained as

$$P_{\mathrm{MP}}(t) = \sum_{i=1}^{n_{\mathrm{T}}}\sum_{j=1}^{n_{\mathrm{S}}}V_{\mathrm{MP},ij}(t)\cdot I_{\mathrm{MP},ij}(t) \tag{32}$$

6.3 Multistring CPV System

The advantage of string CPV system is maximizing the string power independently. However, each string requires its own inverter, which requires additional cost. A multistring PV system takes advantage of having a central inverter per each tracker and optimizing power of each string independently. The basic condition is that each string voltage after DC/DC converters is uniform within a tracker. The DC power $P_{\mathrm{MP}}(t)$ based for multistring PV system can be obtained as

$$P_{\mathrm{MP}}(t) = \left\{ \sum_{i=1}^{n_{\mathrm{T}}} \sum_{j=1}^{n_{\mathrm{S}}} V_{\mathrm{MP},ij}(t) \cdot I_{\mathrm{MP},ij}(t) \middle| \; j_1 \neq j_2, \forall i : V_{\mathrm{MP},ij_1}(t) = V_{\mathrm{MP},ij_2}(t) \right\} \quad (33)$$

6.4 DC Module CPV System

In a DC module CPV system, each CPV module is connected to its own DC/DC converter that is in series with other DC/DC converters followed by an inverter. The main advantage of this scheme is maximizing energy harvest in each CPV module. The output voltage of each DC/DC converter is independently controlled, but the string current is uniform within a tracker. The DC power $P_{\mathrm{MP}}(t)$ based for a DC module PV system can be obtained as

$$V_{\mathrm{MP},ijk}(t) = V_{\mathrm{MP}}\left[(1 + \varepsilon_{\mathrm{V},ijk})(1 - \mathrm{FS}_{ijk}(t)) - n_{\mathrm{BD}} V_{\mathrm{BD}} \mathrm{FS}_{ijk}(t)\right] \quad (34)$$

$$I_{\mathrm{MP},ij}(t) = \left\{ I_{\mathrm{MP},ijk}(t) \middle| \; k_1 \neq k_2, \forall i,j : I_{\mathrm{MP},ijk_1}(t) = I_{\mathrm{MP},ijk_2}(t) \right\} \quad (35)$$

$$P_{\mathrm{MP}}(t) = \sum_{i=1}^{n_{\mathrm{T}}} \sum_{j=1}^{n_{\mathrm{S}}} \sum_{k=1}^{n_{\mathrm{M}}} V_{\mathrm{MP},ijk}(t) \cdot I_{\mathrm{MP},ij}(t) \quad (36)$$

6.5 AC Module CPV System (Microinverter CPV System)

Unlike other configurations, an AC module CPV system makes each CPV module completely independent from another one, which enhances power generation under self-shading and mismatch conditions. However, increased components may reduce the rated power under normal operation, and the higher cost for making electronics is a big hurdle for it to be applied for utility-scale CPV systems. $V_{\mathrm{MP},ijk}(t)$ is

identical to Eq. (34). The module current $I_{\mathrm{MP},ijk}(t)$ and the DC power $P_{\mathrm{MP}}(t)$ based for an AC module PV system can be obtained as

$$P_{\mathrm{MP}}(t) = \sum_{i=1}^{n_{\mathrm{T}}} \sum_{j=1}^{n_{\mathrm{S}}} \sum_{k=1}^{n_{\mathrm{M}}} V_{\mathrm{MP},ijk}(t) \cdot I_{\mathrm{MP},ijk}(t) \tag{37}$$

6.6 Centralized CPV System Without an MPPT

For the initial investment in a centralized CPV system to be lowered, which may not lead to lower LCOE, MPPT capability can be omitted and strings connected in parallel followed by a central inverter. In this case, the DC output voltage of a string is forced to a fixed ratio of its open-circuit voltage V_{OC} (e.g., 87 %). Because the partial-shading and mismatch losses are significant, this configuration is not recommended for utility-scale CPV systems. Basic equations for this configurations to calculate the total power harvested are as follows

$$V_{ij}(t) = 0.87 \cdot V_{\mathrm{OC},ij} \tag{38}$$

$$I_{ij}(t) = \left\{ I_{ijk}(t) \middle| \; k_1 \neq k_2, \; \forall i,j : \; I_{ijk_1}(t) = I_{ijk_2}(t) \right\} \tag{39}$$

$$P(t) = \sum_{i=1}^{n_{\mathrm{T}}} \sum_{j=1}^{n_{\mathrm{S}}} V_{ij}(t) \cdot I_{ij}(t) \tag{40}$$

7 Partial Shading Loss in Power-Optimization Schemes

Figure 16 illustrates the partial-shading effect in various power-optimization schemes. The 3-by-4 CPV modules on a dual-axis tracker are simulated for two different scenarios, in which the shades move (1) from bottom to top and (2) from left to right. For both cases, the power harvested by CPV modules within a single tracker is strong function of the amount and the shape of shading. The more the shading, in general, the less is the power harvested [16–18]. Distributed CPV systems using DC and/or AC modules are superior to others operating under these shading conditions, but the increased cost for electronics may cause increases in LCOE. For fair comparison, further careful analysis regarding the cost of electronics must be performed, which is out of scope for this section.

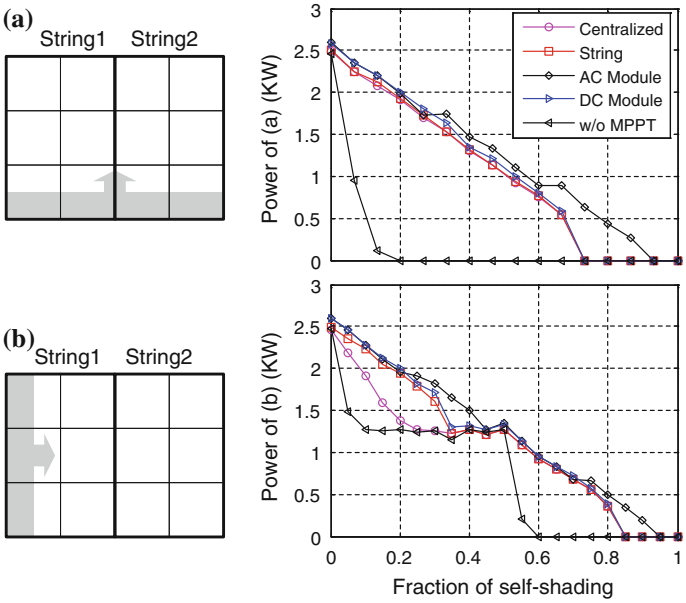

Fig. 16 Various power-optimization strategies of grid-tied HCPV systems

8 Tracker Array Model

The estimation of the total power harvested by a system requires accurate analysis of the geometrical configuration of both a tracker array and each module, especially for analyzing self-shading losses. Thus, all of the system parameters are extracted from the SolFocus prototype HCPV system in Fig. 17. Because most HCPV systems are built with a tracker array, GCR and CF in Eqs. (1) and (2), respectively,

Fig. 17 SolFocus prototype HCPV system used for extracting tracker and module parameters

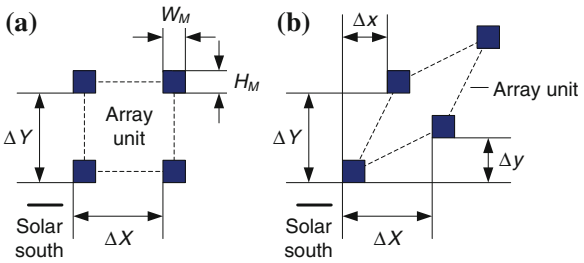

Fig. 18 Two types of tracker array units. **a** Rectangular array. **b** Quadrangular array

depend strongly on these geometries and can be redefined with an array unit as shown in Fig. 18.

$$\mathrm{GCR} = \sum A_{\mathrm{module}}/A_{\mathrm{land}} = W_{\mathrm{M}}H_{\mathrm{M}}/(\Delta X \Delta Y) \tag{41}$$

$$\mathrm{CF} = \frac{\sum_1^{365}\sum_1^{24} P(d,t)}{365 \cdot 24 \cdot P_{\max}} \tag{42}$$

where W_{M} and H_{M} are the width and the height of modules in a tracker, respectively, and $P(d, t)$ calculates total power harvested throughout a year on an hourly basis. Figure 19 shows shading by a 3-by-3 tracker array, located at the previously mentioned site, on January 1 at 8 AM. The darker color represents the overlapped shading area by multiple trackers. The more the space in between trackers, the less the self-shading happens.

When calculating the shadow matrix for the *m*-by-*n* tracker array as defined in Eqs. (19) and (21), the computational time is a linear function of the number of trackers. Especially for utility-scale simulations to optimize land use, this method might be too time-consuming. The algorithm in [7] makes the computation time

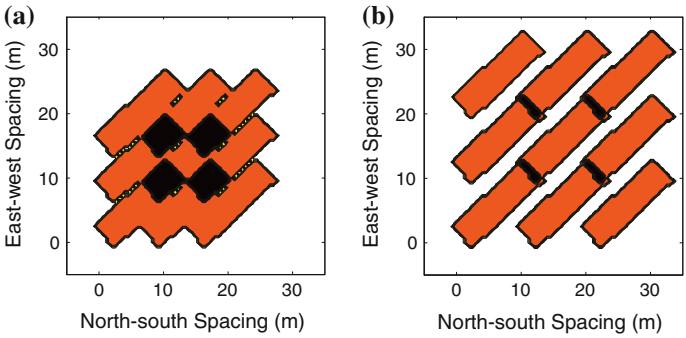

Fig. 19 Top view of shading by a 3-by-3 tracker array on January 1 at 8 AM **a** with 7-m spacing and **b** with 10-m spacing

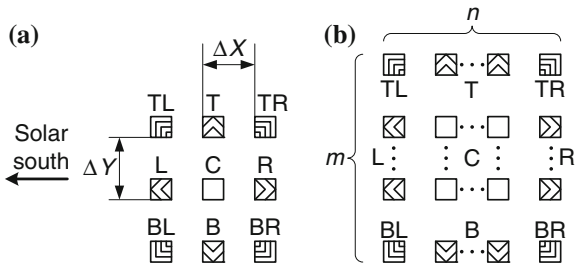

Fig. 20 Top view of a tracker array with CPV modules flat to the ground. **a** 3-by-3 tracker array. **b** *m*-by-*n* tracker array

independent of the scale of an HCPV system. Letting SMA(t) be a shadow matrix of a 3-by-3 tracker array at time t, SMA(t) can be separated into nine sections: (1) top left (TL), top, top right (TR), left, center, right, bottom left (BL), bottom, and bottom right (BR) as depicted in Fig. 20a. For calculating SMA(t) for the *m*-by-*n* tracker array, the array can also be divided into nine sections: $1 \times$ TL, $(n-2) \times$ T, $1 \times$ TR, $(m-2) \times$ L, $(m-2) \times (n-2) \times$ C, $(m-2) \times$ R, $1 \times$ BL, $(n-2) \times$ B, and $1 \times$ BR. Note that the most of trackers in *m*-by-*n* tracker array will be shaded, as with the center tracker in 3-by-3 tracker array, as the number of trackers increases.

9 Simulation Results

For comparison, we will consider two different simulations: simulation I for maximizing CF according to given GCR and simulation II for minimizing the cost function in Eq. (5) by varying the east–west and the north–south spacing. The procedure for each simulation I is as follows:

- Simulation I
  1. Gather monthly averaged DNI data for the site (only DNI is required for HCPV systems).
  2. Calculate hourly DNI from the monthly averaged DNI data.
  3. Find the *m*-by-*n* tracker array with a given GCR that maximizes CF by using the shadow matrix.
  4. Calculate the optimal CF according to GCR.
  5. Repeat steps 3 and 4 for various power-optimization schemes.

Figure 21 shows DC energy harvested by an *m*-by-*m* tracker array based on the simulation I where ΔX, ΔY, Δx, and Δy are set to 10, 10, 0, and 0 m, respectively. The modeling can be applied to any type of tracker and module array. It can be seen that the lager tracker array gives more self-shading energy loss, especially in the

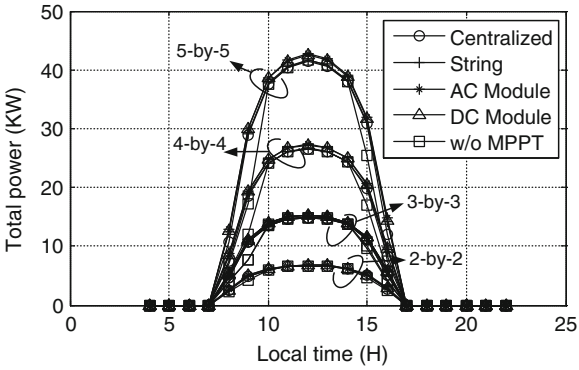

Fig. 21 DC energy harvested by an *m*-by-*m* tracker array on January 1 where GCR = 0.2 and 3-by-4 modules are on each tracker

morning and the evening. DC module–based and AC module–based CPV systems alleviate mismatch losses among CPV modules; thus, they harvest more energy than other types of power-optimization scheme even at solar noon without self-shading. In a centralized PV system, a shaded string may affect the performance of the unshaded strings resulting in equal or lower power harvest than other types.

Each power-optimization scheme for the 4-by-4 module array is compared in Fig. 22. Orientation of the tracker array is set to the mean value of solar noon to minimize the maximum shadow length by each tracker. For fast simulation, hourly DNI on the first day of each month is considered. Tracker array and sampling days can be larger at the expense of longer computational time. The CF-versus-GCR plot shows the optimum spacing of the tracker array. As GCR increases, the optimum CF decreases due to aggravated self-shading losses. However, in Fig. 22, the values of GCR and CF for minimizing LCOE cannot be obtained. Thus, we needs to obtain the cost function as follows:

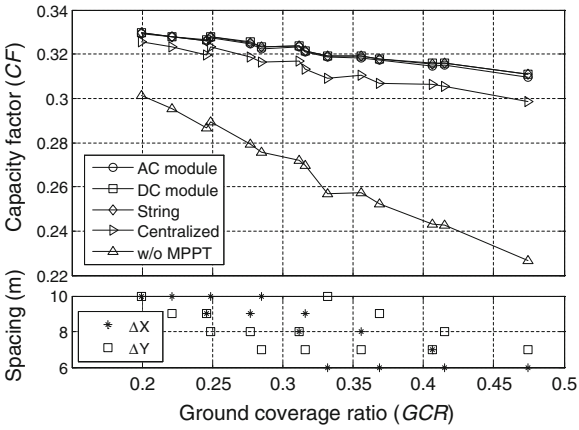

Fig. 22 Capacity factor for various ground coverage ratios of a 4-by-4 tracker array. Optimum spacing among dual-axis trackers is given for each point

- Simulation II

1. Perform steps 1 and 2 from the simulation I.
2. Obtain the value of k in the cost function.
3. Find the 3-by-3 shadow matrix and calculate the overall power and the cost function.
4. Based on the step 3, calculate the overall power that minimizes the cost function of the m-by-n tracker.
5. Repeat steps 3 and 4 for various power-optimization schemes.

Figure 23 depicts hours of shading by a 3-by-3 tracker array. The simulation only includes time with $\alpha < 0$. As with simulation I, the first day of each month is sampled for reducing the computational time. The darker the color at the particular points, the more the hours of shading occur. It can be seen that more shading occurs in the east–west direction than that in the north–south direction, which indicates that greater spacing is required for the east–west direction.

The most narrow tracker spacing that minimizes the cost function according to the value of k is shown in Fig. 24 based on DNI from NASA. To investigate the dependency of tracker size, both 3-by-3 and m-by-n arrays (where $m = n = 20$) are simulated and compared. Trackers located on the boundary of the 3-by-3 array are affected less by shading than the tracker in the center. However, the portion of trackers located on the boundary of the m-by-n array is smaller than that of the 3-by-3 array, resulting in more self-shading losses. Therefore, larger spacing is required for m-by-n array. The range of spacing is limited to $7 \leq \Delta X \leq 11$ and $7 \leq \Delta Y \leq 12$ for reducing the run time. DNI data from TMY3 are applied to the same analysis as depicted in Fig. 25. The values of ΔX are equal or less than those from Fig. 24 mainly due to lower DNI in winter TMY3 data. The optimization is weighted more to performance in the summer. Finally, the run time to obtain data for Fig. 22 is linear to the number of trackers; however, the run time to obtain Figs. 24 and 25 takes 13 min with a 2.2-GHz dual-core processor regardless of the number of trackers.

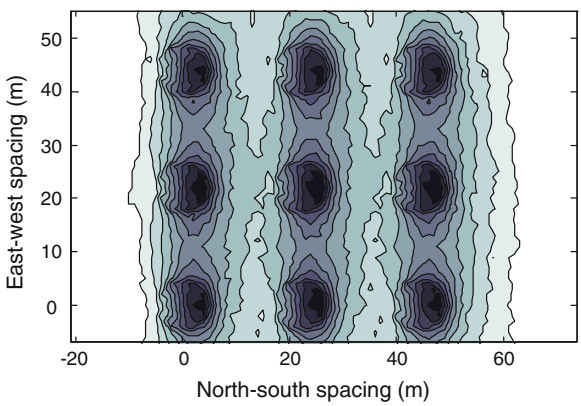

Fig. 23 Hours of shading by a 3-by-3 tracker array with both east–west and north–south spacing of 11 m

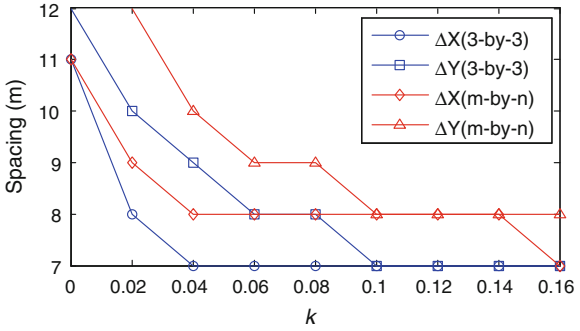

Fig. 24 Most narrow tracker spacing that minimizes the cost function with DNI data from NASA

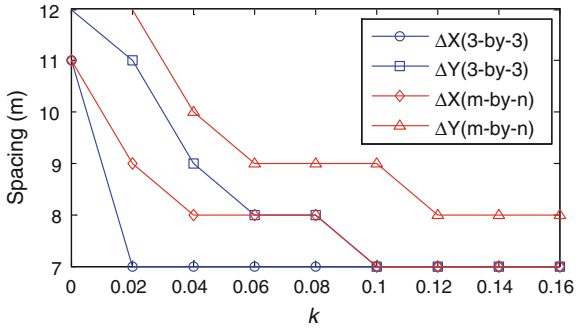

Fig. 25 Most narrow tracker spacing that minimizes the cost function with DNI data from TMY3

10 Conclusion

This chapter presents a comprehensive model of HCPV systems including location-dependent DNI, various configurations of tracker and module arrays, mismatch and misalignment, and power-optimizing schemes. This model can be widely used by the solar industry to estimate how much energy can be generated with given system parameters and to maximize energy harvest of the system. Moreover, the cost function that considers CF, GCR, and the relative cost of land minimizes the LCOE cost of energy by optimizing the space among dual-axis trackers. For fast simulation, the performance of a 3-by-3 tracker array is matched to an *m*-by-*n* tracker array resulting in a constant run time regardless of the number of trackers.

Acknowledgments This work was supported by the Human Resources Development program (Grant No. 20124030200120) of the Korea Institute of Energy Technology Evaluation and Planning grant funded by the Korea government Ministry of Trade, Industry and Energy. This research was also supported by Basic Science Research Program through the National Research Foundation of Korea (NRF) funded by the Ministry of Science, ICT and Future Planning (Grant No. NRF-2014R1A1A1003771).

References

1. Roy S (2006) optimal planning for utility generation by photovoltaic sources spread across multiple sites. IEEE Trans Energy Conv 21:181–186
2. Carrasco JM, Franquelo LG, Bialasiewicz JT, Galvan E, Guisado RCP, Prats MAM, Leon JI, Moreno-Alfonso N (2006) Power-electronic systems for the grid integration of renewable energy sources: A survey. IEEE Trans. Ind. Electron. 53:1002–1016
3. Campbell M, Blunden J, Smeloff E, Aschenbrenner P (2009) Minimizing utility-scale PV power plant LCOE through the use of high capacity factor configurations. In: Proceedings of photovoltaic specialists conference, June 2009, pp 421–426
4. Narvarte L, Lorenzo E (2008) Tracking and ground cover ratio. Prog Photovoltaics Res Appl 16(8):703–714
5. Kim YS, Kang SM, Winston R (2013) Modeling of a concentrating photovoltaic system for optimum land use. Prog Photovoltaics Res Appl 21(2):240–249
6. Panico D, Garvison P, Wenger H, Shugar D (1991) Backtracking: a novel strategy for tracking PV systems. In: Proceedings of photovoltaic specialists conference, Oct 1991, pp 668–673
7. Kim YS, Winston R (2011) Optimal spacing of dual-axis trackers for concentrating photovoltaic systems. In: 7th international conference on concentrating photovoltaic systems: CPV-7, Apr 2011, pp 370–373
8. Walraven R (1978) Calculating the position of the sun. Sol Energy 20:393–397
9. Duffie JA, Beckman WA (2013) Solar engineering of thermal process. Wiley, New York
10. Kasten F, Young AT (1989) Revised optical air mass tables and approximation formula. Appl Opt 28:4735–4738
11. Meinel AB (1976) Applied solar energy: an introduction. In: Addison-Wesley series in physics
12. Spertino F, Akilimali JS (2009) Are manufacturing mismatch and reverse currents key factors in large photovoltaic arrays? IEEE Trans Ind Electron 56:4520–4531
13. Kim YS, Kang SM, Winston R (2014) Tracking control of high concentration photovoltaic systems for minimizing power losses. Prog Photovoltaics Res Appl 22(9):1001–1009
14. Minuto A, Timò G, Groppelli P, Sturm M (2010) Concentrating photovoltaic multijunction (CPVM) module electrical layout optimisation by a new theoretical and experimental "mismatch" analysis including series resistance effects. In: Proceedings of photovoltaic specialists conference, June 2010, pp 3081–3086
15. Kim YS, Winston R (2014) Power conversion in concentrating photovoltaic systems: central, string, and micro-inverters. Prog Photovoltaics Res Appl 22(9):984–992
16. Patel H, Agarwal V (2008) Maximum power point tracking scheme for PV systems operating under partially shaded conditions. IEEE Trans Ind Electron 55:1689–1698
17. Gao L, Dougal RA, Liu S (2009) Parallel-connected solar PV system to address partial and rapidly fluctuating shadow conditions. IEEE Trans Ind Electron 56:1548–1556
18. Carannante G, Fraddanno C, Pagano M, Piegari L (2009) Experimental performance of MPPT algorithm for photovoltaic sources subject to inhomogeneous insolation. IEEE Trans Ind Electron 56:4374–4380

Shading in High-Concentrator Photovoltaic Power Plants

P. Rodrigo, S. Gutiérrez and L.A. Guerrero

Abstract The electrical behavior of high concentrator photovoltaic power plants is affected by self-shading between solar trackers. Partial shading of the concentrator modules on a tracker causes complex effects in the output I–V characteristics. Shadows affect the behavior of the basic component of a concentrator photovoltaic generator, the solar receiver integrated with primary optics, and the electrical connection of receivers with different behavior distortions the system output. In this chapter, measurements of concentrator receivers integrated with partially shaded primary optics are analyzed to understand their electrical behavior and a methodology for characterizing the I–V curve of shaded high concentrator photovoltaic generators under given environmental conditions is described and compared with experimental data. This methodology can be used for carrying out different studies on shading in high concentrator photovoltaic power plants. For instance, time domain simulations that calculate the I–V characteristic curve of a concentrator photovoltaic generator at small time steps can be implemented. These simulations can be used for calculating shading energy losses in grid-connected high concentrator photovoltaic systems or for analyzing important aspects in the design of these plants, such as optimum trackers allocation or inverters configuration. The problem of optimizing trackers allocation is also approached in this chapter with a simplified method based on balancing irradiation losses with energy losses in wires and costs of the land.

1 Introduction

In high concentrator photovoltaic (HCPV) power plants composed of two-axis solar trackers, there are daily shading conditions. These shadows cannot be avoided because the distance between trackers cannot be too large due to wiring and

P. Rodrigo (✉) · S. Gutiérrez · L.A. Guerrero
Panamericana University, Aguascalientes, Mexico
e-mail: prodrigo@up.edu.mx

P. Pérez-Higueras and E.F. Fernández (eds.), *High Concentrator Photovoltaics*,
Green Energy and Technology, DOI 10.1007/978-3-319-15039-0_7

land-use requirements. Moreover, back-tracking techniques [1] cannot be used in these kinds of plants as they are in conventional flat-plate photovoltaic tracking systems because HCPV modules must be always pointing to the sun. These shadows cause distortions in the electrical behavior of the system. The coexistence of different I–V characteristics in the components of a photovoltaic generator originates a deformation of the generator I–V curve and mismatch power losses when connecting the generator to the grid [2].

Mismatch power losses due to shading are not negligible in HCPV generators or in HCPV modules. Figure 1 shows an experimental example of the nonlinear behavior of shading power losses in HCPV modules connected to an inverter with maximum power point tracking. Two HCPV modules were measured by reproducing different shading conditions on the primary lenses. The *x*-axis represents the module shading factor for each measurement (the quotient between the shaded area and the total area of the module primary lenses) whereas the *y*-axis represents the corresponding shading power losses factor (the quotient between the losses in the generated power and the theoretical power that would be generated in absence of shadows). The straight line represents a hypothetical linear behavior (power losses proportional to irradiance losses). As can be seen in the graph, power losses do not follow the linear approximation: they are always greater than irradiance losses and show a highly nonlinear behavior. This behavior, observed in the HCPV modules, also happens in shaded HCPV generators.

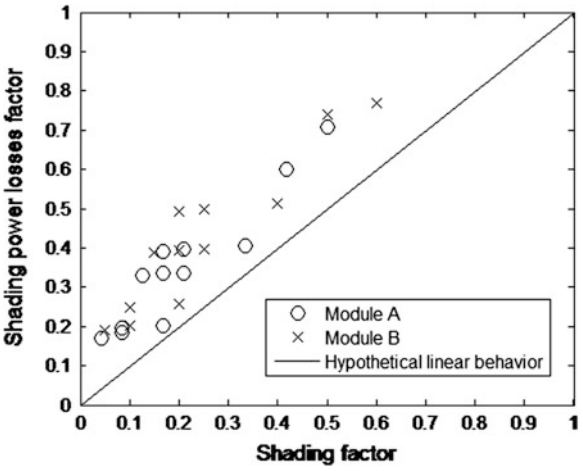

Fig. 1 Shading power losses factor versus shading factor for different measurements on two HCPV modules under shading conditions. Module A was composed of 6 series-connected 1.15 cm^2-sized GaInP/GaInAs/Ge solar cells with one PMMA squared flat Fresnel lens per cell and 500× concentration factor. Module B was composed of 5 series-connected 0.92 cm^2-sized GaInP/GaInAs/Ge solar cells with one PMMA squared flat Fresnel lens per cell and 625× concentration factor. Partial shading on the modules was reproduced by placing opaque cards on the lenses surfaces

Nowadays, there is a wide knowledge on the electrical effects of shading on conventional flat-plate photovoltaic generators [3]. There are models that characterize the electrical parameters of flat-plate solar cells under shading [4–6]. These models in combination with standard one-diode or two-diodes solar cell equivalent circuits allow reproducing the I–V curve of a shaded conventional solar cell. Once the cell I–V curve has been obtained, numerical simulations of solar cells and bypass diodes interconnection circuits can be performed. This has been performed both at the module level [7–12] and at the generator level [13–17].

There are also several studies on shading oriented to HCPV technology [18–21]. In [18], a model for shading energy losses calculation in HCPV plants was introduced with emphasis on finding the optimum trackers allocation in a given land. In [19], two practical methods were proposed for optimizing trackers allocation in small size HCPV systems. In [20], a shading energy losses model was developed which allowed analyzing different inverters configuration to maximize energy harvest in HCPV plants. In [21], the electrical behavior of the basic component of an HCPV generator, the solar receiver integrated with a partially shaded primary optics [22], was investigated. However, these studies do not characterize the complete I–V curve of a shaded HCPV generator, what can help in understanding the electrical effects due to shading and in developing new applications.

The chapter is structured as follows: Sect. 2 gives an overview of the effects of partial shading on the I–V curve of an HCPV module and generator. Section 3 presents an experimental analysis of HCPV receivers operating with partial shading on the primary optics. Section 4 describes a methodology for characterizing the I–V curve of a shaded HCPV generator and compares simulated to experimental behavior. Section 5 calculates monthly and annual shading energy losses in a hypothetical HCPV power plant to be located at Marrakech, Morocco, by applying the proposed methodology, using geometric formulae that determine self-shading between solar trackers and performing time domain simulation of the generator I–V curve. Section 6 introduces a simplified method for determining optimal distances between trackers based on balancing irradiation losses with energy losses in wires and costs of the land and applies the method taking into account typical meteorological data of Aguascalientes, México. Section 7 presents the conclusions of the chapter and Sect. 8 gives future directions in this research line.

2 Effects of Partial Shading on the I–V Curve of an HCPV Module and Generator

In this section, an overview of the electrical behavior of partially shaded HCPV modules and generators from the point of view of their characteristic I–V curve is performed. The study is organized in three sections: Sect. 2.1 explains the operation of solar cells as energy sinks and the effects of bypass diodes; Sect. 2.2 shows how

the I–V curve of an HCPV module can be obtained from the I–V curves of its individual receivers; finally, Sect. 2.3 presents the characteristics of the I–V curve of a shaded HCPV generator.

2.1 Operation of Solar Cells as Energy Sinks and Use of Bypass Diodes

Both, conventional flat-plate solar cells and multijunction solar cells present an I–V curve with similar shape. Figure 2 qualitatively shows the shape of a solar cell I–V curve extended to three quadrants. As can be seen, a solar cell can operate as energy source (first quadrant) or as energy sink (second and fourth quadrants). In the first quadrant, both voltage and current are positive; however, in the second quadrant, voltage is negative and, in the fourth quadrant, current is negative, resulting a negative power, i.e., cell operating as energy sink.

The operation of solar cells as energy sinks is not wanted in photovoltaic systems but can happen in specific conditions such as shading. Indeed, let's consider a string of series-connected solar cells; when one of the cells is shaded, the unshaded cells will force the shaded cell to pass a higher current than its short-circuit current. The only way for the shaded cell to do this is by operating at the second quadrant as energy sink [23].

The operation at the second or fourth quadrants implies cell overheating and if this situation remains a long time, the cell can damage [24]. Because of this, photovoltaic modules incorporate bypass diodes. In HCPV modules, the typical configuration of bypass diodes is one parallel-connected diode per cell mounted in the same solar receiver [21].

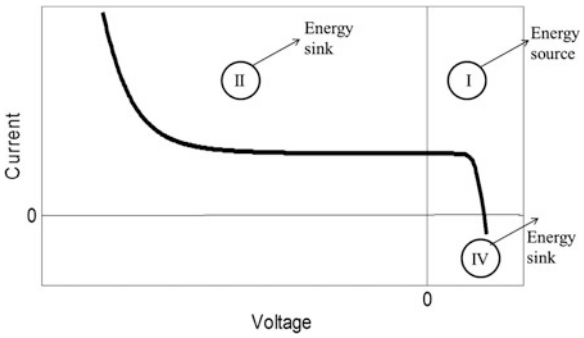

Fig. 2 Qualitative shape of a solar cell I–V curve extended to three quadrants. Standard solar cell one-diode equivalent circuit with a term representing breakdown at the second quadrant was used for the simulation and approximate parameters values of a lattice-matched GaInP/GaInAs/Ge solar cell under 500 suns were chosen

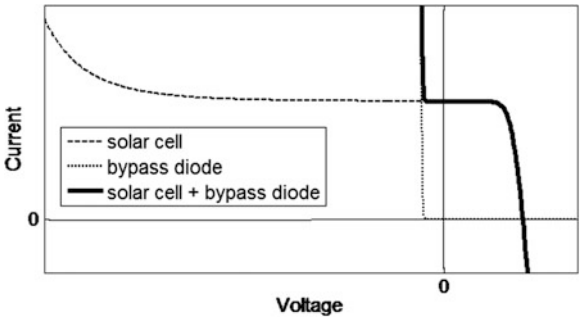

Fig. 3 I–V curve of a solar receiver obtained by the parallel association of a multijunction solar cell and a bypass diode (qualitative simulation). The solar cell curve was reproduced by means of a standard one-diode equivalent circuit with a term representing breakdown at the second quadrant and choosing approximate parameters values of a lattice-matched GaInP/GaInAs/Ge solar cell under 500 suns. The bypass diode curve was reproduced by means of Shockley's diode equation by adjusting the diode threshold voltage to 30 % the solar cell open-circuit voltage. The *bolded curve* was obtained from Kirchhoff's law for the parrallel-connection of two electrical elements

Figure 3 qualitatively shows the effect of adding a bypass diode in parallel with a solar cell. The figure plots the simulated I–V curve of an illuminated multijunction solar cell, the I–V curve of a bypass diode and the I–V curve of a solar receiver obtained by the parallel association of the solar cell and the diode curves. As can be seen, the receiver I–V curve only enters the second quadrant in a negative voltage approximately equal to the diode threshold voltage. Because this voltage is small, the operation of the solar cell with high reverse voltage is avoided due to the activation of the diode. This means that overheating is also avoided.

2.2 I–V Curve of a Partially Shaded HCPV Module

From the electrical point of view, a typical HCPV module is a string of series-connected solar receivers, each solar receiver composed of a solar cell and a bypass diode, Fig. 4 [25, 26]. When this kind of device is partially shaded, different receivers will have different I–V curves as a function of the amount of shading on the different primary optical elements.

When the primary optical element of a solar receiver is partially shaded, the main electrical effect is that the receiver I–V curve moves down on the current axis. Figure 5 shows this behavior from a qualitative point of view. Shading the primary optics has a similar effect than decreasing the incident irradiance, so that the main change in the I–V curve is a decrease of the short-circuit current.

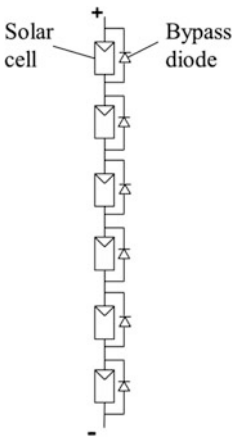

Fig. 4 Electrical configuration of an HCPV module composed of six series-connected solar receivers, with one solar cell and one bypass diode per receiver

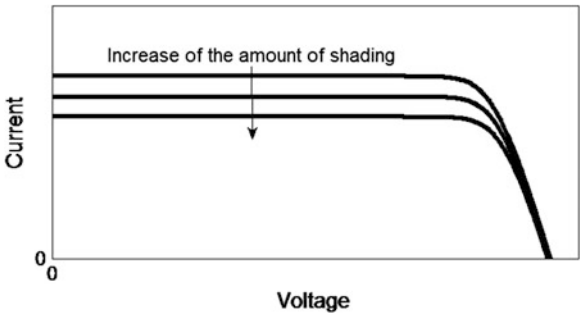

Fig. 5 Change in the I–V curve of a solar receiver when the amount of shading on the primary optics increases (qualitative simulation). Approximate parameters values of a lattice-matched GaInP/GaInAs/Ge solar cell under 500 suns were used for the *upper curve*. Then, the light concentration was decreased to qualitatively obtain I–V curves of the same solar cell when incident irradiance decreases due to partial shading on the primary optics

So, in a partially shaded HCPV module, different solar receivers have different I–V curves. The module I–V curve is obtained by the series association of the individual curves, i.e., individual voltages are added for each value of current. An example of this association law is shown in Fig. 6. The figure qualitatively plots the I–V curve of a receiver with unshaded primary optics, the I–V curve of a receiver with 75 % shaded primary optics and the I–V curve of the series association of them.

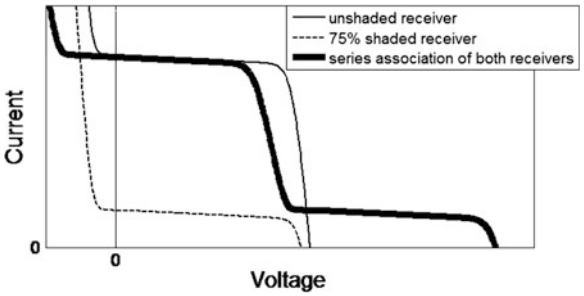

Fig. 6 I–V curve of two series-connected solar receivers, one of them with unshaded primary optics and the other with 75 % shaded primary optics (qualitative simulation). The unshaded receiver curve tries to represent a lattice-matched GaInP/GaInAs/Ge solar cell under 500 suns with a parallel-connected diode adjusted to have a threshold voltage 20 % of the solar cell open-circuit voltage. The *shaded receiver curve* was obtained by 75 % decreasing the incident irradiance on the solar cell. Both curves are intended for approximating the behavior of an HCPV receiver integrated with a primary lens when this lens is unshaded or partially shaded, by neglecting optical losses, nonuniformities of the light falling on the cell, etc. The *bolded curve* was obtained from Kirchhoff's law for the series-connection of two electrical elements

As can be seen, the combined curve shows a stair shape as a result of the two different I–V curves. The maximum power of the combined curve is lower than the sum of the maximum powers of the individual curves due to mismatch losses.

2.3 I–V Curve of a Partially Shaded HCPV Generator

From an electrical point of view, an HCPV generator is composed of HCPV modules interconnected in series and in parallel. The I–V curve of a shaded generator can be obtained by combining the I–V curves of the individual modules. The electrical laws for the series or parallel association of the I–V curves of two electrical elements are as follows:

- For two series connected elements, individual voltages are added for each value of current.
- For two parallel connected elements, individual currents are added for each value of voltage.

According to these electrical laws, the generator I–V curve can be obtained from the I–V curves of the generator components. Figure 7 shows a qualitative example of I–V and P–V curves of an HCPV tracker simulated under realistic shading conditions. As can be seen, these curves are warped because of the presence of shading. The P–V curve presents several local maxima, what can cause additional power losses if the inverter maximum power point tracker is not able to track the absolute maximum of the curve.

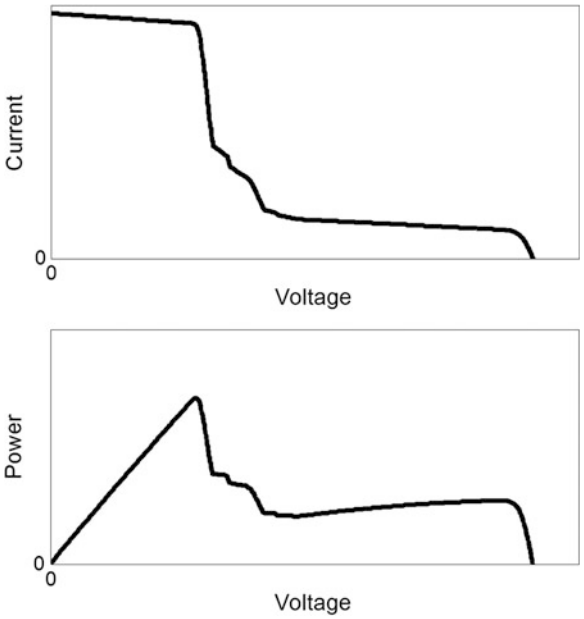

Fig. 7 Current–Voltage and Power–Voltage curves of a solar tracker under realistic shading conditions (qualitative simulation). A rectangular 11.5 × 8.8 m-sized tracker composed of 6 rows of 20 HCPV modules per row was approximately modeled. Modules in a row were connected in series and the different rows were connected in parallel. Each module was represented by 10 series-connected HCPV solar receivers equipped with Fresnel lenses with 625× concentration factor. Realistic shadows on the tracker surface caused by 8 adjacent trackers separated 18 m in the South-North direction and 21 m in the East-West direction were calculated at an instant of the day with low sun elevation angle. DNI was adjusted to a value corresponding to this sun elevation. Summer of a location at the centre of Spain was considered to calculate sun angles

3 High Concentrator Photovoltaic Receivers Operating with Partial Shading on the Primary Optics

In this section, the electrical behavior of HCPV solar receivers operating under partial shading on the primary optics is analyzed. An HCPV solar receiver [22] is typically composed of a multijunction solar cell, a bypass diode, a heat sink and a secondary optical element. The devices analyzed in this study are composed of a single solar receiver integrated with Fresnel lens primary optics and the protection elements required for outdoor operation. Figure 8 shows an example of such a device.

The aim of the study is to characterize the equivalent irradiance that affects the device. This equivalent irradiance, if homogeneously applied on the primary lens surface, would cause the same electrical behavior than is observed on the partially shaded device.

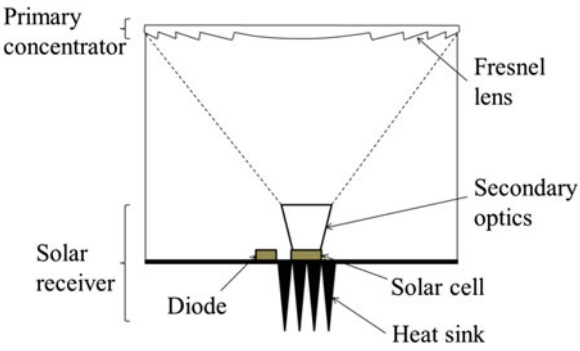

Fig. 8 Structure of a typical HCPV solar receiver integrated with Fresnel lens primary optics

The study is organized in two sections: Sect. 3.1 presents some outdoor measurements performed on solar receivers integrated with primary lens under partially shaded conditions; Sect. 3.2 characterizes the equivalent irradiance that affects these devices based on the collected measurements.

In what follows, the parameter "shading factor" (s) will be used. It is defined as the quotient between the shaded area on the primary lens surface and the total area of the primary lens. Because diffuse components of solar radiation do not affect the behavior of HCPV devices, no correction on this factor is required and it can be calculated by a simple quotient between areas.

3.1 Outdoor Measurements of Solar Receivers Operating with Partial Shading on the Primary Optics

Two solar receivers integrated with primary lens were measured outdoors at Jaén, South of Spain, by reproducing shading conditions on the lens surface [21]. The devices had 500× and 625× concentration factors and incorporated lattice-matched GaInP/GaInAs/Ge solar cells. The measurements included the acquisition of the I–V curve of the device as well as the cell temperature and other atmospheric parameters such as direct normal irradiance, ambient temperature, wind speed and sun elevation angle. For this purpose, the devices were mounted on a two-axis solar tracker.

Multijunction concentrator solar cells are influenced by changes in irradiance, cell temperature and incident light spectrum [27–30]. Therefore, the measured devices were supposed to be influenced by these parameters as well [25, 31, 32]. It was essential for the experiment to analyze the effect of shading on the devices independently of other influencing factors. Because of this, the different measurements were performed at very clear days with low wind speed during 1 h at noon. These selected conditions allowed analyzing the effect of shading by neglecting changes in irradiance, temperature and spectrum.

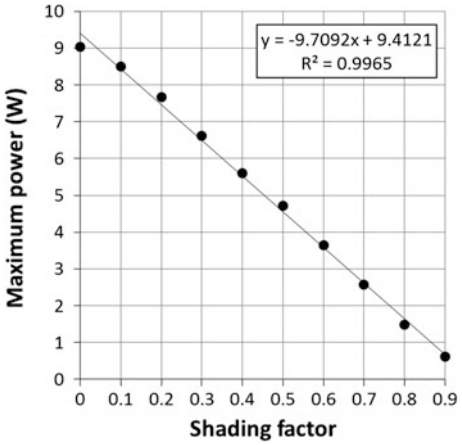

Fig. 9 Results of ten measurements of the maximum power of a solar receiver integrated with primary lens under stable conditions of irradiance, temperature and spectrum by varying the shading factor on the lens. The solar receiver incorporated a 0.92 cm^2-sized GaInP/GaInAs/Ge solar cell with a parallel-connected diode, a refractive quadrangular truncated pyramid made of glass as secondary optical element and was passively cooled through a finned heat-exchanger. A PMMA squared flat Fresnel lens provided 625× concentration factor. Measured environmental conditions during the experiment were direct normal irradiance = 936.5 ± 0.8 % W/m^2, air mass = 1.33 ± 3 %, air temperature = 12.0 ± 5 % °C, wind speed < 2 m/s

In each selected day, different shadows were reproduced on the primary lens of the measured device, covering shading factors of $s = 0.0$, $s = 0.1$, $s = 0.2$, …, and $s = 0.9$, i.e., ten measurements were performed, what took approximately 1 h. The experiment was repeated in different days and for both devices.

The main conclusion when analyzing the measurements was related to the behavior of the maximum power of the devices. It was found that maximum power decreased almost linearly with the shading factor. Figure 9 shows an example of such a behavior. It corresponds to a device measured at the conditions: direct normal irradiance = 936.5 ± 0.8 % W/m^2, air mass = 1.33 ± 3 %, air temperature = 12.0 ± 5 % °C, wind speed < 2 m/s. As can be seen, the correlation coefficient R^2 of the linear regression is 0.9965 (very close to unity). Similar results were obtained for the other device and for other days. This behavior was found to be very similar to that of conventional flat-plate solar cells under partial shading.

3.2 Equivalent Irradiance for Solar Receivers Operating with Partial Shading on the Primary Optics

The equivalent irradiance ($G_{B,eq}$) of an HCPV receiver integrated with partially shaded primary lens is defined as the irradiance that, if homogenously applied on

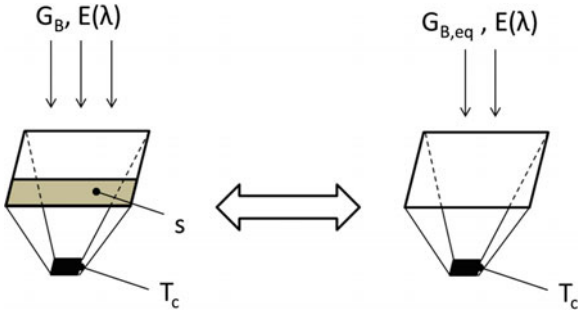

Fig. 10 Definition of the equivalent irradiance: the shaded device operating under direct normal irradiance G_B, cell temperature T_c, spectrum $E(\lambda)$ and shading factor s behaves like the homogenously illuminated device operating under the equivalent irradiance $G_{B,eq}$, cell temperature T_c and spectrum $E(\lambda)$

the lens surface while maintaining the same cell temperature and spectrum, would cause the same electrical behavior in the homogeneously illuminated device than in the shaded device (Fig. 10). This concept is useful because if the equivalent irradiance can be determined, any existing model for receivers with unshaded primary lens can be adapted to receivers with partially shaded primary lens by replacing the direct normal irradiance parameter by the equivalent irradiance parameter.

The measurements of receivers integrated with partially shaded primary lens shown a linear decrease of the maximum power with respect to the shading factor. This suggests that the equivalent irradiance could be characterized from the direct normal irradiance and the shading factor by means of a linear function:

$$G_{B,eq} = (1 - s) \cdot G_B \tag{1}$$

This hypothesis was verified through an experimental campaign performed at Jaén on the two mentioned HCPV devices. For this purpose, a set of measurements were taken outdoors at different levels of direct normal irradiance, cell temperature and spectrum by reproducing different shading conditions on the lens surface of the devices.

The experimental maximum power of the devices for each measurement compared with the calculated maximum power obtained by applying the hypothesis in Eq. (1) combined with the Sandia National Laboratories model for characterizing photovoltaic devices [33]. It was found a reasonable agreement between calculated and measured values (RMSEs of 4.7 and 5.1 % for each device). This means that the proposed expression for characterizing the equivalent irradiance can be used for HCPV receivers integrated with partially shaded primary lens.

The measured devices incorporated a truncated quadrangular pyramid made of glass as secondary optical element. The linear expression for the equivalent irradiance could not be valid for other designs with poorer light homogenization properties.

4 A Methodology for Characterizing the I–V Curve of Shaded HCPV Generators

In this section, a methodology for characterizing the I–V curve of shaded HCPV generators is described and compared with experimental data. The methodology uses three kinds of inputs: ambient conditions, shading factors of the lenses in the generator and generator electrical configuration. It is composed of three blocks, as shown in Fig. 11. The first block (unshaded receiver block) computes the I–V curve of a solar receiver with unshaded primary lens based on ambient conditions; the second block (shaded receiver block) computes the I–V curve of every receiver with partially shaded primary lens in the generator from the unshaded receiver curve and the shading factors of its lens; the third block (shaded generator block) computes the I–V curve of the shaded generator from the I–V curves of the receivers and the generator electrical configuration.

Ambient conditions used as inputs are direct normal irradiance (G_B), ambient temperature (T_{air}), wind speed (WS) and air mass (AM). One of the advantages of the methodology is that these atmospheric parameters are easy to measure or can be easily obtained from meteorological databases. This makes the methodology applicable either for operating HCPV generators or in the early stage of design of HCPV plants. Sections 4.1, 4.2 and 4.3 describe the three blocks that compose the methodology. Section 4.4 compares experimental I–V curves to curves simulated with the developed methodology.

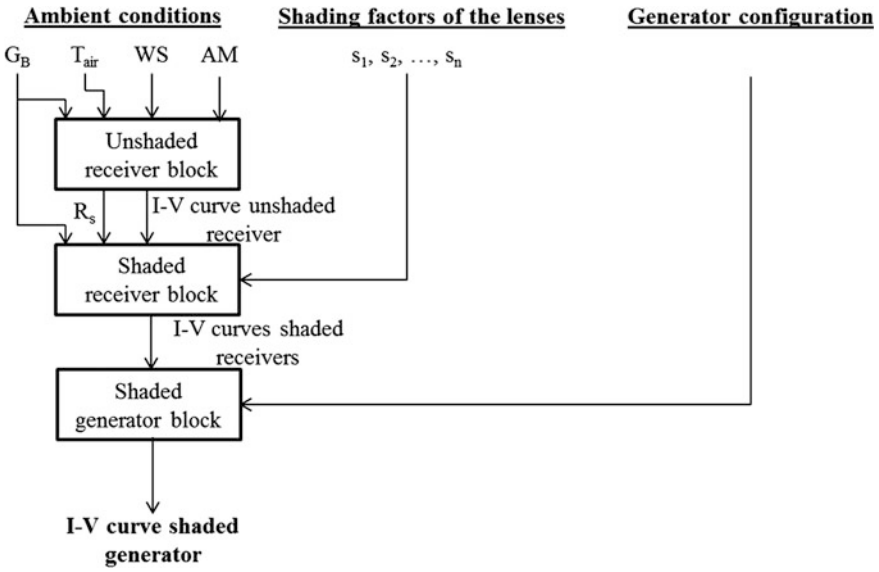

Fig. 11 General scheme of the methodology for characterizing the I–V curve of shaded HCPV generators

4.1 Unshaded Receiver Block

The unshaded receiver block obtains the I–V curve of a receiver integrated with unshaded primary lens based on ambient conditions. For this purpose, several existing models were integrated. Figure 12 shows a scheme of the different models and variables used in the implementation. These models are briefly described later in the text.

- Almonacid's model.
  This model allows estimating the cell temperature (T_c) in an HCPV receiver integrated with unshaded primary lens operating in real conditions [34]. It uses as inputs direct normal irradiance, ambient temperature and wind speed and obtains cell temperature through linear coefficients. Model parameters are obtained from an outdoor experimental campaign by monitoring cell temperature together with atmospheric parameters and applying multilinear regression analysis.
- Sandia's model.
  Core of the unshaded receiver block is the model of Sandia National Laboratories for characterizing photovoltaic devices [33]. This model uses as inputs direct normal irradiance, cell temperature and air mass. It is based on several equations that allow calculating solar cell electrical parameters. Specifically, parameters calculated by this model are as follows: short-circuit current (I_{sc}),

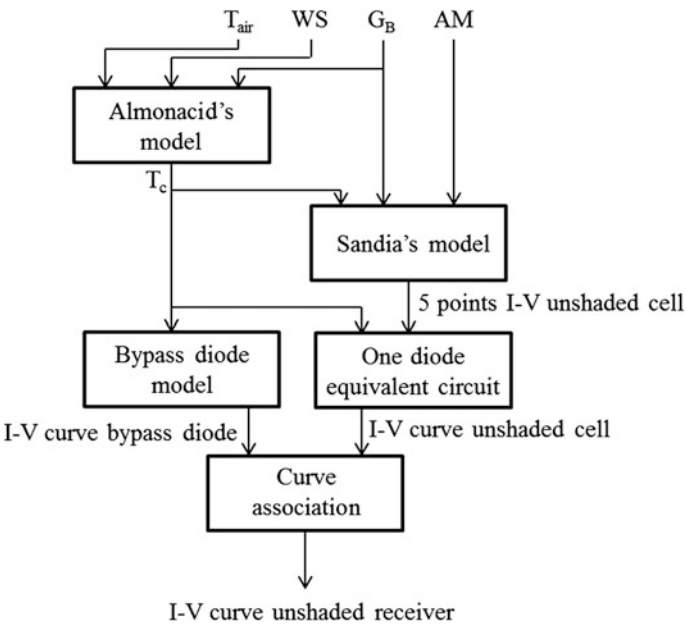

Fig. 12 Scheme of the unshaded receiver block

open-circuit voltage (V_{oc}), maximum power point current (I_{mpp}), maximum power point voltage (V_{mpp}), current at a voltage $V_{oc}/2$ and current at a voltage ($V_{mpp} + V_{oc}$)/2, i.e., five points on the solar cell I–V curve are calculated. Model parameters are obtained from an outdoor experimental campaign by monitoring the I–V characteristic curve, the cell temperature and atmospheric parameters and applying multilinear regression analysis.

- One-diode equivalent circuit.
  It was reported that the solar cell one-diode equivalent circuit is able to characterize the experimental I–V curves of a triple-junction solar cell in an HCPV receiver [35]. This equivalent circuit depends on five parameters: photocurrent (I_{ph}), saturation current (I_0), diode ideality factor (m), series resistance (R_s) and shunt resistance (R_{sh}). These parameters can be calculated given the five points on the solar cell I–V curve calculated from the Sandia National Laboratories model by means of the method developed by Karatepe et al. [16]. The method builds a system of five nonlinear implicit equations that must be numerically solved. A trust-region optimization method is recommended for solving because of the good convergence properties and relative independence of initial parameters values [36]. Once I_{ph}, I_0, m, R_s and R_{sh} have been calculated, the standard solar cell one-diode equivalent circuit allows obtaining as many points of the solar cell I–V curve as wanted.
- Bypass diode model.
  Shockley's diode equation can be used to reproduce the I–V curve of the bypass diode in a solar receiver. However, experimental measurements of bypass diodes integrated in HCPV solar receivers suggest modelling a small resistance in series with the diode. This resistance accounts for the effects of the metallic contacts between the multijunction solar cell and the bypass diode. Shockley's equation parameters depend on diode temperature [37]. In this methodology, these parameters are directly correlated to the cell operating temperature (T_c).
- Curve association.
  Once the solar cell and the bypass diode I–V curves are calculated and given that the cell and the diode in a solar receiver are connected in parallel, currents of both I–V curves are added for each value of voltage. This way, the I–V curve of the solar receiver integrated with unshaded primary lens is obtained.

4.2 Shaded Receiver Block

The aim of the shaded receiver block is to obtain the I–V curve of every solar receiver with partially shaded primary lens in the generator. For this purpose, it uses as inputs the I–V curve of the receiver with unshaded primary lens, the shading factor of each specific lens (s_i), the direct normal irradiance (G_B) and the series resistance of the solar cell in the receiver with unshaded lens as obtained by the unshaded receiver block (R_s). Figure 13 shows the scheme of the shaded receiver block as well as the involved variables.

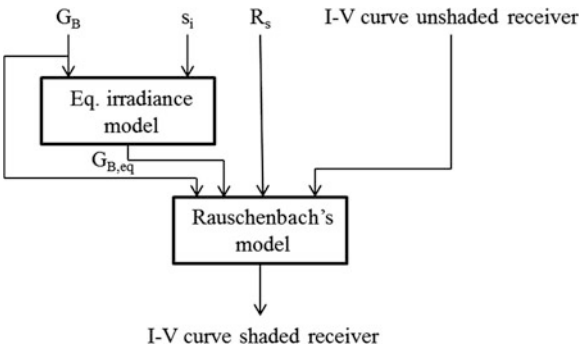

Fig. 13 Scheme of the shaded receiver block

The two models that compose this block are as follows:

- Equivalent irradiance model.
  This model calculates the equivalent irradiance that affects the receiver with partially shaded primary lens ($G_{B,eq}$) as defined in Sect. 3.2. This parameter is obtained from direct normal irradiance and shading factor of the lens. Experimental measurements of solar receivers integrated with partially shaded primary lens shown that a linear equation, Eq. (1), is able to approximate the equivalent irradiance [21].
- Rauschenbach's model.
  The aim of this model is to translate the I–V curve of the receiver with unshaded primary lens to obtain the I–V curve of the receiver with partially shaded primary lens in a point by point basis. For that purpose, it requires as inputs equivalent irradiance, direct normal irradiance and series resistance of the solar cell in the receiver with unshaded lens. An existing procedure for flat-plate solar cells [5] has been adapted to HCPV receivers. Resulting equations are:

$$I_2 = I_1 - \left(1 - \frac{G_{B,eq}}{G_B}\right) \cdot I_{sc} \tag{2}$$

$$V_2 = V_1 + \left(1 - \frac{G_{B,eq}}{G_B}\right) \cdot R_s \cdot I_{sc} \tag{3}$$

(V_1, I_1) being the point on the I–V curve of the receiver with unshaded primary lens, (V_2, I_2) the corresponding translated point on the I–V curve of the receiver with partially shaded primary lens, $G_{B,eq}$ the equivalent irradiance, G_B the direct normal irradiance, R_s the series resistance and I_{sc} the short-circuit current of the receiver with unshaded primary lens.

4.3 Shaded Generator Block

Once the I–V curve of every receiver in the generator has been reproduced, the shaded generator block implements Kirchhoff's electrical laws based on generator electrical configuration. Series connections of receivers that represent each HCPV module and series-parallel connections of HCPV modules that represent the HCPV generator are modelled. This results in a set of nonlinear equations that must be numerically solved for each value of generator voltage. This procedure has been used for the modelling of flat-plate photovoltaic generators, see for instance [15]. By solving the system, current in any branch, voltage in any node and finally, generator current can be calculated, so that the shaded generator I–V curve can be obtained. Implementation of these equations and numerical algorithms can be considerably simplified with the help of dynamic simulation software such as Matlab/Simulink.

4.4 Comparison Between Measured and Simulated I–V Curves

Two HCPV modules were measured outdoors at Jaén, South of Spain, by reproducing different shading conditions on their primary lenses. The measurements included the acquisition of the I–V curve of the partially shaded module simultaneously with direct normal irradiance, air temperature, wind speed and sun elevation angle. Modules were named as A and B. Module A had 6 series-connected solar receivers equipped with lattice-matched GaInP/GaInAs/Ge solar cells, each one integrated with a 500× concentration factor Fresnel lens. Module B had 5 series-connected solar receivers equipped with lattice-matched GaInP/GaInAs/Ge solar cells and 625× concentration factor Fresnel lenses. Module powers at Concentrator Standard Test Conditions [38] were 65.6 and 51.8 W respectively. Both modules had passive cooling.

The I–V curves of the shaded modules were latter simulated with the developed methodology taking into account the registered atmospheric parameters and the shading factors of the lenses. Experimental and simulated curves were then compared. Figures 14 and 15 are examples that illustrate the degree of accuracy obtained by the methodology. Figure 14 shows the comparison between an I–V curve measured on the module A and the corresponding simulated curve when two lenses are partially shaded, one with a 25 % shading factor and the other with a 75 % shading factor. Figure 15 shows an example of measured and simulated curves on the module B with two partially shaded lenses, one with a 50 % shading factor and the other with a 75 % shading factor. In most analyzed cases, it was found a reasonable agreement between experimental and simulated behavior. For instance, the two presented curves got RMSEs of 2.2 and 2.8 % respectively.

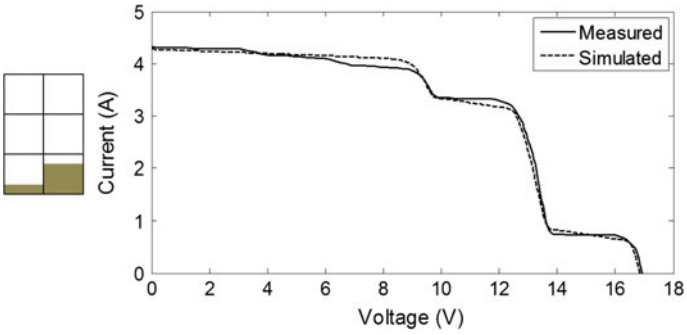

Fig. 14 Example of measured and simulated I–V curves for the module A. The shading pattern for the module is represented at the *left side*. Module A uses GaInP/GaInAs/Ge solar cells with 500× concentration factor provided by flat Fresnel lenses

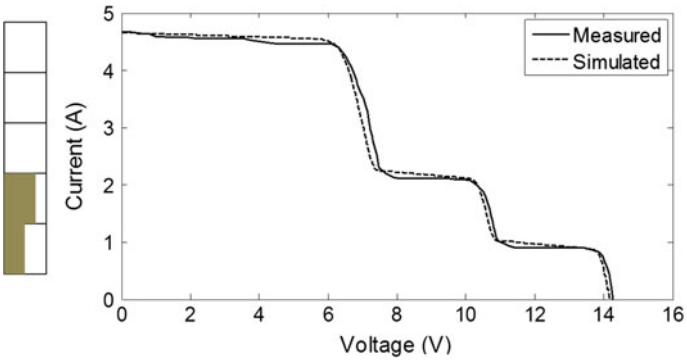

Fig. 15 Example of measured and simulated I–V curves for the module B. The shading pattern for the module is represented at the *left side*. Module B uses GaInP/GaInAs/Ge solar cells with 625× concentration factor provided by flat Fresnel lenses

The experimental measurements indicated that the methodology is adequate for characterizing the I–V curve of shaded HCPV modules. This means that it can be a good choice for carrying out studies on shading in HCPV power plants.

5 Calculation of Shading Energy Losses in HCPV Plants

A possible application of the presented methodology is implementing time domain simulations that reproduce the electrical behavior of a shaded HCPV generator at small time steps. For this purpose, knowledge of atmospheric parameters daily profiles is required (direct normal irradiance, air temperature, wind speed and sun position). In addition, details of the HCPV plant configuration are needed such as

geographic location, dimensions of solar trackers, trackers distribution and HCPV modules interconnection scheme. The electrical behavior of the concentrator modules used in the plant must be previously characterized under unshaded conditions.

In this section, geometric formulae for calculating self-shading between trackers are shown (Sect. 5.1). These formulae together with the methodology described in the previous section are used to calculate monthly and annual shading energy losses in a hypothetical HCPV plant to be located at Marrakech, Morocco (Sect. 5.2).

5.1 Geometric Calculation of Shadows in HCPV Plants

The geometric formulae used for the calculation of self-shading between solar trackers are expressed as a function of solar position, trackers dimensions and relative position between trackers.

Solar position is determined by the elevation angle (γ_s) and the azimuth angle (ψ_s). Solar elevation angle takes values in the range 0° (sunrise and sunset) to 90° (sun upright the observer). Solar azimuth angle takes values in the range −180 to +180°, where $\psi_s = -90°$ indicates sun oriented at East, $\psi_s = 0°$ indicates sun oriented at equator, $\psi_s = +90°$ indicates sun oriented at West, etc.

In this analysis, rectangular trackers are considered. Trackers dimensions are determined by L parameter (rectangle side parallel to ground) and M parameter (rectangle side not parallel to ground).

To determine relative position between two trackers, an obstacle tracker and a shaded tracker, x and y parameters are used. x represents the distance between the shaded tracker and the obstacle tracker in the West-East direction, whereas y represents the distance in the South-North direction (North hemisphere) or in the North-South direction (South hemisphere). Both parameters can take negative values. Figure 16 shows a top view of two trackers in an arbitrary relative position and Fig. 17 shows the corresponding side view.

By analyzing this geometry, the distances d_1 and d_2 shown in the figures can be calculated by:

$$d_1 = x\cos\psi_s - y\sin\psi_s \tag{4}$$

$$d_2 = -(x\sin\psi_s + y\cos\psi_s)\sin\gamma_s \tag{5}$$

In addition, a λ parameter can be calculated to evaluate if the obstacle tracker can shade the central tracker, depending on sun position. This parameter is expressed as:

$$\lambda = -(x\sin\psi_s + y\cos\psi_s)\cos\gamma_s \tag{6}$$

If λ is positive, the obstacle tracker is before the central tracker in the solar rays direction, so that the central tracker can be shaded. If λ is negative, the obstacle

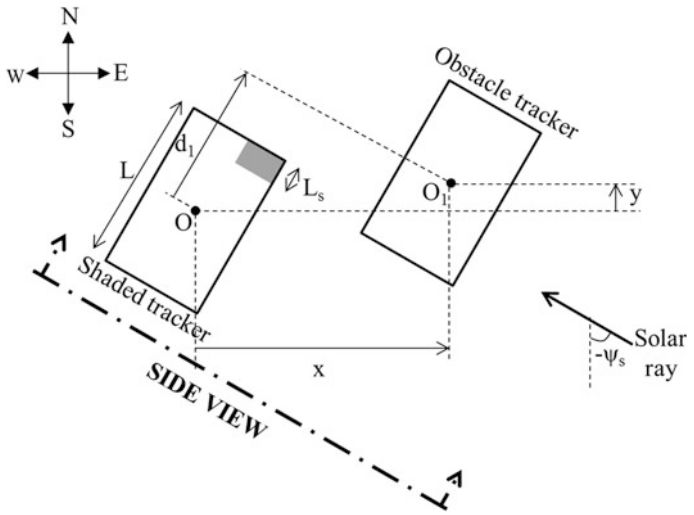

Fig. 16 Top view of two trackers and projected shadow (North hemisphere)

Fig. 17 Side view of two trackers and projected shadow

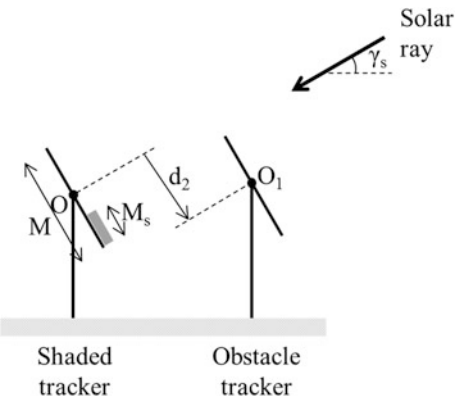

tracker is behind the central tracker in the solar rays direction, so that the central tracker cannot be shaded.

If λ is positive, distances d_1 and d_2 must be calculated and from them, the shaded rectangle on the central tracker can be determined. This rectangle is represented by L_s (shaded rectangle side parallel to ground) and M_s (shaded rectangle side not parallel to ground). The following expressions allow calculating L_s and M_s:

$$L_s = L - |d_1| \tag{7}$$

$$M_s = M - d_2 \tag{8}$$

If one of these parameters results in a negative value, there is no shadow on the central tracker. Once L_s and M_s are determined, the shading factor of the central tracker can be expressed as:

$$s = (L_s M_s)/(LM) \tag{9}$$

This method can also be used to calculate the shading factor of individual lenses on the tracker surface. Each lens is a polygon whose vertices have known coordinates on the plane of the tracker. The shaded area on a specific lens can be obtained by the intersection of the lens area and the shaded rectangle on the tracker. Therefore, the shading factor of a lens can be calculated by the quotient between its shaded area and its total area.

If several obstacle trackers project shadows on the central tracker, the shading pattern on the tracker surface is obtained by combining the different shaded rectangles.

5.2 Application for Calculating Shading Energy Losses

A case study has been defined to apply the procedures described in the previous sections for the calculation of shading energy losses. It corresponds to a hypothetical HCPV plant to be installed at Marrakech, Morocco. Trackers dimensions are L = 11.5 m and M = 8.8 m and distances between trackers are x = 21 m (in the West-East direction) and y = 18 m (in the South-North direction). Each tracker is supposed to be composed of 6 parallel strings of 20 series-connected HCPV modules per string with a total power of 30 kWp per tracker, i.e., 250 Wp HCPV modules are used rated at Concentrator Standard Test Conditions [38]. Each string of 20 series-connected modules is aligned in a horizontal row of the tracker. Each tracker is supposed to have its own inverter.

The HCPV modules are composed of 10 series-connected solar receivers equipped with triple-junction solar cells, with 30 V of module maximum power point voltage and 8.33 A of maximum power point current. Parameters that define the electrical behavior of the modules under unshaded conditions were taken from the outdoor experimental characterization of an HCPV module of typical characteristics performed at the Centre of Advanced Studies in Energy and Environment of Jaén University, South of Spain. This representative module incorporated GaInP/GaInAs/Ge solar cells, a PMMA flat Fresnel lens per receiver with 625× concentration factor and was passive-cooled.

Typical monthly averaged daily profiles of direct normal irradiance, air temperature, sun elevation and azimuth angles for Marrakech were synthesized with the help of a photovoltaic software package. Wind speed was considered negligible for this location. Time steps of 2.5 min were chosen for the simulation.

Table 1 Percentages of irradiation losses and harvested energy losses due to shading for a simulated HCPV plant at Marrakech, Morocco, composed of rectangular 11.5 × 8.8 m-sized solar trackers separated 21 m in the West-East direction and 18 m in the South-North direction

	Irradiation losses (%)	Energy losses (%)
Jan	5.95	9.65
Feb	4.55	7.36
Mar	6.22	8.76
Apr	6.39	7.41
May	4.01	6.43
Jun	4.10	6.79
Jul	4.12	6.69
Aug	5.38	6.98
Sep	7.08	8.17
Oct	4.74	8.42
Nov	5.56	8.46
Dec	7.38	12.01
Annual	5.35	7.91

A representative 250 Wp HCPV module composed of 10 series-connected GaInP/GaInAs/Ge solar cells with a bypass diode per cell, passive cooling and 625× concentration factor provided by flat Fresnel lenses was experimentally characterized under unshaded conditions and the obtained parameters were used for the time-domain simulation. The solar trackers were modeled with 6 parallel-connected rows of modules and 20 series-connected modules per row, by considering a tracker-oriented inverters configuration

Simulation results are shown in Table 1. The table compares the irradiation losses due to self-shading between trackers to the losses in the harvested energy in a monthly basis. As can be seen, shading energy losses between 6.43 % (May) and 12.01 % (December) can be expected. Annual energy losses due to shading were estimated in 7.91 % for this kind of plant and location considering the current state-of-the-art of commercial HCPV technology.

6 A Simplified Method for Determining Optimum Trackers Allocation

In this section, a simplified method for determining optimum trackers allocation in the design of an HCPV plant is described [39]. The procedure is based on balancing shading irradiation losses with energy losses in wires and costs of the land. It has the advantage of simplicity and has proven its usefulness in the practical design of HCPV power plants.

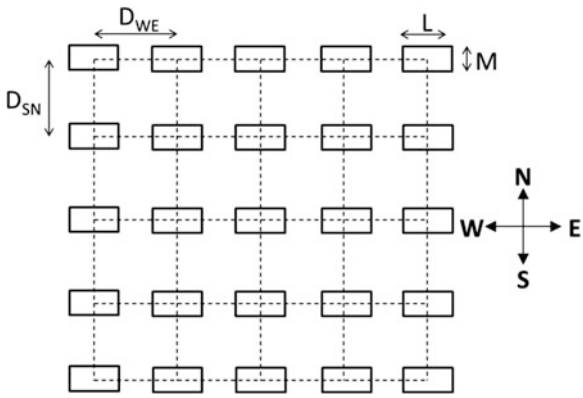

Fig. 18 Geometry of a generic HCPV plant as considered by the method

The procedure uses the following assumptions:

- Land is a horizontal plane.
- Trackers are identical with rectangular surface. This surface is defined by the dimensions L (side parallel to ground) and M (side not parallel to ground), in meters.
- Plant geometry is defined by a rectangular grid oriented in the directions West-East and South-North. Distances D_{WE} and D_{SN} in meters determine this geometry as shown in Fig. 18. The aim of the procedure is to optimize the value of these two parameters.
- Shadows caused by surrounding obstacles or by a nonplanar horizon are neglected. Only self-shading between trackers is considered.

Section 6.1 explains the steps of the procedure. Section 6.2 shows an example of its application.

6.1 Procedure Description

The developed method follows the next steps:

1. *Obtainment of the monthly averaged daily direct normal irradiance profile.*

Knowledge of typical direct normal irradiance data for the considered location is an input of the procedure. A representative day of each month must be characterized with its direct normal irradiance profile. These irradiance functions can be synthetized with meteorological software packages. Another option is to use a simplified method defined in [40].

2. *Calculation of sun position at any instant.*

Sun position can be calculated by means of standardized formulae [41]. These formulae are based on the determination of earth orbit eccentricity and declination for a representative day of each month. Once these parameters are known, the elevation

angle (γ_s) and the azimuth angle (ψ_s) that define sun position at a given instant can be obtained through trigonometric expressions. Results of this step are pairs of values (γ_s, ψ_s) at given time intervals for the representative day of each month.

3. *Calculation of the percentage of shaded area on a tracker caused by another arbitrarily located tracker at any instant.*

Expressions described in Sect. 5.1 allow calculating the shading factor of a central tracker shaded by an arbitrarily located obstacle tracker. As was commented, relative position between two trackers can be defined by x (West-East distance) and y (South-North distance for North hemisphere or North-South distance for South hemisphere) parameters. Distance increments must be defined in the algorithm (Δx, Δy) and for each trackers relative position and sun position, shading factor of the central tracker must be calculated. This procedure is repeated for the representative day of each month.

4. *Calculation of the percentage of annual direct irradiation losses on a tracker caused by the eight adjacent trackers.*

The procedure takes into account shadows on a tracker caused by the eight adjacent trackers. Shadows caused by farther trackers are neglected.

For a plant geometry defined by D_{WE} and D_{SN} distances (Fig. 18), x and y coordinates of each adjacent tracker with respect to the central tracker are known. Thus, eight shading factors s_1, s_2, …, s_8 on the central tracker at each instant can be obtained from the calculations in step 3. The combined shading factor on the central tracker (s) is estimated by:

$$s = \min\left\{\sum_{i=1}^{8} s_i, 1\right\} \tag{10}$$

This implies an overestimation of the real shading factor because at some instants it is possible that two or more of the projected shadows overlap.

Therefore, this step allows knowing the central tracker shading factor at each instant. In contrast, the direct normal irradiance at each instant (G_B in W/m^2) was obtained in step 1. From these data, annual direct irradiation received by the shaded tracker, H_s, and annual direct irradiation that would be received by this tracker in absence of shadows, H, both in kWh/m^2, can be calculated by means of annual summations:

$$H_s = \frac{1}{1000} \cdot \sum_{j=1}^{12\text{months}} n_{\text{days},j} \left[\sum_{i}^{\text{day}} (1 - s_{ij}) G_{\text{B}ij}\right] \cdot \Delta t \tag{11}$$

$$H = \frac{1}{1000} \cdot \sum_{j=1}^{12\text{months}} n_{\text{days},j} \left[\sum_{i}^{\text{day}} G_{\text{B}ij}\right] \cdot \Delta t \tag{12}$$

$n_{\text{days},j}$ being the number of days of the j month and Δt the time step of the simulation in hours. From both values, the annual direct irradiation losses factor due to shading, L_{irr}, can be obtained by:

$$L_{\text{irr}} = 1 - H_{\text{s}}/H \tag{13}$$

5. *Calculation of the annual income by energy production of a tracker.*

The main input in this step is the economic income per kWh generated by the plant, r_{kWh} in USD/kWh. To use this parameter, it is necessary to have an estimation of the annual energy production of a tracker.

In photovoltaics, annual Performance Ratio (PR) is commonly used to calculate harvested energy from annual irradiation. This ratio can be broken down into different losses factors that affect tracker production such as temperature losses, spectral losses, misalignment, optical losses, soiling, shading, etc. All of these losses can be considered independent of relative distances between trackers except shading losses. Because of this, it is convenient to define a modified tracker Performance Ratio (PR′) that includes every existing loss except shading losses:

$$\text{PR} = (1 - L_{\text{s}}) \cdot \prod_{i=2}^{n} (1 - L_i) = (1 - L_s) \cdot \text{PR}' \tag{14}$$

L_{s} being the shading losses factor. The annual energy harvested by a tracker, E, can be expressed as a function of this modified Performance Ratio by:

$$E(\text{kWh}) = \text{PR}' \cdot P_{\text{pk}}(\text{kWp}) \cdot (1 - L_{\text{s}}) \cdot H\left(\text{kWh}/\text{m}^2\right) \tag{15}$$

P_{pk} being the tracker peak power. In this procedure, the shading losses factor (L_{s}) is approximated by the direct irradiation losses factor due to shading (L_{irr}) as calculated in step 4:

$$\begin{aligned} E(\text{kWh}) &\approx \text{PR}' \cdot P_{\text{pk}}(\text{kWp}) \cdot (1 - L_{\text{irr}}) \cdot H\left(\text{kWh}/\text{m}^2\right) \\ &= \text{PR}' \cdot P_{\text{pk}}(\text{kWp}) \cdot H_{\text{s}}\left(\text{kWh}/\text{m}^2\right) \end{aligned} \tag{16}$$

This way, the previous calculations allow estimating the annual energy harvested by a tracker if the modified Performance Ratio value is known for the location and technology of the plant. It is important to remark that replacing L_{s} by L_{irr} implies underestimating the influence of shading on tracker production because mismatch losses that happen in a shaded generator are being neglected. However, this approximation is considered acceptable for the defined procedure because it tends to compensate the overestimation of shading performed in step 4.

Once the annual energy harvested by a tracker has been estimated, the annual income by energy production of a tracker, I, is calculated by:

$$I = r_{\mathrm{kWh}} \cdot E \tag{17}$$

6. *Calculation of annual costs due to energy losses in wires for a tracker.*

Most of the energy losses in wires due to Joule effect take place in the wires that link each group of parallel-connected trackers to the corresponding inverter. The total length of these paths for the plant can be expressed as a function of the distances D_{WE} and D_{SN} that determine the plant geometry if the inverters location is predefined.

As a previous calculation for determining annual energy dissipated in wires, an annual parameter, H_{s}^2, dependent on direct normal irradiance and tracker shading factor, must be evaluated through a quadratic summation:

$$H_{\mathrm{s}}^2 = \frac{1}{1000} \cdot \sum_{j=1}^{12\mathrm{months}} n_{\mathrm{days},j} \left[\sum_{i}^{\mathrm{day}} \left(1 - s_{ij}\right)^2 G_{\mathrm{B}ij}^2 \right] \cdot \Delta t \tag{18}$$

This parameter has units of kWh $\cdot$ (W/m^4) and can be calculated the same way than H_{s}, with the difference that terms $(1 - s)$ and G_{B} are squared. The annual energy dissipated in wires for a tracker, E_{W}, is the total energy dissipated in the plant divided by the number of trackers in the plant:

$$E_{\mathrm{W}} = \frac{2 \cdot \rho \cdot L_{\mathrm{W}}(D_{\mathrm{WE}}, D_{\mathrm{SN}})}{A_{\mathrm{W}} \cdot n_{\mathrm{track}}} \cdot \left(n_{\mathrm{trackparal}} \cdot n_p \cdot I_{\mathrm{mpp}}^* \right)^2 \cdot \frac{H_{\mathrm{s}}^2(D_{\mathrm{WE}}, D_{\mathrm{SN}})}{G_{\mathrm{B}}^{*2}} \tag{19}$$

$L_{\mathrm{W}}(D_{\mathrm{WE}}, D_{\mathrm{SN}})$ being the function that determines the total length of wires between groups of parallel connected trackers to inverters for the plant in meters, A_{W} the cross-sectional area of the wires in mm^2, ρ the Copper resistivity in Ω mm^2/m, n_{track} the number of trackers in the plant, $n_{\mathrm{trackparal}}$ the number of trackers connected in parallel that compose a group to be connected to a inverter, n_{p} the number of parallel strings of series-connected HCPV modules in a tracker, I_{mpp}^* the HCPV module maximum power point current in amperes and G_{B}^* the standard direct normal irradiance at which the modules are rated. Annual costs due to energy losses in wires for a tracker, Q_{W}, can be evaluated by:

$$Q_{\mathrm{W}} = r_{\mathrm{kWh}} \cdot E_{\mathrm{W}} \tag{20}$$

7. *Calculation of annual costs of the land for a tracker.*

These costs can be calculated if the annual costs per m^2 of land, r_{m^2} in USD/m^2, are known. An estimation of the land area corresponding to each tracker (the total plant

area divided by the number of trackers) is required. For instance, a squared plant would have annual costs of the land for a tracker, Q_L, such as:

$$Q_L = r_{m^2} \cdot \frac{\left(\sqrt{n_{track}} - 1\right)^2}{n_{track}} \cdot D_{WE} \cdot D_{SN} \tag{21}$$

8. *Calculation of optimal distances between trackers.*

The annual profit (P) due to the operation of a tracker as a function of D_{WE} and D_{SN} distances is obtained by deducting costs due to energy losses in wires and costs of the land to the income by energy production:

$$P(D_{WE}, D_{SN}) = I - Q_W - Q_L \tag{22}$$

The design problem is then solved by searching for a (D_{WE}, D_{SN}) pair that maximizes the annual profit function.

6.2 Example of Application

In this section, results of applying this method to a hypothetical HCPV plant to be located at Aguascalientes, México, are shown. Aguascalientes latitude is 21.9°N and has an annual averaged daily direct normal irradiation of 5.9 kWh/m^2. The plant would be composed of 100 trackers with 30 kWp per tracker. Trackers dimensions are 11.5 × 8.8 m and are supposed to have a modified annual Performance Ratio PR′ = 0.8. Each tracker has 6 parallel strings of 20 series-connected HCPV modules with 8.33 A of maximum power point current per module measured at 1000 W/m^2 of direct normal irradiance. Groups of 10 parallel-connected trackers are connected to central inverters located at the center of the plant through 200 mm^2 cross-sectional area wires. The economic scenario for the simulation is defined by the following parameters: income per kWh generated by the plant = 0.14 USD/kWh; annual costs per m^2 of land = 1.4 USD/m^2.

Figure 19 represents the results obtained after applying steps 1, 2 and 3 of the procedure. The graph shows the distribution of percentages of shading annual direct irradiation losses on a tracker caused by another tracker as a function of relative distances between them.

Figure 20 represents the distribution of annual prices of the energy generated by a tracker surrounded by eight trackers as a function of D_{WE} and D_{SN} distances that define the plant geometry as calculated by steps 4 and 5 of the procedure. Afterwards, Fig. 21 shows annual costs due to energy losses in wires and land use per tracker as a function of distances between trackers as calculated by steps 6 and 7 of the procedure.

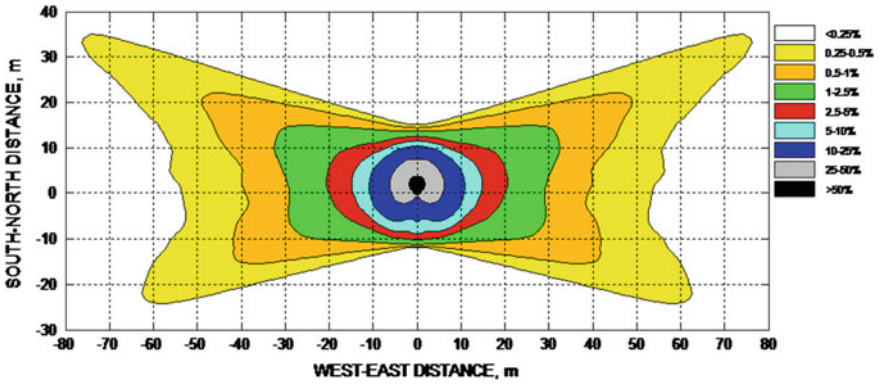

Fig. 19 Percentages of shading annual direct irradiation losses on a tracker caused by another tracker. Trackers dimensions are 11.5 × 8.8 m. Typical direct normal irradiance data and sun position angles of Aguascalientes, México, were used for the calculations

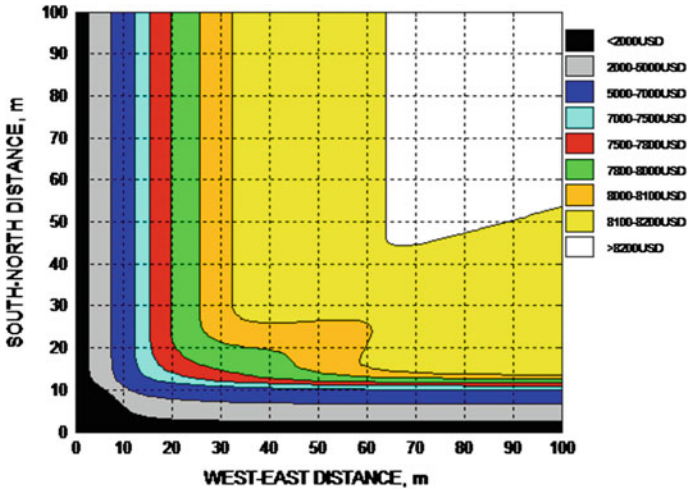

Fig. 20 Annual prices of the energy generated by a tracker surrounded by eight trackers as a function of distances between trackers. 30 kWp trackers were considered, a modified Performance Ratio (excluding shading energy losses) of 80 % was used for a tracker and the income per kWh generated by the plant was adjusted to 0.14 USD/kWh

Finally, Fig. 22 shows the annual profit per tracker as a function of distances between trackers as obtained by deducting costs due to energy losses in wires and land use to the income by energy production (step 8 of the procedure). The point that maximizes annual profit is indicated on the graph (D_{WE} = 24 m; D_{SN} = 17 m) and determines the optimum allocation of trackers for the plant.

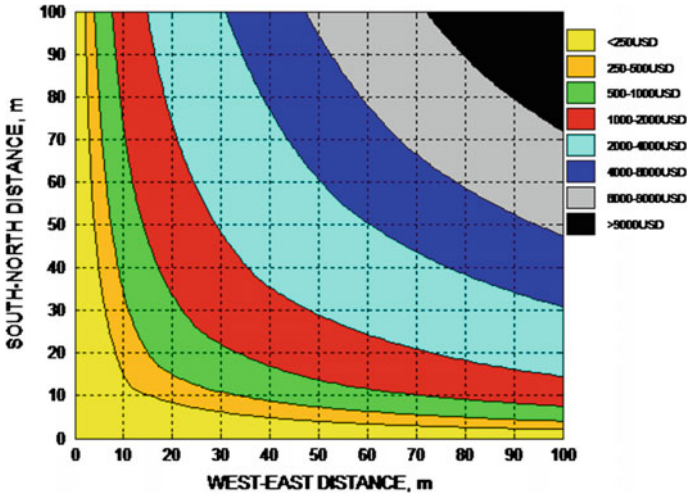

Fig. 21 Annual costs due to energy losses in wires and land use per tracker as a function of distances between trackers. Inverters were supposed to be located at the center of a 3 MWp HCPV power plant composed of 100 trackers, were each group of 10 parallel-connected trackers is linked to the corresponding central inverter through 200 mm^2 cross-sectional area Copper wires. Economic parameters are as follows: income per kWh generated by the plant = 0.14 USD/kWh; annual costs per m^2 of land = 1.4 USD/m^2

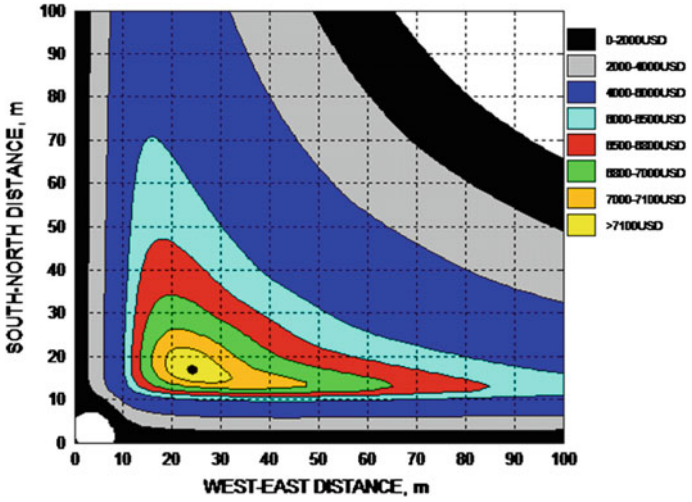

Fig. 22 Annual profit per tracker obtained by deducting costs due to energy losses in wires and costs of the land to the income by energy production and optimum trackers allocation (D_{WE} = 24 m; D_{SN} = 17 m) for an HCPV power plant composed of 11.5 × 8.8 m-sized 30 kWp solar trackers to be located at Aguascalientes, México

7 Conclusions

The characterization of the I–V curve of a shaded HCPV generator under given environmental conditions can be performed from the characterization of the basic component of the generator, the solar receiver integrated with partially shaded primary optics. If the electrical behavior of the different receivers in the generator is known, Kirchhoff's electrical laws allow obtaining the generator I–V curve.

An expression for the equivalent irradiance that affects a solar receiver with partially shaded primary lens was proposed from experimental measurements. As well, a methodology for obtaining the I–V curve of shaded HCPV generators was defined and a comparison between measured and simulated I–V curves was performed. One of the advantages of the methodology is that it uses atmospheric parameters that are easy to measure or can be easily obtained from meteorological databases (direct normal irradiance, ambient temperature, wind speed and air mass). This makes it applicable either for operating HCPV generators or in the early stage of design of HCPV plants. The methodology can be a good choice for carrying out studies on shading in HCPV power plants.

As an example of application of the methodology, typical monthly and annual energy losses for an HCPV plant to be located at Marrakech, Morocco, were calculated by considering geometric formulae that represent self-shading between solar trackers and performing time domain simulation of the generator I–V curve. This example shows the potential of the developed methodology, which could be applied to other kinds of studies, such as optimum trackers allocation or inverters configuration among others.

Another interesting line is developing simpler easy-to-use methods, suitable for designers of HCPV plants. As an example, a simplified method for obtaining optimal distances between solar trackers was introduced and applied to an HCPV plant to be located at Aguascalientes, México.

8 Future Directions

The variety of existing HCPV module designs implies that the methodology for I–V curve characterization must be checked and corrected if needed for other module configurations. This will allow generalizing the results of the analysis to other HCPV technologies.

I–V curves simulated with the developed methodology should be compared with data measured on real operating HCPV plants. For this purpose, some effects not included in the methodology should be analyzed such as misalignment, soiling, energy losses in wires or inverters operation.

The potential of the methodology has not been fully exploited. It is expected that it can be used for developing new methods applicable in the design of HCPV power plants, evaluation of existing systems, energy prediction, etc.

Other possible research line is the development of simplified easy-to-use methods for their integration in industrial photovoltaic software packages.

References

1. Lorenzo E, Narvarte L, Muñoz J (2011) Tracking and back-tracking. Prog Photovolt Res Appl 19:747–753
2. Alonso-García MC, Ruiz JM, Herrmann W (2006) Computer simulation of shading effects in photovoltaic arrays. Renew Energy 31:1986–1993
3. Woyte A, Nijs J, Belmans R (2003) Partial shadowing of photovoltaic arrays with different system configurations: literature survey and field results. Sol Energy 74:217–233
4. Wolf M, Rauschenbach HS (1963) Series resistance effects on solar cell measurements. Adv Energy Convers 3:455–479
5. Rauschenbach HS (1971) Electrical output of shadowed solar arrays. IEEE Trans Electron Dev 18:483–490
6. Quaschning V, Hanitsch R (1996) Influence of shading on electrical parameters of solar cells. In: IEEE photovoltaic specialists conference, p 1287
7. Abete A, Barbisio E, Cane F, Demartini P (1990) Analysis of photovoltaic modules with protection diodes in presence of mismatching. In: Proceedings of IEEE photovoltaic specialists conference, p 1005
8. Kawamura H, Naka K, Yonekura N, Yamanaka S, Kawamura H, Ohno H et al (2003) Simulation of I–V characteristics of a PV module with shaded PV cells. Sol Energy Mater Sol Cells 75:613–621
9. Kajihara A, Harakawa T (2005) Model of photovoltaic cell circuits under partial shading. In: Proceedings of IEEE international conference on industrial technology, p 866
10. Silvestre S, Chouder A (2008) Effects of shadowing on photovoltaic module performance. Prog Photovolt Res Appl 16:141–149
11. Wang YJ, Hsu PC (2011) An investigation on partial shading of PV modules with different connection configurations of PV cells. Energy 36:3069–3078
12. Dolara A, Lazaroiu GC, Leva S, Manzolini G (2013) Experimental investigation of partial shading scenarios on PV (photovoltaic) modules. Energy 55:466–475
13. Bishop JW (1988) Computer simulation of the effects of electrical mismatches in photovoltaic cell interconnection circuits. Sol Cells 25:73–89
14. Quaschning V, Hanitsch R (1995) Numerical simulation of photovoltaic generators with shaded cells. In: Proceedings of universities power engineering conference, p 583
15. Quaschning V, Hanitsch R (1996) Numerical simulation of current voltage characteristics of photovoltaic systems with shaded solar cells. Sol Energy 56:513–520
16. Karatepe E, Boztepe M, Çolak M (2007) Development of a suitable model for characterizing photovoltaic arrays with shaded solar cells. Sol Energy 81:977–992
17. Brecl K, Topi M (2011) Self-shading losses of fixed free-standing PV arrays. Renew Energy 36:3211–3216
18. Araki K, Kumagai I, Nagai H (2010) Theory and experimental proof of shading loss of multi–trackers CPV system. In: Proceedings of world conference on photovoltaic energy conversion, p 114

19. Araki K (2012) Two interactive and practical methods for optimization of tracker allocation in a given land. In: Proceedings of the 8th international conference on concentrating photovoltaic systems, vol 1477. AIP Conf Proc, pp 244–247
20. Kim YS, Kang SM, Winston R (2013) Modeling of a concentrating photovoltaic system for optimum land use. Prog Photovolt Res Appl 21:240–249
21. Rodrigo P, Fernández Eduardo F, Almonacid F, Pérez-Higueras PJ (2013) Outdoor measurement of high concentration photovoltaic receivers operating with partial shading on the primary optics. Energy 61:583–588
22. IEC 62108 (2007) Concentrator photovoltaic (CPV) modules and assemblies—design qualification and type approval, 1.0 edn. Geneve
23. Alonso-García MC, Ruíz JM (2006) Analysis and modelling the reverse characteristic of photovoltaic cells. Sol Energy Mater Sol Cells 90:1105–1120
24. Royne A, Dey CJ, Mills DR (2005) Cooling of photovoltaic cells under concentrated illumination: a critical review. Sol Energy Mater Sol Cells 86:451–483
25. Fernández Eduardo F, Pérez-Higueras PJ, García Loureiro AJ, Gómez Vidal P (2013) Outdoor evaluation of concentrator photovoltaic systems modules from different manufacturers: first results and steps. Prog Photovolt Res Appl 21:693–701
26. Peharz G, Ferrer Rodríguez JP, Siefer G, Bett AW (2011) A method for using CPV modules as temperature sensors and its application to rating procedures. Sol Energy Mater Sol Cells 95:2734–2744
27. Fernández EF, Siefer G, Schachtner M, García-Loureiro AJ, Pérez-Higueras PJ (2012) Temperature coefficients of monolithic III–V triple-junction solar cells under different spectra and irradiance levels. In: Proceedings of the 8th international conference on concentrating photovoltaic systems CPV-8, vol 1477. AIP Conf Proc, pp 189–193
28. Fernández EF, García-Loureiro AJ, Pérez-Higueras PJ, Siefer G (2011) Monolithic III–V triple-junction solar cells under different temperatures and spectra. In: Proceedings of Spanish conference on electron devices CDE 2011, Article No. 5744222
29. Siefer G, Abbot P, Baur C, Schleg T, Bett AW (2005) Determination of the temperature coefficients of various III–V solar cells. In: Proceedings of European photovoltaic solar energy conference, p 495
30. Siefer G, Baur C, Meusel M, Dimroth F, Bett AW, Warta W (2002) Influence of the simulator spectrum on the calibration of multi–junction solar cells under concentration. In: Proceedings of IEEE photovoltaic specialists conference, p 836
31. Fernández EF, Pérez-Higueras PJ, Almonacid F, García Loureiro AJ, Fernández JI, Rodrigo P et al (2012) Quantifying the effect of air temperature in CPV modules under outdoor conditions. In: Proceedings of 8th international conference on concentrating photovoltaic systems CPV-8, vol 1477. AIP Conf Proc, pp 194–197
32. Peharz G, Ferrer Rodríguez JP, Siefer G, Bett AW (2011) Investigations on the temperature dependence of CPV modules equipped with triple-junction solar cells. Prog Photovolt Res Appl 19:54–60
33. King DL, Boyson WE, Kratochvil JA (2004) Photovoltaic array performance model. Sandia National Laboratories, SAND2004-3535
34. Almonacid F, Pérez-Higueras PJ, Fernández Eduardo F, Rodrigo P (2012) Relation between the cell temperature of a HCPV module and atmospheric parameters. Sol Energy Mater Sol Cells 105:322–327
35. Ben Or A, Appelbaum J (2013) Estimation of multi-junction solar cell parameters. Prog Photovolt Res Appl 21:713–723
36. Powell MJD (1970) A Fortran subroutine for solving systems of nonlinear algebraic equations. In: Rabinowitz P (ed) Numerical methods for nonlinear algebraic equations
37. Pierret RF (1996) Semiconductor device fundamentals. Addison Wesley, Boston
38. IEC 62670-1 (2013) Photovoltaic concentrators (CPV)—performance testing—Part 1: standard conditions, 1.0 edn. Geneve

39. Palomino B, Llamas Z, Rodrigo P, Pérez-Higueras PJ (2014) Procedimiento para el cálculo de la distribución óptima de seguidores en un campo fotovoltaico de alta concentración. Pistas Educativas 108:668–690
40. Pérez-Higueras PJ, Rodrigo P, Fernández Eduardo F, Almonacid F, Hontoria L (2012) A simplified method for estimating direct normal solar irradiation from global horizontal irradiation useful for CPV applications. Renew Sustain Energy Rev 16:5529–5534
41. Iqbal M (1983) An introduction to solar radiation. Academic Press, Toronto

High-Concentrator Photovoltaic Systems Configuration and Inverters

Emilio Muñoz-Cerón, Francisco J. Muñoz-Rodríguez, Juan de la Casa and Pedro Pérez-Higueras

Abstract A high-concentrator photovoltaic (HCPV) system is the result of the electrical interconnection of several CPV modules with additional components denominated "balance of system." The wide variety of elements that compose a module makes possible different types of HCPV systems, although the most widespread is the point-focus pedestal type. Among the elements that compose an HCPV system, the inverter, which has been studied deeply for flat-PV systems, should be adapted to the particularities of HCPV technology. A different definition of weighted efficiency is proposed that has been adapted to an HCPV system located in southern Spain. This definition is compared with other ones proposed by some authors within this technology and also with the most used conventional PV systems definitions, which are the European and Californian efficiencies. It is highlighted that the differences are minimal. Beyond that, a novel classification of the most common interconnection configurations is proposed and some experiments were performed to show that the maximum power point tracker methods traditionally used for standard PV systems are somehow also valid for HCPV systems.

1 Introduction

There are several aspects in which the composition of a high-concentrator photovoltaic (HCPV) system differs from silicon-based Photovoltaic (PV) modules. First, the solar cells used are made of several layers of semiconductor material [multijunction (MJ) devices] that fragment the sunlight absorption capacity depending on

E. Muñoz-Cerón (✉)
Center for Advanced Studies in Energy and Environment, University of Jaén, Jaén, Spain
e-mail: emunoz@ujaen.es

E. Muñoz-Cerón · F.J. Muñoz-Rodríguez · J. de la Casa · P. Pérez-Higueras
IDEA Research Group, University of Jaén, Jaén, Spain

P. Pérez-Higueras and E.F. Fernández (eds.), *High Concentrator Photovoltaics*,
Green Energy and Technology, DOI 10.1007/978-3-319-15039-0_8

the spectral composition of the incident light. This division allows better and improved conversion efficiency, but it requires the addition of optical elements that focus and concentrates the incoming light. For that purpose, it is necessary to use a tracking mechanism that is permanently tracking the Sun's daily path. The wide array of possible combinations of MJ solar cells used, the optical stages, and the tracking mechanism increase the different types of HCPV currently existing. In this chapter, a brief overview of the most used systems will be presented.

In addition, standard elements used in flat-PV module systems, such as inverters, will also be necessary for DC/AC conversion of the electricity generated. The types and configurations of inverters will be reviewed, and some modifications focused on the particularities of HCPV technology will be presented. Within this revision of the inverter's configuration, the definition of "weighted average efficiency" adapted to this technology will be studied. Beyond that, a comparison with the most common efficiencies used (European and Californian) will be undertaken.

In any PV system, it is also important how the modules are connected to the grid; thus, for that purpose the possibilities within the particularities of HCPV technology will be analyzed.

Furthermore, the device responsible for providing the maximum power point (MPP) in the array will also be covered. A brief summary of the maximum power point tracking (MPPT) techniques will be described focused especially on direct methods because they are the most used in practice. Among these, perturb-and-observe (P&O) algorithms will be highlighted.

2 Components and Types of HCPV Systems

An HCPV system is the result of the electrical interconnection of several HCPV modules with additional components that are denominated "balance of system" (BOS).

According to the definition found in the recommendation report from the Sandia Laboratories and several CPV standards published, an HCPV module is the smallest, complete, environmentally protected assembly of receivers permanently mounted in the correct orientation relative to the primary optics—together with the appropriate lens and housing seals, electrical and interconnection components, and mounting elements—that accepts nonconcentrated solar radiation and transforms it into electrical energy when aligned with the Sun (Fig. 1).

In this aspect, an HCPV receiver is an assembly of one or more concentrator cells and secondary optics (if used) that accept concentrated sunlight and incorporates the means for thermal energy removal (active or passive heat sinks) and electrical energy transfer [1–3].

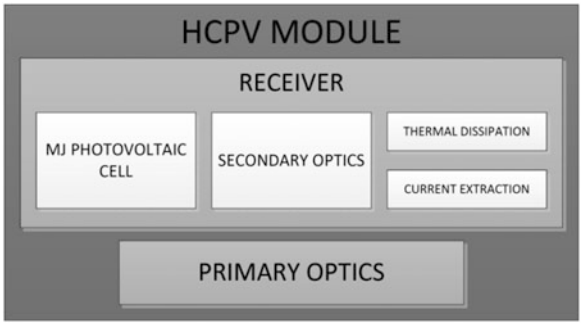

Fig. 1 Composition of a HCPV module

Currently MJ cells are the basis of HCPV systems. These devices are based on different layers of semiconductor materials, so they split their sensitivity to the Sun's spectrum and thus are better matched throughout the Sun's wavelength distribution than single-junction devices such as silicon-based PV cells.

Regarding its manufacturing process, two types of MJ cells can be distinguished: mechanical stacked cells and monolithic cells. The latter ones are the most extended, and they are manufactured by deposition of the semiconductor material under the same substrate. Depending on the lattice constant of the materials used, these monolithic devices are divided into lattice-matched and metamorphic, indicating whether or not the lattice parameters of the material are coincident. In the literature, there is a better detailed explanation of the differences between the monolithic solar cells [4, 5].

The optical element is responsible for concentrating the solar radiation on the cell's surface so that more energy at the output of the cell is obtained as a consequence of the increment in the luminous flux incident on the MJ device. The first consequence of using an optical stage is that the area of semiconductor material, that is, the MJ cell, is reduced, so there is a great potential in decreasing costs because the cells are the most expensive components in a HCPV module.

According to the concentration mechanism used by the optical element, a first division of the HCPV systems can be performed according to reflective or refractive mechanisms and the shape of the focus, which may be linear one or point one. Figure 2 shows the different possible combinations.

Regarding the secondary optics used, there is an extensive catalogue that adds more variety to the sort of HCPV modules that could be manufactured, but its classification is out of the scope of this chapter [6].

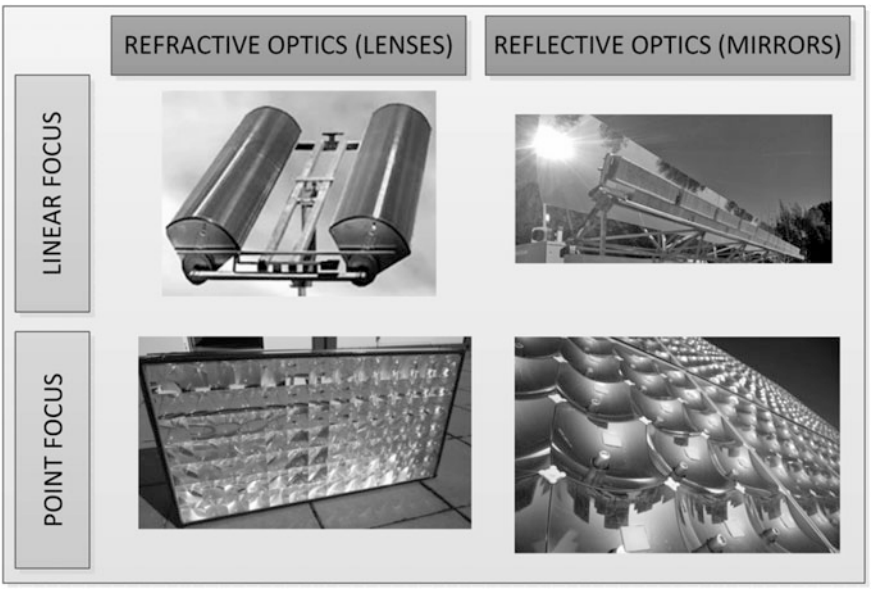

Fig. 2 Typologies based on the optical element

In contrast, the BOS elements that comprise an HCPV system includes any tracking mechanism with its corresponding foundation and supporting structures, the external DC and AC wiring, the connection boxes, the electrical protection devices as well as the inverters or other power-conditioning systems, and the appropriate monitoring equipment.

In the HCPV modules, there are different types of MJ solar cells; several optical typologies, which can be applied in a single stage or a two-concentrating stage; and the tracking mechanism, which may also vary in its constitution. Beyond using an HCPV classification based on the geometrical shape of the modules and/or its concentration ratio, the possible combination of such elements leads to a numerous ways of classifying HCPV systems, but usually the concentrating optics define the types of systems, although there can be a wide variety among these optics.

Although several HCPV classification tables and analysis have been published elsewhere [7, 8], it is more useful to undertake a classification procedure based on the current state of the art regarding the most used and widespread HCPV systems. In this aspect, International Standard IEC 62108 covers up to five different Technologies, which can be observed in the sequence of Figs. 3, 4, 5, 6 and 7.

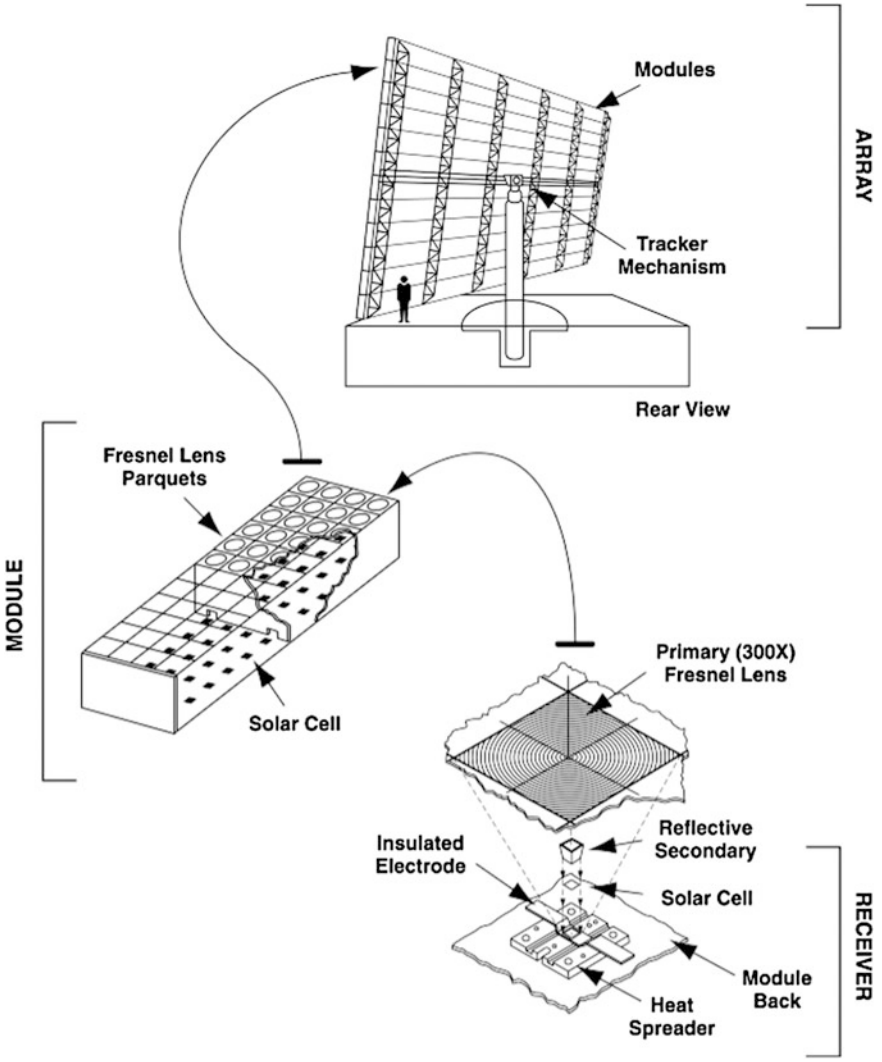

Fig. 3 Point-focus Fresnel lens HCPV system [3]

Among the classification of CPV systems, most of the current manufacturers are designing the Point-focus Fresnel lens HCPV system (Fig. 3) because there is more evidence and proofs of its good operational behavior.

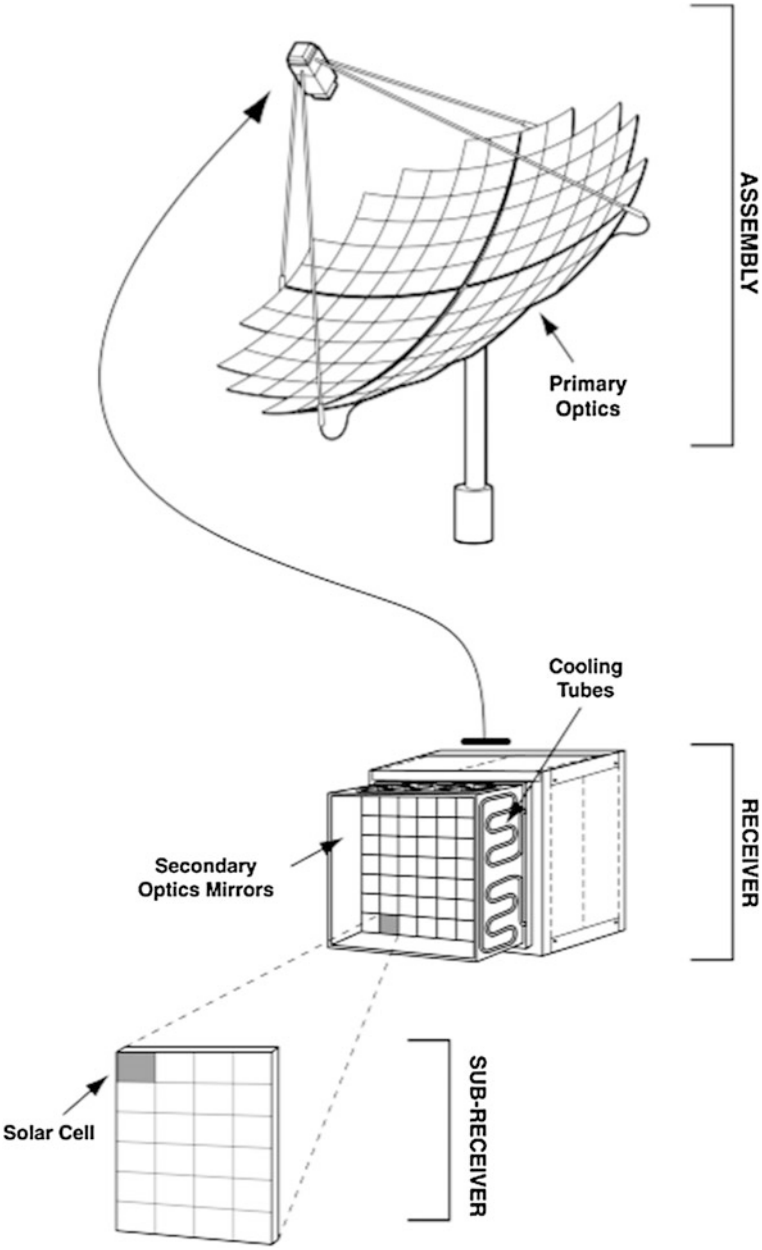

Fig. 4 Point-focus dish CPV system [3]

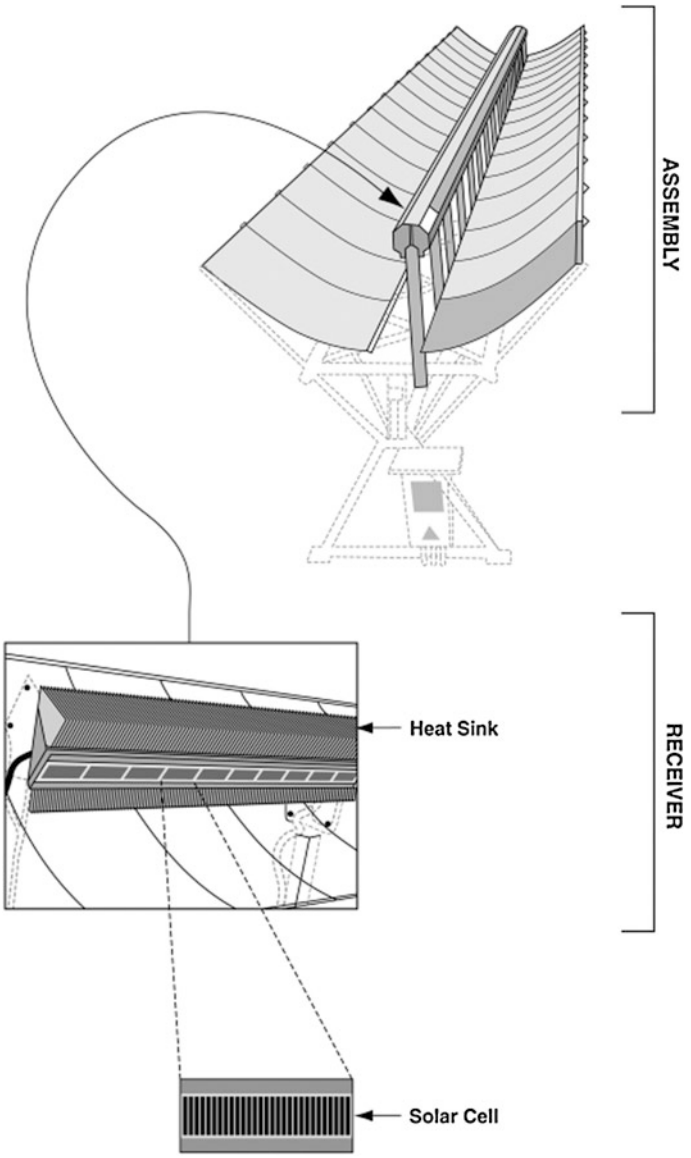

Fig. 5 Linear-focus through CPV system [3]

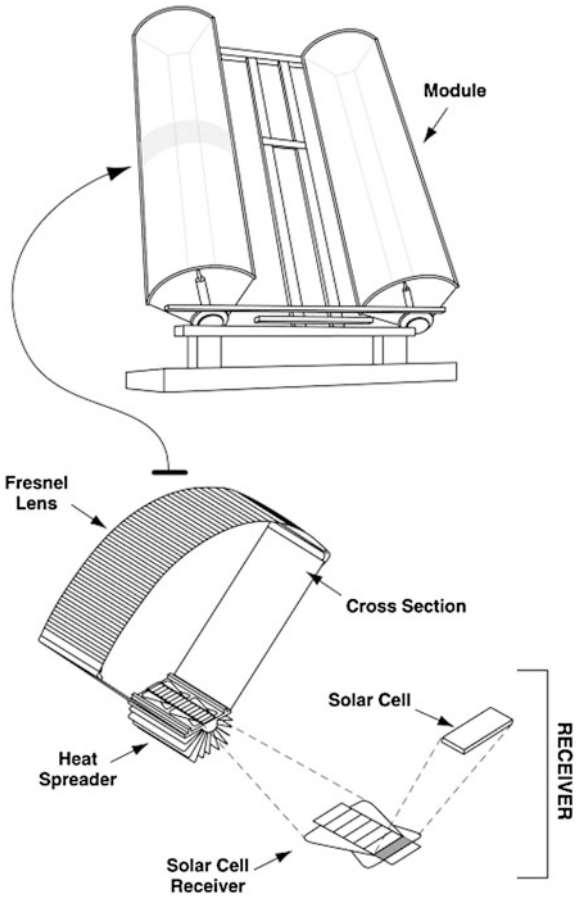

Fig. 6 Linear-focus Fresnel lens CPV system [3]

The following most-widespread HCPV system, albeit in a minor penetration level, is the point-focus dish. It represents an added-value system because of its active cooling system because it can take advantage of the heat transmitted to the thermal fluid so as a whole it can operate as a hybrid CPV/thermal device.

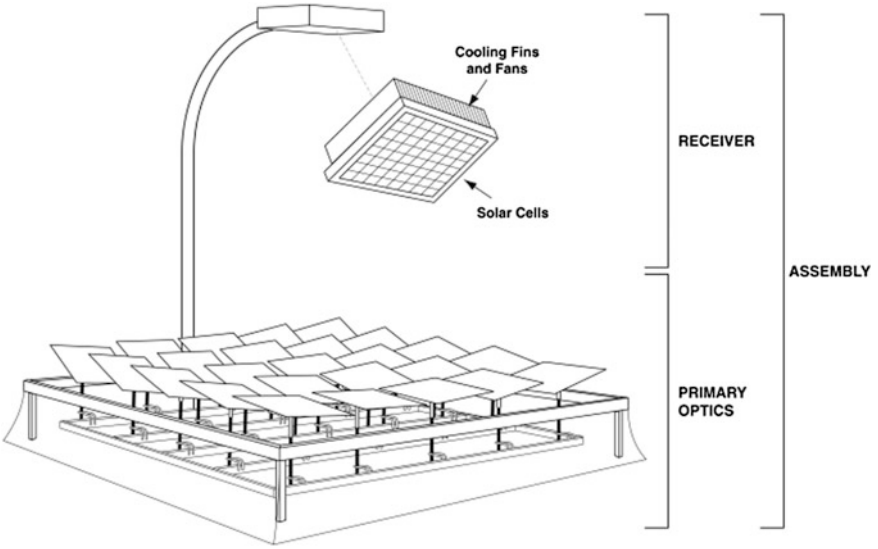

Fig. 7 Heliostat CPV system [3]

3 Inverter

3.1 Definition and General Characteristics

As well as in traditional flat silicon-based PVs, the direct current (DC) electricity generated by HCPV modules must be transformed into alternating current (AC), as well as adapt it to the characteristics of the electrical grid in terms of voltage levels and frequency. The inverter is the electronic equipment responsible for the interface between the PV generator and the electrical-distribution network.

For obtaining the maximum output of a HCPV module or system, the inverter should be always working at the MPP of the current–voltage (I–V) curve. It is well known that the I–V characteristics of a PV module are dependent on the irradiance levels and ambient temperature, among other factors, and in the case of HCPV technology, the spectral content of the incoming sunlight will also be a crucial parameter. Those variations imply that at any moment the MPP would be constantly changing and for that purpose, any inverter should implement a MPPT mechanism to ensure that the module achieves its maximum power. In further sections, different MPPT methods will be discussed.

According to the characteristics that any inverter should possess, in the following tables there is a summary of the main ones, which differentiate DC side characteristics from AC ones (Table 1 and 2).

These characteristics are a brief adaptation of the European Standard EN 50524:2009, which contains the specifications for the data sheet and the name plate for PV inverters. The International Electrotechnical Commission also intends to

Table 1 Typical input characteristics of an inverter

DC main characteristics	
Nominal DC power	$P_{N,DC}$
Maximum input (HCPV) power	$P_{DC,max}$
Nominal DC voltage	$V_{N,DC}$
Maximum input (HCPV) voltage	$V_{DC,max}$
Minimum input (HCPV) voltage	$V_{DC,min}$
MPP voltage range	V_{MPPT}
Nominal DC current	$I_{N,DC}$
Maximum input (HCPV) current	$I_{DC,max}$

Table 2 The inverter's main AC characteristics

AC main characteristics	
Nominal AC power	$P_{N,AC}$
Maximum AC power	$P_{AC,max}$
Power factor	cos φ
Nominal output voltage	$V_{N,AC}$
Output AC voltage range	V_{AC}
Nominal AC current	$I_{N,AC}$
Maximum AC current	$I_{AC,max}$
Nominal frequency	F_N
Frequency range	f
Total harmonic distortion	TDH
Feed-in phases	–

publish a standard with the same purpose (IEC 62894; Photovoltaic inverters—Data sheet and name plate).

Beyond the aforementioned electrical characteristics, the specification of the inverter's efficiency is an important parameter in order to identify the AC/DC conversion losses. This conversion efficiency will depend on the ratio between the AC and DC powers

$$\eta_{CONV} = \frac{P_{OUTPUT}}{P_{INPUT}} = \frac{P_{AC}}{P_{DC}} \quad (1)$$

However, the input power value of the inverter (P_{DC}) constantly changes depending on the ambient parameters, mainly the ones related with the radiation level, spectrum, and temperature. As was stated previously, the MPPT mechanism that incorporates all of the inverters with the aim of making the PV system operate at its optimum point will introduce additional losses depending on the quality of this inverter's adjustment. The differences among the input power (P_{DC}) detected by the tracking mechanism and the real instant maximum power (P_{HCPV_MPP}) of the PV system under the operating ambient conditions will be used for describing the tracking or adaptive efficiency:

$$\eta_{\mathrm{MPPT}} = \frac{P_{\mathrm{DC}}}{P_{\mathrm{HCPV\_MPP}}} \tag{2}$$

The total efficiency, also defined as "static efficiency," is the product of both the conversion and tracking efficiencies and it will vary depending on the load of the inverter:

$$\eta_{\mathrm{TOTAL}} = \eta_{\mathrm{CONV}} \cdot \eta_{\mathrm{MPPT}} \tag{3}$$

After this distinction, it is clear that the nominal and maximum efficiency of an inverter will only be reached under certain environment scenarios and that the instant efficiency will be dependent on the input voltage and the power load, which are also dependent on the irradiance, spectrum, and temperature conditions; thus, it is more useful to plot a efficiency characteristic curve that depends on the relative performance of the inverter, that is, the relation between the instantaneous power delivered and the nominal one ($P_{\mathrm{N,AC}}$) under different input scenarios (Fig. 8).

The different ranges of operation applicable for the static efficiency measurement make it necessary to define some weighted averaging efficiencies that consider different fractions of maximum power and input voltage under certain ambient conditions. The set of weights (F_n) and the values of efficiency (η_n), depending on the fraction of the maximum power, will define this weighted efficiency:

$$\eta_{\mathrm{WEIGHTED}} = \sum_n F_n \cdot \eta_n \tag{4}$$

Depending on the location characteristics (mainly the level of radiation), the distribution of the weights and the values of efficiencies will change. To show those differences and also for comparison purposes, two weighted efficiencies have been defined worldwide depending on the frequency at which certain fractions of efficiency are reached.

The European efficiency is scaled considering the climate values of Central Europe, meanwhile the Californian efficiency (CEC), considers higher values of

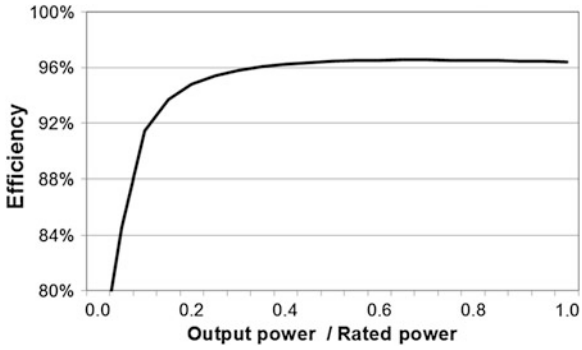

Fig. 8 Typical inverter's efficiency curve

energy at relative performance values >30 %. The formulas with the set of weights and the values of efficiency are described as follows:

$$\eta_{\mathrm{EURO}} = 0.03 \cdot \eta_{5\%} + 0.06 \cdot \eta_{10\%} + 0.13 \cdot \eta_{20\%} + 0.1 \cdot \eta_{30\%} + 0.48 \cdot \eta_{50\%} + 0.2 \cdot \eta_{100\%} \quad (5)$$

$$\eta_{\mathrm{CEC}} = 0.04 \cdot \eta_{10\%} + 0.05 \cdot \eta_{20\%} + 0.12 \cdot \eta_{30\%} + 0.21 \cdot \eta_{50\%} + 0.53 \cdot \eta_{75\%} + 0.05 \cdot \eta_{100\%} \quad (6)$$

The previous weighted-average efficiency definitions were specified for silicon-based PV systems, but due to the particularities of the HCPV technology, it is necessary to adapt the distribution of weighted factors and fractions of maximum power.

First of all, HCPV systems are designed for the use of direct normal irradiation (DNI) in locations where high levels of this component can be achieved. As an example, Fig. 9 shows the differences in the energy generated for a location in the south of Spain where there is a direct normal irradiation level of >2000 kWh m^{-2} $year^{-1}$. The global horizontal irradiation *versus* the DNI values have been considered, and it is clear that the energy produced with an HCPV system is generated at higher levels of irradiance.

Under the previous scenario, it is then recommended to study the percentage distribution of the annual direct irradiation energy classified per DNI levels in a

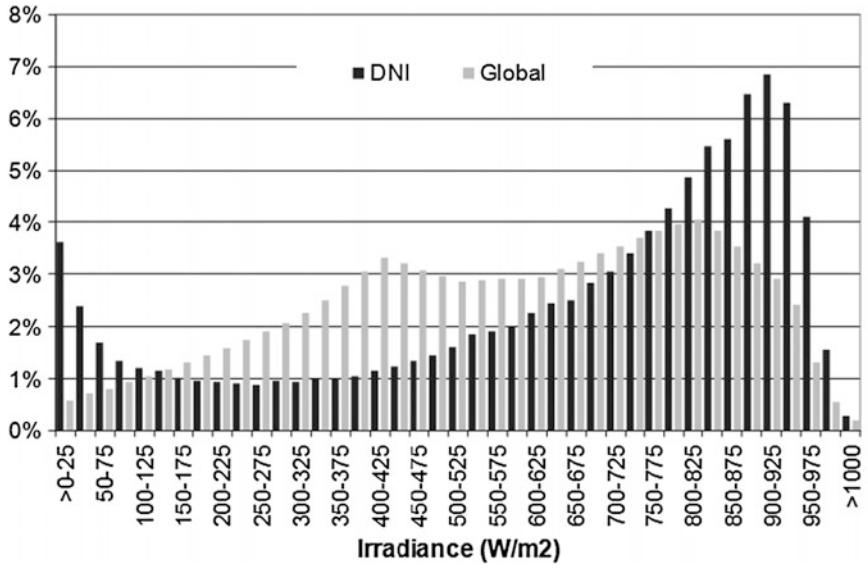

Fig. 9 Global and direct radiation level differences in a location in southern Spain

certain location to analyze the implications of these distribution changes in the efficiency values of HCPV systems.

Some long-term measurements were undertaken at the Centre for Advanced Studies in Energy and Environment of the University of Jaén (Southern Spain) where it was detected that the maximum contribution to the annual energy comes from irradiance levels between 800 and 900 W m^{-2} (see Fig. 10). Moreover, 95 % of the total direct energy received is located in the range 400–1000 W m^{-2} [9].

If it is considered that the energy generated by a HCPV system is proportional to the DNI at the aforementioned location, the following formula of the weighted efficiency of an inverter used in a HCPV system is proposed:

$$\eta_{\mathrm{HCPV}-1} = 0.016 \cdot \eta_{10\%} + 0.036 \cdot \eta_{30\%} + 0.1 \cdot \eta_{50\%} + 0.27 \cdot \eta_{75\%} + 0.58 \cdot \eta_{100\%} \quad (7)$$

Currently some others researchers are working on the definition of weighted average efficiencies for HCPV technology. In the laboratory of Solar Systems at CEA-INES, located in France, Domínguez et al. [10] have analyzed several inverters used in HCPV systems together with the particularities of the distribution of the irradiation levels measured in that location. According to the results obtained, they have proposed certain set of weights (F_n) and efficiency values (η_n) depending on the fraction of the maximum power measured:

$$\eta_{\mathrm{HCPV}-2} = 0.025 \cdot \eta_{10\%} + 0.045 \cdot \eta_{30\%} + 0.11 \cdot \eta_{50\%} + 0.32 \cdot \eta_{75\%} + 0.50 \cdot \eta_{100\%} \quad (8)$$

Comparing the expressions proposed for HCPV technology, there is a significant similarity between the set of weights and the distribution of powers for the two locations chosen.

It is also interesting to compare the efficiencies calculated for the particularities of the HCPV system with the commonly used in silicon-based PV system, which was previously analyzed using the European and CEC efficiencies. In Fig. 11 it can

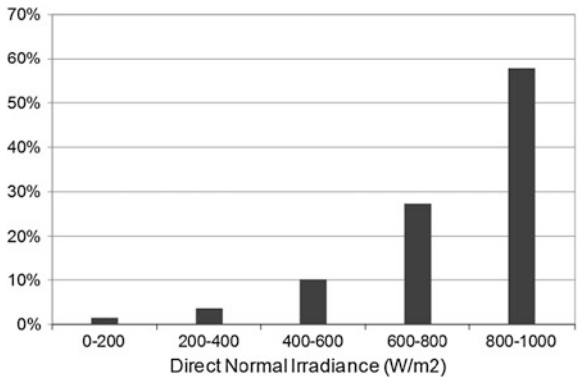

Fig. 10 Percentage of annual direct normal irradiation at Jaén

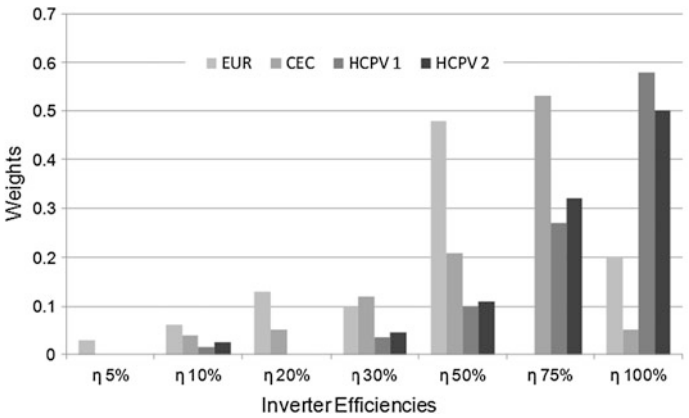

Fig. 11 Distribution of the set of weights for inverter efficiencies

Table 3 Results for the comparison of weighted efficiencies

Inverter's weighted efficiencies	
European efficiency	96.4 %
Californian (CEC) efficiency	96.7 %
HCPV-1	97.0 %
HCPV-2	96.8 %

be observed that these differences are significant as expected. Furthermore, it corroborates the previous statement where it was mentioned that the HCPV system operates at higher levels of power, so the values at those fractions of efficiencies are much greater than those seen with standard flat-panel PV systems.

The results of using the inverter shown in Fig. 8 to calculate the weighted averaging efficiencies expressed in this chapter are listed in Table 3. Although the previously cited visible different distribution of weights, i.e., the variations calculated for each efficiency, are minimal, for practical purposes—and in the case of the HCPV systems analyzed—one could still use the CEC, which it is the most widespread one, assuming some minimum errors.

3.2 Inverter Types and Configurations

There are a wide variety of inverters, depending on the power of the installation, from ones that manage hundreds of watts to devices capable of dealing with powers up to hundreds of kilowatts. The main classification of inverters, regarding their configuration, is related to the number of these devices per PV generator as well as the way they in which they are electrically connected. Based on that definition, in the following section, different configuration types used for HCPV grid connection will be discussed.

3.2.1 Central Inverter for Several HCPV Trackers

A central inverter configuration connects several HCPV trackers to a single large inverter. Normally this type of connection is used in medium-sized plants, in the range of hundreds of kW, although commercial inverters up to 1 MW exist.

This sort of configuration simplifies the AC connection scheme, but the DC section becomes complicated because if the voltage is increased (when HCPV generators are connected serially), the cross-section of the wiring will be decreased but the high electrical risk will be high. Nevertheless, if the system is connected in parallel, the cross-section of the wiring increases and so do the thermal losses in the electrical transportation to the inverter.

Another disadvantage of this configuration within an HCPV plant is related to misalignment issues and self-shadowing problems that cause the overall plant might be limited, or even ruled, by the poor operational state of one tracker. This is the main reason why this configuration is not frequently used in HCPV systems (Fig. 12).

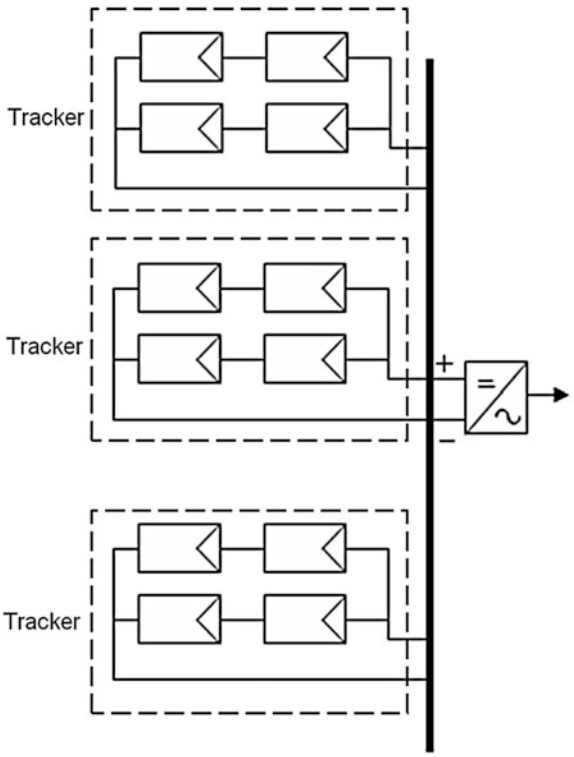

Fig. 12 Typical configuration of central inverter for several trackers

3.2.2 One Inverter at Each HCPV Tracker

This configuration is one of the most widespread in HCPV plants, and it consists of the installation of one inverter per unit of tracking system. Depending on the configuration of the plant, the inverters used may be three-phase or single-phase ones. In the first case, the interconnection of the output is simple, but in the case of using a single-phase inverter per tracker, the AC side interconnection may be deeply studied to balance the electricity supply in each phase. In any case, the interconnection of the subsystems are less critical that in the central inverter's configuration.

Nevertheless, the failure, misalignment, and unpredicted shadowing of one tracker does not mean the complete failure of the entire PV plant, and that it is the main advantage of this configuration. It also allows operational and maintenance protocols without shutting down the complete plant, thus conferring economic and energy savings (Fig. 13).

A particular variation of this configuration has been implemented by some manufacturers. They have designed specific inverters for HCPV where beyond the electronics for the DC/AC conversion and the MPPT methodology used, they have also included the control stage for the tracker's motion. These sorts of devices are denominated "*tracking inverters*" (Fig. 14) [11].

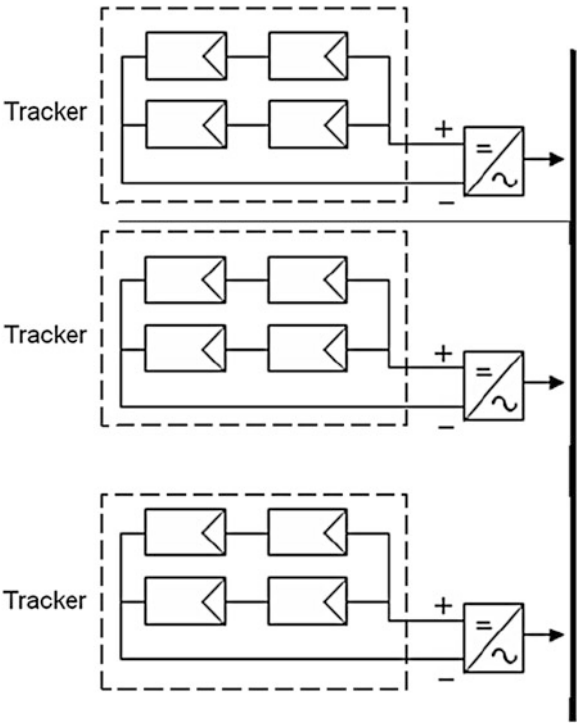

Fig. 13 Tracker oriented inverter configuration

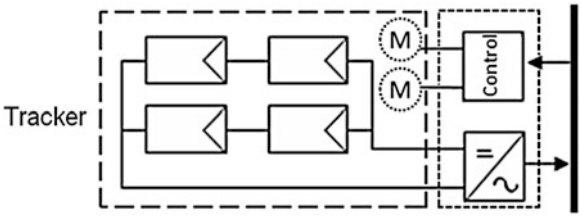

Fig. 14 Diagram of the tracking inverter device

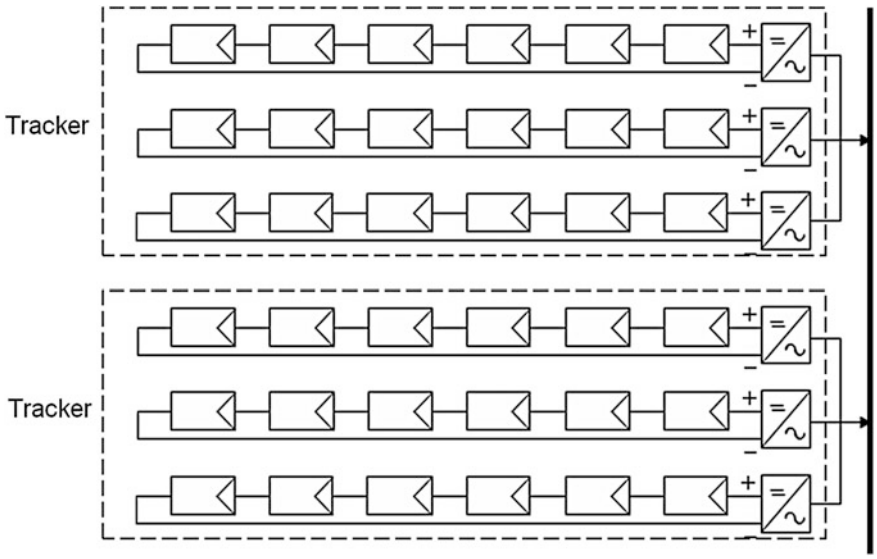

Fig. 15 Several inverters per tracker unit configuration

3.2.3 Several Inverters Per Tracker Unit

This configuration is a variation of the previous one, but instead of connecting all of the modules of a tracker to a single inverter (three-phase or single-phase), the different strings of modules that compose a tracker subsystem are connected to a different inverter, so each tracker has several inverters that afterward are interconnected in the AC side (Fig. 15). Beyond the advantages aforementioned for the tracker oriented configuration, this one adds the reduction of mismatch problems because it will not affect the rest of strings of the tracker.

3.2.4 One HCPV Module One Inverter

This configuration is still under development and consists of installing one low-power inverter (hundreds of watts) per HCPV module. Some authors denominate this device as a "microinverter" (Fig. 16).

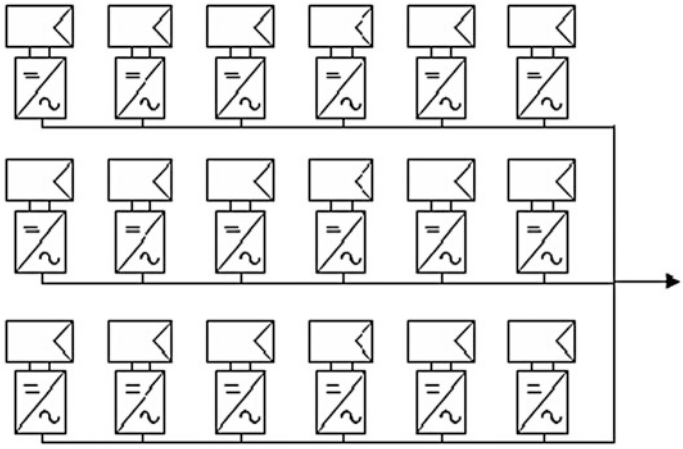

Fig. 16 One HCPV module—one inverter configuration

Each subsystem will have as many inverters as modules that compound the system. From a wide perspective, this configuration is the minimization of the previous configurations, so it increases proportionally the advantages related to misalignments and mismatching issues together with a decrease in Ohmic losses. Nevertheless, this configuration may pose other problems related to the MPP mechanisms.

3.3 Review of Maximum Power Point Tracking Methods

3.3.1 Maximum Power Point Tracker

A PV generator provides a single I–V curve for a given irradiance and temperature. In this curve, there is only one unique point, called the "maximum power point," at which the generator operates with maximum efficiency and delivers its maximum power. The MPP is variable over time because the I–V curve changes with irradiance and temperature as shown in Fig. 17.

The device responsible for maintaining the generator working at MPP is the MPPT. This type of device is a switch-mode power converter and plays an important role in PV systems as they maximize the output power provided by a PV array. In the case of grid-connected systems, this device is placed previous to the input of the inverter and it is mainly constituted by a DC/DC converter and a control system (see Fig. 18).

This control system may be either analog or digital and can monitor one or two variables from the generator to manage the MPP search process. The MPP is not so easy to achieve because it is not previously known, and the function that defines the

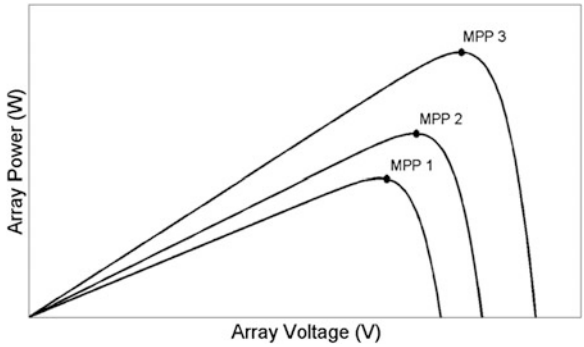

Fig. 17 Typical Power–Voltage curves of a PV generator for different levels of irradiance and temperature

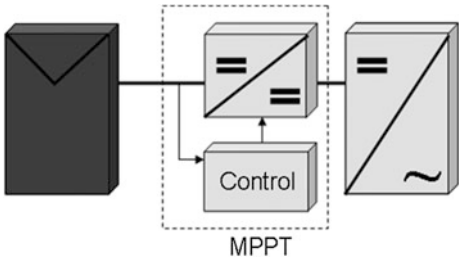

Fig. 18 Block diagram of a Maximum Power Point Tracker

dependency of the MPP on irradiance and temperature is nonlinear. Furthermore, the power–voltage (P–V) curve may have several local maxima due to partial shadowing. This issue increases the complexity of determining the location of the absolute MPP. In this way, this unique point location can be determined through calculations based on mathematical models or through searching algorithms. In the latter case, the MPPT control system, throughout a given MPPT technique or algorithm, may oversee some parameters, such as voltage and current generator, and provide the adequate settings and duty cycle to the DC/DC converter to track and determine the MPP of the PV array.

The levels of DNI may vary in a short interval of time, thus modifying the MPP of a certain HCPV system. A long-term analysis of the frequency and value ranges of the DNI increments has been performed in a location of the south of Spain. In Fig. 19, the percentage of rapid increases (increments) in both global and direct normal irradiance in just a 1-min interval is shown.

In slightly >3 % of the 1-min interval measurements, DNI increases are contained in a range of 100–200 W m^{-2}, and approxiately 1.5 % are in the range of 200–300 W m^{-2}. Beyond this point all higher increments, gathered in a 100 W m^{-2}

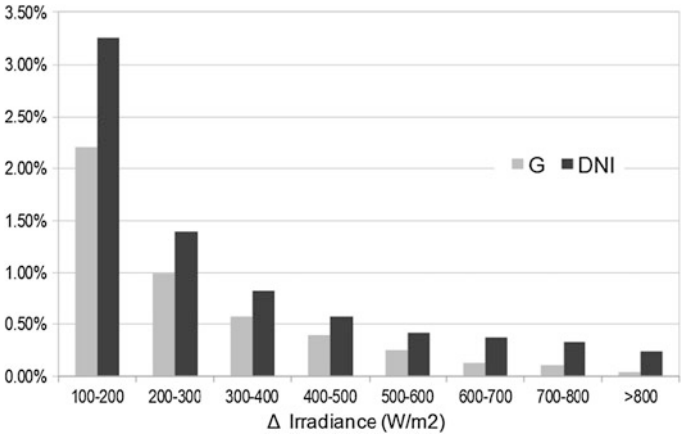

Fig. 19 Rapid increments in global and direct irradiance during 1 min interval measurements in a long-term campaign in the south of Spain

step, are <1 % of the measurements performed. It should be pointed out that the majority (>90 %) of the irradiance increases are <100 W m^{-2}.

In addition, DNI varies a little bit faster than global irradiance values. In this sense, MPPT techniques used in inverters for HCPV systems should be able to overcome these more rapid changes in irradiance.

However, it is shown in Figs. 22 and 23 that MPP trackers in actual inverters may perfectly determine the MPP in HCPV systems. Advanced MPPT algorithms used in inverters for flat PV systems operate successfully under very rapid changing conditions such as the ones that may occur on partly cloudy days when a very sharp increases in irradiance take place.

The next section intends to provide a brief but illustrative summary of MPPT techniques. It will especially focus on direct methods because they are the most used in practice to the detriment of indirect methods. Among the former, perturb-and-observe (P&O) algorithms will be highlighted.

3.3.2 Direct MPPT Techniques

Most MPPT algorithms are based on direct methods in which both PV current and voltage are continuously measured, and the MPP of the array is calculated from these measurements. The most widely used are known as P&O methods. Indirect methods, in which the MPP is estimated either from PV generator models or from a database that includes typical curves of PV generators for different irradiances and temperatures instead of direct measurements, can be found in the literature. This type of method shows some drawbacks because the MPP deviation and thus energy losses are significant when the real conditions differ with respect to those supposed in the considered model. In contrast, direct methods are based on direct

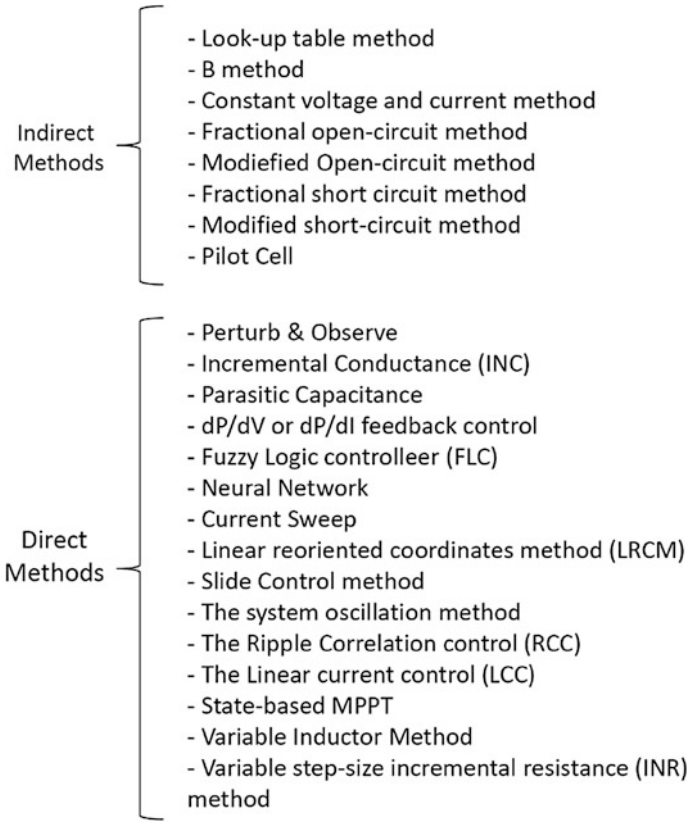

Fig. 20 Classification of MPPT algorithms [13]

measurements and are independent from any irradiance and temperature levels. In this way, the latter (also known as "true seeking methods") offer the advantage of providing the maximum power of the array regardless of the irradiance and temperature.

This section will focus on direct methods. Nonetheless, the reader, if interested, can find further and more detailed information about the different MPPT techniques (Fig. 20), both indirect and direct, in sources [12–14].

Perturb and Observe (P&O) method

Due to its simplicity and ease of implementation, P&O is the most popular algorithm used to obtain the MPP. This direct technique is based on the introduction of periodical perturbations into the system, the effects of which are are used to obtain the MPP. These perturbations are introduced by the algorithm modifying the operating voltage of the PV array by a small increment. Then the PV output power of the array is compared with the one provided in the previous cycle of perturbation, thus obtaining the resulting change in output power, ΔP. The operation point will

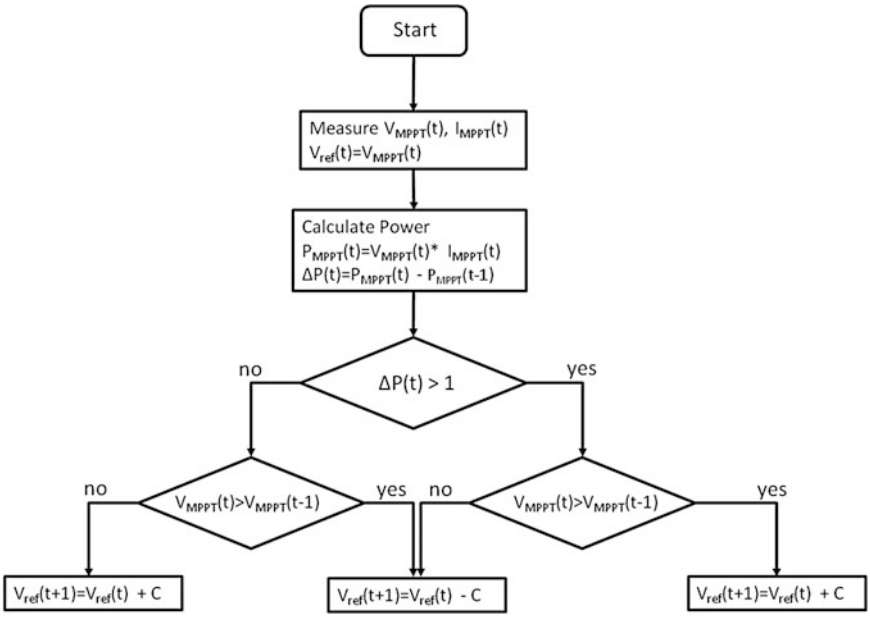

Fig. 21 P&O basic flowchart algorithm

get closer to the MPP if the PV array power has been increased after the perturbation, that is, if the ΔP is positive. In this way, the next perturbation or change in the array voltage will have the same sign as the previous one. In contrast, if the output power provided by the array has diminished (the ΔP is negative), the operation point will have moved away from the MPP. In this case, the sign of the next change in the array voltage will be reversed to move back toward the MPP. This process is repeated until the MPP is determined (see Fig. 21).

Despite its simplicity, the P&O algorithm exhibits some drawbacks that decrease its MPPT efficiency:

1. It cannot determine when the MPP has been reached. In this way, the algorithm involves oscillations around the MPP, changing the sign of perturbation after each cycle.
2. There are increasing difficulties finding determining the MPP because the level of irradiance decreases due to the flattening of the P–V curve, which involves little changes in power associated with the introduced voltage perturbation.
3. P&O can be an inappropriate method for systems subject to rapid changes in irradiance [15] because the operation point may diverge from the MPP instead of coming closer, showing and erratic behaviour in such conditions, and thus diminishing the algorithm efficiency. This situation may appear on partly cloudy days.

The oscillations around the MPP during the steady state can result in energy losses. They can be avoided making not only the perturbation period not so much higher than the system settling time but reducing the step amplitude of the perturbation. However, this solution slows down and makes less efficient the searching process in the case of rapidly changing conditions that obscure the P&O algorithm. Under these conditions, the algorithm is not able to distinguish if the changes in array power are due to the duty cycle modulation or to changes in irradiance [16]. A proper value of the step size perturbation can overcome this problem. In this way, different solutions to this problem involving a variable perturbation size, which becomes smaller as the algorithm becomes closer to the MPP, have been reported in the literature.

To overcome the previously mentioned drawbacks, some variants of the P&O method can be found. They are aimed to decrease the oscillations around the MPP in steady-state irradiance and temperature conditions as well as increase the algorithm's efficiency during cloudy days. In this way, P&O algorithms with adaptive step size have been proposed [17, 18] where the step size is controlled by the slope of the P–V curve (dP/dV); and where P&O techniques with parabolic approximation [19], in which a parabolic interpolation can be used to estimate the MPP.

Incremental conductance method

This technique constitutes an evolution of the P&O method. It is based on the fact that the slope of the PV array curve at the MPP is zero [20], that is, the value of the PV array conductance is equal in magnitude to the absolute value of its incremental conductance, but opposite in sign.

$$\frac{dP}{dV} = \frac{d(V \cdot I)}{dV} = I + V \cdot \frac{dI}{dV} = 0 \Rightarrow -\frac{I}{V} = \frac{dI}{dV} \tag{9}$$

Moreover, the slope of the PV array curve is negative to the right of the MPP and positive to the left. In the first case, the PV array must be diminished to obtain the MPP, whereas in the second case it must be increased. As can be observed, the incremental conductance (INC) algorithm can actually determine the direction of the perturbation introduced by the array voltage so as to reach the MPP. In this way, and compared with P&O algorithms, it will not track in the wrong direction under rapidly changing conditions. Moreover, it can determine when the MPP has been reached. So in an ideal scenario, it will not oscillate around the MPP once it has been reached and will make almost negligible any power loss due in steady-state conditions. However, due to the noise and quantization effects related to the microcontroller that manages this algorithm, this latter advantage vanishes.

Another drawback of this method in HCPV technology is related with local MPPs caused by partial shadowing of the module as was mentioned previously; thus, local zero-slope curves not corresponding with the absolute MPP may be obtained.

There is another method that uses the INC approach: the parasitic capacitance method [21]. In this case, it is considered the solar cell's parasitic union capacitance to obtain the array differential conductance.

d*P*/dV or d*P*/d*I* feedback control

This method is the most natural way to obtain the MPP because it calculates the slope differential power to voltage or differential power to current (d*P*/d*V* or d*P*/d*I*) of the PV power curve. The MPP will be reached when the latter is zero.

Because the relation of d*P*/d*V* versus V is nonlinear, some drawbacks must be considered: increasing complexity, instability, and nonsmoothing. In contrast, the relation between the d*P*/d*V* and output current of the PV array is proved to be almost linear near the MPP region [22]. There are different ways to compute this slope. The algorithm developed in [23] can provide the MPP in a quick and smooth way, thus decreasing the energy losses associated with the P&O method in the stationary state. Moreover, its complexity is less than with the INC method.

Fuzzy Logic Controller

Recently, the use of fuzzy logic controllers (FLC) to achieve the MPP in a PV array has increased because they can obtain the MPP without any detailed knowledge of the PV source model. In that sense, FLC is presented as a good solution to determine the MPP. This type of controller has the following advantages: (1) they are adaptive methods; (2) they do not need exact and detailed knowledge of the PV mathematical models; (3) they can operate with imprecise inputs; and (4) they can handle nonlinearity.

Based on their heuristic nature and fuzzy rule tables, these methods use various ways to determine the MPP from different parameters such as the output circuit voltage together with the short-circuit current and the instantaneous array voltage and current. FLC exhibits a better behaviour than the P&O method by achieving very fast transient response and decreasing the oscillations around MPP in steady state. It has showed a better performance compared with classical MPPT voltage-based techniques [24]. As a drawback, it must be mentioned that a deep knowledge of the system operations is required to determine the computation error and the rule base table.

Neural Network

Neural network is a technique related to FLC, and, like such, it is managed by microcontrollers. Because most HCPV arrays have different characteristics, and meteorological conditions differ from one location to another, a neural network must be specifically trained for the HCPV array for which it is intended. To accurately identify the MPP, the neural network must be trained where the HCPV array is tested over a period of months or years, and the patterns between the inputs and outputs of the neural network are recorded [25]. It must be noted that the characteristics of an HCPV array may also change with time, so the neural network must be also re-trained periodically. However, this limitation is overcome when

Table 4 Maximum power of the HCPV module at standard test conditions (STC)

P (W)	DNI (W/m^2)	Tcell (°C)	Spectrum
250	1000	25	AM1.5d

Table 5 Characteristics of the high-concentrator photovoltaic module used in the study

Geometric concentration	700
Primary optics	SOG squared flat Fresnel lens
Secondary optics	Reflexive truncated pyramid
Optical efficiency	0.80
Type of solar cells	Lattice-matched GaInP/GaInAs/Ge
Solar cells area (cm^2)	0.763
No. of solar cells	20
Cooling type	Passive

Every cell is protected with a bypass diode

using a genetic algorithm that achieves optimal tuning of the membership functions.

With the purpose of validating the current MPPT mechanism on HCPV systems, the following experiment was performed. A HCPV module of 250 W was connected to a microinverter, and both the DC current and DC voltage were monitored. In Tables 4 and 5, the main characteristics and the maximum power of the HCPV module at standard test conditions (STC) are listed.

The microinverter used for the tests had the following characteristics (Table 6).

The experiment was undertaken outdoors with DNI = 910 W/m^2 and an ambient temperature of 28 °C. The module and the inverter are connected and at a certain moment [t = 140 s (Fig. 22)], the HCPV was completely covered with an opaque blanket. After around 40 s (t = 182 s in the figure), the module was uncovered. This process was repeated again 1 min later (t = 240 s).

In Fig. 22, where the DC and AC powers were monitored, it can be observed that around 20 s after uncovering the module, the HCPV module returned to its maximum 100 % power, thus obtaining the rise time for the recovering power.

Another experiment using the same module and microinverter is shown in Fig. 23. This time, they are not connected and instead of measuring the response time under a sudden "shadow," the response time after the connection of the HCPV module with the inverter (t = 0 s) is measured. It can be observed that after

Table 6 Characteristics of the microinverter used in the study

MPP voltage (V)	45–100
Maximum input (HCPV) current (A)	5
Maximum AC power (W)	300
Maximum efficiency (%)	94.8
European efficiency (%)	93.4
MPP efficiency (%)	99

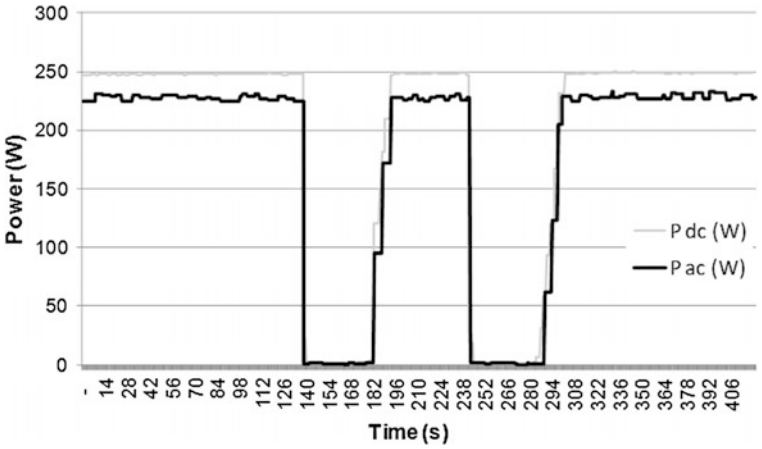

Fig. 22 Rise- and fall-time behaviors of the MPPT of a microinverter connected to a HCPV module under a sudden "shadow"

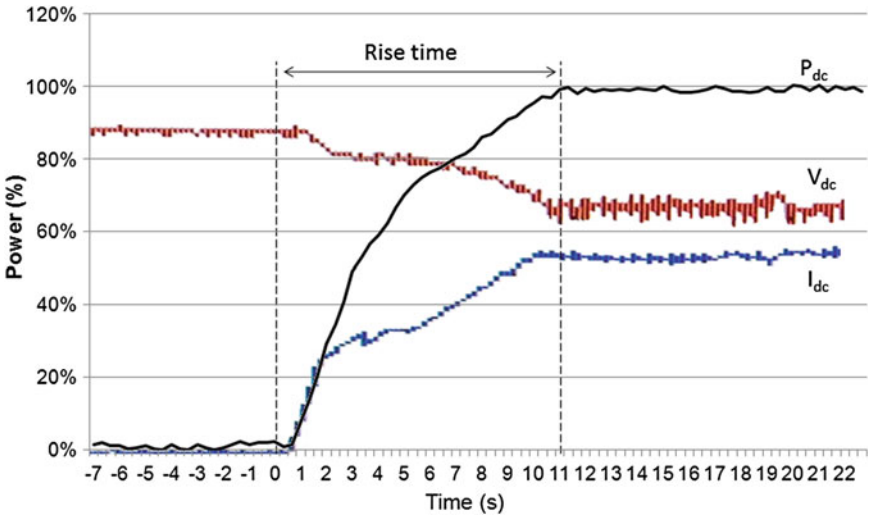

Fig. 23 Off-on rise-time of the MPPT of a microinverter connected to a HCPV module (Color figure online)

approximately 11 s, the MPPT system has reached 100 % power under the operating conditions. In this figure, the voltage (red line) and the current (blue line) are also shown. The DC power has been obtained by multiplying both parameters. The current increases from zero to its maximum power value, (Impp) and the voltage decreases from open-circuit voltage (*V*oc) to the corresponding maximum power-point voltage (*V*mpp). Under these circumstances, the MPPT mechanism of

the microinverter used has been able to rapidly follow changes in the DNI as well as the step from open-circuit voltage to operation at the MPP.

Based on these results, it could be concluded that current MPPT techniques are somehow adequate for HCPV technology. Nevertheless, the particularities of these sorts of devices call for further study to optimize those methods.

4 Other Aspects Related to Inverters

The characteristics and configurations of the inverters described previously correspond to grid-connected devices, but there may be some other installations that could operate off-the grid, that is, SFA, where the characteristics of the inverters used are slightly different. Although there is a wide experience regarding PV stand-alone (SFA) systems, there have been some projects where the use of HCPV for off-the-grid installation was analyzed. In those projects, new inverters and power conditioning devices were developed that adapted to the characteristics of SFA designs [26].

In addition to the use of special inverters for SFA systems, some other variations and complements have been recently introduced. Among them, the inclusion of energy storage for the minimization of the PV power fluctuation, which depends on the MPPT control used, has been studied [27].

The most innovative solution added to standard inverters is related to the self-consumption and net-balance concepts where the generation profile of the PV system is compared with the instant consumption of the final user. In each moment, the HCPV must decide whether to consume electricity from the grid, self-consume its own electricity generated, or inject the energy generated to the grid. Thus, instead of a one-direction traditional DC/AC converter, it must include a management system control together with a back-up device [28]. These sorts of devices seem to have a promising future according to the current policies and trends in PV technology.

5 Conclusions

Owing to the fact that an HCPV system is composed by several elements, the combination of which could result in a wide variety of different HCPV configurations (according to the bibliography consulted), the most common type of HCPV currently used is the pedestal-tracker HCPV where a point-focus mechanism is used in the modules. Looking at the trend in the manufactur of these devices, presumably this sort of system will continue being the most widespread one in the years to come.

Regarding the analysis of the inverter, a significant conclusion is the one related to the definition of weighted efficiencies for inverters. It can be observed that the particularities of HCPV technology produce a translation of the weights to higher

values of efficiency. This is caused by the inherent use of high levels of irradiance values (DNI) needed for such systems to operate normally. This is the reason for calculating a dedicated weighted average efficiency specific for HCPV technology.

Nevertheless, although the visible differences on the distribution of weights when HCPV efficiency is compared with the European or CEC efficiencies, the results obtained when assuming different values for two different locations show that the differences are not so large. In fact, there is not much error if the European efficiency is still used for estimation of the efficiency in an inverter dedicated to an HCPV system.

With the aim of adapting previous concepts used in standard PV systems, a novel classification of the interconnection modes based on the inverter tracker has been proposed. Four different configurations have been identified based on the most widespread HCPV systems currently installed.

In addition, MPPT response time experiments performed with a microinverter showed that the MPPT techniques used for conventional PV systems seem to be fairly adequate for its implementation in HCPV plants. Still, a detailed long-term analysis should be implemented.

References

1. Sandia National Laboratories (1992) Evaluation tests for photovoltaic concentrator receiver sections and modules. Albuquerque, NM
2. IEEE Std 1513 (2001) IEEE recommended practice for qualification of concentrator photovoltaic (PV) receiver sections and modules
3. IEC 62108 (2007) Concentrator photovoltaic (CPV) modules and assemblies—design qualification and type approval
4. Bett A, Dimroth F, Siefer G (2007) Multijunction concentrator solar cells. In: Luque A, Andreev V (eds) Concentrator photovoltaics. Springer, Berlin, pp 67–87
5. Fraas L, Partain L (2010) Solar cells and their applications. Wiley, USA
6. Winston R, Miñano JC, Benítez P (2005) Nonimaging optics. Elsevier Academic Press, Amsterdam
7. Sala G, Antón I (2011) Photovoltaic concentrators. In: Luque A, Hegedus S (eds) Handbook of photovoltaic science and engineering. Wiley, UK, pp 402–451
8. Khamooshi M, Salati H, Egelioglu F, Hooshyar Faghiri A, Tarabishi J, Babadi S (2014) A review of solar photovoltaic concentrator. Int J Photoenergy 17
9. Fernández EF, Pérez-Higueras P, García Loureiro AJ, Vidal PG (2013) Outdoor evaluation of concentrator photovoltaic systems modules from different manufacturers: first results and steps. Prog Photovoltaics 21:693–701
10. Domínguez C, Voarino P, Lazpita B, Bier A, Besson P, Baudrit M (2014) CPV-specific test procedures for evaluating on-grid inverters. In: Proceedings of the 10th international conference on concentrator photovoltaic systems. Albuquerque
11. Stalter O, Burger B, Bacha S, Roye D (2009) Integrated solar tacker positioning unit in distributed grid-feeding inverters for CPV power plants. In: IEEE international conference on industrial technology, pp 1–5
12. Salas V, Olías E, Barrado A, Lázaro A (2006) Review of the maximum power point tracking algorithms for stand-alone photovoltaics systems. Sol Energy Mater Sol Cells 90:1555–1578

13. Eltawil A, Zhao Z (2013) MPPT techniques for photovoltaics applications. Renew Sustain Rev 25:793–813
14. Femia N, Petrone G, Spagnuolo G, Vitelli M (2013) Power electronics and control techniques for maximum energy harvesting in photovoltaic systems. CRC Press, Boca Ratón
15. Gee Wei T, Green T, Hernández-Aramburo C (2007) A current mode controlled maximum power point tracking converter for building integrated photovoltaics. In: Proceedings of European conference on power electronics and applications
16. Hussein HK, Muta I, Hoshino T, Osakada M (1995) Maximum photovoltaic power tracking: an algorithm for rapidly changing atmospheric conditions. IEEE Proc Gener Transm Distrib 142(1):59–64
17. Xiao W, Dunford W (2004) A modified adaptive hill climbing MPPT method for photovoltaic power systems. In: Proceedings of 35th annual IEEE power electronics specialists conference, pp 1957–1963
18. Pandey A, Dasgupta N, Mukerjee A (2006) Design issues implementig MPPT for improved tracking and dynamic perfomance. In: 32nd annual conference on IEEE industrial electronics
19. Fermia N, Granozio D, Petrone G, Vitelli M (2007) Predictive adaptive MPPT perturb and observe method. IEEE Trans Aerosp Electron Syst 43(3):934–950
20. Hussein K, Zhao G (1995) Maximum photovoltic power tracking: an algorithm for rapidly changing atmospheric conditions. IEEE Proc Gener Transm Distrib 141(1):59–64
21. Branbrilla A, Gambarara A, Garutti A, Ronchi F (1999) New approach to photovoltaic arrays maximum power point tracking. In: Proceedings of 30th IEEE power electronics Conference, pp 623–637
22. Kuo Y (2001) Design and implementation of single stsge photovoltaic energy conversion. PhDisertation, Departament of electrical Engineering, National Cheng Kun Unioversity Tainan, Taiwan
23. Dejia Z, Zhengming Z, Eltawil M, Liqiang Y (2008) Design and control of a three phase grid-connected system with developed maximum power point tracking. In: Proceedings of 23rd annual applied power electronics conference and exposition (APEC), pp. 973–979
24. Chiu C, Ouyang Y (2011) Robust maximum power point tracking control of uncertain photovoltaic system: a unified T-S fuzzy model-based approach. IEEE Trans Control Syst Technol 19(6):1516–1526
25. Almonacid F, Fernández E, Rodrigo P, Pérez-Higueras P, Rus-Casas C (2013) Estimating the maximum power of a high-concentrator photovoltaic (HCPV) module using an artificial neural network. Energy 53:165–172
26. Sala G, Pachón D, Leloux J, Victoria M, Bett MW, Banda P (2009) NACIR: an European Initiative dedicated to cooperation with mediterranean partner countries in the field of photovoltaic concentration. In: 24th European photovoltaic solar energy conference. Hamburg
27. De la Parra I, Marcos J, García M, Marroyo L (2014) Minimizing energy storage requirement for PV power ramp-rate limitation controlling the inverters MPPT. In: 29th European photovoltaic solar energy conference and exhibition. Amsterdam
28. García-Domingo B, Torres-Ramírez M, de la Casa J, Aguilera J, Terrados F (2014) Design of the back-up system in patio 2.12 photovoltaic installation. Energy Build 83:130–139

Efficiencies and Energy Balance in High-Concentrator Photovoltaic Devices

Francisco J. Muñoz-Rodríguez, Emilio Muñoz-Cerón, Florencia Almonacid and Eduardo F. Fernández

Abstract Actual and forecast high-concentrator photovoltaic (HCPV) systems efficiencies may provide a scenario where HCPV represents a potential alternative to flat PV technology. The present status of HCPV efficiencies will be studied, and, on this basis, future trends regarding HCPV cells, modules, and systems efficiencies will be forecast. It will be shown that HCPV technology represents a real alternative to the current PV systems. Guidelines and normalized documents are needed to assess the overall performance of HCPV systems and to provide a general assessment of the potential of HCPV technology. The International Standard IEC 61724 publication, Photovoltaic System Performance Monitoring—Guidelines for Measurement Data Exchange and Analysis, will be highlighted. Because these guidelines are specially addressed to flat-PV technology, some suggestions, especially those adapted to the particularities of HCPV systems on both monitored and derived parameters, will be covered. Moreover, different indices of performance and losses that intend to provide comparisons between different HCPV installations will be offered adapted to the HCPV idiosyncrasy. These comparisons may be extremely useful when it comes to optimizing HCPV installation technology.

1 Introduction

Concentration photovoltaic (CPV) and especially high-concentrator photovoltaic (HCPV) systems are considered one of the most promising solutions to achieve cost decrease and to make this technology more competitive by the use of inexpensive optical devices (lenses and mirrors) to concentrate light on a small solar cell. Currently HCPV technology is largely based on the use of high-efficiency III–V multijunction (MJ) solar cells because they have the greatest impact on final efficiency. HCPV modules are made up of MJ solar cells, optical devices, and

F.J. Muñoz-Rodríguez (✉) · E. Muñoz-Cerón · F. Almonacid · E.F. Fernández
IDEA Research Group, University of Jaén, Jaen, Spain
e-mail: fjmunoz@ujaen.es; eduarferfer@gmail.com

P. Pérez-Higueras and E.F. Fernández (eds.), *High Concentrator Photovoltaics*,
Green Energy and Technology, DOI 10.1007/978-3-319-15039-0_9

peripheral components necessary to generate electricity and dissipate the heat produced. Taking this into account, the whole efficiency of an HCPV module will be a function of the solar cell, the optical device efficiencies, the losses in wires, and the rest of the elements that compose the HCPV module. Both MJ cell efficiency and HCPV module efficiency play a determining role to evaluate the potential of HCPV technology and promote its market expansion.

The present status of HCPV efficiencies will be studied, and, based on these studies, future trends in efficiencies of HCPV modules and systems will be forecast. These future trends show that HCPV technology could represent a real alternative to the current PV systems.

Although HCPV technology is still in a deployment stage, HCPV systems are those with the most installed power of the whole CPV technology. Moreover, HCPV systems are based on a technology that in the short and medium term will provide high efficiencies, provide high levels of energy production, and produce large decreases in cost. To assess the overall performance of HCPV systems, which will also provide a general assessment of the potential of HCPV technology, the International Standard IEC 61724 publication, Photovoltaic System Performance Monitoring—Guidelines for Measurement Data Exchange and Analysis, will be highlighted. However, these guidelines are specially addressed to flat-PV technology. In this chapter, some suggestions, especially those adapted to the particularities of HCPV systems on both monitored and derived parameters related to system energy balance and performance, will be covered. It will be shown monitoring parameters, such as direct normal irradiance, spectral solar radiation, and wind speed, will be mandatory. Tracker tilt, azimuth angles, and the error of alignment of the sun using a tracking accuracy sensor should be also measured. Moreover, different indices of performance and losses, addressed to provide a proper performance analysis of HCPV systems and which intend to provide comparisons between different HCPV installations, will be indicated.

2 Efficiencies in HCPV Devices

Efficiency represents the ratio between the output power provided by a system and its input power:

$$\eta = \frac{P_{\text{output}}}{P_{\text{input}}} \tag{1}$$

The concentrator cell is the basic PV device under concentrating solar radiation. The overall cell efficiency (η_{CELL}) can be defined as the electric power supplied by the cell at a given global irradiance (G) on the cell surface (A_{cell}):

$$\eta_{\text{cell}} = \frac{P_{\text{cell}}(W)}{G\left(\frac{W}{m^2}\right) \cdot A_{\text{cell}}(m^2)} \tag{2}$$

The overall electric module efficiency (η_{MOD}) can be defined as the electric power supplied by the module at a determined direct normal irradiance (DNI), on the module surface (A_{mod}):

$$\eta_{\text{MOD}} = \frac{P_{\text{mod}}(W)}{\text{DNI}\left(\frac{W}{m^2}\right) \cdot A_{\text{mod}}(m^2)} \tag{3}$$

Moreover, as a concentrator module is made up of a group of cells, primary and secondary (optional) optics, and other elements, the concentrator module efficiency can be given by:

$$\eta_{\text{MOD}} = \eta_{\text{CELL}} \cdot \eta_{\text{OPT}}(1 - L_{\text{module}}) \tag{4}$$

In this sense, the module's efficiency will be a function of the η_{CELL}, the optical efficiency of the module (η_{OPT}), and the losses in wires and the rest of the elements in a module (L_{module}).

If the losses associated to the wires and the rest of the elements of the array (L_{array}) are considered, the efficiency of the array can be expressed by the following expression:

$$\eta_A = \eta_{\text{MOD}} \cdot \left(1 - L_{\text{array}}\right) \tag{5}$$

Finally, the system efficiency (i.e., the overall plant efficiency (η_{tot}) can be expressed in terms of the array efficiency (η_{A}) and the overall efficiency of the balance-of-system (BOS) components (η_{BOS}):

$$\eta_{\text{tot}} = \eta_{\text{SYS}} = \eta_{\text{A}} \cdot \eta_{\text{BOS}} = \eta_{\text{A}} \cdot \eta_{\text{INV}} \cdot (1 - L_{\text{AC}}) \tag{6}$$

where η_{INV} corresponds to the inverter efficiency and L_{AC} represents the losses associated to the AC side (wires and the rest of the elements).

2.1 Present Status of HCPV Efficiencies and Forecast

MJ cells, which form the basis of HCPV systems, split their sensitivity to the sun's spectrum so they are better matched throughout its wavelength distribution than single-junction devices. This produces a better and more efficient conversion of sunlight into PV electricity.

The high efficiency achieved by MJ solar cells is also explained by the decrease of thermalization and transmission losses in solar cells when the number of p-n junctions is increased [5]. Obviously, these efficiency levels are possible at the

expenses of a substantial increment of the price up to levels where its profitability is questionable when using bare cells for the module composition. This explains the reason for using concentrating optic devices so the cell's area can be decreased while the Sun flux is increased.

The theoretical efficiencies calculated for these devices depend on the number of layers and the considerations estimated. As a global vision, and within a thermodynamic context, the limit is close to 95 %, whereas a detailed balance theory leads to a limit approximately 86.8 % under the black-body consideration or 85 % if AM1.5 DNI [24, 36] is assumed.

It is important to mention that we should distinguish theoretical efficiency of MJ cells in general and the efficiency for a specific structure [34]. Among the monolithic MJ cells there are several structures depending on the manufacturing process and the band gap combination. Under the current state of the art, metamorphic cells seem to achieve slightly greater efficiencies levels regarding the most widespread lattice-matched cells [45, 54].

The historical evolution of best research-cell efficiencies [41] highlights the flattening of the efficiency trend for crystalline silicon cells, which means that it is close to its maximum theoretical limit [35]. Meanwhile, the efficiency records regarding MJ cells have experienced an incremental trend in the last decade, clearly surpassing the 40 % barrier, and have an optimistic roadmap potential because a long gap still exists until getting close to the theoretical limit efficiencies mentioned previously.

The record efficiency of a solar cell currently reported (late 2014) is 44.4 % for an inverted metamorphic monolithic 3-junction cell under a concentration ratio of 302 suns and manufactured by Sharp with the composition InGaP/GaAs/InGaAs [20]. In contrast, Soitec and the research center Fraunhofer Institute for Solar Energy Systems have reached 44.7 % efficiency by means of a 4-junction cell composed by GaInP/GaAs/GaInAsP/GaInAs at 297-times concentration [9].

Nevertheless, the efficiencies of commercial MJ solar cells are slightly lower than these values because the quality of the manufacturing process is diminished in the interest of decreasing prices and increasing production speed. A brief representation of the most widespread commercial MJ solar cells is listed in Table 1.

It was briefly mentioned that the efficiency of the cells differs from the one reached either on modules or on systems because of the occurence of certain intrinsic losses when joining the elements that comprise a HCPV device.

According to the losses mentioned and the current state of the art of commercial MJ cells, the efficiency range of commercial HCPV modules and systems can be identified (Table 2). The module efficiency data are based on the manufacturer's

Table 1 Most representative commercial MJ cell efficiencies (2014)

Manufacturer	Efficiency (%)	Concentration (suns)
Emcore	39	1000
Spectrolab	40	500
Azurspace	41.9	500
Solar junction	41.4	1000

Table 2 Present efficiency status of commercial CPV elements [4]

Device	Efficiency (%)
Cells	~40
Modules	~31
Systems	~26

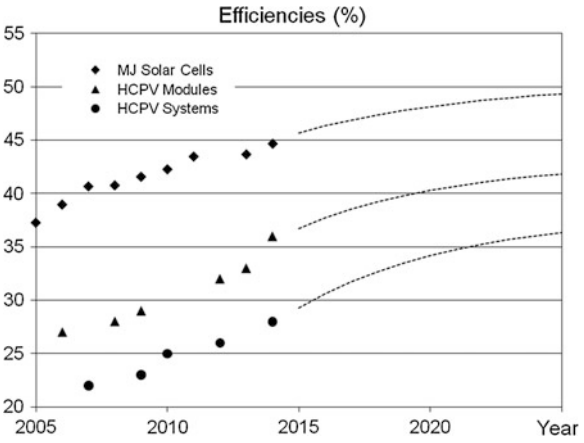

Fig. 1 MJ cell, HCPV module, and HCPV system efficiency roadmap from 2005 to 2025 [21, 44, 51]

data sheet, and the system efficiency is based on the scarce empirical research papers published because most companies are reluctant to offer data on the real operational efficiency of their systems.

Although the efficiency of an MJ cell increases proportionally to the number of layers used, the complexity of stacking different semiconductor materials makes using more than five or six layers unlikely. With the current state of the art regarding the number of layers used, that is, three bands or the recent record four-layer MJ cell, a theoretical limit that clearly surpass efficiencies to >60 % [34] it is expected. Under this scenario, there is still a clear pathway for improvement of efficiency in years to come.

Several studies regarding the forecast in HCPV efficiencies [21, 44, 51] have been published. In Fig. 1, an efficiency forecast for different HCPV devices is shown. Following the previous predictions and assuming a similar trend based on the current state of the art of the cells and the record efficiencies achieved, it is expected that in 2025 the efficiency of the different subelements of HCPV technology could be similar to the ones shown in Table 3.

Table 3 Efficiency forecast for HCPV cells, modules, and systems

Device	Efficiency forecast 2025 (%)
Cells	45–50
Modules	40–45
Systems	35–40

3 Performance Analysis of HCPV Systems: Yields, Indices of Performance, and Efficiencies

Many PV installations use data-acquisition systems to document daily, monthly, or annual derived parameters obtained from monitored data. In the case of HCPV systems, as in any PV system, data obtained during their operation provide valuable information not only to verify whether the design goals have been met but also to improve the design and operation of HCPV systems and to assess the potential of this technology. In this way, the Guidelines for the Assessment of Photovoltaic Plants prepared by the Joint Research Center (JRC) [8] and the International Standard IEC 61724 Photovoltaic System Performance Monitoring—Guidelines for Measurement Data Exchange and Analysis [26] recommend procedures for the analysis of monitored data to assess the overall performance of PV systems. The monitored data in PV systems are processed to determine the daily, monthly, or annual irradiation, overall energy balances, and energy production data which, together with the energy efficiencies and the indices of performance, provide a good indication of the performance of these systems.

The documents mentioned previously can be also used to assess the performance of HCPV systems. However, these documents are intended for flat-PV grid-connected systems. In [40], some considerations were offered to improve the performance analysis from monitored data of stand-alone PV (SAPV) systems without a maximum power point tracker (MPPT). Some particularities must be taken into account when analysing the performance of HCPV systems.

Unlike conventional PV technology that is installed worldwide under different insolation and temperature conditions, HCPV systems are installed in locations with high DNIs. Moreover, this type of system is highly influenced by solar spectrum, whereas the influence of the module temperature on the generated power in an HCPV is not as pronounced as that in a flat-panel PV device. The aim of this section is to provide suggestions on both monitored and derived parameters related to system energy balance and performance, which are calculated from the recorded monitored parameters. Moreover, different indices of performance and losses that intend to provide comparisons between different HCPV installations will be offered adapted to the special features of HCPV technology. These comparisons could be extremely useful when it comes to optimizing HCPV installation technology.

3.1 Monitored Parameters in HCPV Systems

The parameters to be monitored in an HCPV system are shown in Table 4. Most of them correspond to those described in [8, 26]. Although in conventional PV technology without tracking, parameters such as wind speed (S_W), tracker tilt angle (Φ_T), and tracker azimuth angle (Φ_M) are not necessary, in HCPV systems they are mandatory due to the use of trackers. The error of alignment with the Sun

Table 4 Parameters to be measured in real time in HCPV systems

Monitored parameters	Symbol (U)	Installation
Direct irradiance in the plane of the array	DNI (W/m^2)	Meteorological parameters
Ambient air temperature	T_{am} (°C)	
Wind speed	S_W (m/s)	
Spectral power-density distribution	S	
Array output voltage	V_A (A)	Array
Array output current	I_A (A)	
Array output power	P_A (A)	
Cell temperature	T_C (°C)	
Tracker tilt angle	Φ_T (°)	
Tracker azimuth angle	Φ_A (°)	
Sun-pointing error	(°)	
Operating voltage	V_S (V)	Storage
Current to storage	I_{TS} (A)	
Current from storage	I_{FS} (A)	
Power to storage	P_{TS} (kW)	
Power from storage	P_{FS} (kW)	
Load voltage	V_L (V)	Load
Load current	I_L (A)	
Load power	P_L (kW)	
Utility voltage	V_U (V)	Utility grid
Current to utility grid	I_{TU} (A)	
Current from utility grid	I_{FU} (A)	
Power to utility grid	P_{TU} (W)	
Power from utility grid	P_{FU} (W)	
Output voltage	V_{BU} (V)	Back-up sources
Output current	I_{BU} (A)	
Output power	P_{BU} (kW)	

(Sun-pointing error) through a tracking accuracy sensor should be also measured. Moreover, global irradiance in the plane of the array has been substituted for direct irradiance in the plane of the array (DNI), and other parameters, such as the spectral solar radiation and some atmospheric variables, have been included. Meteorological measurements, together with spectral irradiance, manage to determine the relationship between solar resource, temporal meteorological change, and HCPV systems performance.

3.1.1 Direct Normal Irradiance

Due to the use of optical devices, HCPV modules only react to the direct component of the irradiance. The DNI can be measured directly using either a

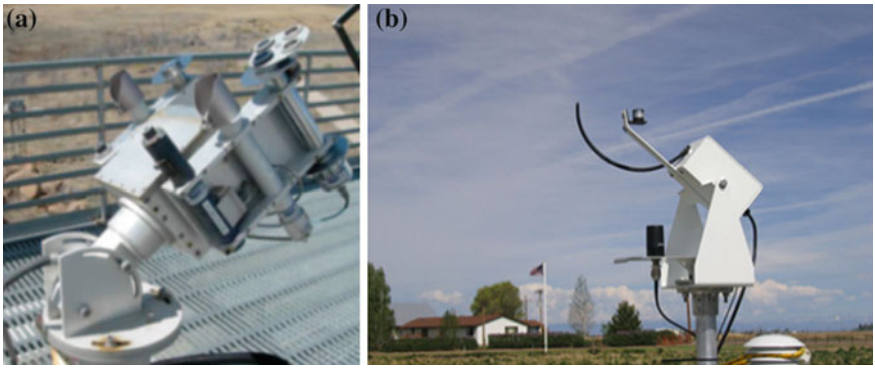

Fig. 2 **a** Pyrheliometer. **b** RSR. *Courtesy* NREL

pyrheliometer or in an indirect way by other pyranometric Systems, such as a rotating shadowband irradiometer (RSR), where the DNI is calculated from the diffuse horizontal irradiance (DHI), the global horizontal irradiance (GHI), and the solar position [53] as shown in Fig. 2. The pyranometric systems offer an alternative to pyrheliometers to decrease the investment and operation/maintenance costs and/or to increase the robustness of the DNI-measurement systems with respect to, for example, misalignment, soiling, or perturbation due to meteorological events.

Pyrheliometers are robust field instruments that provide excellent expanded measurement uncertainty for subhourly DNI measurements (i.e., ±2.5 %) for a well-maintained measurement station equipped with a thermopile-based pyrheliometer. The maintenance implies daily cleaning, regular calibration, and control procedures. They are ideal instruments for high-end research. For RSR, the expanded measurement uncertainty for subhourly DNI measurements is approximately ±5.

The International Orgtanization for Standarization (ISO) and the World Meteorological Organization (WMO) have established classifications and specifications for the measurement of solar irradiance [29, 55]. The aim of these classifications is to provide an estimation of the uncertainty measurement. The user is encouraged to review these documents in more detail as part of the project planning for solar resource measurements before acquiring pyrheliometers or pyranometers. In [53] can be found either WMO and ISO characteristics of operational pyrheliometers and pyranometers for measuring, respectively, DNI and GHI or DHI.

3.1.2 Spectral Solar Irradiation

To accurately evaluate the performance of an HCPV system, temporal references of the spectral variations are required because the behaviour of HCPV modules shows an important dependence on the solar incident spectrum. This type of module is strongly influenced by spectral irradiance due to the use of several junctions

interconnected in series. Moreover, the optical devices, usually Fresnel lenses, used to concentrate the light on the solar cell surface also modify the spectral distribution that falls on the solar cell surface. In this sense, HCPV modules show a large and complex spectral behaviour [13, 37, 50]. Measuring the spectrum constitutes an important task to improve the performance analysis of HCPV systems because the spectral data may permit the determination of the impact of temporal variations in spectra on HCPV system energy yield.

Direct spectral irradiance can be measured with the following:

- *Spectroradiometer.* A spectroradiometer measures quantitative or absolute intensity at different wavelengths of the electromagnetic spectrum. It delivers complete spectral information, thus enabling a detailed study of the solar spectrum. It must be also noted that spectroradiometers are not only expensive, but their use may be relatively complex, and they have multiple disadvantages, especially when outdoor solar spectra are to be measured continuously and reliably over several months to obtain long-term analyses. Moreover, most spectroradiometers are based on semiconductors, and the spectral range covered usually reaches 1100 nm. In the market, there exists a combination of several spectroradiometers that can extend the spectral measurement range from 300 up to ≥1700 nm.
- *Spectroheliometer based on isotype cells*. Either HCPV module and system performance under determined spectral conditions can be obtained from measured monitor cell photocurrents, which provide individual measurements of the effective irradiance in the spectral zones corresponding to each subcell of an MJ solar cell [43] (Fig. 3). Ideally, these monitor cells offer the same spectral response as the subcells in the MJ cell of the HCPV module or system under study. This approach has been used to define spectral matching ratio [10] and the *Z* spectral parameter, which can be used as spectral indexes for the electrical characterization of HCPV systems [19, 42].

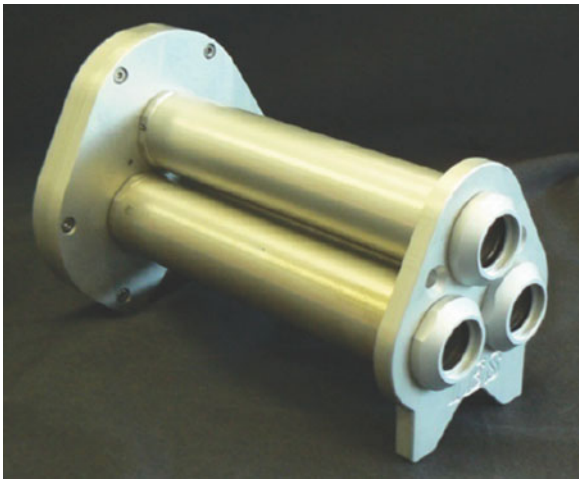

Fig. 3 Tri-band spectroheliometer based on isotype cells. *Courtesy* of Solar Added Value

- *Ground-based measurements of atmospheric parameters*. The atmospheric parameters with the largest influence on the spectral irradiance and the behaviour of HCPV modules are, in order of importance, air mass (AM); aerosol optical depth (AOD), which is usually quantified at 500 or 550 nm; and precipitable water (PW). These parameters, together with radiative models such as the MODerate resolution atmospheric TRANsmission (MODTRAN) and the Model of the Atmospheric Radiative Transfer of Sunshine (SMARTS) [22], manage to analyze the spectral performance of an HCPV module and array [6, 7, 11, 39]. The advantage offered by this method lies in the fact that it allows spectral effects to be evaluated for long-term analysis in remote places if atmospheric parameters are available. Furthermore, this method could be suitable for small HCPV systems where spectroradiometers and Isotype cells can be an expensive solution.

3.1.3 Cell Temperature

Although the influence of the temperature in an HCPV module is not as high as in a flat-PV module, it is still critical to measure the cell temperature of an HCPV module because the cell temperature influences its electrical parameters. Thus, it is imperative for characterizing the behaviour of HCPV modules and systems to know the cell temperature. The cell temperature in HCPV modules is affected by atmospheric parameters such as DNI, air temperature, and S_W [2]:

$$T_{cell} = f(\mathrm{DNI}, T_{air}, S_W) \tag{7}$$

Although cell temperature is a necessary input parameter in any model for the electrical characterization of HCPV modules, the direct measurement of this parameter is a complex task because it is necessary to get inside the module and place a small temperature sensor close to the solar cell. For this reason, different approaches have been followed by several authors to estimate the temperature. Some of these approaches are based on direct measurements (such as heat-sink temperature or open-circuit voltage) on the HCPV module, whereas others attempt to resolve this issue through the relationship between atmospherics parameters and the cell temperature. Although the methods based on direct measurements of an HCPV module provide better results than methods based on atmospheric parameters, the use of atmospheric parameters have the advantage of allowing the cell temperature of an HCPV module to be estimated for a specific location without directly measuring any parameter in the module. Furthermore, experimental analysis has shown that all of the methods can be used for the estimation of cell temperature with an acceptable degree of accuracy [12, 14, 48]. Table 5 shows a summary of existing methods for measuring or estimating the cell temperature in HCPV modules.

Table 5 Methods for measuring or estimating cell temperature on an HCPV module

Model	Reference	Required inputs
Methods based on direct measurement on the HCPV module		
Sandia's model	[31]	Module heat-sink temperature, DNI
ISFOC/IES-UPM model	[49]	
Muller's model	[38]	Module heat-sink temperature, open-circuit voltage
Fernández's model	[17]	Module heat-sink temperature, DNI, generated electrical power density
IEC 60904-5	[27]	DNI, open-circuit voltage
Fernández's model	[18]	
Ju's model	[30]	Open-circuit voltage, short-circuit current
Peharz's model	[42]	
Yandt's model	[56]	DNI, cell temperature at open circuit, current-voltage curve, ambient temperature
Methods based on atmospherics parameters		
Almonacid's model	[2]	DNI, ambient temperature, wind speed
Hornung's model	[25]	
Fernández ANN	[14]	

It is important to note that the most of the methods shown in Table 6 measure or estimate the cell temperature of an HCPV module when it operates at open circuit. However, when the module is connected to an inverter and is working at the MPP, the cell temperature is considerable lower. This can be explained by the power that is not transformed into heat when the HCPV module is connected to an inverter. This difference was theoretically studied in [56], and the authors found a difference of ≤14 °C in the studied modules. Bearing this in mind, a method that takes into account this issue and provides the average cell temperature at the MPP of the cells of a module connected to an inverter was introduced in [15].

3.1.4 Sun-Pointing Error

The error of alignment with the Sun (Sun-pointing error) can be calculated using both Φ_T and Φ_A, respectively. However, to certify proper tracking, this error can be measured using a tracking-accuracy sensor (Fig. 4).

Generally, all of the parameters shown in Table 4 should be sampled at a common rate during the specified monitoring period [26]. The temporal resolution for the measurements is important because temporal records are required for monitoring variations in the incident spectra due to conditions such as change in sky cloud cover, turbidity, air pollutants, water vapour, and AM. In addition, the time resolution must be justified by the fact that sky cloud cover, AM, and, therefore, spectral solar radiation, are known to vary with the solar elevation, location, time of day, and season. In this

Table 6 Derived parameters: system performance indices

Derived parameters: BOS component performance and system performance indices			
Parameter	Symbol	Unit	Equation
BOS efficiency	η_{BOS}	–	$E_{L,\tau} + E_{TSN,\tau} - E_{FSN,\tau} + E_{TUN,\tau} - E_{FUN,\tau} / \left(E_{A,\tau} + E_{BU,\tau}\right)$
Reference yield	Y_r	kWh/(d Wp) or h d^{-1}	$DNI_\tau / DNI_{STC} = PSH_{D,day}$
Array yield	Y_A	kWh/(d Wp) or h d^{-1}	$E_{A,day} / P_0$
Final yield	Y_f	kWh/(d Wp) or h d^{-1}	$E_{usePV,day} / P_0 = Y_A \cdot \eta_{LOAD}$
Capture losses	L_C	kWh/(d Wp) or h d^{-1}	$Y_r - Y_A$
BOS losses	L_{BOS}	kWh/(d Wp) or h d^{-1}	$Y_f - Y_A = Y_A \cdot (1 - \eta_{BOS})$
Performance ratio	R_P (PR)	–	Y_f / Y_r
Mean array efficiency	$\eta_{A,mean,\ \tau}$	–	$E_{A,\tau} / \left(A_a \cdot \tau_r \cdot \sum_\tau DNI\right)$
Overall HCPV plant efficiency	$\eta_{tot,\tau}$	–	$\eta_{A,mean\tau} \cdot \tau_r \cdot \eta_{LOAD}$

P_0 and A_a, Corresponds respectively, to the nominal array power and to the overall array area

Fig. 4 Tracking accuracy sensor BPI-TA1. Courtesy of Black Photon

way, the IEC recommendation can be followed, and a *sampling interval* of 1 min can be chosen. Moreover, this sampling interval can match the *recording interval* (τ_r) instead of processing the sampled data from each parameter into time-weighted averages and recording at a given recording interval expressed in hours.

3.2 Derived Parameters in the Performance Analysis of HCPV Systems

The derived parameters are system-performance indices (Table 6) and meteorological and electrical energy quantities (Table 7), which are calculated from the recorded monitored parameters with a given recording interval over the *reporting or reference periods* (τ) such as days, weeks, months, or years.

It must be stated that some indices of performance require the nominal power of the array. However, the scientific community has been slow to embrace a unified method for assessing a nameplate rating. The choices of whether to use 850, 900, or

Table 7 Derived parameters: meteorological and electrical parameters

Parameter	Symbol	Unit	Equation
Direct irradiation in the plane of the array	DNI_τ	kWh/d or h/d	$\int_\tau \mathrm{DNI}\,\mathrm{d}t = \left(\sum_\tau \mathrm{DNI}\cdot\tau_\mathrm{r}\right)/1000 = \left(\tau_\mathrm{r}\cdot\sum_\tau \mathrm{DNI}\right)/1000$
Net energy from array	$E_{\mathrm{A},\tau}$	kWh/τ	$\int_\tau I_\mathrm{A}\cdot V_\mathrm{A}\,\mathrm{d}t = \tau_\mathrm{r}\cdot\sum_\tau I_\mathrm{A}\cdot V_\mathrm{A}$
Energy to storage	$E_{\mathrm{TS},\tau}$	kWh/τ	$\int_{\mathrm{day}} I_\mathrm{TS}\cdot V_\mathrm{S}\,\mathrm{d}t = \tau_\mathrm{r}\cdot\sum_\tau I_\mathrm{TS}\cdot V_\mathrm{S}$
Energy from storage	$E_{\mathrm{FS},\tau}$	kWh/τ	$\int_{\mathrm{day}} I_\mathrm{FS}\cdot V_\mathrm{S}\,\mathrm{d}t = \tau_\mathrm{r}\cdot\sum_\tau I_\mathrm{FS}\cdot V_\mathrm{S}$
Net energy to storage	$E_{\mathrm{TSN},\tau}$	kWh/τ	$(E_\mathrm{TS}-E_\mathrm{FS})^+$
Net energy from storage	$E_{\mathrm{FSN},\tau}$	kWh/τ	$(E_\mathrm{FS}-E_\mathrm{TS})^+$
Net energy to loads	$E_{\mathrm{L},\tau}$	kWh/τ	$\int_\tau I_\mathrm{L}\cdot V_\mathrm{L}\,\mathrm{d}t = \tau_\mathrm{r}\cdot\sum_\tau I_\mathrm{L}\cdot V_\mathrm{L}$
Net energy from back-up	$E_{\mathrm{BU},\tau}$	kWh/τ	$\int_\tau I_\mathrm{BU}\cdot V_\mathrm{BU}\,\mathrm{d}t = \tau_\mathrm{r}\cdot\sum_\tau I_\mathrm{BU}\cdot V_\mathrm{BU}$
Energy to utility grid	$E_{\mathrm{TU},\tau}$	kWh/τ	$\int_\tau P_\mathrm{TU}\,\mathrm{d}t$
Energy from utility grid	$E_{\mathrm{FU},\tau}$	kWh/τ	$\int_\tau P_\mathrm{FU}\,\mathrm{d}t$
Net energy to utility grid	$E_{\mathrm{TUN},\tau}$	kWh/τ	$(E_\mathrm{TU}-E_\mathrm{FU})^+$
Net energy from utility grid	$E_{\mathrm{FUN},\tau}$	kWh/τ	$(E_\mathrm{FU}-E_\mathrm{TU})^+$
Total system input energy	$E_{\mathrm{in},\tau}$	kWh/τ	$E_{\mathrm{A},\tau}+E_{\mathrm{BU},\tau}+E_{\mathrm{FUN},\tau}+E_{\mathrm{TUN},\tau}$
Total system output energy	$E_{\mathrm{use},\tau}$	kWh/τ	$E_{\mathrm{L},\tau}+E_{\mathrm{TUN},\tau}+E_{\mathrm{TSN},\tau}$
Fraction of total system input energy contributed by HCPV array	$F_{\mathrm{A},\tau}$	–	$E_{\mathrm{A},\tau}/E_{\mathrm{in},\tau}$
Direct PV contribution to E_use	$E_{\mathrm{use,PV}}$	kWh/τ	$F_\mathrm{A}\cdot E_\mathrm{use}$
Load efficiency	η_LOAD	–	$E_{use,\tau}/E_{in,\tau}$

τ Indicates the reporting or reference period
τ_r Indicates the recording interval

Table 8 IEC 62670-1 CSCT and CSOC

	CSTC	CSOC
Irradiance (W/m^2)	1000	900
Temperature (°C)	25	20
Temperature location	Cell	Air
Wind Speed (m/s)	–	2
Spectrum	Direct normal AM1.5 spectral irradiance distribution consistent with conditions described in IEC 60904-3	Direct normal AM1.5 spectral irradiance distribution consistent with conditions described in IEC 60904-3

1000 W/m^2 for DNI and whether to link the rating to ambient or cell temperature may affect how CPV modules are rated and compared with other technologies [33]. Finally, the CPV community has agreed [28] to the concentrator standard test conditions (CSTC), i.e., T_{cell} = 25 °C, DNI = 1000 W/m^2, G173/AM 1.5. Moreover, concentrator standard operating conditions (CSOC) have also been defined: T_{air} = 20 °C, DNI = 900 W/m^2, wind speed = 2 m/s, and direct normal spectral irradiance distribution consistent with conditions described in 60904 (Table 8).

3.3 Indices of Performance of HCPV Systems

The yields and indices of performance of the system (Table 6) are also derived parameters calculated from the recorded monitored parameters, which enable the performance comparison of systems installed at different locations.

Reference yield. This parameter is obtained by dividing the daily direct irradiation ($DNI_{,day}$) by the module's reference in-plane direct irradiance, DNI at STC (1000 W/m^2). It represents the number of direct peak solar hours (PSH_D) that would provide the same monitored daily direct normal irradiation.

Capture losses (L_C). This represents the losses due to array operation. However, this is a very wide concept, which, in the case of HCPV Systems, may include the following:

- *Spectral losses*. These are produced when the solar spectrum differs from AM1.5 spectrum (due to changes in AM, clouds, atmospheric turbidity, etc.).
- *Thermal cell capture losses*. These losses are caused by cell temperatures >25 °C. They are caused by a decrease of generator efficiency when the cells operate at temperatures greater than standard (25 °C for concentrating).
- *Thermal optical losses*. These are due to the effects of the temperature on the optical devices.
- *Shading losses*. These are due to the presence of obstacles, mainly other trackers with their corresponding arrays.

- *Tracking error losses*. This type of loss is produced when sunlight direction differs from normal incidence.
- *Tolerance and degradation losses*. These occur due to the fact that effective module power is lower than the one given by the manufacturer. In addition, degradation occurs as a decrease in module power with their use over time.
- *Mismatch losses*. These are due to the dispersion of the electrical characteristics of the modules and strings. The series–parallel connection of the modules implies that the worst module defines the output of the generator. In this way, the output power from the array will be lower than the sum of the individual power of each module that constitutes the array.
- *Ohmic losses*. These occur due to the voltage decrease across the wires that interconnect the modules and across the wires that connect the generator to the inverter.
- *Low irradiance losses*. These are due to the decrease of the efficiency of the cells when they operate under low irradiance levels.
- *Dirt and dust losses*. These optical losses are due to the deposition of dirt and dust on the generator surface.

Maximum power-tracking error, decrease of array power caused by inverter failures or when the accumulator is fully charged in SAPV systems.

Array yield ($\mathbf{Y_A}$). This is the daily net energy from array (E_A) per kW of the array-rated power (P_0). It also represents the time in hours that the array must operate at its nominal power (P_0) to provide the same monitored net energy from array E_A.

System ($\mathbf{L_s}$) or BOS Losses ($\mathbf{L_{BOS}}$). These are system losses due to the following:

- Inverter efficiency
- Inverter disponibility and failures
- Ohmic losses due to the voltage decrease across the wires that interconnect the AC side
- Transformer station if an HCPV power plant is considered
- Accumulator storage losses in HCPV SAPV systems.

Final yield ($\mathbf{Y_F}$). This represents the time expressed in hours that the array must operate at its rated power to provide the monitored direct PV contribution to E_{use} ($E_{use,PV}$). It can be also seen as the portion indicated by η_{LOAD} of the array yield.

Performance ratio (PR). This parameter indicates the fraction of the available solar energy used, and it can be used for the evaluation of grid-connected systems, thus reflecting the technical operation of a system. In the case of HCPV systems, the most influential parameter on the PR is usually the solar spectrum instead of temperature, which constitutes a determining parameter when studying the PR in flat-PV systems.

At present, the different losses in a PV system specified by the International Standards are only classified into two groups (e.g., system losses and capture losses). This classification may not properly discriminate the different types of losses in a HCPV as indicated previously. Moreover, it does not permit differentiation between avoidable and unavoidable losses. This fact is especially relevant in the case of capture losses, into which category fall thermal, spectrum (unavoidable losses), and the rest of capture losses, which are due to possible malfunctions (avoidable losses) and configure the so-called miscellaneous capture losses (L_{CM}). Because spectrum and thermal losses may represent, in a well-designed and installed HCPV system, a considerable portion of the capture losses, the identification of any other type of loss may be not easy, which may delay its solution. Thermal capture and spectrum losses may be relatively easy to determine from other parameter readings. The rest of capture losses configure the L_{CM}. This type of loss is generally occasional and sporadic because a well-planned and well-realized grid-connected system normally should exhibit only minimal L_{CM} [23].

In the next paragraphs, a method to estimate different losses—such as thermal cell losses, optics capture losses, or spectrum losses—will be indicated. It must be highlighted that these parameters are not derived parameters calculated from monitored data but estimations that are calculated from the monitored parameters. However, they can quantify these types of losses and may improve the performance analysis of HCPV systems, thus helping to find a possible system malfunction.

3.3.1 Capture Loss Estimation from Derived Parameters

It is known that MJ concentrator solar cells are influenced by changes in irradiance, spectrum cell temperature, and optics temperature. Because of this, the MPP of the array can mainly be expressed as a function of:

$$P_{mpp} = f\left(\mathrm{DNI}, S, T_{cell}, T_{opt}\right) \tag{8}$$

Due to the special characteristics of HCPV modules, conventional methods used in flat-PV panel Systems are not valid for HCPV technology. Because of this, there are different methods to estimate the maximum power of an HCPV module that tackle the special features of these kinds of devices [47]. Table 9 shows a summary of the main existing methods for estimating the MPP in HCPV modules.

Once the power harvested by the array has been determined using some of the methods available for HCPVs, special attention must be paid to capture losses because they include several types of losses, which makes it difficult to detect array malfunctions. In this sense, a simple method is provided to discriminate between the different capture losses and help to find the avoidable ones, that is, the L_{CM}.

Table 9 Methods for estimation of MPP in HCPV modules

Methods	References	Required inputs
ASTM E 2527	[3]	DNI, ambient temperature, wind speed
Peharz's method	[42]	DNI, cell temperature, subcell photocurrents
Steiner's method	[52]	DNI, PW, cell temperature, optics temperature, AOD, amsgtrom exponents (α_1 and α_2), tracking error
Rivera's method	[46]	DNI, ambient temperature, wind speed, average photon energy
Almonacid's method	[1]	DNI, ambient temperature wind speed, PW, AM
Fernández's method	[13, 16]	DNI, ambient or cell temperature, AM, AOD (optional)
Sandia's method	[31]	DNI, cell temperature, AM

Spectrum capture loss estimation
Spectrum capture losses can be defined as follows:

$$L_{\mathrm{CS}} = Y_{\mathrm{r}} - Y_{\mathrm{A,S}} \tag{9}$$

where $Y_{\mathrm{A,S}}$ represents the array yield due only to the solar spectrum and DNI, that is, it represents the daily energy output considering only the effects of solar spectrum and DNI ($E_{\mathrm{A,S}}$) per kW of rated array power. $Y_{\mathrm{A,S}}$ can be estimated from the monitored DNI and the solar spectrum:

$$Y_{\mathrm{A,S}} = \frac{E_{\mathrm{AS,day}}}{P_0} = \frac{\sum_{\mathrm{day}} P_{\mathrm{mpp}}(\mathrm{DNI}, S) \cdot \tau_r}{P_0} \tag{10}$$

where P_{mpp}(DNI,S) corresponds to an estimation of the HCPV array power as a function only of the DNI and the solar spectrum.

Thermal cell capture loss estimation
Thermal capture losses can be defined as follows:

$$L_{\mathrm{CTC}} = Y_{\mathrm{A,S}} - Y_{\mathrm{A,TS}} \tag{11}$$

where $Y_{\mathrm{A,TS}}$ represents the array yield due to cell temperature and solar spectrum, that is, it represents the daily energy output considering only the effects of these two monitored parameters ($E_{\mathrm{A,TS}}$) per kW of rated array power. $Y_{\mathrm{A,TS}}$ can be estimated from the monitored DNI, the solar spectrum, and the cell temperature as follows:

$$Y_{\mathrm{A,TS}} = \frac{E_{\mathrm{A,TS,day}}}{P_0} = \frac{\sum_{\mathrm{day}} P_{\mathrm{m}}(\mathrm{DNI}, S, T_{\mathrm{c}}) \cdot \tau_{\mathrm{r}}}{P_0} \tag{12}$$

where P_{m}(DNI, S, T_{c}) corresponds to an estimation of the HCPV array power as a function only of the monitored DNI, T_{c} (the cell temperature), and the solar spectrum.

Thermal optics capture loss estimation
In the same way, thermal optics capture losses can be expressed as:

$$L_{\mathrm{CTO}} = Y_{\mathrm{A,TS}} - Y_{\mathrm{A,TOS}} \tag{13}$$

where $Y_{\mathrm{A,TOS}}$ represents the array yield due to cell temperature, the solar spectrum, and the lens temperature, that is, it represents the daily energy output considering only the effects of these monitored parameters ($E_{\mathrm{A,TOS}}$) per kW of rated array power.

$$Y_{\mathrm{A,TOS}} = \frac{E_{\mathrm{A,TOS,day}}}{P_0} = \frac{\sum_{\mathrm{day}} P_{\mathrm{m}}(\mathrm{DNI}, S, T_{\mathrm{c}}, T_{\mathrm{OPT}}) \cdot \tau_r}{P_0} \tag{14}$$

where $P_{\mathrm{m}}(\mathrm{DNI}, T_{\mathrm{C}}, S, T_{\mathrm{OPT}})$ corresponds to an estimation of the HCPV array power as a function only of DNI, the T_{m}, the solar spectrum, and the lens temperature.

$\mathbf{L_{CM}}$ estimation
L_{CM} can be defined as follows:

$$L_{\mathrm{CM}} = Y_{\mathrm{A,TOS}} - Y_{\mathrm{A}} \tag{15}$$

The sum of the four different capture losses mentioned previously provides the entire capture losses of the array:

$$\begin{aligned} L_{\mathrm{C}} = L_{\mathrm{CS}} + L_{\mathrm{CTC}} + L_{\mathrm{CTOS}} + L_{\mathrm{CM}} = Y_{\mathrm{r}} - Y_{\mathrm{A,S}} + Y_{\mathrm{A,S}} - Y_{\mathrm{A,TS}} \\ + Y_{\mathrm{A,TS}} - Y_{\mathrm{A,TOS}} + Y_{\mathrm{A,TOS}} - Y_{\mathrm{A}} \end{aligned} \tag{16}$$

In this way, the estimations mentioned previously can help not only to quantify these types of losses but also differentiate avoidable *versus* unavoidable losses. This fact may improve the performance analysis of HCPV systems, thus helping to find a possible array malfunction.

4 Conclusions

The present status of the HCPV efficiencies has been provided. Although the efficiency of commercial cells can be slightly greater the 40 %, it must be noted that cell efficiency differs from either modules and systems efficiencies as determined intrinsic losses must be considered when joining the elements that comprise an HCPV device. In this sense, and taking into account the manufacturer's data sheet,

the efficiency values associated with commercial HCPV modules is decreased to 31 %. Meanwhile, system efficiency stands at approximately 26 %. This value is based on the scarce empirical research papers published.

Following predictions based on different studies and assuming a similar trend based on the current state of the art of the cells and the record efficiencies achieved, it is expected that in 2025 the efficiency of the commercial cells may lie between 40 and 45 %. Meanwhile, for modules and systems, the efficiency ranges could be, respectively, 40–45 % and 35–40 %. These values highlight the great potential of HCPV systems.

Guidelines and normalized documents are needed to assess the overall performance of HCPV systems and to provide a general assessment of the potential of HCPV technology. However, the current documents (i.e., IEC 61724 and the Guidelines for the Assessment of Photovoltaic Plants prepared by the Joint Research Center) are focused on flat PV technology. Therefore, in Sect. 3 different suggestions and recommendations about the monitored and derived parameters in the performance analysis of HCPV systems have been provided. Concerning the monitored parameters, it has been shown that the DNI can be achieved using either a pyrheliometer or in an indirect way by other pyranometric systems such as RSR. Direct spectral irradiance can be measured with a spectroradiometer or a spectroheliometer based on isotype cell and using ground-based measurements of atmospheric parameters. Moreover, it has been shown that although the influence of the temperature in an HCPV module is not as high as that in a flat-PV module, it is still critical to measure the cell temperature of an HCPV module because the temperature influences its electrical parameters. However, the direct measurement of this parameter is a complex task because it is necessary to get inside the module and place a small temperature sensor close to the solar cell. For this reason, different approaches to estimate cell temperature have been provided.

Finally, regarding the indices of performance, a method to estimate different types of capture losses (spectrum, thermal cell, thermal optics, and miscellaneous) from monitored parameters have been shown. This approach can quantify these types of losses and may improve the performance analysis of HCPV systems, thus helping to find a possible system malfunctions. It must be highlighted that this estimation from monitored parameters is based on the calculation of the maximum power of an HCPV module. Therefore, the main existing methods for estimating the MPP in HCPV modules methods have been indicated.

References

1. Almonacid F et al (2013) Estimating the maximum power of a High Concentrator Photovoltaic (HCPV) module using an artificial neural network. Energy 53:165–172
2. Almonacid F, Pérez-Higueras PJ, Fernández EF, Rodrigo P (2012) Relation between the cell temperature of a HCPV module and atmospheric parameters. Solar Energy Mater Sol Cells 105:322–327

3. ASTM (2009) ASTM E 2527. Standard test method for electrical performance of concentrator terrestrial photovoltaic modules and systems under natural sunlight. American Society for Testing and Materials, West Conshohocken
4. Bett A (2014) High-efficiency—a key for CPV. CPV-10, 10th international conference on concentrator photovoltaic systems. Albuquerque, USA
5. Bett A, Dimroth F, Siefer G (2007) Multijunction concentrator solar cells. In: Luque A, Andreev V (eds) Concentrator photovoltaics. Springer, Berlin, pp 67–87
6. Chan N, Brindley H, Ekins-Daukes N (2014) Impact of individual atmospheric parameters on CPV system power, energy yield and cost of energy. Prog Photovolt Res Appl 22(10):1080–1095
7. Chan N et al (2013) Validation of energy prediction method for a concentrator photovoltaic module in Toyohashi Japan. Prog Photovolt Res Appl 21:1598–1610
8. Commission of the European Communities: Photovoltaic System Monitoring (1997) Guidelines for the assesement of photovoltaic plants, documents A&B, version 4.3
9. Dimroth F et al (2014) Wafer bonded four-juntion GaInP/GaAs/GaInAsP/GaInAs concentrator solar cells with 44.7 % efficiency. Prog Photovolt Res Appl 22(3):277–282
10. Domínguez C, Antón I, Sala G, Askins S (2013) Current-matching estimation for multijunction cells within a CPV module by means of component cells. Prog Photovolt Res Appl 21:1478–1488
11. Fernández EF, Almonacid F, Micheli L, Mallick T (2014) Comparison of methods for estimating the solar cell temperature and their influence in the calculation of the electrical parameters in a HCPV module. AIP Conf Proc 183–186:1616
12. Fernández EF et al (2013) A two subcell equivalent solar cell model for III–V triple junction solar cells under spectrum and temperature variations. Sol Energy 92:221–229
13. Fernandez E, Almonacid F, Rodrigo P, Perez-Higueras P (2013) Model for the prediction of the maximum power of a high concentrator photovoltaic module. Sol Energy 97:12–18
14. Fernández E, Almonacid F, Rodrigo P, Pérez-Higueras P (2014) Calculation of the cell temperatura of a high concentrator photovoltaic (HCPV) module: a study and comparison of different methods. Sol Energy Mater Sol Cells 121:144–151
15. Fernández E, Almonacid F, Ruiz-Arias J, Soria-Moya A (2014) Analysis of the spectral variations on the performance of high concentrator photovoltaic modules operating under different real climate conditions. Sol Energy Mater Sol Cells 127:179–187
16. Fernandez EF, Almonacid F, Mallick KT, Perez-Higueras P (2015) Analytical modelling of high concentrator photovoltaic modules based on atmospheric parameters. Int J Photoenergy 2015:8
17. Fernández EF, Rodrigo P, Almonacid F, Pérez-Higueras P (2014) A method for estimating cell temperature at the maximum power point of a HCPV module under actual operating conditions. Energy Mater Sol Cells 124:159–165
18. Fernandez E et al (2013) Calculation of cell temperature in a HCPV module using Voc. In: Proceedings of the 2013 Spanish conference on electron devices, CDE, 2013, art no 6481406
19. García-Domingo B, Aguilera J, de la Casa JFM (2014) Modelling the influence of atmospheric conditions on the outdoor real performance of a CPV (concentrated photovoltaic) module. Energy 70:239–250
20. Green MA et al (2014) Solar cell efficiencies tables (version 43). Prog Photovolt Res Appl 22:1–9
21. GTM Research (2011) CPV consortium
22. Gueymard C (2001) Parameterized transmítance model for direct beam and circumsolar spectral irradiance. Sol Energy 71(5):325–346
23. Haberlin H (2012) Photvoltaics. System design and practice. Wiley, West Sussex
24. Henry C (1980) Limiting efficiencies of ideal single and multiple energy gap terrestrial solar cells. J Appl Phys 51(13):4494–4500
25. Hornung TS (2012) Estimation of the influence of Fresnel lens temperature on energy generation of a concentrator photovoltaic system. Sol Energy Mater Sol Cells 99:333–338

26. IEC (1998) International standard IEC 61724: photovoltaic system performance monitoring—guidelines for measurement, data exchange and analysis, 1st edn, Geneve
27. IEC (2011) IEC60904-5, photovoltaics devices—part 5: determination of the equivalent cell temperature (ECT) of photovoltaic (PV) devices by the open-circuit voltage method
28. IEC (2012) IEC 62670-1. Concentrator photovoltaic (CPV) module and assembly performance testing-standard conditions
29. ISO (1990). ISO 9060: specification and classification of instruments for measuring hemispherical solar and direct solar radiation, Geneva
30. Ju X et al (2013) An improved temperature estimation method for solar cells operating at high concentrations. Sol Energy 93:80–89
31. King D, Boyson W, Kratochvil J (2004) SAND2004-3535. Photovoltaic array performance model. Sandia National Laboratories, Albuquerque
33. Kurtz S, Muller M, Marion, B, Emery K (2010) Considerations for how to rate CPV. In: Proceedings 6th international conference on concentrating photovoltaic systems (CPV 6), Freiburg
34. Kurtz S et al (2008) A comparison of theoretical efficiencies of multi-junction concentrator solar cells. Prog Photovolt Res Appl 16:537–546
35. Landsberg PT, Markvart T (2003) Ideal efficiencies. Practical handbook of photovoltaics. Elsevier, UK, pp 124–134
36. Martí A, Araújo GL (1996) Limiting efficiencies for photovoltaic energy conversion in multigap systems. Sol Energy Mater Sol Cells 43:203–222
37. McMahon W et al (2008) Fill factor as a probe of current-matching for GaInP2/GaAs tandem cells in a concentrator system during outdoor operation. Prog Photovolt Res Appl 16(3):213–224
38. Muller M et al (2011) Determining outdoor CPV cell temperature. In: AIP conference proceedings, pp 331–335
39. Muller M, Marion B, Kurtz S, Rodriguez J (2010) An investigation into spectral parameters as they impact CPV module performance. AIP conference proceedings, Freiburg, pp 307–311
40. Muñoz FJ, Almonacid G, Nofuentes G, Almonacid F (2006) New method based on charge parameters to analyze the performance of stand-alone photovoltaic systems. Sol Energy Mater Sol Cells 90:1750–1763
41. NREL (2014) National Center for Photovoltaics. [Online] available at: http://www.nrel.gov/ncpv/images/efficiency_chart.jpg. Accessed 15 May 2014
42. Peharz G, Ferrer Rodríguez J, Siefer G, Bett A (2011) A method for using CPV modules as temperature sensors and its application to rating procedures. Sol Energy Mater Sol Cells 95:2734–2744
43. Peharz G, Siefer G, Bett AW (2009) A simple method for quantifying spectral impacts on multi-junction solar cells. Sol Energy 83(9):1588–1598
44. Pérez-Higueras P, Muñoz-Cerón E, Almonacid G, Vidal P (2011) High concentrator photovoltaics efficiencies: present status and forecast. Renew Sustain Energy Rev 15:1810–1815
45. Philipps S et al (2010) Energy harvesting efficiency of III–V triple-junction concentrator solar cells under realistic spectral conditions. Sol Energy Mater Sol Cells 94:869–877
46. Rivera A, García-Domingo B, del Jesús M, Aguilera J 2013. Characterization of concentrating photovoltaic modules by cooperative competitive radial basis function networks. Expert Syst Appl 40:1599–608
47. Rodrigo P, Fernández E, Almonacid F, Pérez-Higuera P (2013) Models for the electrical characterization of high concentration photovoltaic cells and modules: a review. Renew Sustain Energy Rev 26:752–760
48. Rodrigo P, Fernández E, Almonacid F, Pérez-Higueras P (2014) Review of methods for the calculation of cell temperature in high concentration photovoltaic modules for electrical characterization. Renew Sustain Energy Rev 38:478–488

49. Rubio F et al (2008) Deploying HCPV powerplant—ISFOC experiences. In: Proceedings of the 33rd IEEE photovoltaic specialists conference, PVSC'08, San Diego
50. Siefer G, Bett AW (2014) Analysis of temperature coefficients for III–V multijunction junction concentrator cells. Prog Photovolt Res Appl 22:515–524
51. Sinke W, Bett A et al (2011) A strategic research agenda for photovoltaic solar energy technology, 2nd edn
52. Steiner M et al (2014) YieldOpt, a model to predict the power output and energy yield for concentrating photovoltaic modules. Prog Photovolt Res Appl. doi:10.1002/pip.2458
53. Stoffel T, Renné D, Myers D, Wilcox S (2010) Concentrating solar power. Best practices handbook for the collection and use of solar resource data. National renewable energy laboratory. Technical report NREL/TP-550-47465
54. Tobías I, Luque A (2002) Ideal efficiency of monolithic, series-connected multijunction solar cells. Prog Photovolt Res Appl 10:323–329
55. WMO (2008) WMO guide to meteorological instruments and methods of observation, WMO-no 8, 7th edn, Geneve
56. Yandt MD et al (2012) Estimating cell temperature in a concentrating photovoltaic system. In AIP conference proceedings, pp-172–175

Solar Resource for High-Concentrator Photovoltaic Applications

José A. Ruiz-Arias and Christian A. Gueymard

Abstract Direct solar radiation is the main fuel for concentrating photovoltaic (CPV) technologies. At any instant, the magnitude and spectral distribution of incoming direct normal irradiance (DNI) on the concentrator determines the instantaneous power produced by the generator. On a seasonal or mean annual basis, the magnitude of the DNI resource also directly affects the design of the whole system. Therefore, detailed knowledge of the available solar resource—essentially in terms of broadband DNI—is required at the system's design stage to evaluate the anticipated power to be produced by the projected CPV plant. This chapter is devoted to providing a better understanding of the current methods used in solar resource assessment to accommodate the specific needs of CPV projects. To this aim, the chapter starts with an introductory discussion on extraterrestrial solar radiation and its transfer throughout the Earth's atmosphere. Later on, the most common solar radiation modelling approaches for solar energy applications are discussed preceding a brief review of the best current measuring techniques and data quality-control methods for solar radiation. This includes important measurement recommendations for CPV applications. The chapter ends with brief discussions on spectral and circumsolar solar radiation.

1 Introduction

A key feature of photovoltaic (PV) and concentrating photovoltaic (CPV) technologies is their relatively high scalability. Large projects, however, require considerable financial investments that are usually supported by private financial institutions. Therefore, their "bankability" rules must be satisfied. Considering that

J.A. Ruiz-Arias (✉)
University of Malaga, Malaga, Spain
e-mail: jararias@ujaen.es

C.A. Gueymard
Solar Consulting Services, Colebrook, USA
e-mail: chris@solarconsultingservices.com

P. Pérez-Higueras and E.F. Fernández (eds.), *High Concentrator Photovoltaics*,
Green Energy and Technology, DOI 10.1007/978-3-319-15039-0_10

the gross revenue of CPV plants is proportional to their power production—and thus also essentially proportional to the available direct normal irradiance (DNI)—the proper evaluation of the available solar resource during a long-term period is critical to secure financing. This must be performed with a sufficient degree of certainty as to guarantee not only the project's bankability but also its optimal design and ultimately its correct performance over time. The long-term (interannual and decadal) DNI variability is important to predict the power output and revenue during the lifetime of the system assuming, of course, that historical trends can be extrapolated into the future. In addition, the short-term temporal variability of the historical DNI and its ramp rates may be important in the context of inverter safety, grid stability, and complementarity with other variable energy sources.

The bankability issue is important in CPV because the technology itself is not as mature as other solar technologies, such as PV or concentrating solar thermal power, which tends to make CPV projects appear more risky to investors. Providing high-quality solar resource assessments is a way to objectively improve bankability while subjectively compensating for this perception at least to some extent. In addition to these key quantitative aspects, various other considerations may affect the performance of CPV systems as discussed in the following text.

The spectral quality of sunlight is important because CPV cells have various spectral responses. With current multijunction HCPV cells, the power production is directly affected by the spectral distribution of DNI, which varies rapidly over time and space, and thus must be predicted so that accurate performance simulations of HCPV modules and systems can be obtained. Recent research has been geared toward the development of "tunable" multijunction cells whose design would be customizable according to the prevalent spectral conditions at each projected CPV power plant site. If this avenue proves successful and cost-effective, it can be anticipated that this would make the local solar resource become a key element toward the selection of the most suitable CPV technology from the type of PV cell to the concentrating optics. Various aspects of spectral solar irradiance are discussed in Sect. 6.

A fraction of incident irradiance, known as circumsolar irradiance (CSI), emanates from the sky rather than from the Sun's disc. It may affect the performance of concentrator optics, etc., as well as what is really incident on the CPV system compared with local DNI measurements. This issue is discussed in Sect. 7.

1.1 Concepts and Definitions

At the Earth's surface, sunlight is a heterogeneous and variable combination of electromagnetic waves with wavelengths ranging from 0.3 to 4 μm (known customarily as "shortwave" spectral range). In the present context of terrestrial solar applications, the term solar "radiation" refers to the electromagnetic radiation in this shortwave spectral range, which contains most of the solar spectrum's total energy that reaches the Earth's surface.

Solar radiation transports photonic energy. In the present context, the flux density of monochromatic solar radiant energy F_λ, that is, the solar radiant energy per unit wavelength, unit time, and perpendicular unit area, is referred to as "solar irradiance" and is typically measured in W m^{-2} nm^{-1}. The total broadband flux over an extended spectral band with limits $[\lambda_1, \lambda_2]$ is obtained by summing F_λ over all wavelengths in that interval resulting in a broadband solar irradiance with unit of W m^{-2}. In contrast, the radiant intensity I_λ, or solar spectral "radiance" in the present context, is defined as the flux density of solar radiant energy per unit solid angle. It is usually expressed in W m^{-2} nm^{-1} sr^{-1}.

2 Extraterrestrial Solar Radiation

In the study of solar radiation at the Earth's surface, the atmosphere can be considered as a filter that selectively modifies the spectral power distribution of solar radiation at the top of the atmosphere (TOA), also referred to as "extraterrestrial irradiance." Thus, it is logical to start the characterization of solar radiation by studying the incoming solar spectrum at TOA before it is perturbed by the Earth's atmosphere. Both the total amount of the Sun's radiated energy that is received at TOA and its spectral distribution are described in this section. The former, which is referred to as "total solar irradiance" (TSI or E_{n0}), is measured on a plane normal to the Sun's rays and reduced to the average Sun Earth distance ($R_0 = 1.496 \times 10^{11}$ m, or ≈ 1 AU). It can be observed directly with a spaceborne broadband radiometer or computed from the solar spectral irradiance $E_{n\lambda}$ as:

$$E_{n0} = \int_0^\infty E_{n\lambda} \mathrm{d}\lambda \tag{1}$$

2.1 Total Solar Irradiance

The output energy from the Sun varies with solar activity. Long-term variability is a direct consequence of the solar cycle, which has an average duration of 11 years. Because of these time variations, the term "total solar irradiance" should be preferred rather than the older concept of solar constant (SC), which is, however, still used to refer to the long-term average value of TSI.

After nearly a century of unsuccessful attempts at determining TSI from surface measurements, satellites started to routinely acquire relatively precise and stable observations in 1978. Since then, many space missions have been providing time series of TSI. Their combination and corrections led to continuous long-term estimates of TSI, such as the World Radiation Center Physikalisch-Meteorologisches Observatorium Davos (PMOD) composite [21], which currently covers 36 years

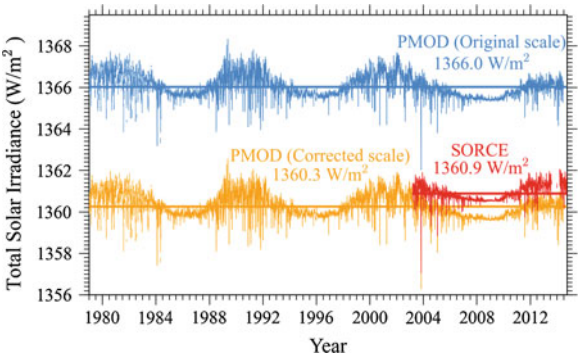

Fig. 1 Daily total solar irradiance from the PMOD (version 42_64_1406) and SORCE data sets. Both original and corrected TSI values are shown for the PMOD data set. The *horizontal lines* are the average daily TSI value in each case (SC), whose numeric value is annotated in the plot

(since November 17, 1978). An extended version of it adds estimated values for the period January 1, 1976, to November 16, 1978, to provide data over the entire solar cycle that started at the former date.

The TSI observations obtained by NASA's Solar Radiation and Climate Experiment[1] (SORCE) space mission surprisingly disagreed with the PMOD and other data. During the period 2003 to 2014, the mean difference between the SORCE daily TSI and its PMOD counterpart was ≈5 W m^{-2}, which could finally be traced to a systematic error in older measurements and thus in the historical PMOD data set.[2] This problem is now corrected in version 42_64_1410 (the latest as of this writing).[3] As a consequence, the SC value of 1366 W m^{-2} previously obtained with the PMOD data decreased to 1360.3 W m^{-2}. In parallel, the 2003 to 2014 average TSI value from SORCE amounts to 1360.9 W m^{-2}. Therefore, a notable agreement has now been achieved between these two independent datasets. It can be expected that the results from newer spaceborne instruments, such as a four-channel precision filter radiometer or the future total and spectral solar irradiance sensor, might change the value of SC by a few tenths of a Watt.

Figure 1 shows the daily TSI observations from PMOD and SORCE. Normal short-term solar activity results in daily TSI variability with a standard deviation of 0.39 W m^{-2} in both the PMOD and SORCE data. Because such a small departure from the mean value of TSI can be considered negligible in engineering applications, the use of a fixed SC value to characterize TSI is considered perfectly adequate. In Fig. 1, low TSI values are associated with sunspots, whereas high values are caused by the hot and bright areas called "faculae." The 11-year solar cycles are clearly apparent from the time series.

[1]Available at http://lasp.colorado.edu/lisird/sorce/sorce_tsi/

[2]For details see ftp://pmodwrc.ch/pub/Claus/VIRGO-TSI/VIRGO_Char2Space.pdf

[3]Available at ftp://pmodwrc.ch/pub/data/irradiance/composite/

Due to the eccentricity of the Earth's orbit around the Sun, the Sun Earth distance is continuously changing. Therefore, the SC value must be corrected by a multiplicative factor S to yield the actual TSI at TOA. As described by Michalsky [60], the daily correction factor S—which varies seasonally within the range ±3.34 %—can be computed precisely from:

$$S = [1.00014 - 0.01671 \cos g - 0.00014 \cos(2g)]^{-2} \quad (2)$$

where g is the mean anomaly (in radians) calculated from the number n of days elapsed since the current astronomical epoch (January 1, 2000 Universal Time) as:

$$g = 6.24006 + 0.0172019699\, n. \quad (3)$$

2.2 Solar Spectral Irradiance

Planck's law describes the spectral radiation emitted by a perfect blackbody at a known absolute temperature T. A perfect blackbody absorbs all of the energy it receives and emits it at the same rate. Assimilating the Sun as a blackbody, Planck's law leads to a straightforward approximation of the emission spectrum of the Sun. Furthermore, Stefan Boltzmann's law, $E = \sigma T^4$, which results from the spectral integration of Planck's law over a complete sphere, can be used to evaluate the effective absolute temperature of the Sun from, e.g., TSI observations. Specifically, considering $\sigma = 5.67 \times 10^{-8}$ W m^{-2}K^{-4} (the Stefan Boltzmann constant) and the-mean solar radius $R_s = 6.96 \times 10^8$ m, the radiant output of the Sun is $E = \text{SC}\,(R_0/R_s)^2$. Hence, $T_s = 5770$ K for SC = 1360.3 W m^{-2}.

Figure 2 shows the spectral irradiance of perfect blackbodies at absolute temperatures of 5500, 5770, and 6000 K. It also shows the extraterrestrial spectrum of

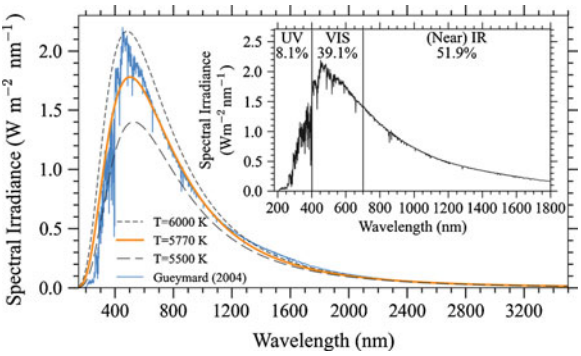

Fig. 2 Spectral irradiances for perfect spectral blackbodies at 5500, 5770, and 6000 K compared with the Gueymard [31] solar spectrum. The inset shows an expansion over the ultraviolet (UV), visible (VIS), and near infrared (NIR) spectral regions as well as the fraction of sunlight contained in each band

Gueymard [31] that is here scaled down by a factor of 1360.3/1366.1 = 0.99575 to reflect the revised value of SC suggested in Sect. 2.1. The difference between the smooth 5770 K curve and the Gueymard spectrum simply results from the fact that the Sun is not a perfect blackbody.

The precise measurement of the spectral distribution of solar irradiance is cumbersome and much less accurate than the observation of TSI because detectors of varying characteristics must be used to cover different parts of the spectrum. Their absolute calibration is also approximately an order of magnitude less accurate than that of absolute radiometers used for TSI. A complete spectrum necessitates an appropriate combination of multiple sources of data obtained from different sensors and usually from different solar activity periods. This piecewise combination, in practice, additionally involves different scaling factors so that the total irradiance exactly amounts to a preselected value of SC as described by Gueymard [31].

The solar spectrum is broadly made of three different spectral bands: ultraviolet (UV), visible (VIS), and infrared (IR) as shown in the inset of Fig. 2. The UV band (approximately 0.1–0.4 μm) is the most energetic part of the shortwave spectrum in terms of photonic activity, but its total power is small (≈8 % of SC). Some of its photons have sufficient energy to initiate photochemical reactions that may result in tissue injuries and DNA damage. Fortunately, approximately 99 % of these photons are absorbed by oxygen (O_2) and ozone (O_3) molecules in the mesosphere and the stratosphere. The VIS band (approximately 0.4–0.7 μm) comprises the part of the spectrum to which human eyes respond. It also contains the wavelengths at which the Sun's emissivity is the highest and a notable fraction of SC (≈39 %). The IR band extends beyond 0.7 μm and includes the NIR, which contains ≈52 % of SC between 0.7 and 4 μm. The residual TOA irradiance beyond 4 μm (far IR) amounts to <1 % of SC.

3 Solar Radiation at the Earth's Surface

Throughout its path from TOA to the Earth's surface, solar radiation undergoes significant attenuation, in terms of both magnitude and spectral distribution, which depends on the amount of the traversed constituents and their optical properties. From this standpoint, and considering that some of these constituents are variable over time and space, the atmosphere can be conveniently abstracted as an optical spectral filter whose properties change dynamically. In this section, the most important interactions between sunlight and the atmosphere are introduced.

3.1 Sun-Earth Geometry

The relative Sun-Earth geometry determines the Sun's rays' pathlength through the atmosphere, which is an essential factor that affects the extinction of solar radiation.

The position of the Sun with respect to an observer on the Earth's surface is described in a spherical coordinate system in which the Sun's position is defined by its zenith and azimuth angles. The Sun's zenith angle (θ_z) is the angle subtended between the imaginary line that joins the local observer and the Sun and the imaginary line that joins the Earth's center and the local observer's position (Fig. 3). The Sun's azimuth angle (ψ) is the angle subtended between the plane that contains the former two imaginary lines and the plane that contains the great circle determined by the north-pointing local meridian. It is conventionally measured clockwise from north (0°) to east (90°), south (180°), and west (270°). For our purposes, which exclude shading considerations, only θ_z is of importance. The Sun's zenith angle is computed from:

$$\cos\theta_z = \sin\delta\sin\varphi + \cos\delta\cos\varphi\cos\omega \tag{4}$$

where δ is the Earth's declination, φ is the local geographical latitude, and ω is the local hour angle (zero at solar noon). The main Sun-Earth geometry variable here is δ. It can be calculated from a number of formulas that have been proposed in the literature with varying degrees of accuracy. For CPV applications, where tracking accuracy is of the utmost importance, accuracy of the calculated θ_z should be of the order of ±0.001° or better [7, 9, 25, 60, 77, 78]. Currently, the most accurate algorithm—but also the slowest—is that of Reda and Andreas [78].

The *optical mass* (m) is defined as the ratio between a slant path-length for any zenith direction and the vertical path-length (Fig. 3). Because the atmospheric constituents have different vertical density profiles, they also normally have different specific optical masses for the same zenith angle. The optical mass accounts for the increased amount of substance that is traversed by the Sun's rays with respect to a vertical trajectory. In the particular case of molecules and uniformly mixed gases, the optical mass is referred to as *optical air mass* or simply *air mass*. It is the one reported most usually. The optical mass of constituents that are concentrated at high altitude (e.g., O_3) is lower than the air mass. Vice versa, the optical mass of constituents concentrated in the lower atmosphere (e.g., aerosols and water vapour) is larger than the air mass. By definition, the minimum air mass is 1 (AM1) for a vertical Sun ($\theta_z = 0$). However, it is customary to refer to air mass 0 (AM0) for the TOA irradiance. Some authors use the concept of "absolute air mass" where

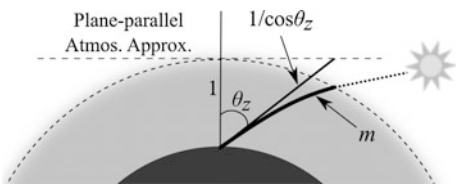

Fig. 3 Optical air mass, m, and solar zenith angle, θ_z. The *dark thick line* shows the bending of the sunlight path due to atmospheric refraction

m is corrected by the relative atmospheric pressure (i.e., surface pressure divided by standard pressure), but this can be confusing and thus is not recommended.

Assuming a hypothetical plane-parallel atmosphere, the air mass would be $1/\cos\theta_z$ (Fig. 3). Although this assumption is very convenient to solve the radiative transfer (RT) problem in the atmosphere, it is not appropriate for solar radiation calculations at large solar zenith angles. For this reason, it is quite common to use empirical corrections that account for the Earth's sphericity. Such is the case, for instance, of the spherical approximation proposed by Gueymard [29, 30]:

$$m = \left[\cos\theta_z + 0.48353\theta_z^{0.095846} \Big/ (96.7412 - \theta_z)^{1.754}\right]^{-1}, \tag{5}$$

where θ_z is in degrees and should consider light refraction for low sunlight.

3.2 Atmospheric Extinction and Direct Solar Radiation

The atmosphere absorbs and scatters solar radiation. The former process results from the capture of light photons by molecules (such as O_3) or particles (such as soot). In the latter process, the atmosphere scatters the light photons out of their direction of origin into all possible directions. This is how air molecules, aerosol particles, and clouds scatter incident sunlight generating the (variable) sky diffuse radiance. The combined effects of absorption and scattering are often referred to as either *extinction* or *attenuation* and are physically quantified by means of their respective optical depth (τ). Precise modelling of all extinction processes is necessary to evaluate the direct irradiance at the surface at any point in time or space.

Specifically, the downward solar irradiance flux incident on a surface normal to the Sun's rays is referred to as DNI. It can be considered in the form of either a broadband irradiance, noted as B_N, or a spectral irradiance, noted as $B_{N\lambda}$. Because the extinction processes are a strong function of wavelength, the precise evaluation of $B_{N\lambda}$ requires detailed information about the optical depth, $\tau_{i\lambda}$, of each extinction process i at wavelength λ (in μm) as:

$$B_{N\lambda} = E_{n\lambda} \exp\left(-\sum_i m_i \tau_{i\lambda}\right) \tag{6}$$

More details on spectral irradiance are provided in Sect. 6. Because spectral calculations are complicated and time consuming, an alternate way to the use of (Eq. 6) and its subsequent spectral integration is to develop a simpler radiation model that determines B_N directly with limited or no spectral information. This can be performed with simplified, broadband radiation models (Sect. 4).

Because measurements of DNI are much less common than those of global horizontal irradiance (G), also commonly referred to as GHI, it is worth mentioning that B_N can be obtained from G using:

$$B_N = (G - D)/\cos\theta_z, \tag{7}$$

where D is the diffuse horizontal irradiance. Because measurements of D are again less common than those of G, it is often necessary to estimate D empirically from G. This approach is discussed in Sect. 4.2.

3.3 Atmospheric Constituents: Gases, Aerosols, and Clouds

The radiatively active constituents of the atmosphere spread over three different broad types: gases, which act at the molecular level; aerosols, which are small particles suspended in the air; and clouds, which are made principally, although not exclusively, of water droplets and/or ice crystals.

Up to 98 % of the atmosphere is made up with only two constituents: nitrogen and O_2. The remaining 2 % is constituted by water vapour (mostly near the ground), inert gases such as argon, and trace gases such as carbon dioxide (CO_2), methane (CH_4), O_3, nitrous oxide, carbon monoxide, and chlorofluorocarbon compounds (of anthropogenic origin). Very importantly, however, the radiative effect of the components in this 2 % of the atmosphere is disproportionally large compared with their reduced amount. All atmospheric gases contribute to the extinction of solar radiation through molecular scattering, also known as "Rayleigh scattering." In addition, some gases, such as O_2, O_3, CO_2, CH_4, or water vapour, absorb radiation (some very strongly) in various parts of the solar spectrum (Sect. 6).

Aerosols are particles suspended in the atmosphere. Their shape is variable and intricate, so they are typically abstracted as spheroid particles. Their sizes sweep a wide range, from <0.1 up to >20 μm, resulting in intricate size distributions. Aerosols can be of (1) natural origin such as dust and sand dragged from deserts, salt particles from the sea surface, smoke and soot from wildfires or volcanic eruptions, etc.; or (2) anthropogenic origin such as smoke and soot from pollution. Aerosol particles are mostly concentrated in the lower troposphere, typically lower than 2 km, although they can also be lifted higher up to the upper atmosphere and transported thousands of kilometres away. This frequently occurs as a consequence of strong dust storms [44].

Clouds are mostly formed by water droplets and ice crystals. Normally, water clouds are concentrated in the lower layers of the atmosphere (up to approximately 6 km above the ground) and ice clouds (cirrus type) in the highest layers (above appoximately 6 km). Thin clouds (typically of the cirrus type) can transmit a large fraction of direct irradiance and are thus of significance in CPV applications as shown in Sect. 3.4.

3.4 Broadband Extinction of Solar Radiation

The combination of variable amounts of atmospheric constituents and their corresponding optical properties determine how much DNI is available at the Earth's surface. Figure 4 shows an estimate of the individual atmospheric transmittances for uniformly mixed gases, water vapour, aerosols, and clouds. The uniformly mixed gases absorb solar radiation depending on their total columnar amounts, which are typically proportional to surface pressure. In particular, Fig. 4a shows that, on

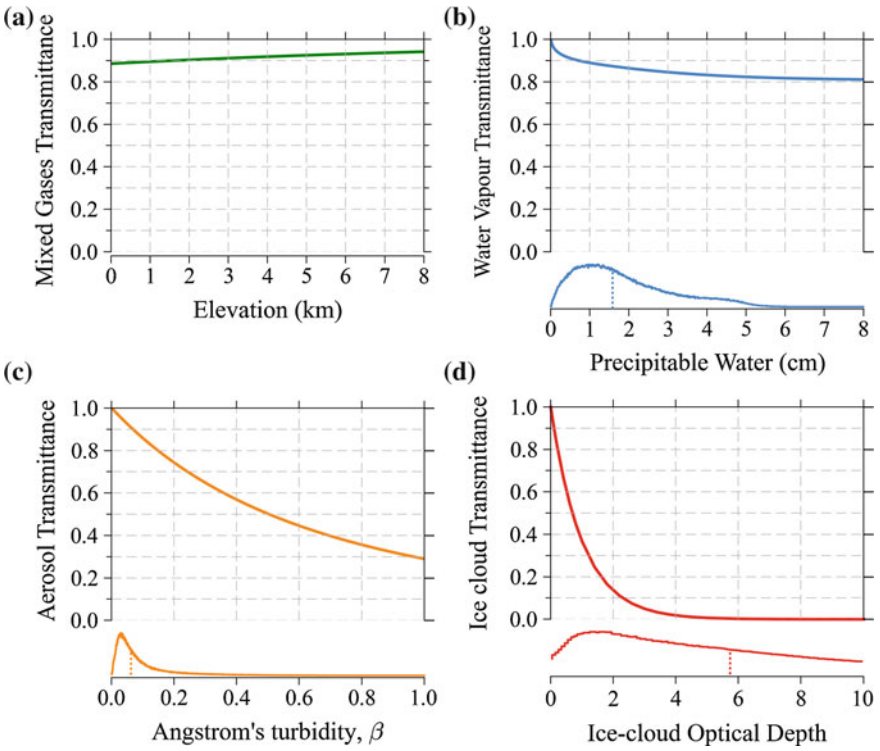

Fig. 4 Individual atmospheric transmittances of different atmospheric constituents for a zenith Sun ($m = 1$). **a** Zenith transmittance of uniformly mixed gases against surface elevation. **b** Zenith transmittance of water vapour against PW (*upper curve*) and frequency distribution of global PW values (*lower curve*). **c** Zenith transmittance of aerosols against Ångström turbidity β (*upper curve*) and frequency distribution of global β values (*lower curve*). **d** Zenith transmittance of ice clouds against cloud optical depth (COD) (*upper curve*) and frequency distribution of global COD values (*lower curve*). All atmospheric transmittances are calculated with the libRadtran radiative transfer library, v1.7 (http://www.libradtran.org). The global frequency distributions of PW and β are obtained from multiyear data from the Aerosol Robotic Network (AERONET) (http://aeronet.gsfc.nasa.gov), whereas that of COD is obtained from 1 year of satellite retrievals from the Climate Monitoring Satellite Facility [CM-SAF (http://www.cmsaf.eu)]. Note that the y-axes for the frequency distributions are not shown because only the relative distribution of data is of interest here. The *vertical dotted lines* in the frequency distributions curves show the median value of each distribution, i.e., it splits the distributions into two halves with exactly the same number of samples

average, the transmission of DNI by uniformly mixed gases is quite stable at approximately 90 %, and slightly increases with increasing surface elevation.

Precipitable water (PW) is a commonly used variable to represent the total columnar amount of water vapour. If the water vapour in a vertical column of 1 cm^2 base area were condensed, PW would be the height (cm) of that column. (Because the mass of 1 cm^3 of water is 1 g, equivalent units for PW are g/cm^2 or g/cm^3.) Considering the global distribution of PW shown in Fig. 4b, solar radiation attenuation by water vapour is normally in the range of 10–15 %.

Solar radiation extinction by aerosols and clouds mostly occurs by scattering, along with some absorption, of sunlight photons. The exact relative proportions of scattering and absorption are not relevant to CPV applications because only the total attenuation impacts DNI. The total (scattering + absorption) aerosol optical depth (AOD) depends on the refraction index of the aerosol particles, their size distribution, and the sunlight's wavelength. The AOD at 1 μm is known as the Ångström turbidity coefficient (β) and is a customary variable to characterize atmospheric turbidity. The extinction of direct solar radiation for β values less than approximately 0.1 is comparable to the one normally produced by PW (Fig. 4b, c). However, for greater AODs, the aerosol-induced extinction increases steadily. If the aerosol transmittance curve is analyzed in combination with the global distribution of β values shown in Fig. 4c, it is concluded that approximately half of the β values—specifically, the upper half of β values—lie on the high-extinction region. Therefore, extinction of DNI by aerosols may be quite important and is typically the main source of extinction under cloudless conditions by far.

Desert areas, which are most interesting for solar applications, are generally characterized by low cloudiness and occasionally or frequently high AOD values. Therefore, a proper characterization of AOD and other aerosol optical properties is crucial to correctly model DNI and obtain accurate solar resource assessments, but is difficult and costly in practice.

Conversely to AOD and other optical depths COD is fairly independent of wavelength. Therefore, very often its spectral dependence is neglected, and a single value is used. As a general rule, low- and middle-altitude clouds are optically thick because they are made of liquid droplets. Their COD is typically >5. High-altitude clouds (e.g., cirrus), in contrast, are mostly made of ice crystals, which makes them optically thin. Their COD ranges from a fraction of 1 to a few tenths. Clouds can only transmit DNI if their COD is lower than ≈5. Figure 4d shows that approximately 50 % of all ice clouds covering Earth produce a complete extinction of DNI. The remaining 50 % only attenuate DNI partially.

From a solar resource perspective, the modelling of DNI's attenuation is not very sensitive to errors in the estimation of PW [41] but conversely is very sensitive to errors in AOD and COD (as can be interpreted from Fig. 4). Significant errors in modelled DNI may typically ensue. Such errors may be large because both AOD and COD are quite complex to observe and the current remote-sensing techniques from satellite platforms are still affected by considerable noise. This makes the modelling of DNI quite difficult and its uncertainty significant over difficult areas [13].

4 Solar Radiation Modelling Approaches

Solar radiation can be modelled in various ways from simple yet limited statistical parameterizations to complex and computationally intensive physical methods. The most suitable approach depends on the specific application for which solar radiation is required and the boundary conditions of the problem at hand (i.e., which input variables are known and with what accuracy). In this section, the most widespread current modelling approaches are introduced along with a highlight of their intended applications, strengths, and weaknesses.

4.1 Clear-Sky Models

Because solar power production peaks under cloudless or quasi-cloudless situations, the accurate modelling of clear-sky radiative processes is key to the proper evaluation of the surface DNI and hence of CPV power production.

In this context, clear-sky radiative transfer (CSRT) models are of particular interest. Because they do not need to consider the vertical profile of atmospheric attenuation or the radiative effects of clouds, large modelling simplifications are possible. In particular, many such models assume a single-layer atmosphere, i.e., the radiatively active properties of the atmosphere are considered to be homogenously distributed along the vertical column. CSRT models are numerical parameterizations based on statistical correlations and, to some extent, on physical foundations. These functions are derived from precise observations and/or detailed simulations using more rigorous models for the transfer of radiation throughout the atmosphere. Compared with rigorous (physical) models, simple CSRT models typically only require a simple description of the atmosphere such as total column quantities (e.g., precipitable water and surface pressure). They also simplify the spectral issue by relying on bulk computations over—most generally—just a single band (i.e., the full spectrum) or, at most, a few large spectral bands. Thus, most CSRT models directly produce the broadband radiative quantities, such as DNI and GHI, that are familiar to the solar community. However, when spectral information is necessary, fast models, such as SMARTS [27, 32] or SPCTRAL2 [6], also produce irradiance estimates with a moderate spectral resolution (Sect. 6).

During recent decades, the complexity of CSRT models has evolved to reflect the rapid improvements in observing methods of the atmosphere and particularly that of remote sensing. Thus, new generations of CSRT models have been devised to reconcile the availability and reliability of information and theoretical knowledge. For an illustration of this evolution, consider the European Solar Radiation Atlas model [82], which was proposed at the turn of this century and had a large effect on the European solar energy community. In this very simple CSRT model, the total atmospheric optical depth is represented by only one variable, namely the Linke turbidity factor, which combines the broadband effects of all attenuations.

More recent CSRT models not only separate these effects by requiring various inputs, such as PW and AOD, but they also even consider the spectral effect of aerosol extinction through the Ångström exponent (AE [see Sect. 6]). This step ahead in CSRT modelling was made possible by the steady increase in the amount and quality of observed variables of the Earth's system.

In recent benchmarking studies [3, 39, 45], the REST2 [33] and Ineichen broadband models [46] obtained the highest marks. They consist of a set of statistical and physical parameterizations that provide estimates of broadband surface irradiance from surface pressure, PW, AOD and, in the case of REST2, some other parameters such as AE. The McClear model has also been introduced recently [53]. Unlike the REST2 and Ineichen models, McClear estimates are based on a large assembly of precomputed solar irradiance values originally obtained with accurate RT models. The output values of McClear are then interpolated from these precomputed tables ("look-up table" approach). McClear's irradiance estimates are available worldwide from 2004 to present with only a few days lag (see http://www.soda-pro.com/es/web-services/radiation/mcclear).

Figure 5 compares 1-min GHI and DNI observations under clear-sky conditions at the Southern Great Plains ARM site in Oklahoma during 2011 *vis-à-vis* the simulated values with the McClear, Ineichen, and REST2 models. The GHI and DNI predictions of the Ineichen and REST2 models were produced using collocated observations of pressure, the PW and AOD. In contrast, McClear uses synthetic input data from numerical weather prediction (NWP) models (Sect. 4.4) and thus does not depend on any local ground observations of atmospheric constituents. Considering all data points ($N = 3853$), the three models produce reasonable values of GHI with a slight advantage to REST2. In contrast, only REST2 provides nearly unbiased estimates of DNI. In particular, McClear largely underpredicts DNI because the AOD input it uses is modelled rather than locally observed and is thus significantly too large for this site due to shortcomings in the underlying aerosol

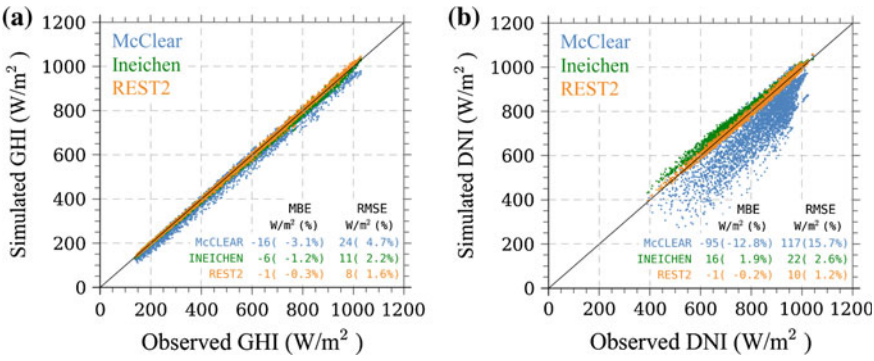

Fig. 5 Simulated values (using the McClear, Ineichen, and REST2 models) *versus* research-class cloudless solar irradiance observations from the Atmospheric Radiation Measurement (ARM) site in Oklahoma, USA, for **a** GHI and **b** DNI. The mean bias error and root mean square error values are shown in both W m^{-2} and percent in each case

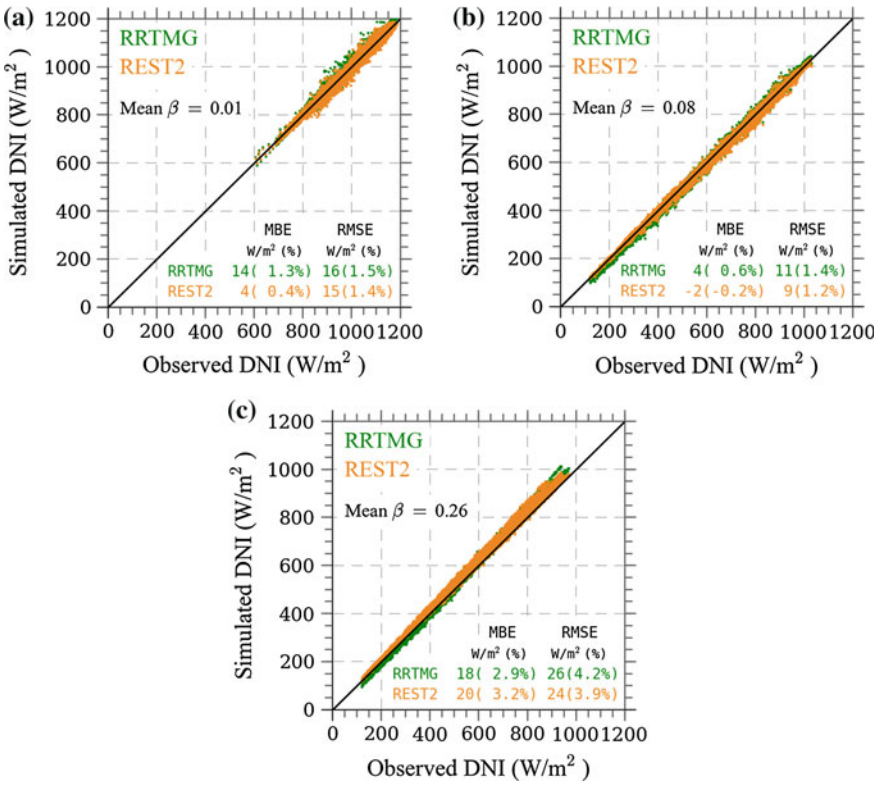

Fig. 6 Simulated clear-sky DNI values with the REST2 and RRTMG models *versus* research-class cloudless DNI observations at **a** Mauna Loa, Hawaii, **b** Plataforma Solar de Almeria, Spain, and **c** Masdar Institute, Abu Dhabi

model. This example shows the much greater impact of input errors on DNI than on GHI and also the underlying need for local atmospheric observations to undertake reliable DNI modelling.

The results shown in Fig. 5 correspond to a temperate site where turbidity is moderate, and therefore the attenuation caused by aerosols is not as high or as low as it can be in other regions. Figure 6, in contrast, shows the predictions made with REST2 and the rapid radiative transfer model (RRTMG) at three sites experiencing a wide range of aerosol regimes: (1) Mauna Loa (Hawaii), a high-elevation station considered representative of areas where turbidity is lowest and solar resource is highest; (2) Plataforma Solar de Almeria (Spain), located in a dry but temperate climate with intermediate atmospheric turbidity; and (3) Masdar Institute (Abu Dhabi), a station that experiences frequent haze episodes and thus high AOD. The RRTMG model uses 14 spectral bands over the shortwave spectrum and a detailed 2-stream algorithm with a precise description of the vertical profiles of atmospheric constituents. REST2 uses only 2 spectral bands and no vertical

profiling, which makes it up to 6 times faster than RRTMG. Nonetheless, it compares fairly well against cloudless DNI observations and even favourably against the DNI estimates of the detailed RRTMG model, including under high-turbidity conditions.

4.2 All-Sky Separation Models

The measurement of DNI involves more costly equipment than that of GHI (Sect. 5). Consequently, most historical records of solar radiation have only included GHI data and, only occasionally, DNI data. Adding DNI observations to radiometric networks has gained support only recently in part to help solar energy applications. Nonetheless, the radiometric sites observing only GHI still outnumber those where DNI is also measured. Using models to derive DNI from GHI offers a means to exploit GHI data for the many solar applications that also require DNI. As discussed later in Sect. 4.3, such models also provide DNI estimates whenever semiempirical GHI predictions are derived from satellite imagery. This makes an evaluation of the capabilities of such models all the more important.

Since the pioneering work of Liu and Jordan [56], the literature on "separation models" (strictly speaking these models separate GHI into its direct and diffuse components) has been rich and profuse probably because all are of an empirical nature and are thus simple to derive. Recently, Gueymard and Ruiz-Arias [42] presented a validation study of such models, with a specific focus on the evaluation of DNI over arid regions, where a large potential for solar power applications exists. Although 36 models were tested, nearly 90 were found in the historical literature. All of these models have the same approach of exploiting the underlying correlation between GHI and DNI: if DNI increases, so does GHI. Most models, however, rather exploit the empirical correlation between the ratio $K_d = D/G$, known as "diffuse fraction," and the ratio $K_t = G/G_0$, known as "clearness index," where G_0 is the extraterrestrial counterpart of G. Once K_d is determined from K_t, DNI can be derived from $B_N = (1 - K_d)\, G/\cos\theta_z$ in virtue of Eq. (7).

In addition to K_t, other predictors may be considered such as air mass, temperature, relative humidity, etc. A few separation models also incorporate a temporal variability index to help discriminate between the radiative impacts of stable conditions (cloudless or overcast conditions) and those of rapidly changing conditions (scattered clouds). Many functional forms have been proposed in the literature: piecewise functions [18, 79], polynomials [67], logistic functions [11, 86], artificial intelligence methods [17], and even approximate physical foundations [57, 73, 74, 92, 93].

Despite these developments, the multiple processes that occur in the atmosphere are so intricate that the performance achievable with such simple models is limited. This translates into large random errors in particular. In addition, the vast majority of existing separation models have no physical foundation and are rather empirical in essence because they are derived directly from observations at a few specific sites.

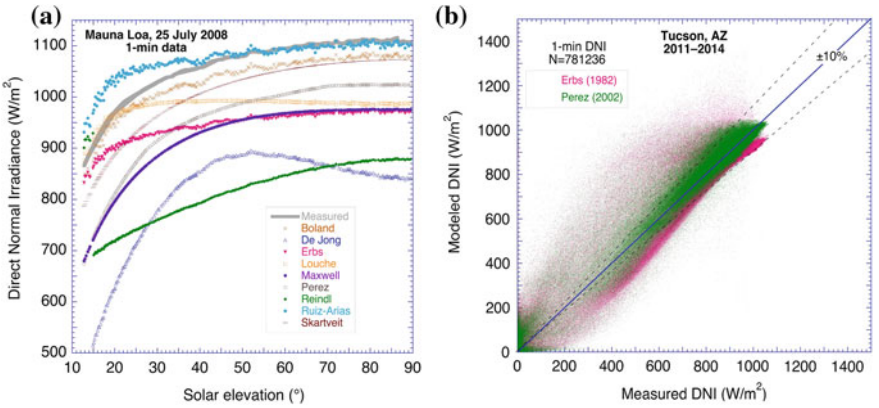

Fig. 7 Validation against DNI observations of DNI estimates using separation models from GHI observations. **a** Variation of DNI with solar elevation during a clear summer morning at Mauna Loa as measured and predicted by eight separation models. Figure based on data from Gueymard [37]. **b** Scatter plot of predicted *versus* measured 1-min DNI using the models proposed by Erbs et al. and Perez et al. [18, 74] at Tucson, AZ. Figure based on data from Gueymard and Ruiz-Arias [42]

Therefore, their performance varies from site to site depending on their respective atmospheric conditions. Similarly, it is virtually impossible to correctly guess which model would be best at any new site without preliminary validation of existing models or development of a new "local" model.

Figure 7 shows a comparison of observed and estimated DNI values from GHI observations using eight separation models. In particular, Fig. 7a shows results for a clear morning at Mauna Loa as a function of solar altitude. The estimation errors are high and very different between models suggesting the already noted strong "location" dependence of their performance. Figure 7b shows another particular case, this time using the popular models proposed by Erbs et al. [18] and Perez et al. [74], for the estimation of DNI from 1-min GHI observations at Tucson, Arizona. The latter model is also known as DIRINDEX. In detailed benchmarking studies [37, 42], DIRINDEX was found to generate fewer random errors than other models of its class. Even for this low-cloudiness location, the random errors in DNI estimates are remarkably large. Interestingly, this GHI-to-DNI model is used in two of the most well-known satellite-based solar radiation models,[4] as discussed further in Sect. 4.3.

4.3 Satellite-Based Models

The radiometers aboard satellite platforms observe the multispectral back-scattered radiance from the Earth's system. This includes scattered radiance from the Earth's

[4]SolarGIS (http://geomodelsolar.eu) and SolarAnywhere (https://www.solaranywhere.com

surface (land, water, ice), aerosol layers, and clouds. By combining this multispectral information in different ways, multiple properties of the Earth's system, including some cloud information, can be derived for each observed pixel. This cloud information can consist of either (1) derived physical and optical properties (such as COD, cloud fraction, cloud height) if using radiative transfer retrieval methods; or (2) just simple reflectance properties if not. In the former case, the solar irradiance at the surface can be evaluated from this detailed cloud information using an appropriate radiation model. This physical approach involves complex numerical processes and requires a detailed and precise description of the atmosphere [43, 65], which is still rarely available in the practice of solar resource assessment. Nevertheless, because this method provides a comprehensive description of solar fluxes in the atmosphere, and super-computing power now makes it operationally possible, this approach will probably become more prevalent in the near future.

The latter case, usually referred to as *semiempirical modelling*, is much simpler and more commonly used. It exploits the existing correlation between the radiance sensed by the satellite radiometer and the solar irradiance at the Earth's surface [12, 52, 55, 74, 75, 83].

Overall, the semiempirical modelling of DNI entails a three-step procedure. First, the ideal clear-sky GHI is modelled with a CSRT model (Sect. 4.1) using ancillary data of pressure, water vapour, aerosols, etc. Second, the cloud extinction estimate obtained from the satellite radiance observations is superimposed on the clear-sky GHI value. Finally, DNI is evaluated from the satellite-based GHI estimate using an all-sky solar radiation separation model (Sect. 4.2).

For any given location, the maximum back-scattered radiance sensed by the satellite radiometer occurs in presence of clouds, whereas the minimum is sensed under cloudless conditions. In that case, the radiance is due uniquely to the clear atmosphere and surface reflectance (generally referred to as *surface albedo*). This albedo varies over time depending on the biological cycle of the present vegetation, groundwater content, or presence of ice or snow. To separate the backscattered radiance reflected by the surface from that coming from clouds, a relative index, referred to as the *cloud index* (n), is used. This index varies linearly from 0 to 1 as sky conditions change from completely cloudless to completely overcast, respectively. The cloud index, which gives a quantitative assessment of cloud extinction, is correlated with the so-called *clear-sky index*, defined as $k_t^* = G/G_c$ where G_c is the ideal clear-sky GHI mentioned previously. The $n - k_t^*$ relationship is determined empirically. It is not unique, and it varies between semiempirical models [74, 75, 83]. The basic algorithmic chain in semiempirical models is therefore as follows: n is determined from the satellite radiance observations, then k_t^* is determined from n using the $n - k_t^*$ empirical relationship, and, finally, G is obtained as $k_t^* G_c$ using the G_c value obtained with the CSRT model. To derive DNI from G, an additional step, involving an all-sky solar radiation separation model, such as DIRINDEX [74], is required. However, according to Gueymard and Ruiz-Arias [42], this step typically introduces some bias and large random errors depending on location.

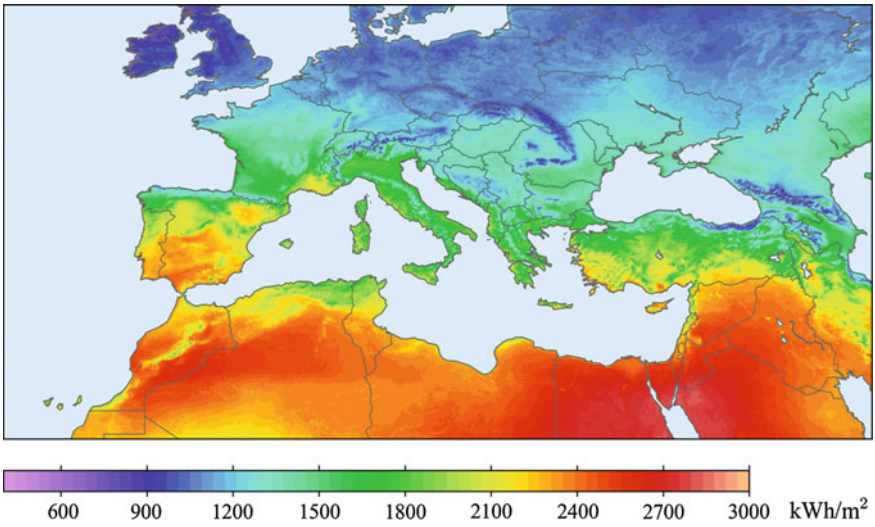

Fig. 8 Mean annual sum of DNI obtained during the period 2003 to 2005 from the CM-SAF (http://www.cmsaf.eu), which uses Meteosat Second-Generation satellite imagery and an approach based on Mueller et al. [66]

An example of a DNI map that results from the application of a semiempirical method, namely that of Mueller et al. [66], appears in Fig. 8. The method is used to construct the CM-SAF database from imagery generated by the SEVIRI sensor onboard the Meteosat Second-Generation geostationary satellite.

Although the semiempirical methodology is most widely used in solar-resource assessment studies, there are sources of uncertainty associated with it, the relative importance of which was discussed by Cebecauer et al. [13]. In particular, the proper evaluation of DNI under cloudless conditions requires an accurate evaluation of aerosol extinction. Because of shortcomings in most simple clear-sky models and in the aerosol data they use, large biases in monthly or annual DNI are frequently observed over arid areas in particular [39].

Ineichen [47] performed a thorough long-term validation study of 7 satellite-derived solar irradiance databases (in the public domain or not) derived with some of the most current models, thus representing the state-of-the-art in semiempirical modelling. Their simulated GHI and DNI hourly values were compared with high-quality ground observations from 18 stations in the European and Mediterranean region. The author found that the overall accuracy of the satellite-derived hourly GHI is characterized by a negligible bias and an SD between 17 and 24 %. For DNI, the models' bias and SD vary between −9 and +12 % and between 34 and 49 %, respectively. At a daily scale (respectively, monthly scale), the DNI models' bias and SD values vary between −9 and +11 % (−9 and +12 %), and between 21 and 35 % (10 and 16 %). Although large discrepancies may exist for specific sites and models, all of the products normally

provide an average annual GHI within one SD of the interannual variability. In the case of DNI, 8 of the 9 satellite models provided estimates within 1 SD of the interannual variability with the best SD being 6 %.

4.4 Numerical Weather Prediction Models

NWP models are mainly intended to provide weather forecasts. Indeed such models are routinely used by all meteorological services to predict the weather. NWP models typically generate forecasts by combining a more or less precise description of the atmosphere at an initial time, and a computer model that casts the state of the atmosphere to future times. The skill of weather forecasts therefore has a twofold component: (1) the accuracy of the atmosphere description at the initial time; and (2) the skill of the computer model to represent the physical processes of the atmosphere.

The description of the atmospheric initial conditions for NWP modelling is based on routine worldwide observations from, e.g., ground stations, radiosondes, geostationary and polar satellites, marine buoys, aircraft, or Global Positioning System sensors [97]. All of these data sources are ingested every few hours, quality controlled, and combined with other observations through a complex computational process called *data assimilation* [48, 49].

The computer model of the atmosphere consists of a set of complex partial differential fluid dynamics equations supported by numerical models of physical processes unaccounted in these equations. One such process is the transfer of solar radiation throughout the atmosphere, which is modelled with RT models. One of them is the popular RRTMG model already introduced in Sect. 4.1 (see Fig. 6). An RT model allows the NWP system to predict and evaluate the radiation absorbed at each level of the atmosphere (which causes its heating) as well as the total flux reaching the Earth's surface.

Because the solar feedback in most of the processes that occur in the atmosphere and at the surface can be well represented with only GHI, the specific calculation of DNI is usually not considered in NWP modelling. Recently, however, the interest in DNI has considerably increased, boosted mostly by requests from the solar energy community. In particular, the solar industry increasingly depends on accurate solar radiation and solar power production forecasts. The weather research and forecasting (WRF) NWP model [91] is one of the first NWP models to incorporate specific capabilities for DNI modelling. The WRF model's prediction skills for GHI and DNI have been evaluated by, e.g., Lara-Fanego et al. [50] and Perez et al. [76]. Its specific use to forecast DNI for CPV applications has also been discussed by Lara-Fanego et al. [51].

Atmospheric RT calculations are one of the most computationally intensive processes in NWP modelling. Consequently, the RT algorithms included in NWP models have been largely simplified and customized for the evaluation of GHI only. Fortunately, the steady increase in computational power allows a more detailed

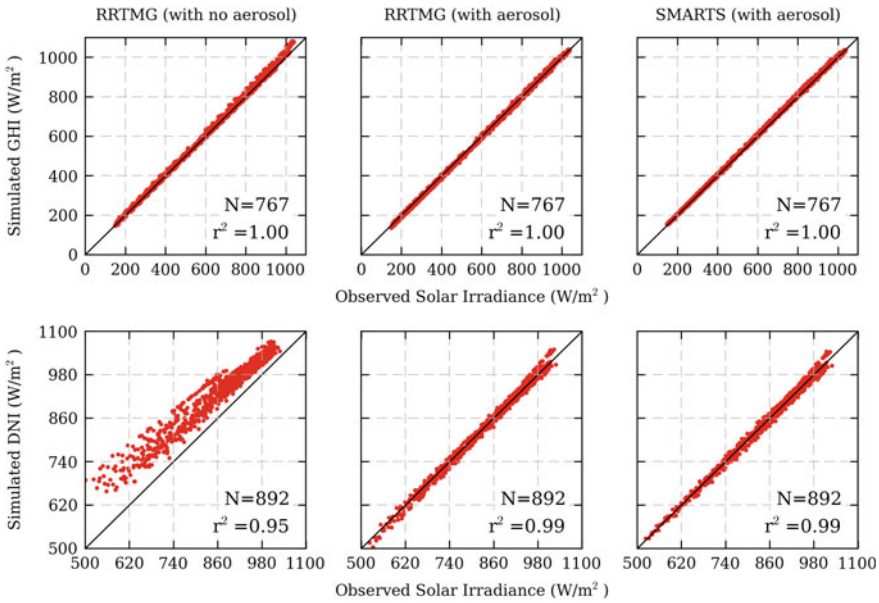

Fig. 9 WRF-simulated *versus* measured GHI (*upper panels*) and DNI (*lower panels*). WRF is used here with the RRTMG radiation model assuming either an ideal atmosphere with zero aerosols [*left column*] or a realistic atmosphere with aerosol optical properties observed at AERONET stations [*middle column*]. The rightmost column shows alternate simulations obtained by the SMARTS spectral RT model in lieu of the WRF/RRTMG model still using the same aerosol inputs. The number (N) of samples and the linearly explained variance (r^2) are shown in each panel

representation of the radiative processes that occur in the atmosphere. In this context, the comprehensive evaluation undertaken by Ruiz-Arias et al. [87] showed the good skill of WRF at predicting GHI and DNI under clear conditions.

Provided the aerosol optical properties are well described (from, e.g., AERONET data), Fig. 9 shows that WRF provides highly reliable estimates of clear-sky GHI and DNI comparable with those from the SMARTS spectral RT model [27, 32]. In contrast, when the radiative aerosol effects are oversimplified—which is the general rule in NWP modelling—or even neglected, such as in the case of the RRTMG simulation with no aerosols in Fig. 9, a noticeable systematic bias appears in the simulated DNI (but not GHI) values. To improve this situation, Ruiz-Arias et al. [88] proposed a versatile numerical scheme—now implemented into WRF—that evaluates the aerosol radiative effects at the Earth's surface from regular AOD observations. Assuming that these are sufficiently accurate, this parameterization delivers results comparable with those shown in Fig. 9.

Although NWP models are mainly intended for weather forecasts, they can also be used for a retrospective weather evaluation called *reanalysis* [15, 81, 90]. This includes multidecadal evaluations of solar radiation time series [10] even predating the period covered by the satellite methods described in the previous section. Nonetheless, satellite-based methods still provide a more accurate representation of

clouds, and they are generally preferred over NWP models for the evaluation of solar radiation. Very recently, however, Ruiz-Arias et al. [89] proposed a methodology to fuse satellite- or NWP-based irradiation data and ground observations. With this method, NWP models may become a valid approach for regional solar resource assessments if a sufficient density of ground radiometric stations exists.

5 Solar Radiation Measurement and Quality Control

Solar radiation can be measured with different types of radiometers. They differ by their detector, time response, quality of materials and construction, maintenance requirements, uncertainty, field performance, and cost. Although DNI can be measured with a single instrument, it is strongly suggested to add separate instruments to measure the two other components (global and diffuse) independently. This is an essential part of the best practice in this field [95]. The goal here is twofold:

- Redundant measurements allow a much improved quality-assurance process (see Sect. 5.4) and thus less uncertainty in the resulting data stream.
- Redundancy also provides a way to replace missing data points in virtue of (Eq. 7) in case of data breaks, which occur frequently in practice. Data breaks are a major issue in solar resource assessments because they degrade the quality of the overall database and the bankability of future projects.

5.1 Conventional Instrumentation

Direct normal radiation is conventionally measured with pyrheliometers. They have a narrow angular aperture now standardized to 5° (or 2.5° half-angle) to measure unscattered sunlight with, however, some inadvertent contribution from diffuse radiation emanating from the Sun's aureole, also referred to as the *circumsolar region* (Sect. 7). Remarkably, a well-maintained and calibrated pyrheliometer provides irradiance data with the best possible accuracy compared with any other field radiometer. However, pyrheliometers must permanently point to the Sun and, for that reason, must be mounted on a tracking device such as a dedicated Sun tracker (see Fig. 10, left). This requires electricity and regular maintenance to guarantee correct tracking. Modern trackers are computer controlled and can point at the Sun very accurately even before it rises. Such trackers are, however, much more expensive than the radiometer itself, which makes the long-term monitoring of DNI a costly proposition.

The sensor in pyrheliometers is a black receiver connected to a thermopile detector, which converts solar heat into an electric signal. The typical time constant of modern pyrheliometers is a few seconds. Some newer compact models have an

Fig. 10 Equipment for the measurement of solar radiation. To the *left*, a dedicated Sun tracker on which a pyrheliometer and two pyranometers (shaded and unshaded) are mounted. To the *right*, a rotating shadowband irradiometer. Photo (c) C. A. Gueymard

advanced design that includes a faster thermopile, which decreases the signal time constant. Such models have the benefit to improve precision in situations when DNI changes rapidly over time. The receiver is protected from stray light by a collimator, whose inside surface is black and equipped with baffles. This attachment is also protected from the elements by a quartz window, which has a high transmittance over the whole shortwave domain (≈0.2–4 μm).

Global hemispherical radiation (G) is measured with a pyranometer, which is a fixed, horizontally mounted radiometer with a 180° field of view. If appropriately shaded from the Sun with a shading element (ideally a shading ball mounted on a Sun tracker), it then senses diffuse radiation (D). Pyranometers use the same thermopile technology as pyrheliometers, and their time constant is thus comparable. The detector is here protected by a double glass dome whose transmittance is somewhat decreased compared with that of pyrheliometers, i.e., typically from 0.3 to 2.8 μm. The slight loss of energy beyond 2.8 μm is compensated for by the calibration process, but this introduces some uncertainty. Overall, pyranometers have more sources of uncertainty than pyrheliometers (see Sect. 5.5). To decrease uncertainty in the measurement of G, the state-of-the-art technique—contrarily to conventional wisdom—consists in obtaining it *indirectly* by the component-sum technique, in which DNI is observed with a pyrheliometer, its horizontal component calculated using the Sun zenith angle, and D sensed with a shaded pyranometer. This approach mitigates a number of errors that are typically present in pyranometric observations of global irradiance [61]. In parallel, this indirect determination of G can be compared with its direct measurement from the unshaded pyranometer, thus providing a powerful way to detect experimental issues (Sect. 5.4). The installation of specially designed ventilation units for all of these radiometers is

Table 1 Recommended instrument specifications for solar resource assessment and long-term monitoring

Pyrheliometer specifications	
Operating temperature	−40 to +80 °C
Response time	<5 s
Full opening view angle	5° ± 0.2°
Spectral range	200–4000 nm
Calibration accuracy	<±1.1 %
Sensitivity temperature correction	<±0.5 % (−20 to +50 °C)
Measurement accuracy (linearity, drift)	<±0.7 %
Maximum expanded uncertainty* (U95)	<2 %
Prevention of soiling	Desirable (optional collimator ventilator)
Pyranometer specifications	
Operating temperature	−40 to +80 °C
Response time	5 s
Spectral range	285–2800 nm
Thermal zero offset	<±10 W m^{-2}
Sensitivity temperature correction:	<±1 % (−20 to +50 °C)
Directional error	<±10 W m^{-2}
Calibration accuracy	<±1.1 %
Measurement accuracy (linearity and drift)	<±0.8 %
Maximum expanded uncertainty* (U95)	<6 %
Prevention of soiling	Desirable (optional ventilation unit)

*The expanded uncertainty (U95) is 1.96 times the standard uncertainty. The latter is the most usually reported by manufacturers, which might be confusing

desirable as a way to minimize soiling (from, e.g., dew or dust) and experimental errors. The recommended specifications of thermopile radiometers for optimal irradiance measurement are listed in Table 1.

5.2 Specific Considerations for Solar Resource Assessment

The previous section is of general validity and thus applies to any type of "permanent" radiometric station. For solar resource assessment studies, which take place before a CPV project is built or even financed and may be of a temporary nature, the optimal setup can be different. Based on considerable practical experience, this section offers basic considerations as well as important recommendations on the practice of solar-resource assessment for solar power applications, in the context of future CPV projects, particularly those to be built in arid areas.

The role of radiometric stations aimed at solar projects is to gather high-quality irradiance data with established methods toward the confirmation of satellite-derived modeled solar resource data (long-term time series) obtained

independently. Due to the failure of some projects that overestimated the DNI resource by the use of incorrectly modeled data, lenders now most generally require on-site measurements to confirm modeled estimates, the uncertainty of which is significant with regard to arid areas [13, 96]. On-site measurements must deliver appropriate high-quality data in support of the project *before* it reaches the final design and financing stages, which implies swift diligence, expertise, and close supervision to avoid data losses or inacceptable overall uncertainties.

In case of disagreement between the on-site measurements and the modeled data, which frequently occurs in the case of DNI, the former can be efficiently used to correct the latter. This process is referred to as *site adaptation* or *record extension* [5, 40, 54, 96]. The resulting corrected data can in turn be used to refine the energy simulations of the projected plant output [based on, e.g., revised typical meteorological years (TMY)] and ultimately improve bankability.

The best practice in solar-resource assessment should include the following tasks and activities:

- Selection of a suitable ground measurement station exactly at the project site or close to it (within 3-km distance, assuming a smooth terrain)
- Acquisition of on-site ground observations under controlled conditions for a period of at least 12 months
- Acquisition of long-term (>15 years) solar irradiation data from satellites
- Correction and gap filling of measured data
- Assessment of measured data quality and uncertainty
- Comparison of satellite and ground observations, and long-term bias correction of the former
- Derivation of corrected long-term averages, solar resource variability, TMY, and overall uncertainty in the solar resource assessment.

A professional assessment of a project's solar resource is to a solar power plant what a geological survey is to a gold mine: Without solid evidence of the presence of gold, no banker would invest in a mine. It is generally considered that a minimum annual average DNI resource of 2000–2200 kWh/m^2 is necessary for CPV applications. The best-known sites in the world have an annual DNI resource >2600 kWh/m^2 (or 7.1 kWh/m^2/days on average). The best possible resource assessment study uses a combination of onsite measurements and long-term satellite-derived modeled data to establish the DNI resource with a low (and proven) uncertainty as well as its seasonal and interannual variability.

The previous section described the use of thermopile radiometers for irradiance measurement. Such instruments correspond to the standard practice, which is followed, e.g., by meteorological networks or research-class stations. However, such instruments have some drawbacks, such as the following, that may make them less appropriate in the practice of solar resource assessments:

- Substantial power requirements, particularly for the Sun tracker, which may be difficult to provide at remote sites or may require a costly autonomous PV system

- Frequent maintenance and cleaning requirements, particularly in arid/desert areas, where a daily cleaning cycle might be necessary, thus leading to personnel and budget constraints
- Substantial first cost of the equipment.

For all of these reasons, many stations being deployed for CPV projects are instead equipped with a kind of instrument often referred to as *rotating shadowband irradiometer* (RSI), which does not have these limitations. Such a device basically consists of two main parts (see Fig. 10, right): a single photodiode sensor placed horizontally and a small motor-activated shadowband rapidly rotating around the sensor at regular intervals, thus intermittently blocking the direct radiation component from the sensor [24, 100]. The global and diffuse irradiances are determined from the unshaded and shaded sensor response, respectively, and the direct irradiance is ultimately calculated at each instant by difference using Eq. (7). An RSI has its own drawbacks, however, as follows:

- Strong spectral selectivity and temperature dependence of the photodiode, which must be corrected in the software as completely as possible
- Difficult, lengthy, and uncertain calibration process
- Greater measurement uncertainty than thermopile instruments
- Difficulty to thoroughly quality control the data because only two independent components (global and diffuse) are actually measured.

The response time of an RSI is only a few milliseconds, i.e., approximately 2–3 orders of magnitude faster than thermopiles. Although this is obviously ideal to track high-frequency changes in irradiance due to cloud passages, this is not a decisive advantage when evaluating the solar resource because the focus is on monthly and annual averages, which themselves are derived from data delivered at 1- to 10-min intervals.

The temperature and spectral sensitivity of the silicon sensor, and its total lack of response below approximately 0.4 μm and above approximately 1.05 μm, generate systematic and time-variable deviations in its response compared with a reference thermopile instrument [71]. These deviations must be appropriately corrected to obtain usable measurements. To that end, some variables, such as sensor temperature and air mass, must be determined. There are presently different empirical correction formulas available that differ somewhat in their method and accuracy [22–24, 99]. More sophisticated correction procedures have now been developed by RSI manufacturers, but these are proprietary.

Photodiode sensors are usually much less sensitive to soiling than thermopile instruments, and their power requirement is also much less. Therefore, they can easily be designed as part of a self-sufficient remote station with a small autonomous power supply (PV panel and battery). Their raw solar irradiance signal must be postprocessed (in the data logger's software) to include the corrections just mentioned. Although their nominal accuracy is lower than that of thermopiles, RSIs have proved to be very reliable at remote sites even in difficult environments. Moreover, their accuracy is generally considered good enough to finance

utility-scale solar power projects. The total hardware cost for a complete RSI-based solar resource station (equipped to measure all components of solar radiation, temperature, barometric pressure, relative humidity, and wind speed and direction) is 2–3 times less than that of a conventional thermopile-based station.

Various studies have been published to evaluate the comparative performance of various types of radiometers [4, 24, 36, 62, 64, 101]. Such studies can help make sound decisions about the most appropriate type and brand of sensor to buy depending on the specificities of each project including budget.

Once the solar power plant becomes operational and is therefore manned on a daily basis, a thermopile-based station might become advantageous for precise long-term monitoring of the plant's performance. This monitoring station could be the same as the initial solar resource station or could be added to it. The latter option is recommended if the power plant has a large size, in which case two DNI measurements at some distance are better than one. Moreover, this dual-station arrangement provides the necessary redundancy to avoid data breaks.

Additional requirements and specifications include an appropriate measurement sampling rate (typically 1 Hz). The time step of data records should be 1–10 min—the shorter the better. The average, maximum, minimum, and standard deviation values of each variable should be reported by the data logger at the end of each time step. The equipment should be properly grounded to prevent lightning damage and shielded to prevent radio frequency interferences. In addition, the equipment must be capable of fast data transfer to the main data center where the data are quality controlled and analysed.

5.3 Siting, Calibration, and Maintenance

Proper site selection for an automatic weather and radiometric station is an important issue during the planning stage of any large-scale solar power installation [95, 100]. In general, the site should be representative of the whole area of interest and should not be affected by obstructions or local sources of aerosols (e.g., dust from dirt roads). Other general guidelines for optimal site selection are contained in the WMO Guide to Instruments and Measurements [107].

The proper calibration of any radiometer is a key factor that determines its accuracy from day 1. Calibration procedures have evolved over time and are now more sophisticated than ever, thus keeping uncertainties as low as possible [35]. Proper calibration of a broadband radiometer essentially means that it is traceable to the World Radiometric Reference (WRR) maintained at the World Radiation Center in Davos, Switzerland. The transfer of calibration from the WRR to the field instrument is an essential multistep procedure that should be performed by qualified personnel only. The overall uncertainty of the instrument under laboratory conditions should be mentioned in all data files for further reference and better judgment of data accuracy. Each radiometer should be calibrated just before or during

installation of the weather station and then on a regular basis per the manufacturer's recommendations or best practice.

The initial calibration of RSI-type sensors requires additional steps and should be performed either on site or under climatic conditions comparable with those anticipated at the prospected site. Most particularly, the aerosol and temperature conditions at the calibration site should be similar to those of the prospected site because they both have a notable incidence on the RSI's spectral effects to be corrected. Due to remaining inaccuracies in the sensor response under variable weather and aerosol conditions, the calibration period of RSI sensors should last at least 2-4 weeks during which a pyrheliometer is maintained next to the RSI to provide the reference DNI.

5.4 Data Quality Control

Even with regular calibration and maintenance of field radiometers, problems still do occur due to, e.g., power failure, loss of tracking, sudden soiling (e.g., bird droppings, frost), progressive drift, data logger issues, etc. Quality control (QC) is an essential near real-time and a posteriori procedure necessary to detect any departure from normal operation, flag the quality of each data point, attempt to correct problematic data points, and even fill in data breaks [106].

For three-component measurements using independent thermopile instruments, various tests exist to exploit the redundancy that allows G to be obtained in two different ways (e.g., [59, 84, 85]). Visual quality-assessment tools [104] are helpful. More sophisticated QC procedures (e.g., [47, 58]) also exist, but they may require substantial manual intervention and expertise. Therefore, an algorithm or procedure should be available to enable *automatic* data collection, screen the collected data regularly for measurement failures, evaluate data quality in near real time, and perform data analyses. Rapid detection of measurement problems is an asset because it translates into less risk of data loss and decreased uncertainties in the final database. A procedure for analysis and correction of soiling effects should be included in the analysis software. Flagging of each data point is an important safety measure because it allows a more informed analysis in the future, which is conducive to decreasing uncertainty. Clever flagging procedures exist to summarize a quantity of information using only 1 or 2 characters [105]. Proper QC leads to an easier evaluation of the measurement uncertainty (discussed in the next section), which itself conditions the overall project's uncertainty [54]. For all QC tasks, expert assistance may be critical to guarantee the quality of the data.

5.5 Measurement Uncertainty

Under cloudless situations, it is possible to use high-performance CSRT models to predict the solar irradiance components—and most importantly DNI—with an

uncertainty close to that of regular measurements [39, 87]. This, however, requires favorable conditions (rarely fulfilled in practice) such as the local availability of high-quality and high-frequency atmospheric data that provide the required inputs to the model. In any case, the uncertainty in modeled irradiance increases considerably under cloudy or partly cloudy conditions. This explains why good measurements are always assumed to have much lower uncertainty than modeled data and why the evaluation of the measurement uncertainty is a key aspect in any solar resource assessment.

As mentioned previously, the observation of DNI with pyrheliometers is normally the most accurate among all broadband irradiance measurements. Long-term outside observations under clean atmospheric conditions and tightly controlled laboratory supervision [64] resulted in a daytime expanded uncertainty (U95) of approximately 1.7 % for the best instruments currently available on the market. This value is similar to the 1.8 % quoted by Gueymard and Myers [35] for the estimated calibration uncertainty of pyrheliometers in general. If restricted to cloudless conditions only, the uncertainty of the same instruments decreases to approximately 0.6 % [64]. In parallel, that study found that the long-term bias is negligible with the best commercial instruments. These results are remarkable, but they cannot be easily extrapolated to any other condition. In particular, suboptimal equipment, irregular calibration, or insufficient cleaning and maintenance under atmospheric conditions prone to soiling would lead to additional sources of discrepancy and bias. Whenever DNI is measured with a good pyrheliometer under the appropriate maintenance schedule, a conservative long-term daily uncertainty of 2–3 % is reasonable in general. Under difficult field conditions or inappropriate care, somewhat greater values can be expected [70].

The U95 uncertainty in pyranometric observations of global or diffuse irradiance, reaching at least approximately 5 % under long-term field conditions, is greater than that of DNI. Some pyranometers are affected by a strong thermal offset issue, which results in too-low readings [36]. The instrument's cosine error and calibration are other main sources of bias and uncertainty. All of these effects are highly variable from one brand and model to the next or even from one specimen to the next of the same model. On a long-term basis, using a 6-year data series, monthly differences between various pyranometers and reference (component-sum) measurements of ≥8 % for global irradiance and 14 % for diffuse irradiance were observed under laboratory supervision [36]. The risk of bias is therefore much more important in practice than what can be assumed from manufacturer specifications or conventional wisdom.

The uncertainty in RSI measurements is more difficult to establish because it highly depends on the calibration and spectral correction methods as well as on cloudiness and the variability of the local solar spectrum due to, e.g., rapidly changing aerosol conditions. Based on the limited error analyses and field tests currently available [24, 71], and on still unpublished results from the BSRN Payerne station in Switzerland (Personal communication with Dr. Laurent Vuilleumier, MeteoSwiss, 2014), it is only possible to suggest a rather large range of 3–9 % for the long-term uncertainty in DNI. Using a well-calibrated RSI and a collocated reference

pyrheliometer at a research-class site in Kuwait under stringent daily maintenance schedule, it was found that, compared with thermopile radiometers, the monthly RSI bias can be within 2 % for DNI and 4 % for GHI [1]. This gives confidence in the long-term solar resource data obtained with RSI instruments if they are properly characterized and maintained.

6 Spectral Solar Radiation

In Sect. 3, the broadband transfer of solar radiation throughout the atmosphere was introduced. Here, further spectral details are discussed starting with spectral transmission for key atmospheric constituents.

6.1 Atmospheric Constituents

Figure 11 shows the transmittance of various gases under a cloud- and aerosol-free mid-latitude summertime atmosphere for a zenith Sun ($m = 1$). Rayleigh scattering is produced by the combined effect of all atmospheric molecules. It varies as approximately λ^{-4}, so that it is only important in the VIS and UV regions, which is why the sky is blue on very clear days.

In addition to scattering, some gas molecules also absorb sunlight. In particular, CH_4 and CO_2 absorb in the IR beyond 1 μm. Throughout most part of the VIS band, the atmosphere is quite transparent except for some thin O_2-absorption lines and a weak O_3-absorption band. In the UV, however, O_3 strongly absorbs, which is essential for life on Earth because it blocks the most energetic and harmful photons from the Sun's rays before they reach the surface.

The spectral absorption pattern of water vapour is very intricate (Fig. 11). For wavelengths beyond approximately 0.6 μm, it absorbs in successive bands with increasing intensity and spectral width as wavelength sweeps the IR spectrum.

The radiative properties of atmospheric aerosols depend on particle type and shape as well as their size distribution. The shortwave spectral AOD ($\tau_{A\lambda}$) normally varies according to Ångström's empirical law, $\tau_{A\lambda} = \beta\lambda^{-\alpha}$, where λ is expressed in μm, β is the Ångström's turbidity coefficient (see Sect. 3), and α is the Ångström exponent, which usually varies from approximately 0.5 (for large aerosol particles such as desert dust or sea salt) to approximately 2.5 (for fine aerosol particles such as those originating from pollution). In contrast, β typically varies from approximately 0.02 for very clean and unpolluted areas to >1 under extremely hazy conditions. Figure 12a shows the spectral aerosol transmittance of solar radiation for three typical aerosol types: rural, urban/polluted, and dust. The urban/polluted aerosol type has a steeper spectral variability of sunlight extinction for wavelengths <1 μm because it is made up of relatively small particles (high α). Conversely, the large size of dust particles makes the spectral variability in dusty environments very

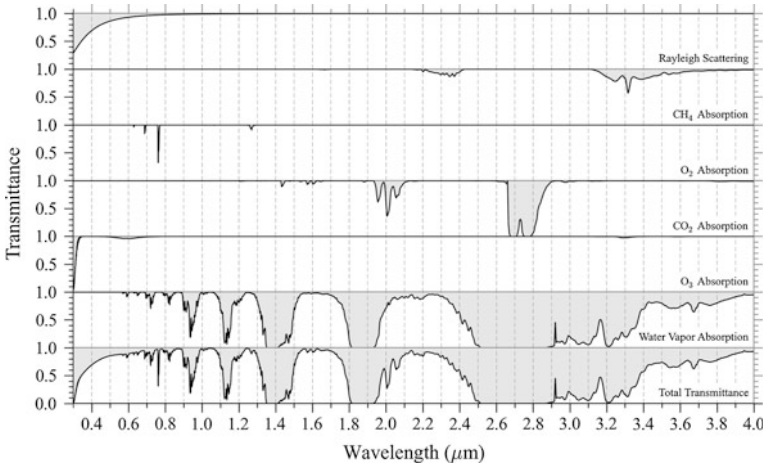

Fig. 11 Zenith (m = 1) transmittance of different attenuation processes under a typical cloud- and aerosol-free mid-latitude summertime atmosphere. The *bottom panel* shows the combined spectral transmittance of the *upper panels*

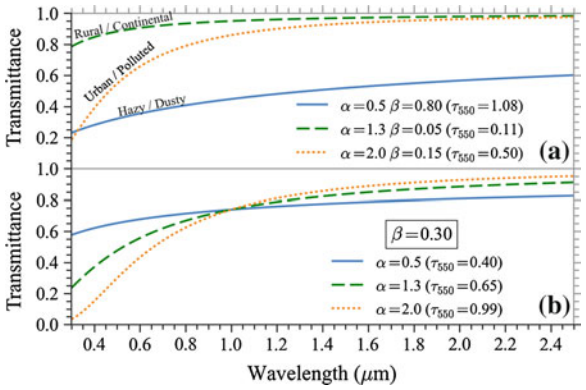

Fig. 12 Zenith (m = 1) transmittance of a hypothetical atmosphere with only aerosols **a** for typical aerosol values in three broad environments and **b** for fixed β and three values of α

flat (low α). Figure 12b shows the effect of α on the spectral aerosol transmittance for a fixed, moderate value of β. In particular, the smaller the α, the flatter the spectral dependence of sunlight extinction.

Clouds act as a grey filter because their optical depth (COD or τ_C) changes very little for wavelengths <2 μm. Below 1 μm, clouds absorb none or very little radiation, so essentially all extinction is caused by scattering. Thus, although they are rather opaque, clouds appear white or grey to the naked eye. Beyond 1 μm, however, they feature some strong absorption bands similar to water vapour. Figure 13 shows the transmittance of GHI and DNI through ice clouds of varying τ_C when the Sun is at the zenith (m = 1). Transmittance of ice clouds for direct radiation is always equal to $\exp(-m\ \tau_C)$ and is thus wavelength independent.

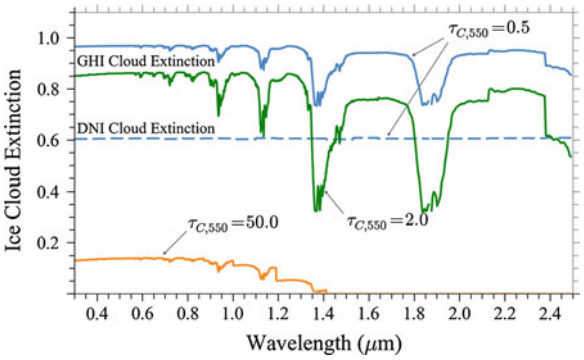

Fig. 13 Zenith (m = 1) transmittance of GHI and DNI throughout a hypothetical atmosphere with only ice clouds with different COD values at 550 nm. Values obtained with the libRadtran v1.7 radiative transfer code

Therefore, the *relative* spectral distribution of direct irradiance under ice clouds is the same as under cloudless conditions.

6.2 Effect of Air Mass

The variation of air mass during the course of a day results in noticeable changes in the spectral distribution of direct irradiance at the Earth's surface. This effect is illustrated in Fig. 14a for six different zenith angles between 0° and 70°. As θ_z increases, the extinction of sunlight becomes stronger at shorter wavelengths resulting in a progressive red shift in the direct spectrum. This explains the Sun's reddish color at sunrise and sunset. The increased spectral extinction at lower wavelengths is dominated by scattering from molecules and aerosols.

6.3 Spectral Modelling

Modelling of the solar spectrum at the Earth's surface is made possible by fundamental knowledge in electromagnetic theory (for scattering) and spectroscopy (for absorption). Like with broadband radiation modelling, only the surface direct irradiance is of interest to CPV applications, which allows the use of simpler and faster models than those typically developed, e.g., for atmospheric sciences.

If only moderate spectral resolution (122 wavelengths between 0.3 and 4 μm) and accuracy is required, the SPCTRAL2 model [6] is suggested. For more demanding applications, SMARTS [26, 27, 68] is the model of choice. It evaluates the spectrum at 2002 wavelengths between 0.28 and 4 μm and includes optional calculations such as the CSI or the simulation of spectroradiometers. The model has been extensively

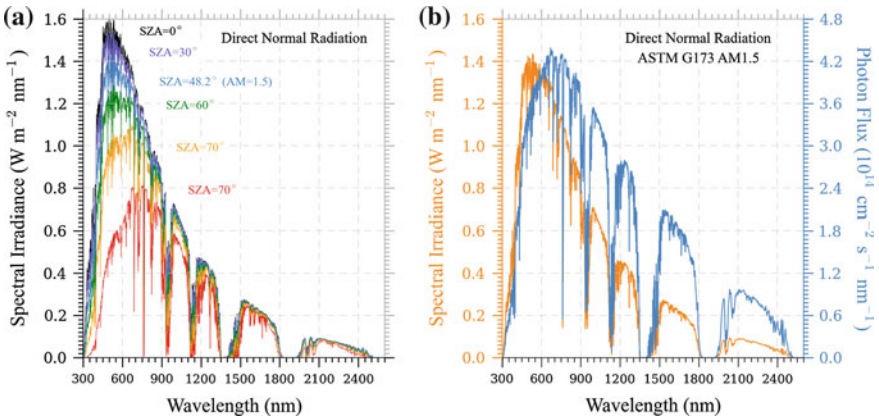

Fig. 14 Spectral direct solar radiation simulated with SMARTS **a** for six different solar zenith angles from 0° to 70° and the atmospheric parameters defined for the American Society for Testing and Materials (ASTM) G173 AM1.5 standard [2]. **b** Direct ASTM G173 AM1.5 standard reference spectrum (left axis) and the corresponding photon flux (right axis)

validated [26, 27, 34, 63, 69, 87] and has generated reference spectra for the PV industry [28], which eventually became standardized (see next section).

More generally, the flexibility and performance of SMARTS are key to evaluate the power output and energy yield of CPV systems under widely different climatic conditions [14, 19, 20, 94]. Another promising avenue is the development of "tunable" multijunction cells that can be adapted to a local climate based on SMARTS simulations [16, 108].

6.4 Standard Reference Spectrum: Irradiance and Photon Flux

Per the discussions in Sects. 6.1 and 6.2, the spectrum of incoming direct solar radiation at the Earth's surface is highly variable in both time and space. A consensus spectrum is thus needed to rate the performance of many different CPV cells relatively to a commonly accepted basis. In the early 2000s, it became obvious that the atmospheric clarity of the southwest United States would be ideal for the development of CPV projects. This prompted the study of the atmospheric conditions and DNI resource of the region [28]. Using a "typical" mean AOD of 0.084 at 500 nm, a reference direct spectrum was obtained with then-current SMARTS version 2.9.2. The integrated broadband irradiance was 900 W m^{-2}, i.e., 10 % less than with the global spectrum used for the rating of regular PV cells.

In 2003, and based on that base study, the American Society for Testing and Materials (ASTM) promulgated the standard G173 containing two reference solar spectra at air mass 1.5. This standard is still current [2]. Figure 14b shows the main

part of the direct G173 spectrum, usually referred to as AM1.5D. For future reference and to maintain accessibility to the underlying model, the ASTM also increased SMARTS to the status of adjunct standard, thus allowing its use in all applications that require consistency with the standard spectrum.

In addition to irradiance, a concept that is of major importance in PV applications is that of photon flux, which is the number of photons incident on a normal unit surface per unit of time. It is directly related to the quantum effect of photons and is therefore the appropriate quantity to convolve with the external quantum efficiency of CPV cells. The photon flux (F_λ) can be derived from the spectral irradiance (E_λ) through $F_\lambda = k\, E_\lambda \lambda/(hc)$ where c is the speed of light in vacuum (2.99792458×10^8 m s^{-1}), h is the Planck constant ($6.62606896 \times 10^{-34}$ J s), and k is a numerical constant to reconcile units. For instance, it equals 1×10^{-13} for λ in nm, E_λ in W m^{-2} nm^{-1}, and F_λ in cm^{-2} s^{-1} nm^{-1}. The photon flux corresponding to the G173 AM1.5D spectrum is shown in Fig. 14b.

6.5 Spectral Measurement

Spectral irradiance can be measured with a spectroradiometer. Modern instruments of this type are usually built around a solid-state detector, which has no moving part and is much faster than older instruments based on a scanning mechanism. A silicon detector is most generally used for spectral measurements between approximately 0.35 and 1.05 μm. Over this range, spectral irradiance is sensed most typically at 512 or 1024 wavelengths depending on detector performance and cost. To obtain the direct spectrum, the spectroradiometer must be mounted on a solar tracker and equipped with a collimator much like a pyrheliometer.

Separate instruments, or a single instrument with multiple detectors, must be used to extend the spectrum into the UV or NIR, which increases the difficulty (and cost) of such an experimental undertaking. A possible alternative is to use only a VIS instrument (spectroradiometer or sunphotometer), derive the most important atmospheric parameters at a few key wavelengths with the help of an appropriate model, and extend the spectrum by calculation [72]. This, however, requires expertise and might be difficult to perform under rapidly changing atmospheric conditions. This technique is also highly dependent on the accuracy of the instrument's calibration.

The calibration of spectroradiometers is more tedious than that of broadband radiometers because it usually must be performed against a standard calibrated lamp inside a specialized laboratory. This explains why only a few laboratories in the world have the resources to monitor the solar spectrum on a quasi-continuous basis. One of these laboratories is the National Renewable Energy Laboratory (NREL) in Golden, Colorado, where a few spectroradiometers are deployed to measure the spectral distribution of global horizontal, global tilted, and direct normal irradiance automatically and at high frequency (typically 1- to 5-min intervals).

Figure 15 shows an experimental AM1.5 direct spectrum recently measured with two collocated instruments: An Eko WISER covering the spectral range

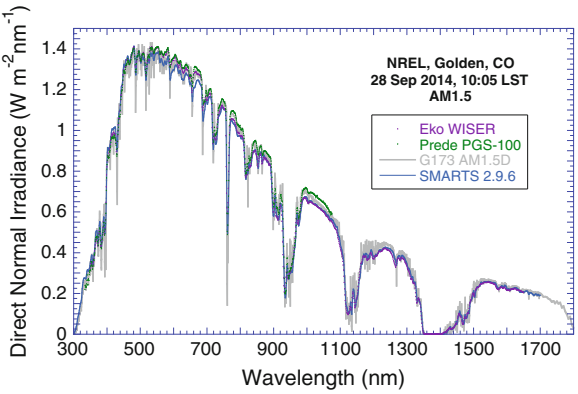

Fig. 15 Direct AM1.5 spectrum measured at NREL with two collocated solid-state spectroradiometers, compared with a simulation with the SMARTS model and the G173 standard spectrum, at full resolution

350–1650 nm at 1-nm intervals, and a Prede PGS-100 covering 334–1075 nm at approximately 0.73-nm intervals. In addition, two modelled spectra are also shown: the G173 AM1.5D spectrum and a simulation obtained with SMARTS version 2.9.6 based on observed atmospheric information for that specific time. This particular calculation makes use of the instrument's bandpass characteristics and the SMARTS postprocessor to smooth the modelled spectrum and properly simulate the instrument's response. The comparison in Fig. 15 illustrates the fact that spectral measurements typically remove a significant part of the fine structure in the spectrum. Although the two instruments are collocated and calibrated the same way, they disagree by as much as 8 % around 1 μm. Finally, the measured and simulated spectra on that day were only slightly different from the G173 standard, which is reassuring but unexpected considering the greater AOD at measurement time [0.115 compared with 0.084 for the standard spectrum (at 500 nm)]. The resulting stronger aerosol extinction, however, is compensated for by decreased molecular scattering because the experimental site is at high elevation (1830 m compared with sea level for the standard spectrum). This discussion illustrates the benefit of comparing modelled and measured spectra to better understand and precisely characterize local spectral effects on CPV systems.

7 Circumsolar Radiation

As discussed in Sect. 5, modern pyrheliometers have an opening angle, ε_p, of approximately 2.5°, which is an order of magnitude greater than the apparent Sun's radius (0.266° at the average Sun Earth distance). This means that in addition to the pure direct irradiance emanating from the Sun's disc itself, these instruments also sense diffuse radiation emanating from the Sun's aureole, commonly referred to as

CSI. This sky area is usually very bright due to the forward-peaking characteristic of the aerosol and ice cloud scattering processes. Although CSI is diffuse in nature, it behaves like direct radiation and therefore can be concentrated. However, HCPV systems have an acceptance angle that is much lower than ε_p. This means that pyrheliometer measurements tend to systematically overestimate the direct irradiance that can be really used by HCPV systems. Conversely, pyrheliometer measurements would normally underestimate the irradiance incident on LCPV systems.

Contrarily to pyrheliometers, solar radiation models normally do not include any circumsolar radiation in their DNI predictions; thus, they tend to slightly underestimate the actual irradiance incident on any type of CPV system. A notable exception is the SMARTS model [27, 32, 38].

Research has shown that the ratio CSI/DNI is nearly proportional to the receiver's opening angle [38]. Under clear skies, this contribution is typically small, <1%. It is a function of both m and AOD and also depends on the type of dominant aerosol. Scattering by dust aerosols, most noticeably, has a stronger forward-peaking characteristic than other aerosol types, which results in a greater CSI for a fixed AOD. It can therefore be expected that CPV systems built in or around deserts can experience significant contributions during hazy periods.

Results from theoretical calculations [80, 98] have shown that the CSI generated by ice clouds is much greater than that generated under cloudless conditions. Observations have indeed confirmed this: Circumsolar contributions to the reading of a pyrheliometer can reach up to approximately 50 % when DNI is still >400 W m^{-2}, which is remarkable [8].

Various methods exist to evaluate the broadband CSI experimentally [38, 102, 103]. For CPV applications, however, the spectral distribution of CSI also must be taken into consideration, which complicates the issue. Under clear skies, CSI can be evaluated spectrally with SMARTS [27] if the aerosol conditions are known. Under cloudy conditions, a more sophisticated type of model and more data are needed [80, 98], which means that the real-time simulation of CSI at high frequency is still not a realistic possibility in practice. For further reading, a recent publication offers a comprehensive discussion on the issues related to the relative determinations of CSI and DNI and on how CSI affects concentrating solar technologies [8].

8 Summary

Current methods to model and measure the solar resource for CPV applications were introduced in this chapter. At any instant, the magnitude and spectral distribution of incoming DNI on the concentrator determine the instantaneous power produced by the generator. In the long-term, an accurate evaluation of the solar resource is required to secure the financing of large solar projects. In the short-term, detailed knowledge of the rapid variations in DNI is required to track the frequency and magnitude of irradiance ramp rates. Such studies may be important in the

context of inverter safety, grid stability, spatial variability of power generation, and complementarity with other variable energy sources.

Throughout the atmosphere, sunlight is attenuated by various atmospheric constituents, three of which are both strong and highly variable over time and space: water vapour, aerosols, and clouds (in increasing order of potential attenuation). Accurate modelling of DNI requires a proper characterization of the atmospheric state regarding both aerosols and clouds. This is highly challenging because their respective optical depths (AOD and COD) are difficult to obtain precisely at any instant and location.

The common approaches currently used in DNI modelling have been discussed. In particular, clear-sky radiation models constitute an essential tool to determine the solar potential over regions with high solar resource, which are typically characterized by low cloudiness. When only GHI measurements are accessible (which is a frequent situation), the numerous all-sky separation models in the literature offer a means to easily estimate DNI. However, they are not "universal" and introduce significant estimation errors. Satellite-based solar radiation models provide the most accurate and reliable synthetic solar radiation time series, particularly for GHI. For DNI, however, remaining modelling challenges significantly increase its uncertainty particularly over arid areas. NWP models represent the current state-of-the-art in atmospheric modelling, although their skill at evaluating solar radiation (and DNI in particular) is still limited compared with methods based purely on satellite imagery. Still, they will certainly become the standard approach for solar radiation assessment and forecasting in the future.

An important part of this chapter has been devoted to the current instruments and techniques—including discussions on station siting and maintenance, data quality control, and experimental uncertainty—for solar radiation measurement. The pros and cons of thermopile radiometers and photodiode-based sensors have also been discussed in the context of solar resource assessments and short measurement campaigns at remote sites.

Finally, although this has not been directly discussed in this chapter, the study of the variability in DNI over the short-term future (from 1 s to a few days) constitutes a research topic known as *solar forecasting*, which deserves to be mentioned here. The forthcoming DNI's magnitude and probability of occurrence are key inputs that condition important decisions to be taken every day, even every 15 min, by plant operators and electric grid regulators. Considering the technological, financial, and economical implications of a rapidly increasing penetration of variable electric generation (such as from CPV and solar systems in general), the role of solar forecasting appears essential. Although this kind of forecasting is still in its infancy, the existing tools already improve the dispatchability of all kinds of solar power plants and the management and stability of the electric grid, decrease the need for costly spinning reserves, and ultimately decrease the overall cost of electricity production at the country scale. Considerable improvements are expected in the coming few years that will benefit the development of solar energy in general.

References

1. Al-Rasheedi M, Gueymard CA, Ismail A, Hajraf SA (2014) Solar resource assessment over Kuwait: validation of satellite-derived data and reanalysis modeling. In: Proceedings of EuroSun ISES conference, Aix-les-Bains, France
2. ASTM (2012) Standard tables for reference solar spectral irradiances: direct normal and hemispherical on 37° tilted surface. Standard G173-03, American Society for Testing and Materials, West Conshohocken, PA. Available at http://www.astm.org/Standards/G173.htm
3. Badescu V, Gueymard CA, Cheval S, Oprea C, Baciu M, Dumitrescu A, Iacobescu F, Milos I, Rada C (2012) Computing global and diffuse solar hourly irradiation on clear sky. Review and testing of 54 models. Renew Sustain Energy Rev 16:1636–1656. doi:10.1016/j.rser.2011.12.010
4. Badosa J, Wood J, Blanc P, Long CN, Vuilleumier L, Demengel D, Haeffelin M (2014) Solar irradiances measured using SPN1 radiometers: uncertainties and clues for development. Atmos Meas Tech 7:4267–4283. doi:10.5194/amt-7-4267-2014
5. Bender G, Davidson F, Eichelberger S, Gueymard C A (2011) The road to bankability: improving assessments for more accurate financial planning. In: Proceedings of Solar 2011 conference. American Solar Energy Society, Raleigh, NC, USA
6. Bird RE, Riordan C (1986) Simple solar spectral model for direct and diffuse irradiance on horizontal and tilted planes at the Earth's surface for cloudless atmospheres. J Clim Appl Meteorol 25:87–97
7. Blanc P, Wald L (2012) The SG2 algorithm for a fast and accurate computation of the position of the Sun for multi-decadal time period. Sol Energy 86:3072–3083. doi:10.1016/j.solener.2012.07.018
8. Blanc P, Espinar B, Geuder N, Gueymard C, Meyer R, Pitz-Paal R, Reinhardt B, Renné D, Sengupta M, Wald L, Wilbert S (2014) Direct normal irradiance related definitions and applications: the circumsolar issue. Sol Energy 110:561–577. doi:10.1016/j.solener.2014.10.001
9. Blanco-Muriel M, Alarcón-Padilla DC, López-Moratalla T, Lara-Coira M (2001) Computing the solar vector. Sol Energy 70:431–441
10. Boilley A, Wald L (2015) Comparison between meteorological re-analyses from ERA-Interim and MERRA and measurements of daily solar irradiation at surface. Renew Energy 75:135–143. doi:10.1016/j.renene.2014.09.042
11. Boland J, Ridley B, Brown B (2008) Models of diffuse solar radiation. Renew Energy 33:575–584. doi:10.1016/j.renene.2007.04.012
12. Cano D, Monget JM, Albuisson M, Guillard H, Regas N, Wald L (1986) A method for the determination of the global solar radiation from meteorological satellite data. Sol Energy 37(1):31–39. doi:10.1016/0038-092X(86)90104-0
13. Cebecauer T, Šúri M, Gueymard CA (2011) Uncertainty sources in satellite-derived direct normal irradiance: how can prediction accuracy be improved globally? In: Proceedings of SolarPACES conference, Granada, Spain
14. Chan NLA, Brindley HE, Ekins-Daukes NJ (2014) Impact of individual atmospheric parameters on CPV system power, energy yield and cost of energy. Prog Photovolt: Res Appl 22:1080–1095. doi:10.1002/pip.2376
15. Dee DP et al (2011) The ERA-interim reanalysis: configuration and performance of the data assimilation system. Q J R Meteorol Soc 137(656):553–597. doi:10.1002/qj.828
16. Dobbin A, Norton M, Georghiou GE, Lumb M, Tibbits TND (2011) Energy harvest predictions for a spectrally tuned multiple quantum well device utilising measured and modelled solar spectra. AIP Conf Proc 1407:21. doi:10.1063/1.3658286
17. Elminir HK, Azzam YA, Younes FI (2007) Prediction of hourly and daily diffuse fraction using neural network, as compared to linear regression models. Energy 32(8):1513–1523. doi:10.1016/j.energy.2006.10.010

18. Erbs DG, Klein SA, Duffie JA (1982) Estimation of the diffuse radiation fraction for hourly, daily and monthly-average global radiation. Sol Energy 28(4):293–302
19. Fernández EF, Almonacid F, Rodrigo P, Pérez-Higueras P (2013) Model for the prediction of the maximum power of a high concentrator photovoltaic module. Sol Energy 97:12–18. doi:10.1016/j.solener.2013.07.034
20. Fernández EF, Almonacid F, Ruiz-Arias JA, Soria-Moya A (2014) Analysis of the spectral variations on the performance of high concentrator photovoltaic modules operating under different real climate conditions. Sol Energy Mat Sol Cells 127:179–187. doi:10.1016/j.solmat.2014.04.026
21. Fröhlich C (2006) Solar irradiance variability since 1978: revision of the PMOD composite during Solar Cycle 21. Space Sci Rev 125:53–65. doi:10.1007/s11214-006-9046-5
22. Geuder N, Pulvermüller B, Vorbrugg O (2008) Corrections for rotating shadowband pyranometers for solar resource assessment. In: Proceedings of SPIE 7046, optical modeling and measurements for solar energy systems II, p. 70460F. doi:10.1117/12.797472
23. Geuder N, Hanussek M, Haller J, Affolter R, Wilbert S (2011) Comparison of corrections and calibration procedures for rotating shadowband irradiance sensors. In: Proceedings of SolarPACES conference, Granada, Spain
24. Geuder N, Affolter R, Kraas B, Wilbert S (2014) Long-term behaviour, accuracy and drift of LI-200 pyranometers as radiation sensors in rotating shadowband irradiometers (RSI). Energy Procedia 49:2330–2339. doi:10.1016/j.egypro.2014.03.247
25. Grena R (2008) An algorithm for the computation of the solar position. Sol Energy 82:462–470. doi:10.1016/j.solener.2007.10.001
26. Gueymard CA (1995) Simple model of the atmospheric radiative transfer of sunshine, version 2 (SMARTS2): algorithms description and performance assessment. Technical report FSEC-PF-270-95, Florida Solar Energy Center. Available at http://rredc.nrel.gov/solar/models/smarts/relatedrefs/smarts2_report.pdf
27. Gueymard CA (2001) Parameterized transmittance model for direct beam and circumsolar spectral irradiance. Sol Energy 71:325–346
28. Gueymard CA, Myers DR, Emery K (2002) Proposed reference irradiance spectra for solar energy systems testing. Sol Energy 73:443–467. doi:10.1016/S0038-092X(03)00005-7
29. Gueymard CA (2003) Direct solar transmittance and irradiance predictions with broadband models. Part 1: Detailed theoretical performance assessment. Sol Energy 74:355–379. doi:10.1016/S0038-092X(03)00195-6
30. Gueymard CA (2004) Direct solar transmittance and irradiance predictions with broadband models. Corrigendum. Sol Energy 76:513. doi:10.1016/j.solener.2003.11.002
31. Gueymard CA (2004) The sun's total and spectral irradiance for solar energy applications and solar radiation models. Sol Energy 76:423–453. doi:10.1016/j.solener.2003.08.039
32. Gueymard CA (2005) Interdisciplinary applications of a versatile spectral solar irradiance model: a review. Energy 30:1551–1576. doi:10.1016/j.energy.2004.04.032
33. Gueymard CA (2008) REST2: high-performance solar radiation model for cloudless-sky irradiance, illuminance, and photosynthetically active radiation—validation with a benchmark dataset. Sol Energy 82:272–285. doi:10.1016/j.solener.2007.04.008
34. Gueymard CA (2008) Prediction and validation of cloudless shortwave solar spectra incident on horizontal, tilted, or tracking surfaces. Sol Energy 82(3):260–271. doi:10.1016/j.solener.2007.04.007
35. Gueymard CA, Myers D (2008) Solar radiation measurement: progress in radiometry for improved modeling. In: Badescu V (ed) Modeling solar radiation at the earth's surface: recent advances. Springer, Berlin, pp 1–27
36. Gueymard CA, Myers DR (2009) Evaluation of conventional and high-performance routine solar radiation measurements for improved solar resource, climatological trends, and radiative modeling. Sol Energy 83:171–185. doi:10.1016/j.solener.2008.07.015
37. Gueymard CA (2010a) Progress in direct irradiance modeling and validation. In: Proceedings of Solar 2010 conference. American Solar Energy Society, Phoenix, AZ

38. Gueymard CA (2010b) Spectral circumsolar radiation contribution to CPV. CPV-6 conference, Freiburg, Germany. AIP conference proceedings, vol 1277, p 316. doi:10.1063/1.3509220
39. Gueymard CA (2011) Clear-sky irradiance predictions for solar resource mapping and large-scale applications: improved validation methodology and detailed performance analysis of 18 broadband radiative models. Sol Energy 86(6):2145–2169. doi:10.1016/j.solener.2011.11.011
40. Gueymard CA, Gustafson WT, Bender G, Etringer A, Storck P (2012) Evaluation of procedures to improve solar resource assessments: optimum use of short-term data from a local weather station to correct bias in long-term satellite derived solar radiation time series. In: Proceedings of Solar 2012 conference. American Solar Energy Society, Denver, CO, USA
41. Gueymard CA (2014) Impact of on-site atmospheric water vapour estimation methods on the accuracy of local solar irradiance predictions. Sol Energy 101:74–82. doi:10.1016/j.solener.2013.12.027
42. Gueymard CA, Ruiz-Arias JA (2014) Performance of separation models to predict direct irradiance at high frequency: validation over arid areas. EuroSun conference, Aix-les-Bains, France
43. Habte A, Sengupta M, Wilcox S (2013) Validation of GOES-derived surface radiation using NOAA's physical retrieval method. National Renewable Energy Laboratory, Technical report NREL/TP-5500-57442. Available at: http://www.nrel.gov/docs/fy13osti/57442.pdf
44. Husar RB, Tratt DM, Schichtel BA et al (2001) Asian dust events of April 1998. J Geophys Res 106(D16):18317–18330. doi:10.1029/2000JD900788
45. Ineichen P (2006) Comparison of eight clear sky broadband models against 16 independent data banks. Sol Energy 80:468–478. doi:10.1016/j.solener.2005.04.018
46. Ineichen P (2008) A broadband simplified version of the Solis clear sky model. Sol Energy 82:758–762. doi:10.1016/j.solener.2008.02.009
47. Ineichen P (2014) Long term satellite global, beam and diffuse irradiance validation. Energy Procedia 48:1586–1596. doi:10.1016/j.egypro.2014.002.179
48. Kalnay E (2003) Atmospheric modeling, data assimilation, and predictability. Cambridge University Press, Cambridge
49. Lahoz W, Khattatov B, Ménard R (2010) Data assimilation and information. In: Lahoz W, Khattatov B, Ménard R (eds) Data assimilation: making sense of observations. Springer, Berlin
50. Lara-Fanego V, Ruiz-Arias JA, Pozo-Vázquez D, Santos-Alamillos FJ, Tovar-Pescador J (2012) Evaluation of the WRF model solar irradiance forecasts in Andalusia (southern Spain). Sol Energy 86(8):2200–2217. doi:10.1016/j.solener.2011.02.014
51. Lara-Fanego V, Ruiz-Arias JA, Pozo-Vázquez D, Gueymard CA, Tovar-Pescador J (2012) Evaluation of DNI forecast based on the WRF mesoscale atmospheric model for CPV applications. Am Ins Phys Conf Proc 1477(1):317–322. doi:10.1063/1.4753895
52. Lefèvre M, Wald L, Diabaté L (2007) Using reduced data sets ISCCP-B2 from the Meteosat satellites to assess surface solar irradiance. Sol Energy 81:240–253. doi:10.1016/j.solener.2006.03.008
53. Lefèvre M, Oumbe A, Blanc P, Espinar B, Gschwind B, Qu Z, Wald L, Schroedter-Homscheidt M, Hoyer-Klick C, Arola A, Benedetti A, Kaiser JW, Morcrette JJ (2013) McClear: a new model estimating downwelling solar radiation at ground level in clear-sky conditions. Atmos Meas Tech 6:2403–2418. doi:10.5194/amt-6-2403-2013
54. Leloux J, Lorenzo E, García-Domingo B, Aguilera J, Gueymard CA (2014) A bankable method of assessing the performance of a CPV plant. Appl Energy 118:1–11. doi:10.1016/j.apenergy.2013.12.014
55. Linares-Rodriguez A, Ruiz-Arias JA, Pozo-Vázquez D, Tovar-Pescador J (2013) An artificial neural network ensemble model for estimating global solar radiation from Meteosat satellite images. Energy 61:636–645. doi:10.1016/j.energy.2013.09.008

56. Liu BYH, Jordan RC (1960) The interrelationship and characteristic distribution of direct, diffuse and total solar radiation. Sol Energy 4(3):1–19. doi:10.1016/0038-092X(60)90062-1
57. Maxwell EL (1987) A quasi-physical model for converting hourly global horizontal to direct normal insolation. In: Proceedings of Solar '87, annual American Solar Energy Society conference, Portland, OR
58. Maxwell E, Wilcox S, Rymes M (1993) User's manual for SERI_QC Software—assessing the quality of solar radiation data. National Renewable Energy Laboratory technical report NREL/TP-463-5608, Golden, CO. Available at: http://www.nrel.gov/docs/legosti/old/5608.pdf
59. McArthur LJB (2005) Baseline Surface Radiation Network (BSRN). Operations Manual Version 2.1, WCRP-121, WMO/TD-No. 1274. Available at: http://bsrn.awi.de/fileadmin/user_upload/redakteur/Publications/McArthur.pdf
60. Michalsky JJ (1988) The astronomical Almanac's algorithm for approximate solar position (1950–2050). Sol Energy 40:227–235
61. Michalsky J, Dutton E, Rubes M, Nelson D, Stoffel T, Wesley M, Splitt M, DeLuisi J (1999) Optimal measurement of surface shortwave irradiance using current instrumentation. J Atmos Oceanic Technol 16:55–69. doi:10.1175/1520-0426(1999)016%3C0055:OMOSSI%3E2.0.CO;2
62. Michalsky JJ, Dolce R, Dutton EG, Haeffelin M, Jeffries W, Stoffel T, Hickey J, Los A, Mathias D, McArthur B, Nelson D, Philipona R, Reda I, Rutledge K, Zerlaut G, Forgan B, Kiedron P, Long C, Gueymard C (2005) Toward the development of a diffuse horizontal shortwave irradiance working standard. J Geophys Res 110(D06107). doi:10.1029/2004JD005265
63. Michalsky JJ, Anderson GP, Barnard J, Delamere J, Gueymard C, Kato S, Kiedron P, McComiskey A, Ricchiazzi P (2006) Shortwave radiative closure studies for clear skies during the atmospheric radiation measurement 2003 aerosol intensive observation period. J Geophys Res 111:D14S90. doi:10.1029/2005JD006341
64. Michalsky J, Dutton E, Nelson D, Wendell J, Wilcox S, Andreas A, Gotseff P, Myers D, Reda I, Stoffel T, Behrens K, Carlund T, Finsterle W, Halliwell D (2011) An extensive comparison of commercial pyrheliometers under a wide range of routine observing conditions. J Atmos Oceanic Technol 28:752–766. doi:10.1175/2010JTECHA1518.1
65. Miller SD, Heidinger AK, Sengupta M (2013) Physically based satellite methods. In: Kleissl J (ed) Solar energy forecasting and resource assessment. Academic Press, Oxford, pp 49–80
66. Mueller R, Matsoukas C, Gratzki A, Behr H, Hollmann R (2009) The CM-SAF operational scheme for the satellite based retrieval of solar surface irradiance—a LUT based eigenvector hybrid approach. Remote Sens Environ 113(5):1012–1024. doi:10.1016/j.rse.2009.01.012
67. Muneer T, Younes S, Munawwar S (2007) Discourses on solar radiation modeling. Renew Sustain Energy Rev 11:551–602. doi:10.1016/j.rser.2005.05.006
68. Myers DR, Gueymard CA (2004) Description and availability of the SMARTS spectral model for photovoltaic applications. In: Proceedings of SPIE 5520, Organic Photovoltaic V. doi:10.1117/12.555943
69. Myers DR, Emery K, Gueymard CA (2004) Revising and validating spectral irradiance reference standards for photovoltaic performance evaluation. J Sol Energy Eng 126(1):567–574. doi:10.1115/1.1638784
70. Myers DR (2005) Solar radiation modeling and measurements for renewable energy applications: data and model quality. Energy 30:1517–1531. doi:10.1016/j.energy.2004.04.034
71. Myers DR (2010) Comparison of direct normal irradiance derived from silicon and thermopile global hemispherical radiation detectors. In: Proceedings of SPIE 7773, reliability of photovoltaic cells, modules, components, and systems III, p 77730G. doi:10.1117/12.859732
72. Osterwald CR, Emery KA (2000) Spectroradiometric Sun Photometry. J Atmos Oceanic Technol 17:1171–1188. doi:10.1175/1520-0426(2000)017<1171:SSP>2.0.CO;2

73. Perez R, Ineichen P, Maxwell EL, Seals R, Zelenka A (1992) Dynamic global-to-direct irradiance conversion models. ASHRAE Trans 98(1):354–369
74. Perez R, Ineichen P, Moore K, Kmiecik M, Chain C, George R, Vignola F (2002) A new operational model for satellite-derived irradiances: description and validation. Sol Energy 73:307–317. doi:10.1016/S0038-092X(02)00122-6
75. Perez R, Cebecauer T, Šùri M (2013) Semi-empirical satellite models. In: Kleissl J (ed) Solar energy forecasting and resource assessment. Academic Press, Oxford, pp 21–48
76. Perez R, Lorenz E, Pelland S, Beauharnois M, Van Knowe G et al (2013) Comparison of numerical weather prediction solar irradiance forecasts in the US, Canada and Europe. Sol Energy 94:305–326. doi:10.1016/j.solener.2013.05.005
77. Reda I, Andreas A (2004) Solar position algorithm for solar radiation applications. Sol Energy 76:577–589. doi:10.1016/j.solener.2003.12.003. See also Reda I, Andreas A (2007) Corrigendum to Solar position algorithm for solar radiation applications. Solar Energy 76 (2004) 577–589, doi:10.1016/j.solener.2003.12.003
78. Reda I, Andreas A (2008) Solar position algorithm for solar radiation applications. NREL technical report NREL/TP-560–34302. National Renewable Energy Laboratory, Golden, CO. http://www.nrel.gov/docs/fy08osti/34302.pdf
79. Reindl DT, Beckman WA, Duffie JA (1990) Diffuse fraction correlations. Sol Energy 45:1–7
80. Reinhardt B, Buras R, Bugliaro L, Wilbert S, Mayer B (2014) Determination of circumsolar radiation from meteosat second generation. Atmos Meas Tech 7:823–838. doi:10.5194/amt-7-823-2014
81. Rienecker MM et al (2011) MERRA: NASA's modern-era retrospective analysis for research and applications. J Clim 24:3624–3648. doi:10.1175/JCLI-D-11-00015.1
82. Rigollier C, Bauer O, Wald L (2000) On the clear sky model of the ESRA—European Solar Radiation Atlas—with respect to the Heliosat method. Sol Energy 68:33–48
83. Rigollier C, Lefèvre M, Wald L (2004) The method Heliosat-2 for deriving shortwave solar radiation from satellite images. Sol Energy 77(2):159–169. doi:10.1016/j.solener.2004.04.017
84. Roesch A, Wild M, Ohmura A, Dutton EG, Long CN, Zhang T (2011a) Assessment of BSRN radiation records for the computation of monthly means. Atmos Meas Tech 4:339–354. doi:10.5194/amt-4-339-2011
85. Roesch A, Wild M, Ohmura A, Dutton EG, Long CN, Zhang T (2011b) Assessment of BSRN radiation records for the computation of monthly means. Corrigendum, Atmos Meas Tech 4:973
86. Ruiz-Arias JA, Alsamamra H, Tovar-Pescador J, Pozo-Vázquez D (2010) Proposal of a regressive model for the hourly diffuse solar radiation under all sky conditions. Energy Convers Manage 51:881–893. doi:10.1016/j.enconman.2009.11.024
87. Ruiz-Arias JA, Dudhia J, Santos-Alamillos FJ, Pozo-Vázquez D (2013) Surface clear-sky shortwave radiative closure intercomparisons in the weather research and forecasting model. J Geophys Res-Atmos 118(17):9901–9913. doi:10.1002/jgrd.50778
88. Ruiz-Arias JA, Dudhia J, Gueymard CA (2014) A simple parameterization of the short-wave aerosol optical properties for surface direct and diffuse irradiances assessment in a numerical weather model. Geosci Model Dev 7:1159–1174. doi:10.5194/gmd-7-1159-2014
89. Ruiz-Arias JA, Quesada-Ruiz S, Fernández EF, Gueymard CA (2015) Optimal combination of gridded and ground-observed solar radiation data for regional solar resource assessment. Sol Energy. doi:10.1016/j.solener.2014.12.011
90. Saha S et al (2010) The NCEP climate forecast system reanalysis. Bull Am Meteorol Soc 91(8):1015–1057. doi:10.1175/2010BAMS3001.1
91. Skamarock WC, Klemp JB, Dudhia J, Gill DO, Barker DM et al (2008) A description of the advanced research WRF Version 3. NCAR Technical note NCAR/TN–475+STR
92. Skartveit A, Olseth JA (1987) A model for the diffuse fraction of hourly global radiation. Sol Energy 38:271–274
93. Skartveit A, Olseth JA, Tuft M (1998) An hourly diffuse fraction model with correction for variability and surface albedo. Sol Energy 63:173–183

94. Steiner M, Siefer G, Hornung T, Peharz G, Bett AW (2014) YieldOpt, a model to predict the power output and energy yield for concentrating photovoltaic modules. Prog Photovolt: Res Appl. doi: 10.1002/pip.2458
95. Stoffel T, Renné D, Daryl M, Wilcox S, Sengupta M et al (2010) Concentrating solar power: best practices handbook for the collection and use of solar resource data (CSP). Report No. NREL/TP-550-47465. National Renewable Energy Laboratory (NREL), Golden, CO. http://www.osti.gov/scitech/biblio/989017. Now superseded by http://www.nrel.gov/docs/fy15osti/63112.pdf
96. Šúri M, Cebecauer T (2014) Satellite-based solar resource data: model validation statistics versus user's uncertainty. In: Proceedings of solar 2014 conference. American Solar Energy Society, San Francisco, CA
97. Thépaut J-N, Andersson E (2010) The global observing system. In: Lahoz W, Khattatov B, Ménard R (eds) Data assimilation: making sense of observations. Springer, Berlin
98. Thomalla E, Kopke P, Muller H, Quenzel H (1983) Circumsolar radiation calculated for various atmospheric conditions. Sol Energy 30:575–587
99. Vignola F (2006) Removing systematic errors from rotating shadowband pyranometer data. In: Proceedings of solar 2006 conference. American Solar Energy Society, Denver, CO
100. Vignola F, Michalsky J, Stoffel T (2012) Solar and infrared radiation measurements. CRC Press, Boca Raton
101. Vuilleumier L, Hauser M, Félix C, Vignola F, Blanc P, Kazantzidis A, Calpini B (2014) Accuracy of ground surface broadband shortwave radiation monitoring. J Geophys Res Atmos 119. doi:10.1002/2014JD022335
102. Wilbert S, Reinhardt B, DeVore J, Roeger M, Pitz-Paal R, Gueymard CA, Buras R (2013) Measurement of solar radiance profiles with the sun and aureole measurement system. J Sol Energy Eng 135:1–11. doi:10.1115/1.4024244
103. Wilbert S, Pitz-Paal R, Jaus J (2013b) Comparison of measurement techniques for the determination of circumsolar irradiance. In: Proceedings of international conference on concentrator photovoltaic systems (CPV-9), Miyasaki, Japan. AIP conference proceedings, vol 1556, p 162. http://dx.doi.org/10.1063/1.4822222
104. Wilcox S (1996) A visual quality assessment tool for solar radiation data. In: Proceedings of annual conference. American Solar Energy Society, Boulder, CO
105. Wilcox S (2012) National solar radiation database 1991–2010 update: user's manual. National Renewable Energy Laboratory technical report NREL/TP-5500-54824, Golden, CO. Available from http://www.nrel.gov/docs/fy12osti/54824.pdf
106. Wilcox S, McCormack P (2011) Implementing best practices for data quality assessment of the National Renewable Energy Laboratory's solar resource and meteorological assessment project. In: Proceedings of solar 2011 conference. American Solar Energy Society, Raleigh, NC
107. WMO (2008) Guide to meteorological instruments and methods of observation, 7th edn. World Meteorological Organization WMO-No. 8, Geneva, Switzerland. Available from http://www.wmo.int/pages/prog/gcos/documents/gruanmanuals/CIMO/CIMO_Guide-7th_Edition-2008.pdf
108. Zhang C, Gwamuri J, Andrews R, Pearce JM (2014) Desing of multijunction photovoltaic cells optimized for varied atmospheric conditions. Int J Photoenergy 2014:514962. doi:10.1155/2014/514962

Standards for Testing High-Concentrator Photovoltaic Modules

I. Petrina, A.B. Cueli, J. Díaz, J. Moracho and A.R. Lagunas

Abstract A key concept when deciding the investment in a determined photovoltaic (PV) product is to know if it passed enough tests to ensure its good performance and its safety and durability characteristics. Testing under internationally recognized standards has some advantages. From the point of view of the designers and manufacturers, the certification obtained according to international standards allows them to test their designs against common parameters and, based on the results, to define the extent of their warranties. From the point of view of end users, the employment of certified products involves that they are reliable enough to ensure reasonable sustained performance over the years and to minimize the appearance of risks during installation and operation.

1 Introduction

The first standard for concentrator photovoltaic (CPV) modules and assemblies was released in 2001 by the Institute of Electrical and Electronics Engineers (IEEE). The publication "IEEE1513-2001—Recommended Practice for Qualification of Concentrator Photovoltaic (PV) Receiver Sections and Modules" [1] established the

I. Petrina (✉) · A.B. Cueli · J. Díaz · J. Moracho · A.R. Lagunas
CENER (Renewable Energy National Centre), Sarriguren, Spain
e-mail: ipetrina@cener.com

A.B. Cueli
e-mail: abcueli@cener.com

J. Díaz
e-mail: jdiaz@cener.com

J. Moracho
e-mail: jmoracho@cener.com

A.R. Lagunas
e-mail: alagunas@cener.com

P. Pérez-Higueras and E.F. Fernández (eds.), *High Concentrator Photovoltaics*,
Green Energy and Technology, DOI 10.1007/978-3-319-15039-0_11

minimum tests and inspections required to evaluate photovoltaic concentrating modules as well as a common approach (e.g., between producer and purchaser) in conducting qualification tests.

If no weaknesses were identified during the qualification process, both manufacturer and customer could expect a more reliable product.

Later, in 2002, the Technical Committee (TC) 82 of IEC began the development of a new standard for the qualification of CPV modules and assemblies.

The International Electrotechnical Commission (IEC) is the world's leading organization that prepares and publishes international standards for all electrical, electronic, and related technologies. It is divided in 174 TCs, each of them with various working groups. The technical committee for PV systems—TC82, Working Group 7 (WG7), which is inside TC82—develops international standards for PV concentrators and receivers. The first standard developed by this working group was the IEC62108, the initial draft of which was based on IEEE1513-2001. That was withdrawn on December 2006, before the publication of the IEC62108:2007, "Concentration Photovoltaic Modules and Assemblies—Design Qualification and Type Approval" [2] in December 2007.

IEC62108:2007 is actually the most important standard for CPV modules and assemblies to enter the market. The experience of testing laboratories applying this standard has already produced the need for a revision of the first edition. The application of the IEC62108 standard is more difficult due to the fact of the great variety of CPV systems ranging from small modules of a few watts to larger systems of various kilowatts [3]. In the case of large components, the laboratory must discuss with the manufacturer the definition and fabrication of representative samples that might be used for some tests. In cases where a requirement for the real size product exists, such in outdoor exposure, testing might be performed in situ (e.g., in CPV plants) instead of in the laboratory facilities. In addition, different severities defined for the same tests allow the manufacturer to choose the option that better matches the particulars of their product. All of these facts require more active communication between the manufacturer and the laboratory than in the case of flat PV module technologies.

Apart from this standard, the IEC TC82 Working Group 7 released IEC62670-1:2013 "Photovoltaic Concentrators (CPV)—Performance Testing—Part 1: Standard Conditions" [4] and, recently, IEC62817:2014 "Photovoltaic Systems—Design Qualification of Solar Trackers" [5].

IEC WG7 is also working on other standards as:

- IEC62688 CPV Module and Assembly Safety Qualification," which will probably be released by 2016;
- IEC62670-2 CPV Performance Testing Part 2: Energy Measurement;
- IEC62670-3 CPV Performance Testing Part 3: Performance Measurements and Power Rating;
- IEC62108 (ed. 2) CPV Modules and Assemblies—Design Qualification and Type Approval;

- IEC62787 CPV Solar Cells and Cell-on-Carrier (CoC) Assemblies—Reliability Qualification;
- TS/IEC62789 Technical Specification of Concentrator Cell Description;
- IEC62925 (ed. 1) Thermal Cycling Test for CPV Modules to Differentiate Increased Thermal Fatigue Durability;
- New Proposal for CPV Solar Simulators; and
- New Proposal for CPV optics specification.

Apart from the IEC, Underwriters Laboratories (UL) released, in 2011, UL8703 Issue No. 3 [6], which, in terms of safety, it is mandatory for the United States market. All of these standards will be discussed in this chapter.

2 IEC62108:2007 CPV Modules and Assemblies—Design Qualification and Type Approval

2.1 Introduction

Released in December 2007, IEC62108 is accepted worldwide as citing the minimum requirements that a CPV module or assembly must fulfill to enter the international market.

IEC62108 specifies the minimum requirements for the design qualification and type approval of CPV modules and assemblies suitable for long-term operation in open air climates as defined in IEC60721-2-1. The standard is partially based in IEEE513-2001 and IEC61215 "Crystalline Silicon Terrestrial PV Modules—Design Qualification and Type Approval" [7], and it consists of a sequence of tests specific for the CPV product.

The object of the standard is to determine the electrical, mechanical, and thermal characteristics of the CPV modules and assemblies and to show, as far as possible, that they are capable of withstanding prolonged outdoor exposure. The life of CPV units depends on their design, production, environment, and—as a less controlled aspect—the conditions under which they are operated.

If the CPV unit under test has not been qualified, the entire sequence of tests must be performed. However, if the sample under test is already qualified and has undergone any changes (in materials, components, design, or manufacturing process) from the previously approved model, the manufacturer and also the certifying body and testing laboratory should discuss the retesting sequence for the newer model. To have consistent criterion, a retesting guideline was released in 2010 as a decision sheet by IECEE, and it will be included in the second edition of this standard as an annex.

2.2 Sampling

There is a wide variety of CPV modules and assemblies. For every "type" of CPV system, the concentration standard defines two items to be tested: the receivers and the modules/assemblies. The receiver is the group of one or more concentrator cells and secondary optics (if present) that accepts concentrated sunlight and incorporates the means for thermal and electric energy transfer. The module/assembly is the group of receivers, optics, and other related components such as interconnection and mounting that accepts unconcentrated light. Usually the modules are prefabricated as one unit, and the focus point is not field-adjustable. In contrast, the assemblies usually are shipped separately; they require some field installation; and the focus point is field-adjustable.

For CPV module qualification purposes, seven modules and two receivers—plus one receiver for the bypass/blocking diode thermal test—are required to be run through all of the specified tests. In the case of assemblies, nine receivers (including secondary optics sections if applicable) and seven primary optics—plus one receiver for the bypass/blocking diode thermal test—are required to be run through all of the specified tests. If a full-size module or assembly is too large to fit into available testing equipment, or a if a full-sized module or assembly is too expensive, a smaller representative sample may be used.

Representative samples must include all components except for some repeated parts. They must achieve maximum similarity to the full-size component in all electrical, mechanical, and thermal characteristics related to quality and reliability. The cell string in a representative sample should be long enough to include at least 2 bypass diodes and no fewer than 10 cells. The encapsulations, interconnects, terminations, and clearance distances around all edges should be the same as on the actual full-sized products.

The testing laboratory must be involved in the design of the representative samples and discuss it with the manufacturer to take into account all of the possible weaknesses that the module might have.

However, even if representative samples are used for other tests, a full-sized module or assembly should be installed and tested for outdoor exposure.

2.3 Test Sequence

As in IEC61215, the test sequence of IEC62108 includes some preliminary diagnosis tests. After this initial diagnosis, the samples are divided into five sequences where they are submitted to different aging/environmental tests. At the end, a final diagnosis is made to compute the total degradation that occurred during the qualification process. Figures 1 and 2 define the test sequence for modules and assemblies, respectively.

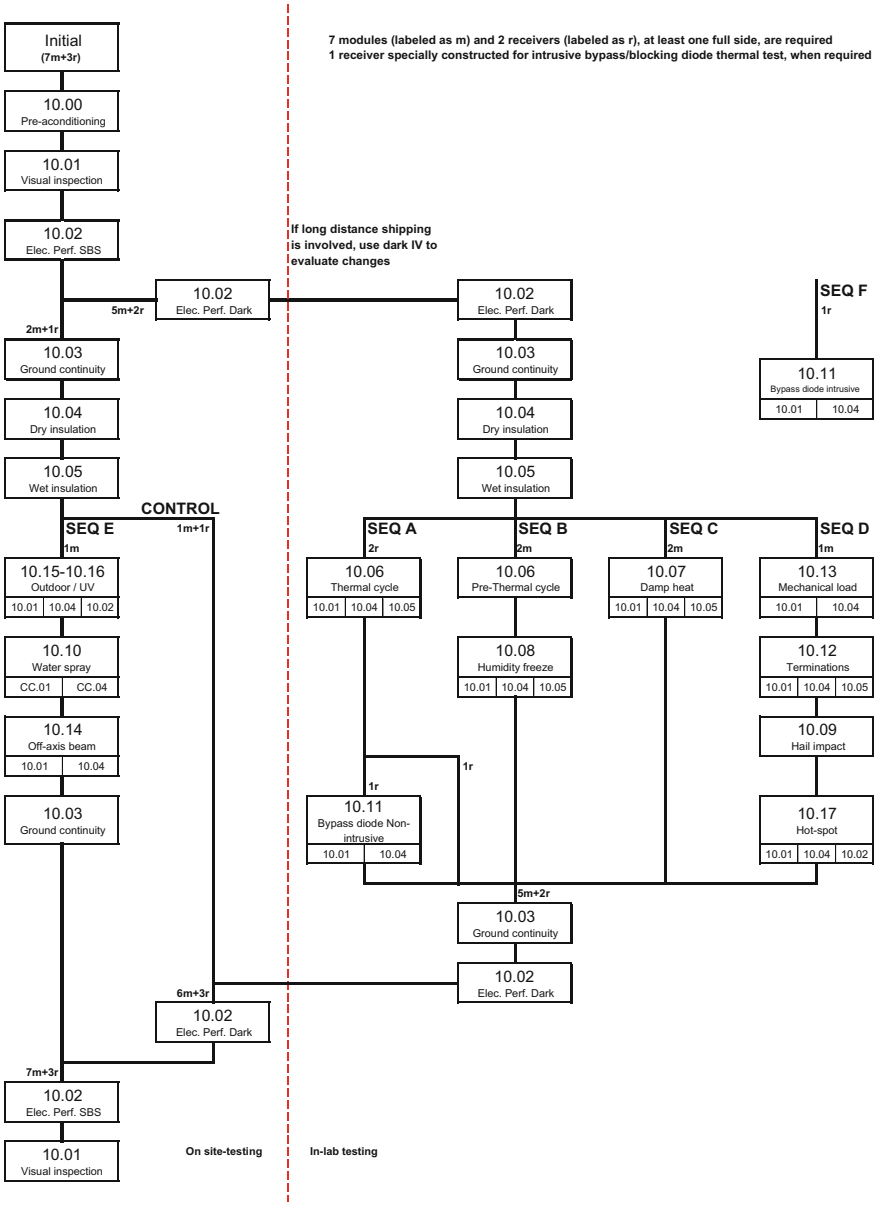

Fig. 1 Test sequence for CPV modules

2.3.1 Diagnostic Tests

As it can be seen in both figures, the first tests before the beginning of the sequences are considered diagnostic tests. These tests can be classified as visual diagnostic,

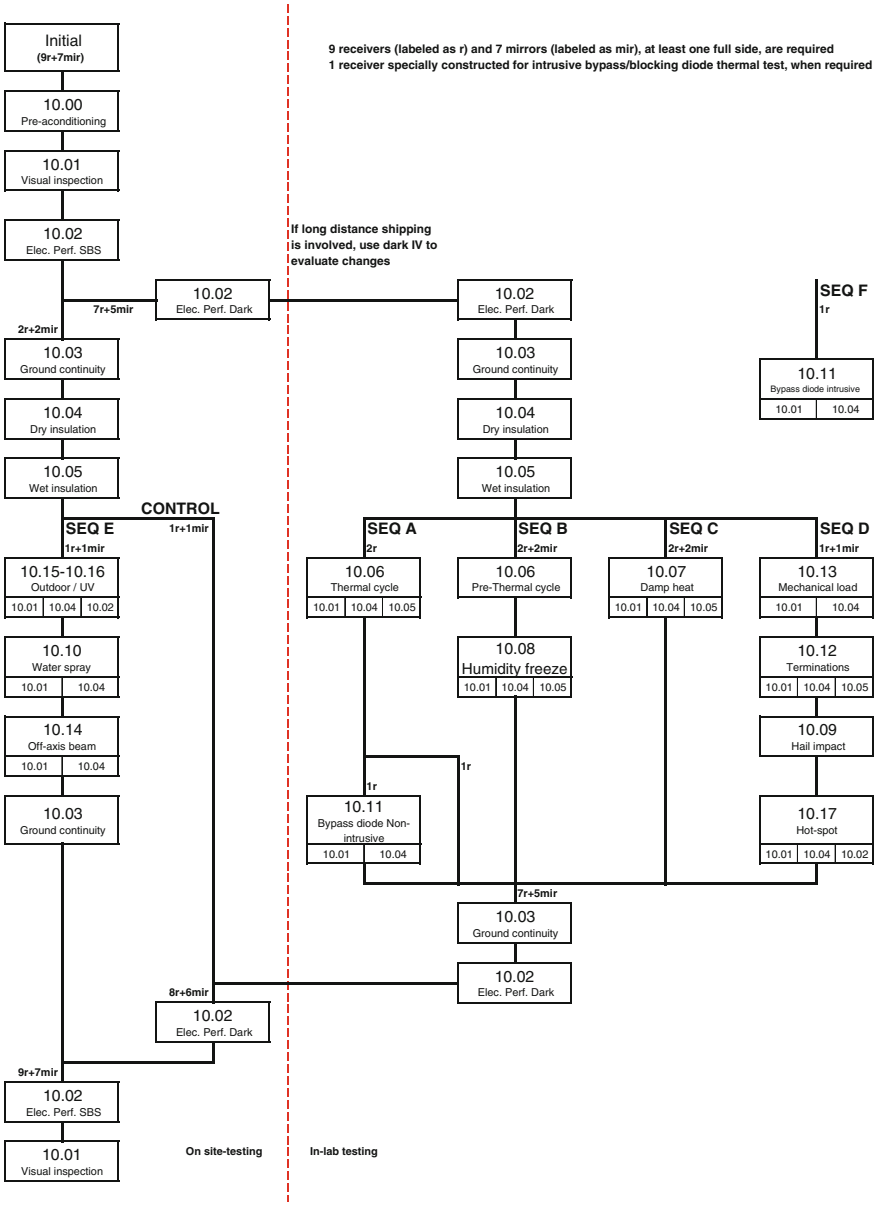

Fig. 2 Test sequence for CPV assemblies

electrical diagnostic/safety (dry and wet insulation tests and ground-continuity test), and performance diagnostic (electrical performance side-by-side and dark IV).

The visual inspection allows the examiner to identify defects such as broken parts or cells, sealant failures, faulty terminations, exposed live parts, corrosion and

other conditions that may affect reliability or performance. According to the standard, the samples must be free of major visual defects, which are defined as follows:

- Broken, cracked, bent, misaligned, or torn external surfaces including lens, mirror, receiver body, frame, and junction box;
- Broken or cracked cells;
- Bubbles or delamination forming a continuous path between any part of the electrical circuit and the edge of the receiver;
- Visible corrosion of any of the active circuitry of the sample;
- Adhesive or sealant failures; and
- Loss of mechanical integrity to the extent that the installation and/or operation of the modules or assemblies would be impaired.

The electrical insulation test determines if the CPV sample is well-insulated between all active parts of the module and the frame or the outside world. The test is performed in two steps. First, a voltage of 1000 V plus twice the maximum system voltage (as rated by the manufacturer) is applied between the shorted positive and negative terminals and the frame. This voltage is maintained for 2 min, and no dielectric breakdown must appear. Then the voltage is reduced to 500 V and maintained for another 2 min. After this time, the insulation resistance is measured.

The purpose of the wet insulation test is to evaluate the insulation of the CPV system under wet conditions and also to verify if moisture from the weather conditions might cause corrosion, a ground fault, or a safety hazard. In this test, the sample is immersed, or sprayed, for at least 5 min with an special solution made of water and a surfactant product. The resistivity of the solution must be <3500 Ω cm. After this time, a voltage of 500 V is applied between the short-circuit terminals and the solution that is in contact with the system. Two minutes later the insulation resistance is measured.

In both tests, the pass criteria are that no dielectric breakdown, surface tracking, or bubbles appear in the samples; and the insulation resistance must be >50 MΩ for samples with an overall receiver aperture of ≤0.1 m^2, and >5 MΩ m^2 for samples with an overall receiver aperture >0.1 m^2.

The ground continuity test is performed to verify that all of the exposed conductive parts and the grounding point of the system have good electrical continuity under high-current conditions. A current equal to two times the short-circuit current of the system is applied between the grounding point and any accessible part. The resistance measured during the current injection must be <0.1 Ω, and no damage should appear in the joints of the exposed conductive parts. This test is carried only at the beginning and at the end of each test sequence.

For the electrical performance measurement, two tests are defined in the standard. The outdoor side-by-side current voltage (I–V) measurement identifies the power degradation of a test sample comparing its relative power before and after each test sequence. This relative power is defined as the maximum power of the sample under test divided by the maximum power of the control sample, which are both measured under similar test conditions. This method assumes that the changes

in the control sample electrical performance are insignificant. For conducting this method, the following meteorological conditions are required:

- DNI must be >700 W/m^2, under a clear sky, and with a variation <2 % in every 5-min interval.
- Wind speed must be <6 m/s, and there must be no gust >10 m/s in 10 min before any measurement.
- The sample temperature cannot vary >2 °C in <1 min.

The test sample and the control sample must be mounted on a two-axis tracker. It is also possible to mount both samples on adjacent trackers, but in both cases the samples should be aligned according to the manufacturer's specifications. If there are no specifications, the I_{SC} of the module can be used as an indicator of the alignment. The misalignment should not cause a decrease of >2 % of the I_{SC} according to its maximum value.

Once the samples are aligned, I–V curves of both samples must be taken as quickly as possible so the change in the power output caused by the meteorological conditions is <2 %. Once the measurements are taken, the relative power of the test sample is calculated as:

$$P_r = \frac{P_m}{P_{mc}} \cdot 100\,\% \tag{1}$$

where P_r is the sample's relative power (in %), P_m is the test sample's maximum power (in W), and P_{mc} is the control sample's maximum power (in W).

Once the sequence is completed, another side-by-side measurement must be made. The relative power degradation of the test sample is calculated as:

$$P_{rd} = \frac{P_{ri} - P_{rf}}{P_{ri}} \cdot 100\,\% \tag{2}$$

where P_{rf} is the relative power after a given test, and P_{ri} is the relative power before a given test.

This test is used as a pass/fail criteria after the test sequence steps have been performed. For the sample under test, the relative power degradation of the module should be <13 % for outdoor measurements and <8 % for indoor measurements. This 5 % difference is for taking into account the uncertainty in outdoor measurements.

The last electrical performance test is the dark I–V measurement, in which the series resistance of the sample is measured before and after one test. It is mandatory to perform this test if the sample has been tested at different locations to evaluate possible changes due to shipping. If the series resistance shows a 10 % increase, the side-by-side test should be performed. In this test, a power supply is connected to the test sample; if the sample has a blocking diode, this must be shorted by placing a jumping lead across its terminals. After this, a current from 0.9 to 1.6 I_{SC} must flow across the sample registering the values of voltage and current. This must be

performed as quickly as possible to avoid heating of the sample cells. At least 10 values must be recorded. Finally, a chart of the voltage in the vertical axis and the current in the horizontal axis must be plotted, and a linear regression in the region of the linear part of the curve must be made. Then the following equation is obtained:

$$V = R \times I + V_0 \tag{3}$$

where R is the module's series resistance, and V_0 is the linear-regression constant.

This test is not used as a pass/fail criteria, but it is an easy procedure to identify possible degradations of the sample after each test.

2.3.2 Sequence A

In this sequence, which is applied only to the receivers, the main test is the thermal cycling test, in which the ability of the receivers to withstand the thermal mismatch, fatigue, and other stresses caused by the rapid, nonuniform, or repeated changes in temperature is determined. If the receivers are too large to fit in the environmental chamber, or they are very expensive to use, a representative sample can be used.

The thermal cycle test must be performed without adding humidity, and there are three options to fit the different materials. A dwell time of 10 min minimum at T_{max} and T_{min}, within ±3 °C in both temperatures, is required. The thermal frequency must be between 10 and 18 cycles/day. In addition, the current cycling speed should be on and off for 10 cycles in 1 thermal cycle, but for temperatures <25 °C, the current injection should be switched off. The three options and the cycle profile are shown in Table 1 and Fig. 3, respectively.

This test is being reviewed by IEC TC82–WG7 due to the impossibility of reaching a steady temperature in the T_{max} dwell time when the current is being injected on the receiver. Another important point to take into account is the time needed for accomplishing the test, which could vary from 1 month (if 110 °C is selected and the environmental chamber can achieve 18 cycles/day) to >6 months (if 65 °C is selected, and the thermal speed is 10 cycles/day). At the end of the test, the samples should be subjected to the visual inspection and dry insulation tests with the same requirements as in the initial diagnosis.

After this test, one of the receivers should be subjected to the bypass/blocking diode thermal test. With this test the capability of the diodes used in the samples to limit the detrimental effects of the hotspots in the system is assessed. A thermal

Table 1 Thermal cycle test options for sequence A

Option	Maximum cell temperature (°C)	Total cycles	Applied current
TCA-1	85	1000	Apply 1.25 × I_{SC} when T > 25 °C Cycle speed is 10 electrical/thermal
TCA-2	110	500	
TCA-3	65	2000	

sensor must be attached to the diode. If a special sample must be prepared to perform this test, the test is called an "intrusive bypass/blocking diode thermal test"; otherwise, it is called a "nonintrusive test." In any case, the receiver should be manufactured with a low-mass thermal sensor attached to the case of the diode with minimum disturbance to the diode and its thermal environment.

The sample under test must be heated to 75 ± 5 °C. Once this temperature is reached, a current equal to the short-circuit current must be applied to the diode for 1 h while its temperature is recorded. In that situation, the junction temperature of the diode must be calculated using the information provided by the manufacturer. This calculated temperature should not exceed the diode manufacturer's maximum junction-temperature rating. If the result is acceptable, a current injection of $1.25 \times I_{SC}$, must be applied to the diode during another hour. After this second hour, the diode should still function as a diode. Finally, the sample under test must be subjected to a visual inspection and a dry insulation test.

2.3.3 Sequence B

This sequence is applied only to modules or assemblies. The first step is a pre-thermal cycling test according to the temperature profile of Fig. 3, but this is without current injection. The options for the maximum temperature and number of cycles are described in Table 2.

After this test, the sample is subjected to the humidity freeze test. The objective of the test is to see the ability of the modules or assemblies to withstand the effects of high humidity and temperature followed by a period of freezing temperature. It is important to note that this is not a thermal shock test. As in all of the tests, except

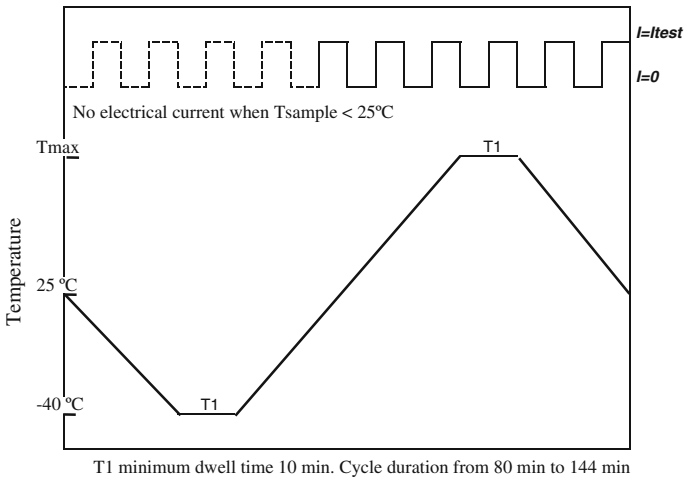

Fig. 3 Temperature and current profile of thermal cycle test

Table 2 Thermal cycle test options for sequence B

Option	Maximum cell temperature (°C)	Total cycles	Applied current
TCB-1	85	200	None
TCB-2	110	100	
TCB-3	65	400	

the ones of the sequence E, the use of representative samples is allowed if the sample under test is too big to fit on to the climatic chamber or if it is too expensive to use.

The thermal and humidity profile is shown in Fig. 4. As for the thermal-cycling test, there are two different options for the maximum temperature, which will be set by the manufacturer depending on the materials used on the samples. These options are detailed in Table 3.

After the humidity–freeze cycles, and between 2 and 4 h of removal from the environmental chamber, the sample under test should be subjected to dry and wet insulation tests. Finally, the sample should be also subjected to the visual

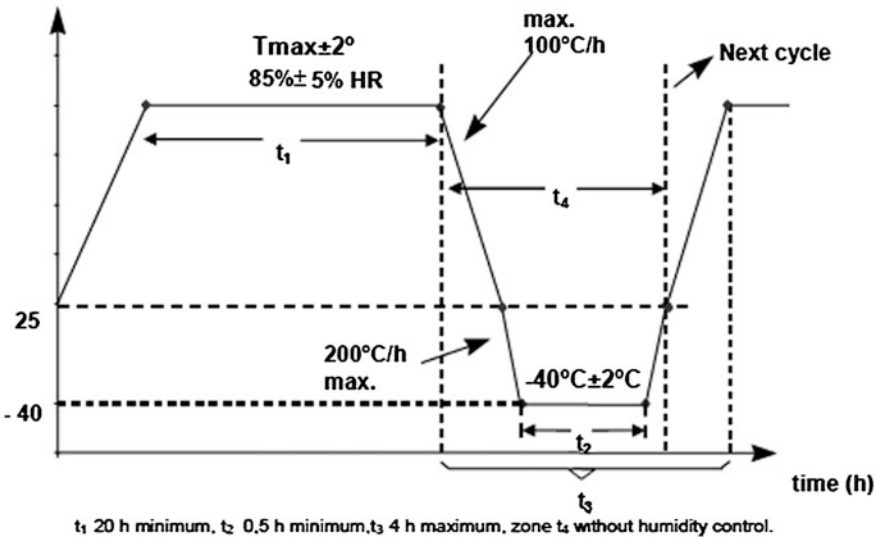

Fig. 4 Temperature and humidity profile of the humidity freeze test

Table 3 Options for the humidity–freeze test in sequence B

Option	Maximum cell temperature (°C)	Humidity (%)	Total cycles	Applied current
HFC-1	85	85	20	None
HFC-2	65	85	40	

inspection test. The requirements for the diagnosis tests are the same as in the initial diagnosis step.

2.3.4 Sequence C

In this sequence there is only the damp-heat test. This test is applied to modules or assemblies. Its main purpose is to check if the module or assembly can withstand the effects of long-term penetration of humidity. As in the previous sequence, if the design under test is too big to fit in the environmental chamber, or if it is too expensive to use, representative samples may be used. The samples under test are placed in an environmental chamber in which the relative humidity is maintained at 85 ± 5 % with a temperature of 85 ± 2 °C. The length of time needed for accomplishing the test is 1000 h. If the materials of the sample are not suitable for working at that temperature, it is also possible to perform the test at 65 °C and with the same relative humidity. If this option is selected, the time needed for accomplishing the test is 2000 h.

At the end of this exposure, and between 2 and 4 h of the removal of the samples from the chamber, dry and wet insulation tests must be performed. The samples are also subjected to the visual inspection test, and the requirements for the results of the diagnosis tests remain the same as in the initial diagnosis.

2.3.5 Sequence D

This sequence is applied only to one module or assembly. The first test in the sequence is the mechanical load test, which determines the ability of the module or assemblies to withstand wind, snow, or ice load.

In this test, the sample is mounted on to a structure according to the mounting method provided by the manufacturer, and during the whole test the internal circuit continuity should be monitored. A pressure of 2400 Pa is applied gradually on the entire front surface. This pressure is maintained for 1 h. The same procedure is applied to the back surface and then repeated twice until three entire cycles are achieved. After the test, visual inspection and dry insulation tests should be performed.

If the module or assembly is not suitable for installation in areas of extreme climate conditions, the manufacturer should specify the load limits that apply to the product so that the test pressure level will match these specifications. If the product is suitable to withstand heavy accumulation of snow and ice, the load applied during the last cycle onto the front surface of the module is increased until 5400 Pa.

After the mechanical load test, the sample is subjected to the robustness-of-terminations test. This test is analogous to the test applied to flat-plate modules. The test attempts to assure that the terminations of the sample and their attachments can withstand the stresses caused by its installation and operation. The test procedure is dependent on the kind of termination used (wire or flying leads,

threated nuts or screws, and, finally, connectors). All of them are described in the IEC60068-2-21 standard, and in all cases it consists of a tensile test and a bending test. At the end of the test, the sample shall be subjected to visual inspection and dry insulation and wet insulation tests, for which the sample shall accomplish the same requirements as in the initial diagnosis.

The hail test determines if all of the exposed parts of the sample, mainly the lens and mirrors, can survive a hailstorm. The sample is shot with ice balls (diameter 25.4 mm) at a speed of 22.4 m/s at a minimum of 10 different locations on the sample. The selected points should meet the following guidelines:

- Any point that may be hit by a hailstorm falling from 45° around the vertical when the module is under normal operation or stow positions;
- Corners that are no more than 25 mm from the edge;
- Edges and points that are no more than 12 mm from the side or the fixing structure;
- Farthest points from the fixing points to supporting structures; and
- Any other point vulnerable to hail impact.

There is no specific pass/fail criteria for this test, but the result of every impact should be recorded and reported in detail. As in the mechanical test, if the sample is intended to be used in areas where a hailstorm is unlikely, this test can be omitted, but this should be detailed in the test report and product certificate.

The last test of the sequence is the hotspot test, which determines if the module or assembly is able to withstand long-term of periodic hot-spot heating. The test procedure is similar to the one described in IEC61215 for crystalline silicon flat-plate modules but with adding an extra 3 % of relative power degradation if the measurement is made by a solar simulator or 5 % if this measurement is made under natural sunlight for the entire sequence. The procedure depends on the configuration of the bypass diodes in the sample and actually is under revision by IEC TC82. Finally, the sample shall be subjected to visual inspection and dry insulation tests, and the sample shall accomplish the same requirements as in the initial diagnosis. If the module or assembly has a bypass diode per cell, this test can be omitted.

2.3.6 Sequence E

This sequence comprises the tests related with the sample exposure in the field. The main characteristic of this test sequence is that the use of a representative sample is not allowed.

Outdoor exposure and the ultraviolet (UV) conditioning are both performed at the same time. The purpose of the outdoor test is to realize a preliminary analysis of the ability of the sample to withstand exposure to outdoor conditions, whereas the UV conditioning test attempts to show possible failures due to limited UV exposure.

The sample under test is mounted onto the solar tracker and connected to the grid, and the DNI, UV irradiation and ambient and module temperatures are recorded all along the duration of the test. The total dose that the sample must receive is 1000 kWh/m^2 of DNI and 50 kWh/m^2 for UV light. This latter dose is only counted when the DNI is >600 W/m^2.

When the exposure is complete, the sample is subjected to visual inspection and dry insulation tests. In addition, the side-by-side test is performed with an accepted relative power degradation of 5 % if the measure is performed under a solar simulator or 7 % if performed under natural sunlight measurement. The allowed relative power degradation on these tests is lower than in the rest of sequence because the outdoor exposure is not an aging test.

After the outdoor test, the sample is subjected to the water-spray test, which evaluates if rain can enter the module or assembly under operating conditions and if the entered water can produce a ground fault or a safety hazard. In this test, the module is mounted in four different orientations (with the front face at 45° from the horizontal, in the stow position, at the normal limit of its allowed tracking, and upside down, when applicable). In every one of these positions, a rain-test fixture (according to the requirements of ANSI/UL1703:2002) is placed over the most vulnerable location of the sample for every orientation. The sample is then exposed to a water spay for 1 h at each orientation. After each exposure, the sample must be examined for evidence of water penetration. Finally, between 1 and 2 h after the final exposure, the module is subjected to the dry insulation test. In addition, visual inspection shall be performed.

The last test of the sequence is the off-axis test, which determines if a fault in the tracking system can produce a fault in the sample due to the concentrated solar radiation. If the system has a fully redundant and failsafe protection for the misalignment issues, the system can be exempt from undergoing this test. The sample shall be inspected to detect possible materials that could be damaged by high temperature or intense solar radiation. All of the selected points are tested by focusing the concentrated light under every point for at least 15 min at an irradiation >800 W/m^2. If no specific locations are observed, then the module is aligned toward the Sun, and then the tracking system is stopped allowing the Sun to "walk off" at an angle of 45°. During this test the DNI should be >800 W/m^2. The sample is finally subjected to visual inspection and a dry insulation test.

2.4 Pass Criteria

A CPV module or assembly will be IEC62108 type approved if each sample meets all of the following criteria:

- The relative power degradation in sequences A to D is <13 % for outdoor measurement or <8 % for solar simulator measurements.
- The relative power degradation in sequence E is <7 % for outdoor measurement or <5 % for solar-simulator measurements.

- No sample shows an open circuit during the tests.
- There is no major visual defect as defined in the visual inspection test.
- The dry and wet insulation requirements are met at the beginning and end of every test sequence.
- The specific requirements for the individual tests are met.

If one sample does not meet these "pass" criteria on a sequence, two more samples should be subjected to the entire test sequence. If these two new samples meet the "pass" criteria, the model will be approved. If any of the two samples do not meet the "pass" criteria, the model shall be deemed not to have met the qualification criteria, and the entire test program should be repeated.

3 Safety Standards for CPV Modules

3.1 Introduction

There are two safety standards for CPV modules: UL8703:2011 and IEC62688 [8]. The UL is a minimum requirement for entry in the United States markets, and its third edition was released in May 2011. In contrast, IEC62688 is currently in draft form, but most of the requirements and test procedures are described; therefore, most of the manufacturers test their modules against both standards.

Both standards describe the minimum requirements for a CPV module or assembly to be used in general and restricted areas depending on the module's application class. They are divided in two main parts, which are analogous to the safety standard for flat-plate modules (UL1703 [9] and IEC61730 [10], respectively). The first part includes the requirements for construction, and the second part includes the requirements for testing.

The test sequences for both IEC and UL standards are designed to coordinate with that of IEC62108 so that a single set of samples may be used to perform both the safety and performance evaluation of a CPV module or assembly.

3.2 Sampling

For UL8703 qualification, at least 10 modules or assemblies and 4 receivers are needed for the completion of the test sequence. The IEC62688 requires only 8 modules and 3 receivers for the completion of its test sequence. The main different on the sequences is that for UL qualification, there are 3 samples/test stream instead of the 2 samples required in the IEC62688.

Table 4 Minimum sample requirements and nominal test time [11]

Standard	No. of samples for separate testing	Nominal testing time if performed sequentially (months)	No. of samples for combined testing	Nominal testing time for combined testing (months)
IEC62108	7 modules + 3 receivers	6		
IEC62688	8 modules + 3 receivers	6		
UL8703	10 modules + 4 receivers	6		
IEC62108 + IEC62688	15 modules + 6 receivers	12	8 modules + 3 receivers	6
IEC62108 + UL8703	17 modules + 7 receivers	12	10 modules + 4 receivers	6
IEC62108 + IEC62688 + UL8703	25 modules + 10 receivers	18	10 modules + 4 receivers	6

To save time and money, and also to have faster access to the market, it is highly recommended to perform IEC62108 testing and the safety standards at the same time. Table 4 shows the minimum number of samples and the time required for testing depending on the case of the standards being applied separately (and sequentially) or as a combined sequence. For the calculation, it has been considered that the outdoor-exposure test is performed in approximately 5 months (for very sunny locations).

3.3 Requirements for Construction

The first part of the safety standards consists on the study of all of the materials used for the construction of the module or assembly as well as also the requirements for documentation supplied by the manufacturer, mainly the installation instructions describing the methods for the electrical and mechanical installation of the CPV unit.

The requirements for construction are classified by the type of material used to manufacture the module, the material's function inside the sample and the physical design of the sample (in terms of clearance and creepage distance between active and insulated parts). Depending on these aspects, different requirements must be fulfilled by the materials. There are also requirements for other components such as the connectors, external cables, junction box, grounding, etc.

The application of the different requirements depends on the applicable class of the sample. The different classes of application are as follows:

- class A: General access, hazardous voltage; and hazardous energy application;
- class B: Restricted access, hazardous voltage; and hazardous energy application;
- class X(UL)/B-X(IEC): Restricted access, hazardous voltage; and hazardous energy application with additional flame or concentrated light hazards; and
- class C: General access, with limited voltage, current; and power; the voltage limit is 30 V for the UL and 75 V for the IEC.

3.4 Requirements for Testing and Performance

Figures 5, 6 and 7 describe the test sequences for IEC62108, IEC62688, and UL8703 standards. As in IEC62108, the use of representative samples is allowed, but a full module is needed to perform the outdoor-exposure test.

Both UL and IEC standards allow running some tests separately from the sequences shown in the previous figures to have a combined sequence to conduct IEC62108, IEC62688, and UL8703 at the same time.

The IEC classifies the tests in different categories detailed in Table 5 (the tests marked in bold type are related only to the safety standard):

In some cases, the only difference among standards for a test is related to the levels of severity applied; e.g., the dry-insulation test and ground/bonding path-continuity test have as differences between UL and IEC only proposals of the level of voltage or current to be applied. Taking this into account, it is always possible to perform the tests in the most severe condition to fulfill both standards.

Specific tests that belong only to the safety standards and that are not included in the IEC62108 are described in Table 6.

3.5 Pass Criteria

In the section of construction aspects, the materials, design, and documents of the module or assembly must comply with all specific requirements. In addition, all of the supplied documents for the mechanical and electrical installation must comply with their specific requirements.

Regarding the requirement for testing, the “pass” criterion is that all of the samples must meet the criteria of each individual test applied. If any module does not meet these test criteria, the product under evaluation shall be deemed not to have met the safety test requirements. In this last case, the nature of the failure will determine the extent of retesting requirements.

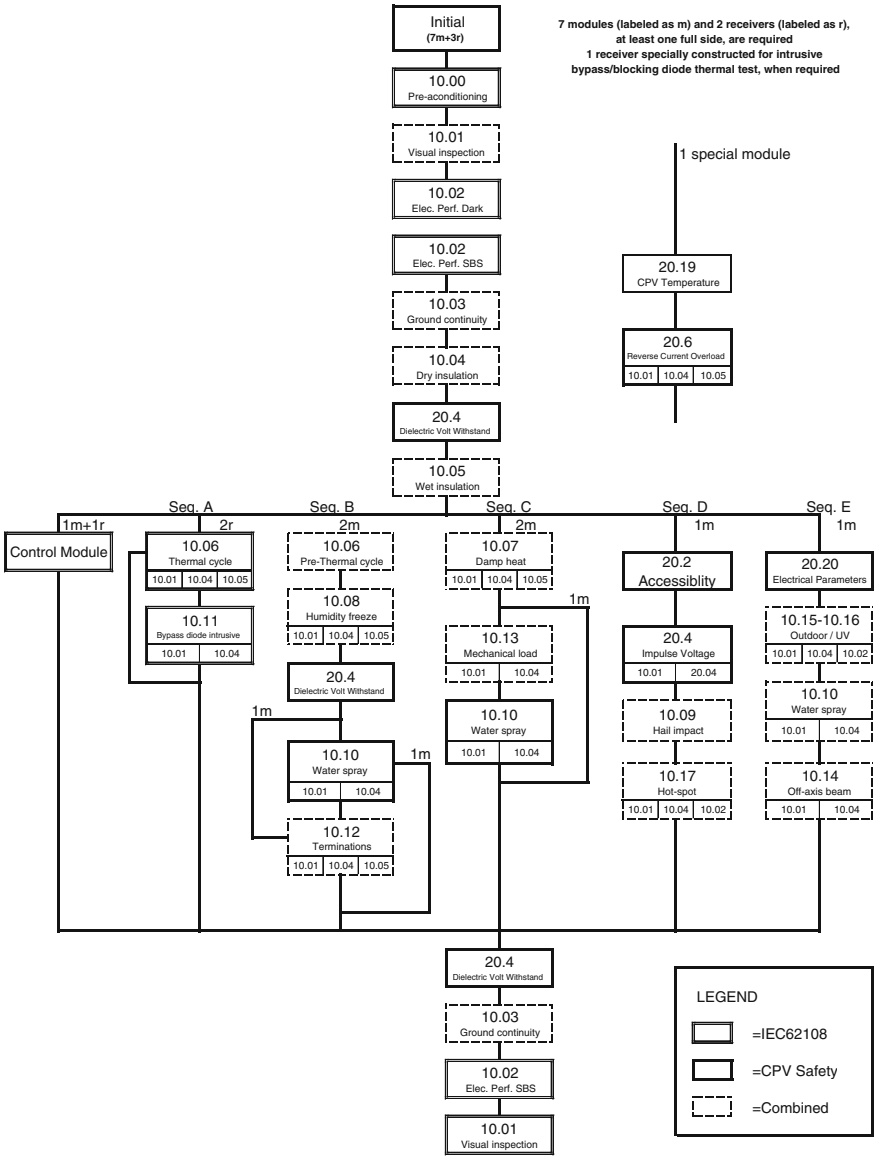

Fig. 5 Combined IEC62108 and IEC62688 for CPV modules

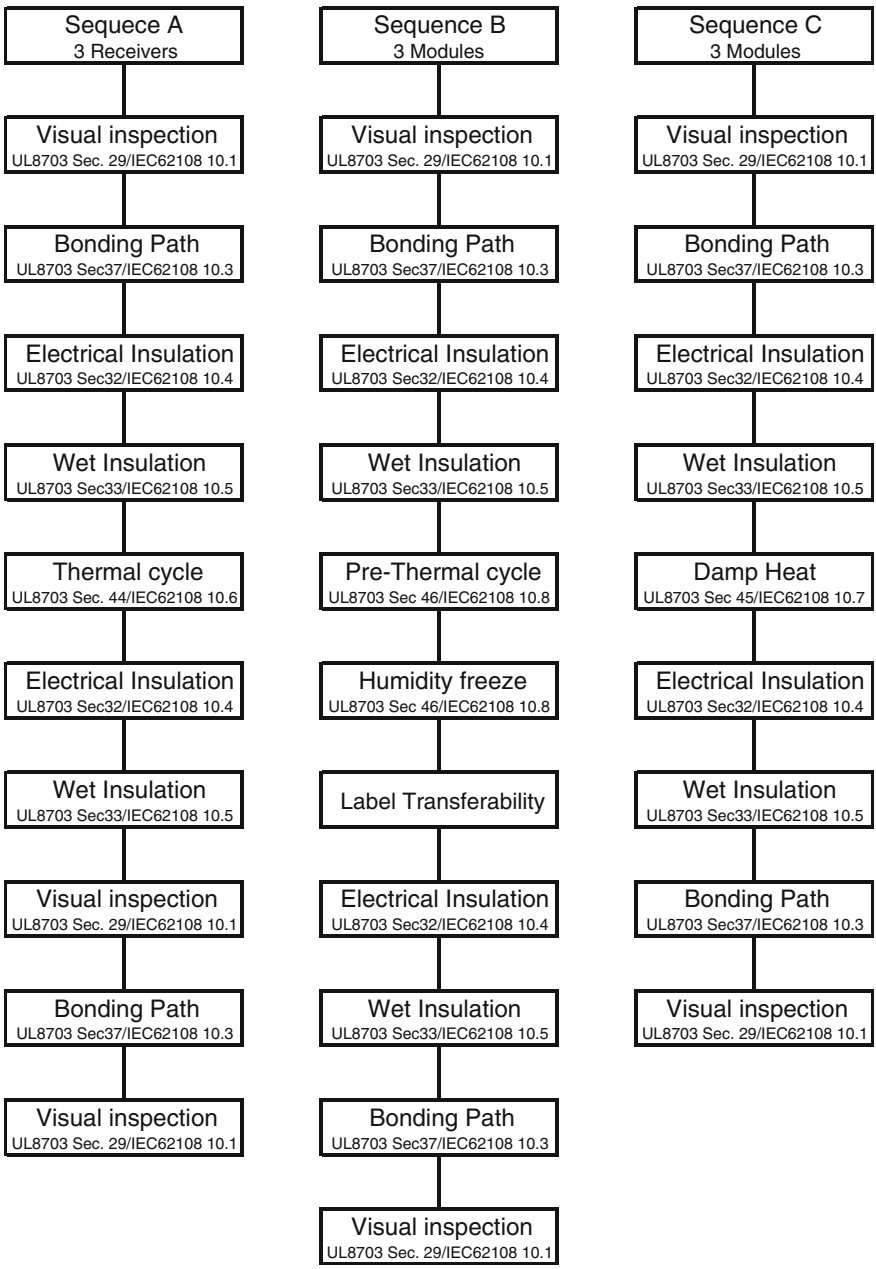

Fig. 6 UL8703 test sequence (part 1)

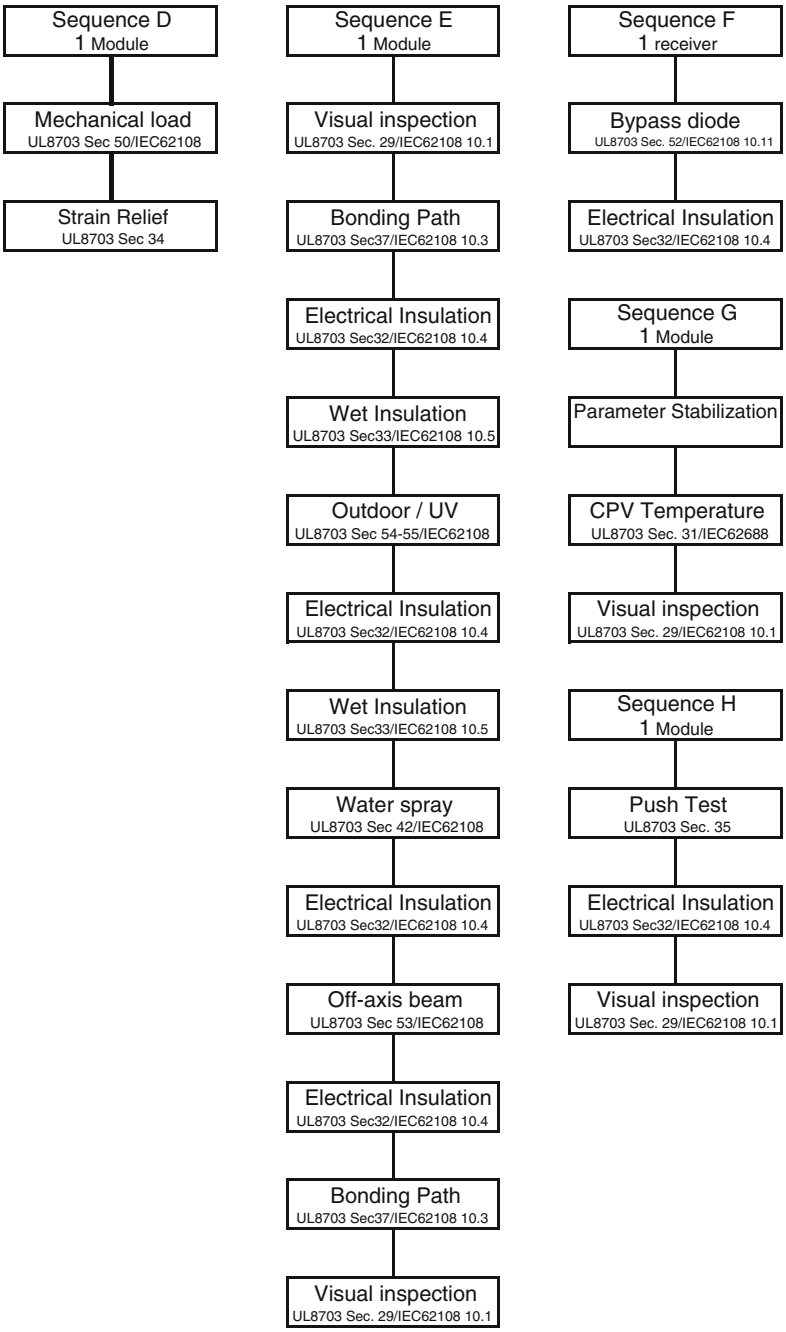

Fig. 7 UL8703 test sequence (part 2)

Table 5 Tests categories according to IEC62688

Tests categories	Tests
Preconditioning tests	Thermal cycling, damp heat, humidity freeze, ultraviolet conditioning, outdoor exposure
General Inspection tests	Visual inspection, **CPV electrical parameters**, **sharp edges**
Electrical shock hazard tests	Electrical insulation, dielectric voltage withstand, wet insulation, **accessibility**, ground path continuity, **impulse voltage**, robustness of terminations, water spray
Fire hazard tests	**CPV temperature**, hot spot endurance, **reverse current overload**, bypass diode thermal, off-axis beam damage
Mechanical stress tests	Mechanical load, hail impact

Table 6 Specific safety tests

Test	IEC	UL	Purpose
CPV electrical parameters test	X	X	Maximum voltage and current are calculated from various worst-case environmental and irradiance conditions, and they must be used for selection and design of other components, such as conductors, connectors, disconnects and overcurrent protection
Sharp-edges test	X	X	Determine the potential personal injury related to the sharpness of edges that are part of or associated with the module. In the IEC it is included as an appendix, and in the UL this test is included as a requirement for construction
Accessibility test	X	X	Determine if the uninsulated electrical live parts of the module or assembly represent a shock hazard to personnel. In the UL this test is included as a requirement for construction
Impulse-voltage test	X		Verify the capability of the solid insulation of the module to withstand over-voltages of atmospheric origin (e.g., lightning). It also covers over-voltages due to switching of low-voltage equipment
CPV temperature test	X	X	Determine the maximum reference temperatures for various components and materials used to construct the module to establish the suitability of their use
Reverse current overload test	X	X	Determine the acceptability of the risk of ignition or fire under reverse current fault conditions
Spread-of-flame test	X	X	This test apply to units intended for roof mounting, and designated for installation above, upon, or integral with a building roof structure. The test procedure is detailed in the UL790. In the IEC standard, this procedure is under construction

(continued)

Table 6 (continued)

Test	IEC	UL	Purpose
Burning-brand test	X	X	This test apply to units intended for roof mounting, and designated for installation above, upon, or integral with a building roof structure. The test procedure is detailed in the UL790 for both standards
Blocked heat-sink test	X		Ensures there is no fire or shock hazard present in the event of an accidental clogging condition on any heat sink employed in a module's construction
Locked rotor test	X		Ensures there is no fire or shock hazard present in the event of an accidental locked rotor condition on any motor employed in a module system
Strain-relief test		X	This test is analogous to the robustness of termination test of the IEC62108
Push test		X	The purpose of this test is the same as the accessibility test of the IEC62688
Terminal-torque test		X	Determine if a screw or nut used on a wiring terminal will withstand stresses as are likely to be applied during normal installation or handling operations
Cut test		X	Determine if the sample is able to withstand the application of a sharp object drawn across any exposed thin insulating surfaces without creating an increased risk of electric shock. The glass surfaces are not required to be submitted to this test
Impact test		X	Determine if the impact of a steel sphere of a certain weight and falling from a certain height can produce an electric shock hazard

4 Other Standards Released and Under Development by the IEC WC7

4.1 Standards Released

At the moment, there are two more standards published by the IEC. The first one, after the publication of IEC62108:2007, is IEC62670-1:2013, which describes the two standard conditions for CPV modules and assemblies. Defining agreed-upon test conditions will allow the manufacturers to be rated against the same reference values.

IEC62817:2014 is the standard for the design qualification of solar trackers. Because every CPV module or assembly needs a tracker to work, this standard ensures the user of the said tracker that parameters reported in the specifications are measured by consistent and accepted industry procedures, also the standard will allow consistency in comparing the products from different vendors, thus verifying the quality of the products under the same conditions.

4.1.1 IEC62670-1:2013 Concentrator Photovoltaic (CPV) Performance Testing—Part 1: Standard Conditions

This standard was released in September 2013. The object of this standard is to define a consistent set of conditions to be used for rating the power noted on data sheets and nameplates. Two sets of conditions are included in the standard; one of them is similar to the ones for flat-plate PV modules [i.e., Concentrator Standard Test Conditions (CSTC)], the other takes into consideration more operative aspects of CPV technology [i.e., Concentrator Standard Operating Conditions (CSOC)]:

- CSOC is defined as follows: irradiance = 900 W m^{-2} direct normal irradiance (DNI); temperature = 20 °C ambient temperature; wind speed = 2 m s^{-1}; and spectrum = direct normal AM1.5 spectral irradiance distribution consistent with conditions described in IEC60904-3;
- CSTC is defined as follows: irradiance: 1000 W m^{-2} DNI; cell temperature = 25 °C; and spectrum = direct normal AM1.5 spectral irradiance distribution consistent with conditions described in IEC60904-3.

4.1.2 IEC62817:2014 Photovoltaic Systems—Design Qualification of Solar Trackers

Released in August 2014, the standard defines test procedures for both key components and the complete tracker system. Some of the tests, e.g., the tracking-accuracy procedure, define parameters to be reported on the tracker-specification sheet (TS62727:2012 "Specification for Solar Trackers"). In other cases, e.g., mechanical testing, environmental testing, and the accelerated mechanical cycling procedures, the test procedure results in a pass/fail criterion. This standard ensures the user of the said tracker that parameters reported in the specification sheet were measured by consistent and accepted industry procedures. The tests with pass/fail criterion are engineered with the purpose to identify whether the design is suitable as specified by the manufacturer.

This standard is not applicable to CPV modules or assemblies; however, because all of the CPV modules need a tracker to operate, it has been a main objective for WG7. The qualification standard gives confidence to the manufacturers and customers.

4.2 Standards Under Development

Because the CPV industry is a relative young industry, and to take in account all of the particularities of the technology, there are several standards under development. Because there is a wide variety of concentration systems, the hardest part of the development of these new standards is to make them applicable for all kind of CPV systems.

4.2.1 IEC62670-2 Concentrator Photovoltaic (CPV) Performance Testing—Part 2: Energy Measurement

Actually at the committee-draft-for-vote (CDV) stage, this standard describes the requirements for measuring the energy output and performance ratio for all kind of CPV modules, assemblies, arrays, and power plants. The standard defines the testing method to stablish a standard energy measurement and to specify the minimum reporting data. It is important to remark that the results are only valid for a specific location indicated in the report.

The test procedure is as follows:

- Selection and description of the device under test (DUT);
- Description of the site where the test is performed, location of the DUT in the power plant, and location of the sensors (if more than one location is used);
- Calibration and installation of the data acquisition system (DAS);
- Measurement of:
  - Time and DNI
  - Global plane of array irradiance (GPOAI) for systems with a concentration ratio of <10×;
  - At least two of these three parameters: gross power/energy, parasitic power/energy, and net power/energy;
  - Ambient temperature;
  - Wind speed;
  - Coolant temperature (only for active cooling systems);
  - Voltage, current, and module/receiver temperature (optional); and
- Documentation of the operation-and-maintenance program, as well as unscheduled maintenance events, rainfall events, etc., and registration of the data in the log book.

At the end of the measurements, the DAS should be rechecked for possible deviations. The data collected should be inspected to identify incorrect data. After inspection and filtering of the data, the following parameters are calculated and included in the report:

- DNI energy;
- Gross active energy (AC and DC);
- Net active energy (AC and DC);
- Parasitic active energy (AC and DC);
- Reference yield (Y_r);
- Final AC yield ($Y_{f,AC}$) and/or final DC yield ($Y_{f,DC}$);
- Performance ratio (AC and DC); and
- Uncertainty values.

DC = direct current; AC = alternating current.

4.2.2 IEC62670-3 Concentrator Photovoltaic (CPV) Performance Testing—Part 3: Performance Measurements and Power Rating

This standard is under development, and the CDV has been not submitted yet. The purpose of the standard is to stablish a unique procedure for the calculation of the power rating of a CPV module or assembly under the conditions detailed in IEC62670-1:2013. It will cover the indoor and outdoor procedures for obtaining the power rating of the sample under test at the two standard conditions detailed in IEC62670-1. There will be also a procedure to translate the power rating of the sample from one condition to the other. The requirements for all of the instruments used to perform the measurement (indoor or outdoor) will also be included in the standard.

4.2.3 IEC62108 Concentrator Photovoltaic (CPV) Modules and Assemblies—Design Qualification and Type Approval (Ed. 2)

After application of the standard for a few years, the second edition was issued to improve some tests and modify procedures or severities. The main changes in this second edition at the moment are described later in the text:

- A new procedure for the thermal cycling test for receivers using active cooling systems. The current injection profile for this test is also changed.
- The UV conditioning test is omitted, but UV radiation is recorded during the outdoor exposure test.
- The procedure for the bypass diode thermal test is changed with the inclusion of an alternative procedure for measuring the diode junction temperature. In addition, the number of bypass diodes under test should be at least three.
- The prethermal cycling test for the modules (sequence B) is not performed.
- A dust ingression test is now included in the standard.
- Finally, the retesting guidelines will be included in the standard as an annex.

4.2.4 IEC62787 Concentrator Photovoltaic (CPV) Solar Cells and Cell-on-Carrier (CoC) Assemblies—Reliability Qualification

This standard is under development, and no CDV has been published yet. It specifies the minimum requirements for the qualification of CPV cells and cell-on-carrier (CoC) designs for their incorporation into CPV receivers, modules, and systems.

The test is designed to show that cell or CoC components are suitable for typical assembly processes, and that when they are properly assembled, are capable of passing IEC62108. The standard tries to determine the electrical, thermal, and processing characteristics of the CPV Cells and CPV CoC packages to show that they are capable of withstanding assembly processes and CPV application

environments. The test sequence (under development) specifies the tests performed for cell and CoC packages. Some of these tests are performed on both kinds of samples.

4.2.5 TS/IEC62789 Technical Specification of Concentrator Cell Description

This technical specification provides guidelines for the parameters to be specified for concentrator solar cells (of any technology) and provides recommendations and references for measurement techniques. No attempt is made to determine pass/fail criteria for concentrator solar cells.

4.2.6 IEC62925 Thermal Cycling Test for CPV Modules to Differentiate Increased Thermal Fatigue Durability (Ed. 1)

This standard, actually give a comparative analysis associated with thermal fatigue failure of the HCPV die-attach of the receivers. It is mainly based on the thermal cycling test, applied in sequence A, of the IEC62108:2007. This test provides more thermal stress than the IEC62108 one by increasing the number of cycles of the test. The final result will be a rating number depending on the total number of cycles completed.

4.2.7 New Proposal for CPV Solar Simulators

For indoor testing of CPV samples, the standard defines the requirements for solar simulator specific for CPVs and therefore collimated solar simulators. In addition, there are more requirements than those listed on the IEC60904-9 Photovoltaic Devices—Part 9: Solar Simulator Performance Requirements [12], but the most important modifications are focused on the following:

- Use of AM1.5D as the reference spectrum;
- Definitions and measurement method for collimation angle; and
- Special procedures to deal with multijunction cells

Collimated beam solar simulators will be classified based on the existing criteria of spectral distribution match, irradiance nonuniformity on the test plane, and temporal instability from IEC60904-9. The value of the collimation angle will be used as an additional criterion for classification.

The purpose of this standard is to provide standardized definitions, specifications, measurement methods, and classifications for collimated beam solar simulators. This standard will help the design and development of CPV solar simulators and also can be used by CPV industry on the procurement specification, acceptance test, calibration, and operation of such simulators.

4.2.8 New Proposal Technical Specification for Primary Optics for Concentrator Photovoltaic Systems

This technical specification will cover key characteristics of primary optical elements (lenses and mirrors) for CPV units. It will include optical performance, mechanical geometry, mechanical strength, materials, and surface morphology. The specification will identify the essential characteristics and the corresponding parameters of interest, thus providing a method for the measurement of each parameter.

This will allow to all interested parties (optics and CPV manufacturers, laboratories, etc.) to define lens/mirror qualities and inspect lenses and mirrors. As in the technical specification for solar trackers and cells, there will not be pass/fail criteria.

5 Summary

In this chapter, the most important standards issued for CPV technology as well as the ones under development have been reviewed. As a relatively new PV technology, only four standards have been released—IEC62108:2007, UL8703:2011, IEC62670-1:2014, and IEC62817:2014—while the others are still under development. The great variety of CPV concepts makes it difficult to deploy procedures and standards to cover all of the possible models and designs. In a general way, the CPV product is formed by receivers, modules, and assemblies. The receiver is the element (typically cell plus secondary optics if it exists) that receives concentrated light. The module is the group of cells or receivers, optics, and other components that receive unconcentrated Sunlight, and its focus point is not field adjustable. The assembly is the combination of cells, receivers, and components, which are usually shipped separately and require to be field adjusted.

Most of the differential points with respect to flat-plate standards come from the fact that some CPV systems are moving from small modules (maximum power in the range of 30 W) to larger ones (with a maximum power in the range of 25 kW). These circumstances imply that the equipment for testing must be versatile to cover all of the possible values (both physical and electrical) and that the tests and severities proposed must consider a larger variety of materials and components.

In most cases, in the first steps of the testing proposal, the manufacturer and laboratory staff meet to identify a representative sample that should be used for some of the tests instead of the full CPV component. This is accepted due to the sizes and physical characteristics of some of the CPV products. Outdoor tests always require a full CPV module.

Regarding the aging tests included in IEC62108 (the first one to be issued and the most exercised one), the humidity–freeze test and the damp-heat test (sequences B and C) are the most critical of the whole sequence due to the condensation problems that might arise as a result of variations of the module temperature. The maximum temperatures of testing on both tests, among the various severities

defined in the standard, must be agreed upon between the laboratory and the designer. It is the same for the thermal-cycling test for CPV modules and receivers. In addition, in the case of receivers, a new procedure for the thermal cycling is under development due to the difficulty of fulfilling all of the requirements of the test as it is currently written. This usually happens when working with new technologies and laboratories feedback their experiences to standard development committees and work to improve all tests included in the standards.

Regarding the standards still under development, an important one is IEC62670-3, which is about performance measurements and power rating. This procedure will be used for the rating of modules and for checking the electrical parameters of the modules during the installation or for checking the warranties. Again, due to the great variety of the CPV systems, the standardization of these kind of measurements is complicated because it is necessary to define two set of testing conditions as: (1) STC at 1000 W/m^2 AM1.5D and 25 °C cell temperature as in the case of flat-plate technology; and (2) SOC at 900 W/m^2 AM1.5D, 20 °C ambient temperature, and wind speed of 2 m/s in the case of CPV technology.

Based on its previous experience on testing flat-plate modules (IEC-61215 and IEC-61730), National Renewable Energy Centre (CENER) has been testing CPV modules since 2007 and has been formally accredited since 2009 for testing under IEC62108 (first issue was in December 2007). CENER also tests CPV modules with respect to draft safety proposals for CPV products (IEC-62688 with a forecasted publication date of 2016). CENER also participates on the WG7 of IEC TC82 of IEC. This Working Group, which is dedicated to development of standards for CPV technology, is where laboratories and manufacturers come together to establish the optimum testing conditions and severities to apply.

References

1. The IEEE1513-2001—recommended practice for qualification of concentrator photovoltaic (PV) receiver sections and modules. ISBN 9780738128337
2. IEC62108:2007 Concentrator photovoltaic (CPV) modules and assemblies—design qualification and type approval. ISBN 2-8318-9430-1
3. Petrina I, Cueli AB, Díaz J, Moracho J, Ariztimuño X, Lagunas AR (2009) Challenges for IEC62108 testing. Paper presented at the photovoltaic specialists conference (PVSC), 34th IEEE, Philadelphia, 7–12 June 2009
4. IEC62670-1:2013 Photovoltaic concentrators (CPV)—performance testing—part 1: standard conditions. ISBN 978-2-8322-1120-5
5. IEC 62817:2014 Photovoltaic systems—design qualification of solar trackers. ISBN 978-2-8322-1826-6
6. UL8703:2011 Concentrator photovoltaic modules and assemblies. Underwriters Laboratories, 2011
7. IEC61215:2005 Crystalline silicon terrestrial PV modules—design qualification and type approval. ISBN 2-8318-7963-9
8. IEC62688 Concentrator photovoltaic (CPV) Module and assembly safety qualification draft N. 2014

9. UL1703:2002 Standard for flat-plate photovoltaic modules and panels. ISBN 0-7629-0760-6
10. IEC61730:2004 Photovoltaic (PV) module safety qualification. ISBN 2-8318-7682-6
11. Robusto PF, Rai S (2013) CPV standards: update of the current testing standards and future developments. SOLAR 2013 conference, Baltimore, Maryland, 16–20 Apr 2013
12. IEC60904-9:2007 Photovoltaic devices—part 9: solar simulator performance requirements. ISBN 2-8318-9347-X

Applications of ANNs in the Field of the HCPV Technology

Florencia Almonacid, Adel Mellit and Soteris A. Kalogirou

Abstract High-concentrator photovoltaic (HCPV) devices are based on the use of multijunctions solar cells and optical devices. Therefore, the electrical modelling of an HCPV device presents a great level of complexity. Several artificial neural network (ANN)—based models have been developed to try to address this issue. In this chapter, a review of the developed ANN—based models developed to try to address some issues related with the field of high concentrator PV technology is reported. In addition, the results obtained from the application of some of these models to estimate the electrical parameters of an HCPV module—such as maximum power, short-circuit current, and open-circuit voltage—are presented. The results show that the ANNs are a useful tool for modelling HCPV applications.

1 Introduction

High-concentrator photovoltaic (HCPV) technology is based on the use of optical devices that focus the light received from the Sun on the solar cell surface. The aim of these systems is to decrease the cost of the electricity by decreasing the semiconductor material by mounting less expensive optical devices [1]. HCPV technology is widely based on the use of high efficiency multijunction (MJ) solar cells; a primary optical element (usually a Fresnel lens), which concentrates the light; and a secondary optical element, which receives the light from the primary one to

F. Almonacid (✉)
IDEA Research Group, University of Jaén, Campus Lagunillas, 23071 Jaén, Spain
e-mail: facruz@ujaen.es

A. Mellit
Faculty of Sciences and Technology, Renewable Energy Laboratory, Jijel University, 18000 Jijel, Algeria

S.A. Kalogirou
Department of Mechanical Engineering and Materials Sciences and Engineering, Cyprus University of Technology, P.O. Box 50329, 3603 Limassol, Cyprus

P. Pérez-Higueras and E.F. Fernández (eds.), *High Concentrator Photovoltaics*, Green Energy and Technology, DOI 10.1007/978-3-319-15039-0_12

homogenize light and improve the angular acceptance angle [2]. An HCPV module is made up of MJ solar cells, an optical system for each cell, and the rest of the components required to generate electricity and dissipate the heat produced on the solar cell surface. MJ solar cells and HCPV modules have already reached high efficiencies, which are expected to continue growing in the next few years [3–5]. Thus, HCPV could play an important role in the energy generation market in the coming years [6]. However, due to the use of MJ solar cells and optical elements, the electrical modelling of HCPV devices shows a significant level of complexity than for conventional photovoltaic (PV) technology.

Artificial neural networks (ANNs) have proven to be helpful in solving complex problems and studying nonlinear systems. In the field of PVs, ANNs have been successfully applied to solve different issues [7–9]. For instance, ANNs have been used to:

- estimate and predict solar radiation data [10–14],
- estimate the maximum power (P_m) and normal operating power of a flat PV module [15, 16],
- size, model, and simulate both stand-alone PV systems [17, 18] and PV systems with a maximum power-point tracking controller [19, 20],
- predict the equivalent circuits parameters of a flat PV module [21],
- select a suitable model for characterising PV devices [22],
- obtain the current–voltage (I–V) curves of different flat-plane panels [23, 24],
- or to estimate the energy production of grid-connected PV systems [25, 26].

Due to the advantages of the ANNs to solve complex and nonlinear problems related with the field of PVs and the great level of complexity of electrical modelling of HCPV devices, in the recent years several authors have applied different ANNs to solve various problems related with this new technology. In this chapter, a review of the ANNs developed to address various issues related with the HCPV is presented, and examples of the application of ANNs in this field are given. In particular, the results obtained in the application of some of these ANNs to estimate the main electrical parameters of an HCPV module—including P_m, short-circuit current (I_{sc}), and open-circuit voltage (V_{oc})—are presented.

2 Application of ANNs to Estimate of Direct Solar Irradiation

Due to the use of lenses that concentrate light on the solar cell, the HCPV devices operate only with direct normal irradiance (DNI). So the DNI is especially important for the characterization, management, and operation of HCPV modules, systems, and power plants. DNI is affected by phenomena that are difficult to forecast such as cirrus clouds, wildfires, dust storms, and episodic air pollution events, which can decrease DNI by ≤30 % on otherwise cloud-free days [27].

Because of this, the modelling and prediction of the DNI is a difficult task, and several authors have used ANN-based models to address this issue. A complete review about the solar data forecast by using artificial intelligence methods including DNI and neural network can be found in [28].

A Bayesian neural network was developed to model direct solar irradiance by Lopez et al. [29]. A relevance-determination method was also employed to obtain the relative relevance of a large set of meteorological and radiometric variables. Results show that the more relevant parameters are the clearness index (K_t) and air mass (AM).

In [30], the authors developed an ANN model to estimate beam solar radiation. A new parameter known as the "reference clearness index" was introduced, which is defined as the ratio of the measured beam solar radiation at normal incidence to the beam solar radiation as computed by Hottel's clear-day model. Results show that root mean square error (RMSE) in the ANN model varies 1.65–2.79 % for Indian regions.

Mishra et al. [31] developed a self-consistent model for the estimation of direct solar radiation in the Indian zone. An ANN-based model was used for the estimation of the K_t. The model predictions for the Indian region were found to be in good agreement with the measurements.

An adaptive model for predicting hourly global, diffuse, and direct solar irradiance was developed in [32]. A comparison between a Feed-Forward Neural Network (FFNN) and the proposed adaptive model was also presented. It was shown that the FFNN was able to predict the DNI with acceptable accuracy at Jeddah, King of Saudi Arabia (KSA). They observed that ANN performed better than the designed adaptive alpha-model with a correlation coefficient of 98 %.

In [33], the author developed an ANN model for estimating of monthly average daily direct solar radiation. According to the author, a correlation coefficient of 0.998 was obtained with mean bias error (MBE) of 0.005 MJ/m^2 and an RSME of 0.197 MJ/m^2.

In [34], the authors developed forecasting models for hourly solar irradiation using ANNs for lead times of ≤6 days. Model inputs included current and forecasted meteorological data obtained from the United States National Weather Service's forecasting database and solar geotemporal variables. The gamma test was combined with a genetic algorithm to select the more relevant inputs. According to the authors, the estimation of DNI is much more difficult to predict reliably; the RMSE values obtained on same-day forecasts are in the range of 28–35 %.

Several ANNs were developed by Rodrigo et al. [35] for the generation of DNI hourly time series for some Spanish locations. In particular, different architectures of multiple linear perceptron (MLP) neural networks were used with three different configurations. The designed model could be used for the estimation of the energy that will be produced by concentrating PV systems, to perform economic analysis, and to supervise plant operation. The developed models were tested in different locations. The RMSE among real data and synthetic data for the three configurations and for the different locations considered are in the range 0.01–0.27. Results show that the ANNs yield better results for locations in the south of Spain.

Rehman and Mohandes [36] used a radial basis function (RBF) network for modelling the diffuse and direct normal solar radiation for sites in KSA based on

Table 1 Summary of the applications of ANNs for predicting the DNI

#	Authors	Ref.	Year	ANN
1	Mellit	[28]	2008	Feed-forward neural network, radial basis function neural network, and neural networks
2	Lopez et al.	[29]	2005	Bayesian neural network with Automatic Relevance Determination (ARD)
3	Alam et al.	[30]	2006	Feed-forward back-propagation neural network
4	Mishra et al.	[31]	2008	Feed-forward back-propagation neural network
5	Mellit et al.	[32]	2010	Feed-forward back-propagation neural network
6	Mubiru	[33]	2011	Feed-forward back-propagation neural network
7	Marquez and Coimbra	[34]	2011	Feed-forward back-propagation neural network
8	Rodrigo et al.	[35]	2012	Feed-forward back-propagation neural network
9	Rehman and Mohandes	[36]	2012	Radial basis function neural networks
10	Marpu et al.	[37]	2013	Feed-forward back-propagation neural network
11	Chu et al.	[38]	2013	Feed-forward neural network with genetic algorithm

input data such as day number, global solar radiation, ambient temperature, and relative humidity. The results indicate that the RBF (with 50 hidden neurons and 0.1 spread constant) predicts direct normal solar radiation with mean absolute percentage error of 0.016 and 0.41 for diffuse solar radiation.

A regionally based ANN model to retrieve the DNI at the surface of the United Arab Emirates (UAE) was developed by Marpu et al. [37]. The results are promising when estimating the solar irradiance at a 15-minute temporal resolution and a 3-km spatial resolution. The inputs of the designed model were six SEVIRI (on-board Meteosat Second Generation satellite) thermal channels along with several time- and season-dependent parameters, namely the solar zenith angle, solar time, day number, and eccentricity correction.

Recently, Chu et al. [38] designed a novel smart forecasting model for intra-hour DNI. The authors combined sky image processing with ANN optimization schemes. The hybrid forecast models achieved statistically robust forecasting skills in excess of 20 % over persistence both for forecasts 5 and 10 min ahead, respectively. Table 1 lists the applications of ANNs for modelling and prediction of DNI and lists the type of ANN employed in each case.

3 Application of ANNs for the Electrical Modelling of HCPV Devices

As in any kind of energy system, modelling the electrical output of a PV device is crucial for the system design and energy prediction. However, the electrical modelling of HCPV modules and systems shows a significantly greater level of

complexity than conventional PV technology. Due to the use of MJ solar cells and optical devices, HCPV modules and systems show a strong spectral dependence. To quantify the spectral changes and to evaluate how these affect the behaviour of an HCPV device is not a trivial issue [39, 40]. In addition, as in conventional PV technology, the cell temperature (T_c) is an important input in models used for the electrical characterization of HCPV devices because the temperature at which cells are working in an HCPV module affects its performance. However, one of the problems in HCPV technology is that the direct measurement of this temperature is a complex task because it requires access inside the module [41].

Because of this difficulty, in recent years the scientific community has devoted efforts in developing ANN-based models which try to solve some of these issues.

3.1 Application of ANNs to Modelling Multi-junction Solar Cells

The PV solar cells used in HCPV technology are made of several p-n junctions (usually three junctions) of III–V semiconductor materials of the periodic table. Each p-n junction has a different band gap and is interconnected in series with the others to optimize the absorption of the solar spectrum and increase the efficiency of the solar cell electricity conversion [42]. Thus, although single-junction (SJ) solar cells are mainly influenced by changes in irradiance and temperature, MJ solar cells show complex behaviour because their performance is also strongly influenced by changes in solar spectrum. Due to this, Patra et al. [43–46] proposed approaches based on ANN to characterize these devices.

In [43] and [44], an ANN based-model was proposed to characterize dual-junction (DJ) GaInP/GaAs solar cells. The authors used four multilayer perceptrons: one for estimating the tunnelling effects of a solar cell and the other three for estimating the external quantum efficiency (EQE) and the I–V characteristic, both under 1 sun and in dark, for the DJ solar cell. The inputs for ANNs are the voltage for estimating the tunnelling effects and the I–V characteristic as well as the irradiation wavelength (λ) for estimating the EQE. The results were compared with experimental and simulated data through Silvaco ATLAS software [47]. The results showed that compared with the results obtained through ATLAS, the MLP-based model was able to predict DJ solar cell parameters more closely to that of experimental ones.

In [45], a novel Chebyshev neural network-based model for a DJ GaInP/GaAs solar cell was developed to predict the EQE and the I–V characteristics, both at one sun and dark levels. The inputs of the model are the same as those in the previous case.

In [46], an ANN-based model was used to estimate the EQE and the performance of triple-junction InGaP/GaAs/Ge solar cells under the influence of a wide range of charged particles. The inputs of the models are the wavelength (λ), the proton energy (η), and the fluence (f). The results show that the ANN-based models

perform quite well in the estimation of EQE of the solar cell under the influence of proton energy ranging from 30 keV to 10 MeV with fluence levels ranging from 10^{10} to 10^{14} ion/cm^2.

3.2 Application of ANNs to Modelling HCPV Modules

3.2.1 Application of ANNs to Estimate the Maximum Power of a HCPV Module

Due to the use of MJ solar cells and lenses, HCPV modules are mainly influenced by changes in irradiance, spectrum, temperature, and wind speed (W_s). Taking this into account, the output of HCPV modules could be expressed as a function of these parameters:

$$P_m = f(B, S, T, W_s) \tag{1}$$

The relation between these parameters and the output of an HCPV module is complex and nonlinear, so the use of ANN-based models has been proposed by several authors to try to find this relation.

Almonacid et al. [48] developed an ANN-based model, in particular an MLP, to find the relation between the output of an HCPV and the main parameters that affected its performance. The input parameters used by the model are as follows:

- the DNI to evaluate how the changes in the irradiance affect the performance of an HCPV module
- AM and precipitable water (PW) to evaluate the spectrum because these are, together with clouds and aerosol optical depth (AOD), the parameters with the largest impact on spectral changes [49, 50] and are also easy to obtain from the data provided by a meteorological station [51–54]
- air temperature (T_{air}) to evaluate the temperature of the HCPV module; and
- the wind speed (W_s).

Coefficients of neural networks are obtained from outdoor monitored data. The results show that the ANN based-model could be used to estimate successfully the output of an HCPV module with a MBE of 0.07 %, an RMSE of 2.91 %, and an R^2 of 0.99.

This approach has also been followed by Rivera et al. [55]. In this case, a cooperative competitive hybrid algorithm for RBF networks was implemented. This model uses as input the average photon energy [56, 57] to quantify the spectral influences on the P_m of an HCPV module. This is a single value in eV that characterizes the shape of the spectrum. A spectroradiometer is required for obtaining this input. The rest of the inputs of the model are DNI to evaluate how the changes in the irradiance affect the performance of an HCPV module, T_{air} to evaluate the temperature, and W_s. The coefficients of the neural network are obtained from outdoor monitored data. The model obtained gives an error of approximately 3.3 %.

3.3 Application of ANNs to Estimate the Electrical Characteristics of an HCPV Module

As already indicated, the output of an HCPV module is significantly affected by changes in irradiance, spectrum, and temperature. A different approach for electrical modelling of these devices is based on the premise that the electrical parameters of an HCPV module can be estimated by applying models and equations used for conventional PV technology from the DNI, corrected spectrally, and the T_c [58, 59]. According to this approach, two ANNs for estimating these parameters have been proposed in [41, 60].

Application of ANNs to estimate the spectrally corrected direct normal irradiance

The spectrally corrected DNI (DNI_c) is defined as the portion of the incident spectrum that an HCPV module is able to convert into electricity expressed here as:

$$DNI_c = \frac{\min\left(\int E_b(\lambda)\eta(\lambda)SR_i(\lambda)d\lambda\right)}{\min\left(\int E_{b,ref}(\lambda)\eta(\lambda)SR_i(\lambda)d\lambda\right)} \int E_{b,ref}(\lambda)d\lambda \quad (2)$$

where the index i represents the junction considered, λ is the wavelength, $SR_i(\lambda)$ is the spectral response of the i-junction, $E_b(\lambda)$ is the spectral distribution of the DNI, and $\eta(\lambda)$ is the optical efficiency of the HCPV module.

The advantage of this approach is that the spectral effects of an HCPV device are quantified by adjusting only the incident DNI [58].

Taking this into account, an ANN-based model for DNI_c was presented in [60]. The inputs of the model are the main meteorological parameters that influence the spectral distribution of the DNI and the performance of an HCPV module: AM, AOD, and PW. Results show that the method is able to predict spectrally corrected normal irradiance with an RMSE of 2.92 %, an MBE of −0.12 %, and a R^2 of 0.98.

Application of ANNs to estimate the cell temperature of a HCPV module

The operating temperature of the solar cell is a crucial issue to characterize the electrical behaviour of a PV device. However, the measurement of this temperature in an HCPV module is a complex task due to its special features that do not allow one to access the cell. To solve this problem, several authors have attempted different approaches [41, 61]. One of these is based on the premise that the T_c can be obtained from the main meteorological parameters that have an influence in this temperature: DNI, T_{air}, and W_s. Using a linear expression [62]:

$$T_c = T_{air} + a\text{DNI} + bW_s \quad (3)$$

where a and b are empirical parameters obtained from outdoor monitored data.

Table 2 Summary of applications of artificial neural networks for modelling HCPV devices

No.	Authors	Ref.	Year	ANNs
ANN for modelling MJ solar cells				
1	Patra and Maskell, Patra	[43, 44]	2010 2011	Feed-forward back-propagation neural network
2	Patra	[45]	2011	Chebyshev neural network
3	Patra and Maskell	[46]	2012	Feed-forward back-propagation neural network
ANNs for modelling HCPV modules				
4	Almonacid et al.	[48]	2014	Feed-forward back-propagation neural network
5	Rivera et al.	[55]	2013	Radial basis function network with a cooperative-competitive hybrid algorithm
6	Fernández et al.	[41]	2014	Feed-forward back-propagation neural network
7	Fernández and Almonacid	[60]	2014	Feed-forward back-propagation neural network

According to this approach, an ANN-based model was presented in [41]. This model attempts to characterise the relationship between the T_c and the main meteorological parameters that affect it. The input parameters are DNI, T_{air}, and W_s. Results show that the ANN-based model significantly improves the results of the method based on a linear expression with an R^2 of 0.95, a relative RMSE of 4.80 %, and an absolute RMSE of 3.24 °C. Table 2 lists the applications of ANNs for modelling HCPV devices and also indicates the type of ANN employed in each case.

4 Examples of Applications

In this section, some examples of the applications of the ANNs for the characterization of HCPV modules are presented. The first example concerns the P_m of an HCPV estimated using the ANN developed by Almonacid et al. in [48]. In the second part, the V_{oc} and the I_{sc} of an HCPV module will be calculated from the DNI_c and the T_c according to the approach presented in [58, 59]. The ANNs developed in [41, 60] have been used to estimate the spectrally corrected normal irradiance and the T_c for an HCPV module.

4.1 Experimental Campaign

To conduct this study, an HCPV module was measured for 6 months in the Centro de Estudios Avanzados en Energía y Medio Ambiente at the University of Jaén. The module is made up of 20 lattice-matched MJ solar cells connected in series (N_s)

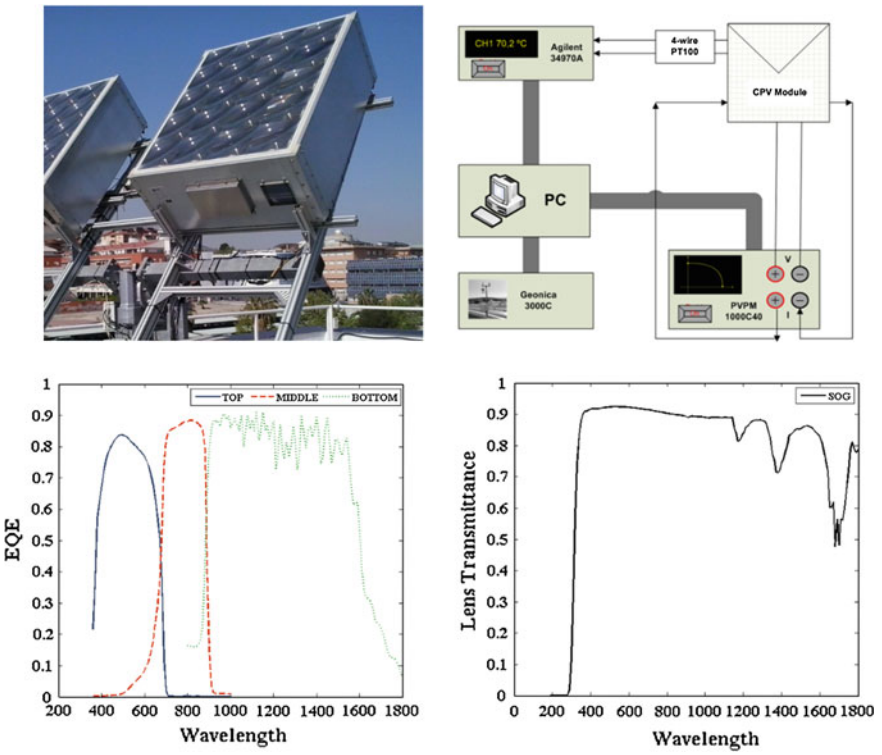

Fig. 1 *Top left* Photograph of the HCPV module considered in the study. *Top right* Scheme of the experimental set-up to measure the electrical parameters of the HCPV module and the main parameters necessary to train the ANN. *Bottom left* EQE of the MJ solar cells of the HCPV module. *Bottom right* Transmittance of the Fresnel lenses used in the HCPV module considered

with a silicon-on-glass Fresnel lens on each cell (Fig. 1, top left). Figure 1 shows the EQE of the MJ solar cells and the transmittance of the lens of the HCPV module used in this study. Table 3 shows the main electrical parameter of the HCPV module.

The experimental set-up (Fig. 1, top right) used to measure the electrical characteristic of the HCPV module and the main parameters necessary to train the ANNs for estimating P_m, DNI_c and the T_c, is made up of the following:

Table 3 Electrical characteristics of the module under study measured at outdoor reference conditions: DNI = 900 W/m^2, T_{air} = 20 °C, and AM = 1.5, for wind speed lower than 1 m/s

Electrical parameters of the HCPV module	
Maximum power (P_m)	232 W
Open circuit voltage (V_{oc})	57.6 V
Short circuit current (I_{sc})	5.3 A

Table 4 Maximum, minimum, and average values of the parameters used as inputs of the ANNs for estimating P_m, DNI_c, and T_c

Parameter	Maximum	Minimum	Average
DNI (W/m^2)	978.42	235.27	763.00
T_{air} (°C)	40.36	3.74	26.12
W_s (m/s)	9.76	0.00	1.34
AM	9.05	1.02	1.92
AOD	0.55	0.04	0.19
PW (cm)	3.29	0.39	1.71

- a high-accuracy two-axis solar tracker to keep the HCPV module always pointing toward the solar rays so lenses are able to focus the radiation on the small solar cell area;
- a four-wire electronic load to measure the electrical parameters of the module;
- a four-wire PT100 placed close to the solar cell to measure the T_c; and
- a meteorological station placed at the roof of the centre to record the main atmospheric parameters such as DNI, T_{air}, W_s, or humidity.
- the values of AOD and PW, which were not provided by the meteorological station, were obtained from MODIS Daily Level-3 data source [63].

Table 4 shows the maximum, minimum, and average values of the parameters used as inputs of the different ANNs used in the study.

4.2 Estimation of the Maximum Power of a HCPV Module

The ANN developed in [48] has been applied to estimate the P_m of the HCPV module. The inputs of the ANN-based model are DNI, AM, PW, T_{air}, and W_s. The structure of the ANN consists of tree layers: the input layer, which has five nodes; the hidden layer, which has seven nodes; and the output layer, which has one node that corresponds to the P_m of the HCPV module. This architecture was trained with the Levenberg–Marquardt back-propagation algorithm to determine the coefficients of the ANN. To train and test the ANN, a set of outdoor measurements, including the output of the HCPV module and the meteorological parameters, were used for a wide range of operating conditions (Table 4). Table 5 shows the coefficient of multiple determination (R^2), the RMSE, the mean absolute error (MAE), and the MBE between actual data and data predicted by the ANN-based model.

Figure 2 shows an example in the estimation of the P_m of the HCPV module using the ANN based-model for two different days (summer and winter days).

Table 5 Values of the parameters R^2, RMSE, MAE, and MBE between actual data and predicted data by the ANN-based model for estimating the maximum power of the HCPV module considered

R^2	RMSE (%)	MAE (W)	MBE (%)
0.98	2.78	4.09	−0.01

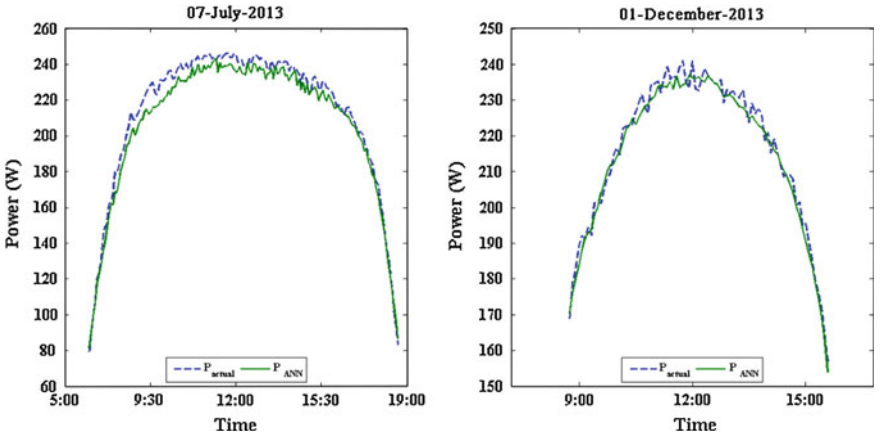

Fig. 2 *Left* Actual maximum power of the HCPV module considered versus predicted maximum power by the ANN-based model for a summer day (07 July 2013). *Right* Actual maximum power of the HCPV module considered versus predicted maximum power by the ANN-based model for a winter day (01 December 2013)

Table 6 Maximum, minimum, and average values of the parameters used as inputs for the two examples days (summer and winter day)

	Summer day (07/07/2013)			Winter day (01/12/2013)		
Parameter	Maximum	Minimum	Average	Maximum	Minimum	Average
DNI (W/m^2)	924.87	378.46	797.77	931.97	674.10	863.94
T_{air} (°C)	36.8	27.8	33.24	13.12	4.72	9.44
W_s (m/s)	6.70	0.25	3.93	3.91	0	1.25
AM	6.42	1.00	1.82	4.30	1.87	2.42
AOD	0.15	0.15	0.15	0.09	0.09	0.09
PW (cm)	1.82	1.82	1.82	0.78	0.78	0.78

Table 6 shows the maximum, minimum, and average values of the parameters used as input of the ANN for the two example days.

4.3 Estimation of the Electrical Parameters of a HCPV Module

According to the approach that the electrical performance of an HCPV device can be quantified from the DNI_c and T_c [58, 59], the V_{oc}, and the I_{sc} of the HCPV module considered can be estimated from equations used in conventional PVs:

$$I_{sc} = \frac{I_{sc}^*}{G^*} G\left(1 + \gamma\left(T_c^* - T_c\right)\right) \tag{4}$$

$$V_{oc} = V_{oc}^*\left(1 + \beta\left(T_c^* - T_c\right)\right) + N_s \frac{mkT_c}{q} \ln\left(\frac{G}{G^*}\right) \tag{5}$$

where I_{sc}^*, G^*, T_c^*, and V_{oc}^* are the I_{sc}, solar global irradiance, T_c, and V_{oc} at reference conditions; γ and β are the T_c coefficient of the I_{sc} and the V_{oc}, respectively; m is the effective ideality factor of the cell; k is the Boltzmann constant; and q is the electron charge.

Equations (4) and (5) must be adapted to HCPV as follows:

$$I_{sc} = \frac{I_{sc}^*}{\mathrm{DNI}^*} \mathrm{DNI}_c\left(1 + \gamma\left(T_c^* - T_c\right)\right) \tag{6}$$

$$V_{oc} = V_{oc}^*\left(1 + \beta\left(T_c^* - T_c\right)\right) + N_s \frac{mkT_c}{q} \ln\left(\frac{\mathrm{DNI}_c}{\mathrm{DNI}^*}\right) \tag{7}$$

where DNI^* is the DNI at reference conditions and DNI_c is the spectrally corrected DNI. The various parameters for the module considered are $m = 3$, $\gamma = 0.002\ ^\circ\mathrm{C}^{-1}$ and $\beta = 0.0015\ ^\circ\mathrm{C}^{-1}$ for the HCPV.

4.4 Estimation of the Spectrally Corrected Direct Normal Irradiance

To estimate the DNI_c of the HCPV module considered, the ANN developed in [60] was applied. The inputs of the ANN are AM, AOD, and PW, and the ANN has five nodes in the hidden layer and one node in the output layer corresponding to the spectral correction function. This architecture was trained with the Levenberg–Marquardt back-propagation algorithm to determine the coefficients of the ANN. To train and test the ANN, a set of outdoor measurements were used for a wide range of operating conditions listed in Table 4. Table 7 lists the R^2, the RMSE, the MAE, and the MBE—all of which are considered very adequate—between actual and predicted data using the ANN-based model.

Figure 3 shows an example of the DNI measured during 2 days (summer and winter) versus the DNI_c predicted by the ANN based-model for the HCPV module.

Table 7 Values of the parameters R^2, RMSE, MAE, and MBE between actual data and predicted data by the ANN-based model for estimating the spectrally corrected direct normal irradiance

R^2	RMSE (%)	MAE (W/m^2)	MBE (%)
0.98	3.19	17.50	−0.16

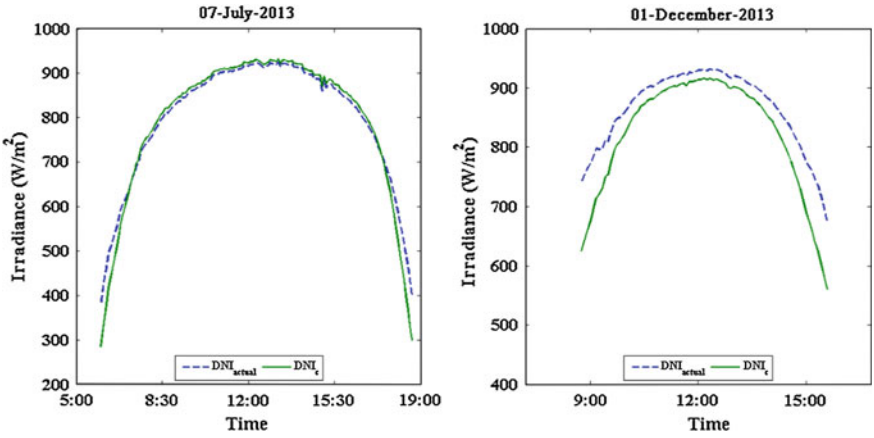

Fig. 3 *Left* Actual direct normal irradiance versus spectrally corrected direct normal irradiance predicted by the ANN-based model for a summer day (07 July 2013). *Right* Actual direct normal irradiance versus spectrally corrected direct normal irradiance predicted by the ANN-based model for a winter day (01 December 2013)

Table 6 shows the maximum, minimum, and average values of the parameters used as input to the ANN for the 2 example days.

As can be seen from Fig. 3, although the maximum level of DNI reached on winter and summer is similar (approximately 900 W/m^2), the DNI$_c$ is lower in winter. This could be mainly explained because the AM values are significantly greater in the winter than in summer, so the portion of the incident spectrum that an HCPV module is able to convert into electricity is lower due to spectral losses. This also can be observed at the sunrise and sunset (both in winter and summer) when the AM values are greater and the DNI$_c$ is lower than DNI.

4.5 Estimation of the Cell Temperature

To estimate the T_c of the HCPV module considered, the ANN developed in [41] has been used. The inputs of the ANN are: T_{air}, DNI and W_s, and the ANN has five nodes in the hidden layer and one node in the output layer corresponding to the T_c of the HCPV module. This architecture was trained with the Levenberg–Marquardt back-propagation algorithm, to determine the coefficients of the ANN. To train and test the ANN, a set of outdoor measurements including the T_c of the HCPV module and the meteorological parameters were used for a wide range of operating conditions, listed in Table 4. Table 8 shows the R^2, RMSE, MAE and the MBE between actual data and predicted data using the ANN-based model.

Table 8 Values of the parameters R^2, RMSE, MAE, and MBE between actual data and predicted data by the ANN-based model for estimating the cell temperature of the HCPV module considered

R^2	RMSE (%)	MAE (°C)	MBE (%)
0.90	5.16	2.51	0.00

Figure 4 shows an example of the T_c of the HCPV module measured during 2 days (summer and winter day) versus the T_c predicted by the ANN based-model. Table 6 shows the maximum, minimum, and averages values of the parameters used as input of ANN for the two example days.

4.5.1 Estimation of the Short-Circuit Current and the Open-Circuit Voltage

Once the values of the DNI_c and T_c are available, it is possible to estimate the I_{sc} and the V_{oc} using Eqs. (6) and (7). Table 9 shows the R^2, RMSE, MAE, and MBE between actual and predicted data using Eqs. (6) and (7).

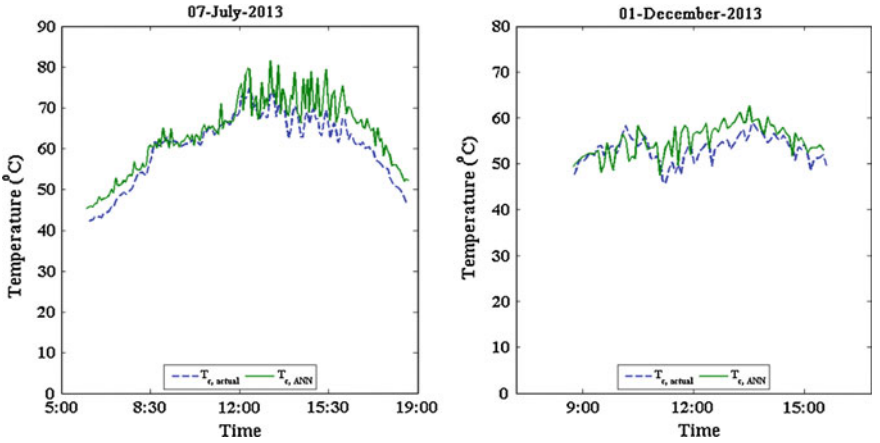

Fig. 4 *Left* Actual cell temperature versus predicted cell temperature by the ANN-based model for a summer day (07 July 2013). *Right* Actual cell temperature versus predicted cell temperature by ANN-based model for a winter day (01 December 2013)

Table 9 Values of the parameters R^2, RMSE, MAE, and MBE between actual and predicted data using Eqs. (6) and (7) for estimating the short-circuit current and the open-circuit voltage of the HCPV module considered

	R^2	RMSE (%)	MAE	MBE (%)
I_{sc}	0.97	3.53	0.12 A	−0.23
V_{oc}	0.90	0.66	0.29 V	0.01

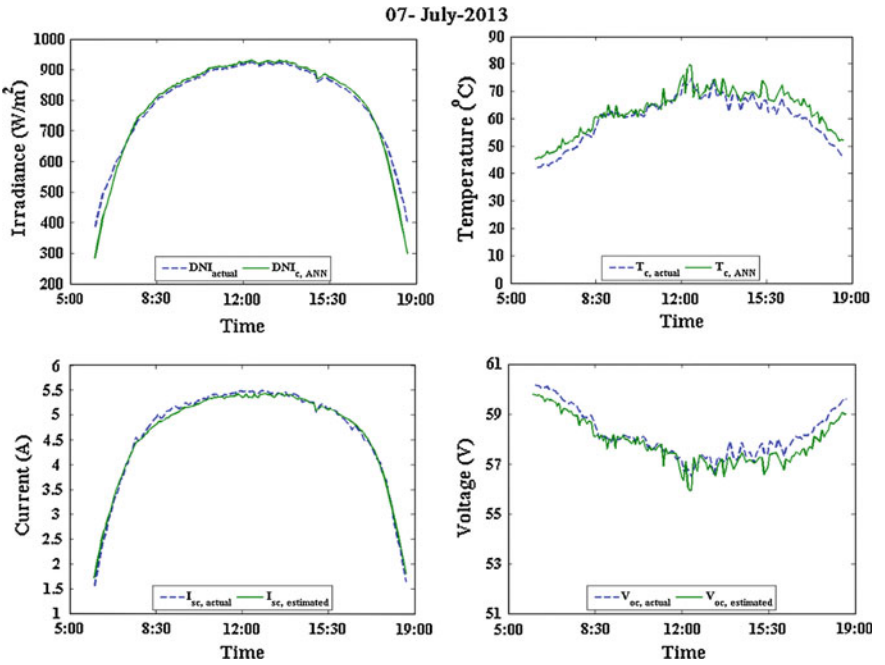

Fig. 5 *Top left* Direct normal irradiance measured during a summer day versus the spectrally corrected direct normal predicted by the ANN presented in [60]. *Top right* cell temperature measured during a summer day versus cell temperature predicted by the ANN presented in [41]. *Bottom left* Actual short-circuit current versus estimated short-circuit current using Eq. (6) for the HCPV module considered during a summer day. *Bottom right* Actual open-circuit voltage versus open-circuit voltage using Eq. (7) for the HCPV module considered during a summer day

Figures 5 and 6 bottom-left show the actual versus the predicted I_{sc} for the HCPV module considered for 2 example day. Figures 5 and 6 bottom-right show the actual versus the predicted V_{oc} for the HCPV module considered for 2 example days.

5 Conclusions

In this chapter, a review of ANN-based models developed for solving some problems related with HCPV technology is presented. In addition, several examples of the application of some of these models for estimating the main electrical parameters of an HCPV module—such as the P_m, the I_{sc}, and the V_{oc}—are presented.

The ANN based-model developed in [48] was applied to estimate the P_m of an HCPV. This model takes into account the main meteorological parameters that affect the output of an HCPV module. The approach presented in [58, 59] was

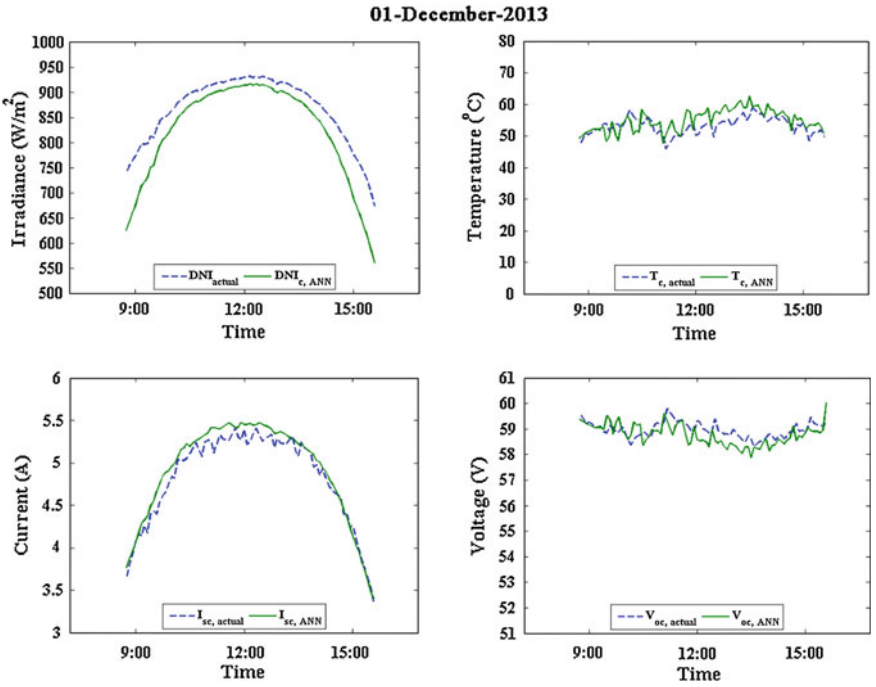

Fig. 6 *Top left* Direct normal irradiance measured during a winter day versus the direct normal predicted by the ANN presented in [60]. *Top right* cell temperature measured during a winter day versus cell temperature predicted by the ANN presented in [41]. *Bottom left* Actual short-circuit current versus estimated short-circuit current using Eq. (6) for the HCPV module considered during a winter day. *Bottom right* Actual open-circuit voltage versus open-circuit voltage using Eq. (7) for the HCPV module considered during a winter day

followed to estimate the I_{sc} and the V_{oc}. In this case, these electrical parameters were estimated from the DNI_c, the T_c, and use of the equations of conventional PVs. The values of the DNI_c and the T_c were obtained by applying the ANNs developed in [25, 60].

From the analysis of results, it can be concluded that ANNs are a useful tool for the electrical characterization of HPCV devices.

References

1. Luque A, Sala G, Luque-Heredia I (2006) Photovoltaic concentration at the onset of its commercial deployment. Prog Photovoltaics Res Appl 14(5):413–428
2. Xie W, Dai Y, Wang R, Sumathy K (2011) Concentrated solar energy applications using Fresnel lenses: a review. Renew Sustain Energy Rev 15(6):2588–2606
3. Pérez-Higueras P, Muñoz E, Almonacid G, Vidal P (2011) High concentrator photovoltaics efficiencies: present status and forecast. Renew Sustain Energy Rev 15(4):1810–1815

4. Dimroth F, Grave M, Beutel P et al (2014) Wafer bonded four-junction GaInP/GaAs/GaInAsP/GaInAs concentrator solar cells with 44.7 % efficiency. Prog Photovoltaics Res Appl 22(3):277–282
5. Ghosal K, Lilly D, Gabriel J, Whitehead M, Seel S, Fisher B, Wilson J, Burroughs S (2014) Semprius field results and progress in system development. IEEE J Photovoltaics 4(2): 703–708
6. Globaldata (2014) Concentrated photovoltaics (CPV)—global market size, competitive landscape and key country analysis to 2020. UK
7. Kalogirou S (2001) Application of artificial neural networks in renewable energy systems applications: a review. Renew Sustain Energy Rev 5:373–401
8. Mellit A, Kalogirou S (2008) Artificial intelligence techniques for photovoltaic applications: a review. Prog Energy Comb Sci 34:574–632
9. Kalogirou S (2000) Application of artificial neural networks for energy systems. Appl Energy 67:17–35
10. Hontoria L, Aguilera J, Riesco J, Zufiria P (2001) Recurrent neural supervised models for generating solar radiation. J Intell Rob Syst 31:201–221
11. Hontoria L, Aguilera J, Zufiria P (2002) Generation of hourly irradiation synthetic series using the neural network multilayer perceptron. Sol Energy 72(5):441–446
12. Al-Alawi S, Al-Hinai H (1998) An ANN-based approach for predicting global radiation in location with no direct measurement instrumentation. Renew Energy 14:199–204
13. Mellit A, Benghanem M, Hadj Arab A, Guessoum A (2005) A simplified model for generating sequences of global radiation data for insolates sites: using neural network and library of Markov transition matrices. Sol Energy 79(5):468–482
14. Mellit A, Benghanem M, Kalogirou S (2006) An adaptative wavelet-network model for forecasting daily total solar. Appl Energy 83:704–722
15. Bahgat A, Helwa N, Ahamd G, El Shenawy E (2004) Estimation of the maximum power and normal operating power of a photovoltaic module by neural networks. Renew Energy 29: 443–457
16. Himaya T, Katabayashi K (1997) Neural network based estimation of maximum power generation from PV module using environmental information. IEEE Trans Energy Convers 12 (3):241–247
17. Mellit A, Benghanem M, Hadj Arab A, Guessoum A (2005) An adaptive artificial neural network model for sizing stand-alone photovoltaic systems: application for isolated sites in Algeria. Renew Energy 30(10):1501–1524
18. Mellit A, Benghanem M, Kalogirou S (2007) Modelling and simulation of standalone photovoltaic system using an adaptative artificial neural network. Renew Energy 32(2): 285–313
19. Veerachary M, Yadaiah N (2000) ANN based peak power tracking for PV supplied motors. Sol Energy 69(4):343–350
20. Bahgat A, Helwa N, Ahamd G, El Shenawy E (2005) Maximum power point tracking controller for PV systems using neural networks. Renew Energy 30:1257–1268
21. Karapete E, Boztepe M, Colak M (2006) Neural network based solar cell model. Energy Convers Manag 47:1159–1178
22. de Blas M, Torres J, Prieto E, García A (2002) Selecting a suitable model for characterizing photovoltaic devices. Renew Energy 25:371–380
23. Almonacid F, Rus C, Hontoria L, Fuentes M, Nofuentes G (2009) Characterisation of Si-crystalline PV modules by artificial neural networks. Renew Energy 34:941–949
24. Almonacid F, Rus C, Hontoria L, Muñoz FJ (2010) Characterisation of PV CIS module by artificial neural networks. A comparative study with other methods. Renew Energy 35: 973–980
25. Almonacid F, Rus C, Pérez-Higueras P, Hontoria L (2011) Calculation of the energy provided by a PV generator. Comparative study: Conventional methods versus artificial neural networks. Energy 36:375–384

26. Almonacid F, Rus C, Pérez-Higueras P, Hontoria L (2009) Estimation of the energy of a PV generator using artificial neural network. Renew Energy 34:2743–2750
27. Coimbra CF, Kleissl J, Marquéz R (2013) Chapter 8: overview of solar-forecasting methods and a metric for accuracy evaluation. In: Solar energy forecasting and resource assessment, Elsevier, pp 172–192
28. Mellit A (2008) Artificial intelligence technique for modelling and forecasting of solar radiation data: a review. Int J Artif Intell Soft Comput 1(1):52–76
29. Lopez G, Batlles F, Tovar-Pescador J (2005) Selection of input parameters to model direct solar irradiance by using artificial neural networks. Energy 30:1675–1684
30. Alam S, Kaushik S, Garg S (2006) Computation of beam solar radiation at normal incidence using artificial neural network. Renew Energy 31:1483–1491
31. Mishra A, Kaushika N, Zhang G, Zhou J (2008) Artificial neural network model for the estimation of direct solar radiation in the Indian zone. Int J Sustain Energ 27(3):95–103
32. Mellit A, Eleuch H, Benghanem M, Elaoun C, Pavan A (2010) An adaptive model for predicting of global, direct and diffuse hourly solar irradiance. Energy Convers Manag 51:771–782
33. Mubiru J (2011) Using artificial neural networks to predict direct solar irradiation. Advan Artif Neural Syst 2011:1–6
34. Marquez R, Coimbra C (2011) Forecasting of global and direct solar irradiance using stochastic learning methods, ground experiments and the NWS database. Sol Energy 85: 746–756
35. Rodrigo J, Hontoria L, Almonacid F, Fernández E, Rodrigo P, Pérez-Higueras PJ (2012) Artificial neural networks for the generation of direct normal solar annual irradiance synthetic series. In: AIP conference proceedings of 8th international conference on concentrating photovoltaic systems: CPV-8, Toledo
36. Rehman S, Mohandes M (2012) Splitting global solar radiation into diffuse and direct normal fractions using artificial neural networks. Energy Sources 34(14):1326–1336
37. Marpu EYP, Gherboudj I, Ghedira H, Taha BO, Chiesa M (2013) Artificial neural network based model for retrieval of the direct normal, diffuse horizontal and global horizontal irradiances using SEVIRI images. Sol Energy 89:1–16
38. Chu Y, Pedro HT, Coimbra CF (2013) Hybrid intra-hour DNI forecasts with sky image processing enhanced by stochastic learning. Sol Energy 98:592–603
39. Fernández EF, Pérez-Higueras P, Garcia Loureiro A, Vidal P (2013) Outdoor evaluation of concentrator photovoltaic systems modules from different manufacturers: first results and steps. Prog Photovoltaics Res Appl 21(4):693–701
40. Fernandez EF, Almonacid F, Ruiz-Arias J, Soria-Moya A (2014) Analysis of the spectral variations on the performance of high concentrator photovoltaic modules operating under different real climate conditions. Sol Energy Mater Sol Cells 127:179–187
41. Fernández EF, Almonacid F, Rodrigo P, Pérez-Higueras P (2014) Calculation of the cell temperature of a high concentrator photovoltaic (HCPV) module: a study and comparison of different methods. Sol Energy Mater Sol Cells 121:144–151
42. Ef Fernández, Siefer G, Almonacid F, García Loureiro AJ, Pérez-Higueras P (2013) A two subcell equivalent solar cell model for III–V triple junction solar cells under spectrum and temperature variations. Sol Energy 92:221–229
43. Patra J, Maskell D (2010) Estimation of dual-junction solar cell characteristic using neural networks. In: 35th IEEE photovoltaic specialists conference, PVSC 2010, Honolulu
44. Patra J (2011) Neural network-based model for dual-junction solar cells. Prog Photovoltaics Res Appl 19:33–44
45. Patra J (2011) Chebyshev neural network-based model for dual-junction solar cells. IEEE Trans Energy Convers 26(1):132–139
46. Patra J, Maskell D (2012) Modeling of multi-junction solar cells for estimation of EQE under influence of charged particles using artificial neural networks. Renew Energy 44:7–16
47. "SILVACO," Available: http://www.silvaco.com/products/tcad/device_simulation/atlas/atlas.html

48. Almonacid F, Fernández EF, Rodrigo P, Pérez-Higueras P, Rus-Casas C (2013) Estimating the maximum power of a high concentrator photovoltaic (HCPV) module using an artificial neural network. Energy 53:165–172
49. Emery K, Del Cueto J, Zaaiman Z (2002) Spectral correction based on optical air mass. In: Proceeding of 29th IEEE PV specialist conference, New Orleans
50. Faine P, Kurtz SR, Riordan C, Olson J (1991) The influence of Spectral solar irradiance variations on the performance of selected single-junction and multijunction solar cells. Sol Cells 31:259–278
51. Kasten F, Young A (1989) Revised optical air mass tables and approximation formula. Appl Opt 28(22):4735–4738
52. Gueymard C (1992) Assesment of the accuracy and computing speed of simplified saturation vapour equations using a new reference dataset. J Appl Meteorol 32:294–300
53. Gueymard C (1994) Analysis of monthly average atmospheric precipitable water and turbidity in Canada and Northern United States. Sol Energy 53(1):57–71
54. Rigolliere C, Bauer O, Wald L (2000) On the clear sky model of the Esra—European Solar Radiation Atlas—with respect to the heliosat method. Sol Energy 68:33–38
55. Rivera A, García-Domingo B, Del Jesus M, Aguilera J (2013) Characterization of concentrating photovoltaic modules by cooperative competitive radial basis function networks. Expert Syst Appl 40(5):1599–1608
56. Williams S, Betts T, Helf T, Gottschalg R, Beyer H, Infield D (2003) Modeling long term module performance based on realistic reporting conditions with consideration to spectral effects. In: Proceedings of the world conference on photovoltaic energy conversion
57. Takashi M, Yasuhito N, Hiroaki T, Hideyuki T (2009) Uniqueness verification of solar spectrum index of average photon energy for evaluating outdoor performance of photovoltaic modules. Sol Energy 83:1294–1299
58. Antón I, Martinez M, Rubio F, Núñez R, Herrero R, Dominguez C, Victoria M, Askins S, Sala G (2012) Power rating of CPV systems based on spectrally corrected DNI. AIP Conf Proc 1477:331–335
59. King DL, Boyson WE, Kratochvil JA (2004) Sandia national laboratories. Photovoltaic array performance model SAND2004-3535, Albuquerque
60. Fernández E, Almonacid F (2014) Spectrally corrected direct normal irradiance based on artificial neural networks for high concentrator photovoltaic applications. Energy 74:941–949
61. Rodrigo P, Fernández E, Almonacid F, Pérez-Higueras P (2014) Review of methods for the calculation of cell temperature in high concentration photovoltaic modules for electrical characterization. Renew Sustain Energy Rev 38:478–488
62. Almonacid F, Pérez-Higueras P, Fernández EF, Rodrigo P (2012) Relation between the cell temperature of a HCPV module and atmospheric parameters. Sol Energy Mater Sol Cells 105:322–327
63. MODIS Daily Level-3 data (2013) Available: http://gdata1.sci.gsfc.nasa.gov/daac-bin/G3/gui.cgi?instance_id=MODIS_DAILY_L3. (Accessed 2013)

Building-Integration of High-Concentration Photovoltaic Systems

Daniel Chemisana and Aggelos Zacharopoulos

Abstract The chapter addresses building-integration (BI) issues from the basic concepts to the most specific concerns related to high-concentration photovoltaic (HCPV) systems. The reader is introduced to the topic by learning the main aspects of the true BI of PV systems. Although CPVs were developed to generate electricity at a decreased price compared with nonconcentrating systems, their BI can provide additional advantages related to a range of building energy needs and functions. Characteristic case studies of building-integrated concentrating systems are presented and discussed to show how different types of optical arrangements are designed to be architecturally integrated. BI HCPV systems require two-axis tracking arrangements, which poses a range of challenges in addition to those general for low-concentration or nonconcentrating BI solar systems. Two examples of truly BI HCPV, from the very few that can be found at present, are presented.

1 Introduction to Building-Integration of Solar Energy Systems

Energy use in buildings represents 40 % of the total primary energy used in the European Union. The Energy Performance of Buildings Directive (EPBD) requires member states to set minimum energy performance requirements for buildings taking into account the positive contribution of renewable energy sources [1]. Therefore, developing building-integrated renewable energy technologies that offer effective energy alternatives is vital.

D. Chemisana (✉)
Applied Physics Section of the Environmental Science Department, Polytechnic School, University of Lleida, 25001 Lleida, Spain
e-mail: daniel.chemisana@macs.udl.cat

A. Zacharopoulos
Centre for Sustainable Technologies, School of the Built Environment, Ulster University, Jordanstown Campus, Shore Road, Newtownabbey, Co. Antrim BT37 0QB, UK
e-mail: a.zacharopoulos@ulster.ac.uk

P. Pérez-Higueras and E.F. Fernández (eds.), *High Concentrator Photovoltaics*, Green Energy and Technology, DOI 10.1007/978-3-319-15039-0_13

Solar energy systems (SES) can be integrated onto roofs, facades, and other building elements offering several advantages such as the following:

- They do not require additional land use and can be used in highly built-up areas.
- They can produce electrical/thermal energy to cover part or all of the building's needs.
- They can decrease the building's energy needs by providing thermal insulation, natural daylight, and shading.
- They supply energy at the point of use, thus decreasing infrastructure costs.
- They replace conventional building materials and components, thus enhancing investment payback periods.
- They can improve aesthetic appearance.

In particular, building-integrated PVs (BIPV) offer the extra advantage of producing power at peak demand times, thus decreasing the utilitiy's peak grid loads.

- They do not requiring any additional infrastructural installations.
- They can produce power at peak demand times, thus decreasing the utilitiy's peak grid loads.

By superimposing a SES on a building structure, it is possible to achieve architectural integration and provide good aesthetic appearance. However, a SES is considered to be truly BI when it becomes a component that provides integrity and functionality to the building. Being part of the building structure it means that when dismounted, it will affect or will require the replacement of the adjacent building component(s). A dismounted BI SES must be replaced partly or totally by a conventional/appropriate building component to preserve the integrity of the building. Therefore, in addition to generating energy (heat, electricity, etc.), a BI SES must provide a combination of the following:

- mechanical rigidity and structural integrity;
- weather impact protection from rain, snow, wind and hail;
- life expectancy from the various materials involved (at least equal to the life of the building);
- fire protection;
- noise protection; and
- environmental benefit/influence (LCA, embodied energy, emissions).

It is essential for the wider acceptance of BI SES that apart from good energy performance and cost-effectiveness, they provide flexibility on a wide range of characteristics that affect the building aesthetics and the wider public acceptance. These include employed material and surface textures, colour of the solar absorber, shape and size of the units, and methods for interconnection and thermal/electrical storage options. Toward this end, solar concentrating systems have several advantages compared with non-concentrating ones. Nevertheless, at present, the use of concentrating technologies is limited, and most of the existing installations are stand-alone devices of considerable size (e.g., solar power towers, parabolic-trough

concentrators, parabolic-dish concentrators, and large Fresnel concentrators with two-axis tracking).

The use of concentrating systems for BI requires development of reliable systems from the manufacturers. An important issue is the tracker mechanism, which must be simple to decrease the complexity and the cost of the system. When comparing such a system with a flat-panel PV device built for the same application, the additional cost of the tracker and its maintenance must be compensated for by the advantages provided by the use of the concentrating technology. In contrast, flat-panel systems can be used to replace structural elements of a building, which in most cases is not possible with concentrating technologies [2].

The way of integration of SES and the perception from people of how well-integrated is the system is a complex issue to define because there are many factors (cultural, economical, political, etc.) to consider. For instance, in a certain location where a solar concentrating collector is superimposed onto a façade, it could be considered an aesthetically pleasing system because the tracking movements provide a more dynamic image to the building. However in another location of the same façade, integration could be considered totally anaesthetic and incorrect. Reijenga [3] established a classification of the BIPV systems that has an inherent subjectivity. Five categories were defined based on the increasing extent of architectural integration:

1. applied invisibly,
2. adds to the design,
3. adds to the architectural image,
4. determines the architectural image, and
5. leads to new architectural concepts.

Now that the concept of BI of solar systems has been introduced, the next sections deals with the particular restrictions and requirements that an HC BIPV system should fulfill.

2 Characteristics of a Well-Integrated Solar System

The characteristics that a solar system should cover to be successfully building-integrated should be in balance between architectural and engineering issues. In other words, a good balance between aesthetics and engineering should be created.

Regarding the above-mentioned balance, Munari Probst and Roecker [4] performed a survey on how architects and engineers perceive integration quality. The study focused on building-integrated solar thermal systems, but the results can be effectively be applied to any solar device. This research was part of the Task 41: Solar Energy and Architecture from the Solar Heating and Cooling program (SHC) of the International Energy Agency (IEA). From the collected survey data, the authors defined the following criteria:

1. The multifunctionality of the solar energy system allows the architect to define a more effective project because fewer elements must be considered, e.g., when the solar device is also a construction element (facade cladding, roof covering, etc.).
2. The position as well as the dimensions of the collector field should be evaluated by considering the building as a whole. This implies taking into consideration energy production goals and formal integration needs (colour, size, shape, etc.). In some of the cases, the use of dummy elements (non-active) may help to achieve more coherence between the solar system and the rest of the building.
3. The choice of colours and materials for the system should match with colours and materials characterising building and context. The initial choice of technology is fundamental because it imposes the material of the external-visible-system layer (glass, metal, plastic, etc). In the frame of the chosen technology, material treatments (surface colour, texture) offered by the various available products can be considered.
4. Module size and shape should be chosen by taking into consideration building and facade/roof composition dimensions and characteristics (or vice versa). The proposed module jointing types should also be considered while choosing the product (different jointing types differently underline the modular grid of the system in relation to the building).

The criteria stated from the collected survey data were used by Munari Probst and Roecker [4] to define a design methodology. Figure 1 depicts the sequence of steps involved in the collector design. As indicated previously, the guidelines consider solar thermal collectors and, within them, concentrating hydraulic systems; however the design methodology for obtaining a well-integrated collector can be applied either for thermal or PV systems. Sometimes, the integration requirements are difficult to achieve as the currently available collectors on the market have been developed with insufficient awareness of BI aspects [5]. In the case of BI high-concentration photovoltaic (HCPV) systems, most of the collectors do not consider BI issues, and very few examples can be found. In Sect. 6, two representative cases will be described.

Almost in parallel to the work performed by IEA SHS Task 41 regarding PV systems, Task 7 of the IEA on the Photovoltaic Power Systems program evaluated the aesthetic quality of building-integrated PV systems. As a result, a set of requirements of a well-integrated PV system were defined [6]:

- natural integration;
- architecturally pleasing design;
- good composition of colours and materials;
- dimensions that fit the gridula, harmony, and composition;
- conformity to the context of the building; and
- well-engineered and innovative design.

As indicated for the case of BI solar thermal systems, these requirements can be used for any solar-collector type. In addition to the requirements listed, BI HCPV should overcome successfully a series of constraints caused by tracking requirement, extra weight, etc. These aspects are further discussed in Sect. 4.

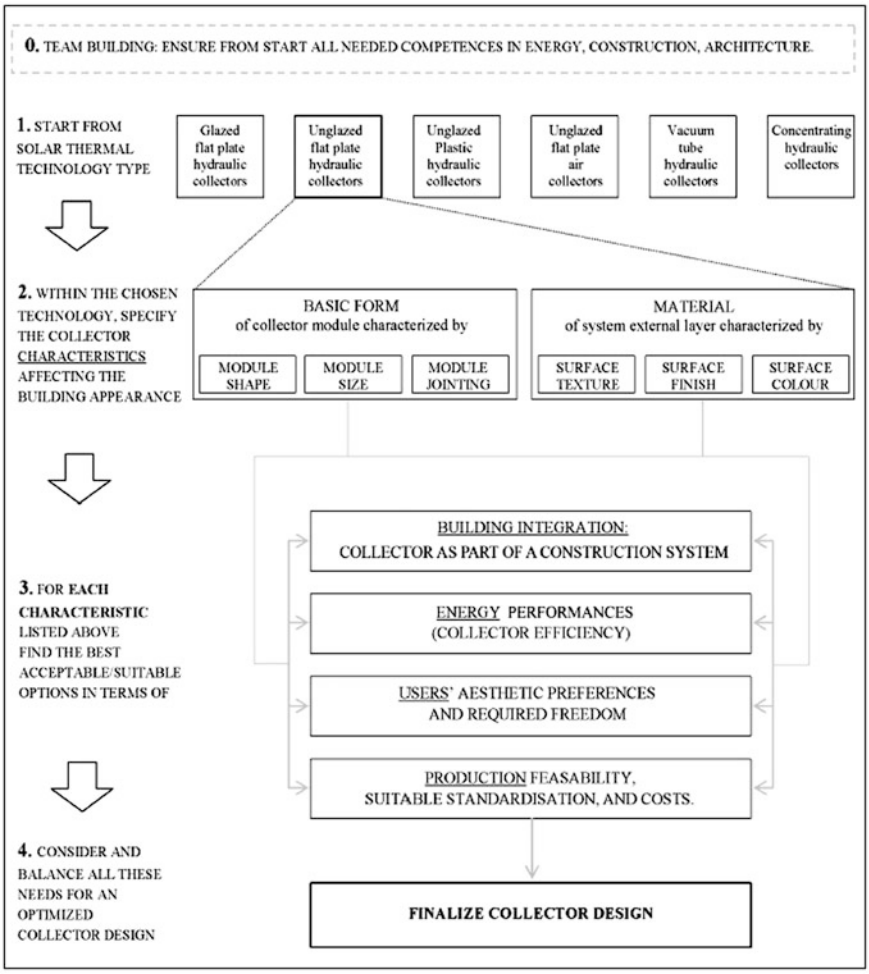

Fig. 1 Design methodology for a BI solar collector [4]

3 Representative Case Studies of Building-Integrated Concentrating Photovoltaic Systems

3.1 The Concentrating Photovoltaic Evacuated Glazing (CoPEG)

The incorporation of PV cells onto conventional gazing restricts daylight transmission, thus increasing the requirement for artificial lighting in the building. Recent concepts have attempted to improve transparency by removing sections of the PV material; however, this decreases the electrical-generating capacity of the

system and offers no lighting control for the building's interior. Dielectric concentrating covers for PV façade BI enable increased electricity generation per unit area of PV material compared with conventional PV panels [7, 8]. In addition lighting control can be achieved by tailoring the dielectric concentrating lens design to allow daylight to enter the building for prespecified range of incidence angles of solar radiation. Evacuated glazing systems have significant potential in decreasing heat loss from buildings [9]. Laboratory evacuated glazing prototypes have shown that U-values as low as 0.6 Wm-2K-1 can be achieved [10].

The innovative CPV evacuated glazing (CoPEG) concept developed by the Centre of Sustainable Technologies at the University of Ulster [11] integrates evacuated glazing technology with transparent concentrating PV lens into a single multifunctional facade element. Integrated onto a building façade, CoPEG provides significant thermal insulation with enhanced optical daylight control whilst incorporating a concentrating PV lens to generate electricity.

The CoPEG concept can form part of the building envelope providing the following:

- high thermal insulation for the building decreasing heating and cooling requirements;
- low-cost and carbon-free electricity generation from the Sun; and
- control of daylight penetration into the building.

The concept technology consists of an evacuated glazing panel where one pane of glass is shaped into a series of linear concentrating lenses. A patented low-temperature sealing technique that uses indium [12] has been utilised to create an effective and consistent seal around the edges of the evacuated space formed by the flat and the concentrating glass panes. PV cells are placed at the focus of the concentrating lens. The vacuum between the outside glass pane and the PV concentrating lens pane minimises convective and conductive heat transfer, thus providing high thermal insulation to the building. The solar radiation is transmitted through the outer glass pane and concentrated onto the PV cells to generate electricity. The concentrating PV lenses are designed to allow a certain fraction of the beam incident solar radiation to reach the building interior at times when natural lighting is needed (Fig. 2). The lenses can also be designed to produce a seasonal effect with more direct sunlight allowed into the building in the winter months and less in the summer. In cooling-dominated climates, CoPEG can significantly decrease solar heat gain to the building by concentrating all incident sunlight onto the PV cells. At the same time, the generated electricity can be utilised to supplement air-conditioning cooling power requirements.

The technology is currently undergoing proof-of-concept to advance it to Technology Readiness Level (TRL) 4. The linear concentrating lenses are of prismatic shape and offer a geometrical concentration ratio of 2.7×. They are cut onto a 500 mm × 500 mm × 15 mm (length × width × thickness) opti-white glass pane using especially designed computer numerical control cutting tools. Multicrystalline PV cells, 14 mm-wide, are bonded onto the focal (absorber) area of the prismatic lens. To produce a building-integrated component with superior aesthetics, green

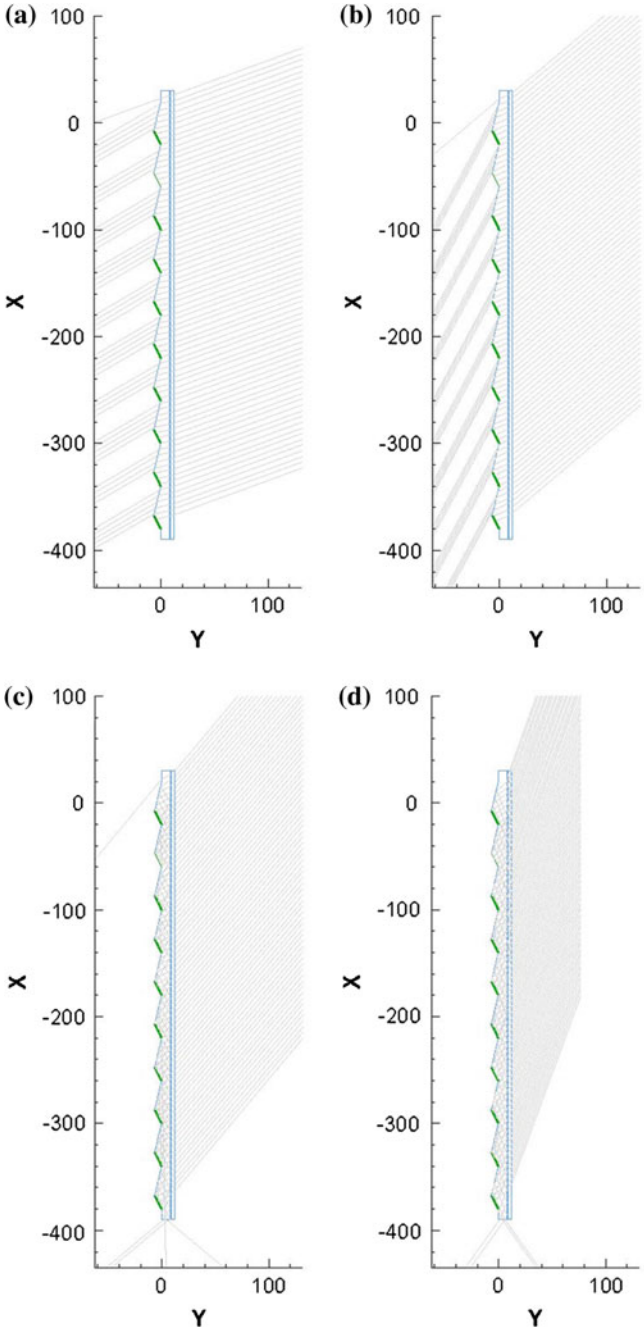

Fig. 2 Series of ray traces demonstrating the interaction between the linear concentrating lens of the CoPEG concept and direct sunlight incident at different angles (measured from the perpendicular to the outer glass pane): (**a**) 20°, (**b**) 40°, (**c**) 50°, and (**d**) 70°

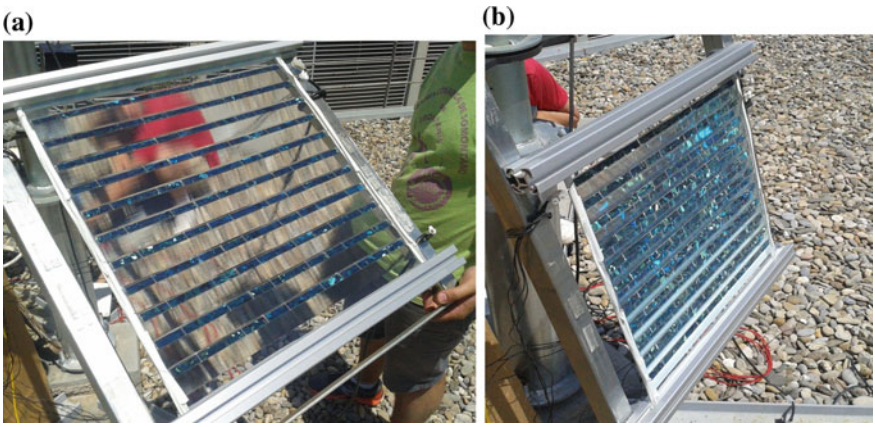

Fig. 3 The effect of the angle of incidence on the amount of beam solar radiation that reaches the PV cells concentrating PV glass pane: (**a**) at low incidence angles the PV cells receive only the solar radiation which is directly incident onto their surface. The remaining radiation penetrates behind the glass mane, (**b**) at high incidence angles the larger part of beam solar radiation is reaching the PV cells either directly or after total internal reflection at the prismatic surface

coloured cells are used. The effect that the incidence angle of solar radiation has on the amount of sunlight reaching the PV cells can be observed in Fig. 2. At low incidence angles, the PV cells receive the fraction of beam solar radiation that is directly incident on them (Fig. 3a). The remaining beam radiation penetrates behind the glass. At high incidence angles, most of the beam radiation reaches the PV cells either directly or after been totally internally reflected at the prismatic surfaces. This is indicated by the overall green colour of the prototype in Fig. 3b.

3.2 Hybrid Solar Wall Element

A hybrid solar wall element—which combines active and passive heating, PV electricity, and control of daylight penetration into the building—was developed by Fieber et al. [13]. The solar wall element uses a PV/Thermal (PV/T) hybrid absorber with tracking insulated reflectors integrated into a window (Fig. 4). The tracking reflectors offer an effective concentration ratio of 2.45, and they also act as sun-shades and added internal insulation for the window.

The hybrid absorber is fixed in an angle of 20° from the horizontal and made of 2 mm-thick aluminium sheet. PV cells are laminated on its upper side, and pipes are attached to the bottom for circulation of water. To maximise the fraction of solar radiation that reaches the PV/T absorber, highly transparent glass with an antireflective coating is used for the window.

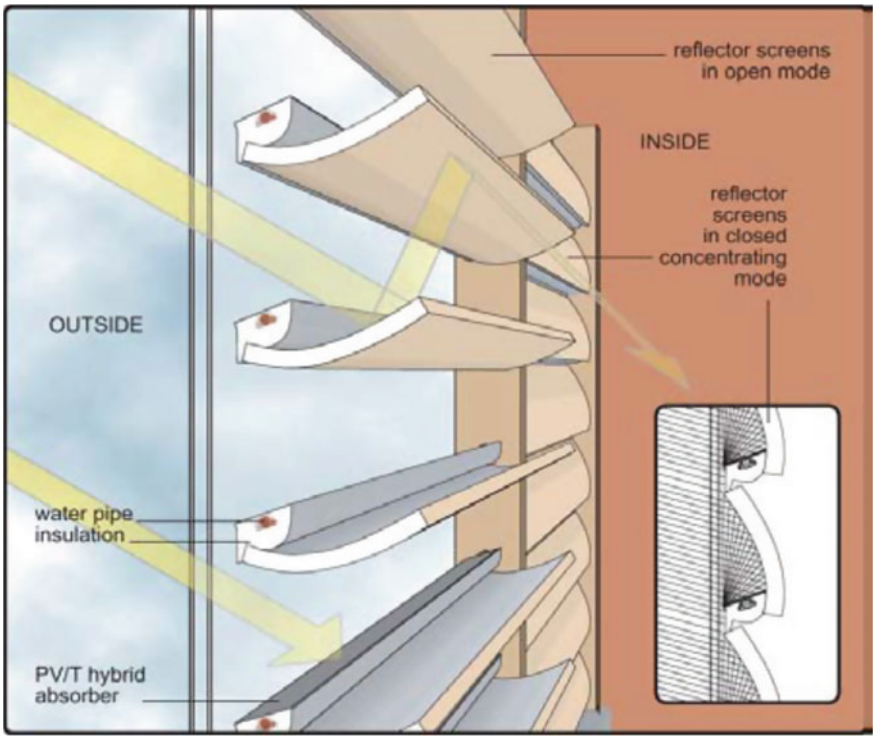

Fig. 4 The hybrid solar wall element [13]

The tracking reflectors can be set to achieve a range of combinations of solar radiation concentrated onto the PV/T absorbers and light penetrating the building interior. With the reflectors fully closed, all of the incident solar radiation is concentrated onto the absorbers, thus maximising electricity or heat generation and minimising solar gains for the building. In passive solar house designs that use large south-facing windows, this feature of the solar wall element-combined with the insulated reflectors—can minimise risks of overheating during daytime or thermal losses during night time. With the reflectors fully opened, all incident solar radiation penetrates the building to provide maximum natural lighting and solar gains.

The system is a visible element in the exterior of the building, particularly in the interior, and its performance is directly connected to the user's behaviour due to the wide range of different operating modes of the reflectors.

A 1 m^2 prototype of the system was fabricated and experimentally evaluated regarding its Sun shading and U-value properties and its photovoltaic and active thermal output [14]. For a double-glazed antireflectively coated window, the U-value was found to range between 1.2 (with reflectors fully closed) and 2.8 W/m^2 K (with reflectors fully open). The estimated annual energy gain was estimated to be 609 kWh/m^2, of which approximately 10 % was expected to be delivered as

electricity-generated PV absorber elements (assuming that the reflectors are fully closed at all times). However, because providing natural daylight to the building interior is a more efficient strategy than using PV-generated electricity to power artificial lighting, it was suggested that the reflectors should not be closed at incident solar radiation levels <300 W/m^2.

A simulation program calibrated using actual data from installed prototypes in Lund, Southern Sweden, and a family house at Solgarden, Central Sweden, predicted that the hybrid solar wall element annually can produce approximately 35 % more electric energy per unit of employed PV area compared with a vertically installed flat PV module [15]. In comparison, a wall-integrated low-concentration PV system optimised purely for electricity production at similar latitudes (approximately 60°) was predicted to generate 120 kWh/m^2 of PV area, 72 % greater than that generated by a flat PV module [16].

Hybrid solar wall technology is not fully integrated onto the building façade because it is simply installed (superimposed) behind a window in the building's interior. It does offer the advantage of decreasing the total price of the construction compared with a conventional solar PV/T collector because it utilizes the frame and the window's double glazing for cover. It also offers improved thermal insulation to the building by using insulated reflectors. However, because it is an active system that requires tracking of the reflectors to operate effectively, it incurs operating and maintenance costs. The reflector and PV/T absorber assembly, even when the reflectors are fully opened, will impair the view of the building occupants toward the outside and prevent penetration of the sunlight into the building.

3.3 The Fresnel Lens PV/T Collector

The ability of linear Fresnel lenses to separate the beam from the diffuse solar radiation makes them useful for illumination control in the building interior space. Fresnel lenses are advantageous because they can combine within them both the concentrating element and the optically transparent window. In addition, nonimaging Fresnel lenses are much less demanding in tracking requirements than the image-forming ones. This feature is very interesting for BI as it simplifies the control needs, the weight, and the complexity. Based on these characteristics, the Applied Solar Energy group, at the University of Lleida, designed a solar concentrator that consists of a stationary wide-angle optical concentrator, which, for Sun position in the sky, transmits the incident solar radiation into a small moving focal area, which in turn is tracked by the absorber. The absorber is a hybrid PV/T collector that controls the cells from overheating to maximize electrical yield and simultaneously generates low-temperature thermal energy for domestic hot-water use [17].

The system combines a linear Fresnel lens (5×) with a secondary CPC reflector (2×). This option was selected to maximize the concentration ratio and to obtain optimum illumination for the PV cells (mainly homogeneity in the focal area). The secondary concentrator increases the acceptance angle of the lens and at the same

time mitigates the non-uniformity caused by the Fresnel unit, thus obtaining a more uniform profile on the cell. The optical performance of the system was found to be consistent throughout the year. Figure 5 shows the concentration ratio as a function of the relative angles in the direction perpendicular to the focal plane (θ) and in the direction of the focal plane (ψ). The lens was placed at the latitude plane, and the angle variation was θ (−25°, 25°) and ψ (−70°, 70°) [18].

The system allows a range of different BI options because the lens is static, and the acrylic material of it [with the adequate ultraviolet (UV) treatment] is waterproof, light, easy to fix, etc. Therefore, it can be installed as an external element, e.g., in windows, and can be used for either the façade or roof closing element. Figure 6a illustrates the view of the concentrating system from the indoors and the effect of the sunlight that reaches the building interior. Clear shading is observed, which is caused by the large percentage of the incident irradiance that is

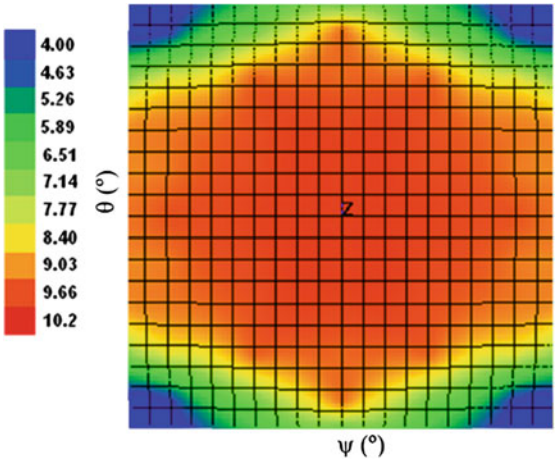

Fig. 5 Dependence of concentration ratio on angles of incidence

Fig. 6 **a** Architectural design of the Fresnel PVT collector. **b** Prototype system built using a structure of metallic profiles that supports the Fresnel lenses and the PV/T absorber

concentrated onto the PV/T absorber where the diffuse fraction enters the interior space. The lens was placed with its longitudinal axis horizontal and the PV/T absorber just outside the window. Figure 6b shows the prototype that was built using a structure of metallic profiles. The structure was designed to support the module and the lens in the same position as they would be in a real building-integrated installation.

3.4 Photovoltaic Facades of Decreased Costs Incorporating Devices with Optically Concentrating Elements (PRIDE)

Dielectric nonimaging concentrating covers for PV-integrated building facades make use of total internal reflection of sunlight to redirect the incident solar radiation onto PV cells placed at the absorber of dielectric nonimaging concentrators. They were designed as a replacement for the glass panes covering conventional PV modules while offering higher electrical outputs per unit of PV material employed. An asymmetric CPC was specifically designed for use in for building façade BIPV (Fig. 7a). The asymmetric design was shown to be more suitable compared with symmetric concentrators. It offered (after truncation) a geometrical concentration ratio of 2.46 with a 1.39 aperture width-to-depth ratio [7]. Refraction of the incident solar radiation at its aperture allowed it to collect beam solar radiation incident at any angle between 0° and 66.4° from the perpendicular to its aperture. A 5.3 mm deep concentrator was predicted to achieve optical efficiencies of up to 91 % when made from opti-white glass. A three-dimensional optical analysis predicted that the asymmetric CPC maintained optical efficiencies of >40 % (Fig. 7b) even for

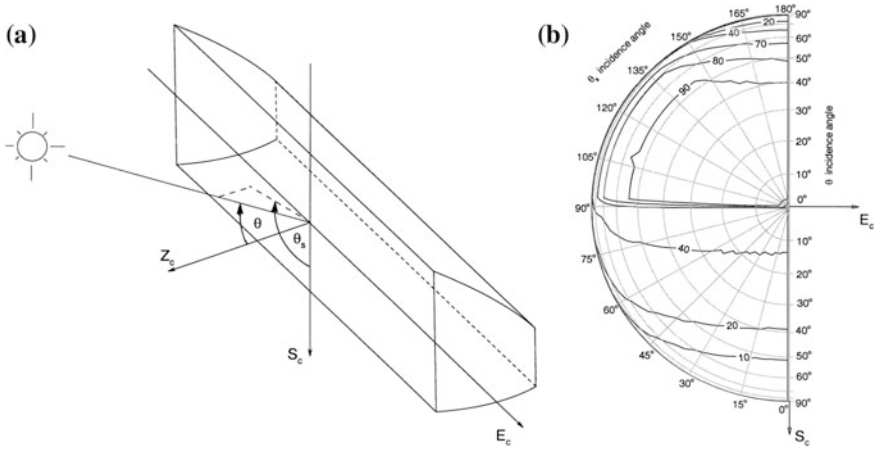

Fig. 7 The dielectric asymmetric CPC designed for use in façade-integrated PV covers (**a**) and its predicted optical efficiency (%) in the three dimensions (**b**)

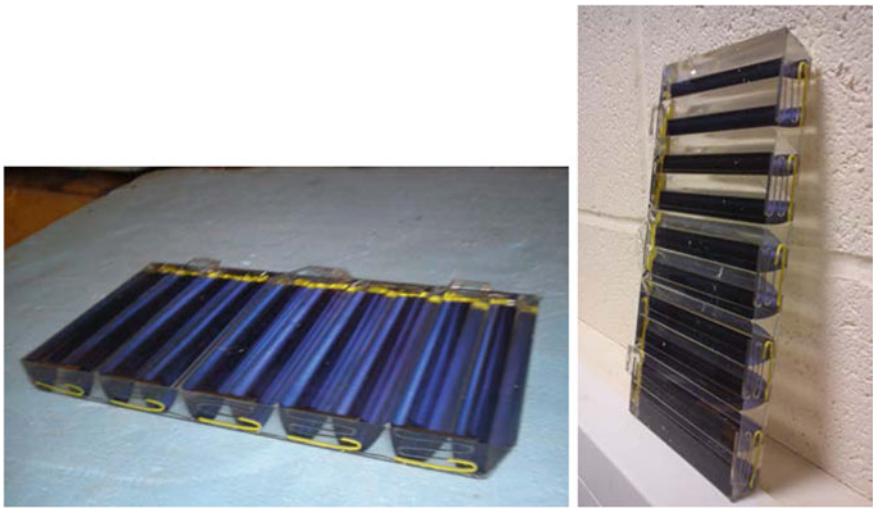

Fig. 8 Prototype concentrating PV covers made by casting acrylic material into a mould. The covers use 9 mm-wide PV cells at the absorber of asymmetric CPCs specifically designed for building-integration

incidence angles outside of its two-dimensional angular acceptance range. Compared with a nondielectric concentrating system, it offered increased acceptance of solar radiation for incidence angles both inside and outside its meridian.

The asymmetric CPC design was used in prototype covers of PV facades incorporating devices with optically concentrating elements that were fabricated using casting into moulds (Fig. 8). The prototype covers were compared with similar nonconcentrating systems under controlled simulated conditions and showed excellent power output. An injection moulding method was used to fabricate covers out of clear acrylic material using 6 mm-wide cells at the absorber of the dielectric asymmetric CPCs [8]. The method allowed large-scale manufacturing with improved durability and decreased weight and cost of the covers. The fabricated covers were optically characterised and evaluated outdoors compared with similar non-concentrating panels. The measured power ratios between the two systems showed a 2× power concentration (Fig. 9). The decrease in relation to the geometric concentration ratio of 2.45 was due to optical losses. The maximum solar to electrical conversion efficiency achieved for concentrating covers was 10.2 %. The power output from a 950 × 1000-mm cover measured at standard test conditions was 78 W.

The quality of the finish of the acrylic surfaces of the asymmetric CPCs was the main factor affecting the optical performance of the prototype concentrating covers. The employed asymmetric CPC design provides the optimum optical performance for building façade integration (with wide acceptance angle, high optical efficiency, concentration ratio of 2.46 and 1.4 with aperture width-to-depth ratio). However, the complexity of its geometry makes it difficult to fabricate accurately and

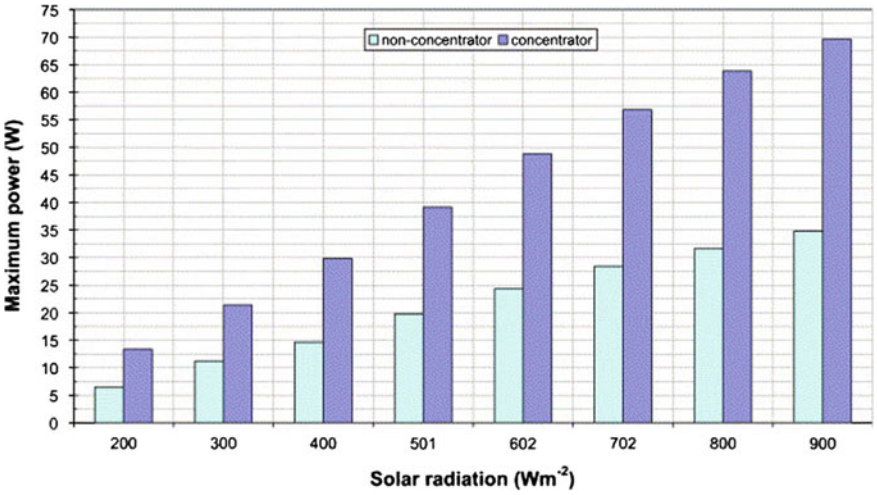

Fig. 9 Comparison of power outputs at different solar intensities for the prototype concentrating PV and a similar non-concentrating panel using the same area of PV material [8]

inexpensively. Although small concentrator depths mean shorter paths for the sunlight inside the concentrator body before reaching the PV cell and in turn greater optical efficiencies, achieving good fabrication quality becomes more challenging at small scales (such as when using 3 mm-wide PV cells). Baig et al. [19] modelled and experimentally evaluated a building-integrated CPV system based on symmetric elliptical hyperboloid dielectric elements. The geometric concentration ratio of the system was 6×. A power ratio of 3.7 was determined at normal incidence and an average ratio of 2.1 was determined over the entire incidence angle range. Fabrication defects, spectral transmission, and temperature losses were identified as the main loss mechanisms for decreased performance. However, the effect of the high nonuniformity of the solar flux incident on the cell surface was found to be negligible.

The concentrating PV covers were developed as a method of decreasing the unit price of electricity by using less PV material to achieve the same electricity output compared with conventional PV. Decreases in the price of PV cells over the last 10 years meant that the costs of fabricating the dielectric concentrators became greater compared with the costs saving from using less PV material. Any façade-integrated BIPV technology is exposed to lower levels of solar radiation compared with roof-mounted systems. This results in decreased electricity outputs and longer investment payback periods. To achieve cost-effectiveness, façade-integrated BIPV should provide other functions or advantages than just generating solar electricity. Ease of integration, good thermal insulation, natural daylighting, solar gain control and aesthetics must be part of the competitive offering package of the technology.

4 High-Concentration Systems: Critical Aspects

Compared with BI PV and BI CPV, BI HCPV offers the opportunity of achieving greater overall electrical conversion efficiencies by using HC solar cells, which achieve conversion efficiencies >40 %. In this way, significant amounts of power can be generated by the limited space available on building facades, roofs, and other elements. Furthermore, the cost-effectiveness of the system can be improved when the high-temperature waste heat generated by the large concentration fluxes (400×) incident on the PV absorber is used for other applications such as cooling and power generation [20].

By the two-axis tracking of the Sun, BI HCPV systems ensure that incident solar radiation is received within a very narrow angular range, which maximises acceptance and in turn power generation. Moreover, the tracking system can allow a more versatile use of a BI HCPV system. Connected to the appropriate control systems, the tracking mechanism can be used to control or allow daylight penetration into the building in response to changing ambient conditions and building occupant needs. During night time, the tracking mechanism can arrange the position of the concentrating system elements in such a way that improves the insulation properties of the building skin and decreases heat loss.

HCPV systems require a highly collimated light on their aperture, which is then focused on a very narrow area where the PV cell is located (point focus). It is possible to use this method in reverse and employ it for lighting purposes [21].

In HC systems, a distinguishing aspect compared with other PV technologies (e.g., flat-plate PV modules without concentration or PV of low concentration) is the requirement for two-axis tracking that can achieve the desired power densities. Due to this characteristic and the magnitude of the concentrated radiative flux itself, a number of critical factors, related with BI, arise:

1. The requirement for additional structural and mechanical elements to fix or attach the tracking system itself. Thus, the structural load of HC systems integrated into a building is always greater than that of a conventional solar system.
2. The space occupied (as part of the building) increases due to the moving parts of the tracking system and the PV generator. Therefore, in these devices it is necessary to consider the swept volume required to track the solar height and azimuth. The density of the elements on the surface where the system is installed is decreased by having gaps between them for tracking movements. In turn, the volume of the layer, understood as a constructive system, is also increased because of solar-tracking trajectories. The best method, which allows for low swept volume, is to install modules with the smallest possible size (one optical element–one PV cell). This means that more mechanical pieces will be used to fix each of the individual concentrating units, but the volume occupied is lower and the possibilities for BI improved (Fig. 10).
3. As a result of the previous requirement, moving parts mean that the interconnections of all of the installations involved (electrical circuits, hydraulic circuits, control circuits) should be prepared for these movements. This is a bigger

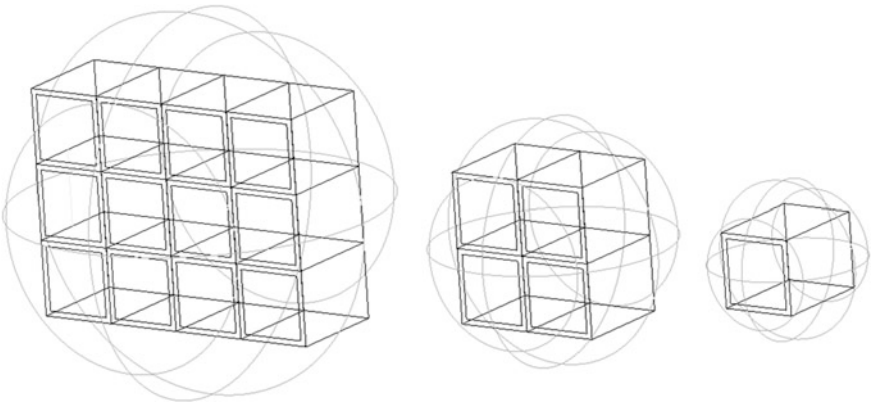

Fig. 10 Swept volume as a function of the elements forming the concentrating module

challenge in the case of PV concentrators equipped with active cooling, whereby an additional flexibility for pipe connections is required. It is worth mentioning that the majority of HC systems are equipped with passive heat sinks that work successfully due to the small size of the PV cell and its isolated placement in the module. These two factors allow using evacuation devices with high-dissipation active area with respect to the cell surface to be cooled.

4. In addition to generating electrical power, the system has an electrical consumption for the tracking system; thus, the net output is decreased. Moreover, this consumption implies the use of an additional electrical circuit to feed the tracking system and its corresponding control.
5. The solar tracking for HC systems is demanding with angular tolerances of approximately ≤0.2°. Because small deviations could cause several problems in addition to the consequent loss of production, the control must be precise and proper maintenance is required.
6. A large amount of the incident concentrated energy, between 60 and 70 %, is not converted into electricity and is lost as waste heat. Thus, hot spots with temperatures ranging from 50 to 100 °C should be managed by appropriate heat sinks and should be the air flow to which the waste heat is transferred.

Considering what has been presented in the previous sections, the majority of HCPV systems are not designed to be architecturally integrated. The most feasible option is to incorporate them on flat roofs where they are not visible from the street level. However, these configurations fall outside the "building integrated system" concept because they are instead superimposed on the building structure.

In addition to the requirements inherent to HC, these systems must comply with the general principles of a solar system well-integrated into the building. In this direction, the HCPV that are more suitable for integration in buildings are made by refractive optical systems, and their main components are Fresnel lenses. Refractive systems have a highly desirable property, which is their transparency; this enables

them to be part of façades or roofs while allowing natural lighting to interior spaces. The direct fraction of the solar irradiance is concentrated onto a high-efficiency solar cell, and the diffuse fraction provides natural lighting inside the building. Depending on the arrangement of the concentrator elements, a portion of the solar irradiance passes directly through the interspaces of the modules needed to perform the two-axis tracking. The light-guiding devices, which combine refraction and total internal reflection, also have the property of transparency. The Light-Guide Solar Optics Sun Simba, commercialised by Morgan Solar, is a leading exponent of this typology [22]. This system operates with a geometric concentration of 500× and III-V cells of 5 mm^2. It is highly compact (similar to a conventional PV module) because the PV cell and the concentrator form a single element. In addition, the waste heat-removal system is minimized as the concentrator removes the infrared (IR) from the incident spectrum [23].

Parabolic-dish concentrators have the same constraints derived from two-axis tracking and volume occupied as the refractive systems using Fresnel lenses. However, being reflective systems, natural lighting of interior spaces is achieved only through the gaps between the array elements. Improving the compactness of the system, cassegrain-type concentrators combine several optical systems achieving a similar thickness as a conventional module but with a concentration of approximately 500× [24–26]. It is possible to allow lighting into the building by using spectral-selective reflectors that permit part of the incident irradiance to enter and other bandwidths to be concentrated onto the cell [27–29]. This is more suitable for PV technologies, such as the silicon or GaAs PV cells, that utilise narrow spectral bandwidths and a spectral response at a distinct maximum zone. A possible configuration is to use a reflector that only concentrates irradiance from a zone around the spectral response peak (i.e., approximately 900 nm in the case of silicon cells) while it is transparent in the rest of the visible region. However, in the case of multijunction cells where spectral response ranges from the UV to the near-IR region with very high external quantum efficiency, the benefits depend on other factors rather than the efficiency. Nevertheless, a band-pass filter configuration could be designed to satisfy the specific application.

5 Examples of BI HCPV Systems

5.1 Integrated Concentrating Solar Facade (ICSF) System

A BI HCPV system that fulfils the criteria for a well-integrated system in buildings is the integrated concentrating solar facade by researchers at the Rensselaer Polytechnic Institute [Center for Architecture Science and Ecology (CASE)] and the Harvard University [30]. The technical challenges addressed by the researches, in addition to developing a low-cost system, are as follows:

- to maximise the direct beam irradiance gain for producing electricity;
- to use the maximum amount of incident diffuse irradiance to provide natural daylight;
- to minimise maintenance issues;
- to capture and utilise the waste heat produced by the PV; and
- to be aesthetically pleasant and prevent glare effects for the building's occupants.

The solution adopted to meet all of the desired characteristics is a Fresnel lens optical system that concentrates the direct irradiance (approximately 600×) towards a III-V high-efficiency cell. The structure supporting the lens and the PV cell is completely transparent (made from either borosilicate glass or acrylic), and it constitutes the concentration module. The modules are suspended between parallel hanging fins that rotate to track the solar azimuth. On the front of the modules, thin vertical cables, which are practically invisible, are attached on the aperture area of the concentrator. The cables hold the module and track the solar altitude (Fig. 11).

To use the incident energy that is not converted into electricity, the system includes an active cooling system comprising a heat exchanger placed at the back of the PV cell and a hydraulic circuit located inside the vertical tube that connects the apexes of the modules. The connector of the hydraulic circuit with the cooler is flexible to absorb solar tracking movements. Because the hydraulic system is decoupled from the structural fins that track the solar azimuth, the connector between the heat exchanger and the distribution circuits must absorb only the limited movements required for tracking the solar altitude.

Fig. 11 Concentrating Fresnel lens module with detail of the individual concentranting element. *Courtesy* of CASE

The system minimizes the load impact on the building by using lightweight materials and by providing additional functions to the structural elements such as tracking element or hydraulic circuit housing. The fasteners are designed to be vertical, thereby bending deformation because all loads act in the main direction of the element is avoided. This fact enables the use of smaller section profiles. Thermal expansion of components is considered carefully to minimize stresses and maintain tracking within optical tolerances. By contrast, the fins performing the azimuth tracking are subjected to torques that may be important; therefore, it is necessary to take into account the distance from where the torque is applied (transmission system) and the different elements that rotate as well as the materials and the section of the twisting profiles. The ladder construction of the module axle and fin assembly is designed to delocalize the stresses from these torques.

In terms of swept volume, the researchers considered including an array of individual elements so that the occupied volume is minimized. These elements are housed between two glass panes in a curtain wall.

The system functions are illustrated in Fig. 12. Depending on the temperature of the heat-removal fluid and the available technology for utilising it, a wide range of combinations are possible that also produce, apart from the PV electricity, heat for different uses: space cooling, dehumidification, service hot water, desalination and wastewater treatment, power generation, heating, etc.

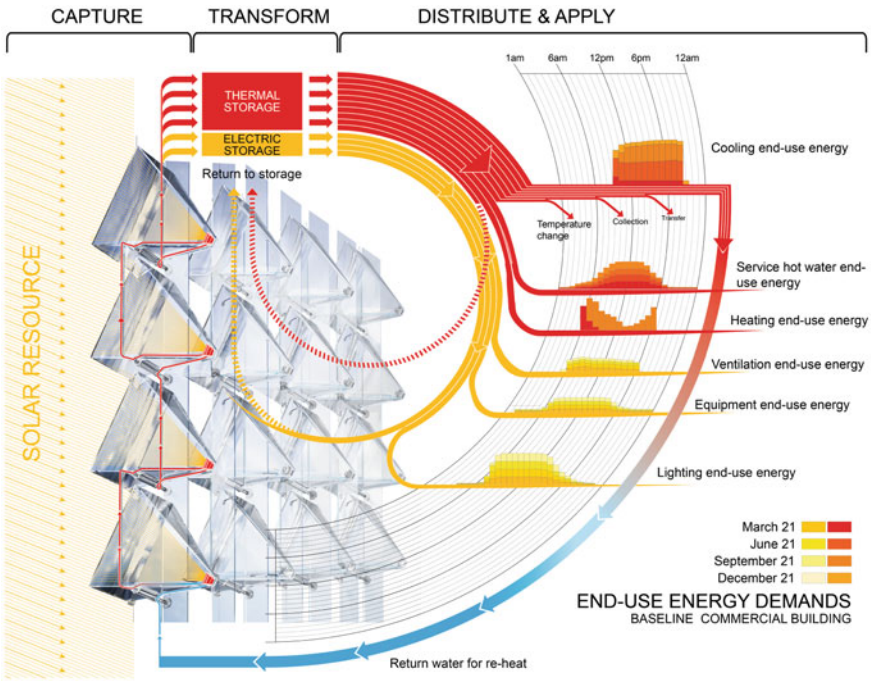

Fig. 12 Schematic of the applications of high-quality thermal energy collected through an envelope-integrated solar-harvesting system. *Courtesy* of CASE

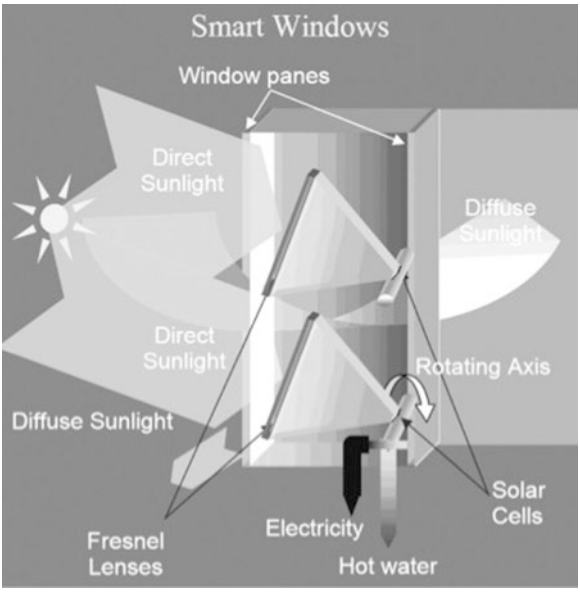

Fig. 13 Schematic of the concentrating system [31]

The proposed device has been tested in the SyracuseCoE Centre of Excellence and the SOM-NY Headquarters and is commercialised by HeliOptix.

The hybrid device ensures that the cell does not overheat; it works in optimum conditions and increases the overall efficiency of the system by producing thermal energy. However, even with a dissipater, a warm zone is produced behind the cells. Heat flux is transferred mainly by convention to the air located in the cavity between the two glass panes. This effect has been numerically investigated by Sabry et al. [31] in a very similar BI HCPV system. This system has the major support axis positioned horizontally so that the rotation achieves the solar altitude tracking. In this case, the loads of the structure are more demanding due to the bending deformation in addition to the torque (Fig. 13).

5.2 Spherical Solar Concentrator

The second example of a BI HCPV system, designed by the company Rawlemon, is based on acrylic spheres. The diameter of the spheres ranges between 50 and 1800 mm. Systems with smaller spheres are made from solid acrylic material and called MicroTrack 324. Larger spheres are made from a spherical acrylic shell with the internal cavity filled with water. The larger diameter systems are a hybrid receiver, using the water for cooling, and can reach a combined efficiency of approximately 57 %.

All of the systems are designed with a geometric concentration ratio of 100×. The smallest device (50-mm diameter) incorporates a single 5 × 5 mm^2

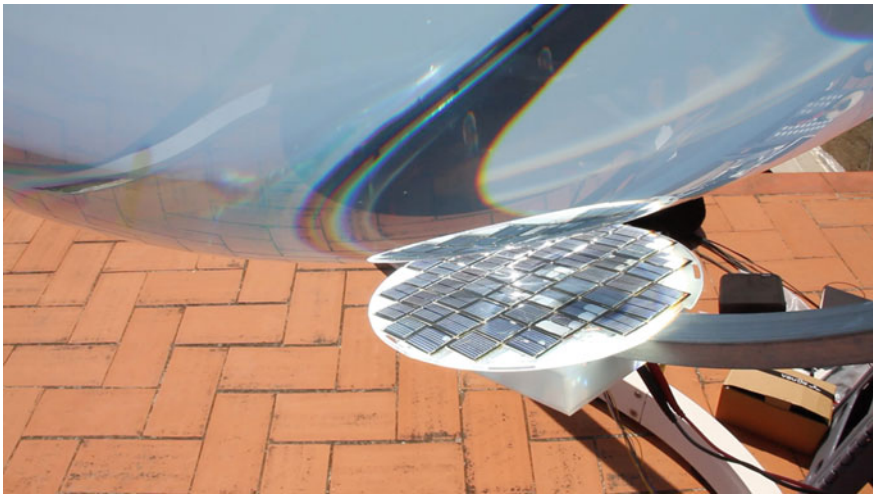

Fig. 14 Photograph of the receptor formed by a matrix of cells. *Courtesy* of Rawlemon

Fig. 15 Solar spherical concentrator. *Courtesy* of Rawlemon

concentration cell. The rest of the systems present an array of concentration cells with variable surface, depending on the sphere diameter, to achieve 100× concentration. Figure 14 shows a photograph of the matrix of PV cells for one of the large-size spheres.

The design is fully adapted for architectural integration with the concentrating element (array of spheres) manufactured as a single panel. Two-axis tracking is used on the PV element to track the focal point of the sunlight after being concentrated by the spheres as shown in Fig. 15. The PV cell is the element that moves to track the focus. The system is fully modular and does not need additional elements to support its operation. As defined in the technical specifications, it is the first concentrating solar module that allows complete integration. The designer

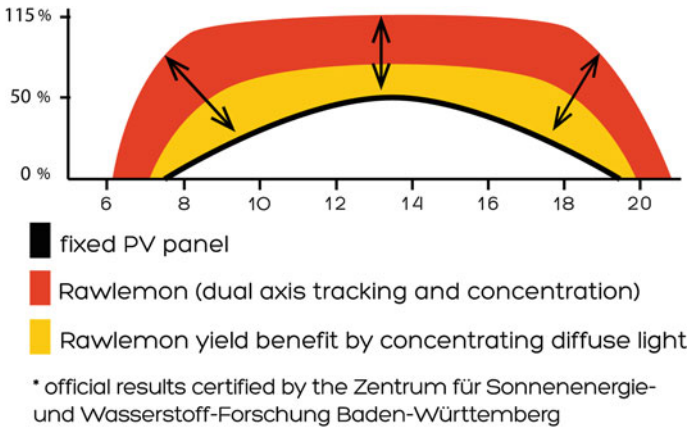

Fig. 16 Comparative performance between a Rawlemon system and a conventional PV panel. *Courtesy* of Rawlemon

claims that it can utilise 15 % of the diffuse irradiance with a transparency of 99 % [32]. However, due to the increased lengths of paths the sunlight travels inside the sphere before reaching the PV absorber, it suffers large optical losses. In addition to generating electricity, or electricity and heat, the system also provides an alternative function for night lighting by placing a series of light-emmitting diodes in the focal points of the spheres.

The system has been experimentally analyzed by the Centre for Solar Energy and Hydrogen Research Baden-Württemberg showing that it can deliver up to 70 % surplus yield compared with a conventional PV panel also placed vertically (Fig. 16).

6 Conclusions

Building-integrated solar energy technologies such as PV systems can play an important role in covering part of the building energy needs and helping achieve the challenging targets such as EPBD. BIPV generates energy in situ where the consumption of it takes place. This does not require a distribution grid from the centralised power-generation unit; therefore, losses from supply side to the demand side are minimised.

Truly building-integrating systems are multifunctional offering extra benefits than just producing energy. They can work as structural elements of the building, such as windows or facades; they can provide and/or control the natural lighting to the interior spaces; they can improve the aesthetics of the building; and they enhance the insulation properties of the building's skin. In contrast, some BI configurations, where the system is superimposed onto the building structure,

achieve less electrical yield compared with a PV system placed at the optimum tilt angle for a specific location.

Concentration of the direct sunlight decreases the amount of solar cell material required and makes the system more cost-effective. Solar concentrators may also help in increasing the amount of incident energy by means of increasing the acceptance of direct incident solar radiation for the full collection period and because they use more efficient cells, which can double the system's performance compare with using conventional cells such as silicon-based technologies.

Most documented building-integrated concentrating systems are of low concentration ratios. When the concentration ratio is low, the system can be static, which facilitates the integration into the building. Few high-concentrating PV collectors are designed to be architecturally integrated. HC systems need two-axis tracking to operate, which means that parts of or the whole system moves. This imposes extra requirements to consider when designing such collectors. Nevertheless, if the BI issues are considered from the beginning of the design and given the same priority as those issues related with the efficiency, suitable devices and good performance can be obtained.

Two HC building-integrated PV systems have been described. Both systems operate with cell efficiencies >30 % and increase the energy performance considerably compared with a similarly integrated standard PV system. From an aesthetic and architectural point of view, the concentrating devices are integrated in a way that improves the image of the building and enhances its public acceptance.

Further research should be performed into developing solutions for truly building-integrated HCPV systems that can offer high cost-effectiveness while enhancing building aesthetics and comfort for its occupants.

References

1. EPBD (Energy Performance of Buildings Directive) (2002) Official Journal of the European Communities, Directive 2002/91/Ec of the European Parliament and of the Council. http://eur-lex.europa.eu/LexUriServ/LexUriServ.do?uri=OJ:L:2003:001:0065:0071:EN:PDF
2. Swanson RM (2000) The promise of concentrators. Prog Photovolt Res Appl 8:93
3. Reijenga TH (2003) Handbook of photovoltaic science and engineering. In: Luque A, Hegedus S (eds). Wiley, New York
4. Munari Probst MC, Roecker C (2007) Towards an improved architectural quality of building integrated solar thermal systems (BIST). Sol Energy 81:1104
5. Munari Probst MC et al (2005) Architectural integration of solar thermal collectors: results of a European survey. In: Proceedings of ISES solar world congress, Orlando, 8–12 Aug 2005
6. Reijenga TH, Kaan HF (2011) Handbook of photovoltaic science and engineering. In: Luque A, Hegedus S (eds). Wiley, New York
7. Zacharopoulos A, Eames PC, McLarnon D, Norton B (2000) Linear dielectric non-imaging concentrating covers for PV integrated building facades. Sol Energy 68:439
8. Mallick TK, Eames PC (2007) Power losses in an asymmetric compound parabolic photovoltaic concentrator. Sol Energy Mater Sol Cell 91:597
9. Griffiths PW, di Leo M, Cartwright P, Eames PC, Yianoulis P, Leftheriotis G, Norton B (1998) Fabrication of evacuated glazing at low temperature. Sol Energy 63:243

10. Papaefthimiou S, Leftheriotis G, Yianoulis P, Hyde TJ, Eames PC, Fang Y, Pennarun PY, Jannasch P (2006) Development of electrochromic evacuated advanced glazing. Energy Build 38:1455
11. Zacharopoulos A, Mondol JD, Hyde TJ, Smyth M (2011) Publication Number WO2011101682, International Patent Application No. PCT/GB2011/050327, 25 Aug 2011
12. Eames PC, Norton B, Griffiths PW, Hyde TJ (2000) International Patent Application No. PCT/GB2000/001495, Publication number WO2000063130, 26 Oct 2000
13. Fieber A et al (2003) Design, Building integration and performance of a hybrid solar wall element. In: Proceedings of ISES solar world congress, Gothenburg, 14–19 June, 2003
14. Fieber A (2004) PV performance of a multifunctional PV/T hybrid solar window. In: Proceedings of 19th european photovoltaic solar energy conference and exhibition, Paris, 7–11 June 2004
15. Davidsson H, Perers B, Karlsson B (2012) System analysis of a multifunctional PV/T hybrid solar window. Sol Energy 86:903
16. Gajbert H, Hall M, Karlsson B (2007) Optimization of reflector and module geometries for stationary, low-concentrating, façade-integrated photovoltaic systems. Sol Energy Mater Sol Cell 91:1788
17. Chemisana D, Ibáñez M, Rosell JI (2011) Characterization of a photovoltaic-thermal module for fresnel linear concentrator. Energy Convers Manag 52:3234
18. Chemisana D, Ibáñez M, Barrau J (2009) Comparison of Fresnel concentrators for building integrated photovoltaics. Energy Convers Manag 50:1079
19. Baig H, Sellami N, Mallick TK (2015) Sol Energy Mater Sol Cell 134:29
20. Chemisana D, López-Villada J, Coronas A, Rosell JI, Lodi C (2013) Building integration of concentrating systems for solar cooling applications. Appl Therm Eng 50:1472
21. Parkyn WA et al (2004) Edge-ray design of compact etendue-limited folded-optic collimators. In: Proceedings of SPIE, vol 5185, p 6
22. Myrskog S et al (2012) Experimental results of Morgan Solar Inc.'s HCPV Sun Simba. In: Proceedings of 8th international conference on concentrating photovoltaic systems, Toledo, 16–18 Apr 2012
23. Morgansolar Sun Simba specifications. www.morgansolar.com. Accessed Sept 2014
24. Gordon JM, Feuermann D (2005) Optical performance at the thermodynamic limit with tailored imaging designs. Appl Opt 44:2327
25. Winston R, Gordon JM (2005) Planar concentrators near the etendue limit. Opt Lett 30:2617
26. Mcdonald M, Barnes C (2008) Spectral optimization of CPV for integrated energy output. In: Proceedings of SPIE, conference: optical modeling and measurements for solar energy systems II. San Diego, 13–14 Aug 2008
27. Maghanga CM, Niklasson GA, Granqvist CG, Mwamburi M (2011) Spectrally selective reflector surfaces for heat reduction in concentrator solar cells: Modeling and applications of TiO_2:Nb-based thin films. Appl Opt 50:3296
28. Liu Y, Hu P, Zhang Q, Chen Z (2014) Thermodynamic and optical analysis for a CPV/T hybrid system with beam splitter and fully tracked linear Fresnel reflector concentrator utilizing sloped panels. Sol Energy 103:191
29. Ulavi TU, Davidson JH, Hebrink T (2014) Analysis of a hybrid PV/T concept based on wavelength selective mirror films. J Sol Energy Eng Trans ASME 136:1
30. Dyson A et al (2007). Integrated concentrating (IC) Solar façade system. In DOE solar energy technologies program review meeting, Colorado, 17–19 Apr 2007
31. Sabry M, Eames PC, Singh H, Yupeng W (2014) Smart windows: thermal modelling and evaluation. Sol Energy 103:200
32. Rawlemon (2014) www.rawlemon.com. Accessed Sept 2014

Analysis of Present and Future Financial Viability of High-Concentrating Photovoltaic Projects

Steve Tomosk, David Wright, Karin Hinzer and Joan E. Haysom

Abstract Three metrics for the financial analysis of high-concentrating photovoltaic (HCPV) systems are assessed: capital costs for fully installed systems (in $/W), the levelized cost of electricity [in $/kilowatt-hours (kWh)], and the net present value [NPV (in $)]. First, capital costs for HCPV systems are shown to have fallen at a steady rate and are characterised by a learning rate of 18 % with a 90 % confidence interval of 14–22 %. The analysis further combines this learning rate with future scenarios for volume growth rates to provide "lower," "middle," and "upper" projections for future capital costs of HCPV systems. These capital cost projections are used as inputs to the LCOE and NPV calculations, from which present and future project viability is assessed for a number of different project conditions. A case study for an HCPV deployment in Las Vegas exhibited an LCOE of $0.125/kWh in 2014 under the "middle" capital cost scenario, which decreases to $0.072/kWh by 2020. For project locations and situations where electricity rates vary according to different hours of the day, the NPV calculation provides a better assessment of financial viability. A detailed methodology with month-hour computation of revenues was developed and applied to two offsetting case studies: Las Vegas, Nevada (with time-of-use electricity prices for small businesses) and Ottawa, Ontario (with a large business rate structure that depends on peak demand). HCPV provides a good match for peak demand times, and the correspondingly high tariffs improve profitability compared with flat electricity rates. Both case studies exhibited profitability by 2015 (2018) under the "low" ("middle") capital cost scenarios. The research as a whole indicates that HCPV systems are already competitive with other solar energy technologies and in certain locations may already be able to deliver market-competitive

S. Tomosk · D. Wright
Telfer School of Management, University of Ottawa, 55 Laurier Ave. E, Ottawa K1N 6N5, Canada

K. Hinzer · J.E. Haysom (✉)
SUNLAB Centre for Research in Photonics, University of Ottawa, 800 King Edward, Ottawa K1N 6N5, Canada
e-mail: jhaysom@uottawa.ca

P. Pérez-Higueras and E.F. Fernández (eds.), *High Concentrator Photovoltaics*,
Green Energy and Technology, DOI 10.1007/978-3-319-15039-0_14

electricity costs. As prices continue to fall between now and 2020, many more projects will be profitable in both high- and low-DNI locations depending on the electricity rates and their structure.

1 Introduction

In this chapter, we describe some of the financial analysis necessary to show the economic viability of high-concentrating photovoltaic (HCPV) systems. We take the perspective of the HCPV system manufacturer as well as that of the owner/manager of an installed system, both of whom need to show a profit on their part of the supply chain for solar-generated electric power. We cover the current situation at the time of writing, i.e., the fourth quarter of 2014, as well as projections over the remainder of this decade.

HCPV system manufacturers play into a quickly growing but highly competitive market for solar energy technologies, thus competing against established options such as silicon PV and concentrating solar power. An important metric on which they compete is the capital cost of a complete installed system, which is measured in dollars per watt ($/W). Dollars is the price at which the complete system—including modules, racking, trackers, inverters, cabling, and installation—is sold to the solar farm (herein assumed to be 2014 US dollars). Watts is the peak direct current (DC) power generated by the system in Concentrator Standard Test Conditions of 1 kW of solar irradiance per square meter at a module temperature of 25 °C [1]. Although this is a simple measure, it contains some subtleties.

- First, it subsumes energy conversion efficiency in the multijunction cell and in the concentrating optics in the sense that it focuses on the watts of DC power that result from those efficiencies. It also subsumes cost-effective efficiencies in manufacturing processes and in deployment methods. Because a system producer improves these efficiencies [2], those improvements (and the associated costs) are automatically reflected in a new figure for $/W and therefore do not need to be taken into account separately.
- Second, although $/W is a good measure for comparing among different HCPV systems, it is less useful for comparing HCPV with other electricity-generating technologies. Our estimate of the average capital cost of HCPV in 2014 is $2.40/W [3], and the world median capital cost of nuclear power is $4.10/W [4]. However, a nuclear power plant operates at near full capacity 24 h/day, whereas each peak watt of HCPV can generate far less electrical energy because it only produces during sunny conditions. Moreover, $/W refers only to the capital cost and does not include operating costs (e.g., fuel), which are very different among the various electricity generating technologies.

From the viewpoint of a solar farm operator, it is important to note that the $/W metric does not provide information about the amount of electrical energy, in kilowatt-hours, that the system can be expected to produce because that will depend

on where geographically the system is installed due to factors such as solar resource, temperature, shading, and soiling. A solar farm operator needs to deploy the HCPV system at a location that produces enough kWh of electrical energy that can be sold for a sufficient price in $/kWh to cover the capital cost of the system in $/W. There are two metrics that can be used for such an assessment:

- The levelized cost of electricity (LCOE) is a measure of the average cost of producing electricity over the lifetime of the system, and it can be used to compare among alternative power-generation technologies. It also enables the comparison between the effective cost of production and current electricity market rates: If the market rates are constant, this is an easy comparison.
- There are many situations when the value of electricity varies with the hour, month, and year, typically increasing at times of high demand. In these cases, an appropriate metric is the net present value (NPV) of the HCPV system, which takes into account the capital and operating costs together with the time-dependent value of the power generated.

Section 2 of this chapter covers the $/W metric for HCPV systems including analysis of future trends; Sect. 3 provides a discussion of LCOE; and Sect. 4 presents the NPV metric for the operation of HCPV systems under different tariff structures.

2 Capital Costs with Future Projections

2.1 Historic Capital Costs

HCPV systems have been deployed commercially since 2007 at capital costs varying from $2.09 to $10.00/W [3]. Costs have in general declined since 2007, but there has also been considerable variability in the price at which deals were negotiated within a single year (see Fig. 1).

To make a decision to invest in an HCPV system, a solar farm operator needs to consider not just the economics of investing today but also the economics of waiting to invest at a future point in time. The decline in HCPV system prices can be expected to continue into the future, which, coupled with increasing electricity prices in the future, may imply that it is more profitable to defer the investment decision until a future date. This option is explored in detail in Sects. 4.2 and 4.3 of this chapter. Hence, in addition to current system prices, the operator needs to have estimates of future prices.

A projection of capital costs to 2020 based on a log/linear regression analysis is given in Fig. 1, which shows 90 % confidence intervals (CIs) on the projections to illustrate the extent of the price variability. Such a projection is based entirely on historical trends over time continuing into the future. It does not take into account other factors, such as why prices have declined in the past or whether price trends early in the deployment of a new technology, such as HCPV, might be different from trends after the technology is more established.

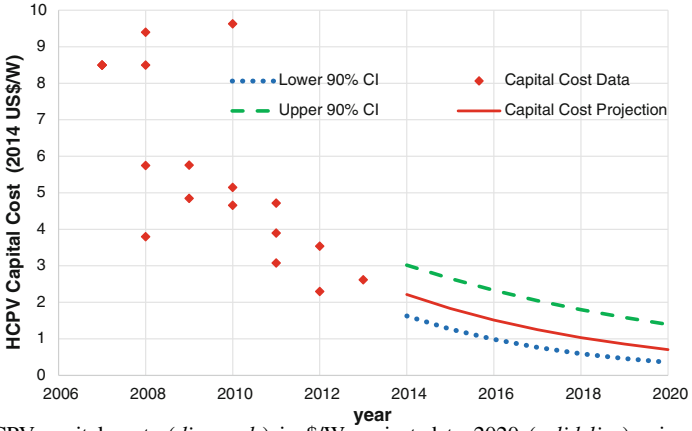

Fig. 1 HCPV capital costs (*diamonds*) in $/W projected to 2020 (*solid line*) using log linear regression with 90 % CIs. The *dashes* represent the upper CI, whereas the *dots* represent the lower CI. Log(capital cost) = −0.190 (year−2000) + 3.46

2.2 Learning Analysis

An improved methodology for projecting technology prices is to relate prices not to time but to deployment volume. This approach has been used in a number of industries including solar power [5] and is based on the "experience curve" or "learning curve." The rationale behind this approach is that as HCPV is deployed, the industry gains experience and hence is able to operate more efficiently. Larger deployment volumes bring more revenue, and thus more research and development money is available to fund efficiency improvements in system technologies. In addition, increased deployments result in improvements in manufacturing and installation methods as well as efficiencies in scale, which further decrease costs. The learning curve equation is:

$$C = \alpha V^{\beta} \tag{1}$$

where C is the cost of HCPV in $/W, and V is the cumulative deployment volume to date in megawatts (MW).

When deployment volume doubles, cost will change in the ratio 2^{β}, thus resulting in a price reduction because typically β is negative. The "learning rate" is defined as the proportional reduction in price and is given by:

$$\mathrm{LR} = 1 - 2^{\beta} \tag{2}$$

In [3], we give HCPV deployment volumes for the period 2007–2013. They are likely more robust than the costs because industry players are more willing to disclose the size of a project in MW than the cost in $/W. A log/log regression of the data according to Eq. (1) results in an estimate of the learning rate of HCPV to

be 18 % with a 90 % CI of 14–22 % [3]. This is a rapid learning rate compared with 11 % for concentrated solar power (CSP) systems [6] and 14 % for PV systems [7]. A higher learning rate for HCPV technology puts the technology in a good competitive position relative to other solar technologies for two reasons. First, doubling in deployment volume can be expected to result in an 18 % reduction in HCPV system price compared with lower percentages for CSP and PV. Second, because current cumulative deployment of HCPV (217.5 MW at the end of 2013) is <1 % of the solar global total, doubling can be achieved with a relatively small number of new MW-sized solar farms compared with the much higher volume required to double the cumulative deployment of CSP and PV.

We next show how the learning curve developed for HCPV can be used to derive more robust price projections than those shown in Fig. 1.

2.3 Projections in Future Capital Costs

The learning curve of Eq. (1) can be used to forecast future costs, C, as long as we know future deployment volume, V. Commercial market projections of deployment volume were obtained from Yole [8] and IHS [9] covering the period 2014–2020.

Three price projections were obtained based on three volume projections: Yole conservative, Yole optimistic, and IHS [3]. Each price projection has a 90 % CI resulting in 9 graphs. As a simplified summary of the many curves, Fig. 2 shows the three projections with only their outermost CIs shown.

These three forecasts give 2020 projections of $1.32, $1.13, and $1.17/W, respectively, based on cumulative deployment volumes of 3.02, 5.12, and 4.65 GW. Comparing Figs. 1 and 2, it can be seen that the trend extrapolation in Fig. 1 results in a price of $0.71/W in 2020, which is significantly lower than those in Fig. 2. The learning curve shows that to achieve a price of $0.71/W in 2020, the cumulative deployment would need to be 26.5 GW, which is excessive compared with the projected volumes from Yole and IHS. In subsequent sections of this chapter, we therefore focus on a price projection derived from the Fig. 2 curves.

3 LCOE with Future Projections

The LCOE is a gauge of the costliness of an energy-generating technology over its operational lifetime. The LCOE for any electricity-generating system can be thought of as the break-even price today for selling electricity produced over all future years of operation [10, 11]. The LCOE is particularly useful for comparing energy producing technologies that sell electricity to the energy marketplace at a consistent price over their operational lifetimes.

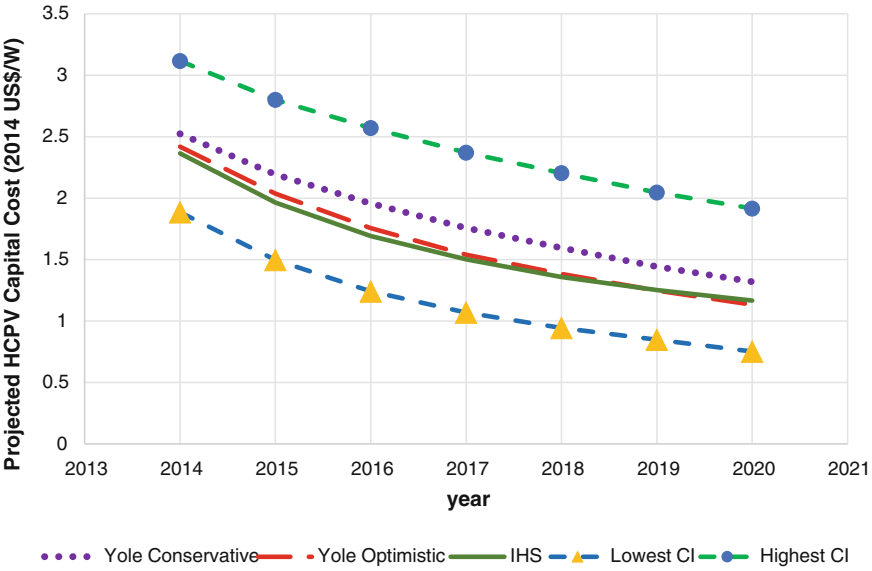

Fig. 2 Projections of HCPV costs in $/W based on the learning curve shown in Eq. (1) and projections of deployment volume from the Yole conservative [8] (*dots* conservative; *long dashes* optimistic) and IHS [9] (*solid line*). The outermost of the 90 % CIs for all three projections are also shown, whereas lowest CI (*dashes* with *triangles*) is derived from the IHS and highest CI (*dashes* with *circles*) is derived the from Yole conservative

We can calculate the LCOE for a solar installation using:

$$\text{Levelized Cost of Electricity} = \frac{I + \sum_{t=1}^{T} M_t \div (1+r)^t}{\sum_{t=1}^{T} E_0(1-dt) \div (1+r)^t} \tag{3}$$

where I is the initial capital expenditure, which occurs in year zero; M_t is the operation and maintenance cost at time t; and E_0 is the amount of energy produced by the system in its first year. The HCPV module degradation rate is denoted by d; r represents the risk-adjusted discount rate; and the total number of operating years is T.

The discount rate is regarded as a rate of required return on invested capital. It can be interpreted as the rate of return an investor could obtain from an alternate investment with a similar amount of risk [12]. Alternatively, the discount rate can be thought of as the cost of financing the debt owed to investors by an organization. For our analysis, we assume a discount rate of 7 % based on [13, 25–27].

Operation and maintenance costs are incurred annually and depend on the kW size of the PV system. We assume these expenditures to be $33.25/kW/year for HCPV, which is 1.75 times the average cost for PV systems [20] due largely to tracking-equipment maintenance. Two additional one-time operational and maintenance expenses for inverter replacement and module recycling are included as fixed costs in our analysis in years 13 and 25, respectively. The cost to replace the inverter

is proportional to the kW size of the HCPV system, whereas the recycling expenditure is dependent on the physical size of the HCPV installation measured in square meters (m^2). The price to replace the inverter in year 13 of the analysis is presumed to be \$0.16/W, and this figure rests on an average 2012 commercial PV system inverter replacement charge of \$0.19/W [13]. The expense to dismantle and recycle HCPV modules at the end of their operational lifetime is taken to be \$18.25/m^2 based on an up-to-date PV module dismantling and recycling fee [14] converted to American dollars at the 2014 average euro/dollar exchange rate at the time of writing.

Degradation is the gradual decrease over time in the energy output capability of solar modules resulting from their ongoing exposure to the outdoor elements [15]. Although an installation's degradation rate could vary over its operational lifetime [16], our HCPV analysis assumes a small, linear rate of 0.5 % based on PV studies [23, 24]. Given that HCPV degradation rates are currently unknown, and a recent publication indicated no measureable degradation after seven years [17], our analysis will assume that the HCPV degradation rate is the same as an accepted rate for PV technologies.

It is important to disclose the assumed input values for each variable found in Eq. (3), and these assumptions are given in Table 1. We presume that system prices are based on projections from Sect. 2.3, and for clarity, the yearly values are tabulated in Table 2. The amount of energy produced by the system, E_0, has been calculated using direct normal irradiance (DNI) data for Las Vegas, Nevada, from the National Solar Radiation Data Base [18] and the Measurements and Instrumentation Data Center [19]. The former is a "typical meteorological year" DNI data set crafted from historic measured values in Las Vegas spanning 1979–2001. The latter data set, in contrast, contains consecutive hourly DNI data for Las Vegas spanning the period 2006–2013. The average of the two datasets provides a yearly DNI value of 2406 kWh/m^2/year. The first year's HCPV energy production is calculated by multiplying the amount of DNI by an assumed HCPV module efficiency and balance-of-system efficiency as follows:

$$E_0 = \text{DNI} \times A \times \eta_{\text{CPV}} \times \eta_{\text{SYS}} \tag{4}$$

where DNI is the annual DNI, η_{CPV} represents HCPV module efficiency, and η_{SYS} denotes HCPV system efficiency. The area, A, is the module area in m^2 derived from the system size:

$$A = \frac{P}{\eta_{\text{CPV}} \times \text{CSTC}} \tag{5}$$

where P is the rated DC power of the HCPV modules in watts, and CSTC is the DNI used for HCPV standard test conditions [1].

Inputting the "middle" 2014 input capital cost of \$2.44/W together with the values of Table 1 into Eq. (3), the LCOE is found to be \$0.125/kWh. Thus, our solar installation would need to sell the electricity it produces at a price of \$0.125/kWh over its 25-year life span of operation to break even.

Table 1 Input values for LCOE calculation using a 100-kW solar installation

Parameter	Symbol	Value	Reference	Notes
HCPV-module power rating	P	100 kW		
Input capital costs	I	\$312,000, \$244,000, \$189,000		2014 values from Eq. (1) and Table 2 costs C, using $I = CP$
Operation and maintenance costs	M_t	\$33.25/kW	[20]	1.75 × PV operation and maintenance costs
DNI solar resource	DNI	2406 kWh/m^2/year	[18, 19]	For Las Vegas
HCPV module efficiency	η_{CPV}	30 %	[21, 22]	
HCPV system efficiency	η_{SYS}	80 %		
Concentrating standard test condition	CSTC	1000 W/m^2	[1]	
HCPV module area	A	333 m^2		By way of Eq. (5)
HCPV energy production	E_0	192,493 kWh/year		By way of Eq. (4)
HCPV degradation rate	d	0.5 %	[23, 24]	
Discount rate	r	7 %	[13, 25–27]	
Project life span	T	25 year		

Table 2 HCPV capital cost scenarios (in \$/W) used in our analysis

Year	Upper (\$/W)	Middle (\$/W)	Lower (\$/W)
2014	3.12	2.44	1.89
2015	2.80	2.06	1.50
2016	2.57	1.80	1.24
2017	2.37	1.60	1.07
2018	2.20	1.45	0.94
2019	2.05	1.31	0.85
2020	1.92	1.21	0.75

Looking toward future trends, we can incorporate the predicted declining capital costs from Table 2 to determine future LCOE values. Here we use the system prices from each of the "upper," "middle," and "lower" cost scenarios for each year, which modify I from Eq. (3). At the same time, we maintain all other assumed values from Table 1. The result is a clearly declining LCOE with time as illustrated by Fig. 3.

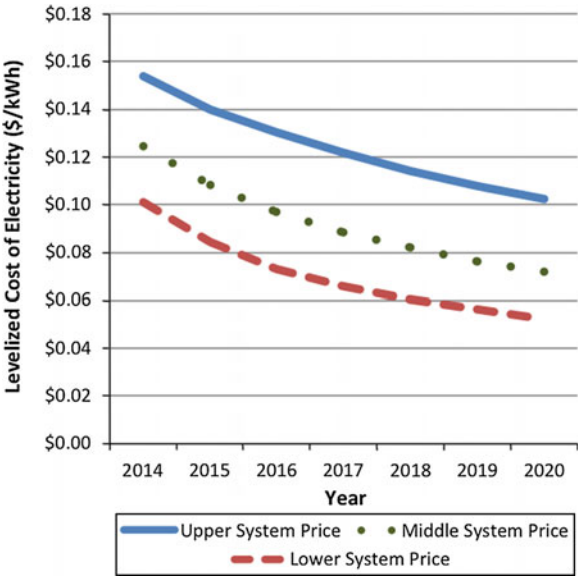

Fig. 3 The LCOE decreases over time due to decreasing HCPV system costs

Thus, diminishing capital costs have a significant impact on the LCOE. The "middle" curve, for example, exhibits an LCOE of $0.072/kWh in 2020, a decrease of 42 % compared with 2014.

From Fig. 2, the "upper" prices correspond to system prices from the "highest CI," whereas the "lower" prices correspond to capital costs projections from the "lowest CI." The "middle" prices are a yearly average of Yole conservative, Yole optimistic, and IHS estimates also from Fig. 2.

The amount of DNI received by a solar installation also affects the LCOE. Las Vegas has a moderately strong solar resource compared with other geographic locations. Regions such as Northern Chile, Southern Africa, and Central China may achieve values in the range of 2600–3000 kWh/m^2/year, whereas the Northeastern United States, Southern Canada, and Central Europe have lower DNI resources in the range of 1300–1600 kWh/m^2/year. To study the sensitivity, we maintain all assumptions from Table 1 with the exception of E_0, which is modified to represent DNI levels spanning 1300–3000 kWh/m^2/year. As illustrated by Fig. 4, the LCOE decreases as the HCPV installation receives more DNI. Even a small increase in DNI by 100 kWh/m^2/year has a noticeable impact on the LCOE.

3.1 LCOE Discussion

The LCOE incorporates many different variables to determine the price at which electricity must be sold over the operational lifetime of the technology to break even. Combining its calculation with the projected future capital cost trends

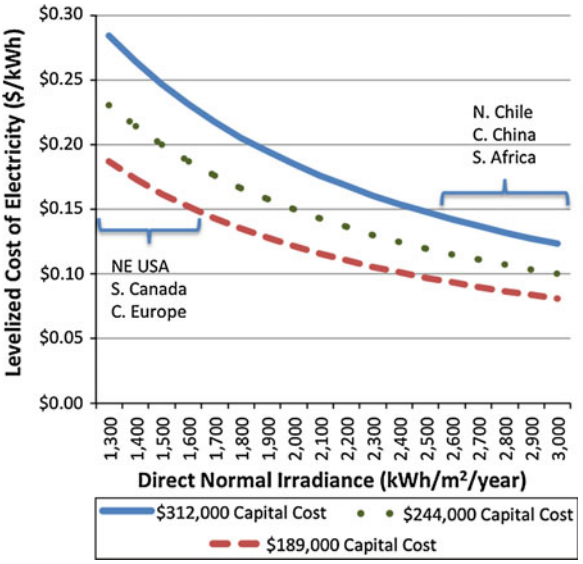

Fig. 4 The sensitivity of the LCOE to the solar resource, shown here for 2014; all curves will shift downwards in future years.

provides a useful indication of the future financial viability of HCPV projects. LCOE values will decrease as HCPV system prices decrease and may be less than the price of grid-produced electricity in some locations presently; this will spread to more locations as prices continue to decrease. The amount of DNI received by an HCPV installation has a significant impact on the LCOE; thus, locations with high DNI will achieve lower LCOE values before locations with low DNI resources. But this will be a dynamic situation: In future years, all prices will decrease. For example, again using the "middle" capital cost curve, Fig. 4 shows that a location with a low DNI of 1400/kWh/m^2/year will have an LCOE of \$0.214/kWh in 2014. However, this will decrease 42 % by 2020 (applying the same trends as in Fig. 3) resulting in a value of \$0.124/kWh, which again may be competitive with 2020 electricity market prices.

The LCOE has limitations and is not an accurate indicator of an HCPV project's financial viability if the project sells its electricity at variable energy market prices. In addition, LCOE calculation is incapable of accounting for the *value* of electricity produced at different times of the day by intermittent energy-producing technologies such as HCPV. Both of these shortcomings, along with disagreements over the values of the inputs used in LCOE calculations, have led some to criticize the application of the LCOE to solar electricity generation [13, 23, 28]. Given these drawbacks, we will now explore an alternative method of assessing the economic viability of a solar installation. This method, often referred to as a "net present value" (NPV) analysis, enables us to take into account the varying wholesale electricity market prices and the time-dependent solar electricity production. As a result, we can obtain a clearer picture of the economic attractiveness of solar energy.

4 NPV with Future Projections

4.1 Methodology

The NPV calculation incorporates several factors into one computation to gauge financial viability, which is measured by the present value of a series of future revenues and expenditures. A typical NPV calculation includes such items as the initial outlay of capital, yearly cash flows, and a discount rate. The yearly cash flows of a HCPV project incorporate the following items:

- Expenses: This includes operation and maintenance costs, an inverter replacement charge, and a recycling fee to be paid at the end of the project's life.
- Revenues: This includes value of the electricity produced by an HCPV installation over each year of operation subject to degradation of equipment over time and variable electricity rates.

To assess financial attractiveness, the sum of the HCPV installation's discounted revenue and expenses is compared with the initial outlay of capital. If the sum of the discounted revenue is greater than the initial outlay of capital, the project is said to have a positive NPV and is economically appealing. The NPV is calculated as:

$$\text{Net Present Value} = -I + \sum_{t=1}^{T} \frac{R_t - M_t}{(1+r)^t} \tag{6}$$

where I is equal to the capital cost incurred in year zero; T denotes the number of years the HCPV installation is operational; and r signifies the discount rate. For each year t of operation, R_t is the revenue attributed to solar electricity production, and M_t represents operation and maintenance costs. Assumptions and values for I, T, $M_{t,}$ and r are taken to be the same as indicated in Sect. 3 for the LCOE calculations. R_t is new and requires further explanation.

At the beginning of year 1, the HCPV installation is assumed to be fully operational. The HCPV modules generate electricity and revenues during this first year of operation as well as in each subsequent year. Revenues, R_t, are equal to the amount of electricity produced, which is measured in kWh, multiplied by an hourly electricity price as follows:

$$R_t = \sum_{\text{mh}} E_{\text{mh}}(t) \times p_{\text{mh}}(t) \tag{7}$$

where $E_{\text{mh}}(t)$ is the alternating current (AC) energy yield from the HCPV system, and $p_{\text{mh}}(t)$ is the electricity price. Both of these variables depend on the month (m) and hour (h), which is the main differentiation from LCOE calculations that derive a fixed value for electricity costs. We assume that the values can be approximated as constant within a given hour of a given month and hence use the subscripts m and h for month and hour, respectively. For example, for 15:00–16:00

in July, an energy yield and electricity price is determined by taking an average of all of the date from 15:00 to 16:00 in the month of July.

The annual energy yield of the HCPV modules begin with an energy yield of $E_{\mathrm{mh}}(0)$ and experience yearly linear degradation, d, as per:

$$E_{\mathrm{mh}}(t) = E_{\mathrm{mh}}(0) \times (1 - d \times t) \tag{8}$$

in the same manner as for the LCOE calculation. As well, the (t) dependence of the variable $p_{\mathrm{mh}}(t)$ is due to the fact that electricity rates may change year by year as will be examined in the case studies to follow.

Furthermore, the derivation of the AC energy yield follows similar lines as Eq. (4) from Sect. 3, but it now also maintains the month hour variability of the raw hourly DNI data:

$$E_{\mathrm{mh}}(0) = \mathrm{DNI}_{\mathrm{mh}} \times A \times \eta_{\mathrm{CPV}} \times \eta_{\mathrm{SYS}} \tag{9}$$

with A, η_{CPV}, and η_{SYS} as defined in Table 1.

Clearly, $\mathrm{DNI}_{\mathrm{mh}}$ and $p_{\mathrm{mh}}(t)$ will be dependent on the project's location, so complete calculations will be undertaken as two case studies in the upcoming sections. We will again use Las Vegas as an example, but we will also include an example calculation for Ottawa, Ontario, Canada. Las Vegas, with similar DNI levels as much of Western and Central Australia, Western South Africa, and Northwestern Saudi Arabia [29], is a more typical HCPV host site than Ottawa, at latitude 45°. For reference, Ottawa has similar DNI levels as Northern Italy and Southern Japan [29]. In our case study, we will show the economic viability of HCPV in Ottawa under the electricity-cost structure of a large business customer with peak demand >3 MW.

We will consider the NPV for a project commencing in year 2014 as well as for investments deferred until future years. Unlike the LCOE analysis, which maintained a fixed system size of 100 kW, the NPV analysis will instead maintain a fixed starting investment value of $1000 in the year 2014. As a result, the deployed system size will vary with each calculation based on the $/W capital cost and project start date. As was the case for the LCOE analysis, the calculations are performed for each of the "lower," "middle," and "upper" system price projections, which are shown in Table 2.

Finally, we note that our NPV analyses will calculate electricity bill *cost savings* instead of revenues. In contrast to selling the electricity produced by our HCPV modules, we will assume that all power is consumed on-site, which consequently avoids the use of an equal amount of electricity from the power grid. By foregoing grid-produced electricity and associated fees, cost savings are generated. This distinction is particularly relevant to the Ottawa case study, where demand charges are decreased by the HCPV generation.

4.2 Las Vegas Case Study

We now provide a detailed NPV calculation for an HCPV project in Las Vegas using the above-mentioned assumptions plus location-specific data for electricity rates and DNI. The same DNI datasets of [18, 19] are employed again to calculate an average $\mathrm{DNI}_{\mathrm{mh}}$.

For electricity prices, we employ time-of-use tariffs currently in effect for small businesses in Las Vegas as shown in Table 3. One can observe that the peak electricity price, which is significantly higher than off-peak prices, occurs over the course of the summer months during the afternoon and early evening. This time frame happens to coincide with the times at which solar modules typically produce their greatest amount of electricity, meaning that our HCPV system will, in all likelihood, generate a disproportionate amount of cost savings when electricity prices are at their peak. The inherent ability of HCPV to match peak electricity prices with peak electricity output is a significant benefit of employing the technology for the purpose of offsetting.

Our analysis assumes that electricity prices will increase at a rate of 0.4 %/year, which is the average rate at which commercial electricity prices in the United States are expected to increase between now and 2040 [31]. We also assume that the hourly structure of the electricity prices remains the same in all years of operation. Thus, the value generated by offsetting, which we denoted as R_t in Fig. 7, can be calculated using the more specific formula:

$$R_t = \sum_{\mathrm{mh}} E_{\mathrm{mh}}(t) \times p_{\mathrm{mh}}(0) \times (1.004)^t \tag{10}$$

where the $p_{\mathrm{mh}}(0)$ is obtained from Table 3.

Table 4 displays an example complete NPV analysis for an HCPV project commencing in 2014 assuming a capital cost of \$1.89/W in year zero and using the assumptions and calculation methods stated previously in this chapter.

According to Table 4, raw cost savings somewhat increase each year due to the assumed slight increase in electricity prices. However, once solar module degradation, the discount rate, as well as costs for operation and maintenance, inverter replacement, and recycling are taken into account, we observe decreasing present values of our net cost savings during the 25-year operational time frame. The result is a negative NPV of −\$188.87 meaning that the HCPV system does not generate

Table 3 Current time-of-use electricity prices for small businesses in Las Vegas, Nevada [30]

Period	Time	Electricity price (per kWh)
June 1st–September 30th	13:00–19:00	\$0.30149
June 1st–September 30th	19:01–12:59	\$0.06262
October 1st–May 31st	00:00–23:59	\$0.05005

Table 4 Complete NPV analysis for a $1000 HCPV-offsetting project beginning in 2014

Year	Cost savings ($)	Degradation (%)	Degradation cost savings ($)	Inverter replacement cost ($)	Recycling cost ($)	Operation maintenance cost ($)	Net cost savings ($)	Discount rate (%)	Present value of net cost savings ($)
0	−1000.00	0.0	−1000.00	0.00	0.00	0.00	−1000.00	7.00	−1000.00
1	92.25	−0.5	91.79	0.00	0.00	17.59	74.20	7.00	69.34
2	92.61	−1.0	91.69	0.00	0.00	17.59	74.10	7.00	64.72
3	92.98	−1.5	91.58	0.00	0.00	17.59	73.99	7.00	60.40
4	93.34	−2.0	91.48	0.00	0.00	17.59	73.88	7.00	56.37
5	93.71	−2.5	91.37	0.00	0.00	17.59	73.77	7.00	52.60
6	94.07	−3.0	91.25	0.00	0.00	17.59	73.66	7.00	49.08
7	94.44	−3.5	91.13	0.00	0.00	17.59	73.54	7.00	45.80
8	94.80	−4.0	91.01	0.00	0.00	17.59	73.42	7.00	42.73
9	95.17	−4.5	90.88	0.00	0.00	17.59	73.29	7.00	39.87
10	95.53	−5.0	90.75	0.00	0.00	17.59	73.16	7.00	37.19
11	95.90	−5.5	90.62	0.00	0.00	17.59	73.03	7.00	34.70
12	96.26	−6.0	90.48	0.00	0.00	17.59	72.89	7.00	32.37
13	96.63	−6.5	90.34	84.66	0.00	17.59	−11.90	7.00	−4.94
14	96.99	−7.0	90.20	0.00	0.00	17.59	72.61	7.00	28.16
15	97.35	−7.5	90.05	0.00	0.00	17.59	72.46	7.00	26.26
16	97.72	−8.0	89.90	0.00	0.00	17.59	72.31	7.00	24.49
17	98.08	−8.5	89.75	0.00	0.00	17.59	72.15	7.00	22.84
18	98.45	−9.0	89.59	0.00	0.00	17.59	72.00	7.00	21.30
19	98.81	−9.5	89.43	0.00	0.00	17.59	71.83	7.00	19.86
20	99.18	−10.0	89.26	0.00	0.00	17.59	71.67	7.00	18.52
21	99.54	−10.5	89.09	0.00	0.00	17.59	71.50	7.00	17.27

(continued)

Table 4 (continued)

Year	Cost savings ($)	Degradation (%)	Degradation cost savings ($)	Inverter replacement cost ($)	Recycling cost ($)	Operation maintenance cost ($)	Net cost savings ($)	Discount rate (%)	Present value of net cost savings ($)
22	99.91	−11.0	88.92	0.00	0.00	17.59	71.32	7.00	16.10
23	100.27	−11.5	88.74	0.00	0.00	17.59	71.15	7.00	15.01
24	100.64	−12.0	88.56	0.00	0.00	17.59	70.97	7.00	13.99
25	101.00	−12.5	88.38	0.00	32.19	17.59	38.60	7.00	7.11
								Net present value	−188.87

any net cost savings. Additional advantageous financial incentives—such as a tax rebate on solar equipment capital costs, renewable energy credits that supplement the price paid for clean energy, or even avoidance of paid sales taxes by the offset—would improve the final financial result. However, these items are outside of the scope of our analysis.

Both of the 2014 "middle" and "upper" $/W capital costs from Table 2 also yield negative NPV results. At installed costs of $2.44/W and $3.12/W, our calculations produce NPVs of −$371.71 and −$508.64, respectively.

Without additional incentives, an HCPV system installed today in Las Vegas to offset grid-produced electricity charges for a small business will not generate a positive NPV over 25 years under any of the 3 pricing scenarios. However, given the steady decrease in HCPV capital costs between 2014 and 2020 as illustrated in [3] and shown in Table 2, we would be wise to investigate future NPVs from investing in an HCPV-offsetting project at a later time. By delaying investment, we can take advantage of a lower capital cost for the HCPV project as well as greater electricity rates to offset. Justification for deferral will be determined by comparing the NPV of projects with start dates between 2015 through to 2020 with each discounted back to 2014.

The idea of forward-looking financial evaluation is a key component of our NPV analysis. When we defer investment, we assume that the $1000 of investment capital is reinvested in risk-free United States treasury notes between 2014 and the start date of the project as per the rates in Table 5. This adds an additional incentive to defer investment because the interest collected, albeit small, increases the total amount of investment capital available.

For projects beginning in 2018 and 2020, we presume that interest on the $1000 of investment capital is accrued for 4 years at 0.88 % and for 6 years at 1.64 %, respectively.

In Fig. 5, we observe the negative NPVs in 2014 stated previously under each of the three pricing scenarios. However, looking no further than the following year, we can see a small, positive NPV for an HCPV system installed at the "lower" 2015 capital cost. Continuing further into the future, we can expect a positive NPV in 2018 according to the "middle" pricing scenario. The "upper" installation costs do not produce any positive NPVs for a HCPV-offsetting project in Las Vegas, Nevada, between 2014 and 2020.

Table 5 Average United States treasury yield rates for 1-, 2-, 3-, and 5-year treasury notes between January 1st and October 31st 2014 [32]

Period (year)	Average 2014 rate (%)	Project start date
1	0.11	2015
2	0.44	2016
3	0.88	2017
5	1.64	2019

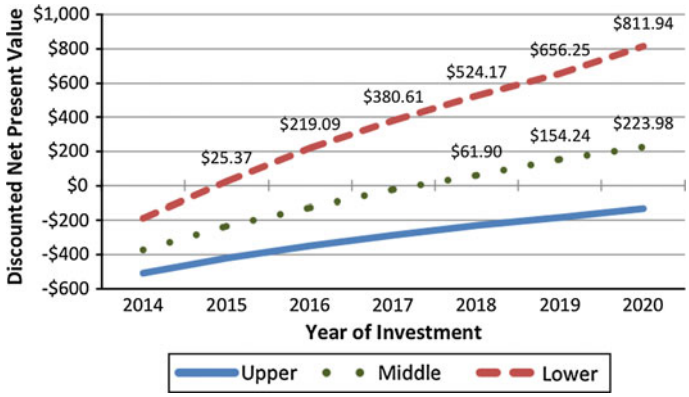

Fig. 5 Net present values calculated using the "upper," "middle," and "lower" capital cost scenarios for Las Vegas, Nevada. Each symbol represents a complete NPV analysis discounted back to 2014

In summary, we examined the prospect of using HCPV to offset electricity costs at a small business in Las Vegas, Nevada, according to current time-of-use rates. Per our results, HCPV investment in Las Vegas for offsetting will be profitable as soon as 2015 if installation prices are low. Otherwise, investment will not be profitable until 2018 or later depending on the capital cost scenario. We will now turn our attention to an HCPV-offsetting project in Ottawa, Ontario, for comparison with these results.

4.3 Ottawa Case Study

One might expect an HCPV project to be unviable in Ottawa, Ontario, given the much lower DNI solar resource in this location compared with Las Vegas, Nevada. However, because of a significantly different electricity rate structure for Ontario customers, with peak energy demands in excess of 3 MW, the actual result is rather interesting. Our Ottawa analysis will employ the same assumptions about HCPV performance, capital, and operating costs from the previous sections but with different DNI data and additional electricity charges to offset for cost savings.

We obtained DNI data for Ottawa from the Canadian Weather Energy and Engineering Datasets [33]. The Ottawa data set contains hourly DNI readings between January 1, 1953, and December 31, 2005, and has an average yearly DNI total of 1455 kWh/m^2/year. From this data set, we developed average $\mathrm{DNI}_{\mathrm{mh}}$ data, which were used to derive AC energy yield values $E_{\mathrm{mh}}(0)$ and $E_{\mathrm{mh}}(t)$ in the exact same manner as Las Vegas. What is unique to this case study is that the calculation of cost savings, R_t, will require three subcalculations due to the manner in which

customers consuming a large quantity of electricity are charged for electricity[1] and how the value from offsetting each of these charges is calculated. The solar project works toward offsetting electricity bill charges by providing both kWh of energy and kW of power, which decrease demand charges using the following formula:

$$R_t = \sum_{\text{mh}} E_{\text{mh}}(t) p_{1,\text{mh}}(t) + 12 p_2(t) \sum_{\text{mh}} \gamma_{2,\text{mh}} \frac{E_{\text{mh}}(t-1)}{1\ \text{h}} + p_3(t) \sum_{\text{mh}} \gamma_{3,\text{mh}} \frac{E_{\text{mh}}(t)}{1\ \text{h}} \tag{11}$$

The centre term in (11) is not present for $t = 1$ because the CPV system is being built in year zero and thus generates no power in that year. In addition, in Eq. (11) the γ_i terms represent probabilities, and the p_i terms represent the three different rate charges, as will be explained in the following paragraphs.

First, customers who consume a large amount of electricity in Ontario are charged the wholesale price of electricity for the energy they consume, which is measured in hourly increments. They also pay other fees that are charged per kWh of energy consumed, which for large customers in Ottawa averaged approximately 50 % of wholesale costs in 2013. Thus, the price p_1 represents both of these charges and is computed herein as 1.5 times the Hourly Ontario Electricity Price data set for 2013. When we multiply p_1 by the HCPV energy yield E_{mh} corresponding to the same hour, we determine that particular hour's cost savings. An overall summation of all hours in the year is performed.

Second, there is a monthly charge based on a *grid peak* demand pricing structure. For each month, the charge is based on the customer's proportion of the Ontario grid's total electricity demand during the *province's five greatest demand peaks* from the *previous* calendar year [34] multiplied by the month's grid demand charge. Those grid peaks typically occur on hot, sunny afternoons in the summer due to air conditioning use. To calculate the average expected power generation that an HCPV project will have in those hours, we multiply the probability of the grid peak occurring during a particular hour $\gamma_{2,\text{mh}}$ [34] by the average expected HCPV energy yield for the same hourly interval $E_{\text{mh}}(t)$. This figure is then divided by 1 h to convert into power. A graph displaying the hours in which grid peak demands have occurred, and the associated probability of these occurrences is shown in Fig. 6. The overall sum of the hours provides the decrease in net grid peak demand that the customer can expect to have achieved in the previous year and which will become their factor for all charges in the subsequent year. Thus, the sum is then multiplied by the monthly grid peak demand charge p_2 of $24.35/kW (converted from 26.70 CAD/kW [34, 35]) and then by 12 to calculate the total peak demand cost savings for 1 year.

Third, the local distribution company charges a monthly delivery fee based on the kW consumed during the *customer's* consumption peak each month. For our analysis, we assume a simplified customer whose peak demand occurs between

[1]Canadian electricity prices and related charges are converted to American dollars.

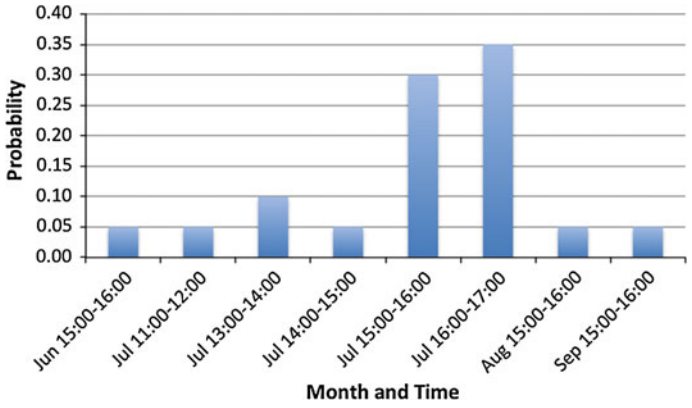

Fig. 6 Historical grid peak demand charge occurrences and associated probabilities. All individual hours for which the probability is nonzero during the 4 years of the program are provided

09:00 and 10:00 from November to March and between 13:00 and 14:00 from April to October. These times represent substantial air conditioner use in summer afternoons and morning peaks in the colder months of the year when the business commences daily operations. This is equivalent to setting the probability $\gamma_{3,\mathrm{mh}}$ to 1 for these 12 h of the year and to zero for all others hours. HCPV energy $E_{\mathrm{mh}}(t)$ is again divided by 1 h to convert into power. The sum is multiplied by the monthly delivery charge p_3 of \$6.42/kW for large consumers of Hydro Ottawa (converted from 7.04 CAD/kW [36]) and then multiplied by 12 to calculate the total customer demand cost savings for 1 year.

A sum of these three terms provides us with the total cost savings for 1 year for offsetting electricity charges. The next step is to consider how the rates $p_{1,\mathrm{mh}}(t)$, $p_2(t)$, and $p_3(t)$ will change over time in years t to estimate the quantity of cost savings our HCPV installation will generate during each of its 25 years of operations. We turn to the Government of Ontario's most recent Long-Term Energy Plan, which was released in 2013 [37]. It provides estimates for future changes to wholesale electricity prices and rates of peak demand charges, which we incorporate into the NPV calculation for future years [38]. For example, the Long-Term Energy Plan projects that wholesale electricity prices $p_{1,\mathrm{mh}}(t)$ are expected to nearly double between 2013 and 2023, while at the same time grid peak charges $p_2(t)$ are anticipated to slightly decrease. The large energy customer's monthly peak consumption charges, $p_3(t)$, are assumed to remain relatively stable over time [37].

Clearly, this is a complex calculation, and more detailed explanations can be found in [38]. The entire NPV calculation is once again analysed for HCPV projects commencing in 2014–2020 (inclusive) and discounted back to 2014 with results shown in Fig. 7.

According to Fig. 7, we will realize negative discounted NPVs if we make an HCPV investment in 2014 under any of the three pricing scenarios from Table 2. However, similar to the case of Las Vegas, deferring HCPV investment by just

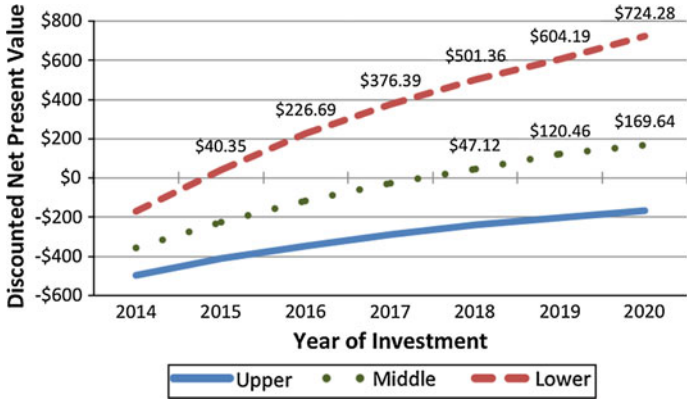

Fig. 7 Discounted NPVs for each of the "upper," "middle," and "lower" HCPV pricing scenarios for Ottawa, Ontario. The $/W capital costs used to calculate these values are shown in Table 2

1 year to 2015 yields a positive NPV under the "lower" pricing scenario even when the NPV is discounted back to 2014 at a discount rate of 7 %. By 2018, there is a positive NPV for the "middle" price projection, and profitability increases with each successive year. Regarding the "higher" installed capital costs, Fig. 7 shows an increase in NPV between 2014 and 2020, but these figures fail to cross into positive territory during this time frame.

4.4 NPV Discussion

Compared with Las Vegas, Ottawa is not a typical location for an HCPV installation. However, we illustrated in Sect. 4.3 that an HCPV-offsetting project for a large business in Ottawa can generate cost savings given the electricity pricing structure in place in Ontario. We observe multiple commonalities between the NPV results for Ottawa and Las Vegas. In 2014, HCPV offsetting projects in both locations did not generate any positive net cost savings. But we do observe positive cost savings in both Ottawa and Las Vegas beginning in 2015 under the "lower" pricing scenario and in 2018 according to the "middle" capital costs. Neither location realizes positive net cost savings under the "upper" pricing scenario.

In 2015, when positive net cost savings are realized under the "lower" pricing scenario in both locations, Ottawa's discounted NPV of $40.35 is greater than the $25.37 discounted NPV in Las Vegas. In 2016, Ottawa also has a higher discounted NPV of $226.69 compared with Las Vegas' $219.09. However, we see a changeover in 2017 when Las Vegas replaces Ottawa as the city with the greater discounted NPV from offsetting electricity charges. This is due to projections of diminishing grid peak rates in Ontario [37, 38]. Although DNI levels for Las Vegas are significantly greater than those for Ottawa, the electricity charge structure in

Ontario keeps Ottawa's NPVs in line with those observed in Las Vegas. Under average projected prices, our Ottawa and Las Vegas analyses have shown that HCPV projects built in 2018 or thereafter are expected to be profitable when selling electricity at market rates without any subsidies or incentives.

5 Conclusions

HCPV technology has exhibited strong efficiency improvements and provides a compelling promise toward further significant efficiency gains. The marketplace for HCPV is considered nascent, meaning it has room for manufacturing cost-efficiencies as it further matures and expands. This chapter shows, conclusively, that HCPV technology also has a strong track record and promises decreasing system costs and financial viability in the future.

The three metrics for financial analysis assessed in this chapter were capital costs (in $/W), LCOE (in $/kWh), and NPV (in $). First, capital costs for HCPV systems were shown to have decreased at a steady, significant rate. The trend is characterised by a learning rate of 18 % with a 90 % CI of 14–22 %. This is greater than those for other solar system technologies. Our analysis further combines this learning rate with future scenarios for HCPV-deployed volume growth rates from three different market scenarios to provide projections for future capital costs of HCPV systems. By 2020, prices are projected to reach $1.32, $1.13, and $1.17/W corresponding to cumulative deployment volumes of 3.02, 5.12, and 4.65 GW, respectively. It should be noted that these cumulative volumes are all extremely small compared with the size of the entire solar industry and thus allow for strong growth to quickly enable the further realization of very low cost HCPV. The research as a whole indicates that HCPV systems are already competitive with other forms of solar energy and are projected to show the strongest decreases in capital costs over time. Thus, now is a realistic time to begin considering HCPV technologies for future projects.

Using these capital cost projections, we evaluated the cost of electricity produced from HCPV using the LCOE method. This method is useful for generalized evaluations, in particular when electricity is sold at a flat rate, and for comparisons with other electricity-generating technologies. We undertook a case study for a HCPV deployment in Las Vegas, which has an average yearly DNI of 2406 kWh/m^2. We calculated an LCOE of $0.125/kWh in 2014 under the "middle" capital cost scenario, which decreased to $0.072/kWh by 2020. The analysis was further augmented to include "lower" and "upper" capital cost projections. Furthermore, the sensitivity of LCOE to the DNI resource was explored again for multiple capital cost projections. Clearly, the LCOE depends on both DNI and capital costs: For "middle" cost projections, the LCOE may be as low as $0.10/kWh in high-DNI regions today. These electricity prices are extremely competitive with market rates for electricity in most parts of the world, and these low prices will rapidly extend to lower DNI regions in future years.

For project locations and situations where electricity rates vary according to different hours of the day, alternate approaches must be employed to assess financial viability. We have developed an NPV methodology with month hour computation of revenues. Two case studies were undertaken using this methodology: Las Vegas, Nevada (with time-of-use electricity prices) and Ottawa, Ontario (with a complex rate structure and dependencies on grid and customer peak demands). HCPV provides a good match for high electricity prices and peak demand hours, which typically occur around midday during the summer months. This matching improves HCPV system profitability much more so than if non-peaking average electricity rates were in place. Both case studies showed negative, nonattractive NPVs for 2014. However, when considering future capital cost projection scenarios for the years 2014 and 2020, both studies exhibited profitability for 2015 (2018) under "lower" ("middle") capital cost scenarios. Any subsidies or incentives, if available, for HCPV projects would further aid with profitability at earlier dates.

Given that project development can often take ≥3 years from initial concept to a fully realized system, our predictions indicate that interested institutions, installers, developers, and policymakers should already have HCPV technology on their radar as a profitable candidate for renewable energy generation.

References

1. IEC (2013) IEC 62670-1 Photovoltaic concentrators (CPV)—performance testing—part 1: standard conditions
2. National Renewable Energy Laboratory (2014) Best research cell efficiencies. http://www.nrel.gov/nCPV/images/efficiency_chart.jpg. Accessed 12 Sept 2014
3. Haysom JE, Jafarieh O, Anis H, Hinzer K, Wright D (2014) Learning curve analysis of concentrated photovoltaic systems. In: Prog Photovoltaics: Res Appl doi:10.1002/pip.2567
4. World Nuclear Association (2014) The economics of nuclear power. http://www.world-nuclear.org/info/Economic-Aspects/Economics-of-Nuclear-Power/. Accessed 15 Sept 2014
5. Luque A, Hegedus S (2011) Handbook of photovoltaic science and engineering, 2nd edn. Wiley, Chichester
6. Hernandez-Moro J, Martınez-Duart JM (2013) Analytical model for solar PV and CSP electricity costs: present LCOE values and their future evolution. Renew Sustain Energy Rev 20:119–132. doi:10.1016/j.rser.2012.11.082
7. Kersten F, Doll R, Kux A, Huljić DM, Görig MA, Breyer C, Müller JW, Wawer P (2011) PV learning curves: past and future drivers of cost reduction. In: Proceedings of the 26th European photovoltaic solar energy conference (EUPSEC), Hamburg, Germany, 5–9 Sept 2011
8. Yole Développement (2013) High-concentration photovoltaics business and technology update report. http://www.i-micronews.com/reports/High-Concentration-Photovoltaics-Business-Update-report/5/358/. Accessed 13 Sept 2014
9. IHS (2013) Concentrated photovoltaic solar installations set to boom in the coming years. http://press.ihs.com/press-release/design-supply-chain/concentrated-photovoltaic-solar-installations-set-boom-coming-year. Accessed 13 Sept 2014
10. Darling SB, You F, Veselka T, Velosa A (2011) Assumptions and the levelized cost of energy for photovoltaics. Energy Environ Sci 4:3133–3139. doi:10.1039/c0ee00698j

11. Borenstein S (2012) The private and public economics of renewable electricity generation. J Econ Perspect 26(1):67–92. doi:10.1257/jep.26.1.67
12. Pratt SP, Grabowski RJ (eds) (2014) Defining cost of capital. In: Cost of capital: applications and examples. Wiley, Hoboken, pp 1–10
13. Bazilian M, Onyeji I, Liebreich M, MacGille I, Chased J, Shahf J, Gieleng D, Arenth D, Landfeari D, Zhengrongj S (2013) Re-considering the economics of photovoltaic power. Renew Energy 53:329–338. doi:10.1016/j.renene.2012.11.029
14. Di Francia G (2013) The impact of recycling policies on the photovoltaic levelized cost of the electricity. In: Proceedings of the international conference on renewable energy research and applications (ICRERA), Madrid, Spain, 20–23 Oct 2013
15. Lyden S, Haque ME, Gargoom A, Negnevitsky M, Muoka PI (2012) Modelling and parameter estimation of photovoltaic cell. In: Proceedings of the 22nd Australasian universities power engineering conference (AUPEC), Bali, Indonesia, 26–29 Sept 2012
16. Phinikarides A, Kindyni N, Makrides G, Georghiou GE (2014) Review of photovoltaic degradation rate methodologies. Renew Sustain Energy Rev 40:143–152. doi:10.1016/j.rser.2014.07.155
17. Gerstmaier T, Rottger M, Zech T, Moretta R, Braun C, Gombert A (2014) Five years of CPV field data: results of a long-term outdoor performance study. Paper presented at the 10th international conference on concentrating photovoltaics, Albuquerque, New Mexico, 7–9 Apr 2014
18. National Renewable Energy Laboratory (2014) 723860 Las Vegas McCarran Intl AP. In: National solar radiation data base 1991-2005 update: typical meteorological year 3. http://rredc.nrel.gov/solar/old_data/nsrdb/1991-2005/data/tmy3/723860TY.csv. Accessed 2 Oct 2014
19. Nevada Power (2014) DAILY PLOTS and RAW DATA FILES 27 Mar 2006–1 Oct 2014. http://www.nrel.gov/midc/apps/day.pl?NPC. Accessed 2 Oct 2014
20. National Renewable Energy Laboratory (2013) Distributed generation energy technology operations and maintenance costs. http://www.nrel.gov/analysis/tech_cost_om_dg.html. Accessed 2 Oct 2014
21. Fernández EF, Pérez-Higueras P, Garcia Loureiro AJ, Vidal PG (2013) Outdoor evaluation of concentrator photovoltaic systems modules from different manufacturers: first results and steps. Prog Photovoltaics Res Appl 21(4):693–701. doi:10.1002/pip.1262
22. Kurtz S (2012) Opportunities and challenges for development of a mature concentrating photovoltaic power industry. Available via National Renewable Energy Laboratory Publications. http://www.nrel.gov/docs/fy13osti/43208.pdf. Accessed 3 Oct 2014
23. Branker K, Pathak MJM, Pearce JM (2011) A review of solar photovoltaic levelized cost of electricity. Renew Sustain Energy Rev 15(9):4470–4482. doi:10.1016/j.rser.2011.07.104
24. Reichelstein S, Yorston M (2013) The prospects for cost competitive solar PV power. Energy Policy 55:117–127. doi:10.1016/j.enpol.2012.11.003
25. Swift KD (2013) A comparison of the cost and financial returns for solar photovoltaic systems installed by businesses in different locations across the United States. Renew Energy 57:137–143. doi:10.1016/j.renene.2013.01.011
26. Barbose G, Darghouth N, Weaver S, Wiser R (2013) Tracking the sun VI: an historical summary of the installed price of photovoltaics in the United States from 1998 to 2012. Available via Lawrence Berkeley National Laboratory. http://emp.lbl.gov/sites/all/files/lbnl-6350e.pdf. Accessed 6 Oct 2014
27. Poullikkas A, Hadjipaschalis I, Kourtis G (2013) Parametric assessment of concentrated photovoltaic parks for the Mediterranean region. Int J Sustain Energ 32(1):42–52. doi:10.1080/14786451.2011.595794
28. Joskow PL (2011) Comparing the costs of intermittent and dispatchable electricity generating technologies. Am Econ Rev Pap Proc 100(3):238–241. doi:10.1257/aer.100.3.238
29. GeoModal Solar (2013) World map of direct normal irradiation. http://solargis.info/doc/_pics/freemaps/1000px/dni/SolarGIS-Solar-map-DNI-World-map-en.png. Accessed 30 Oct 2014

30. NV Energy (2014) Business time of use for southern service territory. https://www.nvenergy.com/business/paymentbilling/timeofuse.cfm. Accessed 7 Oct 2014
31. U.S. Energy Information Administration (2014) Annual energy outlook 2014. Available via U.S. Energy Information Administration Independent Statistics & Analysis. http://www.eia.gov/forecasts/aeo/pdf/tbla8.pdf. Accessed 8 Oct 2014
32. U.S. Department of the Treasury (2014) Daily treasury yield curve rates. http://www.treasury.gov/resource-center/data-chart-center/interest-rates/Pages/TextView.aspx?data=yieldYear&year=2014. Accessed 31 Oct 2014
33. Government of Canada (2013) Index of /Pub/Engineering_Climate_Dataset/Canadian_Weather_Energy_Engineering_Dataset_CWEEDS_2005/ZIPPED FILES/ENGLISH/. ftp://client_climate@ftp.tor.ec.gc.ca/Pub/Engineering_Climate_Dataset/Canadian_Weather_Energy_Engineering_Dataset_CWEEDS_2005/ZIPPED%20FILES/ENGLISH/ONTARIO.zip. Accessed 6 Oct 2014
34. Independent Electricity Service Operator (2014) Global adjustment for class A. http://www.ieso.ca/Pages/Participate/Settlements/Global-Adjustment-for-Class-A.aspx. Accessed 7 Oct 2014
35. Independent Electricity Service Operator (2014) Global adjustment—archive. http://www.ieso.ca/Pages/Participate/Settlements/Global-Adjustment-Archive.aspx. Accessed 6 Oct 2014
36. Hydro Ottawa (2014) Rates and conditions. https://hydroottawa.com/business/rates-and-conditions/. Accessed 6 Oct 2014
37. Ontario Power Authority (2014) Cost of electricity service 2013 LTEP: module 4. Available via Ontario Power Authority. http://powerauthority.on.ca/sites/default/files/planning/LTEP-2013-Module-4-Cost.pdf. Accessed 7 Oct 2014
38. Tomosk S (2015). An application of photovoltaic offsetting to reduce electricity costs at Ontario data centers. Master's thesis, University of Ottawa (in writing)

Economic Evaluation of High-Concentrator Photovoltaic Systems

D.L. Talavera and G. Nofuentes

Abstract Before the installation of an high-concentrator photovoltaic (HCPV) system, any project developer or prospective owner must assess the economic and financial feasibility of the investment. This chapter has a tutorial content that is aimed at providing the reader with the necessary tools to accomplish that task. Some fundamentals and profitability indices are shown, reviewed, and adapted to the peculiarities of HCPV (i.e., net present value [NPV], benefit-to-cost ratio [BCR], internal rate of return [IRR], etc.). Both economic and financial analyses depend on a wide variety of factors that configure a specific scenario. Two scenarios are provided to illustrate the proposed tools. (1) The first scenario corresponds to the end of 2013 with a cumulative installed HCPV power that adds up to 160 MWp outlined as follows: assumed initial investment cost of 1800 €/kWp with 80 % financed by means of a loan and 20 % funded through equity, a feed-in-tariff scheme of 0.10 €/kWh with an annual direct normal irradiation of 2200 kWh/m^2, and a weighted average cost of capital (WACC) assumed equal to 6.5 %. Such an investment is feasible from an economic viewpoint since IRR = 7.2 % > 6.5 % and BCR = 1.08 > 1. However, this investment fails to be financially feasible because negative cumulative net cash balances appear during the first 15 years of the system's operation. (2) The second scenario is assumed to take place in 2020 so that forecasting both costs and the financial environment has been required. Cumulative installed HCPV power is predicted to be equal to 1400 MWp by the end of 2020. Learning curves, in which a progress ratio of 0.80 is assumed, lead to an initial investment cost of 800 €/kWp, which is also financed by external capital (80 %) and equity (20 %). HCPV-generated electricity is assumed to be entirely fed to the grid at a pool price of 0.05 €/kWh. In addition, there is an annual direct irradiation of 2200 kWh/m^2 and a WACC of 4.5 % are assumed. This investment does not only prove to be feasible from an economic point of view because IRR = 8.5 %, which is well above 4.5 %, and BCR = 1.5 > 1, it is also viewed favourably from a financial viewpoint because positive cumulative net cash balances are obtained over the whole project life cycle. Consequently, the economic and financial viability of

D.L. Talavera (✉) · G. Nofuentes
IDEA Research Group, University of Jaén, Campus las Lagunillas s/n, 23071 Jaén, Spain
e-mail: dlopez@ujaen.es

P. Pérez-Higueras and E.F. Fernández (eds.), *High Concentrator Photovoltaics*,
Green Energy and Technology, DOI 10.1007/978-3-319-15039-0_15

HCPV is likely to take place at the turn of this decade. Last, a sensitivity analysis of IRR and BCR to each considered factor has been performed for both two scenarios. This analysis ranks these factors according to lowest to highest effect on IRR and BCR as follows: annual degradation rate, income tax rate, annual operation and maintenance cost, life cycle of the HCPV system, discount rate, annual direct normal irradiation, and initial investment cost of the HCPV. Annual final yield, performance ratio, and HCPV electricity unitary price exert the same influence on IRR and BCR. Stand out that these three factors are function of the annual direct normal irradiation.

1 Introduction

High-concentrator photovoltaics (HCPV) is an emerging and promising technology: Electricity is produced by means of harnessing an inexhaustible energy source without causing any significant environmental impact. However, project developers and prospective owners of HCPV systems need information regarding the economic and financial feasibility of such systems. This chapter is mainly addressed to provide the tools and enable the reader to carry out this economic and financial assessment. Multiple factors are involved in this analysis, so an effort has been made to take as many as possible of them into account. Just to give an example, income taxation and tax depreciation, which are considered here but often are overlooked by similar works to that presented here. However, unrealistic results might be obtained if their impact is ignored. Likewise, aspects related to financing are frequently missed. In this sense, special care should be taken because financial feasibility implies economic profitability, yet the reverse is not always true.

First, some basic concepts and fundamentals related are presented. Then some methods commonly used to assess the economic profitability analysis of investment projects in renewable energies are reviewed [8, 10, 52, 57, 60, 61]. Namely, expressions to calculate the IRR, the net present value (NPV), the benefit-to-cost ratio (BCR), and the discounted payback time (DPBT) are proposed. Some shortcomings identified in these methods lead to the introduction of the modified internal rate of return (MIRR), the modified net present value (MNPV), and the real net present value (RNPV). The financial dimension of the investment is also approached.

Two scenarios have been considered in which the previously mentioned methods and concepts are applied. One of them assumes technical and economic data corresponding to the end of 2013, whereas the other corresponds to the end of this decade. Learning curves and cumulative installed HCPV power projections, together with some factor forecasting, configure the prospective scenario assumed for 2020.

Last, the above-mentioned two scenarios are considered base cases with which to carry out an analysis of the sensitivity of IRR, NPV, and BCR to the factors on which they depend. This is especially interesting to quantitatively assess how

changes in these factors influence the profitability of HCPV systems. Such an analysis may prove useful to a potential investor if estimates of future values of some factors were to make postponing his/her investment advisable.

2 Fundamentals and Concepts

In this section, some concepts used in the profitability analysis of investment projects, mainly cash inflows (CIs) and cash outflows (COs) generated by the operation and development of the project, are reviewed. In addition, a number of assumptions will be established so as to be considered in the economic evaluation of a project. In addition, the financial dimensions of an investment project will be reviewed.

2.1 Net Cash Flow

Net cash flow (NCF [in €]) over a given time period (t) is the difference between the CIs (in €) and COs (in €) generated by the operating activities of project during this time period. It may be written as:

$$\mathrm{NCF}_t = \mathrm{CI}_t - \mathrm{CO}_t \tag{1}$$

where NCF_t (€) = NCF during t, CI_t (€) = all revenue, specifically sales revenues, collected over t, and CO_t (€) = operating and maintenance cost for period t. Parameter t is usually assumed equal to 1 year.

The above expression may be broken down, according to the concepts where the resources are allocated, so that:

$$\mathrm{NCF}_t = \mathrm{RI}_t + I_t + \mathrm{di}_t + \mathrm{IT}_t + \mathrm{NCB}_t \tag{2}$$

where RI_t (€) = repayment instalments on funds borrowed (debt and/or equity capital) to fund the investment project, I_t (€) = interest charges on debt, di_t (€) = dividends, i.e., return on equity capital, paid, IT_t (€) = taxes paid on income, and NCB_t (€) = net cash balance, which represents the liquidity, i.e., the remaining money after all of these payments. All of these parameters are referred to year t. The above parameters are shown in Fig. 1.

If after-tax net the effect of taxation is taken into account in NCFs, cash flows is obtained during year t ($\mathrm{NCF}_{t(\text{after-tax})}$ [in €]) by:

$$\mathrm{NCF}_{t(\text{after}-\text{tax})} = \mathrm{NCF}_t \cdot (1 - T) + \mathrm{DEP}_t \cdot T \tag{3}$$

where DEP_t (€) = tax depreciation during year t, and T = income tax rate.

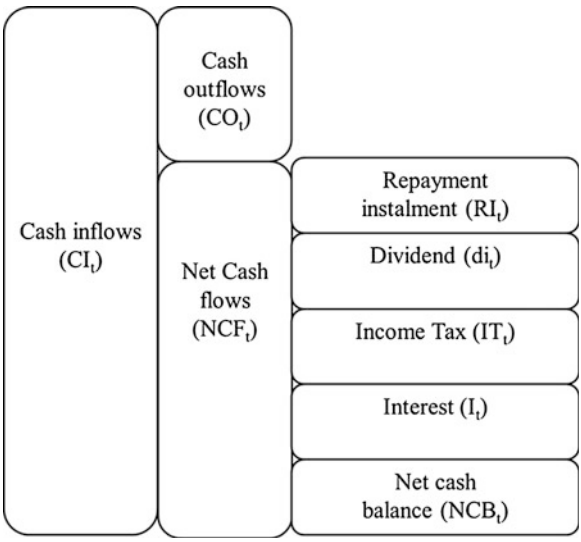

Fig. 1 Breakdown of net cash flows

As with Eq. (2), the above expression may be broken down, according to the concepts where the resources are allocated, so that:

$$\mathrm{NCF}_{t(\mathrm{after-tax})} = \mathrm{RI}_t + I_t(1-T) + \mathrm{di}_t + \mathrm{NCB}_t \tag{4}$$

The influence of taxation on funds borrowed to finance an investment is exerted on the paid debt interest (I_t [in €]) because it is tax deductible. Accordingly, taxation leads to a decrease in the cost of capital. Hence, interests after paying taxes during year t ($I_{t(\text{after-tax})}$ [in €]) are given by:

$$I_{t(\mathrm{after-tax})} = I_t(1-T) \tag{5}$$

2.2 Time Value of Money: The Discount Rate

Money has time value. The value of a certain amount of money today is more valuable than its value tomorrow. Money has time value because of the following reasons:

- Investment opportunities: An investor can profitably employ a certain amount of money received today to give him/her a higher value to be received tomorrow or after a certain period of time.
- Risk and uncertainty: Future is always uncertain and risky. Money you have now is not at risk. Money predicted to arrive in the future is less certain.

- Inflation: in an inflationary scenario, the money received today, has more purchasing power than the money to be received in future. In other words, a sum today represents a greater real purchasing power than a sum a year afterwards.

The time-value of money is the relationship between the previous factors and time. By using the present value approach and assuming an opportunity cost rate (r) and an inflation rate (i), a sum S (€) received at the present time has a future worth of $S[(1 + r)\,(1 + i)]^n$ after n years. Consequently, a sum S to be received after n years has a present worth of $S/[(1 + r)\,(1 + i)]^n$. Factor r is normally termed "real discount rate" so that the nominal discount rate, or simply discount rate, is stated as d, $1 + d = (1 + r)\,(1 + i)$. Last, parameter r is also noted as d_r. Thus, the fundamental principle behind the concept of time value of money is that a sum of money received today is worth more than the same sum received after a certain period of time.

Choosing an appropriate value of d is a controversial issue. The appropriate selection of a value of d for the analysis of a given investment project should be the rate of return for an investment of comparable risk that would be made instead. A widespread practice in organizations is to use a discount rate equal to the organization's weighted average cost of capital (WACC) [56]. WACC is the cost that the owner or investor of the project must pay for using capital sources to finance the investment. It is also common to use a discount rate equal to the opportunity cost of capital. The latter cost is based on opportunities arising from the financial market. Therefore, the value of the discount rate would be equivalent to the price of money determined by the free interplay of supply and demand. It also may represent the rate of return on the best alternative investment available.

2.3 Financial Dimensions of Projects

This section analyzes investment projects from a financial standpoint. An investment project with associated funding will be considered. This financing process implies collecting the funds needed for the investment. Despite the fact that a wide variety of instruments can be used to finance investment projects, the following two are the most widespread ones:

1. "Equity capital: Equity capital is high-risk financing that expects high returns. An equity investment can be made in support of a specific project, or equity funds can be provided to the company carrying out the project. Equity investors maintain the right to get involved in the decision-making process of the project or company to protect their investment.
2. Debt: Debt presents medium risk with modest expected returns. In contrast to equity investors, lenders who provide debt financing to a project do not own shares in the project. They provide capital for the purpose of earning interest. Because lenders must be repaid before distributions can be made to shareholders, lenders bear less risk than equity holders. For this reason, potential return to lenders is limited to risk-adjusted market interest rates" [65].

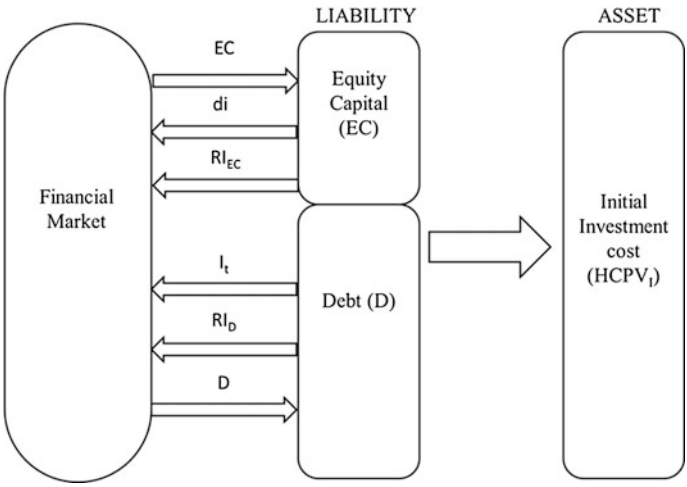

Fig. 2 Financing process of a project

Both types of investment capital are combined to finance the initial investment. The process of financing a project is shown in Fig. 2. The involved parameters are described later in the text.

The initial investment cost ($HCPV_I$ [in €]) is the initial capital expenditure that is set aside to the acquisition of assets of the investment project. It is equal to sum of the equity capital (EC [in €]), e.g., common stocks and preferred stocks, and debt (D [in €]), e.g., long-term loans, Bonds, and mortgage loans, that are used to fund the capital expenditure. The asset of the investment project equals its liability, which is formed by equity capital and debt:

$$\mathrm{HCPV}_I = \mathrm{EC} + \mathrm{D} \tag{6}$$

where RI_{Dt} (€) is the repayment instalments on debt, RI_{ECt} (€) is the repayment installments on equity capital, I_t (€) are the interests paid on debt, and di_{ECt} (€) are the dividends paid on equity capital. All of these parameters are referred to year t.

The result of the financing of a project can be represented as a stream of CIs and COs over time. Because CIs and COs occur at different points in time, it is easier to deal with them using a timeline. A timeline shows the timing and the amount of each CI or CO. This is shown in Fig. 3, which begins with revenue $HCPV_I$, followed by annual periodic costs, so that payment is made at the end of the year. Upward arrows indicate revenues, whereas downward arrows indicate payments.

The investment of the project is analyzed below according to the same criteria used for funding. Once funding is obtained, productive assets purchase market goods. The implementation of the investment will involve a trade with the market as shown in Fig. 4.

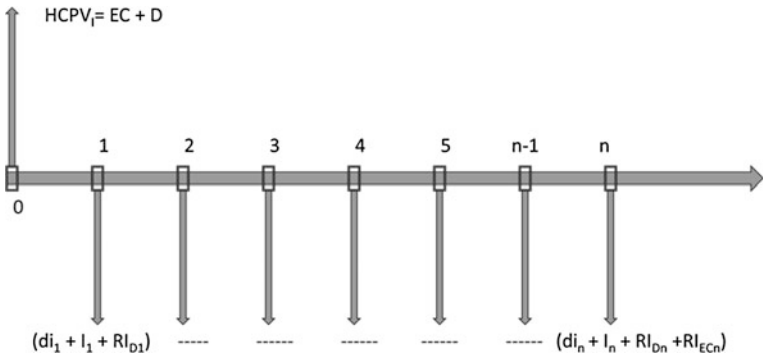

Fig. 3 Financial dimension of financing. In this figure, it has been considered that the loan duration equals the time in which the equity capital is refunded. However, in the most general case, both time periods do not coincide

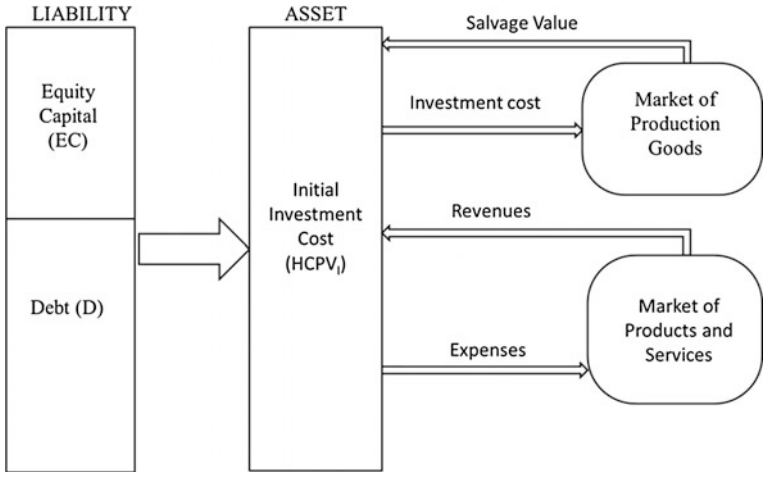

Fig. 4 Investment process of a project

Schneider [55] considers that any investment is characterized from a financial point of view in response to current revenues and payments incurred in the company. The comparison between these two monetary series is important from a practical point of view because it allows us to make an assessment of the investment, thereby obtaining a measure of profitability that it can generate for the company or investor. Consequently, from a financial point of view, i.e., money, any investment project is defined by the following variables:

- Initial investment cost or capital expediture representing an initial payment (HCPV$_I$).
- Net cash flows (NCF$_t$) are the result of the difference between the CIs and COs generated by the operation of the project during year *t*.

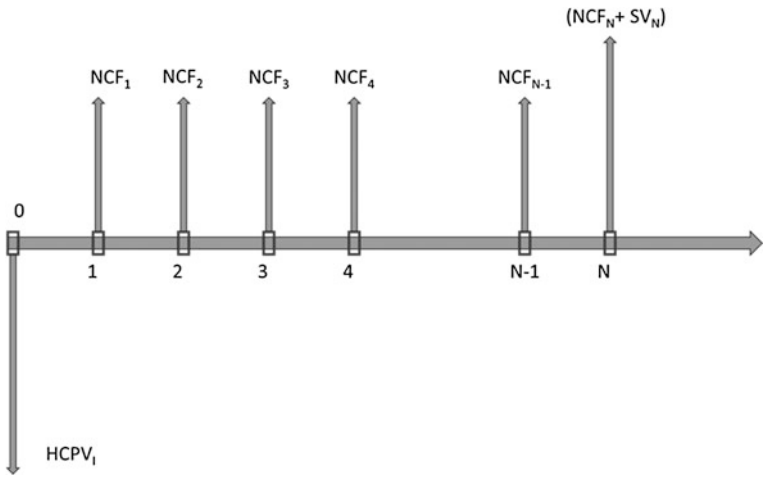

Fig. 5 Financial dimension of an investment

- Analysis period (N [in years]) is the period of time for which an evaluation is performed. N is usually equal to the lifetime of the investment project. The estimate of N is often difficult owing to the amount of variables that influence its quantification.
- Salvage value (SV_N [€]) is a salvage value received by the sale (settlement) of the assets of the investment. This inflow will be obtained by the end of the life cycle of the investment.

Finally, the investment may be represented in the same way as the study of financing of a project. This is shown in Fig. 5: It begins with an $HCPV_I$ payment, followed by a series of NCFs, being effective at the end of the year. At the end of the lifetime of the project, an amount equal to NCF_N plus the salvage value is obtained.

2.4 Evaluation of an Investment Project

The first step in the economic evaluation of a project usually comprises an investment profitability analysis together with a financial analysis. The investment profitability analysis is the measurement of the profitability of the resources allocated to a project, or, in other words, this analysis tries to ascertain the return on the capital investment. Different methods may be used as a basis on which to assess the investment profitability of a project. These methods will be studied in next section.

The financial analysis must take into consideration the financial features of a project to ensure that the disposable finances will permit the smooth implementation

and operation of the project. A simple approach to this financial analysis can be performed for the sum of the CIs and COs on a year-by-year basis, i.e., the financial dimension of the financing and the financial dimension of the investment.

3 Methods for Economic Analysis of a HCPV System

The most common criteria aimed at measuring the profitability of the project, such as the NPV (€), the IRR, the BCR, the DPBT (years), the annualised value (AV [in €]), the MNPV (€), the MIRR, and the RNPV (€) are presented hereafter. Criteria based on NPV, benefdit-to-cost ratio (BCR), AV and IRR, are addressed at measuring profitability, while DPBT is aimed at measuring the liquidity of the investment.

The core idea that lies in the fact that the profitability assessment of investment projects may be broadly summarized as follows: finding a suitable parameter—or a set of them—in which all considered financial factors are taken into account so that a profitability estimation of the investment is provided.

3.1 Net Present Value

The NPV of a project is defined as the difference between the present values of the CIs and COs generated by the investment over the lifetime of the project. The NPV method discounts all of the NCFs of a project to a base year, i.e., the start of the implementation, at a predetermined discount rate. This is given by the expression:

$$\mathrm{NPV} = -\mathrm{HCPV}_I + \mathrm{PV}[\mathrm{NCF}(N)] \tag{7}$$

The present value of the NCFs (PV[NCF(N)] in €) may be written as:

$$\mathrm{PV}[\mathrm{NCF}(N)] = \mathrm{PV}[\mathrm{CI}(N)] - \mathrm{PV}[\mathrm{CO}(N)] + \mathrm{PV}[\mathrm{DEP}(N_\mathrm{d})] \cdot T \tag{8}$$

where PV[DEP(N_d)] (€) is the present value of tax depreciation. The method used in the tax depreciation may be different from one country to another. Usually, the modified accelerated cost recovery system is used as the tax depreciation system in the USA [31]. In any case, readers must refer to the national taxation laws and abide by them.

PV [CO(N)] (€) is the present value of the COs over the lifetime of the project, and it may be written as:

$$\mathrm{PV}[\mathrm{CO}(N)] = \mathrm{PV}[\mathrm{HCPV}_\mathrm{OM}(N)] \tag{9}$$

where PV[$\mathrm{HCPV}_\mathrm{OM}$ (N)] (€) is the present value of the operation and maintenance cost over the system lifetime (N [in years]). It may be written as:

$$\mathrm{PV}[\mathrm{HCPV}_{\mathrm{OM}}(N)] = \left[\mathrm{HCPV}_{\mathrm{AOM}}(1-T)\cdot\frac{Q(1-Q^N)}{1-Q}\right] \tag{10}$$

where $\mathrm{HCPV}_{\mathrm{AOM}}$ (€) is the annual operation and maintenance cost, assumed to be constant over the system's lifetime, while $Q(1 - Q^N)/(1 - Q)$ is the present value interest factor (PVIF[N]). Factor Q is equal to $1/(1 + d)$. Assuming an annual escalation rate of the operation and maintenance cost of the HCPV system (Δ_{OM}), PV[$\mathrm{HCPV}_{\mathrm{OM}}$ (N)] may be rewritten as follows:

$$\mathrm{PV}[\mathrm{CO}(N)] = \left[\mathrm{HCPV}_{\mathrm{AOM}}(1-T)\cdot\frac{Q_{\mathrm{OM}}\cdot(1-Q_{\mathrm{OM}}^N)}{1-Q_{\mathrm{OM}}}\right] \tag{11}$$

where $Q_{\mathrm{OM}} = (1 + \Delta_{\mathrm{OM}})/(1 + d)$.

PV [CI(N)] (€) is the present value of the CIs over the lifetime of the project. Regarding this parameter, CIs are partly obtained by means of the annual HCPV electricity generated that is used for self-consumption (E_{HCPVs} [in kWh]), and consequently saved, instead of buying it from the grid at a given price (p_{s} [in €/kWh]). In addition, CIs are obtained by the annual electricity generation (E_{HCPVg} [in kWh]), partly fed into the grid, that may be compensated for at a different price (p_{g} [in €/kWh]):

$$\begin{aligned}\mathrm{PV}[\mathrm{CI}(N)] = {} & p_{\mathrm{s}}\cdot E_{\mathrm{HCPV_s}}(1-T)\frac{Qp_{\mathrm{s}}\left(1-Qp_{\mathrm{s}}^N\right)}{1-Qp_{\mathrm{s}}} \\ & + p_{\mathrm{g}}\cdot E_{\mathrm{HCPV_g}}(1-T)\frac{Qp_{\mathrm{g}}\left(1-Qp_{\mathrm{g}}^N\right)}{1-Qp_{\mathrm{g}}}\end{aligned} \tag{12}$$

where the factors $Qp_{\mathrm{s}} = (1 + \Delta p_{\mathrm{s}})\cdot(1 - r_{\mathrm{d}})/(1 + d)$ and $Qp_{\mathrm{g}} = (1 + \Delta p_{\mathrm{g}}) \cdot (1 - r_{\mathrm{d}})/(1 + d)$; Δp_{s} and Δp_{g} stand for the annual escalation rate of the electricity price that is consumed and fed from/to the grid, respectively; and factor r_{d} is the annual degradation rate of the efficiency of the PV modules.

As stated previously, this applies to the most general case. However, if the annual HCPV-generated electricity is used for self-consumption in its entirety, Eq. (12) is simplified:

$$\mathrm{PV}[\mathrm{CI}(N)] = p_{\mathrm{s}}\cdot E_{\mathrm{HCPV_s}}(1-T)\frac{Qp_{\mathrm{s}}\left(1-Qp_{\mathrm{s}}^N\right)}{1-Qp_{\mathrm{s}}} \tag{13}$$

Likewise, if the annual HCPV generated electricity is fed into the grid in its entirety, Eq. (12) is also simplified:

$$\mathrm{PV}[\mathrm{CI}(N)] = p_{\mathrm{g}}\cdot E_{\mathrm{HCPV_g}}(1-T)\frac{Qp_{\mathrm{s}}\left(1-Qp_{\mathrm{s}}^N\right)}{1-Qp_{\mathrm{s}}} \tag{14}$$

Regarding the present value of the tax depreciation, it can be calculated by:

$$\mathrm{PV}[\mathrm{DEP}(N_\mathrm{d})] = \sum_{t=1}^{N_\mathrm{d}} \frac{\mathrm{DEP}_t}{(1+d)^t} \tag{15}$$

where N_d (years) is the period of time over which an investment is amortized for tax purposes, and DEP_t (€) is the tax depreciation corresponding to year t. For example, if tax depreciation is assumed linear and constant over a given period of time, the present value of the tax depreciation may be estimated by:

$$\mathrm{PV}[\mathrm{DEP}(N_\mathrm{d})] = \mathrm{DEP}_y \cdot \mathrm{PVIF}(N_\mathrm{d}) \tag{16}$$

where DEP_y (€) is the annual tax depreciation for the HCPV system.

A criticism of the NPV criterion raises the lack of realism on the assumption of reinvestment of intermediate cash flows of the project. NPV assumes reinvestment of interim cash flows, in the same project or a different project, with a rate of return equal to the discount rate until the end of the life cycle of the project. Obviously, such reinvestment rate need not necessarily be equal to the discount rate assumed for the project.

The project is profitable or feasible if the calculated NPV is positive after using a sustainable discount rate. A negative NPV indicates that the project should not be considered. When selecting among alternative projects, the one with the largest NPV is chosen for implementation. The only serious limitation with this approach is that it should not be used to compare projects with unequal lifetimes.

The NPV criterion has the advantage of ease of calculation relative to the criterion of the IRR. Indeed, calculation of the IRR is a cumbersome task up to a certain extent.

3.2 Internal Rate of Return

IRR is defined as the discount rate that makes the NPV of all cash flow equal to zero. It is considered to be the most useful measure of project worth and is used by almost all of the institutions involved in the economic and financial analysis of the project. It represents the average earning power of the money used in the project over the project's lifetime. The IRR is the profitability expected from a project expressed as a percentage, whereas NPV is expressed in monetary value, as an absolute magnitude. Equally, IRR can be defined as the discount rate that makes the NPV equation equal to zero:

$$0 = -\mathrm{HCPV}_I + \mathrm{PV}[\mathrm{NCF}(N)] \tag{17}$$

This criterion also has some drawbacks. One is the lack of realism on the assumption of reinvestment of intermediate cash flows of the project as happened

with the NPV criterion. The IRR criterion presupposes the immediate reinvestment of net positive cash flows until the end of the life cycle of the project, a reinvestment rate equal to the IRR of the project. In addition, it considers that any net negative cash flows are refinanced immediately until the end of the lifetime of the project with average capital of cost equal to the IRR of the project. Obviously such reinvestment or refinanced rates need not necessarily be equal to the IRR of the project.

Another drawback is the difficulty in calculating the result and possible inconsistency. Algebraically, the IRR is defined as the value of d, which satisfies Eq. (17). As can be easily noticed, this is a fairly complex equation to be solved for d. In fact, it is a polynomial of degree N, the lifetime of the project. In general, Eq. (17) can have as many as N solutions for d. The number of solutions will correspond with the number of times NCF changes sign. Fortunately, this will not typically be a problem since, for most projects, NCF will change sign only once, being negative initially while initial investment costs are being incurred, and then positive for the rest of the project life. In these circumstances, IRR will not only be uniquely defined, it will also indicate if the project looks profitable when regarding at it from different angles, e.g., exceeding a cut-off rate given by the opportunity cost, the WACC, or the minimum profitability required by the investor. Then the NPV of the project will be positive.

It should be noted that Eq. (17) leads to the calculation of a "gross" IRR. However, because most projects use financial mechanisms that required to be performed, the net internal rate of return (IRR_n) provides a more realistic assessment. Thus, IRR_n is obtained by subtracting WACC from IRR as calculated by means of Eq. (17) as follows:

$$\mathrm{IRR}_n = \mathrm{IRR} - \mathrm{WACC} \tag{18}$$

Under this criterion, a project should be accepted when the IRR is greater than the company's cost of capital, at the least, and reject those whose IRR falls short of such cost of capital. This cost is usually set equal to WACC or the opportunity cost of capital among others.

3.3 Discounted Pay-back Time

Discounted pay-back time (DPBT, in years) is the number of years required for the sum of the NCFs generated by project to meet the initial investment cost. It is given by the expression:

$$\mathrm{HCPV}_I = \mathrm{PV}[\mathrm{NCF}(\mathrm{DPBT})] \tag{19}$$

$$\mathrm{HCPV}_I = \mathrm{PV}[\mathrm{CI}(\mathrm{DPBT})] - \mathrm{PV}[\mathrm{CO}(\mathrm{DPBT})] + \mathrm{PV}[\mathrm{DEP}(N_\mathrm{d})] \cdot T \tag{20}$$

where PV[NCF(DPBT)] (€) = the present value of the NCFs generated over DPBT, PV[CI(DPBT)] (€) = present value of the CIs generated over DPBT, and PV[CO (DPBT)] (€) = the present value of the COs generated over DPBT.

If N_d is greater than DPBT, Eq. (20) may be written as:

$$\mathrm{HCPV}_I = \mathrm{PV}[\mathrm{CI}(\mathrm{DPBT})] - \mathrm{PV}[\mathrm{CO}(\mathrm{DPBT})] + \mathrm{PV}[\mathrm{DEP}(\mathrm{DPBT})] \cdot T \tag{21}$$

where PV[DEP(DPBT)] (€) = the present value of the tax depreciation over DPBT.

Obviously, the DPBT should not exceed the serviceable life of the project (DPBT < N). Although easily understandable and straightforward, this parameter does not consider the cash flows that are produced after DPBT. Hence, it might hide sound financial opportunities for those deciding to invest in a PV system. DPBT is an indicator of liquidity and risk. The acceptability of the investment is determined by comparison with the investor's required payback period. Thus, the investment should be accepted when the DPBT is less than the investor's required payback period; otherwise, the investment should be rejected.

3.4 The BCR of an Investment

The BCR of an investment project is defined as the ratio between the present value of its CIs and the project's life-cycle cost.

$$\mathrm{BCR} = \frac{\mathrm{PV}[\mathrm{CI}(N)]}{\mathrm{HCPV}_I + \mathrm{PV}[\mathrm{CO}(N)] - \mathrm{PV}[\mathrm{DEP}(N_\mathrm{d})] \cdot T} \tag{22}$$

Using this criterion implies assuming that the project is feasible when BCR is >1 so that if some projects are to be assessed, the one with the greatest BCR should be preferred.

The BCR criterion is closely related to the NPV approach. In fact, if the NPV of a project is positive, the BCR will be >1. In contrast, if the NPV is negative, the project will have a BCR < 1. Therefore, both NPV and BCR are closely related and provide similar information to the investor/user.

3.5 Annualized Value

The annualizing process transforms a stream of cash flows into equivalent annual streams. Cash flows are discounted to their NPV and then annualized by multiplying the present value of the cash flows by $(1 - Q)/(Q(1 - Q^N))$:

$$\mathrm{AV} = \mathrm{NPV} \cdot \frac{1 - Q}{Q(1 - Q^N)} \tag{23}$$

where AV (€) is the annualized value. If the uniform capital recovery factor of k years is stated as $\mathrm{UCRF}(k) = (1 - Q)/(Q(1 - Q^k))$, the annualized value of the HCPV system may rewritten as:

$$\mathrm{AV} = \mathrm{NPV} \cdot \mathrm{UCRF}(N) \tag{24}$$

3.6 Modified Net Present Value

The reinvestment assumption may thus be avoided by using the MNPV. There is no reinvestment assumption associated with the MNPV because the reinvestment rate is specified. Although the simple NPV carries the baggage of the reinvestment assumption, the MNPV does not. The MPNV value considers that positive NCFs are explicitly reinvested at the company's, or an individual's, opportunity cost of capital (r) rather than implicitly reinvested at a rate equal to the discount rate (d), whereas negative NCFs are explicitly refinanced at a rate equal to the discount rate considered.

$$\mathrm{MNPV} = -\mathrm{HCPV}_I + \sum_{t=1}^{N} \frac{\mathrm{NCF}_{p_t} \cdot (1 + r)^{N-t}}{(1 + d)^N} - \sum_{t=1}^{N} \frac{\mathrm{NCF}_{n_t} \cdot (1 + d)^{N-t}}{(1 + d)^N} \tag{25}$$

where $\mathrm{NCF}p_t$ is a positive NCF in year t, whereas $\mathrm{NCF}n_t$ is a negative NCF in year t. It should be understood that $\mathrm{NCF}p_t$ is derived from Eq. (3) on condition that its result is positive; otherwise, $\mathrm{NCF}p_t = 0$. Likewise, $\mathrm{NCF}n_t$ is also derived from Eq. (3) on condition that its result is negative; otherwise, $\mathrm{NCF}n_t = 0$. Given that negative NCFs are explicitly refinanced at a rate equal to the discount rate considered, Eq. (25) can be simplified:

$$\mathrm{MNPV} = \sum_{t=1}^{N} \frac{\mathrm{NCF}_{p_t} \cdot (1 + r)^{N-t}}{(1 + d)^N} - \sum_{t=0}^{N} \frac{\mathrm{NCF}_{n_t}}{(1 + d)^t} \tag{26}$$

The numerator of the first term in the right-hand side of Eq. (26) is the sum of all positive NCFs capitalized at the reinvestment rate until the last year (N) of the project. The second term in the right-hand side is the sum of all of the negative NCFs discounted at the financing rate—this usually equals WACC—until period zero of the project.

The decision criterion associated to the MNPV method is identical to that of the NPV: The project is profitable if the calculated MNPV is positive, whereas a negative value of MNPV means rejection. MNPV equal to zero indicates indifference.

3.7 Modified Internal Rate of Return

The reinvestment assumption can thus be avoided by using the MRR. There is no reinvestment assumption associated with the MIRR because the reinvestment rate is specified. Although the simple IRR carries the baggage of the reinvestment assumption, the MIRR does not. The MIRR is therefore probably a better way to measure the implied return from a project and gives a more reasonable measurement for comparison against other projects.

Modified IRR (MIRR) is similar to IRR, but positive NCFs are explicitly reinvested at the company's, or an individual's, opportunity cost of capital rather than implicitly reinvested at a rate equal to the system IRR, whereas negative NCFs are explicitly refinanced a rate equal to the discount rate considered.

$$0 = -\mathrm{HCPV}_I + \sum_{t=1}^{N} \frac{\mathrm{NCF}_{p_t} \cdot (1+r)^{N-t}}{(1+\mathrm{MIRR})^N} - \sum_{t=1}^{N} \frac{\mathrm{NCF}_{n_t} \cdot (1+d)^{N-t}}{(1+d)^N} \tag{27}$$

or

$$0 = -\mathrm{HCPV}_I + \sum_{t=1}^{N} \frac{\mathrm{NCF}_{p_t} \cdot (1+r)^{N-t}}{(1+\mathrm{MIRR})^N} - \sum_{t=1}^{N} \frac{\mathrm{NCF}_{n_t}}{(1+d)^t} \tag{28}$$

If HCPV_I is considered as a negative NCF corresponding to year 0, Eq. (28) may be rewritten as:

$$\sum_{t=1}^{N} \frac{\mathrm{NCF}_{p_t} \cdot (1+r)^{N-t}}{(1+\mathrm{MIRR})^N} = \sum_{t=0}^{N} \frac{\mathrm{NCF}_{n_t}}{(1+d)^t} \tag{29}$$

The numerator of the term in the left-hand side of Eq. (29) is the sum of all positive NCFs capitalized at the reinvestment rate until the last period (N) of the project. The term in the right-hand side of Eq. (29) is the sum of all of the negative NCFs discounted at the financing rate—usually WACC—until period zero of the project.

The decision criterion associated with the MIRR method is identical to that of the IRR. A project should be accepted when the IRR is greater than the company's cost of capital, at the least, and reject those in which the MIRR falls short of such cost of capital. This cost can be either WACC or the opportunity cost of capital among others.

3.8 Real Net Present Value

Section 2.1 dealt with how the NCFs of an investment project may be broken down according to the concepts where the resources are allocated by means of Eq. (4). Of all components of NCF, only the net cash balance can be actually reinvested

because the remainder are obligations incurred by the company that arise from the financing of the project. If this is taken into account, a much more realistic new measurement of profitability can be proposed. This is aimed at averting the problem of the reinvestment of intermediate NCFs that becomes apparent in the NPV method. Bearing in mind Eqs. (4) and (7), the RNPV (€) is given by:

$$\mathrm{NPV} = -\mathrm{HCPV}_I + \mathrm{PV}[\mathrm{NCF}(N)] \tag{7}$$

$$\mathrm{NCF}_{t(\mathrm{after-tax})} = \mathrm{RI}_t + I_t \cdot (1 - T) + \mathrm{di}_t + \mathrm{NCB}_t \tag{4}$$

$$\mathrm{RNPV} = -\mathrm{HCPV}_I + \sum_{t=1}^{N} \frac{\mathrm{RI}_t + I_t \cdot (1 - T) + \mathrm{di}_t}{(1 + d)^t} + \sum_{t=1}^{N} \frac{\mathrm{NCB}_t \cdot (1 + r)^{N-t}}{(1 + d)^N} \tag{30}$$

Values of NCB_t are reinvested if positive, and r is assumed equal to the reinvestment rate given by the company's, or an individual's, opportunity cost of capital. Values of NCB_t are refinanced if negative, so that r is assumed equal to WACC, whereas d equals the discount rate considered.

It should be noted that the widespread assumption of setting d equal to WACC leads to:

$$0 = -\mathrm{HCPV}_I + \sum_{t=1}^{N} \frac{\mathrm{RI}_t + I_t \cdot (1 - T) + \mathrm{di}_t}{(1 + d)^t} \tag{31}$$

Therefore, the RNPV can be simplified as:

$$\mathrm{RNPV} = \sum_{t=1}^{N} \frac{\mathrm{NCB}_t \cdot (1 + r)^{N-t}}{(1 + d)^N} \tag{32}$$

As shown above, NCB_t can be derived from Eq. (4) as:

$$\mathrm{NCB}_t = \mathrm{NCF}_{t(\mathrm{after-tax})} - \mathrm{RI}_t - I_t \cdot (1 - T) - \mathrm{di}_t \tag{33}$$

The criterion followed to assign the value of r in Sect. 3.5 (MNPV) may also be applied to Eq. (32).

4 Economic and Financial Feasibility of a Project

An investment project is feasible from an economic point of view when the return provided by the assets exceeds the cost of its liabilities, i.e., the NPV is >0, and the IRR is greater than the cost of capital for its liability.

An investment project is feasible from a financial point of view when at all times of its life cycle it has a a positive cumulative net cash balance. Then the financial

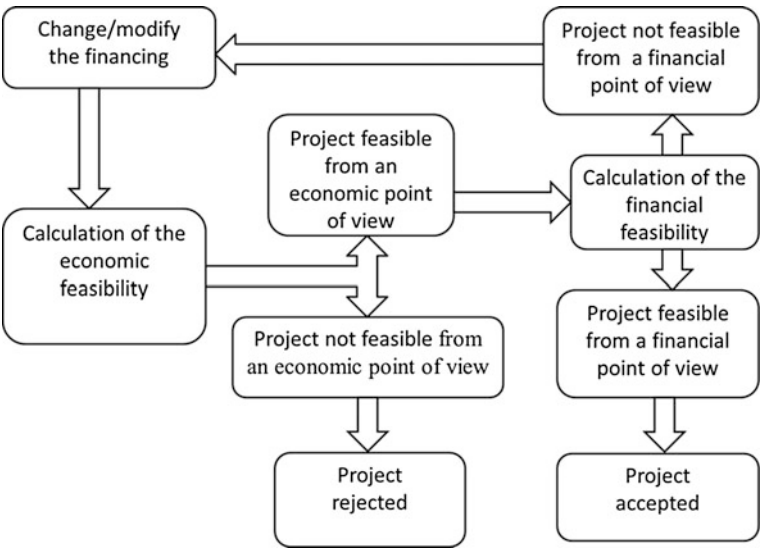

Fig. 6 Process of economic and financial feasibility

feasibility of a project is determined by the sum of the CIs and COs on a year-to-year basis. In other words, this is the financial dimension of the financing and the financial dimension of the investment.

A project might be feasible from an economic but not from a financial point of view. In this case the reverse is not possible: A possible option to turn it into a feasible one from a financial standpoint requires modifying the financing. Such modification may affect the economic feasibility of the project so that the study should be performed again as shown in Fig. 6.

5 Economic Analysis

To provide realistic results in the analysis that follows, some data were obtained from PV market surveys and reports from energy agencies. Two scenarios are proposed for the study of the economic profitability of HCPV systems. The first scenario is configured according to the information available by the end of 2013. Then, a second scenario is hypothesized to take place in 2020 by trying to predict the evolution of the HCPV market up to that year. For each scenario considered, a base case has been defined as a starting point to carry out a profitability analysis of HCPV systems.

5.1 Estimation of Parameters Involved in the Analysis

This review will lead to the identification of the value of the parameters required for a profitability analysis of the HCPV systems for a given scenario (2013) and a prospective scenario (2020). It should be noted that some of the figures presented here referring to costs and electricity yields are all normalized per kWp. The symbols used for these factors are the same for those not normalized except that they are shown in brackets and with the subscript "kWp."

5.1.1 Calculation of the HCPV Initial Investment Cost

Several market analysis [25, 30, 44] indicate that the HCPV world cumulative installed capacity in 2013 accounted for 160 MWp and that this could exceed 1400 MWp in 2020 as shown in Fig. 7. Based on the available information, different average annual growth rates (r_{HCPV} [in %]) of this capacity may be assumed. The company IHS expects an average annual growth rate equal to 36 %, whereas Globaldata expects growth to be 32 %. Bearing in mind both two values, it is assumed that r_{HCPV} 34 % in our analysis. Such an optimistic assumption implies that the installed HCPV capacity will exceed 1200 MWp in 2020.

Learning curves can be used to estimate the evolution of the initial investment cost of HCPV systems for upcoming years. These curves describe the cost reduction as a function of the accumulated experience in the manufacturing and in the use of a particular technology. The learning curve of a HCPV system can be expressed as:

$$\mathrm{HCPV}_{I\mathrm{year}} = \mathrm{HCPV}_{I2013}\left(\frac{Q_{\mathrm{HCPV\ year}}}{Q_{\mathrm{HCPV\ 2013}}}\right)^{\log_2^{(1-\mathrm{LR})}} \tag{34}$$

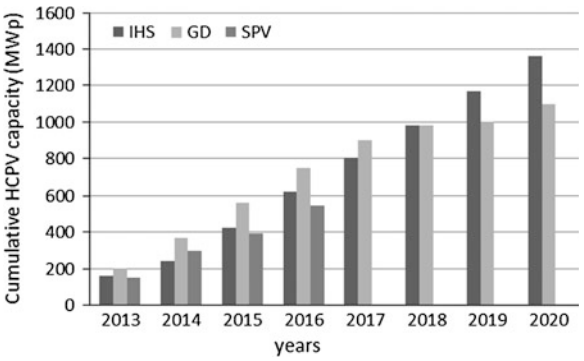

Fig. 7 Forecast of the HCPV world cumulative capacity. Market forecast performed by the private companies IHS (HIS), Globaldata (GD), and SPV Market (SPV)

Table 1 Learning ratio values of conventional PV as estimated by several authors (Poponi [49]; Parente et al. [48]; Bhandari and Stadler [4]

Author/date	Period of time analysed	Region studied	LR (%)
Poponi/2003	1976–2002	World	25
Parente/2002	1981–2000	World	23
Poponi/2003	1989–2002	World	20

where $HCPV_{Iyear}$ (€/kWp) is the HCPV initial investment cost in the year under study, $HCPV_I$ 2013 (€/kWp) is the HCPV initial investment cost in 2013, $Q_{HCPV\ year}$ (kWp) is the HCPV world cumulative installed capacity in the year under study, Q_{HCPV} 2013 is the HCPV world cumulative installed capacity in 2013 (kWp), LR is the learning rate, and $\log_2 (1 - LR)$ is the learning elasticity parameter. In 2013, the typical initial investment cost per kWp in HCPV varied from 1400 to 2200 €/kWp [20, 21]. In this study, an HCPV initial investment cost equal to 1800 €/kWp in 2013 is assumed.

As shown in Table 1, the learning rate of conventional PV has decreased with time as more experience in this technology has been gained. This ratio has sunk from a value of 25 % in the first stage of this technology (1976–2002) to a lower value of 20 % in later stages. As commented, HCPV technology is still in its first stages, and therefore a learning ratio of 25 % may be reasonably assumed. This value configures what is referred to as the "optimistic scenario" in the following text.

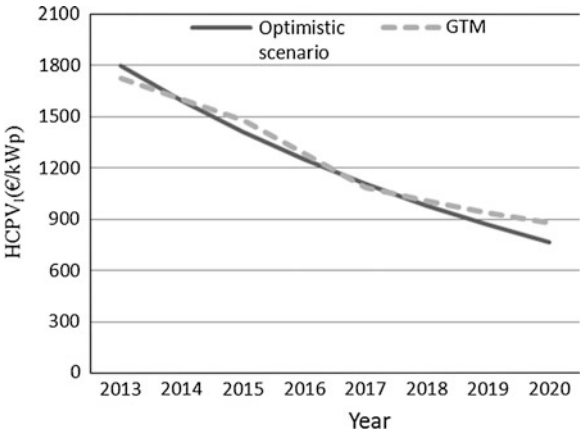

Fig. 8 Learning curve of the initial investment cost of HCPV systems in the assumed scenario (*optimistic scenario*). The initial investment cost of HCPV forecast performed by the private company GTM Research Inc [50] is also depicted

Based on the data described previously, the learning curve of the initial investment cost of HCPV systems could be estimated. Figure 8 shows the results obtained for the envisaged scenario. These results depend on multiple variables that may change over time; therefore, the data obtained might be altered. However, it is possible to expect a prospective scenario in which the initial investment cost of HCPV will fall within the interval of 700–900 €/kWp. In this study, $HCPV_I$ will be set equal to 800 €/kWp in 2020.

5.1.2 Estimation of HCPV Electricity Yield

Several methods have been proposed in the literature to calculate the energy generated by a PV grid connected system [1–3, 22, 27, 28, 37, 39–41, 47, 54, 68]. The method, based on the performance ratio (PR), is one of the most commonly used. The [32] defines that the annual generated electricity by a 1-kWp conventional PV system may be estimated using the following Eq. (35):

$$Y_f = PR \frac{H_A}{G_{STC}} \tag{35}$$

where Y_f [kWh/kW] is the annual final system yield in a conventional 1-kWp PV system, H_A [kWh/m^2] is the in-plane annual global irradiation, and G_{STC} [1 kW/m^2] is the global irradiance at standard test conditions. Values of PR in conventional PV systems usually range from 0.70 to 0.80 [9, 45, 51, 53, 59].

Likewise, the annual generated electricity by a 1-kWp HCPV system can be estimated using the following equation:

$$Y_{fHCPV} = PR \frac{DNI_A}{DNI_{STC}} \tag{36}$$

where Y_{fHCPV} [kWh/kW] is the annual final yield in a HCPV system, DNI_A [kWh/m^2] is the annual direct normal irradiation, and DNI_{STC} [1 kW/m^2] is the DNI at standard test conditions. Values of PR in HCPV systems have been reported to range from 0.75 to 0.90 [26, 29, 35, 36, 38, 46, 58, 66]. In the considered base case, an intermediate value of 0.82 has been used.

5.1.3 Estimation of the Remaining Factors

Initial investment cost of an HCPV system may be financed by means of debt or/and equity capital. Long-term loans and equity capital are chosen in this work. It has been assumed that 80 % of this initial amount is taken on loan ($HCPV_l$ [in €]), i.e., debt, while the remaining investment amount (20 %) is contributed from

stock issue ($HCPV_{eq}$ [in €]), i.e., equity capital. Regarding the loan, the interest rate (i_l) is considered equal to 6 %, whereas N_l is set equal to 20 years [15, 23]. Regarding equity capital, the dividend percentage d_{eq} is assumed equal to 12 % [21], and equity capital is payable in full at the end of the life cycle of the project (N [in years]). The risk related to HCPV projects perceived by investors is higher than that perceived regarding other renewable technologies, so cost of debt and equity capital, i.e., d_{eq} and i_l, take higher values.

The share of external financing and equity financing can be included in the analysis explicitly through the WACC over the discounting factor or nominal discount rate. Given that $HCPV_I = HCPV_l + HCPV_{ec}$, and taking into account taxation, Eq. (37) is obtained:

$$HCPV_I = \left(HCPV_l \cdot \frac{i_l(1-T)}{1-(1+i_l(1-T))^{-N_l}} \cdot \frac{Q \cdot (1-Q^{N_l})}{1-Q} \right) + \left((d_{eq} \cdot HCPV_{eq}) \cdot \frac{Q \cdot (1-Q^{N})}{1-Q} + HCPV_{eq} \cdot Q^{N} \right) \tag{37}$$

The first term of the right-hand side of Eq. (37) refers to loan: As commented previously, $HCPV_l$ is borrowed at an annual loan interest (i_l) to be repaid in N_l years. The second term refers to equity capital, with an annual payback in the form of dividends (d_{eq}), and is amortized at the end of the life cycle of the system. It is worth mentioning that the left-hand side of Eq. (37) only equals its right-hand side if the selected value of d is equal to the WACC of the investment.

The HCPV electricity unitary price, i.e., $p_{u,}$ in (€/kWh), of the HCPV-generated electricity paid to the owner, fed to the grid, or saved by the owner—in situ self-consumption—can be fixed at wholesale or retail price of the market. In the USA, the average retail price of electricity to ultimate customers by the end-use sector was equal to $0.1/kWh (all states' data from May 2013, 2014 [13]). Values of p_u varying between 0.07 and 0.30 €/kWh comprise the value of most market prices and present generation-based incentives for PV in different countries such as Germany, Italy, France, USA, Greece, and the UK among others [6, 7, 19, 33, 67]. For example, for flat-plate PV, Germany offers a minimum of 0.1102 €/kWh for a free-standing facility and Italy from 0.106 to ≤0.176 €/kWh as a function of rated power plus a premium for personal consumption. France offers from 0.0818 to ≤0.3159 €/kWh depending on the rated power. In the USA, net metering is regulated by law in most states, but state policies vary widely [12]. The feed-in tariff values for HCPV in Italy, according to the Ministerial Decree of 05 July 2012, vary from 0.215, 0.201, and 0.174 €/kWh for rated power ranging from 1 to 200, 200.01 to 1000, and >1000 kW, respectively [6]. For an HCPV system with a rated power >1 MWp, a reasonable value for the assumed base case is given by p_u = 0.1 €/kWh for the scenario (2013).

The annual increase rate of the HCPV electricity unitary price (rp_u), which is linked to the evolution of electricity markets, is always difficult to forecast. In the upcoming years 2014–2020 in the EU, retail electricity prices could increase from 2 to 5 % yearly depending of the country (European Photovoltaic Industry Association [17]. In the USA, retail electricity prices are expected to grow in the coming years (2014–2040) at an annual average rate ranging from 2.2 to 2.6 % [63]. In this study, rp_u is set equal to 2.5 %.

Regarding inflation, taking into account averages of historical data related to annual inflation rates (period 2005–2014) for some countries, the obtained values are i = 1.9 % for the Euro area [14, 24]; i = 2.3 % for the USA; i = 1.8 % for Canada; and i = 3 % for China [24]. Thus, i is assumed equal to 2.2 % in the base case.

The annual HCPV electricity yield generated by the system is assumed to decrease every year. Average annual degradation rate (r_d) in the efficiency of flat PV panels is 0.5 %/year [5, 34]. The analysis period equals the lifetime of an HCPV system, which is assumed equal to 30 years; consequently, N is set equal to 30 years. This makes sense because nowadays, flat PV systems have a life cycle of ≥30 years. The salvage value of the system's life cycle (S_V) is considered equal to zero.

The nominal discount rate (d) is assumed equal to the weighted average capital of cost to calculate the profitability criteria [21]. This capital cost will vary depending on how the capital resources are chosen to finance the initial investment cost. In the base case, the after-tax WACC is equal to 6.5 % given the assumptions stated in the first paragraph of this section.

Yearly operation and maintenance cost have been reported to be equal to 28 €/kWh/y for HCPV systems [11, 20]. Other estimates consider an annual fixed percentage of the initial investment cost $HCPV_I$, which is assumed equal to 2 % for [18]. The latter approach has been chosen in this work. The annual escalation rate of the operation and maintenance costs (r_{OM}) is set equal to the value of the annual inflation rate, i.e., r_{OM} = 2.2 %.

The income tax rate (T) for the organization or taxpayer, changes depending on each country's regulations. The value income tax rate is assumed equal to 30 % for this study. The method used in the tax depreciation uses a maximum linear coefficient of 5 % with a tax life for depreciation of 20 years [42, 43, 62]. Table 2 summarises the previous analysis by showing the figures chosen and assumed for each factor that define the case base for HCPV systems in the given scenario.

In a prospective scenario (2020) as described hereafter in Sect. 5.1.1. $[HCPV_I]_{kWp}$ equals 800 €/kWp, whereas the perceived risk of HCPV projects is similar to that of some other renewable technologies; therefore, cost of debt and equity capital is lower—by means of dividends and loan interest rate, respectively—than those stated values of the case base analysed according to Table 2 so that d_{ec} = 8 % and i_l = 4 %. HCPV electricity unitary price is set equal to 0.05 €/kWh,

Table 2 Values of factors assumed for the profitability analysis of HCPV systems in the scenario (2013)

Factors	Base case	Units
$[HCPV_I]_{kWp}$	1800	€/kWp
DNI_{STC}	1	kW/m^2
DNI_A	2200	kWh/m^2
PR	82	%
r_d	0.5	%
p_u	0.10	€/kWh
rp_u	2.5	%
$[HCPV_{OM}]^a_{kWp}$	2.0	%
r_{OM}	2.2	%
T	30	%
d = WACC	6.5	%
i	2.2	%
i_l	6.0	%
N_l	20	Years
d_i	12	%
N	30	Years

[a]This value should be interpreted as the percentage of $[HCPV_I]_{kWp}$ that is spent on operation and maintenance tasks on an annual basis

the pool price [64]; European Commission [16] because generation-based incentives for HCPV are assumed to be unavailable by 2020. The values of the remaining factors are the same to those of the base case of Table 2. Table 3 summarises these

Table 3 Factors values assumed for the profitability analysis of HCPV systems in the prospective scenario (2020)

Factors	Base case	Units
$[HCPV_I]_{kWp}$	800	€/kWp
DNI_{STC}	1	kW/m^2
DNI_A	2200	kWh/m^2
PR	82	%
r_d	0.5	%
p_u	0.05	€/kWh
rp_u	2.5	%
$[HCPV_{OM}]^a_{kWp}$	2.0	%
r_{OM}	2.2	%
T	30	%
d = WACC	4.5	%
g	2.2	%
i_l	4.0	%
N_l	20	Years
d_i	8.0	%
N	30	Years

[a]This value should be interpreted as the percentage of $[HCPV_I]_{kWp}$ that is spent on operation and maintenance tasks on an annual basis

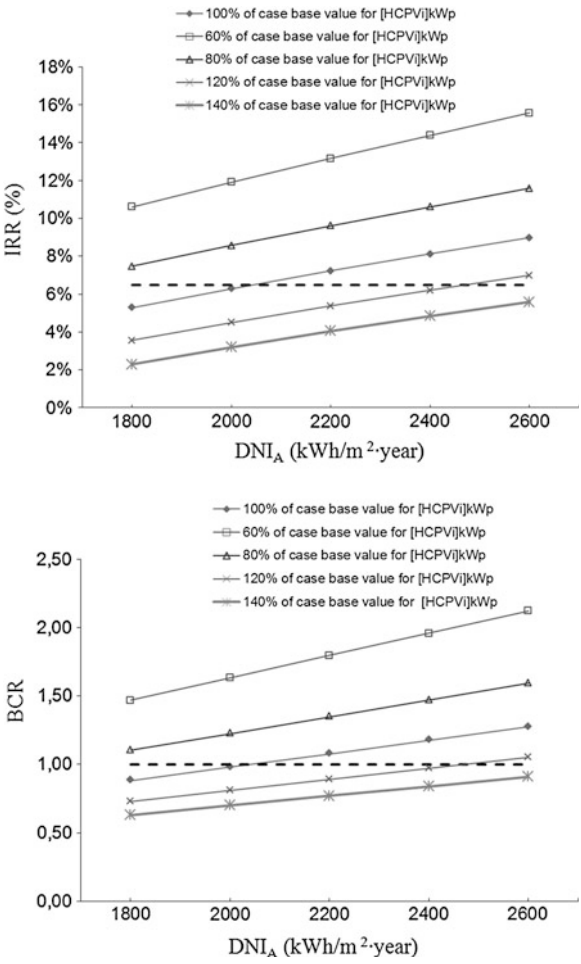

Fig. 9 IRR (*top panel*) and BCR (*bottom panel*) as a function of annual direct normal irradiation for variations of normalized-per-kWp initial investment cost. For each figure the rest of parameters are those stated for the base case in Table 2. The *horizontal dashed line* shows the threshold of economic feasibility for both criteria, i.e., *d* WACC = 6.5 % (*top panel*), and BCR = 1 (*bottom panel*)

considerations by showing the figures assumed for each factor that defines the case base for HCPV systems in the prospective scenario (2020).

5.2 Results

Solving the equations presented in Sect. 3, together with the figures shown in Tables 2 and 3, by means of using a spreadsheet, paves the way to the calculation of the profitability criteria for each base case. Thus, the following indices are obtained

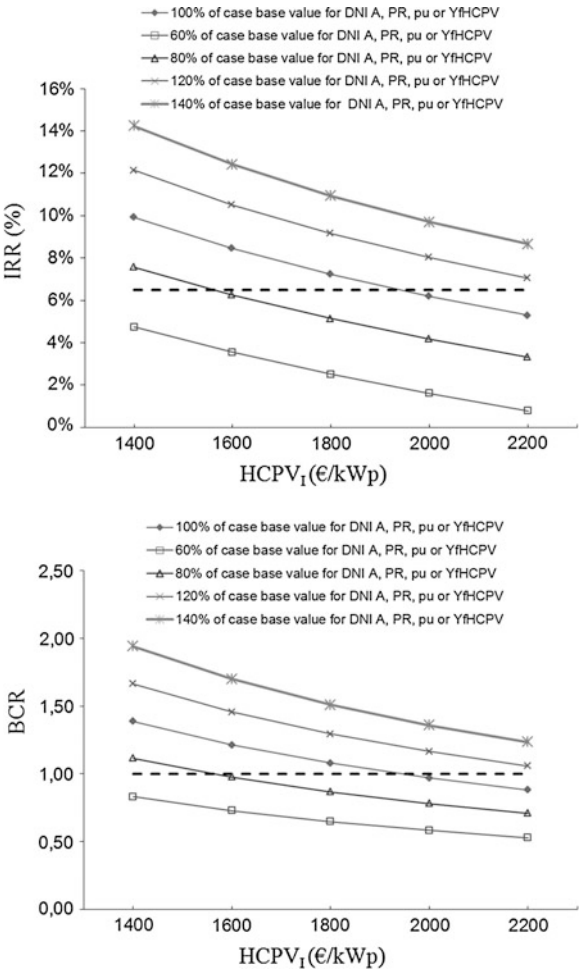

Fig. 10 IRR (*top panel*) and BCR (*bottom panel*) as a function of initial investment cost for variations of annual direct normal irradiation, PR, electricity unitary price, and normalized-per-kWp annual energy yield. For each figure the rest of parameters are those stated for the base case in Table 2. Regarding PR, only percentage values <120 % of the base case (0.82) should be considered given that annual PR cannot exceed the ideal value of 1. The *horizontal dashed line* shows the threshold of economic feasibility for both criteria, i.e., d = WACC = 6.5 % (*top panel*), and BCR = 1 (*bottom panel*)

for the given scenario (2013): IRR = 7.23 %, IRR_n 0.75 %, BCR = 1.08, DPBT = 25 years, NPV = 151 €/kWp, and PI = 0.08. Regarding the prospective scenario (2020), the following results are obtained: IRR = 8.45 %, IRR_n = 3.98 %, BCR = 1.5, DPBT = 15.5 years, NPV = 445 €/kWp, and PI = 0.56. Assuming a reinvestment rate equal to 7 % in Eqs. (26), (28) and (33) leads to the following values for the given scenario: MIRR = 7.05 %, MNPV = 331 €/kWp, and

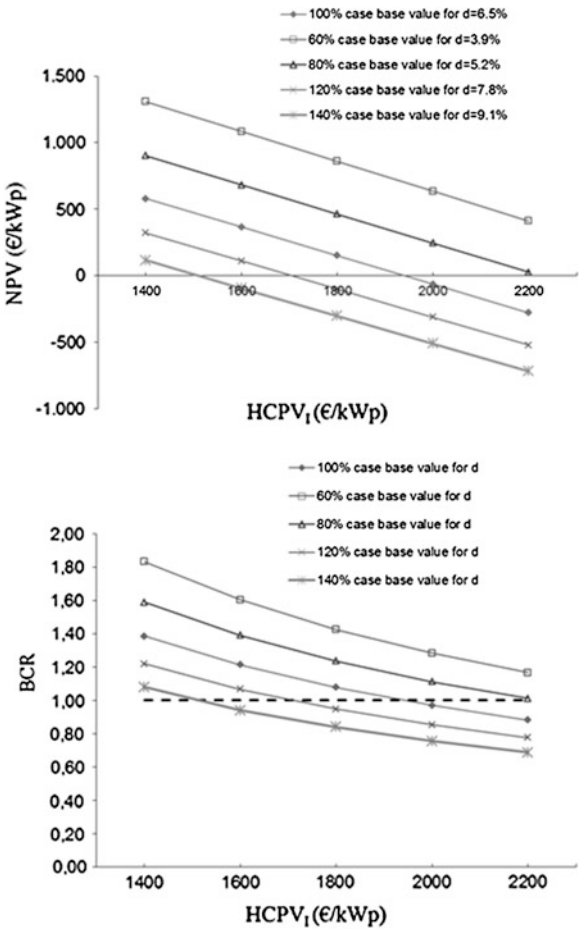

Fig. 11 NPV (*top panel*) and BCR (*bottom panel*) as a function of initial investment cost for variations of nominal discount rate. For each figure the rest of parameters are those of base case shown in Table 2. The *horizontal dashed line* shows the threshold of economic feasibility for both criteria, i.e., NPV = 0 (*top panel*) and BCR = 1 (*bottom panel*)

RNPV = 157 €/kWp. In contrast, assuming a reinvestment rate equal to 5 % in the prospective scenario results in the following values: MIRR = 5.8 %, MNPV = 556/kWp, and RNPV = 477 €/kWp. For both base cases, and given that IRR is greater than WACC, NPV is positive, and BCR is >1, we can conclude that HCPV systems are feasible from an economic point of view.

Regarding the financial feasibility of the base case corresponding to the given scenario (2013), a negative cumulative net cash balance in the first 15 years is obtained, so it would not be feasible from a financial point of view. Therefore, in this case the funding conditions should be modified. However, when calculated in

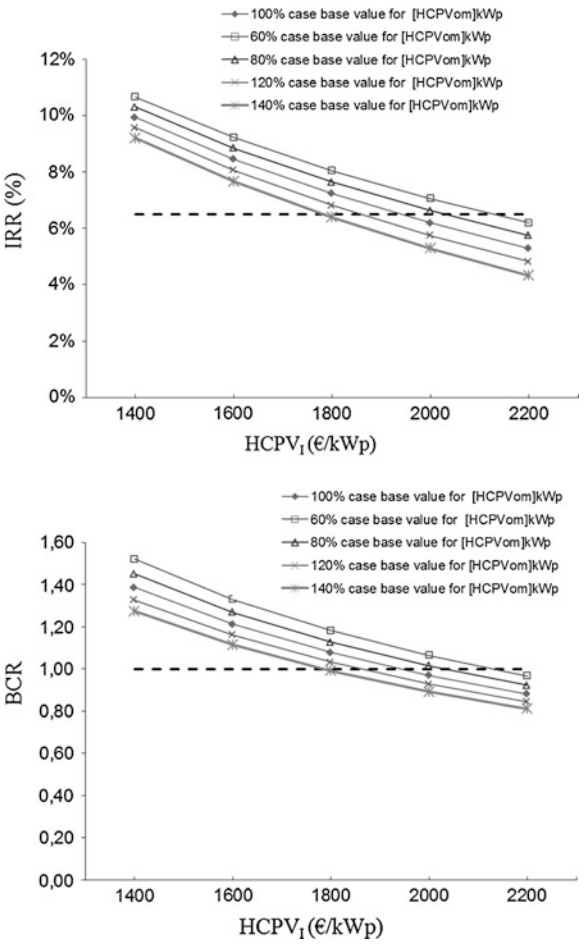

Fig. 12 IRR (*top panel*) and BCR (*bottom panel*) as a function of initial investment cost for variations of normalized-per-kWp annual operation and maintenance cost. For each figure the rest of parameters are those of base case in Table 2. The *horizontal dashed line* shows the threshold of economic feasibility for both criteria, i.e., d = WACC = 6.5 % (*top panel*), and BCR = 1 (*bottom panel*)

the base case for the prospective scenario, a positive cumulative net cash balance appears over the whole life cycle of the HCPV system, so it would be also feasible from a financial point of view.

6 Sensitivity Analysis

Possible changes in the value of the factors that configure both the considered given and future base case scenarios obviously influence an HCPV system's profitability criteria. Therefore, a sensitivity analysis of the latter criteria to those factors is

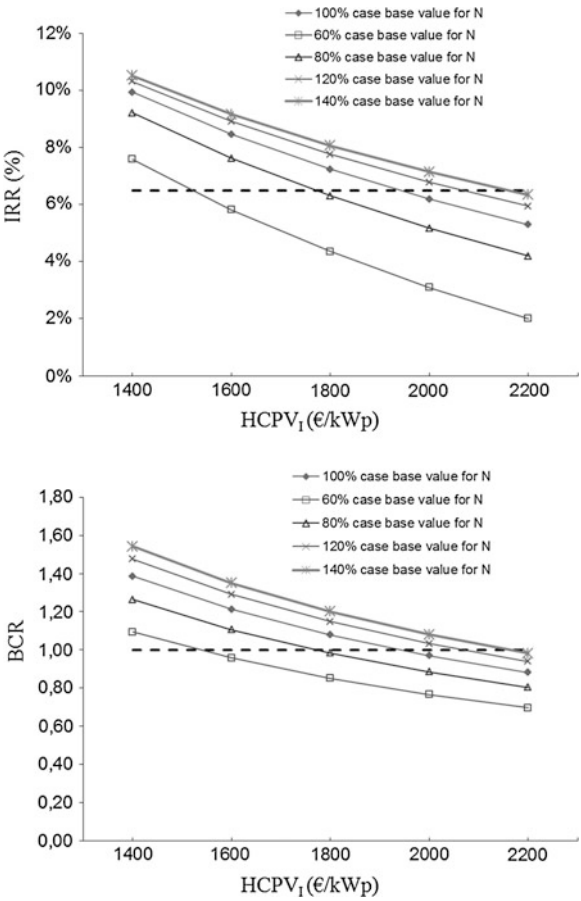

Fig. 13 IRR (*top panel*) and BCR (*bottom panel*) as a function of initial investment cost for variations of life cycle. For each figure the rest of parameters are those of base case in Table 2. The *horizontal dashed line* shows the threshold of economic feasibility for both criteria, i.e., d = WACC = 6.5 % (*top panel*) and BCR = 1 (*bottom panel*)

shown herein. According to Sect. 5, a base case has been defined in each scenario as a starting point to study the deviations of the studied profitability criteria as a function of the variations in the values of the factors that define this base case. Figures 9, 10, 11, 12, 13, 14 and 15 show the effect of deviations of these parameters from the figures that define each base case. Variations of factors within the range from −40 to +140 %, with 20 % increments, have been considered. Figures 9, 10, 11, 12, 13, 14 and 15 show figures of IRR (percentage units), NPV (€/kWp), and BCR (as a function of annual direct normal irradiation or initial investment cost) for deviations of the factors that define the base cases for the current scenario.

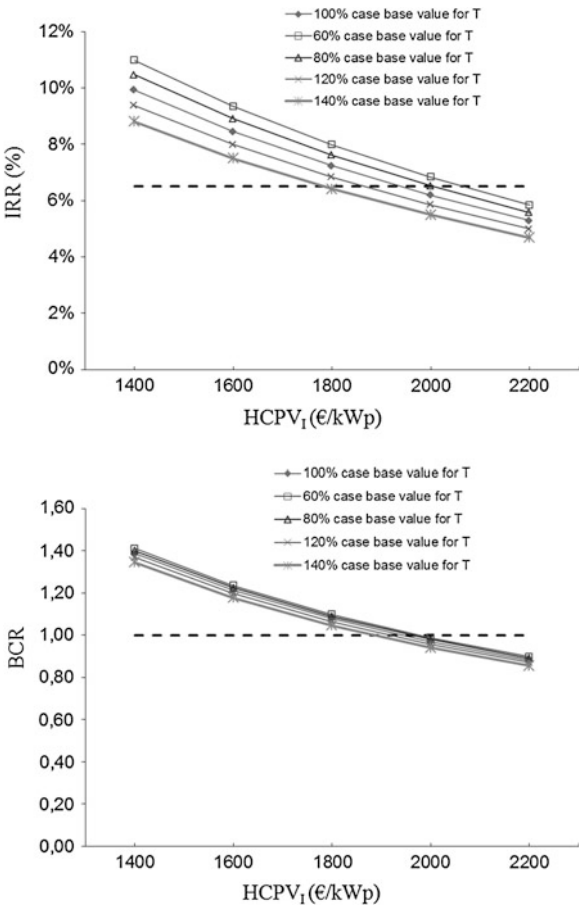

Fig. 14 IRR (*top panel*) and BCR (*bottom panel*) as a function of initial investment cost for variations of tax. For each figure the rest of parameters are those of base case in Table 2. The *horizontal dashed line* shows the threshold of economic feasibility for both criteria, i.e., d = WACC = 6.5 % (*top panel*) and BCR = 1 (*bottom panel*)

6.1 Given Scenario

The results of the sensitivity analysis for the given scenario (2013) are shown in Figs. 9, 10, 11, 12, 13, 14 and Table 4. As commented previously, in these figures the profitability criteria are depicted as a function of annual direct normal irradiation or initial investment cost for variations of the factors that characterize the base case.

When the values obtained for IRR, BCR, and NPV in Figs. 9, 10, 11, 12, 13, 14 and 15 are compared, some conclusions can be drawn. Variations in the annual degradation rate in the efficiency of the PV panels have little influence on IRR and BCR. Variations in certain factors, such as income tax rate and the percentage

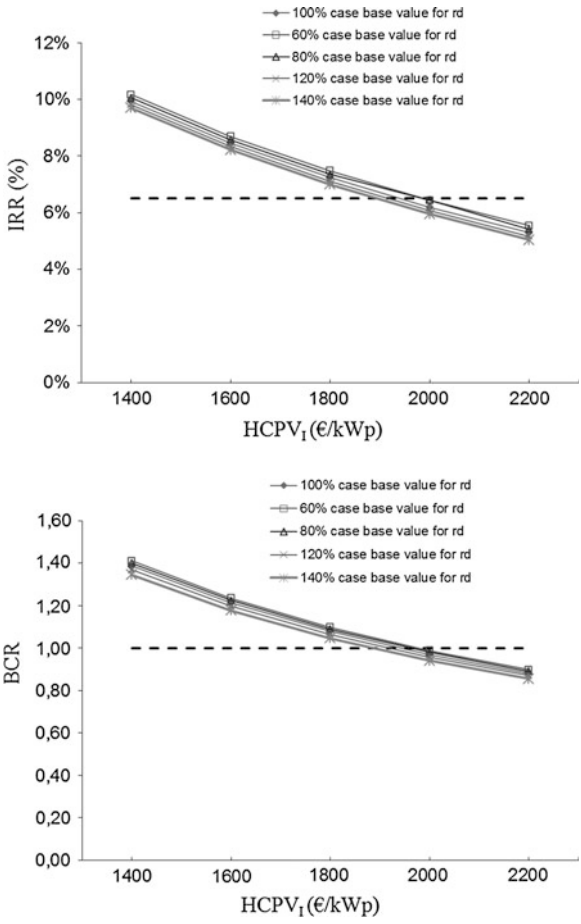

Fig. 15 IRR (*top panel*) and BCR (*bottom panel*) as a function of initial investment cost for variations of annual degradation rate in the efficiency of the PV panels. For each figure the rest of parameters are those of base case in Table 2. The *horizontal dashed line* shows the threshold of economic feasibility for both criteria, i.e., d = WACC = 6.5 % (*top panel*), and BCR = 1 (*bottom panel*)

annual operation and maintenance cost, exert a similar influence on the profitability criteria. Such influence turns out to be greater than that exerted by deviations of the annual degradation rate in the efficiency of the HCPV panels. Variations in the useful life cycle exert a lower impact on the profitability criteria than those of the nominal discount rate, but these criteria show more sensitivity to such variations than to those of all of the previously mentioned factors. IRR, BCR, and NPV are even more sensitive to variations in annual direct irradiation, normalised annual

Table 4 Effect of the variation of the analysed factors on base-case IRR and BCR for the given scenario (2013)

Factor	Units	Factor value range	Range of variation of IRR (%)	Range of variation of BCR
$[HCPV_I]_{kWp}$	€ kWp	1080 ÷ 2520	13.2 ÷ 4.1	1.80 ÷ 0.77
$[HCPV_{OM}]_{kWp}$	%	1.2 ÷ 2.8[a]	8.1 ÷ 6.4	1.18 ÷ 0.99
d	%	3.9 ÷ 9.1	No variation[b]	1.43 ÷ 0.84
r_d	%	0.3 ÷ 0.7	7.5 ÷ 7.0	1.11 ÷ 1.05
N	Year	18 ÷ 42	4.4 ÷ 8.1	0.85 ÷ 1.20
T	%	18 ÷ 42	8.0 ÷ 6.4	1.10 ÷ 1.05
DNI_A	kWh/m^2	1320 ÷ 3080	2.5 ÷ 10.9	0.65 ÷ 1.51
Yf_{HCPV}	kWh/kWp	1016 ÷ 3048	Same as above	
p_u	€/kWh	0.06 ÷ 0.17		
PR	–	0.49 ÷ 1.0	2.5 ÷ 9.2	0.65 ÷ 1.29

[a]These values should be interpreted as the percentage of $[HCPV_I]_{kWp}$ that is spent on operation and maintenance tasks on an annual basis

[b]It should be understood that IRR stands for "gross" IRR so that this profitability criterion remains constant irrespective of the value of d in this work, which is set equal to WACC. However, as commented in a previous section, the IRR_n is directly influenced by WACC because $IRR_n = IRR - WACC$

HCPV electricity yield, PR, and HCPV electricity unitary price. It should be borne in mind that these three factors cause the same effect. Last, the greatest impact on profitability criteria is exerted by deviations from the normalised initial investment cost related to the base case.

The variations of IRR and BCR experienced by the variations of each factor considered are listed in Table 4. In this table, columns 4 and 5 depicts the range of variation of the IRR and BCR for the specific range of the analysed factors. These values of IRR and BCR were drawn from Figs. 9, 10, 11, 12, 13, 14 and 15.

6.2 Prospective Scenario

As shown in the previous section, a short analysis on the factors that most influence the profitability criteria is performed herein. Thus, the results of this sensitivity analysis on the profitability criteria in a prospective scenario are shown in Figs. 16,

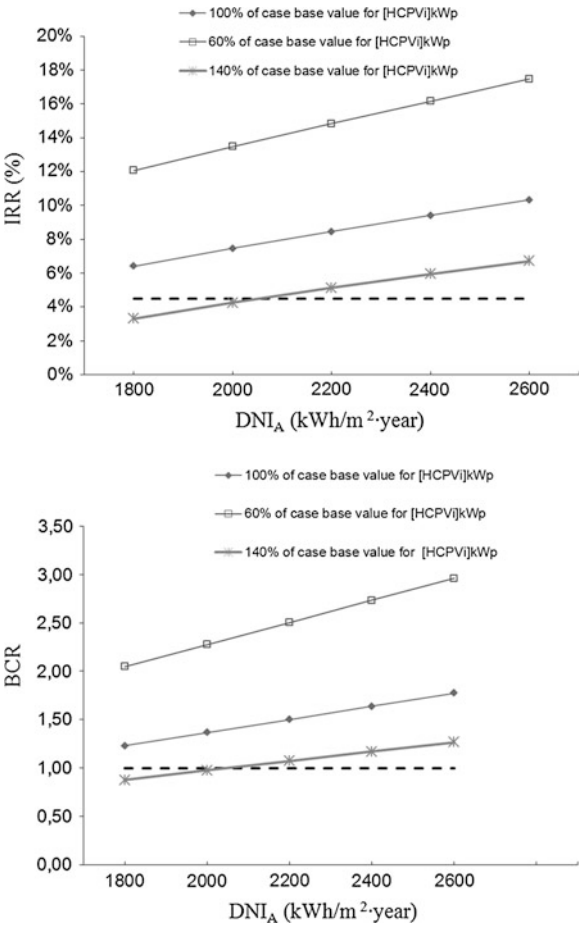

Fig. 16 IRR (*top panel*) and BCR (*bottom panel*) as a function of annual direct irradiation for variations of normalized-per-kWp initial investment cost. For each figure the rest of parameters are those of the base case presented in Table 3. The *horizontal dashed line* shows the threshold of economic feasibility for both criteria, i.e., d = WACC = 4.5 % (*top panel*), and BCR = 1 (*bottom panel*)

17, 18, 19 and Table 5. As is the case in the given scenario, an insignificant impact on IRR, BCR, and NPV is caused by deviations of the annual degradation rate and income tax rate from the values assumed for these two factors in the base case. A similar conclusion holds for the annual operation and maintenance cost. Consequently, no figures are provided regarding the sensitivity of IRR, BCR, and NPV to the previous three factors given their scarce influence compared with that exerted by the remaining ones described with later in the text.

Some sound conclusions may be derived by comparing the values obtained for IRR, BCR, and NPV in the figures mentioned in the preceding paragraph. Variations in the life cycle and nominal discount rate exert a similar influence on the

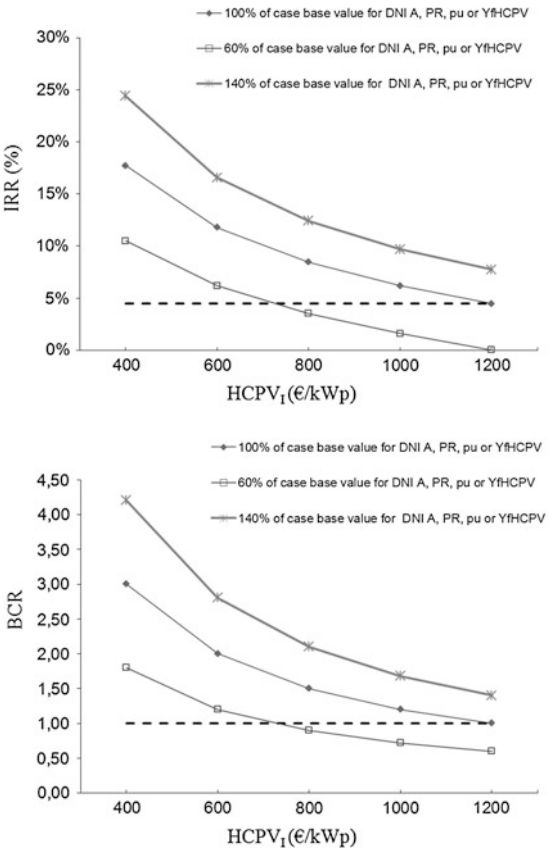

Fig. 17 IRR (*top panel*) and BCR (*bottom panel*) as a function of initial investment cost for variations of annual direct normal irradiation, PR, electricity unitary price, and normalized-per-kWp annual energy yield. For each figure the rest of parameters are those of the base case presented in in Table 3. Regarding PR, only percentage values <120 % of the base case (0.82) should be considered given that annual PR cannot exceed the ideal value of 1. The *horizontal dashed line* shows the threshold of economic feasibility for both criteria, i.e., d = WACC = 4.5 % (*top panel*), and BCR = 1 (*bottom panel*)

profitability criteria, but it is believed to occur a lesser extent than that exerted by the remaining factors studied. The nominal discount rate, the life cycle of the HCPV system, the annual final yield in an HCPV, the HCPV electricity unitary price, the PR, the annual direct normal irradiation, and the normalised initial investment are ordered from lowest to highest impact on profitability criteria related to the base case. As happened in Sect. 6.1, it should be noted that $Y_{f\mathrm{HCPV}}$, p_u, PR, and DNI_A exert the same influence.

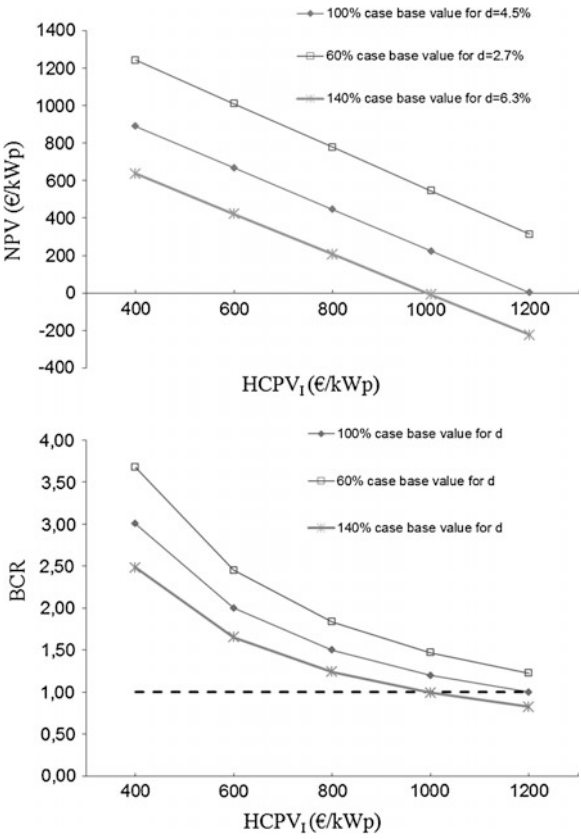

Fig. 18 NPV (*top panel*) and BCR (*bottom panel*) as a function of initial investment cost for variations of nominal discount rate. For each figure the rest of parameters are those of the base case presented in Table 3. The *horizontal dashed line* shows the threshold of economic feasibility for both criteria, i.e., NPV = 0 (*top panel*) and BCR = 1 (*bottom panel*)

The effect of the variation of each factor considered exerted on the value of IRR and BCR are listed in Table 5. In this table, columns 4 and 5 depict the range of variation of the IRR and the BCR for the specific range of the analysed factors, respectively. These values of IRR and BCR were drawn from Figs. 16, 17, 18 and 19.

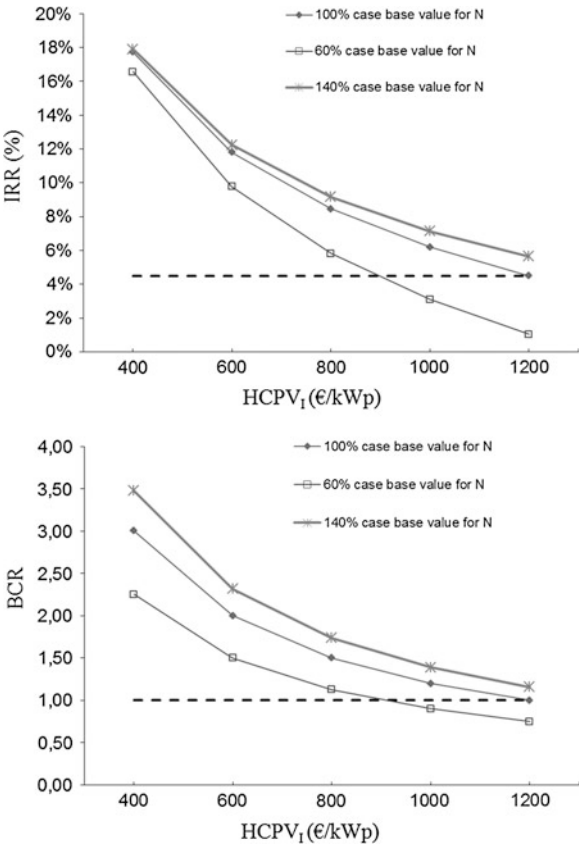

Fig. 19 IRR (*top panel*) and BCR (*bottom panel*) as a function of initial investment cost for variations of life cycle. For each figure the rest of parameters are those of the base case presented in Table 3. The *horizontal dashed line* shows the threshold of economic feasibility for both criteria, i.e., d = WACC = 4.5 % (*top panel*), and BCR = 1 (*bottom panel*)

Table 5 Effect of the variation of the analysed factors on base case IRR and BCR for the prospective scenario

Factor	Units	Factor value range	Range of variation of IRR (%)	Range of variation of BCR
$[HCPV_I]_{kWp}$	€ kWp	480 ÷ 1120	14.8 ÷ 5.1	2.50 ÷ 1.07
d	%	2.7 ÷ 6.3	No variation[b]	1.84 ÷ 1.24
N	Year	18 ÷ 42	5.8 ÷ 9.2	1.13 ÷ 1.74
DNI_A	kWh/m^2	1320 ÷ 3080	3.6 ÷ 12.4	0.90 ÷ 2.10
Y_{fHCPV}	kWh/kWp	1082 ÷ 2526	Same as above	
p_u	€/kWh	0.03 ÷ 0.07		
PR	–	0.49 ÷ 1.0	3.6 ÷ 10.5	0.90 ÷ 1.8

[a]These values should be interpreted as the percentage of $[HCPV_I]_{kWp}$ that is spent on operation and maintenance tasks on an annual basis

[b]It should be understood that IRR stands for "gross" IRR so that this profitability criterion remains constant irrespective of the value of d in this work equal to WACC. However, as commented in a previous section, the IRR_n is directly influenced by WACC because IRR_n = IRR − WACC

7 Conclusions

An introduction to the economic and financial analyses of HCPV systems has been presented throughout this chapter. The proposed mathematical expressions are aimed at taking into account most factors on which these analyses are based. To put them into practice, two different scenarios have been presented so as to provide two base cases.

The first base case corresponds to the year 2013, in which the cumulative installed HCPV power accounted for 160 MWp by the end of that year. This scenario is mainly characterized by an assumed initial investment cost of 1800 €/kWp with 80 % financed by means of a loan and 20 % funded through equity, a feed-in-tariff scheme of 0.10 €/kWh, an annual direct normal irradiation that equals 2200 kWh/m^2, and a perceived risk of the investment considered greater than that associated with other renewable techniques: This results in a WACC assumed equal to 6.5 %. The economic analysis proves that this investment as feasible from this point of view given that the IRR (7.2 %) exceeds the WACC and the BCR is >1 (1.08). However, this investment fails to be feasible from the financial viewpoint due to the negative cumulative net cash balances that are obtained during the first 15 years.

The second base case corresponds to a prospective scenario in 2020. Obviously, making some predictions regarding costs and financial environment has been necessary so that most relevant ones are commented below.

Cumulative installed HCPV power forecast, i.e., 1400 MWp by the end of 2020 —together with learning curves, in which a learning ratio of 0.20 is assumed—lead to an initial investment cost of 800 €/kWp, which is also financed by external capital (80 %) and equity (20 %). HCPV-generated electricity is assumed to be sold in its entirety to the grid at a pool price of 0.05 €/kWh, the same annual direct irradiation as commented previously, and a lower perceived risk of default is considered, which decreases the WACC to 4.5 %. The results derived from the economic analysis prove this investment as feasible from this point of view given that the IRR (8.5 %) nearly doubles the WACC and the BCR equals 1.5. In addition, this investment is feasible from the financial viewpoint because positive cumulative net cash balances are obtained over the whole project life cycle. This a optimistic—but also realistic—promising scenario in which HCPV turns out to be a real alternative to conventionally generated electricity.

The sensitivity of the IRR and the BCR to each considered factor has been ascertained in both scenarios presented herein. This sensitivity analysis provides clear evidence that annual degradation rate, income tax rate, annual operation and maintenance cost, life cycle of the HCPV system, discount rate, annual direct normal irradiation, and initial investment cost of the HCPV system are ordered from lowest to highest impact. It should be noted that annual final yield, PR, and HCPV electricity unitary price exert the same influence on IRR and BCR stand out that these three factors are function of the annual direct normal irradiation.

The results of the sensitivity analysis shown above may prove useful for government bodies and prospective owners of HCPV systems. Indeed, these results shed light on how changes in existing technical and economic factors that shape a given scenario may influence the profitability of the investment on these systems.

Appendix: Terminology

$[\text{HCPV}_{\text{AOM}}]_{\text{kWp}}$	Normalized per-kWp annual operation and maintenance cost of the HCPV system (€)
$[\text{HCPV}_I]_{\text{kWp}}$	Normalized per-kWp initial investment cost of HCPV (€/kWp)
Δ_{OM}	Annual escalation rate of the operation and maintenance cost of the HCPV system (%)
Δp_{g}	Annual escalation rate of the electricity price that is fed to the grid
Δp_{s}	Annual escalation rate of the electricity price that is consumed from the grid
AV	Annualised value (€)
BCR	Benefit-to-cost ratio
CI_t	Cash inflows over t (€)
CO_t	Cash outflows for t (€)
d	Nominal discount rate (%)
D	Debt (€)
d_{ec}	Annual dividend of the equity capital or return on equity (%)
DEP	Annual tax depreciation (€)
DEP_t	Tax depreciation during t (€)
di_t	Dividends-return on equity capital-paid (€)
DNI_A	Annual direct normal irradiation (kWh/m^2)
DNI_{STC}	Direct normal irradiation in standard test conditions (1 kW/m^2)
DPBT	Discounted payback time (year)
d_r	Real discount rate (%)
EC	Equity capital (€)
E_{HCPVg}	Annual HCPV electricity generated which is fed to the grid (kWh)
E_{HCPVs}	Annual HCPV electricity generated that is used for self-consumption (kWh)
G_{STC}	Global irradiance in standard test conditions (1 kW/m^2)
H_A	In-plane annual global irradiation (kWh/m^2)
HCPV_{AOM}	Annual operation and maintenance cost of the HCPV system (€)
HCPV_{eq}	Equity-financed fraction of the initial investment (€)
HCPV_I	Initial investment cost on the HCPV system (€)
HCPV_{l}	Loan-financed fraction of the initial investment (€)
i	Annual inflation rate (%)

(continued)

(continued)

i_l	Annual loan interest (%)
IRR	Internal rate of return (%)
IRR_n	Net internal rate of return (%)
I_t	Interest charges on debt during t (€)
$I_{t(\text{after-tax})}$	Interests after paying taxes during t (€)
IT_t	Taxes paid on income during t (€)
LR	Learning rate
MIRR	Modified internal rate of return (%)
MNPV	Modified net present value (€)
N	Life cycle of the HCPV system, equal to analysis period (year)
NCB_t	Net cash balance during t (€)
$NCFn_t$	Negative net cash flow during t (€)
$NCFp_t$	Positive net cash flow during t (€)
NCF_t	Net cash flow during t (€)
$NCF_{t(\text{after-tax})}$	After-tax net cash flows obtained during t (€)
N_d	Period of time over which an investment is amortized for tax purposes (year)
N_l	Amortization of loan (years)
NPV	Net present value (€)
p_g	Price at which electricity is sold to the grid (€/kWh)
PR	Performance ratio
p_s	Price at which electricity is bought from the grid (€/kWh)
p_u	HCPV electricity unitary price (€/kWh)
PV [DEP(N_d)]	Present value of the tax depreciation (€)
PV[CI(DPBT)]	Present value of the cash inflows generated over DPBT (€)
PV[CI(N)]	Present value of the cash inflows over the lifetime of the project (€)
PV[CO(DPBT)]	Present value of the cash outflows generated over DPBT (€)
PV[CO(N)]	Present value of the cash outflows overthe lifetime of the project (€)
PV[DEP (DPBT)]	Present value of the tax depreciation over DPBT (€)
PV [$HCPV_{OM}(N)$]	Present value of the HCPV system operation and maintenance cost (€)
PV[NCF (DPBT)]	Present value of the net cash flows generated over DPBT (€)
PV[NCF(N)]	present value of net cash flows (€)
PVIF(N)	$Q(1 - Q^N)/(1 - Q)$
Q	$1/(1 + d)$
Q_A	Annual growth installed capacity (%)
Q_{HCPV}	HCPV world cumulative installed capacity
Q_{OM}	$(1 + \Delta_{OM})/(1 + d)$
Qp_g	$(1 + \Delta p_g)\cdot(1 - r_d)/(1 + d)$

(continued)

(continued)

Qp_s	$(1 + \Delta p_s)\cdot(1 - r_d)/(1 + d)$
r_d	Annual degradation rate in the efficiency of the HCPV panels (%)
r_{HCPV}	Average annual HCPV power growth rate (%)
RI_{Dt}	Repayment instalments on debt (€)
RI_{ECt}	Repayment instalments on equity capital (€)
RI_t	Repayment instalments on funds borrowed (debt and/or equity capital) to fund the investment project during t (€)
RNPV	Real net present value (€)
r_{OM}	Annual escalation rate of the operation and maintenance cost of the HCPV system (%)
S_{VN}	Salvage value of the system at the end of its life cycle (€)
t	Period of time (year)
T	Income tax rate (%)
UCRF(k)	$(1 - Q)/(Q(1 - Q^k))$
WACC	Weighted average cost of capital (%)
Y_f	Annual final yield in a conventional flat-plate PV system (kWh/kWp)
Y_{fHCPV}	Annual final yield in a HCPV system (kWh/kWp)

References

1. Almonacid F, Rus C, Hontoria L, Fuentes M, Nofuentes G (2009) Characterisation of Si-crystalline PV modules by artificial neural networks. Renewable Energy 34(4):941–949
2. Araujo GL, Sánchez E (1982) Analytical expressions for the determination of the maximum power point and the fill factor of a solar cell. Solar Cells 5(4):377–386
3. Araujo GL, Sánchez E, Martí M (1982) Determination of the two-exponential solar cell equation parameters from empirical data. Solar Cells 5(2):199–204
4. Bhandari R, Stadler I (2009) Grid parity analysis of solar photovoltaic systems in Germany using experience curves. Sol Energy 83(9):1634–1644
5. Branker K, Pathak MJM, Pearce JM (2011) A review of solar photovoltaic levelized cost of electricity. Renew Sustain Energy Rev 15(9):4470–4482
6. Campoccia A, Dusonchet L, Telaretti E, Zizzo G (2014) An analysis of feed'in tariffs for solar PV in six representative countries of the European Union. Sol Energy 107:530–542
7. Castello S, De Lillo A, Guastella S, Paletta F (2013) National survey report of PV power applications in Italy 2012. International Energy Agency, Paris
8. Danchev S, Maniatis G, Tsakanikas A (2010) Returns on investment in electricity producing photovoltaic systems under de-escalating feed-in tariffs: the case of Greece. Renew Sustain Energy Rev 14(1):500–505
9. Drif M, Pérez PJ, Aguilera J, Almonacid G, Gomez P, de la Casa J, Aguilar JD (2007) Univer project. A grid connected photovoltaic system of at Jaén University. Overview and performance analysis. Sol Energy Mater Sol Cells 91(8):670–683
10. Drury E, Denholm P, Margolis R (2011) The impact of different economic performance metrics on the perceived value of solar photovoltaics. Contract 303:275–3000
11. Drury E, Lopez A, Denholm P, Margolis R (2013) Relative performance of tracking versus fixed tilt photovoltaic systems in the USA. Prog Photovoltaics Res Appl 22:1302–1315

12. DSIRE (2014) Solar policy and information. Database of states of incentives for renewables. http://www.dsireusa.org/solar/index.cfm?ee=1&RE=1&spf=1&st=1. Accessed July 2014
13. EIA (2014) Electric power monthly, Table 5.6.A, Average retail price of electricity to ultimate customers by end-use sector, by State, May 2014 and 2010. http://www.eia.gov/electricity/monthly/epm_table_grapher.cfm?t=epmt_5_06_a. Accessed July 2014
14. European Central Bank (2013a) Inflaction in the Euro area. http://www.ecb.europa.eu/stats/prices/hicp/html/inflation.en.html. Accessed 2013
15. European Central Bank (2013b) MFI interest rates on euro-denominated deposits from and loans to euro area residents. http://sdw.ecb.europa.eu/reports.do?node=100000173. Accessed 2013
16. European Commission DE (2013) Quarterly report on European electricity markets
17. European Photovoltaic Industry Association (2011) Solar photovoltaics competing in the energy sector: on the road to competitiveness
18. Extance A, Márquez C (2010) The concentrated photovoltaics industry report
19. Fang L, Honghua X, Sicheng W (2013) National survey report of pv power applications in China 2012
20. Fraisopi F (2013) The CPV market: an industry perspective
21. Fraunhofer Institute for Solar Energy Systems ISE (2013) Levelized cost of electricity renewable energy technologies
22. Fuentes M, Nofuentes G, Aguilera J, Talavera DL, Castro M (2007) Application and validation of algebraic methods to predict the behaviour of crystalline silicon PV modules in Mediterranean climates. Sol Energy 81(11):1396–1408
23. Global rates.com (2013a) Central banks—summary of interest rates. http://www.global-rates.com/interest-rates/central-banks/central-banks.aspx. Accessed 2013
24. Global rates.com (2013b) Inflation—summary of international inflation figures. http://www.global-rates.com/economic-indicators/inflation/inflation.aspx. Accessed 2013
25. Globaldata (2014) Concentrated photovoltaics (CPV)—global market size, competitive landscape and key country analysis to 2020
26. Gómez-Gil FJ, Wang X, Barnett A (2012) Energy production of photovoltaic systems: fixed, tracking, and concentrating. Renew Sustain Energy Rev 16(1):306–313
27. Huld T, Dunlop E, Beyer HG, Gottschalg R (2013) Data sets for energy rating of photovoltaic modules. Sol Energy 93:267–279
28. Huld T, Friesen G, Skoczek A, Kenny RP, Sample T, Field M, Dunlop ED (2011) A power-rating model for crystalline silicon PV modules. Sol Energy Mater Sol Cells 95 (12):3359–3369
29. Husna H (2013) Impact of spectral irradiance distribution and temperature on the outdoor performance of concentrator photovoltaic system, p 252
30. IHS Solar Solution (2013) Concentrated PV (CPV) report 2013—CPV on the edge of market breakthrough. USA
31. Internal Revenues Service United States, Department of the Treasury (2013) Figuring Depreciation Under MACRS
32. International Electrotechnical Commission (IEC) (1998) IEC 61724: photovoltaic system performance monitoring—guidelines for measurement, data exchange and analysis
33. International Energy Agency (IEA) (2013) Trens 2013 in photovoltaic application: survey report of selected IEA countries between 1992 and 2012
34. Jordan DC, Kurtz SR (2013) Photovoltaic degradation rates—an analytical review. Prog Photovoltaics Res Appl 21(1):12–29
35. King C (2010) Site data analysis of CPV plants. In: Conference record of the IEEE photovoltaic specialists conference, p 3043
36. Kinsey GS, Stone K, Brown J, Garboushian V (2011) Energy prediction of Amonix CPV solar power plants. Prog Photovoltaics Res Appl 19(7):794–796

37. Kroposki B, Emery K, Myers D, Mrig L (1994) Comparison of photovoltaic module performance evaluation methodologies for energy ratings. In: Proceedings of the 24th IEEE photovoltaic specialists conference. Part 2 (of 2), ed. Anon, IEEE, Piscataway, NJ, United States, 5 December 1994 through 9 December 1994, p 858
38. Lecoufle D, Kuhn F (2009) A Place for PV, tracked-PV and CPV
39. Leloux J, Lorenzo E, García-Domingo B, Aguilera J, Gueymard CA (2014) A bankable method of assessing the performance of a CPV plant. Appl Energy 118:1–11
40. Marion B (2002) A method for modeling the current-voltage curve of a PV module for outdoor conditions. Prog Photovoltaics Res Appl 10(3):205–214
41. Marion B, Rummel S, Anderberg A (2004) Current-voltage curve translation by bilinear interpolation. Prog Photovoltaics Res Appl 12(8):593–607
42. Ministry Economic Spain (2008) Royal decree 1793/2008, ministry economic
43. Ministry Economic Spain (2004) Royal decree 1777/2004, ministry economic
44. Mints P (2013) The current status of CPV 2013. PV-insider, UK
45. Mondol JD, Yohanis YG, Smyth M, Norton B (2003) Performance analysis of a frid-connected building integrated photovoltaic system
46. Nishikawa W, Horne S (2008) Key advantages of concentrating photovoltaics (CPV) for lowering levelized cost of electricity (LCOE), p 3765
47. Osterwald CR (1986) Translation of device performance measurements to reference conditions. Solar Cells 18(3–4):269–279
48. Parente V, Goldemberg J, Zilles R (2002) Comments on experience curves for PV modules. Prog Photovoltaics Res Appl 10(8):571–574
49. Poponi D (2003) Analysis of diffusion paths for photovoltaic technology based on experience curves. Sol Energy 74(4):331–340
50. Prior B (2011) Roadmap for CPV technology
51. Ransome SJ, Wohlgemuth JH, Solar BP (2002) kWh/kWp dependency on PV technology and balance of systems performance. In: 29th IEEE photovoltaic specialists conference, 19 May 2002 through 24 May 2002, p 1420
52. Reddy KS, Veershetty G (2013) Viability analysis of solar parabolic dish stand-alone power plant for Indian conditions. Appl Energy 102:908–922
53. Ruiz-Arias JA, Terrados J, Pérez-Higueras P, Pozo-Vázquez D, Almonacid G (2012) Assessment of the renewable energies potential for intensive electricity production in the province of Jaén, southern Spain. Renew Sustain Energy Rev 16(5):2994–3001
54. Rus-Casas C, Aguilar JD, Rodrigo P, Almonacid F, Pérez-Higueras PJ (2014) Classification of methods for annual energy harvesting calculations of photovoltaic generators. Energy Convers Manag 78:527–536
55. Schneider E (1978) Teoría de la Inversión. El Ateneo, Buenos Aire
56. Short W, Packey DJ, Holt T (1995) A manual for the economic evaluation of energy efficiency and renewable energy technologies
57. Spertino F, Di Leo P, Cocina V (2013) Economic analysis of investment in the rooftop photovoltaic systems: a long-term research in the two main markets. Renew Sustain Energy Rev 28:531–540
58. Stone K (2006) Analysis of five years of field performance of the Amonix High Concentration PV system
59. Šúri M, Huld TA, Dunlop ED, Ossenbrink HA (2007) Potential of solar electricity generation in the European Union member states and candidate countries. Sol Energy 81(10):1295–1305
60. Talavera DL, de la Casa J, Muñoz-Cerón E, Almonacid G (2014) Grid parity and self-consumption with photovoltaic systems under the present regulatory framework in Spain: the case of the University of Jaén Campus. Renew Sustain Energy Rev 33:752–771
61. Talavera DL, Muñoz-Cerón E, De La Casa J, Ortega MJ, Almonacid G (2011) Energy and economic analysis for large-scale integration of small photovoltaic systems in buildings: the case of a public location in Southern Spain. Renew Sustain Energy Rev 15(9):4310–4319

62. Thonson Reuters (2014) Consulta A.E.A.T. 128308,. IS. Central fotovoltaica. Amortización. http://portaljuridico.lexnova.es/doctrinaadministrativa/JURIDICO/77405/consulta-aeat-128308-is-central-fotovoltaica-amortizacion
63. U.S. Energy Information Administration (2014a) Annual energy outlook 2014. Table A3, Energy prices by sector and source. http://www.eia.gov/forecasts/aeo/pdf/tbla3.pdf. Accessed Sept 2014
64. U.S. Energy Information Administration (2014b) Wholesale electricity and natural gas market data. http://www.eia.gov/electricity/wholesale/index.cfm. Accessed Sept 2014
65. United States Agency for International Development (2002) Best practices guide: economic and financial evaluation of renewable energy projects
66. Verlinden, P. 2008, "Energy rating of Concentrator PV systems using multi-junction III–V solar cells"
67. Yamada H, Ikki O (2013) National survey report of PV power applications in Japan 2012
68. Zhou W, Yang H, Fang Z (2007) A novel model for photovoltaic array performance prediction. Appl Energy 84(12):1187–1198

High-Concentrator Photovoltaic Power Plants: Energy Balance and Case Studies

Pedro Pérez-Higueras, Francisco J. Muñoz-Rodríguez, Carlos Adame-Sánchez, Leocadio Hontoria-García, Catalina Rus-Casas, Antonio González-Rodríguez, Juan D. Aguilar-Peña, Francisco J. Gallego-Álvarez, Ivan González-Luchena and Eduardo F. Fernández

Abstract High-concentrator photovoltaic (HCPV) power plants are inherently different from conventional photovoltaic (PV) power sources due to the use of concentrator modules and two-axis solar trackers. HCPV technology is a relatively new energy source; therefore, there is limited experience in its application in power plants. Bearing this in mind, this chapter aims to provide information about the special features and performance of HCPV power plants under real operating conditions. The analysis of current concentrator modules and solar trackers is addressed to achieve a better understanding of the main characteristics of this kind of systems. In addition, different methods for estimating the energy yield of an HCPV system or power plant are discussed. This is a crucial task to analyse the potential of such emerging technology. Finally, several HCPV power plants and relevant data concerning their energy yield and performance ratio (PR) are described and commented.

1 Introduction

A photovoltaic (PV) power plant (also known as PV-generating station, PV-power station, or PV-generating plant) (Fig. 1) is an industrial facility for the generation of electric power from PV solar systems. It can be also considered as a grid-connected PV (GCPV) system where all of the electricity generated is fed into the grid. Thus, a PV power plant has the same elements that a GCPV system has, but also has an

P. Pérez-Higueras (✉) · F.J. Muñoz-Rodríguez · L. Hontoria-García · C. Rus-Casas · J.D. Aguilar-Peña · F.J. Gallego-Álvarez
University of Jaén, Jaén, Spain
e-mail: pjperez@ujaen.es

E.F. Fernández
University of Santiago de Compostela, Santiago de Compostela, Spain
e-mail: eduarferfer@gmail.com

C. Adame-Sánchez · A. González-Rodríguez · I. González-Luchena
University of Castilla-La Mancha, Castilla-La Mancha, Spain

P. Pérez-Higueras and E.F. Fernández (eds.), *High Concentrator Photovoltaics*, Green Energy and Technology, DOI 10.1007/978-3-319-15039-0_16

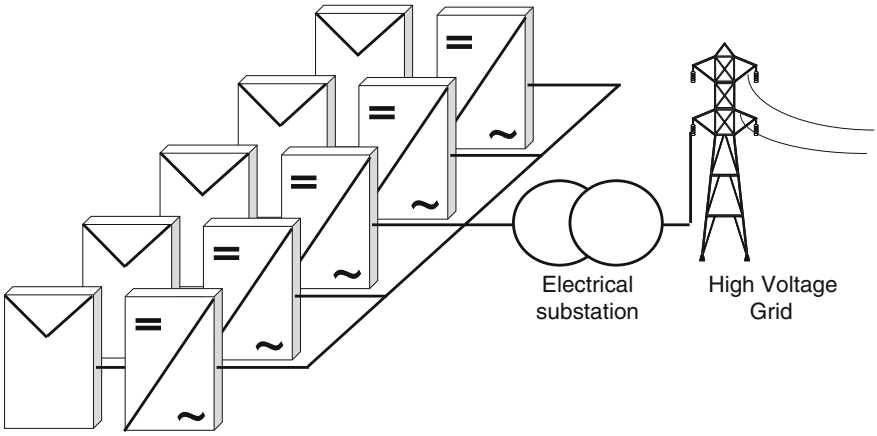

Fig. 1 Basic layout of a photovoltaic power plant

electrical substation to establish a connection with the high-voltage grid. In this sense, a high-concentrator photovoltaic (HCPV) power plant can be defined as a PV power plant where HCPV arrays are used instead of conventional PVs. This type of plant is provided with two-axis solar trackers to keep HCPV modules perpendicularly oriented to the Sun. The remaining elements are similar to those found in any PV power plant (inverter, protection devices, connection elements, electrical substation, monitoring system, etc.).

Although conventional PV power plants have been widely analyzed, and several studies concerning their performance and specific characteristics can be found in the literature, there is narrow experience in the analysis and study of HCPV plants. This is due to that fact that HCPV technology is a new and emergent technology; therefore, the experience in its application in power plants is still scarce. Hence, it is important to devote large efforts to achieve a better understanding of the real performance and special features of this type of power plants. This is the aim of this chapter.

To achieve this goal, this chapter is divided in different sections. Section 2 summarizes the main features of commercial HCPV modules and two-axis trackers. This is crucial to obtain a better understanding about the main components of current HCPV power plants. The energy prediction of power plants is an important task to evaluate the potential and promote the market expansion of HCPV technology. Taking this into account, different methods for estimating the electrical output of HCPV systems or power plants are introduced and discussed in Sect. 3. In addition, and the most relevant atmospheric databases for energy prediction issues are listed in Sect. 4. In Sect. 5, several HCPV power plants are commented and described. Furthermore, valuable information concerning their energy yield and performance is provided. Finally, the main conclusions are outlined in Sect. 6.

2 Components of an HCPV Power Plant

As commented, the main difference between a PV and an HCPV power plant is the fact that HCPV power plants use concentrator modules and two-axis trackers. Bearing this in mind, this section aims to review the characteristics of the main HCPV modules and trackers that are currently being used in power plants. In addition, some trends and proposals to improve the present designs are briefly discussed.

2.1 Commercial HCPV Modules

An HCPV module is made up of solar cells, optical devices, and peripheral components necessary to generate electricity and dissipate the heat produced due to the high temperatures achieved by the solar cells working at high concentration ratios (Fig. 2). Heat dissipation can be performed passively through heat sinks or actively by the flow of fluid, generally water. An HCPV module also incorporates others elements, such as bypass diodes, to avoid the overheating of cells mainly due to mismatch among cells and the shading that may take place when HCPV systems are working under real operating conditions [7, 21, 26, 28, 31].

HCPV is a young technology; therefore, the majority of manufacturing companies of HCPV modules have been recently established. These companies do not provide detailed information about their products mainly due to strategic and confidential commercial purposes. Therefore, currently there is a lack of information on module specifications, features, performance, designs, etc. In addition, most of the published data are incomplete and do not indicate any of the following information:

- measuring conditions,
- measuring laboratory, and
- commercial products or prototypes.

However, in this section relevant information about the following HCPV module manufacturers is provided (Table 1, Fig. 3).

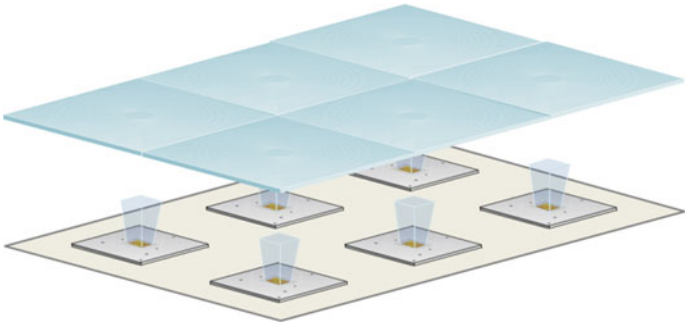

Fig. 2 Schematic of an HCPV module

Table 1 a, b Main data offered by some companies about their HCPV modules

(a)

	Arima CPV-M010	Arima 400 W	Daido 280 W	Emcore G3-1090X	Isofoton GEN-2	Magpower TRK60	Opel Mk-Id
Geometric concentration	476	476	820	1090			
Optical device	Fresnel	Fresnel	Fresnel	Fresnel	Fresnel	Fresnel	Fresnel
Multijunction cells (N°)	48	144	25	15	6	360	6
Test conditions							
Direct normal irradiance (W/m^2)	850	850		1000	1000	850	
Ambient temperature (°C)						20	
Spectrum				1.5D	1.5D		1.5D
Wind speed (m/s)						4	
Performance characteristic under test conditions							
Maximum power (W)	120	440	280	455	93	6600	90
Power tolerance (%)						±5	
Max. power voltage (A)	120	380	68.6	40.4	16.62	305	15.6
Max. power current (A)	1.0	1.15	4.1	11.4	5.73	21.6	5.8
Open-circuit voltage (V)	140		78.0	47.7	18.45	354	17.4
Short-circuit current (A)	1.1		4.4	11.9	6.35	23.1	6.4
Module efficiency (%)	22	25	28	28		23	
Acceptance angle (°)	±0.5		±0.9	±0.7		±1.9	
Max. system voltage (V)			900			500	600
Temperature coefficients							
Power (%/°K)			−0.15	−0.20		−0.16	−0.14
Voltage (%/°K)			−0.12	−0.14		−0.17	−0.15
Current (%/°K)			+0.09	+0.01		+24$^{(*)}$	+200$^{(*)}$

(continued)

Table 1 (continued)

(a)							
	Arima CPV-M010	Arima 400 W	Daido 280 W	Emcore G3-1090X	Isofoton GEN-2	Magpower TRK60	Opel Mk-Id
Mechanical specifications							
Area (m^2)			1	1.7		38	
Length (m)	1.68	1.68	1.00	1.71		8.35	1.58
Width (m)	0.57	1.64	1.00	1.05		5.3	0.28
Depth (m)	0.25	0.25	0.24	0.64			0.31
Weight (kg)	20	60	23.6	57		840	9
Connector				Tyco			MC

(b)							
	Semprius SM-U01	Soitec CX-M400	Soitec CX-M500	Solfocus SF-CPV-205	Solfocus SF-1100P	Soliant SE-1000X	Suncore DDM-1090X
Geometric concentration	1111	530	~500			1000	1090
Optical device	Fresnel	Fresnel	Fresnel	Mirror	Mirror	Fresnel	Fresnel
Multijunction cells (N°)		98				64	
Direct normal irradiance (W/m^2)	1000	1000	1000	850	850	900	900
Cell temperatures (°C)	25	25	25				
Ambient temperature (°C)				20	20	20	20
Spectrum	1.5D		1.5D				1.5D
Wind speed (m/s)				4		4	4
Performance characteristic under test condition							
Max. power (W)	87.5	95	2450	205	315	471	402
Power tolerance (%)	±5	±10	±10		±5		
Max. power voltage (A)	86.6	138	645	40	50	39.8	38.3

(continued)

Table 1 (continued)

(b)							
	Semprius SM-U01	Soitec CX-M400	Soitec CX-M500	Solfocus SF-CPV-205	Solfocus SF-1100P	Soliant SE-1000X	Suncore DDM-1090X
Max. power current (A)	1.01	0.69	3.8	5.2	6.2	11.8	10.5
Open-circuit voltage (V)	101.6	150	740	46	58	47.7	45.2
Short-circuit current (A)	1.06	0.78	4.2	5.4	7.1	13.2	11.1
Module efficiency (%)	33.9		31.8	17		25.3	28
Acceptance angle (°)				±1			±0.7
Max. system voltage (V)	1000			1000	1000	1000	
Temperature coefficients							
Power (%/°K)	−0.14	−0.15	−0.34	−0.16	−0.21	−0.2	−0.2
Voltage (%/°K)	−0.14		−0.14	−0.15	−0.17	−0.02	−0.15
Current (%/°K)			−0.20	+0.8(*)		+0.04	+0.01
Mechanical specifications							
Area (m^2)					1.50		
Length (m)	0.64	0.87	3.67	1.3	1.10	0.71	1.74
Width (m)	0.48	0.43	2.39	1.1	1.37	0.38	1.08
Depth (m)	0.07	0.10	0.10	0.1		0.40	0.64
Weight (kg)	6.8		210	42	32	90	56
Connector	MC4			MC4			

(*)In μA/K°

Fig. 3 Different examples of commercial HCPV modules (*courtesy* of Soitec, Emcore, Solfocus, Opel, and Daido

- Arima EcoEnergy Technologies Corp.: www.arimaeco.com
- Daido Steel Co. Ltd.: www.daido.co.jp
- Emcore Corp.: www.emcore.com
- Isofoton S.A.: www.isofoton.com

- Opel Inc.: www.opelinc.com
- Magpower SA.: www.magpower.eu
- Semprius: www.semprius.com
- Soitec: www.soitec.com
- Solfocus: www.solfcocus.com
- Soliant Energy, Inc.: www.soliantenergy.com
- Suncore Photovoltaic Tech. Co. Ltd.: www.suncorepv.com

Although, some of these companies have closed their operations, it is important show data of the performance of manufactured modules because they show interesting features about current HCPV technology.

Currently, the most industrialized HCPV module is made up of triple-junction (TJ) GaInP/GaInAs/Ge cells. The optical system is made up of one primary optical element based on point-focus Fresnel lenses that focus in a secondary optical element based on a refractive truncated pyramid or similar. The most commonly used material for the lens is usually poly(methylmethacrylate) or silicone-on-glass (SOG). Table 1 lists the main data provided by some companies about their HCPV modules. As can be seen, the concentration factor of the modules varies between 476× from Arima and 1111× from Semprius. Regarding the optics, point-focus Fresnel lens optics is mostly used, and only one module (Solfocus) uses Cassegrain mirror-based optics. The optical devices of the Daido module are somewhat different from the others because they use dome-shaped Fresnel lens. Regarding the acceptance angle, as can be seen, it varies between ±0.5° (Arima module) and ±1.7° (Semprius module). The efficiencies of modules reported by the manufacturers are in the range of 17–33.9 %, although the current world record is 36.7 % efficiency [12] corresponding to a FLATCON® module. This module has an aperture area of 832-cm^2 and concentrates sun light 230 times onto 52 7-mm^2 surface miniature four-junction solar cells with the help of 52 16-cm^2 area Fresnel lenses. In addition, the power of the modules listed in the table varies between 87.5 and 6600 Wp. It is important to note that the Magpower TRK60 module consists of a set of 60 110-Wp modules. In a similar way, Soitec CX-M500 is made up of a set of 12 2014-Wp submodules. Finally, the power temperature coefficient of HCPV modules lies within the range 0.15 and 0.34 %/°K with an average value of 0.20 %/°K. This average value is lower than the typical one of conventional PV modules, which is usually approximately 0.44 %/°K. It is worth mentioning that neither of the manufacturers listed above provide information about the influence of solar spectrum on the electrical output of their HCPV modules. Taking into account the strong spectral dependence of these types of modules, a spectral coefficient could be included in the datasheets to describe their spectral electrical dependence.

The modules commented previously represent an example of the current commercial HCPV modules. Furthermore, several companies and research centers are developing new kind of concentrator modules to achieve greater efficiencies and concentration levels while simultaneously making lighter and more compact designs. For example, Semprius uses 600 × 600-μm microtransfer printed cells for modules with a concentration of 1111× (Fig. 4). The primary optic is an SOG lens

Fig. 4 HCPV alpha module with triple-junction cells concentrating at >1100 suns and scheme of Semprius' HCPV module (*courtesy* of Semprius)

array, and the secondary optic is a ball lens. This module incorporates TJ microcells with efficiencies >41 % as measured by National Renewable Energy Laboratory (NREL), and the module efficiency was measured to be 32.2 % at an ambient temperature of 19 °C and a direct normal irradiance (DNI) of 867 W/m^2 [9]. The use of microcells decreases the optical path of the module, so instead of being an approximately 40–60 cm deep HCPV module, the typical depth for modules with a concentration >1000 (Table 1), Semprius' module is only 6.6-cm deep.

Others possible designs are continuously being discussed by the scientific community to obtain more competitive modules. A module based on new optical configurations to achieve ultra-high concentration levels and to decrease the dimensions of current HCPV modules has been proposed [25]. In addition, the use of optical devices to split the spectral distribution has already showed its potential to create modules with greater efficiencies [2, 33].

2.2 Trackers for HCPV Systems

One of the most important issues of HCPV modules is their efficiency loss when they are not perpendicular to the solar rays. HCPV modules only use the DNI and they have a decreased acceptance angle. The acceptance angle can be defined as the tracking error angle in which the power produced is decreased to 90 %. In Fig. 5, the percentage variation of the power for an HCPV module with the tracking error is shown. In this case, the acceptance angle is 1.7°.

The above discussion highlights the need of HCPV systems of having a high precision of the movement control of their axes. Because of this, HCPV systems are based on the use of two-axis solar trackers. This kind of tracker is able to orientate along the East West direction and along the North South direction, thus acting on both degrees of freedom to make the energetic efficiency greater and, make sure the

Fig. 5 Example of the variation of the module power (%) versus tracking error (°). In this case, the acceptance angle is 1.7°

solar rays are perpendicular to the plane of the PV modules. There are different two-axis tracker configurations; in Figs. 6, 7, 8, 9 and 10, the most used configurations, are shown. This kind of systems could be classified on the following:

- two-axis tracker for point-focus dish PV;
- two-axis tracker for point-focus Fresnel lens PV:
  - pedestal-mounted two-axis tracker;
  - carousel (rotate and roll) two-axis tracker; and
  - "tilt-and-roll" two-axis tracker.

It is also important to note that although there are a wide variety of configurations, the majority of HCPV power plants have pedestal trackers [10]. The most important parts of a pedestal HCPV solar tracker are shown in Fig. 11.

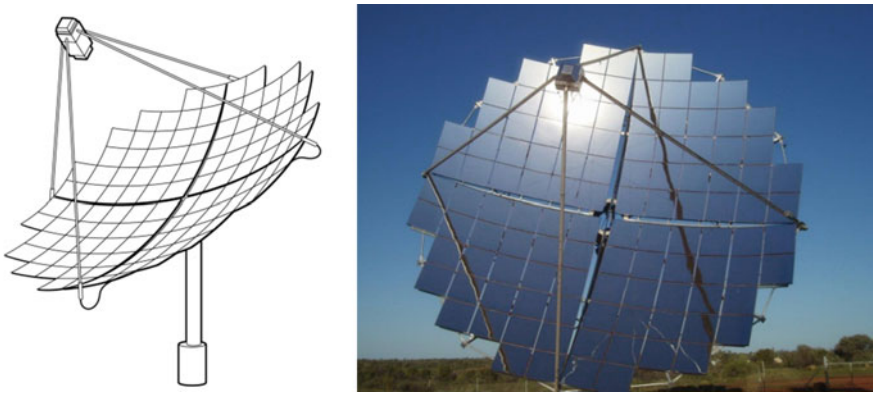

Fig. 6 Two-axis tracker for point-focus dish PV concentrator (*courtesy* of IEC62108 and Solar Systems Pty Ltd.)

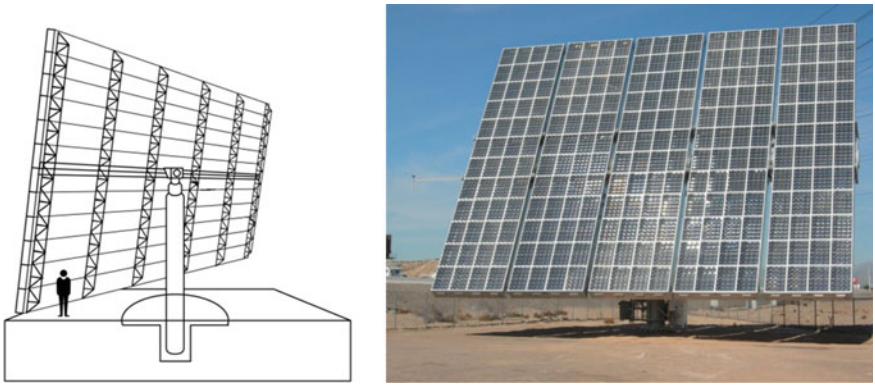

Fig. 7 Pedestal-mounted two-axis tracker for point-focus Fresnel lens PV concentrator (*courtesy* of IEC62108 and Amonix)

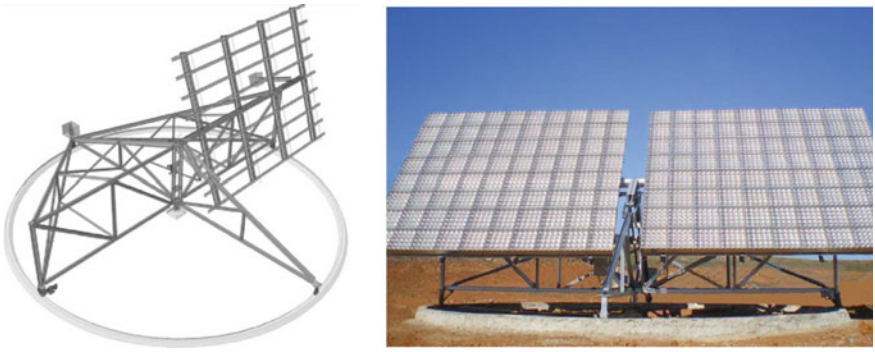

Fig. 8 Carousel (rotate and roll) two-axis tracker for point-focus Fresnel lens PV concentrator (*courtesy* of Titan Tracker)

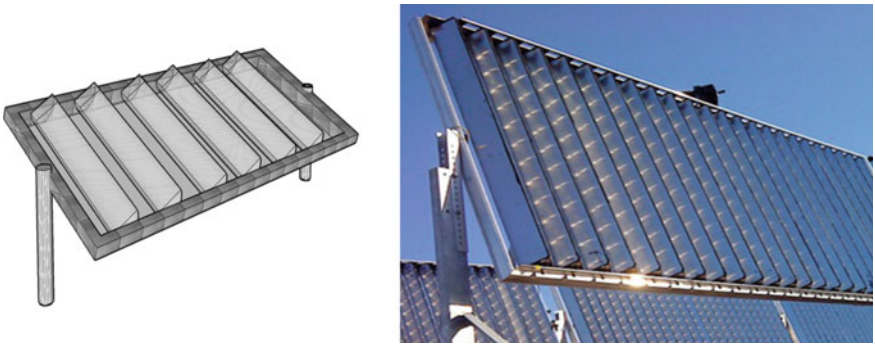

Fig. 9 "Tilt-and-roll" two-axis tracker for point-focus Fresnel lens PV concentrator (*courtesy* of Whitfield Solar)

Fig. 10 Other configuration for "tilt-and-roll" two-axis tracking system for point-focus Fresnel lens PV concentrator (*courtesy* of Emcore)

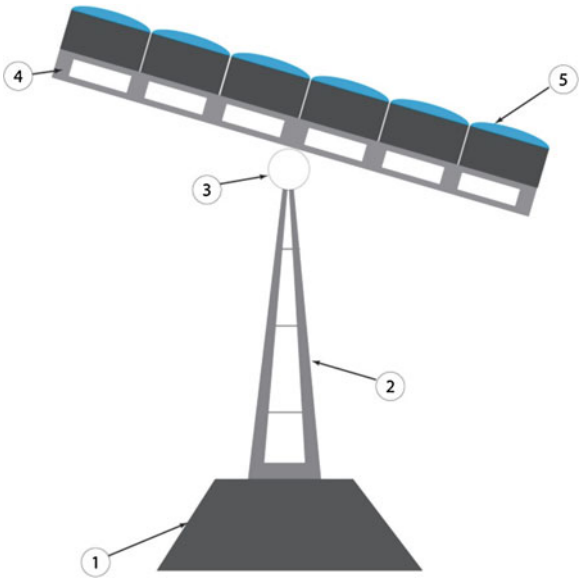

Fig. 11 Main parts of a pedestal solar tracker to HCPV system: *1* Base and embedding in the ground. *2* Picket for raising the structure and avoiding collisions during movement. *3* Mechanical and control systems in charge of the tracker movement. *4* Mechanical structure to support the solar modules and their weight. *5* HCPV solar modules

It is fundamental for this kind of technology to be able to determine and predict the Sun's movement at every moment and in every place. Depending on the coordinate system chosen, the control system in charge of the movement of a solar tracker uses a kind of equation with its control variables (e.g., angular variables in the case of polar coordinate system) to predict the Sun's position. It seems evident that for the required precisions is necessary a be able to reliably control the system, which is able to calculate at any moment to determine possible deviations that may exist. Independent of the control strategy used, the deformation of the structural

elements of the trackers cause unexpected variations in the calculation of the orientation algorithm. For this reason, decreasing the deformation of the structural elements allows the energetic efficiency to be increased and the requirements of the control system to be decreased.

The main target of the mechanical design of the system is to guarantee an optimum orientation. The mechanical system suggested must assure have high precision during movement yet be rigid enough to support external forces. The main condition to maximize the solar radiation is that the solar rays arrive perpendicularly above the plane of the solar HCPV modules. For this reason, providing the structure and the solar modules with a mechanical system that is in charge of the orientation is essential. Throughout past years, gears have been used for system movement as shown in Fig. 12. These configurations are generally built on a fixed structural picket and often break due to the forces that support the gear teeth, thus causing an increment in the cost of the solar tracker.

Apart from its own weight, the solar tracker must support the wind forces above the plane of solar modules during its movement. The wind effect on a plane depends on the incident angle between the velocity profile and the plane. This effect could be not uniform along the plane and is greater or lesser on the edges. For a better understanding of this effect is necessary to explain the gradient velocity of the wind [19], which allows the wind velocity to a height z to be determined according to Eq. 1:

$$v_z = v_g \left(\frac{z}{z_g}\right)^{\frac{1}{\alpha}}, \quad 0 < z < z_g \tag{1}$$

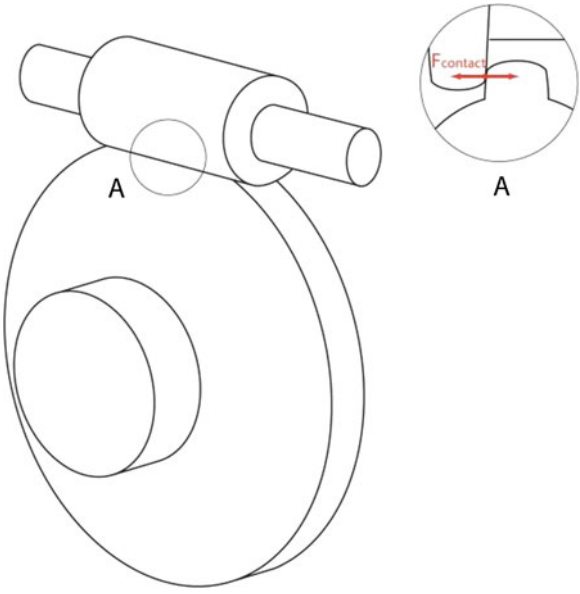

Fig. 12 Schema of the gear system for the solar tracker's movement

As Eq. 2 shows, the wind velocity changes depending on the height that is being analysed. This causes different values of aerodynamic forces that result in a torque that must be supported by the mechanical elements of the solar tracker as shown in Fig. 13 [11, 13]:

$$F_{\text{aerodynamic}} = \frac{1}{2}\rho V^2 S \tag{2}$$

where ρ is the density of the fluid (air in this case); V is the relative velocity of the wind; and S is the surface (in this case the plane of the solar modules). Due to these aerodynamic forces, when the velocity wind reaches values near to 60–70 km/h, the solar tracker is usually placed in the so-called "defensive" position.

The weight of the solar modules and the structure that holds them increase the external torques caused by the wind effect. It is important to mention that the flector moment resultant of the external forces happens independently on the position of the tracker. In the most unfavourable case, i.e., when the instant rotation center of one of the mechanisms do not match with the mass center position of the structure, the stress support by the structural elements will vary depending on the tracker's position.

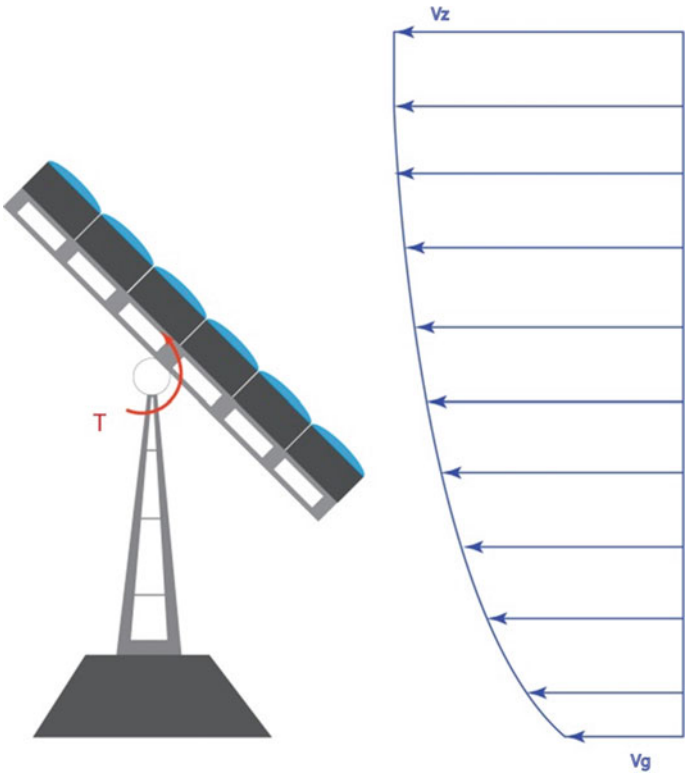

Fig. 13 Torques caused by external aerodynamic forces

The forces described previously are the main ones that must be supported by any solar tracker, and they must be taken into account for calculating the elements in charge of moving their degrees of freedom. Generally the solar trackers use gear systems to move their degrees of freedom, in which case the external forces cause high located stress in the gear teeth in contact. This stress is the main cause of breakage of this type of mechanism. Taking this into account, in the next section the proposal of a new system that is able to properly move the solar tracker and decrease failures as well as the cost of the system, is described.

2.2.1 System Optimization: Alternative Proposal

Most of solar trackers use a gear system to follow the azimuth movement of the Sun, which involves disadvantages. A way to avoid this problem is to link the structure of the solar modules and the structural picket by a series of tridimensional mechanisms replacing the gear system. The European patent EP2484991 [WO2011020931-A1], which belongs to Indra Sistemas S.L., shows how this system would work (Fig. 14).

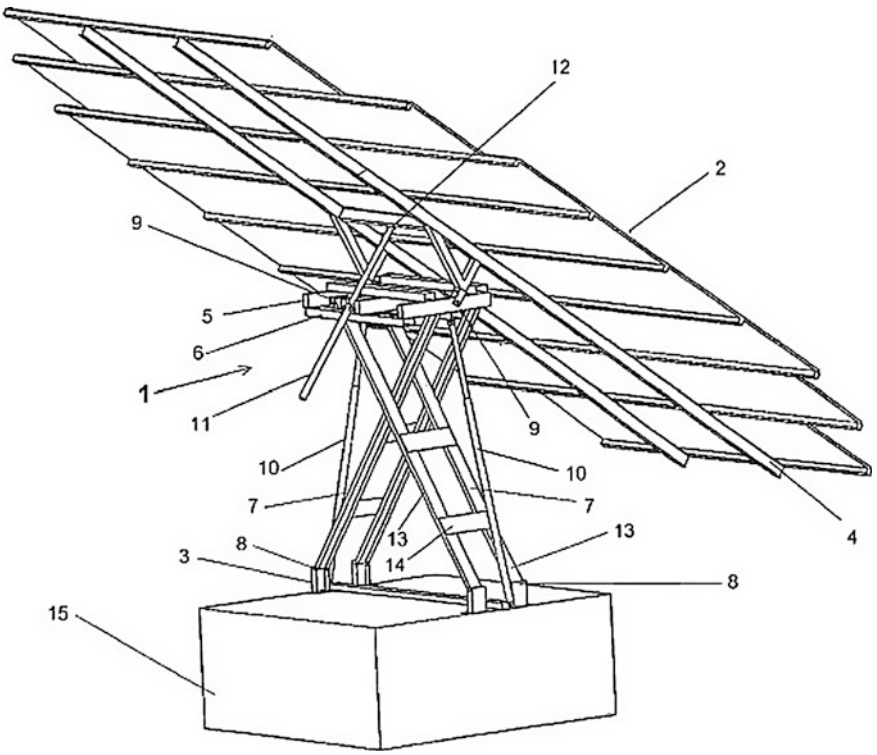

Fig. 14 Schema of a tracker without a gear system

This exposed system utilizes a four-bar mechanism to move the structure of solar modules along two perpendicular directions. The angular interval along the East West direction is greater than the angular interval along the North South direction. Through the East West direction the solar tracker must be able to orientate from the breaking dawn to the sunset. Nevertheless, along the North South direction the top position of the Sun is never too high; because of this, the angular interval is lower. For this reason, a four-bar mechanism is used for the East West direction, and a rotational joint is used for North South direction.

With this configuration, a linear actuators (hydraulic or electromechanical) system can be used to move both mechanisms independently. An essential advantage is that the transmission relationship of these two mechanisms and the linear actuators system allows greater external forces values than the gear systems to be supported.

Figure 14 shows the schema of the European patent commented previously. As can be seen, there is a four-bar mechanism to the East–West orientation. To minimize stress on the orientation of the structure of the solar module, a Chevyshev mechanism of linear trajectory is used. The bars of this mechanism are the "fix bars," and they are labelled with the number "1" in the figure above; number "2" is the actuated bar, and the number "3" is the coupler bar. In this case there are two actuated bars. That situation causes a complication in the control system due to the fact that the mechanical system is over-actuated, although the benefits of the increment of rigidity of the system are greater than the disadvantage of the system being over-actuated. The actuation of the two bars is made with two linear actuators, either hydraulic or electromechanical. These linear actuators are labeled number "4" in the figure. In contrast, the elongation and the retraction of the linear actuator are not proportional to the rotated angle; for this reason, the necessary power depends on the position of the end effector.

Overaction of the employed mechanism using two linear actuators disposed symmetrically causes the maximum power required for each actuator to also be symmetric, which is necessary for constant power during the whole work space. That is to say, when one of the actuators provides minimum power (maximum elongation), the other one provides contrary dynamic conditions (minimum elongation and maximum power) and vice versa. For small solar trackers, electric actuators can be enough, and they have low maintenance costs. For large solar trackers, high-pressure hydraulic actuators are required.

For the other degree of freedom, i.e., the orientation along the North South direction, the mechanism consists of two bars linked by a rotational join actuated by a hydraulic linear actuator. In this mechanism the fix bar is the coupler bar of the previously mechanism. And in the moving bar is where the structure of the solar modules (labeled numbers "5" and "6," respectively, in Fig. 14) is placed. Finally, the actuator for the movement of this mechanism is labeled number "7."

3 Energy Produced by an HCPV Power Plant

Estimating the energy provided by HCPV power plants is an important task for designing plants, monitoring plants, making module life-cycle assessments, and analyse the economic profitability of HCPV technology [8, 16, 20, 24]. The energy provided by such a system mainly depends on atmospheric parameters, such as DNI, solar spectrum, temperature, and wind speed, as well as on the electrical characteristics of the HCPV modules. The tracker, the inverter, and the wires that interconnect the modules and connect them to the inverter must be also considered. Methods for calculating the annual energy produced by an HCPV system or power plant can be grouped into two categories [30]:

- Direct methods: The annual energy harvested is directly calculated taking into account several efficiencies and system performance indices that define both the behaviour of the HCPV array [i.e., the array efficiency or the DC-performance ratio (PR)] and the balance-of-system (BOS) components (i.e., the inverter efficiency or the AC-PR).
- Indirect methods: The annual energy generated by the system is estimated from the power array, which is previously calculated. Afterward, the energy generated by the HCPV system can be obtained by integrating the power harvested by the array for a given time interval and including the efficiencies and losses of the rest of the elements of the system.

3.1 Direct Methods

As mentioned, direct methods calculate the annual energy harvested taking into account efficiencies and system-performance indices. Depending on the parameters considered, several methods can be highlighted.

3.1.1 Energy Estimation of an HCPV Power Plant Based on Efficiencies

The efficiency can be defined as the ratio between the output power provided by a system and its input power.

$$\eta = \frac{P_{\text{output}}}{P_{\text{input}}} \tag{3}$$

It is widely accepted to transform this ratio of powers into a relationship between energies (input and output energies for a given time interval); however, in this case it is more appropriate to use the term “performance.” In this section, the term

"efficiency" will be used to express, indistinctly, the ratio of powers and energies; however, in this last case, it will indicate the mean efficiency:

$$\overline{\eta_{\text{mean}}} = \frac{E_{\text{output}}}{E_{\text{input}}} \tag{4}$$

In this sense, the energy produced by an HCPV power plant for a given time period, τ, can be given as:

$$E_{\text{ouput},\tau} = E_{\text{input},\tau} \cdot \overline{\eta_{\text{tot}}} \tag{5}$$

where η_{tot} represents the overall HCPV power plant efficiency, and $E_{\text{input},\tau}$ indicates the maximum energy available at the input. In an HCPV power plant, they may be expressed as follows:

$$E_{\text{input},\tau} = \text{DNI}_{\tau} \cdot A_{\text{A}} \tag{6}$$

$$\overline{\eta_{\text{tot}}} = \prod_{i=1}^{n} \overline{\eta_i} \tag{7}$$

where DNI_{τ} is the direct normal irradiation (DNI) in the plane of the array for a given period of time expressed in kWh/m^2, A_{A} is the area of the array, and η_i are the different mean efficiencies to be considered in an HCPV power plant.

The annual energy generated by an HCPV system can be defined as follows:

$$E_{\text{ouput,annual}} = \text{DNI}_{\text{annual}} \cdot A_{\text{A}} \cdot \overline{\eta_{\text{tot}}} \tag{8}$$

The overall plant efficiency (η_{tot}) can be expressed in terms of the mean array efficiency (η_{A}) and the overall efficiency of the BOS (η_{BOS}) as:

$$\overline{\eta_{\text{tot}}} = \overline{\eta_{\text{A}}} \cdot \overline{\eta_{\text{BOS}}} \tag{9}$$

Moreover, the mean array efficiency and the overall efficiency of the BOS can be given by the following expressions:

$$\overline{\eta_{\text{BOS}}} = \overline{\eta_{\text{INV}}} \cdot (1 - L_{\text{AC}}) \tag{10}$$

$$\overline{\eta_{\text{A}}} = \overline{\eta_{\text{MOD}}} \cdot (1 - L_{\text{DC}}) \tag{11}$$

where η_{INV} corresponds to the mean inverter efficiency, L_{AC} represents the losses associated with the AC side (wires and the rest of elements), η_{MOD} is the mean HCPV module efficiency, and L_{DC} indicates the losses associated with the DC wires and the rest of elements of the array.

Moreover, the mean array efficiency can be given as a function of the energy harvested by the array and the annual direct irradiation as:

$$\overline{\eta_{\mathrm{A}}} = \frac{E_{\mathrm{array,annual}}}{\mathrm{DNI_{annual}}} = \frac{\sum_{i=1}^{\mathrm{year}} P_{\mathrm{A},i} \cdot \Delta t_i}{A_{\mathrm{A}} \cdot \sum_{k=1}^{\mathrm{year}} \mathrm{DNI}_k \cdot \Delta t_k} \tag{12}$$

where $E_{\mathrm{array,annual}}$ indicates the annual energy harvested by the array; $P_{\mathrm{A},i}$ and DNI_k correspond to the array power and DNI obtained at a given time, respectively; and Δt_i and Δt_k provides the sampling interval corresponding to power and irradiance, respectively.

If the time interval between samples both for the array power and the direct irradiance is equal and constant, Eq. 12 can be simplified as follows:

$$\overline{\eta_{\mathrm{A}}} = \frac{E_{\mathrm{array,annual}}}{\mathrm{DNI_{annual}}} = \frac{\sum_{i=1}^{\mathrm{year}} P_{\mathrm{A},i}}{A_{\mathrm{A}} \cdot \sum_{i=1}^{\mathrm{year}} \mathrm{DNI}_i} \tag{13}$$

In this section, mean array efficiency is defined as shown in Eq. 11.

Because a concentrator module is made up of a group of cells, primary and secondary (optional) optics, and other elements, the concentrator module efficiency can be given by:

$$\overline{\eta_{\mathrm{MOD}}} = \overline{\eta_{\mathrm{CELL}}} \cdot \overline{\eta_{\mathrm{OPT}}}(1 - L_{\mathrm{module}}) \tag{14}$$

In this sense, the module efficiency will be a function of the mean efficiency of cells (η_{CELL}), the mean optical efficiency of the module (η_{OPT}), and the energy lost in wires and the rest of the elements in a module (L_{module}).

In this way, the system efficiency can be expressed as follows:

$$\overline{\eta_{\mathrm{tot}}} = \overline{\eta_{\mathrm{CELL}}} \cdot \overline{\eta_{\mathrm{OPT}}} \cdot \overline{\eta_{\mathrm{INV}}}(1 - L_{\mathrm{module}}) \cdot (1 - L_{\mathrm{DC}}) \cdot (1 - L_{\mathrm{AC}}) \tag{15}$$

Thus, the annual energy produced by an HCPV power plant can be defined as:

$$\begin{aligned} E_{\mathrm{ouput,annual}} = {} & DNI_{\mathrm{annual}} \cdot A_{\mathrm{A}} \cdot \overline{\eta_{\mathrm{CELL}}} \cdot \overline{\eta_{\mathrm{OPT}}} \cdot \overline{\eta_{\mathrm{INV}}}(1 - L_{\mathrm{module}}) \\ & \cdot (1 - L_{\mathrm{DC}}) \cdot (1 - L_{\mathrm{AC}}) \end{aligned} \tag{16}$$

3.1.2 Energy Estimation of an HCPV Power Plant Based on Array and BOS Losses

Another approach to estimate the annual energy generated by an HCPV power plant is to consider its different energy losses. These losses can be classified in array losses, which are those of a PV generator (PV conversion losses, optical losses, thermal cell losses, thermal optics losses, spectral losses, and miscellaneous losses) and BOS losses, which are related to the balance of system (related to inverter, power station, AC wires, etc.).

Some losses are unavoidable losses that depend mainly on HCPV module electrical characteristics and given meteorological conditions (i.e., location); in this

way, they can only be estimated or measured. In contrast, other losses can be limited in the design phase of an HCPV power plant and minimized through adequate operation and maintenance tasks.

Array Losses (L_A): This represents losses due to array operation. However, this is a very wide concept, which in the case of HCPV systems may include the following:

- Photovoltaic conversion losses (L_{PV}): These are produced because not all of the irradiance incident on a concentrator cell is converted into electricity.
- Optics losses (L_{OPT}): These are due to the nonideal optical performance of the lens.
- Spectral capture losses (L_S): These are produced when the solar spectrum differs from the optimal spectral distribution for each particular module, usually the AM1.5D reference spectrum (due to changes in air mass (AM), clouds, atmospheric turbidity, etc.)
- Thermal cell capture losses (L_{TC}): These are due to a decrease of the generator efficiency when the cells operate at temperatures greater than the standard (25 °C for concentrating systems).
- Thermal optics capture losses (L_{TO}): These are due to the influence of lens temperature on the optical performance.
- Low irradiance losses (L_{LI}): These are due to the decrease of the efficiency of the concentrator cells when they operate under low irradiance levels.
- Miscellaneous capture losses (L_M):
  Shading losses ($L_{Mshading}$): These are due to the presence of obstacles, mainly other trackers with their corresponding arrays.
  Tracking error losses ($L_{Mtracking}$): These are produced when sunlight direction differs from normal incidence.
  Tolerance and degradation losses ($L_{Mtolerance}$): These are due to the fact that the effective module power is lower than the one given by the manufacturer. In addition, degradation occurs as a decrease in the power of the modules appears with their use over time.
  Mismatch losses ($L_{Mmismatch}$): These are due to dispersion of the electrical characteristics of the modules and strings. The series–parallel connection of modules with not exactly the same current voltage (I–V) characteristics influences the output of the generator. In this way, the output power from the array will be lower than the sum of the individual power of each module that constitutes the array.
  Ohmic losses (L_{Mohmic}): These are due to the voltage decrease across the wires that interconnect the modules and across the wires that connect the generator to the inverter.
  Dirt and dust losses (L_{Mdirt}): These are due to the deposition of dirt and dust on the optics surface.
  Maximum power tracking error losses (L_{MMPT}): These are due to the decrease of the array power caused by inverter MPPT failures.

In this sense, array losses can be expressed as follows:

$$L_{\mathrm{A}} = L_{\mathrm{PV}} + L_{\mathrm{OPT}} + L_{\mathrm{S}} + L_{\mathrm{TC}} + L_{\mathrm{TO}} + L_{\mathrm{LI}} + L_{\mathrm{M}} \tag{17}$$

where L_{M}:

$$\begin{aligned} L_{\mathrm{M}} = {} & L_{\mathrm{Mshading}} + L_{\mathrm{Mtracking}} + L_{\mathrm{Mtolerance}} \\ & + L_{\mathrm{Mmismatch}} + L_{\mathrm{Mohmic}} + L_{\mathrm{Mdirt}} + L_{\mathrm{MMPT}} \end{aligned} \tag{18}$$

BOS Losses (L_{BOS}): They are losses due to the following:

- Inverter losses (L_{SI}).
- Inverter disponibility and failures (L_{SIF}).
- Self-consumption losses (trackers, inverters, control and monitoring units) (L_{SSC}).
- Ohmic losses (L_{Sohmic}) due to the voltage decrease across the wires that interconnect the AC side of the Power plant.
- Transformer station (L_{ST}).

In this sense, BOS losses can be expressed as:

$$L_{\mathrm{BOS}} = L_{\mathrm{SI}} + L_{\mathrm{SIF}} + L_{\mathrm{SSC}} + L_{\mathrm{Sohmic}} + L_{\mathrm{ST}} \tag{19}$$

and the total energy losses can be expressed as the sum of the array and BOS losses as:

$$L_{\mathrm{tot}} = L_{\mathrm{A}} + L_{\mathrm{BOS}} = \sum_{i=1}^{n} L_i \tag{20}$$

where L_i represents each type of loss mentioned below (given as a fraction).

If the percentage of the annual energy corresponding to each one of these losses is known, the following expression allows the energy generated by an HCPV power plant to be calculated for a determined interval of time:

$$E_{\mathrm{output},\tau} = E_{\mathrm{input},\tau} \cdot (1 - L_{\mathrm{tot}}) \tag{21}$$

It must be highlighted that in this case, like in the previous section, $E_{\mathrm{input},\tau}$ depends on DNI_{τ} and the area of the array. Considering an annual timescale, the energy is given as:

$$E_{\mathrm{input,annual}} = \mathrm{DNI}_{\mathrm{annual}} \cdot A_{\mathrm{A}}$$

$$E_{\mathrm{output,annual}} = \mathrm{DNI}_{\mathrm{annual}} \cdot A_{\mathrm{A}} \cdot \left(1 - \sum_{i=1}^{n} L_i\right) \tag{22}$$

3.1.3 Energy Estimation of an HCPV Power Plant Based on Performance Ratio

The PR of an HCPV power plant may be defined as the quotient of the final yield and the reference yield. PR can be considered for different time intervals (τ)—annual, monthly and daily—and can be expressed as:

$$\mathrm{PR} = \frac{Y_\mathrm{f}}{Y_\mathrm{r}} = \frac{\frac{E_{\mathrm{output},\tau}}{P_{\mathrm{A,CSTC}}}}{\frac{\mathrm{DNI}_\tau}{\mathrm{DNI}_{\mathrm{CSTC}}}} \tag{23}$$

DNI_τ is the annual DNI (kWh/m^2 · τ), and $\mathrm{DNI}_{\mathrm{CSTC}}$ is the direct normal irradiance at Concentrator Standard Test Conditions (CSTC) (DNI = 1000 W/m^2, cell temperature = 25 °C, spectrum = AM1.5D) [15]. $P_{\mathrm{A,CSTC}}$ represents the array power at CSTC conditions.

Moreover, although PR is given for different periods of time (e.g., annual, monthly or daily), instantaneous PR can be considered substituting power and irradiance for energy and irradiation respectively and expressed as:

$$\mathrm{PR}_{\mathrm{inst}} = \frac{\frac{P_{\mathrm{output}}}{P_{\mathrm{A,CSTC}}}}{\frac{\mathrm{DNI}}{\mathrm{DNI}_{\mathrm{CSTC}}}} \tag{24}$$

It must be stated that if the sampling interval is constant, the average value of instantaneous PR in a determined interval of time (τ) matches the PR of the system in this same time interval.

Moreover, it can be also considered a DC-PR ($\mathrm{PR}_{\mathrm{DC}}$) [14]. The PR mentioned above corresponds to the whole system, whereas $\mathrm{PR}_{\mathrm{DC}}$ is applied only to the array. In this case:

$$\mathrm{PR}_{\mathrm{DC}} = \frac{Y_\mathrm{A}}{Y_\mathrm{r}} = \frac{\frac{E_{\mathrm{A},\tau}}{P_{\mathrm{A,CSTC}}}}{\frac{\mathrm{DNI}_\tau}{\mathrm{DNI}_{\mathrm{CSTC}}}} \tag{25}$$

In any case, if annual PR is considered:

$$\mathrm{PR} = \frac{Y_\mathrm{f}}{Y_\mathrm{r}} = \frac{\frac{E_{\mathrm{output,annual}}}{P_{\mathrm{A,CSTC}}}}{\frac{\mathrm{DNI}_{\mathrm{annual}}}{\mathrm{DNI}_{\mathrm{CSTC}}}} \tag{26}$$

In this way, the annual energy generated by the HCPV power plant will be:

$$E_{\mathrm{output,annual}} = \mathrm{PR} \cdot \frac{\mathrm{DNI}_{\mathrm{annual}}}{\mathrm{DNI}_{\mathrm{CSTC}}} \cdot P_{\mathrm{A,CSTC}} \tag{27}$$

Although in PV flat technology, $P_{A,CSTC}$ is always expressed as the sum of the individual power of the different modules of the array, in HCPV arrays, DC losses (L_{DC}) sometimes are also considered. In this case, the $P_{A,CSTC}$ is:

$$P_{A,CSTC} = \sum_{i=1}^{n^{\circ}\,mod} P^{*}_{mod,CSTC,i} \cdot (1 - L_{DC}) \tag{28}$$

To estimate the annual energy generated by an HCPV plant, average monthly PR can be also considered to take into account the different efficiencies and losses as:

$$E_{output,annual} = \sum_{i=1}^{12} PR_i \cdot \frac{DNI_{monthly,i}}{DNI^{*}} \cdot P_{A,CSTC,i} \cdot n_{days,i} \tag{29}$$

where $n_{i,days}$ and $DNI_{monthly,i}$ denote the number of days of each month and the monthly average daily DNI, respectively.

3.2 Indirect Methods

These methods calculate the energy produced by the system from the power of the generator. The procedure followed can be described as:

- Obtain the irradiance, temperature, spectrum and wind speed monthly average daily hourly profiles of the location under study. Although hourly values are usually used, other time intervals can be considered.
- Calculate the maximum power of the HCPV module from each set of DNI, spectrum and temperature profiles:

$$P_{Module} = f(DNI, S, T) \tag{30}$$

- Calculate the maximum power of the array taking into account the DC losses (L_{DC}) not considered in the previous equation, and the number of modules in series (N_S) and/or parallel (N_P) of the array:

$$P_{Array} = N_s \cdot N_p \cdot P_{Module}(DNI, S, T) \cdot (1 - L_{DC}) \tag{31}$$

- Calculate the AC power generated by the HCPV system taking into account the inverter efficiency and the losses associated to the rest of the BOS (L_{AC}):

$$P_{output} = P_{Array} \cdot \eta_{INV} \cdot (1 - L_{AC}) \tag{32}$$

- Finally, the annual energy generated by the system may be computed either by an integral or a summation as:

$$E_{\text{ouput}} = \int_{0}^{\text{year}} P_{\text{output}} \mathrm{d}t = \sum_{0}^{\text{year}} P_{\text{output}} \cdot \Delta t \tag{33}$$

A key issue of this procedure is the estimation of the maximum power of a concentrator module under the time-varying atmospheric parameters. In past years, different models were developed by the scientific community to achieve this goal [29]. Information and a further discussion about these different procedures can be found in previous chapters (Chaps. 5 and 9).

4 Atmospheric Databases and Maps

To estimate the energy yield of an HCPV system or power plant with the methods previously commented, it is necessary to know different atmospheric parameters at the specific location of the power plant. These parameters can be accurately gathered using several instruments and sensors as was commented in previous chapters. However, sometimes it is not possible to have direct measurements of the atmospheric parameters necessary to obtain the energy yield at any desired location. Because of this it is usually appropriate to use of atmospheric databases to predict the energy generated by a power plant when the direct measurements are not available. The most relevant databases for this purpose could be listed as:

- Surface meteorology and solar energy: https://eosweb.larc.nasa.gov/sse/
- NREL Solar Radiation Resource Information: http://www.nrel.gov/rredc/solar_resource.html
- Photovoltaic Geographic Information System (GIS) (PVGIS): http://re.jrc.ec.europa.eu/pvgis/
- Meteronorm: http://meteonorm.com/
- SOLMET/ERSATZ: http://gcmd.nasa.gov/records/GCMD_gov.noaa.ncdc.C00047.html
- SOLDAY: http://gcmd.nasa.gov/records/GCMD_gov.noaa.ncdc.C00087.html
- World Meteorological Organization Data Center (WRDC): http://wrdc.mgo.rssi.ru/
- DLR ISIS: http://www.pa.op.dlr.de/ISIS/
- Solar and Wind Energy Resource Assessment: http://en.openei.org/apps/SWERA/
- Management and Exploitation of Solar Resource Knowledge: http://www.mesor.org

- International Daylight Measurement Program: http://idmp.entpe.fr
- Baseline Surface Radiation Network: http://www.bsrn.awi.de
- Satel-Light: http://satellight.com
- 3-TIER Solar Time Series: http://www.3tier.com
- Solar Energy Mining: http://www.dlr.de/tt/en/desktopdefault.aspx/tabid-2885/4422_read-6581/
- Geomodel: http://geomodelsolar.eu/

These sources offer valuable data to obtain information of the main parameters that affect HCPV systems, such as DNI, air temperature, and spectrum, and pose an alternative for energy-prediction purposes. It is important to note that most of these databases usually provide daily, monthly, or yearly average data of global irradiation or DNI. The DNI can be used as an input parameter for the direct methods commented in the previous section. However, the indirect methods require hourly time series of DNI to allow the energy yield to be estimated. Taking this into account, several methods to generate these times series from other parameters, such as the global horizontal radiation [23, 27], can be found in the literature. It is also important to mention that the majority of these data sources often do not provide hourly time series of air temperature, which is also needed to apply the indirect methods commented. As in the previous case, different procedures have been proposed to predict the hourly air temperature from other more commonly observed values such as daily values of the maximum, minimum, and average of air temperature [1]. Furthermore, neither of the databases listed above provides direct values of the spectral distribution of the incident irradiance. However, they usually offer information about the atmospheric parameters with the highest impact on the spectral irradiance such as aerosol optical depth (AOD), usually at 500 or 550 nm, or precipitable water (PW). These parameters, in conjunction with the AM, offer an excellent tool for evaluating the influence of the spectral changes on the performance of HCPV systems at remote sites where is not possible to have direct measurements of the spectrum [3, 5].

The maps show below some examples of the main atmospheric parameters that can be obtained by using these atmospheric databases. Figure 15 shows a world map of DNI in which is possible to identify the regions with the highest interest to install an HCPV power plant. An interesting world map is also shown in Fig. 16. This map represents the direct normal radiation versus latitude-tilt global radiation. Therefore, it represents the worldwide regions in which more energy is received from the sun for an HCPV system compared with a traditional fixed PV system. At the same time, the rest of the figures show world maps of other relevant parameters that allow the worldwide regions with the highest and lowest temperature and spectral effects on the output of an HCPV plant to be identified (Figs. 17–19, 21–23).

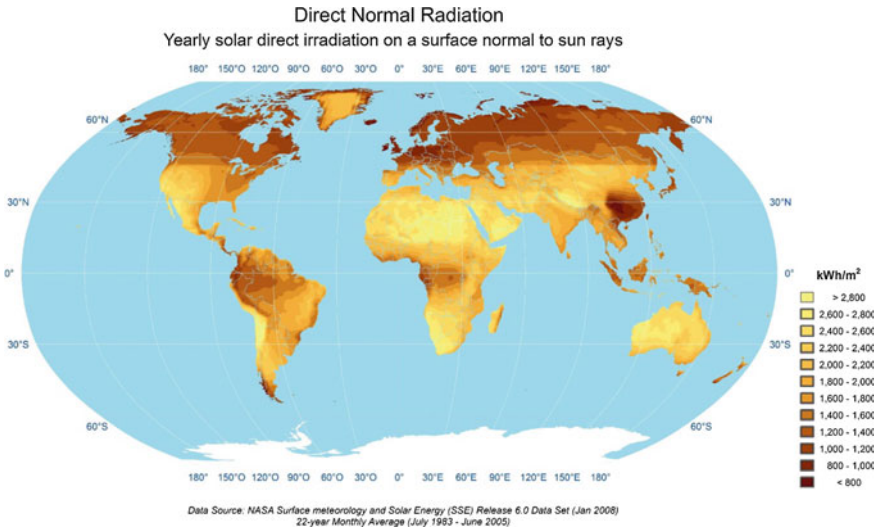

Fig. 15 World map of direct normal radiation

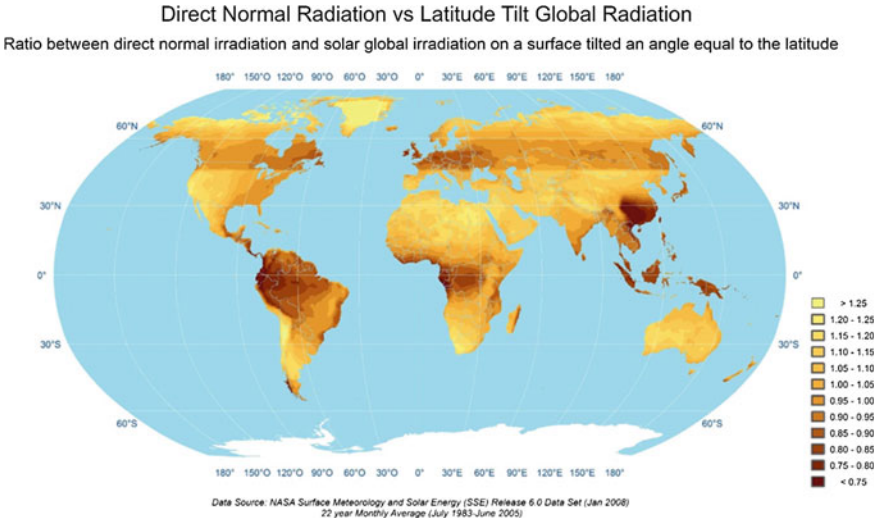

Fig. 16 World map of direct normal radiation versus tilt global radiation

5 HCPV Power-Plant Case Studies

As in other type of energy production systems, the estimation of the energy yield of HCPV systems is a crucial task. Taking this into account, data of energy generated by some HCPV power plants are shown in this section. The objective is to quantify

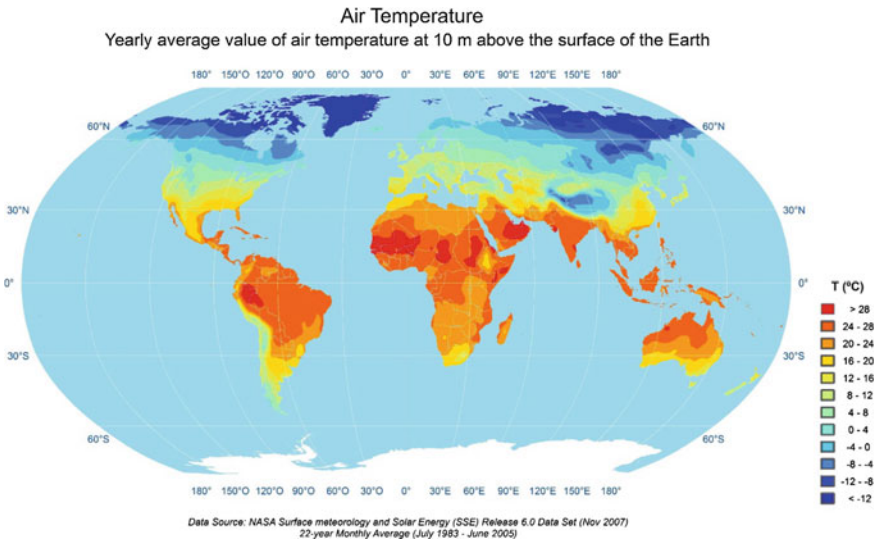

Fig. 17 World map of air temperature at 10 m

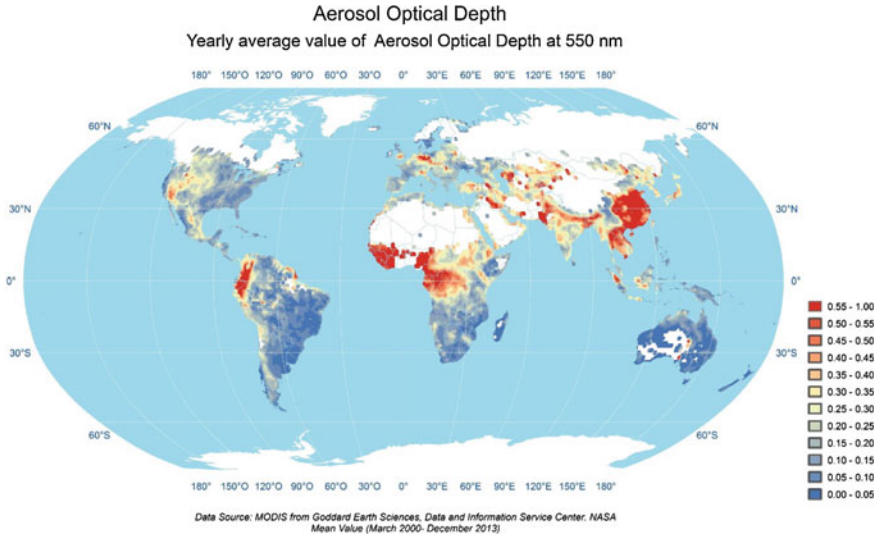

Fig. 18 World map of aerosol optical depth at 550 nm

the energy produced by current HCPV power plants and to provide useful information for energy-prediction assessment of future HCPV power plants. Among the different methods, the PR is a widely used method to estimate and measure the energy generated by a PV system. At the same time, there is a lack of data

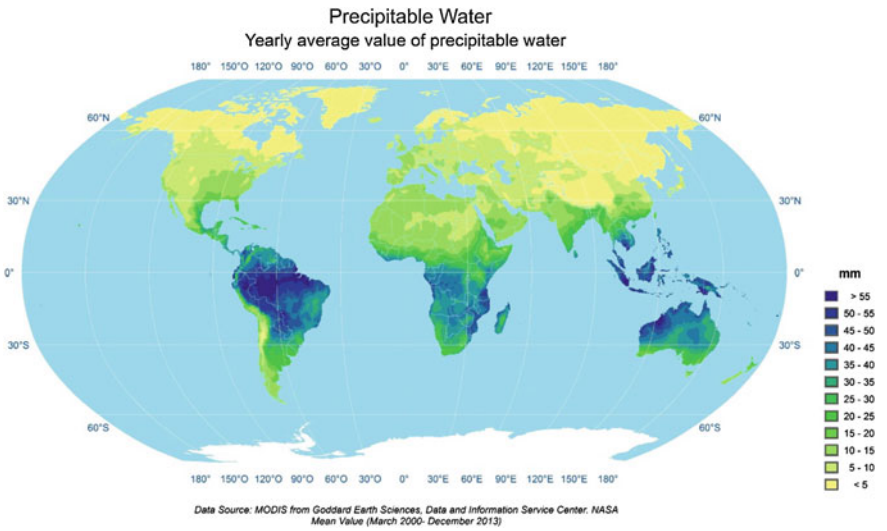

Fig. 19 World map of precipitable water

concerning PR of HCPV power plants due to the current limited experience. Bearing this in mind, this section aims to provide information about the current PR of several HCPV power plants.

HCPV power plants can be ordered accordingly to their installed capacity as shown in Fig. 20: Amonix, Guascor Foton, Soitec, Solfocus, Emcore/Suncore, Greenvolts, Arima, Solar Systems, and Suntrix. However, information about HCPV power plants of all of the companies shown on that figure was not available in the literature. As discussed in previous sections, this is probably due to the fact these data are confidential and strategic for the commercial purposes of the different HCPV companies. Among the different companies mentioned, only data of HPCV power plants from Solfocus, Magpower, Semprius, Soitec, and Solar Systems were available. The main characteristics of these power plants are described later in the

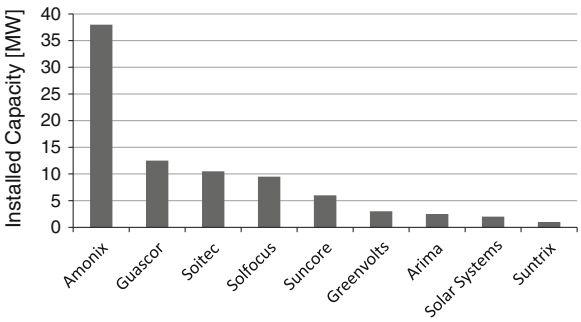

Fig. 20 Total installed capacity of HCPV systems of different companies according to published data. It represents the status as of September 2012 [34]

text. In addition, an HCPV system monitored since 2011 at the University of Jaen (southern Spain) is commented.

Case No. 1: Touwsrivier HCPV power plant

- Company: Soitec
- Location: Touwsrivier, South Africa
- Power: 76.5 kW at CSTC
- System type: CX-P6
- Commissioning: 2010
- Annual estimated DNI (Source Meteonorm): 2447 kWh/m^2/year
- Annual estimated energy production: 144 MWh/year
- Annual estimated final yield: 1878 kWh/kWp/year
- Annual estimated PR: 77 %
- Reference: Consortium [4]
- Observation: The measured data for the period January–October 2011 show a PR of 75.8 % (using unfiltered data). If only a DNI filter is considered (>4 kWh/day), PR is 79.6 %. In addition, if the days implicated in test/upgrade activities and in tracker calibration are eliminated, PR increases to 81 % (Fig. 21).

Case No. 2: APS Star Center HCPV power plant

- Company: Solfocus
- Location: Tempe, AZ

Fig. 21 Touwsrivier HCPV power plant (*courtesy* of Soitec)

- Power: 2.5 kW at a DNI of 850 W/m^2 and an ambient temperature of 20 °C
- Module type: SF-1000 and SF-1100
- Commissioning: 2007
- Historic DNI: 6.9 kWh/m^2/day
- Annual measured PR: 87.4 %
- Reference: King [18]

Case No. 3: ISFOC HCPV power plant

- Company: Solfocus
- Location: Puertollano, Spain
- Power: 6.15 kW at a DNI of 850 W/m^2 and an ambient temperature of 20 °C
- Module type: SF-1000S
- Commissioning: 2008
- Historic DNI: 5.1 kWh/m^2/day
- Annual measured PR: 88.7 %
- Reference: King [18] (Fig. 22)

Case No. 4: Palo Alto Regional Water Plant (PARWP)

- Company: Solfocus
- Location: Palo Alto, CA
- Power: 8.4 kW at a DNI of 850 W/m^2 and an ambient temperature of 20 °C
- Module type: SF-1000 and SF-1100
- Commissioning: 2009
- Historic DNI: 5.1 kWh/m^2/day
- Annual Measured PR: 91.0 %
- Reference: King [18]

Case No. 5: EDF Utility

- Company: Solfocus
- Location: Alto Monte, Italy
- Power: 8.4 kW at a DNI of 850 W/m^2 and an ambient temperature of 20 °C

Fig. 22 Solfocus/ISFOC HCPV power plant (*courtesy* of Solfocus/ISFOC)

- Module type: SF-1100
- Commissioning: 2009
- Historic DNI: 4.8 kWh/m^2/day
- Annual measured PR: 91.1 %
- Reference: King [18]

Case No. 6: Magpower HCPV power plant

- Company: Magpower
- Location: Portugal (Lat 38.1°, Long −8.1°)
- Power: 500 kW at a DNI of 850 W/m^2 and an ambient temperature of 20 °C
- Data collection period: May 2010 to October 2011
- Annual measured DNI: 1978 kWh/m^2/year
- Annual measured final yield: 2113 kWh/kW/year
- Reference: Magpower [22]
- Observation: The power of the plant is measured at the output of the array. The power of the plant at CSTC, considering 5 % of DC losses, would be approximately 650 kW (see Eq. 28) (Fig. 23).

Case No. 7: Semprius HCPV power plant

- Company: Semprius
- Location: Sandia National Laboratories (Albuquerque, NM)
- Power: 3.5 kW at CSTC (DNI 1000 W/m^2 and cell temperature 25 °C)
- Commissioning: 2013
- Data collection period: August 2013 to March 2014
- Average Measured PR_{DC}: 90 %
- Reference: King et al. [17]

Fig. 23 Magpower HCPV power plant (*courtesy* of MagPower)

- Observation: The results presented by Semprius do not take into account all of the components of the BOS. If all BOS losses are considered, PR would be decreased by approximately 5 %.

Case No. 8: Solar Systems HCPV power plant

- Company: Solar Systems
- Location: Hermannsburg, Australia
- Power: 32.2 kW at DNI 1000 W/m^2 and cell temperature 21 °C
- System type: point-focus mirror (aperture area of 130 m^2)
- Commissioning: 2006
- Annual measured PR: 85.4 %
- Reference: Verlinden and Lasich [32]

Case No. 9: UJA HCPV power plant

- Company: University of Jaén
- Location: Jaén, Spain
- Power: 1.35 kW at CSTC
- Commissioning: 2011
- Annual Measured DNI: 2214 kWh/m^2/year
- Annual measured final yield: 1912 kWh/kWp/year
- Annual measured PR: 86.4 %
- Reference: Fernández et al. [6]

Table 2 lists the main data as provided by the companies. As can be seen, PR of HCPV power plants shows an important dispersion with a value ranging from 76 to 91. This can be explained taking into account that the data are provided at different test conditions and therefore are not directly comparable. To allow the comparison of PR of different power plants to be performed, is necessary to know their electrical characteristics under the same test conditions. Table 3 lists the data of the

Table 2 Values provided by HCPV companies concerning plant's power, DNI, yield, and performance ratio at different standard test conditions

	Power (kW)	DNI $_{STC}$ (W/m^2)	Tc $_{STC}$ (°C)	Ta $_{STC}$ (°C)	DNI$_{year}$ (kWh/m^2)	Final yield (kWh/kW)	PR (%)
Soitec/Touwsrivier	76.5	1000	25		2447	1878	76–81
Solfocus/APS	2.5	850		20	2518	2628*	87.4
Solfocus/ISFOC	6.15	850		20	1861	1914*	88.7
Solfocus/PARWP	8.4	850		20	1861	1993*	91.0
Solfocus/APS	8.4	850		20	1752	1878*	91.1
Magpower	500	850		20	1978	2113	91*
Semprius/NREL	3.5	1000	25		2446	2079*	85
Solar Systems	32.2	1000	21		2464	2104*	85.4
HCPV UJA	1.35	1000	25		2214	1912	86.4

Values marked with and asterisk (*) were calculated from data supplied by the HCPV companies according to the procedures described in Sect. 3.

Table 3 Calculated data of performance ratio and annual energy generated by HCPV power plants at concentrator standard test conditions (CSTC)

Power plant	Power (kW_p)	DNI_{CSTC} (W/m^2)	Tc_{CSTC} (°C)	DNI_{year} (kWh/m^2)	$Energy_{year}$ (MWh/year)	PR (%)
Soitec/Touwsrivier	76.5	1000	25	2447	144	76–81
Solfocus/APS	3.2	1000	25	2518	6.6	83
Solfocus/ISFOC	7.8	1000	25	1861	11.8	81
Solfocus/PARWP	10.6	1000	25	1861	16.7	85
Solfocus/APS	10.6	1000	25	1752	15.8	85
Magpower	650	1000	25	1978	1056	82
Semprius/NREL	3.5	1000	25	2446	7.3	85
Solar System	32.2	1000	25	2464	68	85
HCPV UJA	1.35	1000	25	2214	2.6	86

power plants described above at CSTC. As shown, the dispersion of PR of the HCPV plants is significantly decreased and can be considered in the range of 80–85. This suggests that despite the limited experience, the performance of HCPV power plants under real operating conditions could be considered adequate compared with that conventional PV plants. The data of Table 3 were obtained according to the procedures previously commented. Furthermore, it is important to mention that these data were estimated using several approximations and assumptions due to the lack of information available in the literature. Bearing this in mind, the data of Table 3 should be only considered as representative values of current HCPV power plants.

6 Conclusions

A definition of an HCPV plant has been provided. It can be considered as a conventional PV power plant where HCPV arrays are used instead of conventional PVs. In addition, solar trackers are used to keep the modules perpendicularly oriented to the Sun.

A review of the current HCPV modules and trackers used in power plants has been performed. The current HCPV modules are mainly based on TJ GaInP/GaIsAs/Ge solar cells and point-focus Fresnel lens. The concentration factor varies from 476× to 1111×, the acceptance angle from ±0.5° to 1.7°, the efficiency from 17 to 34 %, and the temperature coefficient of maximum power from 0.15 to 0.34 %. Pedestal, carousel, and "tilt and roll" high-accuracy two-axis solar trackers are mainly used. Among them, two-axis pedestal trackers are currently being used in HCPV power plants in the majority of the cases.

The energy yield and performance of HCPV power plants have been also identified as key parameters. Taking this into account, different methods for estimating the energy harvested by a power plant have been discussed: direct methods and indirect methods. The indirect methods estimate the energy produced by using

different indices of the efficiency and performance of the array and the BOS components. In contrast, the direct methods predict the energy yield by integrating the power output of the array and including the efficiencies and losses of the rest of the components of the system. In addition, an analysis of the energy generated and the PR of several HCPV power plants has been performed. Based on this analysis, it can be concluded that the PR of the current HCPV power plants is in the range of 80–85. This indicates reasonable performance compared with current conventional PV power plants.

The ability of HCPV technology as a real alternative energy source will depend mainly on the increase of the efficiency of concentrator solar cells and modules. However, the use of standard procedures and the need to provide detailed information of the performance of HCPV power plants under real operating conditions are also mandatory. This is crucial to increase investor confidence and to promote the market expansion of such technology.

References

1. Almonacid F, Pérez-Higueras P, Rodrigo P, Hontoria L (2013) Generation of ambient temperature hourly time series for some Spanish locations by artificial neural networks. Renew Energy 51:285–291
2. Broderick LZ et al (2015) Design for energy: modeling of spectrum, temperature and device structure dependences of solar cell energy production. Sol Energy Mater Sol Cells 136:48–63
3. Chan N, Brindley H, Ekins-Daukes N (2014) Impact of individual atmospheric parameters on CPV system power, energy yield and cost of energy. Prog Photovoltaics Res Appl 22 (10):1080–1095
4. Consortium C (2011) Concentrator photovoltaic (CPV) workshop. Understanding the technology and related implications for scaled deployment. Solar Power International, Dallas
5. Fernández E, Almonacid F, Ruiz-Arias J, Soria-Moya A (2014) Analysis of the spectral variations on the performance of high concentrator photovoltaic modules operating under different real climate conditions. Sol Energy Mater Sol Cells 127:179–187
6. Fernández EF et al (2015) Model for estimating the energy yield of a high concentrator photovoltaic system. Energy 87:77–85
7. Fernández E, Pérez-Higueras P, Garcia Loureiro A, Vidal P (2013) Outdoor evaluation of concentrator photovoltaic systems modules from different manufacturers: first results and steps. Prog Photovoltaics Res Appl 21(4):693–701
8. Fthenakis V, Kim H (2013) Life cycle assessment of high-concentration photovoltaic systems. Prog Photovoltaics Res Appl 21(3):379–388
9. Ghosal K et al (2013) Performance results from micro-cell based high concentration photovoltaic research development and demonstration systems. Prog Photovoltaics Res Appl 21(6):1370–1376
10. Gómez-Gil F, Wang X, Barnett A (2012) Energy production of photovoltaic systems: fixed, tracking, and concentrating. Renew Sustain Energy Rev 16(1):306–313
11. Gorder P, Kaufman K, Greif R (1996) AIAA, guidance, navigation and control conference. American Institute of Aeronautics and Astronautics, San Diego
12. Green M et al (2015) Solar cell efficiency tables (version 45). Prog Photovoltaics Res Appl 23 (1):1–9
13. Hadlock CR (1998) Mathematical modeling in the environment. s.l.:The Mathematical Association of America

14. Hashimoto J et al (2013) Field experience and performance of CPV system in different climates. In: AIP conference proceedings, vol 1556, pp 261–265
15. IEC (2013) IEC 62670-1 ed1.0. Photovoltaic concentrators (CPV)—performance testing—part 1: standard conditions, s.l.: s.n
16. Kim Y, Kang SM, Winston R (2013) Modeling of a concentrating photovoltaic system for optimum land use. Prog Photovoltaics Res Appl 21(2):240–249
17. King B et al (2014) HCPV characterization: analysis of fielded system data. In: AIP conference proceedings, vol 1616, pp 276–279
18. King C (2010) Site data analysis of CPV plants. In: s.l., 35th IEEE photovoltaic specialists conference
19. Lee C-D et al (2007) HCPV sun tracking study at INER. In: IEEE 4th world conference on photovoltaic energy conversion, WCPEC-4, Waikoloa, p 1
20. Leloux J et al (2014) A bankable method of assessing the performance of a CPV plant. Appl Energy 118:1–11
21. Luque A, Sala G, Luque-Heredia I (2006) Photovoltaic concentration at the onset of its commercial deployment. Prog Photovoltaics Res Appl 14(5):413–428
22. Magpower (2011) Performance in practice CPV versus PV, 1.5 year of operation. In: s.l., 3rd concentrated photovoltaic summit USA
23. Maxwell, E. L., 1987. *A quasi-physical model for converting hourly global horizontal to normal direct insolation,* s.l.: Solar Energy Research Institute
24. Nishimura A et al (2010) Life cycle assessment and evaluation of energy payback time on high-concentration photovoltaic power generation system. Appl Energy 87(9):2797–2807
25. Pérez-Higueras P, Fernández E, Almonacid F, Rodrigo P (2014) Flat photovoltaic modules at ultra high concentration. In: 29th European photovoltaic solar energy conference and exhibition, Amsterdam
26. Pérez-Higueras P, Muñoz E, Almonacid G, Vidal P (2011) High concentrator photovoltaics efficiencies: present status and forecast. Renew Sustain Energy Rev 15(4):1810–1815
27. Pérez-Higueras P et al (2012) Simplified method for estimating direct normal solar irradiation from global horizontal irradiation useful for CPV applications. Renew Sustain Energy Rev 16 (8):5529–5534
28. Razykov T et al (2011) Solar photovoltaic electricity: current status and future prospects. Solar Energy 88(8):1580–1608
29. Rodrigo P, Fernández E, Almonacid F, Pérez-Higueras P (2013) Models for the electrical characterization of high concentration photovoltaic cells and modules: a review. Renew Sustain Energy Rev 26:752–760
30. Rus-Casas C et al (2014) Classification of methods for annual energy harvesting calculations of photovoltaic generators. Energy Convers Manag 78:527–536
31. Swanson R (2000) Promise of concentrators. Prog Photovoltaics Res Appl 8(1):93–111
32. Verlinden P, Lasich J (2008) Energy rating of concentrator PV systems using multi-junction III-V solar cells. In: s.l., 33rd IEEE photovoltaic specialists conference
33. Wang X et al (2012) Lateral spectrum splitting concentrator photovoltaics: direct measurement of component and submodule efficiency. Prog Photovoltaics Res Appl 20(2):149–165
34. Wiesenfarth M et al (2012) Advanced concepts in concentrating photovoltaics (CPV). In: s.l., 27th European photovoltaic solar energy conference and exhibition